



ΕΘΝΙΚΟ ΜΕΤΣΟΒΙΟ ΠΟΛΥΤΕΧΝΕΙΟ
ΣΧΟΛΗ ΠΟΛΙΤΙΚΩΝ ΜΗΧΑΝΙΚΩΝ

**ΜΗ ΓΡΑΜΜΙΚΗ ΔΥΝΑΜΙΚΗ ΑΠΟΚΡΙΣΗ
ΚΑΙ ΣΧΕΔΙΑΣΜΟΣ ΔΙΚΤΥΩΝ ΚΑΛΩΔΙΩΝ**

ΔΙΔΑΚΤΟΡΙΚΗ ΔΙΑΤΡΙΒΗ

ΙΣΑΒΕΛΛΑΣ ΒΑΣΙΛΟΠΟΥΛΟΥ

Διπλωματούχου Πολιτικού Μηχανικού Ε.Μ.Π.

ΕΠΙΒΛΕΠΩΝ:

Χ. Ι. ΓΑΝΤΕΣ

Αναπληρωτής Καθηγητής Ε.Μ.Π.

ΑΘΗΝΑ, Νοέμβριος 2011



**NATIONAL TECHNICAL UNIVERSITY OF ATHENS
SCHOOL OF CIVIL ENGINEERING**

**NONLINEAR DYNAMIC RESPONSE
AND DESIGN OF CABLE NETS**

DOCTORAL THESIS OF
ISABELLA VASSILOPOULOU
Civil Engineering Diploma N.T.U.A.

SUPERVISOR:

C. J. GANTES

Associate Professor N.T.U.A.

ATHENS, November 2011



ΕΘΝΙΚΟ ΜΕΤΣΟΒΙΟ ΠΟΛΥΤΕΧΝΕΙΟ
ΣΧΟΛΗ ΠΟΛΙΤΙΚΩΝ ΜΗΧΑΝΙΚΩΝ

ΜΗ ΓΡΑΜΜΙΚΗ ΔΥΝΑΜΙΚΗ ΑΠΟΚΡΙΣΗ
ΚΑΙ ΣΧΕΔΙΑΣΜΟΣ ΔΙΚΤΥΩΝ ΚΑΛΩΔΙΩΝ

ΔΙΔΑΚΤΟΡΙΚΗ ΔΙΑΤΡΙΒΗ

ΙΣΑΒΕΛΛΑΣ ΒΑΣΙΛΟΠΟΥΛΟΥ

Δίπλωμα Πολιτικού Μηχανικού Ε.Μ.Π. (1995)

Μεταπτυχιακό Δίπλωμα Ειδίκευσης Ε.Μ.Π. (2001)

“Δομοστατικός σχεδιασμός και ανάλυση των κατασκευών”

Η διατριβή υποβλήθηκε στη Σχολή Πολιτικών Μηχανικών του Εθνικού Μετσοβίου Πολυτεχνείου προς εκπλήρωση των προϋποθέσεων του τίτλου της Διδάκτορος Μηχανικού

ΤΡΙΜΕΛΗΣ ΣΥΜΒΟΥΛΕΥΤΙΚΗ ΕΠΙΤΡΟΠΗ:

1. Χ. Ι. ΓΑΝΤΕΣ, Αν. Καθηγητής Ε.Μ.Π. (Επιβλέπων)
2. Ι. ΒΑΓΙΑΣ, Καθηγητής Ε.Μ.Π.
3. Β. Κ. ΚΟΥΜΟΥΣΗΣ, Καθηγητής Ε.Μ.Π.

ΕΠΤΑΜΕΛΗΣ ΕΞΕΤΑΣΤΙΚΗ ΕΠΙΤΡΟΠΗ:

1. Χ. Ι. ΓΑΝΤΕΣ, Αν. Καθηγητής Ε.Μ.Π. (Επιβλέπων)
2. Ι. ΒΑΓΙΑΣ, Καθηγητής Ε.Μ.Π.
3. Β. Κ. ΚΟΥΜΟΥΣΗΣ, Καθηγητής Ε.Μ.Π.
4. Γ. Ι. ΙΩΑΝΝΙΔΗΣ, Καθηγητής Ε.Μ.Π.
5. Μ. ΠΑΠΑΔΡΑΚΑΚΗΣ, Καθηγητής Ε.Μ.Π.
6. Ε. Ι. ΣΑΠΟΥΝΤΖΑΚΗΣ, Αν. Καθηγητής Ε.Μ.Π.
7. Ι. Γ. ΡΑΥΤΟΓΙΑΝΝΗΣ, Επ. Καθηγητής Ε.Μ.Π.

Αθήνα, Νοέμβριος 2011

Η έγκριση της διδακτορικής διατριβής από την Ανώτατη Σχολή Πολιτικών Μηχανικών του Ε. Μ. Πολυτεχνείου δεν υποδηλώνει αποδοχή των γνώμων του συγγραφέα (Ν. 5343/1932, Άρθρο 202)



**NATIONAL TECHNICAL UNIVERSITY OF ATHENS
SCHOOL OF CIVIL ENGINEERING**

**NONLINEAR DYNAMIC RESPONSE
AND DESIGN OF CABLE NETS**

DOCTORAL THESIS OF

ISABELLA VASSILOPOULOU

Civil Engineering Diploma N.T.U.A. (1995)

Postgraduate Specialisation Diploma N.T.U.A. (2001)

"Structural Analysis and Design"

The thesis is submitted to the School of Civil Engineering
of the National Technical University of Athens
in fulfilment of the requirements for the Degree of Doctor of Philosophy

ADVISORY COMMITTEE:

1. C. J. GANTES, Associate Professor N.T.U.A.
(Supervisor)
2. V. K. KOUMOUSIS, Professor N.T.U.A.
3. I. VAYAS, Professor N.T.U.A.

EXAMINATION COMMITTEE:

1. C. J. GANTES, Associate Professor N.T.U.A.
(Supervisor)
2. V. K. KOUMOUSIS, Professor N.T.U.A.
3. I. VAYAS, Professor N.T.U.A.
4. G. I. IOANNIDIS, Professor N.T.U.A.
5. M. PAPADRAKAKIS, Professor N.T.U.A.
6. E. J. SAPOYNTZAKIS, Associate Professor N.T.U.A.
7. I. G. RAFTOYIANNIS, Assistant Professor N.T.U.A.

Athens, November 2011

© Copyright 2011 by Isabella Vassilopoulou

All Rights Reserved

PREFACE

The research work in this thesis was carried out in the Laboratory of Metal Structures, School of Civil Engineering, at the National Technical University of Athens, under the supervision of Associate Professor Charis Gantes.

I would like to express my endless appreciation to my supervisor, for his guidance and support during the course of this study. I thank him from the bottom of my heart for the excellent collaboration we had all these years. Many times he encouraged me and even prevented me from abandoning this effort, always expressing his belief in me and stimulating my interest with new ideas.

I am appreciative to Prof. Vlasis Koumoussis and Prof. Ioannis Vayas for their advice throughout the course of this research.

I would also like to extend my deepest gratitude to Prof. Alexandros Vakakis. I consider myself lucky to have had the opportunity to attend his lectures at the National Technical University of Athens during the short period he stayed in Greece. He opened to me a window with a view to world of science, the existence of which I was not even aware of. I am grateful to him for his undivided availability in explaining in detail new methods, approaches and terms that at first sight appeared to me as "chaotic".

I believe words will never be enough to thank Konstantinos Seferoglou and Xenofondas Botopoulos, directors of Odotechniki LTD, the company where I have been working during the last eight years, for the understanding and trust they have shown to me from the beginning of our collaboration and for all the hours or even days I had to be out of the office for my academic obligations. I am truly indebted to them; without their patience and tolerance, this thesis might have never been completed.

My sincere thanks are also due to Fotis Zoulas and Prof. Massimo Majowiecki for providing me important information about the final design of the Stadium of Peace and Friendship, which has been the starting point of this research.

I am also thankful to Prof. Ted Stathopoulos and Prof. C. Baniotopoulos for their suggestions regarding wind actions, as well as to Prof. Lance Manuel for providing me with data of wind measurements.

Special thanks are due to the postgraduate students Kostantinos Kariniotakis, Pemi Kokkali, Apostolos Vrakas and Ilias Gkimoussis, for their precious help, to Dr. Savvas Triantafyllou for his assistance with the computer software, to Prof. Dimitrios Lignos for sending me bibliographical material and to my dear friends Jolanta Wos, Eva Xenou and Anna Chatzifoti for their valuable suggestions in the preparation of this thesis.

Last, but not least, I would like to thank my colleagues Dr. Thanassis Papageorgiou, Dr. Nikos Pnevmatikos, Dr. Minas Lemonis, Dr. Cyril Douthe, Konstantinos Kalochairetis, Christoforos Dimopoulos, Petros Fortsakis, George Prountzopoulos and Kostas Nikas for their friendship and interest during this course towards our common goal. They all rendered this period of my life unforgettable.

Isabella Vassilopoulou

November 2011

*In Education,
one breathes-in the Past
and breathes-out the Future*

T. P. Tassios

To my teachers who had the ability
to transform their lectures
into a lesson of life



Εθνικό Μετσόβιο Πολυτεχνείο
Σχολή Πολιτικών Μηχανικών
Τομέας Δομοστατικής
Εργαστήριο Μεταλλικών Κατασκευών

Διδακτορική Διατριβή Ισαβέλλας Βασιλοπούλου

Μη γραμμική δυναμική απόκριση και σχεδιασμός δικτύων καλωδίων

Επιβλέπων: Δρ. Χάρης Ι. Γαντές, Αναπληρωτής Καθηγητής Ε.Μ.Π.

Αθήνα 2011

Περίληψη

Σκοπός της εργασίας αυτής είναι η διερεύνηση της απόκρισης δικτύων καλωδίων υπό δυναμικά φορτία, εστιάζοντας την προσοχή στα δυναμικά φαινόμενα που χαρακτηρίζουν τα μη γραμμικά συστήματα. Αρχικώς μορφώνεται η εξίσωση κίνησης ενός απλού δικτύου καλωδίων που αποτελείται από δύο καθέτως διασταυρούμενα καλώδια με ίσο και αντίθετο αρχικό βέλος. Αναπτύσσοντας σε σειρά Taylor και αμελώντας μικρούς όρους, η εξίσωση κίνησης προκύπτει παρόμοια με αυτή του ταλαντωτή Duffing. Η αναλυτική λύση της μόνιμης απόκρισης της εξίσωσης Duffing διατίθεται στη βιβλιογραφία και υιοθετείται σε αυτήν την εργασία για την περίπτωση του ανωτέρω δικτύου καλωδίων. Επιβεβαιώνονται κύριοι και δευτερεύοντες συντονισμοί, όπως είναι ο υπεραρμονικός και ο υποαρμονικός συντονισμός. Η σχέση της μόνιμης παραμόρφωσης με τη συχνότητα της ταλάντωσης απεικονίζεται γραφικά για διάφορες συνθήκες συντονισμού, παρουσιάζοντας καμπύλωση του διαγράμματος της απόκρισης και εξάρτηση της απόκρισης από τις αρχικές συνθήκες. Αυτό επιβεβαιώνεται επιλύοντας αριθμητικά την εξίσωση κίνησης καθώς και χρησιμοποιώντας το λογισμικό ADINA, με το οποίο πραγματοποιούνται μη γραμμικές δυναμικές αναλύσεις. Με τη διερεύνηση αυτού του απλού δικτύου, επιτυγχάνεται ένα πολύ σημαντικό βήμα προς την κατανόηση των δυναμικών φαινομένων που διέπουν τη συμπεριφορά των δικτύων καλωδίων.

Στη συνέχεια, θεωρείται ένα πολυβάθμιο δίκτυο καλωδίων σχήματος υπερβολικού παραβολοειδούς με κυκλική κάτοψη, παρόμοιο με τη στέγη του Σταδίου Ειρήνης και Φιλίας στο Φάληρο. Τα άκρα των καλωδίων θεωρείται ότι αγκυρώνονται είτε σε ακλόνητες στηρίξεις είτε σε έναν παραμορφώσιμο περιμετρικό δακτύλιο, πολύ πιο δύσκαμπτο από το δίκτυο καλωδίων. Υπολογίζονται οι πρώτες συμμετρικές και αντισυμμετρικές ιδιομορφές με τις αντίστοιχες ιδιοσυχνότητες. Παραμετρικές αναλύσεις δείχνουν ότι μεταβάλλοντας το λόγο βέλους προς άνοιγμα και τα μηχανικά χαρακτηριστικά των καλωδίων, η σειρά των πρώτων ιδιομορφών αλλάζει. Μία αδιαστατοποιημένη παράμετρος l^2 , ανάλογη με αυτήν που είναι γνωστή από τη θεωρία των απλών καλωδίων, προτείνεται και για τα δίκτυα καλωδίων σε αυτή την εργασία, η οποία εξαρτάται από το λόγο βέλους προς άνοιγμα και την αρχική ανηγμένη επιμήκυνση των καλωδίων και καθορίζει τη σειρά εμφάνισης των ιδιομορφών. Για διάφορες τιμές αυτής της παραμέτρου, δύο ή περισσότερες ιδιομορφές με διαφορετικό σχήμα έχουν ίσες συχνότητες, φαινόμενο που χαρακτηρίζεται ως εσωτερικός συντονισμός. Γνωρίζοντας το σημαντικό ρόλο που παίζει αυτή η παράμετρος στη δυναμική απόκριση των μη γραμμικών συστημάτων, είναι εύκολο να επιλεγούν κατάλληλα τα μηχανικά και γεωμετρικά χαρακτηριστικά των δικτύων καλωδίων, έτσι ώστε να αποφευχθούν τέτοιου είδους συντονισμοί. Βάσει των αποτελεσμάτων των παραμετρικών αναλύσεων προτείνονται ημιεμπειρικές σχέσεις για τον υπολογισμό των πρώτων ιδιοσυχνοτήτων του συστήματος, ενώ η σύγκριση αυτών με αποτελέσματα ιδιομορφικών αναλύσεων είναι πολύ ικανοποιητική. Αποδεικνύεται επίσης ότι η προσομοίωση του περιμετρικού δακτυλίου επηρεάζει σημαντικά τη συμμετρική ιδιομορφή του δικτύου καλωδίων και την αντίστοιχη

ιδιοσυχνότητα, λόγω της ύπαρξης μιας εντός επιπέδου ιδιομορφής του δακτυλίου. Αντιθέτως, οι αντισυμμετρικές ιδιομορφές παραμένουν ανεπηρέαστες από την παρουσία του δακτυλίου.

Η δυναμική απόκριση ενός πολυβάθμιου συστήματος δικτύου καλωδίων προσεγγίζεται αρχικώς χρησιμοποιώντας ένα ισοδύναμο μονοβάθμιο σύστημα. Η μετατροπή των γεωμετρικών και μηχανικών χαρακτηριστικών από το ένα σύστημα στο άλλο βασίζεται σε μια μέθοδο που χρησιμοποιήθηκε στα αρχικά στάδια της έρευνας αυτής και παρέχει κατάλληλες σχέσεις μετασχηματισμού. Λαμβάνοντας υπόψη διαφορετικές γεωμετρίες δικτύων καλωδίων και διαφορετικές αρχικές τάσεις στα καλώδια δημιουργούνται διαγράμματα μόνιμης απόκρισης για το μονοβάθμιο σύστημα βάσει των αναλυτικών λύσεων, ενώ πραγματοποιούνται μη γραμμικές δυναμικές αναλύσεις για το πολυβάθμιο. Η σύγκριση των διαγραμμάτων των δύο συστημάτων οδηγεί στο συμπέρασμα ότι η μέθοδος αυτή μπορεί να δώσει μία ικανοποιητική εκτίμηση της συμπεριφοράς του πολυβάθμιου συστήματος, με κυριότερο πλεονέκτημα ότι προσδιορίζει το μέγεθος και τη συχνότητα του φορτίου που μπορεί να προκαλέσει μη γραμμικά φαινόμενα με μικρό σφάλμα και σε ελάχιστο υπολογιστικό χρόνο. Παρατηρείται επίσης ότι προκειμένου να πραγματοποιηθούν υπεραρμονικοί ή υποαρμονικοί συντονισμοί απαιτούνται μεγάλα φορτία. Ειδικά για τους υποαρμονικούς συντονισμούς, απαιτούνται και μεγάλα μεγέθη αρχικών παραμορφώσεων και ταχυτήτων. Ο συνδυασμός αυτών των δύο συνθηκών οδηγεί σε αστοχία καλωδίου στην αρχή της ανάλυσης, δηλαδή κατά την παροδική απόκριση, οδηγώντας στο συμπέρασμα ότι ένα πολυβάθμιο δίκτυο καλωδίων δύσκολα μπορεί να συντονιστεί υποαρμονικά.

Η εργασία περιλαμβάνει επίσης μία διερεύνηση της επιρροής της χωρικής κατανομής ενός αρμονικού φορτίου στην απόκριση των δικτύων καλωδίων. Θεωρούνται τρεις διαφορετικές χωρικές κατανομές: μία συμμετρική, μία αντισυμμετρική περί τον έναν οριζόντιο άξονα και μία αντισυμμετρική περί τους δύο οριζόντιους άξονες. Η μόνιμη απόκριση παριστάνεται γραφικά για συχνότητες φορτίου είτε κοντά στην ιδιοσυχνότητα του συστήματος, αποσκοπώντας σε φαινόμενα κύριου συντονισμού, είτε μικρότερες από την ιδιοσυχνότητα, επιδιώκοντας την ενεργοποίηση υπεραρμονικών συντονισμών. Παρατηρείται ότι η καμπύλωση των διαγραμμάτων είναι εντονότερη στην περίπτωση αντισυμμετρικής φόρτισης, και επομένως, για ένα μεγάλο εύρος συχνοτήτων του φορτίου, οι αρχικές συνθήκες καθορίζουν το πλάτος της μόνιμης απόκρισης του συστήματος. Παράλληλα, όταν το δίκτυο καλωδίων φορτίζεται ομοιόμορφα, η παραμορφωσιμότητα του δακτυλίου επηρεάζει σημαντικά το πλάτος της απόκρισης, κάτι που δεν συμβαίνει στην περίπτωση της αντισυμμετρικής φόρτισης.

Τέλος, προκειμένου να μελετηθεί η συμπεριφορά τέτοιων κατασκευών υπό πραγματικά δυναμικά φορτία όπως ο άνεμος, προσδιορίζεται η κατανομή των ανεμοπιέσεων σε τέτοιου είδους επιφάνειες, βασιζόμενη στις συστάσεις του Ευρωκώδικα 1. Η στέγη σχήματος υπερβολικού παραβολοειδούς χωρίζεται σε ζώνες και δίνονται οι συντελεστές πίεσης για κάθε ζώνη χωριστά ανάλογα με την διεύθυνση του ανέμου. Συγκρίνοντας την προτεινόμενη κατανομή ανεμοπιέσεων με αποτελέσματα πειραμάτων στεγών σχήματος υπερβολικού παραβολοειδούς σε αεροδυναμική σήραγγα, επιβεβαιώνεται ότι η προσέγγιση που ακολουθείται σε αυτήν την εργασία οδηγεί σε λίγο μεγαλύτερες τιμές συντελεστών ανεμοπίεσης, ενώ η κατανομή των πιέσεων είναι πολύ ικανοποιητική. Επίσης, πραγματοποιούνται μη γραμμικές δυναμικές αναλύσεις χρησιμοποιώντας την προτεινόμενη χωρική κατανομή πιέσεων και μία πραγματική καταγραφή καθώς και μία τεχνητή ιστορία ανέμου, προκειμένου να εντοπιστούν μη γραμμικά φαινόμενα συντονισμού. Το πλάτος της δυναμικής απόκρισης των δικτύων συγκρίνεται με αυτό που προκύπτει από την ισοδύναμη στατική ανάλυση που προτείνει ο Ευρωκώδικας 1. Παρατηρούνται μεγάλες ταλαντώσεις με συχνότητες ίσες με τις ιδιοσυχνότητες του συστήματος. Το διάγραμμα του ανέμου παρουσιάζει συχνότητες πολύ μικρότερες, ωστόσο προκαλεί υπεραρμονικούς συντονισμούς, ενώ μία μικρή διέγερση, με συχνότητα κοντά στην ιδιοσυχνότητα, προκαλεί κύριο συντονισμό, παρά την ύπαρξη απόσβεσης. Ως αποτέλεσμα παρατηρούνται μεγάλες διαφορές μεταξύ στατικών και δυναμικών αναλύσεων, ενώ, καθώς αυξάνεται η τιμή της παραμέτρου λ^2 , μειώνεται το πλάτος της ταλάντωσης. Βάσει αυτών των αποτελεσμάτων, οι ισοδύναμες στατικές μέθοδοι που λαμβάνουν μόνον έμμεσα υπόψη τα δυναμικά φαινόμενα, δεν θεωρούνται ακριβείς για την ανάλυση και διαστασιολόγηση τέτοιων κατασκευών.



National Technical University of Athens
School of Civil Engineering
Department of Structural Engineering
Laboratory of Metal Structures

Doctoral Thesis of Isabella Vassilopoulou

Nonlinear dynamic response and design of cable nets

Supervisor: Dr. Charis J. Gantes, Associate Professor NTUA
Athens 2011

Abstract

The research presented in this thesis aims at investigating the response of cable nets subjected to dynamic loads, focusing on the dynamic phenomena that characterise nonlinear structures. Firstly a simple cable net is studied, consisting of two crossing cables and the equation of motion is derived. Neglecting small terms of its equation of motion, a simplified single-degree-of-freedom (SDOF) cable net is assumed, which is proved to be similar to a Duffing oscillator with a cubic nonlinear term of the displacement. The analytical solution of its steady-state response, found in the literature, is adopted for this simple cable net and the occurrence of fundamental and secondary resonances, such as superharmonic and subharmonic resonances, is verified for this system. The response diagrams are plotted for different resonant conditions showing bending of the response curve, hardening behaviour and dependence on the initial conditions. This response is confirmed by solving numerically the equation of motion as well as using finite element software and performing time-history analyses, considering also the geometric nonlinearity of the cable net. With this investigation, an important first step towards understanding the dynamic response of cable nets is achieved. Although double curvature renders cable nets stiffer than simple cables and a weakly nonlinear behaviour would be expected, nonlinear dynamic phenomena, established for simple cables, are also detected for these systems.

Proceeding to multi-degree-of-freedom (MDOF) systems, a saddle-form cable net with circular plan view is assumed, similar to the roof of the Peace and Friendship Stadium in Faliro, Greece. The cable net boundary is considered either as rigid, with cable ends modelled as pinned, or as flexible, modelling the deformable edge ring. The first symmetric and antisymmetric vibration modes and the corresponding natural frequencies are calculated. A parametric analysis shows that changing the sag-to-span ratio of the net and the mechanical characteristics of the cables, regarding their axial stiffness and their pretension, the sequence of the first modes changes. A non-dimensional parameter λ^2 , similar to the one used for simple cables to describe this phenomenon, is also introduced for cable nets in this study. It is confirmed that this parameter determines the sequence of their vibration modes, as in simple cables. For specific values of this parameter two or more vibration modes have equal frequencies although they have different shapes, leading to internal resonances. Thus, knowing the important role of this parameter, it is possible to choose appropriately the mechanical and geometric characteristics of the cable net in order to avoid internal resonances. Semi-empirical formulae are also proposed to estimate the frequencies of the first vibration modes of the system with satisfactory accuracy compared to modal analysis results. Modelling the ring is proved to influence significantly the symmetric vibration mode of the net, due to the ring's in-plane mode, which induces

a symmetric oscillation to the net. On the other hand, the antisymmetric modes of the net remain unaltered irrespectively of whether the cable supports are considered as fixed or as flexible.

Having the analytical solution of the simple cable net, the concept of an equivalent SDOF system for estimating the dynamic response of a MDOF system is then explored. The transformation of the characteristics from the large system to the smaller one is obtained by similarity relations adopted from a preliminary method used at the first steps of this research, which is extended here for this purpose. Response diagrams are plotted for both SDOF and MDOF systems, based on the analytical solutions and conducting time-history analyses, respectively. The two responses are compared for several geometries and cable initial stresses in order to define the field of application of this method, showing a good agreement. The main advantage of this method is that it can be used to define with small error and minimum computational time the loading amplitude and frequency for which nonlinear phenomena develop. It is also noted that, in order to have a superharmonic or a subharmonic resonance, large amplitudes of the load are required. Especially for subharmonic resonances, large initial conditions are also necessary. The combination of these two conditions leads to cable tensile failure during the transient response at the beginning of the analysis. Thus, it is unlikely for cable nets to experience subharmonic resonance.

Next, the influence of the spatial load distribution on the response of a cable net subjected to harmonic loads is investigated. Three different spatial load distributions are assumed: a symmetric one, and two antisymmetric ones with respect to one or both horizontal axes. Response diagrams are plotted for loading frequencies either close to the natural frequency, leading to fundamental resonances, or smaller than the eigenfrequency, accounting for superharmonic resonances. The bending of the response curve, which indicates a hardening nonlinear behaviour, is more intense when the net is loaded antisymmetrically rather than symmetrically. As a result, the initial conditions influence the steady-state response for a large range of the loading frequency. The behaviour of the net, when it is uniformly loaded, is altered significantly if the deformability of the boundary ring is also taken into account in the simulation. On the other hand, the presence of the ring does not alter the response of the net for antisymmetric loading, as also noted for the antisymmetric modes.

In order to analyse the behaviour of such structures to actual dynamic loads such as wind actions, the wind pressure distribution on this kind of surfaces is defined based on the recommendations of Eurocode 1. The saddle-form roof is divided into zones and pressure coefficients are provided for each zone according to the wind direction. The proposed wind pressure distribution is also compared with experimental results in order to verify the accuracy of the assumptions made. It is proved that the approach adopted in this thesis results in slightly larger pressure coefficients in some cases, but the spatial distribution of the wind pressure is satisfactory. Finally, a measured wind record and an artificial one are considered and nonlinear time-history analyses are performed to detect nonlinear resonant phenomena for the wind action, as well. The dynamic behaviour of the cable nets is compared with the static one, which is calculated according to the quasi-static procedure recommended by Eurocode 1. Large oscillation amplitudes are also observed in the response spectra for frequencies equal to the eigenfrequencies, although the main frequencies of the wind are much smaller than the eigenfrequencies of the cable nets, while for frequencies close to the natural frequencies, the amplitude of the wind load is small. This leads to the conclusion that the small frequencies with large amplitudes of the wind load cause superharmonic resonances to the net, while a weak excitation with frequency near the eigenfrequency enforces the system to experience a fundamental resonance, although damping is considered. As a result, large differences between static and dynamic responses are observed for all cable nets, while, as the parameter λ^2 increases, the oscillation amplitude becomes smaller. The quasi-static methods cannot predict these nonlinear dynamic phenomena and thus they cannot be considered as accurate for the analysis and design of such structures.

ΠΕΡΙΕΧΟΜΕΝΑ ΕΚΤΕΝΟΥΣ ΠΕΡΙΛΗΨΗΣ

A	Μη Γραμμική Δυναμική Απόκριση και Σχεδιασμός Δικτύων Καλωδίων	A-1
A.1.	ΕΙΣΑΓΩΓΗ	A-1
A.2.	ΒΙΒΛΙΟΓΡΑΦΙΚΗ ΕΠΙΣΚΟΠΗΣΗ	A-2
A.2.1.	Δυναμική απόκριση μη γραμμικών συστημάτων	A-2
A.2.2.	Δυναμική απόκριση απλών καλωδίων	A-3
A.2.3.	Δυναμική απόκριση δικτύων καλωδίων	A-4
A.3.	ΑΝΑΛΥΤΙΚΕΣ ΛΥΣΕΙΣ ΑΠΛΩΝ ΔΙΚΤΥΩΝ ΚΑΛΩΔΙΩΝ	A-5
A.3.1.	Ακριβές προσομοίωμα απλού δικτύου καλωδίων	A-5
A.3.2.	Απλοποιημένο προσομοίωμα απλού δικτύου καλωδίων	A-7
A.3.2.1.	Εξαναγκασμένη ταλάντωση – Θεμελιώδης συντονισμός	A-8
A.3.2.2.	Εξαναγκασμένη ταλάντωση – Υπεραρμονικός συντονισμός	A-8
A.3.2.3.	Εξαναγκασμένη ταλάντωση – Υποαρμονικός συντονισμός	A-9
A.3.3.	Σύγκριση των δύο προσομοιωμάτων	A-10
A.3.3.1.	Γεωμετρία και προένταση	A-10
A.3.3.2.	Ιδιοσυχνότητες	A-10
A.3.3.3.	Συντονισμοί	A-11
A.3.4.	Συμπεράσματα	A-12
A.4.	ΕΠΑΛΗΘΕΥΣΗ ΛΟΓΙΣΜΙΚΟΥ	A-12
A.4.1.	Παραδείγματα	A-12
A.4.2.	Συμπεράσματα	A-13
A.5.	ΙΔΙΟΣΥΧΝΟΤΗΤΕΣ ΚΑΙ ΙΔΙΟΜΟΡΦΕΣ ΔΙΚΤΥΩΝ ΚΑΛΩΔΙΩΝ	A-14
A.5.1.	Γεωμετρία και παραδοχές	A-14
A.5.2.	Ιδιοσυχνότητες και ιδιομορφές	A-14
A.5.3.	Ημι-εμπειρικοί τύποι για υπολογισμό ιδιοσυχνοτήτων	A-16
A.5.4.	Συμπεράσματα	A-18
A.6.	ΙΣΟΔΥΝΑΜΟ ΜΟΝΟΒΑΘΜΙΟ ΔΙΚΤΥΟ ΚΑΛΩΔΙΩΝ	A-18
A.6.1.	Πρωτότυπο και Μοντέλο	A-18
A.6.2.	Σχέσεις μετασχηματισμού	A-18
A.6.3.	Παράδειγμα 1: Δίκτυο καλωδίων με $f/L=1/35$	A-20
A.6.4.	Παράδειγμα 2: Δίκτυο καλωδίων με $f/L=1/20$	A-22
A.6.5.	Συμπεράσματα	A-23
A.7.	ΔΥΝΑΜΙΚΗ ΑΠΟΚΡΙΣΗ ΔΙΚΤΥΩΝ ΚΑΛΩΔΙΩΝ ΥΠΟ ΑΡΜΟΝΙΚΑ ΦΟΡΤΙΑ	A-23
A.7.1.	Προσομοίωμα δικτύου καλωδίων	A-24
A.7.2.	Περιγραφή φορτίου	A-24
A.7.3.	Δίκτυο καλωδίων με ακλόνητες στηρίξεις	A-24
A.7.3.1.	Ιδιομορφές και ιδιοσυχνότητες	A-24
A.7.3.2.	Ομοιόμορφη κατανομή φορτίου (1S)	A-25

A.7.3.3.	Αντισυμμετρική κατανομή φορτίου (1A).....	A-25
A.7.3.4.	Αντισυμμετρική κατανομή φορτίου (2A).....	A-26
A.7.4.	Δίκτυο καλωδίων με περιμετρικό δακτύλιο.....	A-26
A.7.4.1.	Ιδiosisυχνότητες και ιδιομορφές.....	A-26
A.7.4.2.	Ομοιόμορφη κατανομή φορτίου (1S).....	A-27
A.7.4.3.	Αντισυμμετρικές κατανομές φορτίου (1A και 2A).....	A-27
A.7.5.	Παραμετρικές αναλύσεις.....	A-28
A.7.5.1.	Επιρροή της αρχικής τάσης καλωδίων.....	A-28
A.7.5.2.	Επιρροή του λόγου βέλους προς άνοιγμα (f/L).....	A-29
A.7.6.	Συμπεράσματα.....	A-29
A.8.	ΧΩΡΙΚΗ ΚΑΤΑΝΟΜΗ ΠΙΕΣΗΣ ΑΝΕΜΟΥ.....	A-30
A.8.1.	Συντελεστές ανεμοπίεσης σε στέγες υπερβολικού παραβολοειδούς.....	A-30
A.8.2.	Αριθμητικά παραδείγματα.....	A-31
A.8.3.	Συμπεράσματα.....	A-31
A.9.	ΔΥΝΑΜΙΚΗ ΑΠΟΚΡΙΣΗ ΔΙΚΤΥΩΝ ΚΑΛΩΔΙΩΝ ΣΕ ΦΟΡΤΙΑ ΑΝΕΜΟΥ.....	A-31
A.9.1.	Προσομοίωμα δικτύου καλωδίων.....	A-32
A.9.2.	Αρχική κατάσταση ισορροπίας.....	A-32
A.9.3.	Δράση ανέμου.....	A-32
A.9.4.	Απόκριση δικτύου καλωδίων.....	A-33
A.9.5.	Παραμετρικές αναλύσεις.....	A-34
A.9.5.1.	Επιρροή διεύθυνσης ανέμου.....	A-34
A.9.5.2.	Επιρροή παραμέτρου λ^2	A-35
A.9.5.3.	Επιρροή λόγου βέλους προς άνοιγμα f/L.....	A-35
A.9.5.4.	Επιρροή συνοριακών συνθηκών.....	A-36
A.9.5.5.	Τεχνητό διάγραμμα ταχύτητας ανέμου.....	A-36
A.9.6.	Συμπεράσματα.....	A-38
A.10.	ΣΥΝΟΨΗ ΚΑΙ ΣΥΜΠΕΡΑΣΜΑΤΑ.....	A-38
A.11.	ΠΡΩΤΟΤΥΠΗ ΣΥΜΒΟΛΗ ΤΗΣ ΔΙΑΤΡΙΒΗΣ.....	A-40

ΠΕΡΙΕΧΟΜΕΝΑ ΕΚΤΕΝΟΥΣ ΠΕΡΙΛΗΨΗΣ

A	Μη Γραμμική Δυναμική Απόκριση και Σχεδιασμός Δικτύων Καλωδίων	A-1
A.1.	ΕΙΣΑΓΩΓΗ	A-1
A.2.	ΒΙΒΛΙΟΓΡΑΦΙΚΗ ΕΠΙΣΚΟΠΗΣΗ.....	A-2
A.2.1.	Δυναμική απόκριση μη γραμμικών συστημάτων	A-2
A.2.2.	Δυναμική απόκριση απλών καλωδίων	A-3
A.2.3.	Δυναμική απόκριση δικτύων καλωδίων	A-4
A.3.	ΑΝΑΛΥΤΙΚΕΣ ΛΥΣΕΙΣ ΑΠΛΩΝ ΔΙΚΤΥΩΝ ΚΑΛΩΔΙΩΝ	A-5
A.3.1.	Ακριβές προσομοίωμα απλού δικτύου καλωδίων.....	A-5
A.3.2.	Απλοποιημένο προσομοίωμα απλού δικτύου καλωδίων.....	A-7
A.3.2.1.	Εξαναγκασμένη ταλάντωση – Θεμελιώδης συντονισμός	A-8
A.3.2.2.	Εξαναγκασμένη ταλάντωση – Υπεραρμονικός συντονισμός.....	A-8
A.3.2.3.	Εξαναγκασμένη ταλάντωση – Υποαρμονικός συντονισμός	A-9
A.3.3.	Σύγκριση των δύο προσομοιωμάτων	A-10
A.3.3.1.	Γεωμετρία και προένταση.....	A-10
A.3.3.2.	Ιδιοσυχνότητες	A-10
A.3.3.3.	Συντονισμοί.....	A-11
A.3.4.	Συμπεράσματα	A-12
A.4.	ΕΠΑΛΗΘΕΥΣΗ ΛΟΓΙΣΜΙΚΟΥ	A-12
A.4.1.	Παραδείγματα	A-12
A.4.2.	Συμπεράσματα	A-13
A.5.	ΙΔΙΟΣΥΧΝΟΤΗΤΕΣ ΚΑΙ ΙΔΙΟΜΟΡΦΕΣ ΔΙΚΤΥΩΝ ΚΑΛΩΔΙΩΝ.....	A-14
A.5.1.	Γεωμετρία και παραδοχές.....	A-14
A.5.2.	Ιδιοσυχνότητες και ιδιομορφές	A-14
A.5.3.	Ημι-εμπειρικοί τύποι για υπολογισμό ιδιοσυχνοτήτων.....	A-16
A.5.4.	Συμπεράσματα	A-18
A.6.	ΙΣΟΔΥΝΑΜΟ ΜΟΝΟΒΑΘΜΙΟ ΔΙΚΤΥΟ ΚΑΛΩΔΙΩΝ	A-18
A.6.1.	Πρωτότυπο και Μοντέλο	A-18
A.6.2.	Σχέσεις μετασχηματισμού	A-18
A.6.3.	Παράδειγμα 1: Δίκτυο καλωδίων με $f/L=1/35$	A-20
A.6.4.	Παράδειγμα 2: Δίκτυο καλωδίων με $f/L=1/20$	A-22
A.6.5.	Συμπεράσματα	A-23
A.7.	ΔΥΝΑΜΙΚΗ ΑΠΟΚΡΙΣΗ ΔΙΚΤΥΩΝ ΚΑΛΩΔΙΩΝ ΥΠΟ ΑΡΜΟΝΙΚΑ ΦΟΡΤΙΑ	A-23
A.7.1.	Προσομοίωμα δικτύου καλωδίων	A-24
A.7.2.	Περιγραφή φορτίου.....	A-24
A.7.3.	Δίκτυο καλωδίων με ακλόνητες στηρίξεις.....	A-24
A.7.3.1.	Ιδιομορφές και ιδιοσυχνότητες	A-24
A.7.3.2.	Ομοιόμορφη κατανομή φορτίου (1S)	A-25

A.7.3.3.	Αντισυμμετρική κατανομή φορτίου (1A).....	A-25
A.7.3.4.	Αντισυμμετρική κατανομή φορτίου (2A).....	A-26
A.7.4.	Δίκτυο καλωδίων με περιμετρικό δακτύλιο.....	A-26
A.7.4.1.	Ιδiosisυχνότητες και ιδιομορφές.....	A-26
A.7.4.2.	Ομοιόμορφη κατανομή φορτίου (1S).....	A-27
A.7.4.3.	Αντισυμμετρικές κατανομές φορτίου (1A και 2A).....	A-27
A.7.5.	Παραμετρικές αναλύσεις.....	A-28
A.7.5.1.	Επιρροή της αρχικής τάσης καλωδίων.....	A-28
A.7.5.2.	Επιρροή του λόγου βέλους προς άνοιγμα (f/L).....	A-29
A.7.6.	Συμπεράσματα.....	A-29
A.8.	ΧΩΡΙΚΗ ΚΑΤΑΝΟΜΗ ΠΙΕΣΗΣ ΑΝΕΜΟΥ.....	A-30
A.8.1.	Συντελεστές ανεμοπίεσης σε στέγες υπερβολικού παραβολοειδούς.....	A-30
A.8.2.	Αριθμητικά παραδείγματα.....	A-31
A.8.3.	Συμπεράσματα.....	A-31
A.9.	ΔΥΝΑΜΙΚΗ ΑΠΟΚΡΙΣΗ ΔΙΚΤΥΩΝ ΚΑΛΩΔΙΩΝ ΣΕ ΦΟΡΤΙΑ ΑΝΕΜΟΥ.....	A-31
A.9.1.	Προσομοίωμα δικτύου καλωδίων.....	A-32
A.9.2.	Αρχική κατάσταση ισορροπίας.....	A-32
A.9.3.	Δράση ανέμου.....	A-32
A.9.4.	Απόκριση δικτύου καλωδίων.....	A-33
A.9.5.	Παραμετρικές αναλύσεις.....	A-34
A.9.5.1.	Επιρροή διεύθυνσης ανέμου.....	A-34
A.9.5.2.	Επιρροή παραμέτρου λ^2	A-35
A.9.5.3.	Επιρροή λόγου βέλους προς άνοιγμα f/L.....	A-35
A.9.5.4.	Επιρροή συνοριακών συνθηκών.....	A-36
A.9.5.5.	Τεχνητό διάγραμμα ταχύτητας ανέμου.....	A-36
A.9.6.	Συμπεράσματα.....	A-38
A.10.	ΣΥΝΟΨΗ ΚΑΙ ΣΥΜΠΕΡΑΣΜΑΤΑ.....	A-38
A.11.	ΠΡΩΤΟΤΥΠΗ ΣΥΜΒΟΛΗ ΤΗΣ ΔΙΑΤΡΙΒΗΣ.....	A-40

A ΜΗ ΓΡΑΜΜΙΚΗ ΔΥΝΑΜΙΚΗ ΑΠΟΚΡΙΣΗ ΚΑΙ ΣΧΕΔΙΑΣΜΟΣ ΔΙΚΤΥΩΝ ΚΑΛΩΔΙΩΝ

A.1. ΕΙΣΑΓΩΓΗ

Τα δίκτυα καλωδίων ανήκουν στην οικογένεια των εφελκυσμένων κατασκευών. Ξεχωρίζουν από τις συμβατικές κατασκευές για την ικανότητά τους να καλύπτουν μεγάλα ανοίγματα χωρίς ενδιάμεσες στηρίξεις και να μεταφέρουν τα φορτία αναπτύσσοντας μόνο εφελκυσμό στα μέλη τους. Χρησιμοποιούνται για να καλύψουν γήπεδα, πισίνες, υπόστεγα αεροπλάνων, παγοδρόμια, υπόστεγα εκθέσεων, θέατρα, εργοστάσια, εκκλησίες κ.α. Το πιο συνηθισμένο σχήμα δικτύων καλωδίων είναι το υπερβολικό παραβολοειδές, που χαρακτηρίζεται από δύο αντίθετες καμπυλότητες. Η κάτοψη ενός δικτύου καλωδίων μπορεί να είναι τετραγωνική, ρομβοειδής, κυκλική ή ελλειπτική. Το δίκτυο αποτελείται από δύο ομάδες καλωδίων, τα κύρια ή φέροντα καλώδια που στρέφουν τα κοίλα προς τα πάνω και τα δευτερεύοντα ή σταθεροποιητικά καλώδια που στρέφουν τα κοίλα προς τα κάτω. Τα καλώδια αγκυρώνονται σε έναν περιμετρικό δακτύλιο, συνήθως από προεντεταμένο σκυρόδεμα με κοίλη ορθογωνική διατομή, ο οποίος θεωρείται παραμορφώσιμος αλλά είναι πολύ πιο δύσκαμπτος από το δίκτυο καλωδίων.

Τέτοιες κατασκευές είναι πολύ εύκαμπτες με αποτέλεσμα η παραμορφωμένη κατάσταση λόγω των εξωτερικών φορτίων να διαφέρει σημαντικά από την αφόρτιστη κατάσταση. Αντιμετωπίζονται λοιπόν ως μη γραμμικά συστήματα με έντονη γεωμετρική μη γραμμικότητα. Οι μεγάλες παραμορφώσεις περιορίζονται με την προένταση των καλωδίων. Επίσης, οι μεγάλες καμπυλότητες των καλωδίων προσθέτουν δυσκαμψία στο σύστημα. Κατά τον σχεδιασμό των κατασκευών αυτών θα πρέπει να εξασφαλίζεται μία ελάχιστη ένταση στα καλώδια για κάθε συνδυασμό φόρτισης. Σε περίπτωση που χαλαρώνει ένα καλώδιο μιας ομάδας, το δίκτυο μπορεί να παρουσιάσει μεγάλες παραμορφώσεις ή αστοχία καλωδίων της άλλης ομάδας. Τέτοιες κατασκευές διαστασιολογούνται πραγματοποιώντας μη γραμμικές αναλύσεις προκειμένου να ληφθεί υπόψη η γεωμετρική μη γραμμικότητα.

Η πρώτη ανηρτημένη στέγη που κατασκευάστηκε ποτέ ήταν το "velarium", δηλαδή η τέντα που κάλυπτε το Κολοσσαίο στη Ρώμη το 70π.Χ., ενώ το πρώτο δίκτυο καλωδίων που κατασκευάστηκε στη σύγχρονη εποχή ήταν το Raleigh Arena στη Βόρεια Καρολίνα των Η.Π.Α. το 1953. Από τότε ακολούθησαν πολλές παρόμοιες κατασκευές, όπως το Arizona Veterans Memorial Coliseum στο Φοίνιξ της Αριζόνας στις Η.Π.Α. (1965), το Scandinavium Arena στο Gothenburg της Σουηδίας (1971), το Pengrowth Saddledome στο Calgary, Alberta του Καναδά (1983) και το Στάδιο Ειρήνης και Φιλίας στο

Φάληρο (1983). Στις μέρες μας κατασκευάζεται το ποδηλατοδρόμιο στο Λονδίνο που θα χρησιμοποιηθεί για τους Ολυμπιακούς Αγώνες του 2012.

A.2. ΒΙΒΛΙΟΓΡΑΦΙΚΗ ΕΠΙΣΚΟΠΗΣΗ

Κατά τη δυναμική απόκριση των μη γραμμικών συστημάτων παρουσιάζονται διάφορα μη γραμμικά φαινόμενα, άγνωστα στις μελέτες των συμβατικών κατασκευών, που είναι δυνατόν να οδηγήσουν σε μεγάλες παραμορφώσεις ή ακόμα και σε αστοχία. Προκειμένου να γίνουν αντιληπτά τέτοιου είδους φαινόμενα, δίνονται στη συνέχεια μερικά βασικά χαρακτηριστικά της δυναμικής συμπεριφοράς μη γραμμικών συστημάτων βασισμένα στη διεθνή βιβλιογραφία.

A.2.1. Δυναμική απόκριση μη γραμμικών συστημάτων

Σ' ένα σύστημα χωρίς απόσβεση, ακόμα και ένα μικρό αρμονικό φορτίο με συχνότητα Ω ίση με την ιδιοσυχνότητα ω προκαλεί ταλαντώσεις με συνεχώς αυξανόμενο πλάτος, οδηγώντας σε θεμελιώδη ή κύριο συντονισμό. Σε μη γραμμικά συστήματα δευτερεύοντες συντονισμοί μπορούν να συμβούν για συχνότητες του φορτίου μικρότερες ή μεγαλύτερες από αυτές του συστήματος. Έτσι, υπεραρμονικός συντονισμός συμβαίνει στην περίπτωση που η συχνότητα του φορτίου εκφράζεται ως:

$$\Omega = (1/n) \cdot \omega \quad (1)$$

ενώ υποαρμονικός συντονισμός συμβαίνει όταν ισχύει:

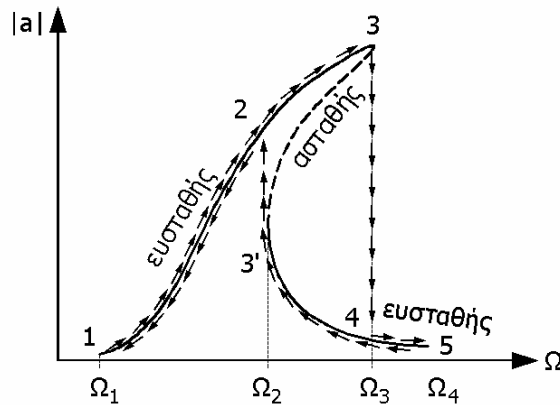
$$\Omega = n \cdot \omega \quad (2)$$

όπου n ακέραιος αριθμός. Και στις δύο περιπτώσεις το σύστημα αποκρίνεται με ταλαντώσεις μεγάλο πλάτους παρά την ύπαρξη απόσβεσης και σε αντίθεση με τα γραμμικά συστήματα στα οποία όταν η συχνότητα του φορτίου είναι μακριά από τη συχνότητα του συστήματος οι ταλαντώσεις έχουν πολύ μικρό πλάτος.

Σε αντίθεση με ένα μονοβάθμιο σύστημα, το οποίο έχει μόνο μία ιδιοσυχνότητα και μία ιδιομορφή, ένα πολυβάθμιο σύστημα n -βαθμών ελευθερίας έχει n ιδιοσυχνότητες και αντίστοιχες ιδιομορφές. Όταν δύο ή περισσότερες ιδιοσυχνότητες μπορούν να συνδεθούν μεταξύ τους με μία σχέση του τύπου $\omega_2 \approx \omega_1$, $\omega_2 \approx 2\omega_1$, $\omega_2 \approx 3\omega_1$, $\omega_3 \approx \omega_2 \pm \omega_1$, $\omega_3 \approx 2\omega_2 \pm \omega_1$, $\omega_4 \approx \omega_3 \pm \omega_2 \pm \omega_1$ κλπ. οι αντίστοιχες ιδιομορφές θεωρούνται συζευγμένες. Σε μία τέτοια περίπτωση συμβαίνουν εσωτερικοί συντονισμοί, κατά τους οποίους η ενέργεια μεταφέρεται από τη μία ιδιομορφή στην άλλη συνεχώς. Οι εσωτερικοί συντονισμοί εξαρτώνται από τα χαρακτηριστικά του συστήματος και μπορούν να συμβούν ακόμα και στις ελεύθερες ταλαντώσεις. Επιπροσθέτως, όταν ένα αρμονικό φορτίο με συχνότητα Ω διεγείρει ένα πολυβάθμιο σύστημα, εκτός από τους κύριους ή δευτερεύοντες συντονισμούς που μπορούν να συμβούν, μπορούν επίσης να ενεργοποιηθούν εσωτερικοί συντονισμοί [2-10].

Το διάγραμμα απόκρισης παριστάνει τη σχέση μεταξύ του πλάτους μόνιμης ταλάντωσης a (στον κατακόρυφο άξονα) και της συχνότητας του φορτίου Ω ή του λόγου συχνοτήτων Ω/ω (στον οριζόντιο άξονα). Σε περίπτωση εξαναγκασμένης ταλάντωσης με ή χωρίς απόσβεση, η απόκριση δίνεται από διάφορες καμπύλες που εξαρτώνται από το μέγεθος της εξωτερικής δύναμης. Στα γραμμικά συστήματα όταν η συχνότητα του φορτίου Ω πλησιάζει την ιδιοσυχνότητα του συστήματος ω , κάθε καμπύλη απόκρισης πλησιάζει ασυμπτωτικά μία κατακόρυφη ευθεία γραμμή που παριστάνει την απόκριση του συστήματος στην περίπτωση της ελεύθερης ταλάντωσης χωρίς απόσβεση, ορίζοντας το φαινόμενο του θεμελιώδους συντονισμού. Στα μη γραμμικά συστήματα, παρατηρείται καμπύλωση του διαγράμματος της απόκρισης όπως φαίνεται στο Σχήμα 1. Στο διάγραμμα αυτό παρατηρείται ότι καθώς η συχνότητα του φορτίου αυξάνεται από Ω_1 έως Ω_4 η απόκριση ακολουθεί τον κλάδο 1-2-3-4-5, όπου από το σημείο 3 στο σημείο 4 παρατηρείται μία απότομη μείωση του πλάτους ταλάντωσης. Αντιθέτως,

καθώς η συχνότητα Ω μειώνεται από Ω_4 σε Ω_1 η απόκριση ακολουθεί τον κλάδο 5-4-3'-2-1, όπου μετά το σημείο 3' η απόκριση αυξάνεται απότομα. Για συχνότητες μεταξύ Ω_2 και Ω_3 παρατηρούνται τρεις κλάδοι που παριστάνουν τη μόνιμη απόκριση, ο 2-3, ο 3-3' και ο 3'-4 όπου μόνο οι δύο από αυτούς είναι ευσταθείς κλάδοι, ενώ ο κλάδος 3-3' είναι ασταθής και δεν πραγματοποιείται ποτέ. Οι αρχικές συνθήκες καθορίζουν ποιος από τους δύο ευσταθείς κλάδους παριστάνει την απόκριση του συστήματος, κι αυτό αποτελεί άλλη μία βασική διαφορά από τα γραμμικά συστήματα [2-19].



Σχήμα 1: Διάγραμμα απόκρισης ενός μη γραμμικού συστήματος

A.2.2. Δυναμική απόκριση απλών καλωδίων

Η δυναμική συμπεριφορά απλών καλωδίων προσεγγίστηκε αρχικώς μέσω των ιδιομορφών και των ιδιοσυχνοτήτων. Ο Rugsley [2-34] έδωσε ημι-εμπειρικούς τύπους για τις ιδιοσυχνότητες των τριών πρώτων εντός επιπέδου ιδιομορφών μιας αλυσίδας με κρέμαση αντιπροσωπεύοντας ένα μη εκτατό κρεμαστό καλώδιο χωρίς προένταση με λόγο βέλους προς άνοιγμα να κυμαίνεται μεταξύ 1/10 έως 1/4. Ο Ahmadi-Kashani [2-35] επέκτεινε την έρευνά του σε μεγαλύτερα βέλη καλωδίων και έδωσε βελτιωμένους τύπους για την εκτίμηση των ιδιοσυχνοτήτων ενός καλωδίου. Οι Irvine και Caughey [2-36] ανέπτυξαν μία γραμμική θεωρία για τις ελεύθερες ταλαντώσεις ενός κρεμαστού καλωδίου με λόγο βέλους προς άνοιγμα (f/L) μέχρι 1/8, συμπεριλαμβάνοντας και προένταση. Μόρφωσαν εξισώσεις που περιγράφουν τις εντός και εκτός επιπέδου ταλαντώσεις και συνέκριναν τα αποτελέσματά τους με πειράματα. Οι εκτός επιπέδου ιδιομορφές ενός καλωδίου με κρέμαση έχουν συχνότητες:

$$\omega_n = \frac{n\pi}{L} \sqrt{\frac{H}{m}} \quad \text{όπου } n=1,2,3\dots \quad (3)$$

όπου H είναι η οριζόντια συνιστώσα της προέντασης, m η μάζα του καλωδίου ανά μέτρο μήκους και L το άνοιγμα. Οι εντός επιπέδου ταλαντώσεις είναι αντισυμμετρικές και συμμετρικές. Οι συχνότητες των αντισυμμετρικών εντός επιπέδου ταλαντώσεων περιγράφονται ως εξής:

$$\omega_n = \frac{2n\pi}{L} \sqrt{\frac{H}{m}} \quad \text{όπου } n=1,2,3\dots \quad (4)$$

ενώ οι συχνότητες ω των συμμετρικών εντός επιπέδου ταλαντώσεων δίνονται από τις λύσεις της εξίσωσης:

$$\tan\left(\frac{\tilde{\omega}}{2}\right) = \frac{\tilde{\omega}}{2} - \frac{4}{\lambda^2} \left(\frac{\tilde{\omega}}{2}\right)^3 \quad (5)$$

όπου:

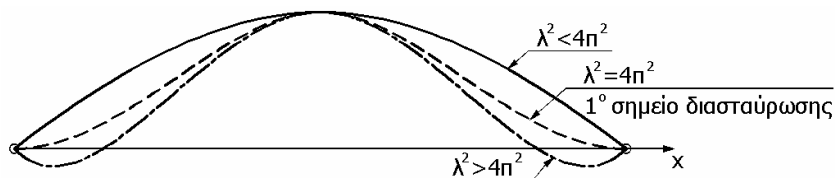
$$\tilde{\omega} = \omega L \sqrt{\frac{m}{H}} \quad (6)$$

και

$$\lambda^2 = 64 \left(\frac{f}{L} \right)^2 \frac{EA}{H} \quad (7)$$

Στην Εξ. (7) Ε είναι το μέτρο ελαστικότητας και Α το εμβαδόν της διατομής του καλωδίου. Η παράμετρος λ^2 , που εξαρτάται από τη γεωμετρία του καλωδίου και την εκτατότητά του, παίζει έναν πολύ σημαντικό ρόλο στις συμμετρικές ταλαντώσεις. Έτσι για:

- $\lambda^2 < 4\pi^2$ η συχνότητα της πρώτης συμμετρικής εντός επιπέδου ιδιομορφής είναι μικρότερη από αυτή της αντισυμμετρικής, και η μορφή ταλάντωσης δεν παρουσιάζει κανένα εσωτερικό σημείο μηδενισμού των παραμορφώσεων (Σχήμα 2).
- $\lambda^2 = 4\pi^2$ η συχνότητα της πρώτης συμμετρικής εντός επιπέδου ιδιομορφής είναι ίση με αυτή της αντισυμμετρικής. Αυτό το φαινόμενο ονομάζεται διασταύρωση ιδιομορφών και η τιμή της παραμέτρου λ^2 ορίζει το πρώτο σημείο διασταύρωσης. Σε αυτήν την περίπτωση, η παραμορφωμένη γεωμετρία του καλωδίου εφάπτεται ως προς την οριζόντιο στα σημεία στήριξής του (Σχήμα 2).
- $\lambda^2 > 4\pi^2$ γίνεται εναλλαγή των ιδιομορφών και πρώτη εμφανίζεται η αντισυμμετρική ιδιομορφή ενώ έπεται η συμμετρική. Επομένως η συχνότητα της πρώτης συμμετρικής εντός επιπέδου ιδιομορφής είναι μεγαλύτερη από αυτή της αντισυμμετρικής. Στην περίπτωση αυτή η πρώτη συμμετρική ιδιομορφή έχει δύο εσωτερικά σημεία μηδενισμού των παραμορφώσεων (Σχήμα 2).
- $\lambda^2 = 16\pi^2$ έχουμε το δεύτερο σημείο διασταύρωσης και η συχνότητα της δεύτερης συμμετρικής ιδιομορφής είναι ίση με αυτή της δεύτερης αντισυμμετρικής ιδιομορφής.
- Γενικώς, όταν η παράμετρος λ^2 παίρνει την τιμή $(\lambda_n)^2 = (2n\pi)^2$ αντιστοιχεί στο n-στό σημείο διασταύρωσης.



Σχήμα 2: Πρώτη συμμετρική ιδιομορφή για διάφορες τιμές της παραμέτρου λ^2

Στην εργασία [2-43] μορφώθηκε η εξίσωση κίνησης ενός ελαστικού καλωδίου παρουσιάζοντας τετραγωνικούς και κυβικούς μη γραμμικούς όρους. Στις εργασίες [2-44] – [2-46] μελετήθηκε η δυναμική απόκριση απλών καλωδίων σε συνθήκες θεμελιώδους, υπεραρμονικού και υποαρμονικού συντονισμού. Στις εργασίες [2-47] – [2-49] αποδείχτηκε ότι οι εσωτερικοί συντονισμοί που συμβαίνουν σε σημεία διασταύρωσης ιδιομορφών οδηγούν σε μηχανισμούς διακλάδωσης.

A.2.3. Δυναμική απόκριση δικτύων καλωδίων

Σχετικά με τα απλά δίκτυα καλωδίων που αποτελούνται από δύο διασταυρούμενα καλώδια, οι Chisalita [2-72] και Leonard [2-32] έδωσαν αναλυτικές λύσεις για ένα επίπεδο δίκτυο καλωδίων ή για ένα σύστημα με αρχικό βέλος, αντίστοιχα. Όσον αφορά σε πολυβάθμια δίκτυα καλωδίων, οι περισσότερες εργασίες που έχουν δημοσιευτεί προτείνουν νέες μεθόδους πεπερασμένων στοιχείων για τον υπολογισμό των ιδιομορφών και ιδιοσυχνοτήτων ή της δυναμικής απόκρισης ενός τέτοιου συστήματος, με στόχο την ελαχιστοποίηση του υπολογιστικού χρόνου. Ενδεικτικά αναφέρονται οι εργασίες [2-77] και [2-84].

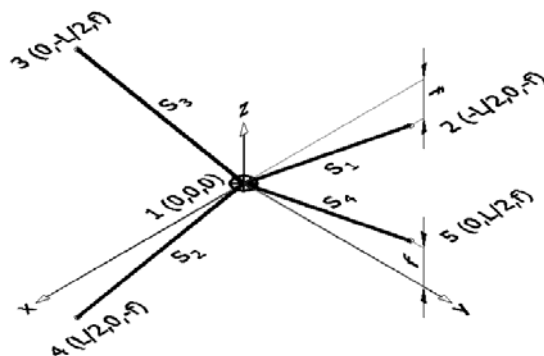
Στην εργασία [2-78] οι συγγραφείς διερεύνησαν την επιρροή των διαφόρων παραμέτρων, όπως η διατομή των καλωδίων, η αρχική προένταση, ο λόγος βέλους προς άνοιγμα, στις ιδιοσυχνότητες τέτοιων συστημάτων. Ο Talvik [2-69] παρατήρησε ότι σε ένα δίκτυο καλωδίων με ελλειπτικό παραμορφώσιμο περιμετρικό δακτύλιο, η πρώτη ιδιομορφή περιλαμβάνει κυρίως ταλάντωση του δακτυλίου ενώ οι επόμενες τέσσερις ιδιομορφές αφορούν κυρίως στο δίκτυο καλωδίων. Οι Geschwindner και West [2-89] μελέτησαν τη δυναμική συμπεριφορά ενός πραγματικού δικτύου καλωδίων σχήματος υπερβολικού παραβολοειδούς με ρομβοειδή κάτοψη, συμπεραίνοντας ότι μία ομοιόμορφη φόρτιση προκαλεί μία σχεδόν γραμμική δυναμική απόκριση, ενώ αντισυμμετρικά φορτία οδηγούν σε έντονη μη γραμμική συμπεριφορά.

A.3. ΑΝΑΛΥΤΙΚΕΣ ΛΥΣΕΙΣ ΑΠΛΩΝ ΔΙΚΤΥΩΝ ΚΑΛΩΔΙΩΝ

Αρχικώς μορφώνεται η εξίσωση κίνησης ενός απλού δικτύου καλωδίων που αποτελείται από δύο καθέτως διασταυρούμενα καλώδια, προκειμένου να προκύψουν αναλυτικές λύσεις που θα οδηγήσουν στη διερεύνηση της δυναμικής απόκρισης και στον εντοπισμό ενδεχόμενων μη γραμμικών φαινομένων.

A.3.1. Ακριβές προσομοίωμα απλού δικτύου καλωδίων

Το δίκτυο καλωδίων που μελετάται φαίνεται στο Σχήμα 3. Αποτελείται από δύο καλώδια με ακλόνητα στηρίξεις. Και τα δύο καλώδια έχουν ίδιο γεωμετρικά και μηχανικά χαρακτηριστικά, δηλαδή άνοιγμα L , διάμετρο D και πυκνότητα μάζας m . Τα άκρα του ενός καλωδίου βρίσκονται χαμηλότερα από τον κεντρικό κόμβο κατά f , ενώ το άλλο καλώδιο αγκυρώνεται σε ένα επίπεδο ψηλότερα από τον κεντρικό κόμβο κατά f . Επομένως τα βέλη των δύο καλωδίων f είναι ίσα και αντίθετα.



Σχήμα 3: Γεωμετρία δίκτυο καλωδίων

Η αρχική προένταση N_0 των δύο καλωδίων εισάγεται ως αρχική ανηγμένη επιμήκυνση ϵ_0 και δίνεται σύμφωνα με το νόμο του Hooke:

$$N_0 = E\epsilon_0 \quad (8)$$

όπου S_N είναι το μήκος κάθε μέλους καλωδίου στην κατάσταση ισορροπίας υπό την προένταση:

$$S_N = \sqrt{(L/2)^2 + f^2} \quad (9)$$

Το αρχικό μήκος S_0 όλων των μελών είναι:

$$\frac{S_N - S_0}{S_0} = \epsilon_0 \Rightarrow S_0 = \frac{S_N}{1 + \epsilon_0} = \frac{S_N}{1 + N_0 / (EA)} \quad (10)$$

Αν θεωρήσουμε u , v και w τις μετατοπίσεις του κεντρικού κόμβου ως προς τους καθολικούς άξονες x , y και z , αντίστοιχα, τα παραμορφωμένα μήκη των μελών θα είναι:

$$S_{1,2} = \sqrt{(L/2 \pm u)^2 + v^2 + (f+w)^2} \quad (11)$$

$$S_{3,4} = \sqrt{u^2 + (L/2 \pm v)^2 + (f-w)^2} \quad (12)$$

Η ένταση του κάθε μέλους στην παραμορφωμένη κατάσταση εκφράζεται ως:

$$N_i = N_0 + EA \left(\frac{S_i - S_N}{S_0} \right) \quad (13)$$

όπου $i=1,2,3,4$, ενώ ο Πίνακας 1 ομαδοποιεί τις συνιστώσες ως προς τους καθολικούς άξονες είναι:

Πίνακας 1: Συνιστώσες εντάσεων καλωδίων ως προς τους καθολικούς άξονες

Μέλος καλωδίου	Άξονας x	Άξονας y	Άξονας z
1	$N_{1x} = N_1 \cdot (L/2 + u) / S_1$	$N_{1y} = N_1 \cdot v / S_1$	$N_{1z} = N_1 \cdot (f+w) / S_1$
2	$N_{2x} = N_2 \cdot (L/2 - u) / S_2$	$N_{2y} = -N_2 \cdot v / S_2$	$N_{2z} = -N_2 \cdot (f+w) / S_2$
3	$N_{3x} = N_3 \cdot u / S_3$	$N_{3y} = N_3 \cdot (L/2 + v) / S_3$	$N_{3z} = -N_3 \cdot (f-w) / S_3$
4	$N_{4x} = -N_4 \cdot u / S_4$	$N_{4y} = N_4 \cdot (L/2 - v) / S_4$	$N_{4z} = N_4 \cdot (f-w) / S_4$

Το άθροισμα των δυνάμεων στον κεντρικό κόμβο ως προς τους καθολικούς άξονες είναι:

$$N_k = N_{1k} - N_{2k} + N_{3k} - N_{4k} \quad \text{όπου } k=x, y, z \quad (14)$$

Παραγωγίζοντας τις Εξ. (14) ως προς u , v και w , αντίστοιχα, και θέτοντας μηδενικές μετατοπίσεις ($u=v=w=0$) ορίζονται οι δυσκαμψίες στην αφόρτιστη και απαραμόρφωτη κατάσταση υπό την προένταση:

$$K_{x0} = K_{y0} = \frac{4 \cdot (EAL^2 + 2N_0L^2 + 8N_0f^2)}{\sqrt{(L^2 + 4f^2)^3}} \quad (15)$$

$$K_{z0} = \frac{4 \cdot (8EAf^2 + 2N_0L^2 + 8N_0f^2)}{\sqrt{(L^2 + 4f^2)^3}} \quad (16)$$

ενώ οι ιδιοσυχνότητες του συστήματος ως προς τους τρεις βαθμούς ελευθερίας είναι:

$$\omega_{x0} = \sqrt{\frac{K_{x0}}{M}} = \omega_{y0} = \sqrt{\frac{K_{y0}}{M}} \quad \text{και} \quad \omega_{z0} = \sqrt{\frac{K_{z0}}{M}} \quad (17)$$

Σε περίπτωση που ένα δυναμικό φορτίο εφαρμόζεται στον κεντρικό κόμβο, οι εξισώσεις κίνησης για τις τρεις διευθύνσεις κίνησης είναι:

$$M\ddot{u} + C\dot{u} + N_x = P_x(t) \Rightarrow M\ddot{u} + C\dot{u} + N_{1x} - N_{2x} + N_{3x} - N_{4x} = P_x(t) \quad (18)$$

$$M\ddot{v} + C\dot{v} + N_y = P_y(t) \Rightarrow M\ddot{v} + C\dot{v} + N_{1y} - N_{2y} + N_{3y} - N_{4y} = P_y(t) \quad (19)$$

$$M\ddot{w} + C\dot{w} + N_z = P_z(t) \Rightarrow M\ddot{w} + C\dot{w} + N_{1z} - N_{2z} + N_{3z} - N_{4z} = P_z(t) \quad (20)$$

όπου $P_x(t)$, $P_y(t)$ και $P_z(t)$ είναι οι τρεις συνιστώσες του εξωτερικού φορτίου ως προς τους καθολικούς άξονες. Η απόσβεση C δίνεται ως συνάρτηση του ποσοστού απόσβεσης ζ , σύμφωνα με τη σχέση:

$$C = \zeta C_{cr} = 2\zeta M \omega_{z0} \quad (21)$$

A.3.2. Απλοποιημένο προσομοίωμα απλού δικτύου καλωδίων

Θεωρείται ένα μονοβάθμιο σύστημα δικτύου καλωδίων, παρόμοιο με αυτό που περιγράφηκε στην παράγραφο A.3.1 με μόνο βαθμό ελευθερίας την κατακόρυφη μετατόπιση του κεντρικού κόμβου. Ένα εξωτερικό φορτίο της μορφής $P_z(t) = P_0 \cos \Omega t$ εφαρμόζεται στον κεντρικό κόμβο. Αντικαθιστώντας τις εκφράσεις των εντάσεων των καλωδίων (Εξ. (13)) και τα μήκη των καλωδίων στην προεντεταμένη, αρχική και παραμορφωμένη κατάσταση, που δίνονται από τις Εξ. (9), (10), (11) - (12), αντίστοιχα, στις κατακόρυφες συνιστώσες της έντασης των καλωδίων (Πίνακας 1), η Εξ. (20) γίνεται:

$$M\ddot{w} + C\dot{w} + N_z = P_z(t) \Rightarrow$$

$$M\ddot{w} + C\dot{w} - \frac{4EA(f+w)}{L\sqrt{1+4\frac{(f+w)^2}{L^2}}} + \frac{4EA(f-w)}{L\sqrt{1+4\frac{(f-w)^2}{L^2}}} + \frac{4w(EA+N_0)}{L\sqrt{1+4\frac{f^2}{L^2}}} = P_z(t) \quad (22)$$

Αναπτύσσοντας σε σειρά Taylor και αγνοώντας όρους $(f/L)^2$ ή ανώτερης δύναμης, η Εξ. (22) απλοποιείται ως εξής:

$$\ddot{w} + \frac{C}{M}\dot{w} + \frac{K_{z0}}{M}w + \frac{16EA}{ML^3}w^3 = \frac{P_0}{M}\cos(\Omega t) \quad (23)$$

όπου K_{z0} είναι η δυσκαμψία του συστήματος της Εξ. (16), η οποία αναπτύσσεται σε σειρά Taylor και αγνοώντας τους όρους $(f/L)^4$ γίνεται:

$$K_{z0} = \frac{4EA}{L} \cdot \left(8\frac{f^2}{L^2} + 2\frac{N_0}{EA} - 4\frac{N_0}{EA}\frac{f^2}{L^2} \right) \quad (24)$$

Παρατηρείται ότι στην Εξ. (23) εμφανίζεται ένας μη γραμμικός κυβικός όρος που εξαρτάται από το μέτρο ελαστικότητας του υλικού των καλωδίων E , από το εμβαδόν της διατομής τους A και από το άνοιγμα L . Η Εξ. (23) μπορεί να πάρει τη μορφή:

$$\ddot{w} + 2\epsilon\dot{w} + \omega_{z0}^2 w + \epsilon a w^3 = P \cos(\Omega t) \quad (25)$$

όπου:

$$2\epsilon\mu = \frac{C}{M} = 2\zeta\omega_{z0} \quad (26)$$

$$\epsilon a = \frac{16EA}{ML^3} \quad (27)$$

$$P = \frac{P_0}{M} \quad (28)$$

$$\omega_{z0} = \sqrt{\frac{K_{z0}}{M}} = \sqrt{\frac{4EA}{ML} \cdot \left(8\frac{f^2}{L^2} + 2\frac{N_0}{EA} - 4\frac{N_0}{EA}\frac{f^2}{L^2} \right)} \quad (29)$$

Η Εξ. (25) είναι γνωστή ως εξίσωση κίνησης του ταλαντωτή Duffing, η διερεύνηση της οποίας δίνεται στη βιβλιογραφία. Στη συνέχεια οι λύσεις της εξίσωσης Duffing υιοθετούνται από τη βιβλιογραφία [3-25] και εφαρμόζονται στο δίκτυο καλωδίων. Η παράμετρος ϵ δηλώνει τη μικρή κλίμακα των όρων

όπου εμφανίζεται σε σχέση με το γραμμικό όρο της μετατόπισης. Η λύση του προβλήματος είναι ανεξάρτητη της παραμέτρου ε , γι' αυτό και η ακριβής τιμή αυτής δεν χρειάζεται να οριστεί.

A.3.2.1. Εξαναγκασμένη ταλάντωση – Θεμελιώδης συντονισμός

Στην περίπτωση θεμελιώδους συντονισμού θεωρείται ότι εφαρμόζεται ένα φορτίο με μικρή τιμή P_0 , το οποίο ορίζεται ως εξής:

$$P_0 = \varepsilon p_0, P = P_0/M = \varepsilon p_0/M = \varepsilon p \quad (30)$$

και συχνότητα κοντά στη συχνότητα του συστήματος, εκφραζόμενη ως:

$$\Omega = \omega_{z0} + \varepsilon \sigma \quad (31)$$

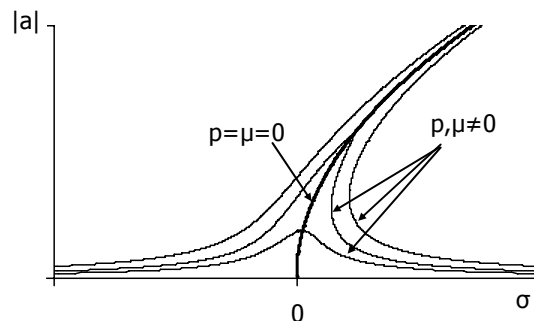
όπου $\varepsilon \sigma$ είναι μία παράμετρος αποσυντονισμού. Και πάλι εισάγεται η παράμετρος ε για να δηλώσει τη μικρή κλίμακα του φορτίου και της συχνότητας αποσυντονισμού. Η μόνιμη απόκριση δίνεται από τη σχέση:

$$w(t) = a \cos(\Omega t - \gamma) + O(\varepsilon) \quad (32)$$

όπου a είναι το πλάτος της μόνιμης ταλάντωσης και γ είναι η φάση. Η σχέση μεταξύ του πλάτους ταλάντωσης a και της συχνότητας αποσυντονισμού ορίζεται ως εξής:

$$\sigma = \frac{3aa^2}{8\omega_{z0}} \pm \sqrt{\frac{p^2}{4\omega_{z0}^2 a^2} - \mu^2} \quad (33)$$

Τυπικές καμπύλες απόκρισης – συχνότητας για μη γραμμικά συστήματα φαίνονται στο Σχήμα 4.



Σχήμα 4: Θεμελιώδης συντονισμός: Καμπύλες απόκρισης – συχνότητας για ένα μη γραμμικό σύστημα

A.3.2.2. Εξαναγκασμένη ταλάντωση – Υπεραρμονικός συντονισμός

Υπεραρμονικός συντονισμός συμβαίνει στην περίπτωση που η συχνότητα φορτίου είναι κοντά στο 1/3 της ιδιοσυχνότητας του συστήματος, δηλαδή:

$$3\Omega = \omega_{z0} + \varepsilon \sigma \quad (34)$$

Η μόνιμη απόκριση του μη γραμμικού συστήματος στην περίπτωση του υπεραρμονικού συντονισμού δίνεται ως εξής:

$$w(t) = a \cos(3\Omega t - \gamma) + P \left(\frac{1}{\omega_{z0}^2 - \Omega^2} \right) \cos \Omega t + O(\varepsilon) \quad (35)$$

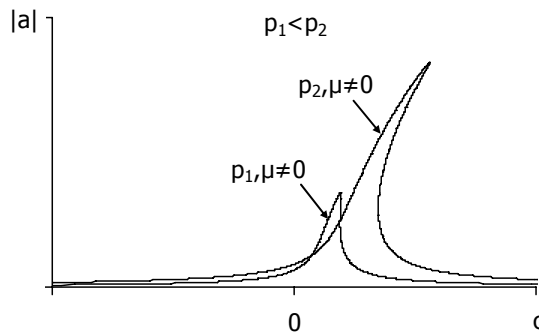
όπου παρατηρείται ένα όρος με τη συχνότητα της διέγερσης (Ω) και ένας όρος με τη συχνότητα του συστήματος (3Ω). Επομένως, αντιθέτως με τα γραμμικά συστήματα, σε ένα μη γραμμικό σύστημα παρατηρούνται μεγάλα πλάτη ταλάντωσης για συχνότητες φορτίου μικρότερες από αυτές του συστήματος, παρά την παρουσία απόσβεσης. Το διάγραμμα απόκρισης – συχνότητας ορίζεται από τη σχέση:

$$\sigma = \frac{3a\Lambda^2}{\omega_{z0}} + \frac{3aa^2}{8\omega_{z0}} \pm \sqrt{\frac{a^2\Lambda^6}{\omega_{z0}^2 a^2} - \mu^2} \quad (36)$$

όπου

$$\Lambda = \frac{1}{2} P \left(\frac{1}{\omega_{z0}^2 - \Omega^2} \right) \quad (37)$$

Τυπικές καμπύλες απόκρισης – συχνότητας στην περίπτωση του υπεραρμονικού συντονισμού φαίνονται στο Σχήμα 5.



Σχήμα 5: Υπεραρμονικός συντονισμός: Καμπύλες απόκρισης – συχνότητας

A.3.2.3. Εξαναγκασμένη ταλάντωση – Υποαρμονικός συντονισμός

Ο υποαρμονικός συντονισμός σε ένα μη γραμμικό σύστημα με έναν κυβικό μη γραμμικό όρο πραγματοποιείται όταν:

$$\Omega = 3\omega_{z0} + \varepsilon\sigma \quad (38)$$

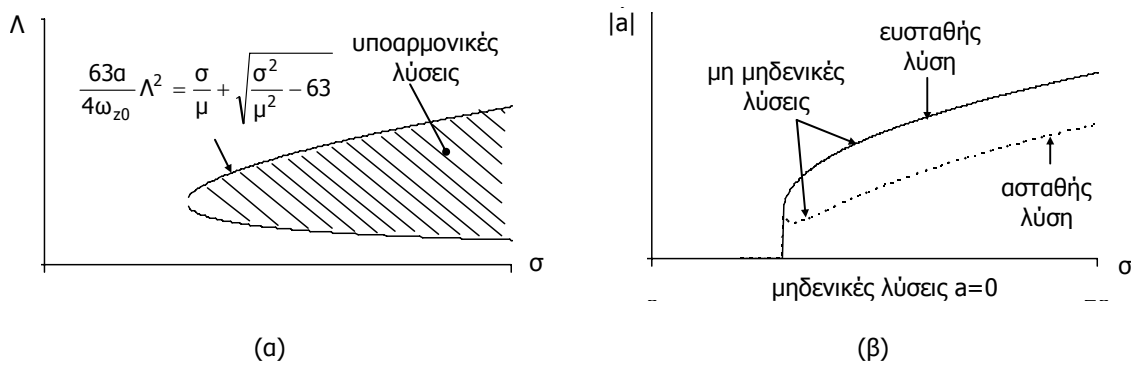
Η σχέση απόκρισης – συχνότητας ορίζεται ως εξής:

$$\left[\left(\sigma - \frac{9a\Lambda^2}{\omega_{z0}} - \frac{9aa^2}{8\omega_{z0}} \right)^2 + 9\mu^2 \right] a^2 = \frac{81a^2\Lambda^2}{16\omega_{z0}^2} a^4 \quad (39)$$

Η Εξ. (39) έχει δύο διπλές μηδενικές λύσεις ($a=0$) και δύο μη μηδενικές ($a \neq 0$) που αντιστοιχούν σε υποαρμονικές λύσεις. Η μία από αυτές είναι ευσταθής λύση και η άλλη ασταθής και δεν μπορεί να πραγματοποιηθεί ποτέ. Υποαρμονικές λύσεις υπάρχουν μόνο αν ισχύει η εξής συνθήκη:

$$\sigma \geq \frac{63a}{8\omega_{z0}} \Lambda^2 + \frac{2\omega_{z0}}{a} \frac{\mu^2}{\Lambda^2} \quad (40)$$

Η ανίσωση (40) ορίζει μία περιοχή όπου εμφανίζονται υποαρμονικές λύσεις. Αυτή η περιοχή και μία τυπική καμπύλη απόκρισης – συχνότητας δίνονται στο Σχήμα 6.



Σχήμα 6: Υποαρμονικός συντονισμός: (α) περιοχή υποαρμονικών λύσεων, (β) καμπύλη απόκρισης – συχνότητας

Οι αρχικές συνθήκες καθορίζουν ποια θα είναι η απόκριση του συστήματος. Για τη μηδενική λύση της Εξ. (39), δηλαδή για $a=0$, η μόνιμη απόκριση εξαρτάται μόνο από το εξωτερικό φορτίο:

$$w(t) = P \left(\frac{1}{\omega_{z0}^2 - \Omega^2} \right) \cos \Omega t + O(\varepsilon) \quad (41)$$

ενώ για υποαρμονικές λύσεις, η μόνιμη απόκριση έχει έναν όρο με τη συχνότητα της διέγερσης και έναν όρο με τη συχνότητα του συστήματος:

$$w(t) = a \cos \left(\frac{\Omega t - \gamma}{3} \right) + P \left(\frac{1}{\omega_{z0}^2 - \Omega^2} \right) \cos \Omega t + O(\varepsilon) \quad (42)$$

A.3.3. Σύγκριση των δύο προσομοιωμάτων

A.3.3.1. Γεωμετρία και προένταση

Προκειμένου να συγκριθούν τα αποτελέσματα της ακριβούς εξίσωσης κίνησης με αυτά της απλοποιημένης, θεωρείται ένα απλό δίκτυο καλωδίων που αποτελείται από δύο καλώδια διαμέτρου $D=10\text{mm}$ και εμβαδόν διατομής $A=7.85 \cdot 10^{-5}\text{m}^2$. Το άνοιγμα των καλωδίων είναι $L=50.00\text{m}$ και το αρχικό τους βέλος $f=2.50\text{m}$. Η αρχική ανηγμένη επιμήκυνση των καλωδίων είναι $\varepsilon_0=0.001$, που αντιστοιχεί σε αρχική προένταση $N_0=12.959\text{kN}$. Το μέτρο ελαστικότητας του υλικού θεωρείται ίσο με $E=165\text{GPa}$, ενώ μία συγκεντωμένη μάζα $M=0.131\text{kN} \cdot \text{sec}^2 \cdot \text{m}^{-1}$ εφαρμόζεται στον κεντρικό κόμβο. Για την επίλυση της ακριβούς εξίσωσης κίνησης, προκειμένου να ληφθεί υπόψη μία ενδεχόμενη χαλάρωση καλωδίου, το υλικό ορίζεται με μηδενικό θλιβόμενο κλάδο. Αντιθέτως, οι αναλυτικές λύσεις της απλοποιημένης εξίσωσης κίνησης δεν λαμβάνουν υπόψη χαλάρωση καλωδίου.

A.3.3.2. Ιδιοσυχνότητες

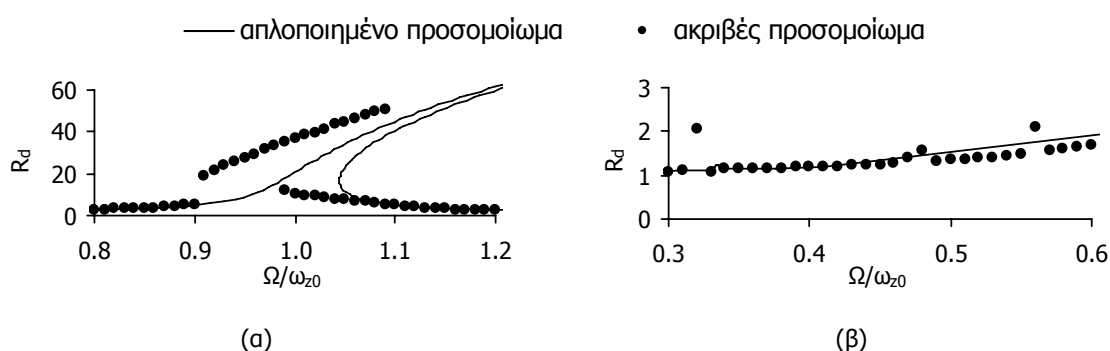
Υπολογίζονται οι δυσκαμψίες και ιδιοσυχνότητες του συστήματος όπως δίνονται στις παραγράφους A.3.1 (Εξ. (16), (17)) και A.3.2 (Εξ. (24), (29)) για το ακριβές και το απλοποιημένο δίκτυο καλωδίων, αντίστοιχα. Ο Πίνακας 2 δίνει τη διαφορά μεταξύ των δύο προσομοιωμάτων, η οποία θεωρείται αμελητέα και για τα δύο μεγέθη.

Πίνακας 2: Δυσκαμψίες και ιδιοσυχνότητες

	Ακριβές	Απλοποιημένο	Διαφορά
Δυσκαμψία K_{z0} (kN/m)	22.49	22.51	0.09%
Ιδιοσυχνότητα ω_{z0} (rad/sec)	13.10	13.19	0.70%

A.3.3.3. Συντονισμοί

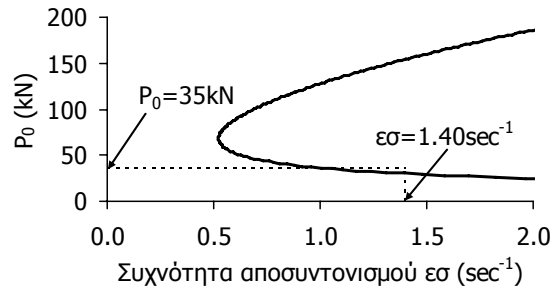
Μελετάται η απόκριση του δικτύου καλωδίων σε συνθήκες συντονισμού για λόγο απόσβεσης $\zeta=0.5\%$ ($\epsilon_m=0.066$) που είναι μία συνήθης τιμή για απλά καλώδια [3-28]. Τα διαγράμματα απόκρισης σε σχέση με το λόγο συχνοτήτων για τα δύο προσομοιώματα συγκρίνονται στο Σχήμα 7α για θεμελιώδη συντονισμό, λαμβάνοντας υπόψη μέγιστη τιμή φορτίου $P_0=1\text{kN}$ ($\epsilon_p=114.50\text{m/sec}^2$) και στο Σχήμα 7β για υπεραρμονικό συντονισμό με $P_0=5\text{kN}$. Στον κατακόρυφο άξονα δίνεται ο λόγος R_d της μόνιμης απόκρισης προς τη στατική απόκριση η οποία αντιστοιχεί στο ίδιο φορτίο. Η συνεχής γραμμή παριστάνει τη μόνιμη απόκριση του απλοποιημένου προσομοιώματος, ενώ η κάθε τελεία παριστάνει τη μόνιμη απόκριση που προκύπτει από μία επίλυση της εξίσωσης κίνησης του ακριβούς προσομοιώματος για τη συγκεκριμένη συχνότητα φορτίου.



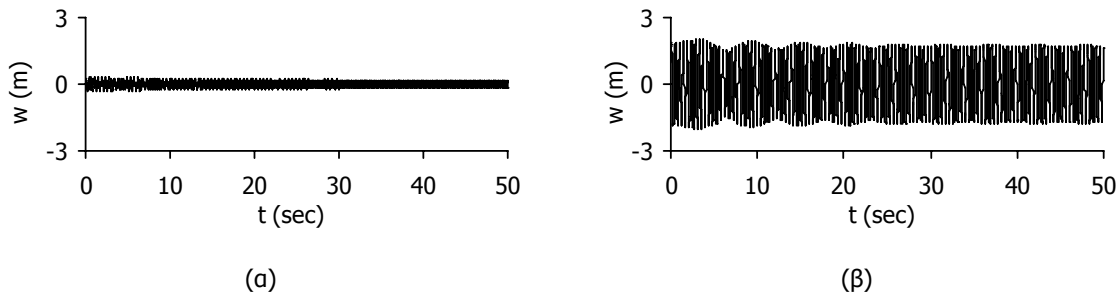
Σχήμα 7: Διάγραμμα απόκρισης – συχνότητας για το ακριβές και το απλοποιημένο προσομοίωμα υπό: (α) θεμελιώδη συντονισμό για $P_0=1\text{kN}$, (β) υπεραρμονικό συντονισμό για $P_0=5\text{kN}$

Παρατηρείται ότι, στην περίπτωση του θεμελιώδους συντονισμού, η αναλυτική λύση της απλοποιημένης εξίσωσης κίνησης μπορεί να προβλέψει με ακρίβεια την καμπύλωση του διαγράμματος, το μέγιστο πλάτος της μόνιμης απόκρισης και το εύρος συχνοτήτων για το οποίο αναμένονται δύο αποκρίσεις που εξαρτώνται από τις αρχικές συνθήκες. Ωστόσο, τα διαγράμματα της απόκρισης του ακριβούς προσομοιώματος, για ένα συγκεκριμένο εύρος λόγων συχνοτήτων, είναι μετατοπισμένα προς μικρότερες τιμές του λόγου Ω/ω_{20} , επειδή για το συγκεκριμένο φορτίο και τις συγκεκριμένες συχνότητες φορτίου συμβαίνει χαλάρωση καλωδίων που καθιστά το σύστημα πιο εύκαμπτο μειώνοντας την δυσκαμψία του και την ιδιοσυχνότητά του. Κατά συνέπεια, ο θεμελιώδης συντονισμός αντιστοιχεί σε μικρότερες συχνότητες. Ωστόσο, η διαφορά μεταξύ των δύο προσομοιωμάτων δεν υπερβαίνει το 7%, και η εκτίμηση της απόκρισης του ακριβούς προσομοιώματος μέσω των αναλυτικών λύσεων του απλοποιημένου κρίνεται ικανοποιητική. Για λόγο συχνοτήτων μικρότερο από 0.91 ή μεγαλύτερο από 1.07, δεν συμβαίνει χαλάρωση καλωδίων και τα δύο διαγράμματα ταυτίζονται απόλυτα. Στην περίπτωση του υπεραρμονικού συντονισμού το διάγραμμα του απλοποιημένου προσομοιώματος προβλέπει με μεγάλη ακρίβεια την απόκριση του ακριβούς προσομοιώματος, όταν δεν συμβαίνει χαλάρωση καλωδίου. Οι κορυφές του διαγράμματος του ακριβούς προσομοιώματος αντιστοιχούν σε υπεραρμονικούς συντονισμούς με μεγάλα πλάτη ταλάντωσης προκαλώντας χαλάρωση καλωδίων, καθιστώντας το σύστημα πιο εύκαμπτο.

Στην περίπτωση του υποαρμονικού συντονισμού εντοπίζονται το μέγεθος και η συχνότητα του φορτίου που μπορούν να τον προκαλέσουν για το απλοποιημένο προσομοίωμα και το φαινόμενο επαληθεύεται για το ακριβές προσομοίωμα. Με βάση την ανίσωση (40) που ορίζει την περιοχή όπου υπάρχουν υποαρμονικές λύσεις (Σχήμα 8), για μέγιστη τιμή αρμονικού φορτίου $P_0=35\text{kN}$ και συχνότητα αποσυντονισμού $\epsilon_s=1.40\text{sec}^{-1}$ αναμένονται υποαρμονικές λύσεις. Για μηδενικές αρχικές συνθήκες το πλάτος της μόνιμης ταλάντωσης είναι μικρό, ενώ λαμβάνοντας υπόψη αρχικές συνθήκες το δίκτυο ταλαντώνεται με πολύ μεγαλύτερο πλάτος όπως φαίνεται στο Σχήμα 9, επιβεβαιώνοντας τον υποαρμονικό συντονισμό.



Σχήμα 8: Περιοχή υποαρμονικών λύσεων για $\zeta=0.5\%$



Σχήμα 9: Ακριβές προσομοίωμα υπό υποαρμονικό συντονισμό: Διάγραμμα μετατόπισης – χρόνου για συχνότητα αποσυντονισμού $\varepsilon\sigma=1.40\text{sec}^{-1}$, ποσοστό απόσβεσης $\zeta=0.5\%$, μέγιστη τιμή φορτίου $P_0=35\text{kN}$ (α) χωρίς αρχικές συνθήκες, (β) αρχική μετατόπιση 1.0m και ταχύτητα 16m/sec

A.3.4. Συμπεράσματα

Η αναλυτική λύση της εξίσωσης Duffing μπορεί να περιγράψει τη συμπεριφορά ενός απλού δικτύου καλωδίων, προβλέποντας με ικανοποιητική ακρίβεια τις συνθήκες για τις οποίες συμβαίνουν μη γραμμικά δυναμικά φαινόμενα. Μικρή διαφορά στην ακριβή συχνότητα φορτίου παρατηρείται μεταξύ των δύο προσομοιωμάτων αν συμβεί χαλάρωση καλωδίου, επειδή οι λύσεις της εξίσωσης Duffing δεν λαμβάνουν υπόψη πιθανή χαλάρωση καλωδίου. Ωστόσο, η διερεύνηση του δικτύου καλωδίων μέσω του απλοποιημένου προσομοιώματος του ταλαντωτή Duffing παρέχει χρήσιμες πληροφορίες για τις συνθήκες για τις οποίες αναμένονται μη γραμμικά φαινόμενα, όπως καμπύλωση του διαγράμματος απόκρισης, απότομες αλλαγές στο πλάτος ταλάντωσης, εξάρτηση της μόνιμης απόκρισης από τις αρχικές συνθήκες ή μη γραμμικοί συντονισμοί.

A.4. ΕΠΑΛΗΘΕΥΣΗ ΛΟΓΙΣΜΙΚΟΥ

Το πρόγραμμα ανάλυσης πεπερασμένων στοιχείων που χρησιμοποιείται στην εργασία αυτή είναι το ADINA ([4-1] – [4-3]). Προκειμένου να ληφθεί υπόψη η ενδεχόμενη χαλάρωση καλωδίου το υλικό των καλωδίων ορίζεται με μηδενικό θλιβόμενο κλάδο. Η ακρίβεια των αποτελεσμάτων του προγράμματος ADINA ελέγχεται για το μονοβάθμιο δίκτυο καλωδίων, για το οποίο η εξίσωση κίνησης επιλύεται αριθμητικά με το πρόγραμμα MATLAB [4-8], στο οποίο η παραδοχή ότι τα καλώδια δεν μπορούν να αναπτύξουν θλίψη πραγματοποιείται θέτοντας ίση με μηδέν την ένταση του καλωδίου όταν αυτή προκύπτει αρνητική, μηδενίζοντας έτσι τη δυσκαμψία του καλωδίου.

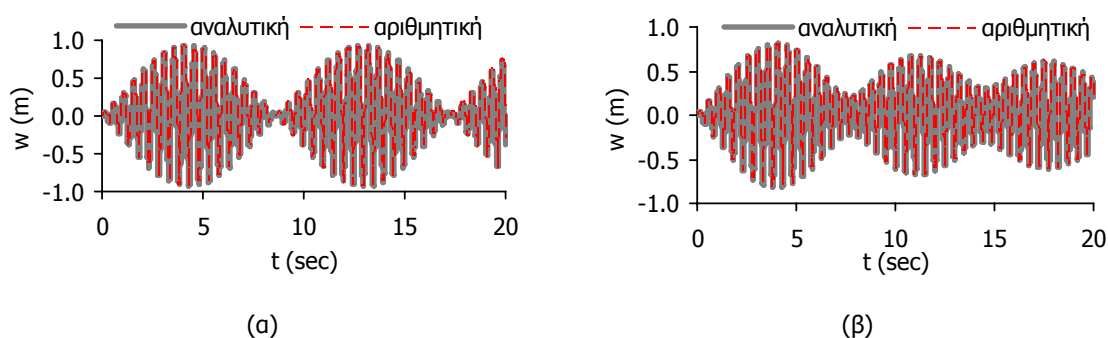
A.4.1. Παραδείγματα

Το απλό δίκτυο καλωδίων που περιγράφηκε στην παράγραφο A.3.3.1 χρησιμοποιείται ως παράδειγμα. Αρχικώς υπολογίζονται οι ιδιοσυχνότητες και οι ιδιοπερίοδοι του συστήματος αριθμητικά (AP) και αναλυτικά (AN) και η διαφορά τους θεωρείται αμελητέα (Πίνακας 3).

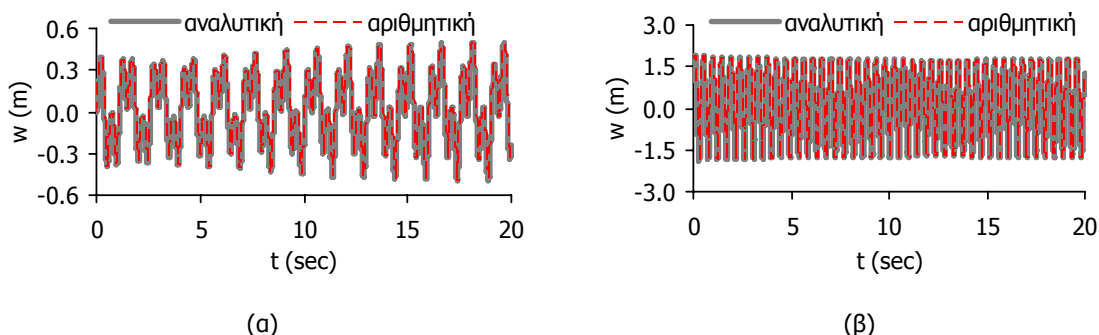
Πίνακας 3: Υπολογισμός ιδιοσυχνοτήτων και ιδιοπεριόδων

Ιδιομορφή	ω (sec^{-1})		T (sec)	
	(AP)	(AN)	(AP)	(AN)
1	13.10	13.10	0.48	0.48
2	88.35	88.39	0.06	0.07
3	88.35	88.39	0.06	0.07

Στη συνέχεια θεωρείται αρμονικό φορτίο στον κεντρικό κόμβο $P(t)=P_0\cos\Omega t$. Στα διαγράμματα της μετατόπισης του κεντρικού κόμβου που ακολουθούν παρουσιάζονται τα αριθμητικά αποτελέσματα που προκύπτουν από το ADINA και τα αναλυτικά που προκύπτουν από το MATLAB. Σημειώνεται ότι το βήμα ολοκλήρωσης παίζει πολύ μεγάλο ρόλο στην ακρίβεια των αποτελεσμάτων που προκύπτουν από τις αριθμητικές αναλύσεις. Στο Σχήμα 10 δίνεται η απόκριση σε θεμελιώδη συντονισμό λαμβάνοντας ή όχι απόσβεση, ενώ στο Σχήμα 11 θεωρούνται συνθήκες υπεραρμονικού ή υποαρμονικού συντονισμού. Έγιναν αναλύσεις υιοθετώντας διάφορα βήματα ολοκλήρωσης. Για απόλυτη συμφωνία μεταξύ των δύο προσεγγίσεων επιλέγεται βήμα ολοκλήρωσης ίσο με $T_{\min}/100$ όπου T_{\min} είναι η μικρότερη περίοδος μεταξύ της ιδιοπεριόδου του συστήματος ή της περιόδου του εξωτερικού φορτίου.



Σχήμα 10: Δυναμική απόκριση κεντρικού κόμβου σε θεμελιώδη συντονισμό με $P=(1\text{kN})\cos(\omega_{20}t)$: (α) χωρίς απόσβεση, (β) με απόσβεση $\zeta=0.5\%$



Σχήμα 11: Δυναμική απόκριση κεντρικού κόμβου με απόσβεση $\zeta=0.5\%$ και αρχικές συνθήκες σε: (α) υπεραρμονικό συντονισμό με $P=(10\text{kN})\cos(\omega_{20}t/3)$, (β) υποαρμονικό συντονισμό με $P=(10\text{kN})\cos(3\omega_{20}t)$

A.4.2. Συμπεράσματα

Το πρόγραμμα ADINA που χρησιμοποιείται για την ανάλυση πολυβάθμιων συστημάτων δίνει πολύ καλά αποτελέσματα. Συγκρίνονται οι ιδιοσυχνότητες και η απόκριση ενός μονοβάθμιου δικτύου καλωδίων με τα αποτελέσματα που προκύπτουν επιλύοντας αριθμητικά την εξίσωση κίνησης αυτού. Ιδιαίτερη προσοχή πρέπει να δίνεται στο βήμα ολοκλήρωσης που επιλέγεται, καθ' ό,τι μικρά βήματα ολοκλήρωσης δίνουν λάθος αποτελέσματα. Το βήμα που θα χρησιμοποιηθεί για τις αναλύσεις πολυβάθμιων συστημάτων λαμβάνεται ίσο με $T_{\min}/100$ όπου T_{\min} είναι η μικρότερη περίοδος μεταξύ της ιδιοπεριόδου του συστήματος ή της περιόδου του εξωτερικού φορτίου.

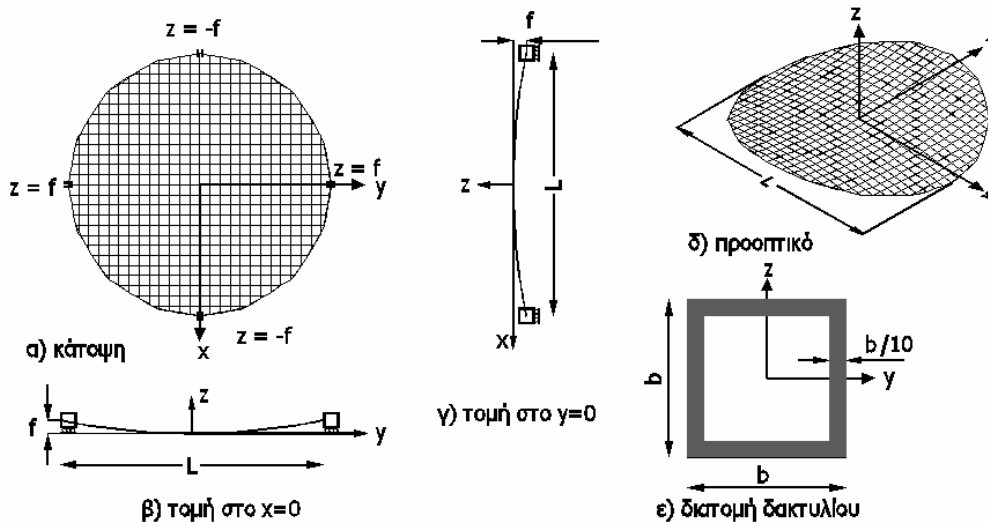
A.5. ΙΔΙΟΣΥΧΝΟΤΗΤΕΣ ΚΑΙ ΙΔΙΟΜΟΡΦΕΣ ΔΙΚΤΥΩΝ ΚΑΛΩΔΙΩΝ

Στη συνέχεια θεωρούνται πολυβάθμια δίκτυα καλωδίων και μελετώνται οι ιδιοσυχνότητες και οι ιδιομορφές τους που όπως αναφέρθηκε στην παράγραφο A.2.1 παίζουν σημαντικό ρόλο στην απόκριση ενός μη γραμμικού συστήματος.

A.5.1. Γεωμετρία και παραδοχές

Θεωρείται ένα δίκτυο καλωδίων σχήματος υπερβολικού παραβολοειδούς με κυκλική κάτοψη διαμέτρου L . Το δίκτυο αποτελείται από N καλώδια ανά κατεύθυνση τοποθετημένα σε τετραγωνικό κάρναβο. Το βέλος του δικτύου καλωδίων είναι f και για τις δύο ομάδες καλωδίων. Όλα τα καλώδια έχουν την ίδια κυκλική διατομή διαμέτρου D και εμβαδού A ενώ το μέτρο ελαστικότητας του υλικού είναι E . Προσομοιώνονται ως στοιχεία δικτυώματος που μπορούν να αναπτύσσουν μόνο εφελκυσμό. Κάθε μέλος μεταξύ δύο συνεχόμενων κόμβων δικτυώματος προσομοιώνεται με ένα ευθύγραμμο στοιχείο δικτυώματος χωρίς καμπτική δυσκαμψία. Η αρχική προένταση N_0 εισάγεται ως αρχική ανηγμένη επιμήκυνση $\epsilon_0 = N_0/EA$. Η πυκνότητα μάζας των καλωδίων είναι ίση με m και μπορεί επίσης να θεωρηθεί και μία πρόσθετη επικόμβια μάζα M .

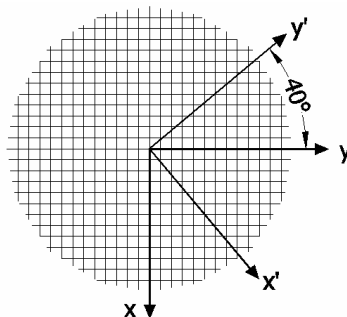
Τα άκρα των καλωδίων θεωρείται ότι αγκυρώνονται είτε σε ακλόνητες στηρίξεις είτε σε έναν παραμορφώσιμο περιμετρικό δακτύλιο (Σχήμα 12). Ο περιμετρικός δακτύλιος θεωρείται ότι έχει τετραγωνική κοίλη διατομή πλάτους b και πάχους τοιχωμάτων $b/10$ με εμβαδόν A_r και ροπή αδράνειας I_r . Το ειδικό βάρος του δακτυλίου είναι ρ_r και το υλικό του έχει μέτρο ελαστικότητας E_r . Σε περίπτωση που θεωρούνται ακλόνητες στηρίξεις καλωδίων δεσμεύονται όλες οι μετακινήσεις στα άκρα των καλωδίων, ενώ όταν προσομοιώνεται ο περιμετρικός δακτύλιος δεσμεύονται οι κατακόρυφες μετατοπίσεις σε όλους τους κόμβους του δακτυλίου, οι κατά x μετατοπίσεις στους κόμβους με συντεταγμένη $x=0$, και οι y μετατοπίσεις στους κόμβους με συντεταγμένη $y=0$. Έτσι επιτρέπεται η ακτινική παραμόρφωση του δακτυλίου αλλά δεσμεύεται η στροφή περί τον κατακόρυφο άξονα.



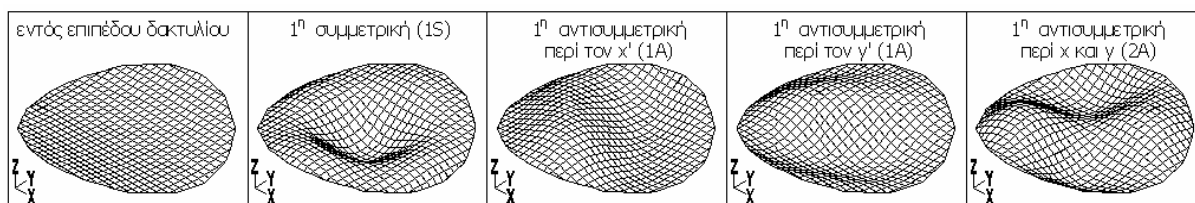
Σχήμα 12: Γεωμετρία δικτύων καλωδίων

A.5.2. Ιδιοσυχνότητες και ιδιομορφές

Πραγματοποιώντας γραμμική ιδιομορφική ανάλυση, υπολογίζονται οι πρώτες συμμετρικές και αντισυμμετρικές ιδιομορφές του συστήματος με τις αντίστοιχες ιδιοσυχνότητες. Για ένα δίκτυο καλωδίων μελετάται η πρώτη συμμετρική ιδιομορφή (1S), οι πρώτες αντισυμμετρικές ιδιομορφές ως προς ένα οριζόντιο άξονα x' και y' αντίστοιχα (1A) και η πρώτη αντισυμμετρική ιδιομορφή ως προς του δύο άξονες (2A). Οι άξονες x' και y' φαίνονται στο Σχήμα 13.

Σχήμα 13: Άξονες x' και y'

Στην περίπτωση που προσομοιώνεται ο περιμετρικός δακτύλιος εισάγεται μία ακόμα ιδιομορφή η οποία είναι η πρώτη συμμετρική εντός επιπέδου ιδιομορφή του δακτυλίου. Οι πρώτες ιδιομορφές ενός τέτοιου συστήματος δίνονται στο Σχήμα 14.



Σχήμα 14: Οι πρώτες ιδιομορφές του συστήματος

Παραμετρικές αναλύσεις δείχνουν ότι μεταβάλλοντας το λόγο βέλους προς άνοιγμα και τα μηχανικά χαρακτηριστικά των καλωδίων, η σειρά των πρώτων ιδιομορφών αλλάζει. Ορίζεται η αδιαστατοποιημένη παράμετρος λ^2 :

$$\lambda^2 = \left(\frac{f}{L}\right)^2 \frac{EA}{N_0} \quad (43)$$

η οποία είναι ανάλογη με αυτήν που είναι γνωστή από τη θεωρία των απλών καλωδίων. Η παράμετρος λ^2 εξαρτάται από το λόγο βέλους προς άνοιγμα f/L του δικτύου καλωδίων και την αρχική ανηγμένη επιμήκυνση των καλωδίων N_0/EA και καθορίζει τη σειρά εμφάνισης των ιδιομορφών. Επίσης, για διάφορες τιμές αυτής της παραμέτρου, δύο ή περισσότερες ιδιομορφές με διαφορετικό σχήμα έχουν ίσες συχνότητες, φαινόμενο που χαρακτηρίζεται ως εσωτερικός συντονισμός. Συγκεκριμένα:

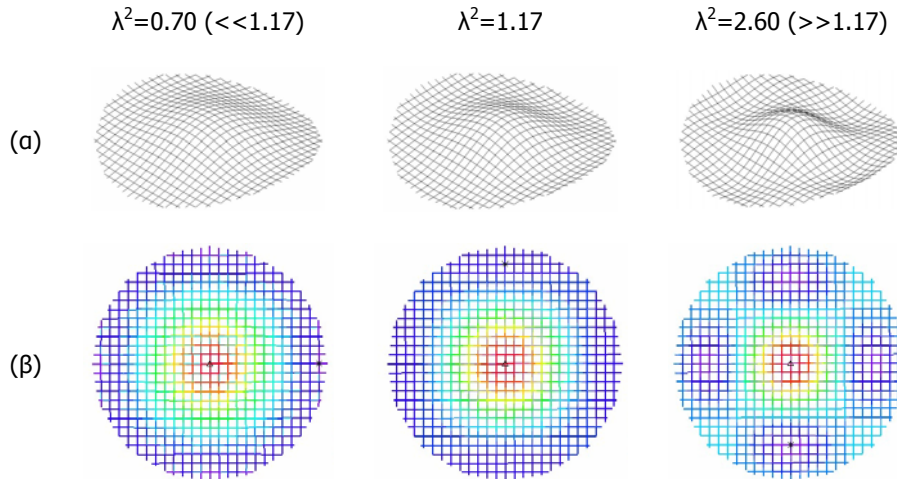
α) όταν $\lambda^2 \leq 0.80$ πρώτη ιδιομορφή του συστήματος είναι η πρώτη συμμετρική ενώ ακολουθούν οι αντισυμμετρικές ιδιομορφές, δηλαδή $\omega_{1S} < \omega_{1A} < \omega_{2A}$. Όταν $\lambda^2 = 0.80$ οι πρώτες τρεις ιδιομορφές έχουν ίσες συχνότητες, δηλαδή $\omega_{1S} = \omega_{1A}$, και αντιστοιχούν σε 1:1 εσωτερικό συντονισμό μεταξύ αυτών των ιδιομορφών.

β) όταν $0.80 < \lambda^2 \leq 0.98$ ισχύει $\omega_{1A} < \omega_{1S} < \omega_{2A}$. Όταν $\lambda^2 = 0.98$ η τρίτη και η τέταρτη ιδιομορφή, 1S και 2A αντίστοιχα, έχουν ίσες ιδιοσυχνότητες, δηλαδή $\omega_{1S} = \omega_{2A}$ αντιστοιχώντας και πάλι σε 1:1 εσωτερικό συντονισμό.

γ) όταν $0.98 < \lambda^2 \leq 1.17$ ισχύει $\omega_{1A} < \omega_{2A} < \omega_{1S}$. Όταν $\lambda^2 = 1.17$ οι συχνότητες της πρώτης, δεύτερης και τρίτης ιδιομορφής είναι ίσες.

δ) όταν $1.17 < \lambda^2$ πρώτη εμφανίζεται η ιδιομορφή 2A και μετά ακολουθούν οι υπόλοιπες, δηλαδή $\omega_{2A} < \omega_{1A} < \omega_{1S}$.

Για μεγαλύτερες τιμές της παραμέτρου λ_2 εναλλαγή των ιδιομορφών παρατηρείται σε ιδιομορφές ανώτερης τάξεως. Το σχήμα της πρώτης συμμετρικής ιδιομορφής αλλάζει ανάλογα με την τιμή της παραμέτρου λ^2 . Έτσι, για τιμές μικρότερες από 1.17, δεν παρουσιάζονται εσωτερικά σημεία μηδενισμού των κατακόρυφων παραμορφώσεων, για τιμές κοντά στο 1.17 η παραμορφωμένη γεωμετρία εφάπτεται ως προς την οριζόντιο στα σημεία στήριξης, ενώ για τιμές μεγαλύτερες του 1.17, εμφανίζονται περιμετρικά εσωτερικά σημεία με μηδενικές παραμορφώσεις (Σχήμα 15).



Σχήμα 15: Πρώτη συμμετρική ιδιομορφή για δίκτυο καλωδίων με ακλόνητες στηρίξεις: (α) προοπτικό, (β) Z- ιδιοδιάνυσμα

A.5.3. Ημι-εμπειρικοί τύποι για υπολογισμό ιδιοσυχνοτήτων

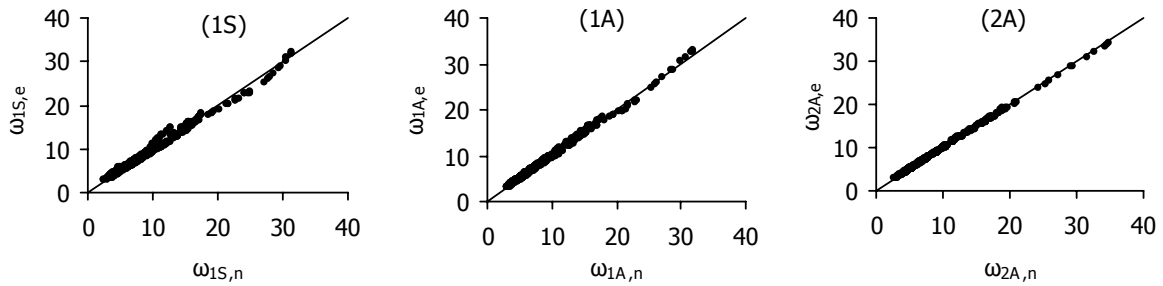
Βάσει των αποτελεσμάτων των παραμετρικών αναλύσεων προτείνονται ημι-εμπειρικές σχέσεις για τον υπολογισμό των πρώτων ιδιοσυχνοτήτων του συστήματος. Έτσι για το δίκτυο καλωδίων προκύπτουν οι εξής σχέσεις:

$$\omega_{1S,e} = \frac{f}{L} \cdot \sqrt{\left(\frac{\frac{50EA}{L}}{mAL + \frac{M(N+1)}{2}} \right)} \sqrt[3]{\left[\frac{N_0}{EA} \left(\frac{L}{f} \right)^2 \right]} \quad (44)$$

$$\omega_{1A,e} = \frac{f}{L} \sqrt{\left(\frac{\frac{50EA}{L}}{mAL + \frac{M(N+1)}{2}} \right)} \sqrt[2.5]{\left[\frac{N_0}{EA} \left(\frac{L}{f} \right)^2 \right]} \quad (45)$$

$$\omega_{2A,e} = \sqrt{\left(\frac{\frac{50N_0}{L}}{mAL + \frac{M(N+1)}{2}} \right)} \quad (46)$$

Οι συχνότητες $\omega_{i,e}$ που υπολογίζονται βάσει των Εξ. (44) -(46) όπου $i=1S, 1A$ ή $2A$, συγκρίνονται με τα αποτελέσματα ιδιομορφικών αναλύσεων $\omega_{i,n}$ και η σύγκριση είναι πολύ ικανοποιητική, όπως φαίνεται στο Σχήμα 16.

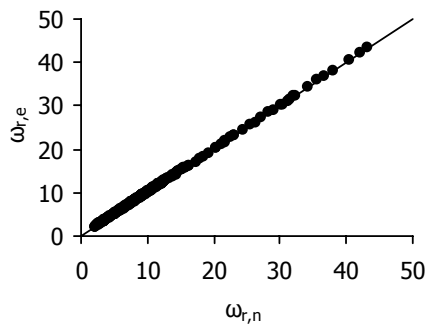


Σχήμα 16: Ακρίβεια ημι-εμπειρικών τύπων για ιδιοσυχνότητες δικτύου καλωδίων

Η ακριβής έκφραση των ιδιοσυχνοτήτων ενός επιπέδου δακτυλίου διατίθεται στη βιβλιογραφία [5-22]. Στην παρούσα εργασία λαμβάνεται υπόψη ότι αυτός δεν είναι επίπεδος. Έτσι, εισάγοντας το λόγο f/L , προκύπτει σχέση υπολογισμού της πρώτης εντός επιπέδου ιδιομορφής:

$$\omega_r = 10.73(1.04 - f/L) \sqrt{\frac{E_r I_r g}{\rho_r A_r L^4}} \tag{47}$$

Η ακρίβεια της σχέσης αυτής φαίνεται στο Σχήμα 17 και θεωρείται πολύ ικανοποιητική.

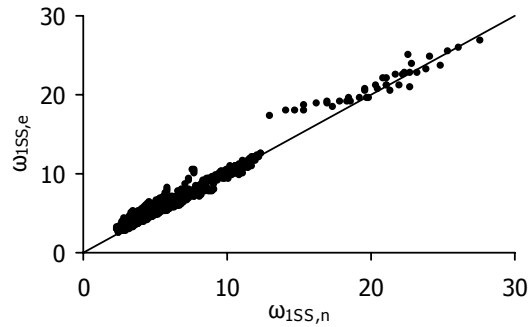


Σχήμα 17: Ακρίβεια ημι-εμπειρικού τύπου για ιδιοσυχνότητα δακτυλίου

Οι παραμετρικές αναλύσεις έδειξαν ότι η προσομοίωση του περιμετρικού δακτυλίου επηρεάζει σημαντικά τη συμμετρική ιδιομορφή του δικτύου καλωδίων και την αντίστοιχη ιδιοσυχνότητα, λόγω της ύπαρξης μιας εντός επιπέδου ιδιομορφής του δακτυλίου. Αντιθέτως, οι αντισυμμετρικές ιδιομορφές παραμένουν ανεπηρέαστες από την παρουσία του δακτυλίου. Σε περίπτωση που προσομοιώνεται ο δακτύλιος, η πρώτη συμμετρική ιδιομορφή του συστήματος, που ονομάζεται στην παρούσα εργασία ως 1SS, είναι ή η εντός επιπέδου του δακτυλίου ιδιομορφή ή η πρώτη συμμετρική ιδιομορφή του δικτύου καλωδίων, ή ένας συνδυασμός αυτών των δύο. Υπολογίζεται βάσει της σχέσης των δυσκαμψιών του μεμονωμένου δακτυλίου και του δικτύου καλωδίων με ακλόνητες στηρίξεις, η οποία ορίζεται από τον λόγο των ιδιοσυχνοτήτων των δύο συμμετρικών ιδιομορφών. Έτσι η πρώτη ιδιομορφή του συστήματος έχει συχνότητα που δίνεται ως εξής:

$$\begin{aligned} &\text{Αν } \omega_r < 0.65 \omega_{1S}, \text{ τότε } \omega_{1SS} = \omega_r \\ &\text{Αν } \omega_r \geq 0.65 \omega_{1S}, \text{ τότε } \omega_{1SS} = \omega_{1S} \left[1 - 0.35 \cdot \left(0.65 \cdot \frac{\omega_{1S}}{\omega_r} \right)^2 \right] \end{aligned} \tag{48}$$

όπου ω_{1S} και ω_r ορίζονται από τις Εξ. (44) και (47), αντίστοιχα. Η ακρίβεια των ημι-εμπειρικών αυτών σχέσεων της Εξ. (48) δίνεται στο διάγραμμα του Σχήμα 18 και κρίνεται ικανοποιητική.



Σχήμα 18: Ακρίβεια ημι-εμπειρικού τύπου για ιδιοσυχνότητα της πρώτης συμμετρικής ιδιομορφής δικτύου καλωδίων με δακτύλιο

A.5.4. Συμπεράσματα

Μελετώντας τις πρώτες ιδιομορφές συμμετρικών δικτύων καλωδίων σχήματος υπερβολικού παραβολοειδούς παρατηρούνται εναλλαγές ιδιομορφών και σημεία διασταύρωσης αυτών που εξαρτώνται από μία αδιαστατοποιημένη παράμετρο λ^2 , παρόμοια με αυτή που αναφέρεται σε απλά καλώδια. Με βάση τις παραμετρικές αναλύσεις που έγιναν, προτείνονται ημι-εμπειρικοί τύποι για την εκτίμηση των πρώτων ιδιοσυχνοτήτων του συστήματος δίνοντας πολύ ικανοποιητικά αποτελέσματα σε σχέση με αυτά των ιδιομορφικών αναλύσεων. Οι τύποι αυτοί μπορούν να χρησιμοποιηθούν σε προκαταρκτικό στάδιο μελέτης κατά το οποίο μπορούν να επιλεγούν γεωμετρικά και μηχανικά χαρακτηριστικά με στόχο την αποφυγή εσωτερικών συντονισμών που αυξάνουν το πλάτος ταλάντωσης λόγω ενεργοποίησης πολλών ιδιομορφών.

Μέρος της ενότητας αυτής έχει παρουσιαστεί στα συνέδρια [5-23] και [5-24] και έχει δημοσιευτεί στο [5-25].

A.6. ΙΣΟΔΥΝΑΜΟ ΜΟΝΟΒΑΘΜΙΟ ΔΙΚΤΥΟ ΚΑΛΩΔΙΩΝ

Η δυναμική απόκριση ενός πολυβάθμιου συστήματος δικτύου καλωδίων, που ονομάζεται «Πρωτότυπο», προσεγγίζεται αρχικώς χρησιμοποιώντας ένα ισοδύναμο μονοβάθμιο σύστημα, που ονομάζεται «Μοντέλο». Η μετατροπή των γεωμετρικών και μηχανικών χαρακτηριστικών από το ένα σύστημα στο άλλο βασίζεται σε κατάλληλες σχέσεις μετασχηματισμού και σε μια μέθοδο που προτάθηκε αρχικώς από τον Gero ([6-10], [6-11]) και που χρησιμοποιήθηκε στα αρχικά στάδια της έρευνας αυτής ([6-12] – [6-15]).

A.6.1. Πρωτότυπο και Μοντέλο

Το Πρωτότυπο έχει κυκλική κάτοψη διαμέτρου L_p και λόγο βέλους προς άνοιγμα f_p/L_p . Το πλήθος των καλωδίων ανά κατεύθυνση είναι $N_p=25$. Το δίκτυο φορτίζεται ομοιόμορφα με ένα αρμονικό κατακόρυφο φορτίο $P_p(t)=(P_0)_p \cos \Omega_p t$ που εφαρμόζεται σε κάθε κόμβο. Η απόκριση του συστήματος μελετάται μέσω του πλάτους μόνιμης ταλάντωσης του κεντρικού κόμβου. Το Μοντέλο που χρησιμοποιείται ως το ισοδύναμο μονοβάθμιο σύστημα είναι παρόμοιο με αυτό που περιγράφηκε στην παράγραφο A.3.2. Αποτελείται από δύο διασταυρούμενα καλώδια, επομένως ισχύει $N_m=1$, με μία συγκεντρωμένη μάζα στον κεντρικό κόμβο M_m , όπου και εφαρμόζεται ένα αρμονικό κατακόρυφο φορτίο $P_m(t)=(P_0)_m \cos \Omega_m t$.

A.6.2. Σχέσεις μετασχηματισμού

Οι σχέσεις μετασχηματισμού που χρησιμοποιούνται για τη μετατροπή των χαρακτηριστικών του Πρωτοτύπου στα αντίστοιχα του Μοντέλου είναι οι ακόλουθες:

$$(P_0)_m = (P_0)_p \left(\frac{E_m}{E_p} \right) \left(\frac{L_m}{L_p} \right)^2 \left(\frac{N_p + 1}{N_m + 1} \right)^2 \sqrt{\frac{f_m / L_m}{f_p / L_p}} \quad \text{:επικόμβιο φορτίο} \quad (49)$$

$$D_m = D_p \left(\frac{L_m}{L_p} \right) \sqrt{\left(\frac{N_p + 1}{N_m + 1} \right) \left(\frac{f_p / L_p}{f_m / L_m} \right)} \quad \text{:διάμετρος καλωδίων} \quad (50)$$

$$A_m = A_p \left(\frac{L_m}{L_p} \right)^2 \left(\frac{N_p + 1}{N_m + 1} \right) \left(\frac{f_p / L_p}{f_m / L_m} \right)^2 \quad \text{:εμβαδόν διατομής καλωδίων} \quad (51)$$

$$(EA)_m = (EA)_p \left(\frac{E_m}{E_p} \right) \left(\frac{L_m}{L_p} \right)^2 \left(\frac{N_p + 1}{N_m + 1} \right) \left(\frac{f_p / L_p}{f_m / L_m} \right)^2 \quad \text{:αξονική δυσκαμψία καλωδίων} \quad (52)$$

$$(N_0)_m = (N_0)_p \left(\frac{E_m}{E_p} \right) \left(\frac{L_m}{L_p} \right)^2 \left(\frac{N_p + 1}{N_m + 1} \right) \quad \text{:αρχική προένταση καλωδίων} \quad (53)$$

$$N_{c,m} = N_{c,p} \left(\frac{E_m}{E_p} \right) \left(\frac{L_m}{L_p} \right)^2 \left(\frac{N_p + 1}{N_m + 1} \right) \quad \text{:ένταση καλωδίων} \quad (54)$$

$$\rho_m = \rho_p \left(\frac{E_m}{E_p} \right) \left(\frac{L_p}{L_m} \right)^2 \left(\frac{f_m / L_m}{f_p / L_p} \right)^2 \quad \text{:ειδικό βάρος καλωδίων} \quad (55)$$

$$M_m = M_p \left(\frac{E_m}{E_p} \right) \left(\frac{L_m}{L_p} \right) \left(\frac{N_p + 1}{N_m + 1} \right)^2 \quad \text{:επικόμβια μάζα} \quad (56)$$

$$w_{d,m} = w_{d,p} \left(\frac{L_m}{L_p} \right) \left(\frac{f_m / L_m}{f_p / L_p} \right) \quad \text{:δυναμική παραμόρφωση} \quad (57)$$

$$w_m = w_p \frac{L_m}{L_p} \quad \text{:στατική παραμόρφωση} \quad (58)$$

$$\omega_m = \omega_p \quad \text{:ιδιοσυχνότητα} \quad (59)$$

$$\Omega_m = \Omega_p \quad \text{:συχνότητα φορτίου} \quad (60)$$

$$\zeta_m = \zeta_p \quad \text{:ποσοστό απόσβεσης} \quad (61)$$

όπου N είναι το πλήθος των καλωδίων ανά κατεύθυνση, L είναι το άνοιγμα του μακρύτερου καλωδίου, E το μέτρο ελαστικότητας του υλικού των καλωδίων, ενώ οι δείκτες m και p αναφέρονται στο Μοντέλο και το Πρωτότυπο αντίστοιχα. Προκειμένου να ελαχιστοποιηθεί το λάθος λόγω της μετατροπής του πολυβάθμιου συστήματος στο μονοβάθμιο, το Μοντέλο επιλέγεται να έχει ίδιο λόγο βέλους προς άνοιγμα f_m/L_m , άνοιγμα καλωδίων L_m και μέτρο ελαστικότητας E_m με το Πρωτότυπο.

A.6.3. Παράδειγμα 1: Δίκτυο καλωδίων με $f/L=1/35$

Αρχικώς μελετάται ένα δίκτυο καλωδίων με $N_p=25$ καλώδια ανά κατεύθυνση, διάμετρο κυκλικής κάτοψης $L_p=100\text{m}$ και λόγο βέλους προς άνοιγμα $f_p/L_p=1/35$. Όλα τα καλώδια έχουν διάμετρο $D_p=50\text{mm}$, και αρχική προένταση $(N_0)_p=600\text{kN}$, ενώ το υλικό τους έχει μέτρο ελαστικότητας $E_p=165\text{GPa}$ με όριο διαρροής $\sigma_y=1570\text{MPa}$. Εφαρμόζεται επικόμβια μάζα σε κάθε κόμβο ίση με $M_p=0.151\text{kNsec}^2/\text{m}$. Το ποσοστό απόσβεσης λαμβάνεται ίσο με $\zeta_p=2\%$. Γι' αυτό το παράδειγμα η αδιαστατοποιημένη παράμετρος λ^2 προκύπτει:

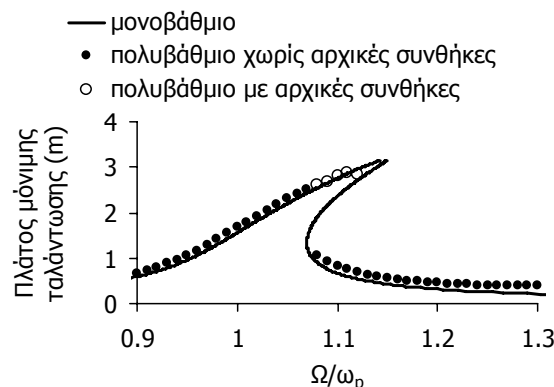
$$\lambda^2 = \left(\frac{f}{L}\right)^2 \frac{EA}{N_0} = \left(\frac{1}{35}\right)^2 \frac{165000000 \cdot 0.00196}{600} = 0.44 < 0.80 \quad (62)$$

Πρώτη ιδιομορφή του δικτύου καλωδίων είναι η πρώτη συμμετρική με συχνότητα $\omega_p=9.902\text{sec}^{-1}$ χωρίς ενδιάμεσα σημεία μηδενισμού των παραμορφώσεων. Τα χαρακτηριστικά του Μοντέλου προκύπτουν από τις σχέσεις μετασχηματισμού (Πίνακας 4).

Πίνακας 4: Χαρακτηριστικά Πρωτοτύπου και Μοντέλου

	Πρωτότυπο	Μοντέλο
Πλήθος καλωδίων N	25	1
Διάμετρος δικτύου καλωδίων L	100m	100m
Λόγος βέλους προς άνοιγμα f/L	1/35	1/35
Μέτρο ελαστικότητας E	165GPa	165GPa
Όριο διαρροής σ_y	1570MPa	1570MPa
Ποσοστό απόσβεσης ζ	2%	2%
Διάμετρος καλωδίων D	50mm	1800mm
Αρχική προένταση καλωδίων N_0	600kN	7800kN
Επικόμβια μάζα M	0.151kNsec ² /m	25.52kNsec ² /m

Για το Πρωτότυπο θεωρείται μέγιστη τιμή αρμονικού φορτίου ίση με $(P_0)_p=1.30\text{kN}$, που αντιστοιχεί σε φορτίο $(P_0)_m=219.7\text{kN}$ για το Μοντέλο. Στο Σχήμα 19 δίνεται το διάγραμμα της μόνιμης απόκρισης του μονοβάθμιου συστήματος που υπολογίζεται σύμφωνα με την παράγραφο A.3.2.1, καθώς επίσης και το διάγραμμα της μόνιμης απόκρισης του πολυβάθμιου συστήματος όπως προκύπτει από μη γραμμικές δυναμικές αναλύσεις, μεταβάλλοντας το λόγο συχνότητας φορτίου προς ιδιοσυχνότητα από 0.90 σε 1.30.

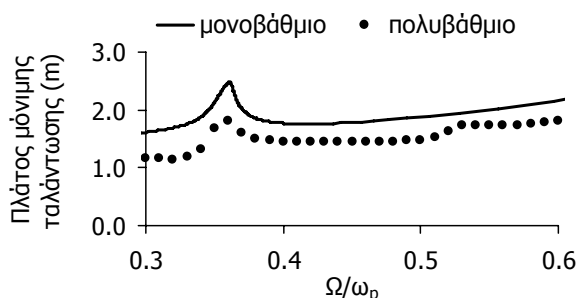


Σχήμα 19: Θεμελιώδης συντονισμός: απόκριση πολυβάθμιου και μονοβάθμιου συστήματος

Αξίζει να σημειωθεί ότι κάθε τελεία και κάθε κύκλος, που παριστάνει την απόκριση του Πρωτοτύπου χωρίς και με αρχικές συνθήκες, αντίστοιχα, είναι το αποτέλεσμα μιας μη γραμμικής δυναμικής ανάλυσης. Επομένως για να δημιουργηθεί ένα τέτοιο διάγραμμα για ένα πολυβάθμιο σύστημα

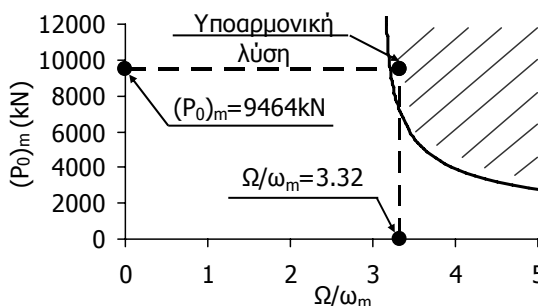
απαιτούνται πολλές αναλύσεις με μικρό βήμα αλλαγής της συχνότητας του φορτίου. Από τα διαγράμματα επιβεβαιώνεται η μη γραμμική συμπεριφορά του δικτύου καλωδίων, εμφανίζοντας καμπύλωση του διαγράμματος, εξάρτηση της μόνιμης απόκρισης από τις αρχικές συνθήκες, απότομη μείωση της απόκρισης και μέγιστη απόκριση για λόγο συχνοτήτων μεγαλύτερο της μονάδας. Παράλληλα, το ισοδύναμο μονοβάθμιο σύστημα εκτιμά με ικανοποιητική ακρίβεια την απόκριση του πολυβάθμιου συστήματος σε συνθήκες θεμελιώδους συντονισμού με διαφορά που ανέρχεται μόλις στο 10%.

Σε περίπτωση υπεραρμονικού συντονισμού, το φορτίο για το Πρωτότυπο είναι $(P_0)_p=14\text{kN}$ που αντιστοιχεί σε φορτίο $(P_0)_m=2366\text{kN}$ για το Μοντέλο. Ο λόγος συχνοτήτων μεταβάλλεται από 0.30 έως 0.60. Στο Σχήμα 20 δίνονται τα διαγράμματα μόνιμης απόκρισης του Πρωτοτύπου και του Μοντέλου, όπου παρατηρείται ότι η απόκριση του Πρωτοτύπου διαφέρει σημαντικά από αυτήν του Μοντέλου. Ωστόσο, η μέθοδος αυτή προβλέπει με ακρίβεια τη συχνότητα του φορτίου για την οποία συμβαίνει ο υπεραρμονικός συντονισμός κι αυτό αποτελεί μεγάλο πλεονέκτημα της μεθόδου, εφόσον για να βρεθεί η συχνότητα αυτή για το πολυβάθμιο σύστημα απαιτούνται πολλές αναλύσεις μεταβάλλοντας τη συχνότητα του φορτίου με μικρά βήματα. Από τη διερεύνηση αυτή επιβεβαιώνεται ότι μπορούν να συμβούν υπεραρμονικοί συντονισμοί στο πολυβάθμιο σύστημα.



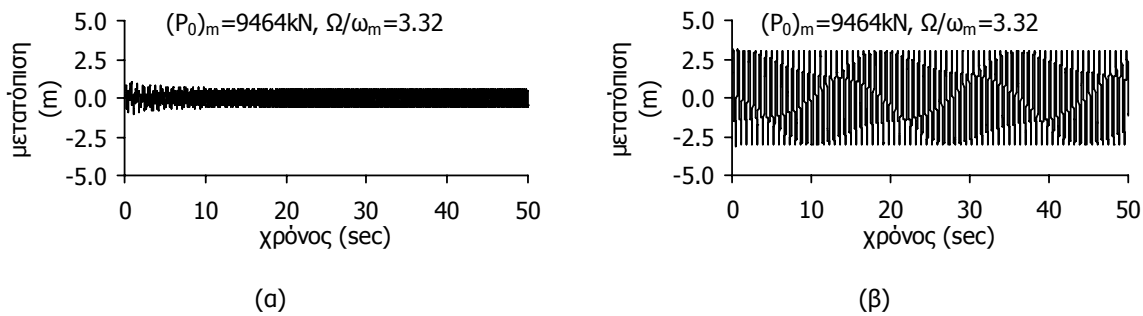
Σχήμα 20: Υπεραρμονικός συντονισμός: απόκριση πολυβάθμιου και μονοβάθμιου συστήματος

Με τις αναλυτικές λύσεις του ισοδύναμου μονοβάθμιου συστήματος μπορούν εύκολα να εντοπιστούν οι συνθήκες για τις οποίες πραγματοποιείται ένας υποαρμονικός συντονισμός. Έτσι, στο Σχήμα 21 ορίζεται η περιοχή όπου υπάρχουν υποαρμονικές λύσεις καθώς και το φορτίο και ο λόγος συχνοτήτων που προκαλούν υποαρμονικό συντονισμό.



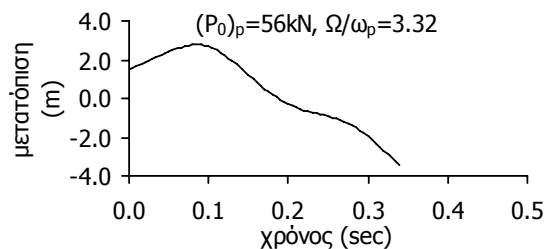
Σχήμα 21: Περιοχή υποαρμονικών λύσεων

Στο Σχήμα 22 εφαρμόζεται στον κεντρικό κόμβο του μονοβάθμιου συστήματος αρμονικό φορτίο με $(P_0)_m=9464\text{kN}$ και $\Omega=3.32\omega_m$, θεωρώντας αρχική παραμόρφωση 1.49m και αρχική ταχύτητα 16m/sec. Συγκρίνοντας τα διαγράμματα με και χωρίς αρχικές συνθήκες παρατηρούμε ότι με αρχικές συνθήκες το πλάτος ταλάντωσης είναι πολύ μεγαλύτερο, επιβεβαιώνοντας τον υποαρμονικό συντονισμό.



Σχήμα 22: Απόκριση κεντρικού κόμβου ισοδύναμου μονοβάθμιου συστήματος: (α) χωρίς αρχικές συνθήκες, (β) με αρχικές συνθήκες

Μετατρέποντας το φορτίο, το λόγο συχνοτήτων και τις αρχικές συνθήκες σύμφωνα με τις σχέσεις μετασχηματισμού στα αντίστοιχα μεγέθη για το Πρωτότυπο και εκτελώντας μη γραμμική δυναμική ανάλυση, το διάγραμμα της μετατόπισης του κεντρικού κόμβου σε σχέση με το χρόνο δίνεται στο Σχήμα 23. Παρατηρείται ότι στα πρώτα βήματα της παροδικής απόκρισης η ανάλυση σταματάει επειδή η μέγιστη ένταση στα καλώδια φτάνει το όριο διαρροής, το οποίο έχει οριστεί ως η μέγιστη ένταση που μπορεί να αναπτύξει το καλώδιο. Αυτό συμβαίνει γιατί τόσο η μέγιστη τιμή του φορτίου όσο και οι αρχικές συνθήκες που απαιτούνται προκειμένου να πραγματοποιηθεί ο υποαρμονικός συντονισμός προκαλούν αστοχία καλωδίου αμέσως μόλις ξεκινήσει η ταλάντωση. Μικρότερα φορτία απαιτούν μεγαλύτερες αρχικές συνθήκες, ενώ, αντίστοιχα, μικρότερες αρχικές συνθήκες απαιτούν μεγαλύτερα φορτία. Επομένως, σε κάθε περίπτωση δεν μπορεί να εξελιχθεί το φαινόμενο του υποαρμονικού συντονισμού πριν την αστοχία των καλωδίων.



Σχήμα 23: Διάγραμμα μετατόπισης κεντρικού κόμβου πολυβάθμιου συστήματος

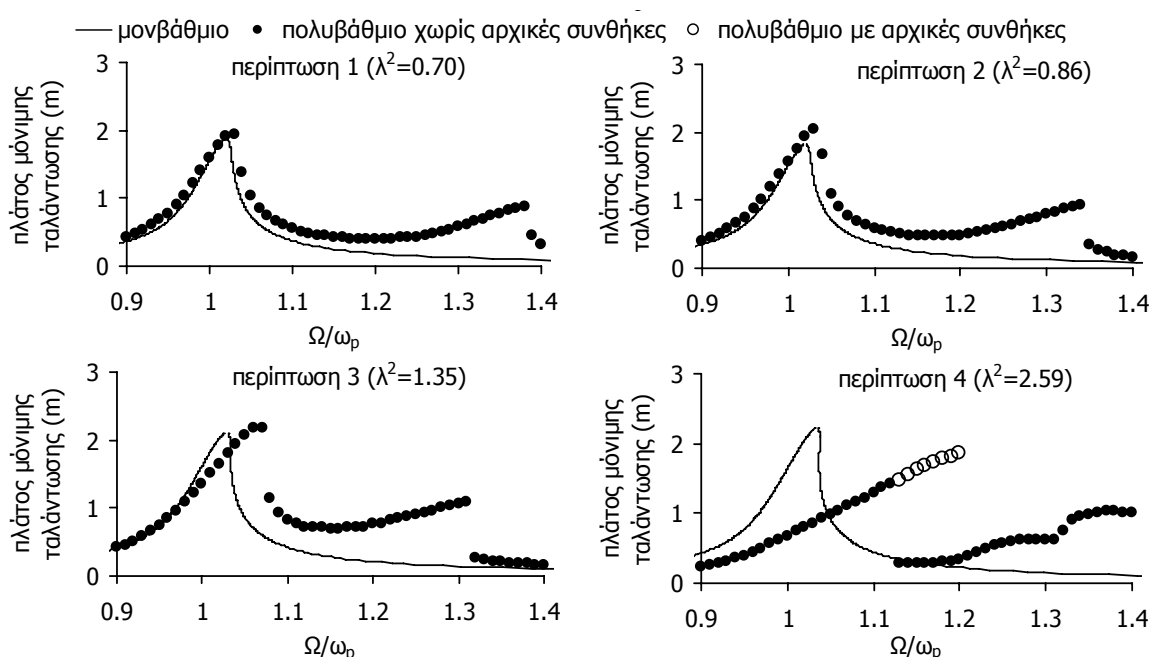
A.6.4. Παράδειγμα 2: Δίκτυο καλωδίων με $f/L=1/20$

Άλλο ένα δίκτυο καλωδίων λαμβάνεται υπόψη με $f/L=1/20$, μέτρο ελαστικότητας $E=165\text{GPa}$, και τέσσερα διαφορετικά επίπεδα αρχικής τάσης καλωδίων. Η διάμετρος των καλωδίων, η αρχική προένταση και το όριο διαρροής, που θεωρείται ως το ανώτερο όριο τάσης καλωδίων, επιλέγονται κατάλληλα ώστε να προκύπτουν χαρακτηριστικές τιμές της παραμέτρου λ^2 . Η μέγιστη τιμή του φορτίου σε κάθε περίπτωση είναι αρκετά μεγάλη ώστε να προκαλεί καμπύλωση του διαγράμματος απόκρισης, χωρίς όμως να προκαλεί αστοχία καλωδίων. Ο Πίνακας 5 περιλαμβάνει τα χαρακτηριστικά των δικτύων καλωδίων για κάθε μία περίπτωση.

Πίνακας 5: Χαρακτηριστικά δικτύων καλωδίων με $f/L=1/20$ και $E=165\text{GPa}$

Περιπτώσεις	P_0 [kN]	D [mm]	N_0 [kN]	σ_v [MPa]	$N_0/(A\sigma_v)$	λ^2
1	1.3	40	735	1670	0.35	0.70
2	1.2	40	600	1570	0.30	0.86
3	2.0	50	600	1570	0.20	1.35
4	5.0	80	800	1570	0.10	2.59

Ακολουθώντας την ίδια διαδικασία όπως περιγράφηκε στην παράγραφο A.6.3, λαμβάνεται υπόψη ποσοστό απόσβεσης $\zeta=2\%$ και μελετάται η απόκριση των δικτύων καλωδίων σε θεμελιώδη συντονισμό για την πρώτη συμμετρική ιδιομορφή. Τα διαγράμματα της μόνιμης απόκρισης του κεντρικού κόμβου για το πολυβάθμιο και το μονοβάθμιο σύστημα φαίνονται στο Σχήμα 24. Για τις δύο πρώτες περιπτώσεις, η μέγιστη μόνιμη απόκριση του πολυβάθμιου συστήματος, καθώς και ο λόγος συχνότητων για τον οποίο αυτή πραγματοποιείται, προβλέπονται με ακρίβεια από το μονοβάθμιο σύστημα. Για την τρίτη περίπτωση, η καμπύλωση του διαγράμματος απόκρισης του πολυβάθμιου συστήματος είναι εντονότερη σε σχέση με αυτή του μονοβάθμιου, ενώ στην τέταρτη περίπτωση η μέθοδος δεν δίνει σωστά αποτελέσματα. Αυτό συμβαίνει επειδή στις δύο αυτές περιπτώσεις η παράμετρος λ^2 είναι μεγαλύτερη από 1.17 (Πίνακας 5), επομένως η πρώτη συμμετρική ιδιομορφή παρουσιάζει εσωτερικά σημεία μηδενισμού των παραμορφώσεων, όπως αποδείχτηκε στην παράγραφο A.5.2, τα οποία δεν μπορούν να προβλεφτούν από το μονοβάθμιο σύστημα.



Σχήμα 24: Θεμελιώδης συντονισμός: διαγράμματα απόκρισης για $f/L=1/20$ και $\zeta=2\%$

A.6.5. Συμπεράσματα

Ο εντοπισμός των κατάλληλων συνθηκών που προκαλούν μη γραμμικά δυναμικά φαινόμενα σε ένα πολυβάθμιο σύστημα απαιτεί πολλές μη γραμμικές αναλύσεις μεταβάλλοντας με μικρά βήματα τη συχνότητα του φορτίου. Η μέθοδος του ισοδύναμου μονοβάθμιου δικτύου καλωδίων εκτιμά με ικανοποιητική ακρίβεια τη συχνότητα και τη μέγιστη τιμή του φορτίου που μπορούν να προκαλέσουν μη γραμμικούς συντονισμούς σε ένα πολυβάθμιο σύστημα για συστήματα που η παράμετρος λ^2 προκύπτει μικρότερη από 1.17.

Μέρος αυτής της ενότητας παρουσιάστηκε στο [6-17].

A.7. ΔΥΝΑΜΙΚΗ ΑΠΟΚΡΙΣΗ ΔΙΚΤΥΩΝ ΚΑΛΩΔΙΩΝ ΥΠΟ ΑΡΜΟΝΙΚΑ ΦΟΡΤΙΑ

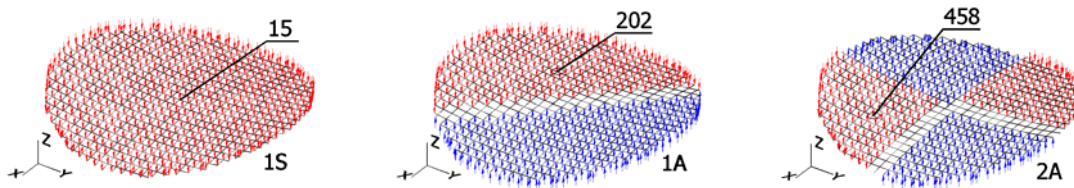
Στη συνέχεια μελετάται η μη γραμμική συμπεριφορά των δικτύων καλωδίων σε αρμονικά φορτία, λαμβάνοντας υπόψη διάφορες κατανομές φορτίου.

A.7.1. Προσομοίωμα δικτύου καλωδίων

Για τις αναλύσεις σε αρμονικά φορτία θεωρείται δίκτυο καλωδίων με διάμετρο κάτοψης $L=100\text{m}$ και αρχικό βέλος $f=L/20=5\text{m}$. Αποτελείται από $N=25$ καλώδια ανά κατεύθυνση διαμέτρου $D=50\text{mm}$, διατομής $A=0.0019635\text{m}^2$, και πυκνότητας μάζας $m=10\text{kN}\cdot\text{sec}^2\cdot\text{m}^{-4}$, ενώ δεν λαμβάνεται υπόψη πρόσθετη επικόμβια μάζα. Θεωρείται μέτρο ελαστικότητας του υλικού των καλωδίων $E=165\text{GPa}$, και αρχική προένταση $N_0=600\text{kN}$. Η μέγιστη επιτρεπόμενη τάση καλωδίων λαμβάνεται ίση με το όριο διαρροής $\sigma_r=1570\text{MPa}$. Σε περίπτωση που προσομοιώνεται και ο περιμετρικός δακτύλιος, αυτός έχει τετραγωνική κοίλη διατομή πλάτους $b=6.0\text{m}$ και πάχους $b/10=0.6\text{m}$, ειδικό βάρος $\rho_r=25\text{kN/m}^3$ και υλικό από προεντεταμένο σκυρόδεμα με μέτρο ελαστικότητας $E_r=39\text{GPa}$. Στις αναλύσεις λαμβάνεται απόσβεση Rayleigh με ποσοστό απόσβεσης ίσο με $\zeta=2\%$.

A.7.2. Περιγραφή φορτίου

Εφαρμόζεται κατακόρυφο αρμονικό επικόμβιο φορτίο σε όλους τους κόμβους του δικτύου, εκφραζόμενο ως $P=P_0\cos(\Omega t)$. Προκειμένου να μελετηθεί η συμπεριφορά του συστήματος σε θεμελιώδη συντονισμό, δηλαδή για συχνότητες φορτίου κοντά στις ιδιοσυχνότητες του συστήματος, η μέγιστη τιμή του φορτίου λαμβάνεται ίση με $P_0=2\text{kN}$, ενώ για υπεραρμονικό συντονισμό και για συχνότητες φορτίου μικρότερες από αυτές του συστήματος, θεωρείται ίση με $P_0=24\text{kN}$. Η κατανομή του φορτίου θεωρείται είτε ομοιόμορφη, με πρόσημο φορτίου αντίστοιχο των μετατοπίσεων της πρώτης συμμετρικής ιδιομορφής, είτε αντισυμμετρική με πρόσημο φορτίου που συμφωνεί με τις ιδιομορφές 1A και 2A. Στο Σχήμα 25 φαίνονται οι κατανομές που θεωρούνται καθώς και οι κόμβοι που παρουσιάζουν τις μέγιστες μετατοπίσεις, για τους οποίους συντάσσονται τα διαγράμματα απόκρισης.

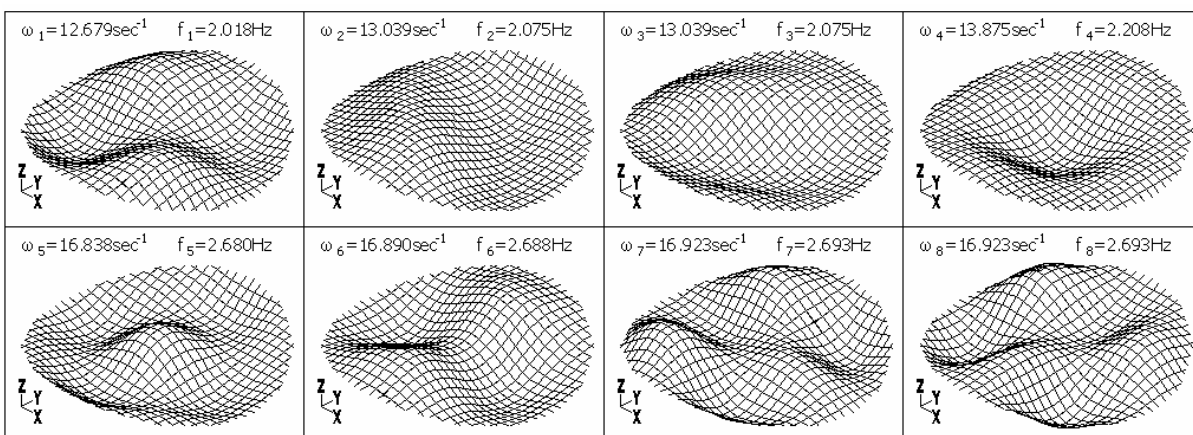


Σχήμα 25: Κατανομές φορτίου και χαρακτηριστικοί κόμβοι

A.7.3. Δίκτυο καλωδίων με ακλόνητες στηρίξεις

A.7.3.1. Ιδιομορφές και ιδιοσυχνότητες

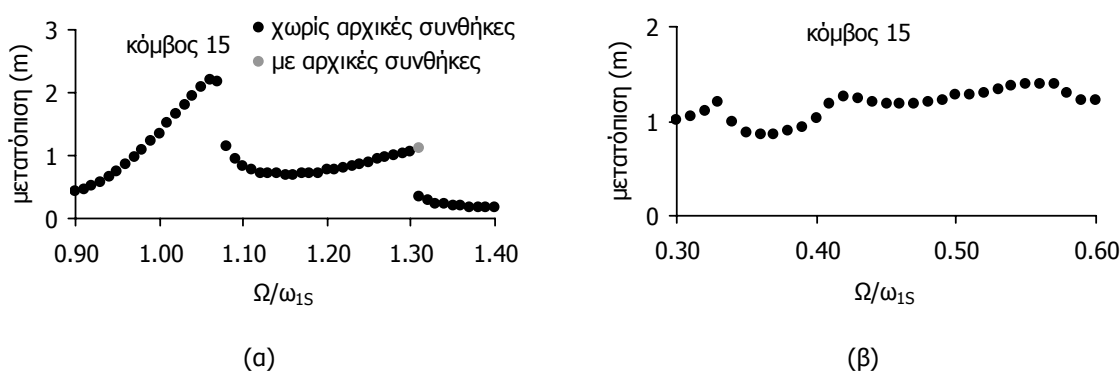
Εκτελώντας γραμμική ιδιομορφική ανάλυση υπολογίζονται οι ιδιοσυχνότητες και ιδιομορφές του συστήματος (Σχήμα 26).



Σχήμα 26: Ιδιομορφές και ιδιοσυχνότητες δικτύου καλωδίων με ακλόνητες στηρίξεις

A.7.3.2. Ομοιόμορφη κατανομή φορτίου (1S)

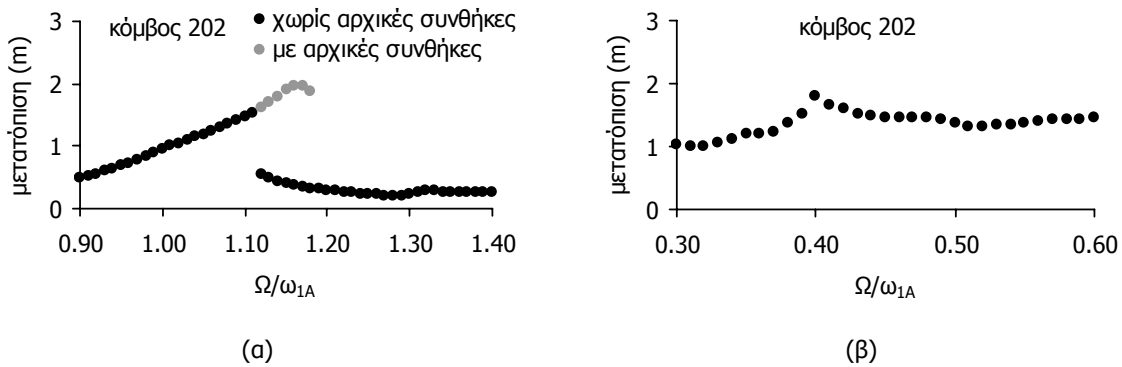
Για ένα ομοιόμορφα καταμεμημένο αρμονικό φορτίο, η μόνιμη απόκριση του κεντρικού κόμβου (κόμβος 15) δίνεται στο Σχήμα 27α, θεωρώντας φορτίο με εύρος $P_0=2\text{kN}$ και συχνότητα που κυμαίνεται μεταξύ $0.90\omega_{1S}$ και $1.40\omega_{1S}$, όπου $\omega_{1S}=\omega_4=13.875\text{sec}^{-1}$ ($f_4=2.208\text{Hz}$, $T_4=0.45\text{sec}$). Η μέγιστη μόνιμη απόκριση ίση με 2.18m , παρατηρείται για $\Omega/\omega_{1S}=1.07$, ενώ για $\Omega/\omega_{1S}=1.08$ μειώνεται απότομα σε 1.14m . Η μέγιστη απόκριση δεν συμβαίνει για λόγο συχνοτήτων ίσο με 1.00 , όπως συμβαίνει στα γραμμικά συστήματα, επιβεβαιώνοντας την καμπύλωση του διαγράμματος. Για $\Omega=1.31\omega_{1S}=1.08\omega_5$, όπου $\omega_5=16.838\text{sec}^{-1}$, παρατηρείται μία ακόμα κορυφή στο διάγραμμα που αντιστοιχεί σε θεμελιώδη συντονισμό για την πέμπτη ιδιομορφή που είναι η δεύτερη συμμετρική ιδιομορφή του συστήματος. Οι αρχικές συνθήκες επηρεάζουν τη μόνιμη απόκριση γι' αυτόν το λόγο συχνοτήτων. Θεωρώντας φορτίο με $P_0=24\text{kN}$ και συχνότητες μεταξύ $0.30\omega_{1S}$ και $0.60\omega_{1S}$, η μόνιμη απόκριση του κόμβου 15 δίνεται στο Σχήμα 27β. Παρατηρούνται δύο κορυφές του διαγράμματος: η πρώτη για $\Omega=0.33\omega_{1S}=4.57\text{sec}^{-1}$ (0.73Hz), και η δεύτερη για $\Omega=0.42\omega_{1S}=0.35\omega_5=5.83\text{sec}^{-1}$ (0.93Hz) που αντιστοιχεί σε έναν υπεραρμονικό συντονισμό τρίτης τάξεως για την τέταρτη και πέμπτη ιδιομορφή, αντίστοιχα. Δύο ακόμα μικρότερες κορυφές παρατηρούνται στο Σχήμα 27β για $\Omega/\omega_{1S}=0.50$ και $\Omega/\omega_{1S}=0.57$ λόγω υπεραρμονικών συντονισμών δεύτερης τάξεως για τις δύο αυτές συμμετρικές ιδιομορφές.



Σχήμα 27: Μόνιμη απόκριση δικτύου καλωδίων με ακλόνητες στηρίξεις υπό συντονισμό για την ιδιομορφή 1S: (α) θεμελιώδης συντονισμός ($P_0=2\text{kN}$), (β) υπεραρμονικός συντονισμός ($P_0=24\text{kN}$)

A.7.3.3. Αντισυμμετρική κατανομή φορτίου (1A)

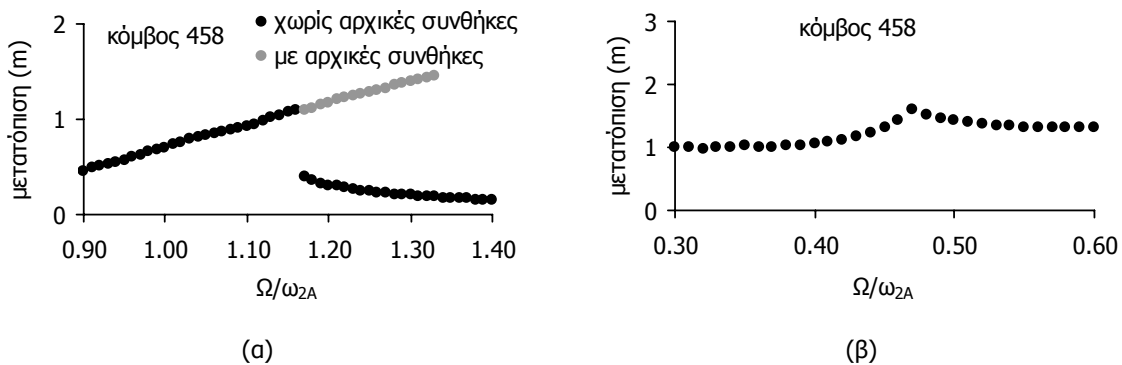
Λαμβάνοντας υπόψη το πρόσημο του δυναμικού φορτίου που εφαρμόζεται σε κάθε κόμβο αντίστοιχο με αυτό της παραμόρφωσης λόγω της ιδιομορφής 1A, το διάγραμμα της μόνιμης παραμόρφωσης για τον κόμβο που παρουσιάζει τη μέγιστη παραμόρφωση (κόμβος 202) (Σχήμα 25) δίνεται στο Σχήμα 28α για φορτίο με μέγιστη τιμή $P_0=2\text{kN}$ και συχνότητα Ω μεταξύ $0.90\omega_{1A}$ και $1.40\omega_{1A}$, όπου $\omega_{1A}=\omega_2=\omega_3=13.039\text{sec}^{-1}$, ($f_{2,3}=2.075\text{Hz}$, $T_{2,3}=0.48\text{sec}$). Για λόγους συχνοτήτων μεταξύ $\Omega/\omega_{1A}=1.12$ και $\Omega/\omega_{1A}=1.19$, υπολογίζονται δύο μόνιμες παραμορφώσεις: η μεγαλύτερη απόκριση προκύπτει λαμβάνοντας υπόψη αρχική παραμόρφωση και ταχύτητα σε όλους τους κόμβους, ενώ η μικρότερη απόκριση υπολογίζεται χωρίς αρχικές συνθήκες. Η καμπύλωση του διαγράμματος είναι πιο έντονη σε αυτήν την περίπτωση φόρτισης, οδηγώντας σε πιο έντονη μη γραμμική δυναμική απόκριση. Το διάγραμμα της μόνιμης απόκρισης του δικτύου για φορτίο με μέγιστη τιμή $P_0=24\text{kN}$ και συχνότητα Ω μεταξύ $0.30\omega_{1A}$ και $0.60\omega_{1A}$ δίνεται στο Σχήμα 28β. Και σ' αυτό το διάγραμμα επιβεβαιώνεται ο υπεραρμονικός συντονισμός τρίτης τάξεως για την ιδιομορφή 1A, εφόσον παρατηρείται μέγιστη μόνιμη απόκριση για $\Omega=0.40\omega_{1A}=5.22\text{sec}^{-1}$ (0.83Hz).



Σχήμα 28: Μόνιμη απόκριση δικτύου καλωδίων με ακλόνητες στηρίξεις υπό συντονισμό για την ιδιομορφή 1A: (α) θεμελιώδης συντονισμός ($P_0=2\text{kN}$), (β) υπεραρμονικός συντονισμός ($P_0=24\text{kN}$)

A.7.3.4. Αντισυμμετρική κατανομή φορτίου (2A)

Θεωρώντας μία αντισυμμετρική κατανομή φορτίου με πρόσημο αντίστοιχο με αυτό της ιδιομορφής 2A, η μόνιμη απόκριση του κόμβου 458 (Σχήμα 25) δίνεται στο Σχήμα 29α για φορτίο με μέγιστη τιμή $P_0=2\text{kN}$ και συχνότητα φορτίου Ω να κυμαίνεται μεταξύ $0.90\omega_{2A}$ και $1.40\omega_{2A}$, όπου $\omega_{2A}=\omega_1=12.679\text{sec}^{-1}$ ($f_1=2.018\text{Hz}$, $T_1=0.50\text{sec}$). Για λόγο συχνοτήτων που κυμαίνεται μεταξύ $\Omega/\omega_{2A}=1.17$ και $\Omega/\omega_{2A}=1.33$ παρατηρούνται δύο πλάτη μόνιμης ταλάντωσης που εξαρτώνται από τις αρχικές συνθήκες, προκαλώντας μεγαλύτερη καμπύλωση του διαγράμματος απόκρισης σε σύγκριση με αυτή των προηγούμενων κατανομών φόρτισης και συνεπώς εντονότερη μη γραμμική δυναμική συμπεριφορά. Θεωρώντας φορτίο με μέγιστη τιμή $P_0=24\text{kN}$ και συχνότητα Ω να κυμαίνεται μεταξύ $0.30\omega_{2A}$ και $0.60\omega_{2A}$, η μόνιμη απόκριση της μετατόπισης του κόμβου 458 δίνεται στο Σχήμα 29β. Η μέγιστη παραμόρφωση παρατηρείται για $\Omega=0.47\omega_{2A}=5.96\text{sec}^{-1}$ (0.95Hz), δηλώνοντας έναν υπεραρμονικό συντονισμό τρίτης τάξεως για την ιδιομορφή 2A.



Σχήμα 29: Μόνιμη απόκριση δικτύου καλωδίων με ακλόνητες στηρίξεις υπό συντονισμό για την ιδιομορφή 2A: (α) θεμελιώδης συντονισμός ($P_0=2\text{kN}$), (β) υπεραρμονικός συντονισμός ($P_0=24\text{kN}$)

A.7.4. Δίκτυο καλωδίων με περιμετρικό δακτύλιο

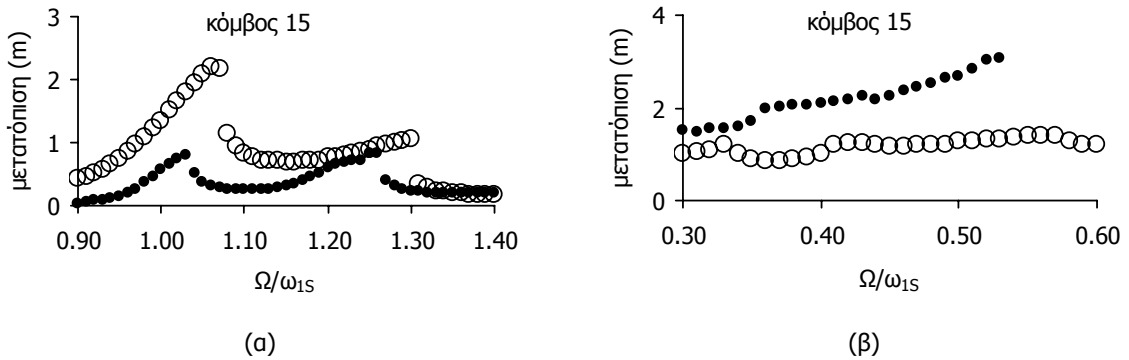
A.7.4.1. Ιδιοσυχνότητες και ιδιομορφές

Η πρώτη ιδιομορφή του συστήματος είναι η εντός-επιπέδου ιδιομορφή του δακτυλίου με συχνότητα $\omega_r=8.679\text{sec}^{-1}$, ενώ ακολουθούν οι ιδιομορφές του δικτύου καλωδίων. Η πρώτη συμμετρική ιδιομορφή του δικτύου καλωδίων είναι η πέμπτη ιδιομορφή με συχνότητα $\omega_r=14.69\text{sec}^{-1}$.

A.7.4.2. Ομοιόμορφη κατανομή φορτίου (1S)

Τα διαγράμματα της απόκρισης του κεντρικού κόμβου σε θεμελιώδη και υπεραρμονικό συντονισμό για την ιδιομορφή 1S δίνονται στο Σχήμα 30, όπου για σύγκριση δίνεται η απόκριση και του δικτύου με ακλόνητες στηρίξεις καλωδίων.

● περιμετρικός δακτύλιος ○ ακλόνητες στηρίξεις



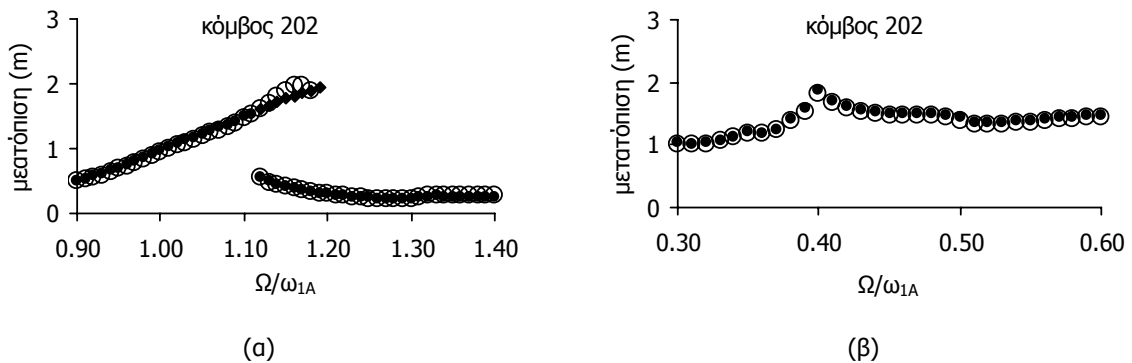
Σχήμα 30: Μόνιμη απόκριση δικτύου καλωδίων με ακλόνητες στηρίξεις υπό συντονισμό για την ιδιομορφή 1S: (α) θεμελιώδης συντονισμός ($P_0=2kN$), (β) υπεραρμονικός συντονισμός ($P_0=24kN$)

Παρατηρείται ότι για την περίπτωση που η συχνότητα του φορτίου είναι κοντά στη συχνότητα 1S, η απόκριση είναι μικρότερη για το δίκτυο καλωδίων με περιμετρικό δακτύλιο. Αυτό συμβαίνει γιατί η εντός επιπέδου ταλάντωση του δακτυλίου προκαλεί αντίθετη ταλάντωση στο δίκτυο καλωδίων από αυτή που προκαλεί το εξωτερικό φορτίο, μειώνοντας έτσι το πλάτος της ταλάντωσης του δικτύου. Αντιθέτως, στην περίπτωση υπεραρμονικού συντονισμού η απόκριση είναι μεγαλύτερη για το δίκτυο με περιμετρικό δακτύλιο, επειδή η συχνότητα του φορτίου είναι πολύ κοντά στη συχνότητα της ιδιομορφής του δακτυλίου προκαλώντας θεμελιώδη συντονισμό γι' αυτήν την ιδιομορφή και επομένως μεγάλες μετατοπίσεις και στο δίκτυο.

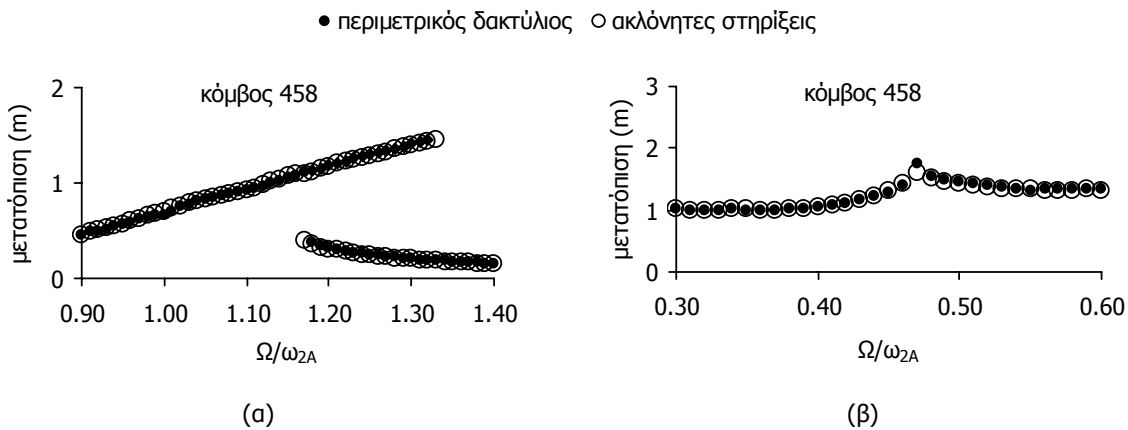
A.7.4.3. Αντισυμμετρικές κατανομές φορτίου (1A και 2A)

Τα διαγράμματα της απόκρισης λαμβάνοντας υπόψη αντισυμμετρική κατανομή του φορτίου σύμφωνα με την ιδιομορφή 1A δίνονται στο Σχήμα 31. Σε αυτήν την περίπτωση η παρουσία του δακτυλίου δεν επηρεάζει την απόκριση του δικτύου καλωδίων. Αντιστοίχως, ο δακτύλιος δεν επηρεάζει και τη μόνιμη απόκριση σε περίπτωση αντισυμμετρικής κατανομής φορτίου σύμφωνα με την ιδιομορφή 2A όπως φαίνεται στο Σχήμα 32.

● περιμετρικός δακτύλιος ○ ακλόνητες στηρίξεις



Σχήμα 31: Μόνιμη απόκριση υπό (α) θεμελιώδη και (β) υπεραρμονικό συντονισμό για την ιδιομορφή 1A

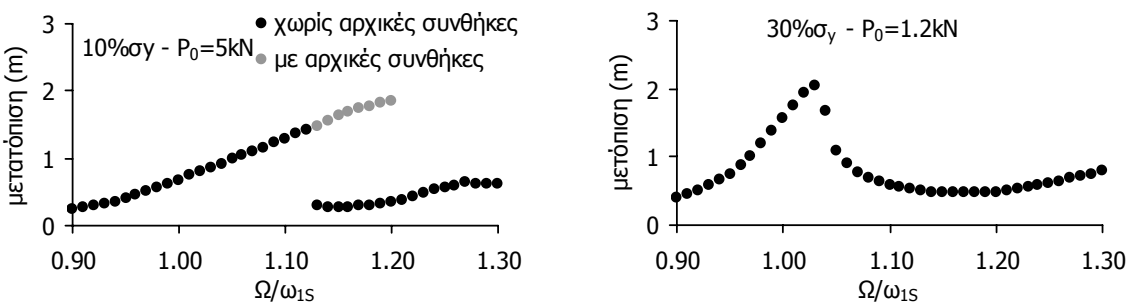


Σχήμα 32: Μόνιμη απόκριση υπό (α) θεμελιώδη και (β) υπεραρμονικό συντονισμό για την ιδιομορφή 2A

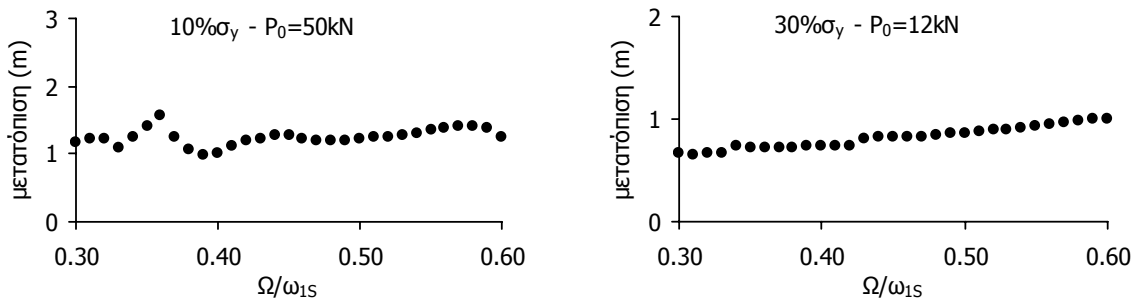
A.7.5. Παραμετρικές αναλύσεις

A.7.5.1. Επιρροή της αρχικής τάσης καλωδίων

Στο παράδειγμα της παραγράφου A.7.1, η αρχική τάση καλωδίων έφτανε στο 19% του ορίου διαρροής. Διατηρώντας τη γεωμετρία του δικτύου και λαμβάνοντας διάμετρο καλωδίου $D=80\text{mm}$ και $D=40\text{mm}$ με αρχική προένταση $N_0=800\text{kN}$ και $N_0=600\text{kN}$, αντίστοιχα, προκύπτουν αρχικές τάσεις καλωδίων 10% και 30%, αντίστοιχα. Το φορτίο επιλέγεται έτσι ώστε να είναι αρκετά μεγάλο χωρίς όμως να προκαλεί μεγάλες τάσεις καλωδίων, ξεπερνώντας το όριο διαρροής. Τα διαγράμματα της μόνιμης απόκρισης υπό θεμελιώδη συντονισμό για την ιδιομορφή 1S δίνονται στο Σχήμα 33 όπου παρατηρείται ότι τα χαμηλά επίπεδα αρχικής τάσης καλωδίων οδηγούν σε μία έντονη μη γραμμική συμπεριφορά, με έντονη καμπύλωση του διαγράμματος, απότομη μείωση της απόκρισης και επιρροή των αρχικών συνθηκών, ενώ τα υψηλά επίπεδα αρχικής τάσης καλωδίων προκαλούν διαγράμματα απόκρισης που πλησιάζουν αυτά ενός γραμμικού συστήματος. Για συχνότητες φορτίου μικρότερες από αυτή της ιδιομορφής 1S, η απόκριση δίνεται στο Σχήμα 34, όπου παρατηρούνται υπεραρμονικοί συντονισμοί δεύτερης και τρίτης τάξεως για το σύστημα με αρχική τάση καλωδίων ίση με 10% σ_y , ενώ για 30% σ_y δεν παρατηρούνται απότομες αυξήσεις στο πλάτος ταλάντωσης, επομένως δεν πραγματοποιούνται υπεραρμονικοί συντονισμοί.



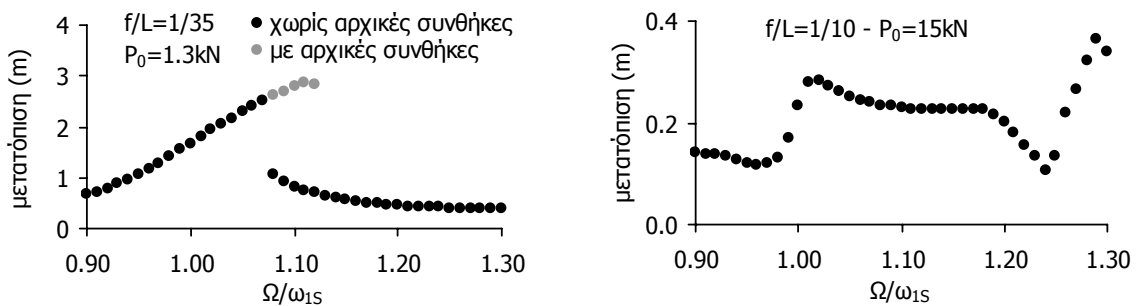
Σχήμα 33: Μόνιμη απόκριση υπό θεμελιώδη συντονισμό για την ιδιομορφή 1S για αρχική τάση καλωδίων 10% σ_y και 30% σ_y



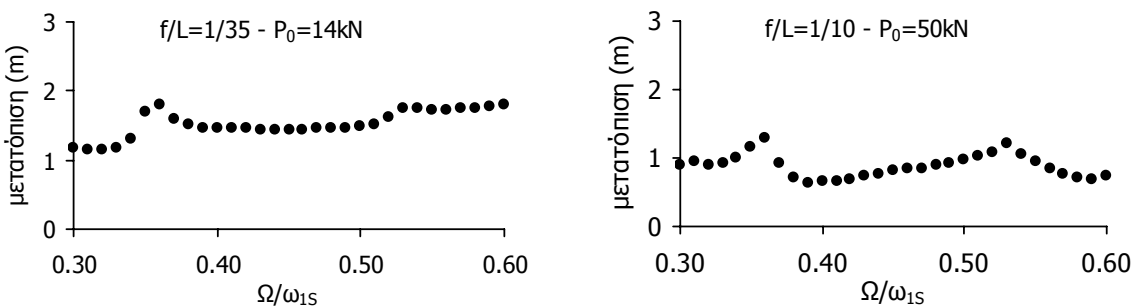
Σχήμα 34: Μόνιμη απόκριση υπό υπεραρμονικό συντονισμό για την ιδιομορφή 1S για αρχική τάση καλωδίων 10%σ_y και 30%σ_y

A.7.5.2. Επιρροή του λόγου βέλους προς άνοιγμα (f/L)

Λαμβάνοντας λόγο βέλους προς άνοιγμα $f/L=1/35$ και $f/L=1/10$ και διατηρώντας όλα τα υπόλοιπα χαρακτηριστικά του δικτύου καλωδίων που περιγράφηκε στην παράγραφο A.7.1, τα διαγράμματα της απόκρισης υπό θεμελιώδη συντονισμό για την ιδιομορφή 1S δίνονται στο Σχήμα 35. Παρατηρείται ότι καθώς ο λόγος f/L μειώνεται, το σύστημα γίνεται πιο εύκαμπτο παρουσιάζοντας μία πιο έντονη μη γραμμική συμπεριφορά, ενώ για μεγάλους λόγους f/L η απόκριση πλησιάζει αυτή ενός γραμμικού συστήματος. Για συχνότητες φορτίου μικρότερες από αυτή της ιδιομορφής, υπεραρμονικοί συντονισμοί δεύτερης και τρίτης τάξεως παρατηρούνται και για τα δύο συστήματα (Σχήμα 36).



Σχήμα 35: Μόνιμη απόκριση υπό θεμελιώδη συντονισμό για την ιδιομορφή 1S για $f/L=1/35$ και $f/L=1/10$



Σχήμα 36: Μόνιμη απόκριση υπό υπεραρμονικό συντονισμό για την ιδιομορφή 1S για $f/L=1/35$ και $f/L=1/10$

A.7.6. Συμπεράσματα

Η συμπεριφορά των δικτύων καλωδίων σε αρμονικά φορτία παρουσιάζει έντονα μη γραμμικά δυναμικά φαινόμενα όπως καμπύλωση του διαγράμματος μόνιμης απόκρισης, απότομη μείωση του πλάτους ταλάντωσης, επιρροή των αρχικών συνθηκών και υπεραρμονικούς συντονισμούς. Το διάγραμμα απόκρισης σε αντισυμμετρική κατανομή του φορτίου παρουσιάζει εντονότερη καμπύλωση από το αντίστοιχο της ομοιόμορφης κατανομής, οδηγώντας σε πιο έντονη μη γραμμική συμπεριφορά. Η

παρουσία του περιμετρικού δακτυλίου επηρεάζει σημαντικά την απόκριση του δικτύου σε ομοιόμορφη φόρτιση, ενώ σε αντισυμμετρική φόρτιση δεν παρατηρούνται διαφορές. Είναι σημαντικό να καθορίζεται μία ρεαλιστική χωρική κατανομή του φορτίου, ειδικότερα στην περίπτωση του ανέμου που η κατανομή στη στέγη εξαρτάται από τη διεύθυνση του ανέμου και από την κλίση της στέγης.

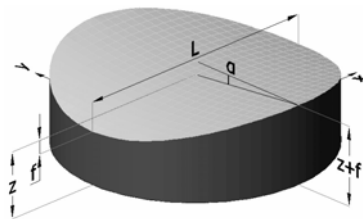
Μέρος της ενότητας αυτής έχει δημοσιευτεί στο [7-19].

A.8. ΧΩΡΙΚΗ ΚΑΤΑΝΟΜΗ ΠΙΕΣΗΣ ΑΝΕΜΟΥ

Προκειμένου να διερευνηθεί η απόκριση τέτοιων στεγών σε ανεμοπιέσεις, ορίζονται οι συντελεστές ανεμοπίεσης c_{pe} , σύμφωνα με τις προτάσεις του Ευρωκώδικα 1 [8-1] για θολωτές και δικλινείς στέγες.

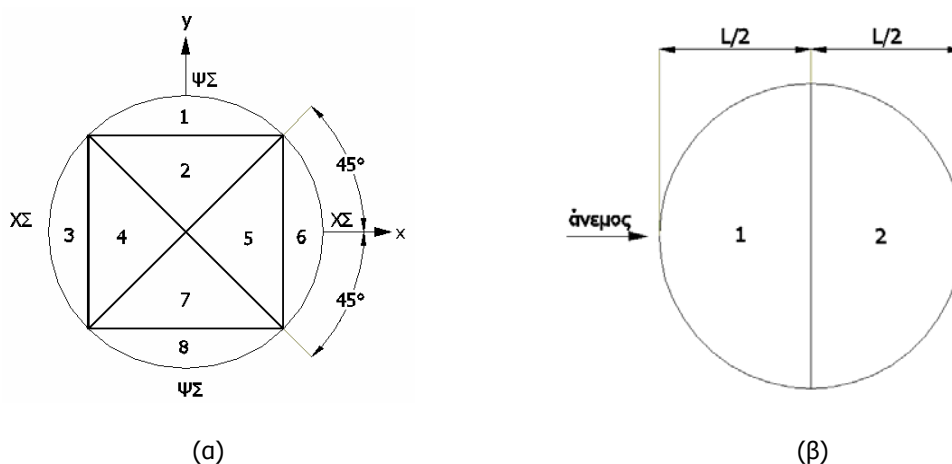
A.8.1. Συντελεστές ανεμοπίεσης σε στέγες υπερβολικού παραβολοειδούς

Η χωρική κατανομή ανέμου βασίζεται στις διατάξεις του Ευρωκώδικα 1. Για να υπολογιστούν οι συντελεστές πίεσης c_{pe} στην επιφάνεια του δικτύου καλωδίων, ορίζεται το υψόμετρο του κεντρικού κόμβου ως τη υψόμετρο όλης της στέγης z και η στέγη χωρίζεται σε ζώνες ανάλογα με την διεύθυνση του ανέμου, και την ισοδύναμη κλίση της στέγης που δίνεται από τη γωνία $\alpha = \arctan(2f/L)$ (Σχήμα 37).



Σχήμα 37: Γεωμετρία δικτύου καλωδίων και ισοδύναμη κλίση στέγης

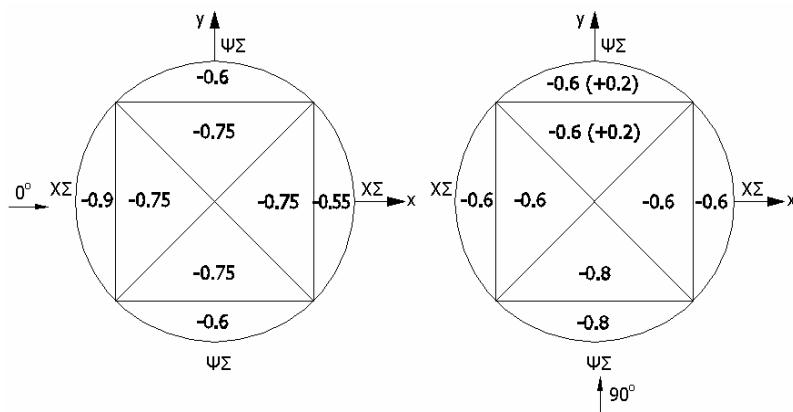
Για γωνίες $\alpha < -5^\circ$ και $\alpha > +5^\circ$, αντιστοιχώντας σε $f/L > 1/22$, η στέγη χωρίζεται σε οκτώ ζώνες (Σχήμα 38α). Για διεύθυνση ανέμου παράλληλα με τον άξονα x (άνεμος 0°), οι ζώνες 2, 3, 4, 5, 6 και 7 προσομοιώνονται ως θολωτή στέγη, ενώ οι ζώνες 1 και 8 ως δικλινής στέγη με αρνητική γωνία ($\alpha < 0$). Για διεύθυνση ανέμου παράλληλα με τον άξονα y (άνεμος 90°), οι ζώνες 1, 2, 7 και 8 προσομοιώνονται ως δικλινής στέγη με $\alpha < 0$, ενώ οι ζώνες 3, 4, 5 και 6 ως δικλινής στέγη με $\alpha > 0$. Για γωνίες $-5^\circ < \alpha < +5^\circ$ που αντιστοιχούν σε $f/L < 1/22$, η στέγη μπορεί να θεωρηθεί ως επίπεδη σύμφωνα με τον Ευρωκώδικα 1. Σε αυτήν την περίπτωση ορίζονται δύο ζώνες ανεμοπίεσης, η προσήνεμη ζώνη 1 και η υπήνεμη ζώνη 2, όπως φαίνεται στο Σχήμα 38β.



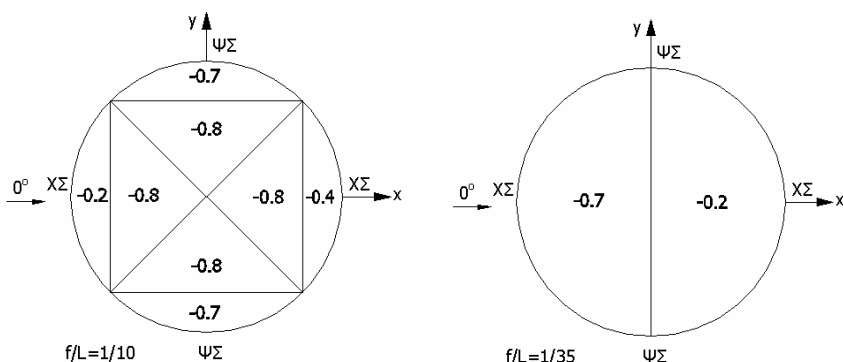
Σχήμα 38: Ζώνες ανεμοπίεσης στέγης υπερβολικού παραβολοειδούς για (α) $f/L > 1/22$ (ΨΣ: Ψηλά Σημεία, ΧΣ: Χαμηλά Σημεία) και (β) $f/L < 1/22$

A.8.2. Αριθμητικά παραδείγματα

Στη συνέχεια μελετούνται τρία δίκτυα καλωδίων με $f/L=1/10$, $1/20$ και $1/35$, για τα οποία οι γωνίες κλίσης είναι 11.31° , 5.71° και 3.27° , αντίστοιχα. Για το δίκτυο καλωδίων με $f/L=1/20$ λαμβάνονται υπόψη δύο κατευθύνσεις ανέμου, για τις οποίες οι συντελεστές ανεμοπίεσης δίνονται στο Σχήμα 39, ενώ για τα υπόλοιπα δίκτυα καλωδίων λαμβάνεται υπόψη μόνο κατεύθυνση ανέμου παράλληλη με τον άξονα x (άνεμος 0°), με αντίστοιχους συντελεστές ανεμοπίεσης που δίνονται στο Σχήμα 40.



Σχήμα 39: Συντελεστές ανεμοπίεσης για δίκτυο καλωδίων με $f/L=1/20$



Σχήμα 40: Συντελεστές ανεμοπίεσης για δίκτυο καλωδίων με $f/L=1/10$ και $f/L=1/35$

Αξίζει να σημειωθεί ότι η προσέγγιση αυτή συγκρινόμενη με αποτελέσματα πειραμάτων παρόμοιων στεγών σε αεροσήραγγες [8-31] δίνει κατανομές με λίγο μεγαλύτερους συντελεστές ανεμοπίεσης χωρίς όμως να ξεπερνά το 20% των μέγιστων τιμών που μετρήθηκαν στα πειράματα.

A.8.3. Συμπεράσματα

Η χωρική κατανομή του ανέμου σε στέγες σχήματος υπερβολικού παραβολοειδούς βασίζεται στις διατάξεις του Ευρωκώδικα 1 για θολωτές και δικλινείς στέγες και κρίνεται ότι προσεγγίζει ικανοποιητικά ρεαλιστικές κατανομές ανέμου.

A.9. ΔΥΝΑΜΙΚΗ ΑΠΟΚΡΙΣΗ ΔΙΚΤΥΩΝ ΚΑΛΩΔΙΩΝ ΣΕ ΦΟΡΤΙΑ ΑΝΕΜΟΥ

Στη συνέχεια μελετάται η δυναμική συμπεριφορά πολυβάθμιων δικτύων καλωδίων στο άνεμο που είναι το σημαντικότερο δυναμικό φορτίο που καταπονεί τέτοιες κατασκευές. Το φορτίο του ανέμου βασίζεται σε πραγματικές καταγραφές ή σε τεχνητά διαγράμματα ταχύτητας ανέμου. Το μέγιστο πλάτος ταλάντωσης συγκρίνεται με αυτό που προκύπτει από ισοδύναμες στατικές μεθόδους όπως προτείνονται από τον Ευρωκώδικα 1 [8-1]. Επίσης διερευνάται η επιρροή της διεύθυνσης ανέμου, του

λόγου βέλους προς άνοιγμα f/L , των ιδιοσυχνότητων του συστήματος και των συνοριακών συνθηκών στη δυναμική απόκριση του δικτύου καλωδίων.

A.9.1. Προσομοίωμα δικτύου καλωδίων

Για τις αναλύσεις σε φορτίο ανέμου λαμβάνεται υπόψη η γεωμετρία του δικτύου καλωδίων της παραγράφου A.7.1. Το υψόμετρο του κεντρικού κόμβου θεωρείται ίσο με $z=25\text{m}$. Η πυκνότητα μάζας των καλωδίων λαμβάνεται ίση με $m=7.85\text{kN}\cdot\text{sec}^2\cdot\text{m}^{-4}$. Επίσης, θεωρείται ένα πρόσθετο μόνο φορτίο ίσο με 0.36kN/m^2 όπως είχε ληφθεί και στη μελέτη του Σταδίου Ειρήνης και Φιλίας [9-10].

A.9.2. Αρχική κατάσταση ισορροπίας

Αρχικώς υπολογίζεται η παραμορφωμένη κατάσταση λόγω των μονίμων φορτίων, η οποία λαμβάνεται ως αρχική κατάσταση για τις δυναμικές αναλύσεις. Παράλληλα πραγματοποιείται ιδιομορφική ανάλυση για να υπολογιστούν οι ιδιοσυχνότητες και οι ιδιομορφές του συστήματος στην ίδια παραμορφωμένη κατάσταση ισορροπίας. Έτσι, η πρώτη ιδιομορφή του συστήματος είναι η αντισυμμετρική 2A με συχνότητα 0.976Hz , ακολουθούν οι δύο ιδιομορφές 1A ως προς του άξονες y και x άξονες, με συχνότητες 0.991Hz και 1.013Hz , αντίστοιχα, οι οποίες δεν έχουν ίσες ιδιοσυχνότητες λόγω της παραμορφωμένης κατάστασης. Η τέταρτη μορφή ταλάντωσης είναι η πρώτη συμμετρική ιδιομορφή με συχνότητα 1.059Hz .

A.9.3. Δράση ανέμου

Σύμφωνα με τον Ευρωκώδικα 1, η μέση τιμή της ταχύτητας ανέμου στο ύψος $z=25\text{m}$ για κατηγορία εδάφους III ($z_0=0.3\text{m}$, $z_{0,II}=0.05\text{m}$, $z_{\min}=5\text{m}$) και για βασική ταχύτητα 30m/sec δίνεται ως εξής:

$$V_m(z)=c_r(z) c_o(z) v_b \Rightarrow V_m(25\text{m})=0.953 \cdot 1.00 \cdot 30\text{m/sec}=28.58\text{m/sec} \quad (63)$$

όπου

$$k_r=0.19(z_0/z_{0,II})^{0.07}=0.19(0.3\text{m}/0.05\text{m})^{0.07}=0.215 \quad (64)$$

$$c_r(z)=k_r \ln(z/z_0) \Rightarrow c_r(25\text{m})=0.215 \ln(25\text{m}/0.3\text{m})=0.953 \quad (65)$$

Η πίεση ταχύτητας αιχμής $q_p(z)$ σε ύψος $z=25\text{m}$ υπολογίζεται ως εξής:

$$q_p(z)=[1+7I_v(z)]1/2\rho(V_m(z))^2 \Rightarrow q_p(25\text{m})=1.32\text{kN/m}^2 \quad (66)$$

όπου $\rho=1,25\text{kg/m}^3$ είναι η πυκνότητα του αέρα, ενώ η ένταση του στροβιλισμού του ανέμου ορίζεται ως:

$$I_v(z)=1/\{\ln(z/z_0) \cdot c_o(z)\}=0.23 \quad (67)$$

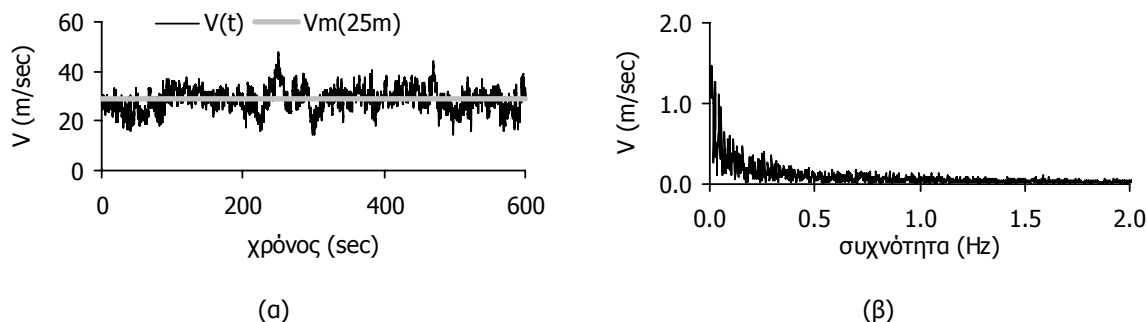
Εφαρμόζοντας την ισοδύναμη στατική μέθοδο που προτείνει ο Ευρωκώδικας 1, η πίεση του ανέμου που δρα στην εξωτερική επιφάνεια της οροφής είναι:

$$w(z)=q_p(z)c_{pe} \Rightarrow w(25\text{m})=1.32c_{pe} \text{ (kN/m}^2) \quad (68)$$

όπου c_{pe} είναι οι συντελεστές πίεσης που δίνονται στο Σχήμα 39. Όπως προτείνεται από τον Ευρωκώδικα 1, ο συντελεστής μεγέθους c_s λαμβάνεται υπέρ της ασφαλείας ίσος με 1, ενώ ο δυναμικός συντελεστής c_d προκύπτει ίσος με 1.054, θεωρώντας ως βασική μορφή ταλάντωσης την πρώτη συμμετρική ιδιομορφή με συχνότητα 1.059Hz . Λαμβάνοντας υπόψη την επιφάνεια επιρροής του κάθε κόμβου, το φορτίο του ανέμου που εφαρμόζεται κατακόρυφα σε κάθε κόμβο του δικτύου είναι:

$$F= c_s c_d w(z)A_{ref}=20.58c_{pe} \text{ (kN)} \quad (69)$$

Το διάγραμμα της ταχύτητας του ανέμου που λαμβάνεται υπόψη στις αναλύσεις προέρχεται από το πείραμα LIST που διεξήχθη στις Η.Π.Α. [9-8]. Η χρονοϊστορία της ταχύτητας και το διάγραμμα Fourier δίνεται στο Σχήμα 41 όπου παρατηρούνται ότι οι βασικές συχνότητες του ανέμου είναι πολύ μικρότερες του 1Hz. Η ελάχιστη και μέγιστη τιμή της ταχύτητας ανέμου είναι 14.35m/sec και 47.41m/sec, αντίστοιχα.



Σχήμα 41: Διαγράμματα ταχύτητας ανέμου: (α) διάγραμμα χρονοϊστορίας, (β) διάγραμμα Fourier

Σε αυτήν την περίπτωση η πίεση ταχύτητας αιχμής $q_p(z)$ σε ύψος $z=25m$ υπολογίζεται ως εξής:

$$q_p(z,t)=1/2\rho(V(t))^2 \Rightarrow q_p(25m)=0.000625 V(t)^2(kN/m^2) \tag{70}$$

Η πίεση του ανέμου που δρα στην εξωτερική επιφάνεια της οροφής είναι:

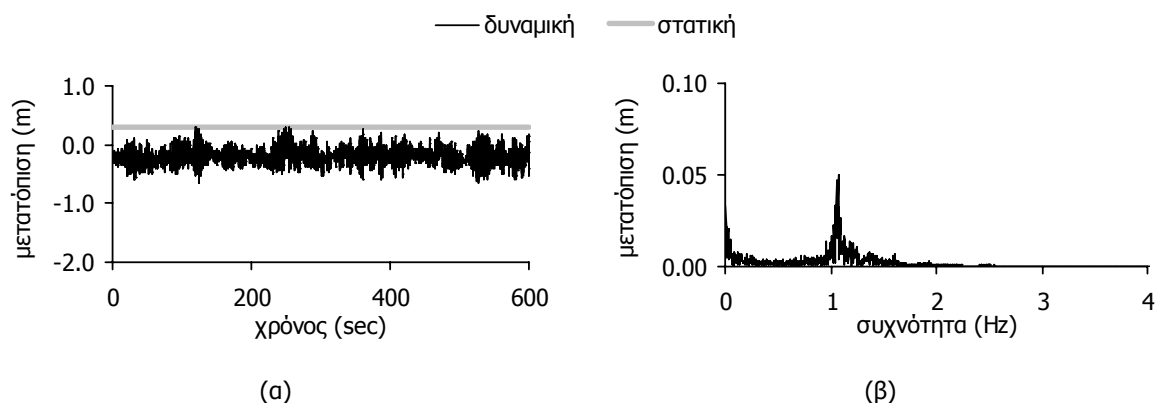
$$w(z,t)=q_p(z,t)c_{pe} \Rightarrow w(25m)= 0.000625 V(t)^2c_{pe} (kN/m^2) \tag{71}$$

Το φορτίο του ανέμου που εφαρμόζεται σε κάθε κόμβο του δικτύου είναι:

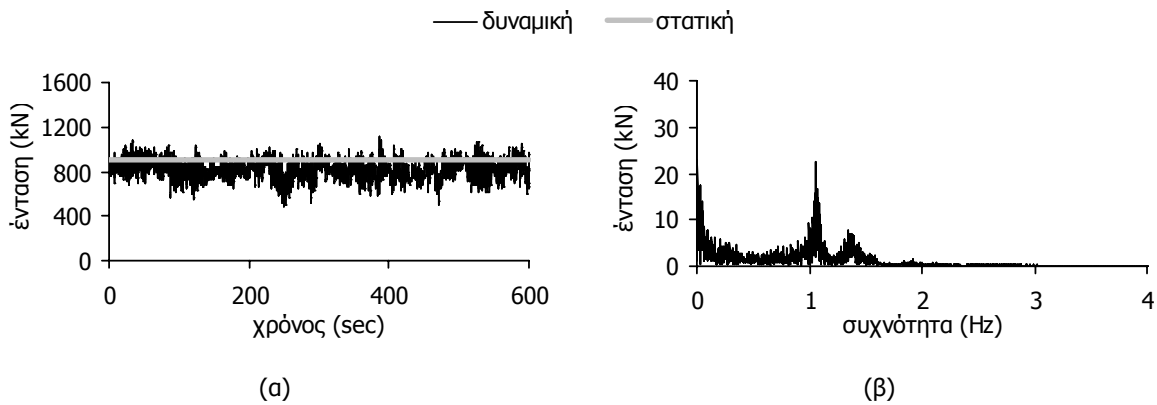
$$F= w(z)A_{ref}=0.00924 V(t)^2c_{pe} (kN) \tag{72}$$

A.9.4. Απόκριση δικτύου καλωδίων

Τα διαγράμματα της απόκρισης του δικτύου καλωδίων στο δυναμικό φορτίο ανέμου δίνονται σε όρους μέγιστης μετατόπισης κεντρικού κόμβου (Σχήμα 42) και μεγίστων εντάσεων καλωδίων (Σχήμα 43). Η μέγιστη θετική παραμόρφωση (προς τα πάνω) που προκύπτει από τη δυναμική ανάλυση είναι περίπου ίση με αυτή της ισοδύναμης στατικής ανάλυσης, ωστόσο, η στατική μέθοδος δεν μπορεί να προβλέψει τη μέγιστη αρνητική παραμόρφωση (προς τα κάτω) του δικτύου. Αντιθέτως η μέγιστη δυναμική ένταση καλωδίων προκύπτει μικρότερη από την αντίστοιχη στατική. Στα φάσματα απόκρισης παρατηρείται ότι το δίκτυο καλωδίων ταλαντώνεται με συχνότητες κοντά στις ιδιοσυχνότητες παρ' όλο που οι συχνότητες του ανέμου είναι πολύ μικρότερες.



Σχήμα 42: Μετατόπιση κεντρικού κόμβου: (α) χρονοϊστορία, (β) φάσμα απόκρισης



Σχήμα 43: Μέγιστη ένταση καλωδίων: (α) χρονοϊστορία, (β) φάσμα απόκρισης

Ένα πολύ μικρό μέγεθος εξωτερικής διέγερσης με συχνότητα κοντά στις ιδιοσυχνότητες του συστήματος μπορεί να προκαλέσει θεμελιώδη συντονισμό παρά την ύπαρξη απόσβεσης. Παράλληλα, οι μικρές συχνότητες του ανέμου μπορούν να διεγείρουν τις ιδιομορφές του δικτύου καλωδίων και να προκαλέσουν υπεραρμονικό συντονισμό, αυξάνοντας το πλάτος της ταλάντωσης και καταλήγοντας σε δυσμενέστερα αποτελέσματα σε σχέση με αυτά των ισοδύναμων στατικών μεθόδων.

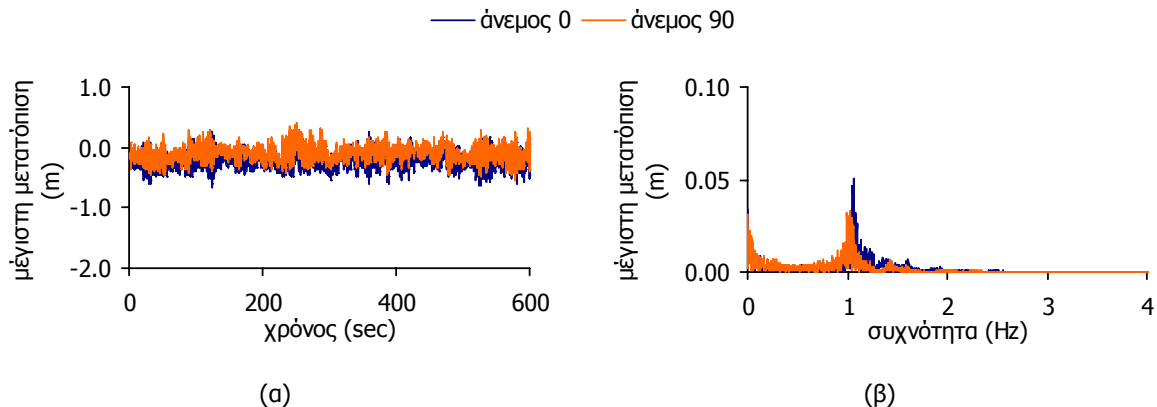
A.9.5. Παραμετρικές αναλύσεις

A.9.5.1. Επιρροή διεύθυνσης ανέμου

Για διεύθυνση ανέμου κάθετα στον άξονα x (άνεμος 90°) οι συντελεστές ανεμοπίεσης c_{pe} για το δίκτυο καλωδίων που μελετάται δίνονται και πάλι στο Σχήμα 39. Από τις δύο τιμές της υπήνεμης πλευράς λαμβάνεται υπόψη η θετική τιμή ($c_{pe}=+0.20$) για την οποία προκύπτει μία αντισυμμετρική κατανομή ανεμοπίεσης στο δίκτυο καλωδίων. Σε αυτήν την περίπτωση το στατικό φορτίο ανέμου υπολογίζεται για δυναμικό συντελεστή $c_d=1.06$, λαμβάνοντας υπόψη ως κύρια μορφή ταλάντωσης την τρίτη ιδιομορφή που είναι η ιδιομορφή 1A με ιδιοσυχνότητα 1.013Hz. Επομένως:

$$F = c_s c_d w(z) A_{ref} = 1.06 \cdot 1.32 \cdot (3.846\text{m})^2 c_{pe} = 20.70 c_{pe} \text{ (kN/node)} \quad (73)$$

Στο Σχήμα 44 δίνονται τα διαγράμματα των παραμορφώσεων του δικτύου καλωδίων, όπου φαίνεται ότι η μέγιστη αρνητική παραμόρφωση παρουσιάζεται για διεύθυνση ανέμου 0° . Τα φάσματα απόκρισης δίνουν και πάλι μεγάλα πλάτη ταλάντωσης για συχνότητες ίσες με τις ιδιοσυχνότητες, οδηγώντας στο συμπέρασμα ότι συμβαίνουν θεμελιώδεις και υπεραρμονικοί συντονισμοί.



Σχήμα 44: Μέγιστη παραμόρφωση δικτύων καλωδίων ανάλογα με τη διεύθυνση ανέμου: (α) χρονοϊστορίες, (β) φάσματα απόκρισης

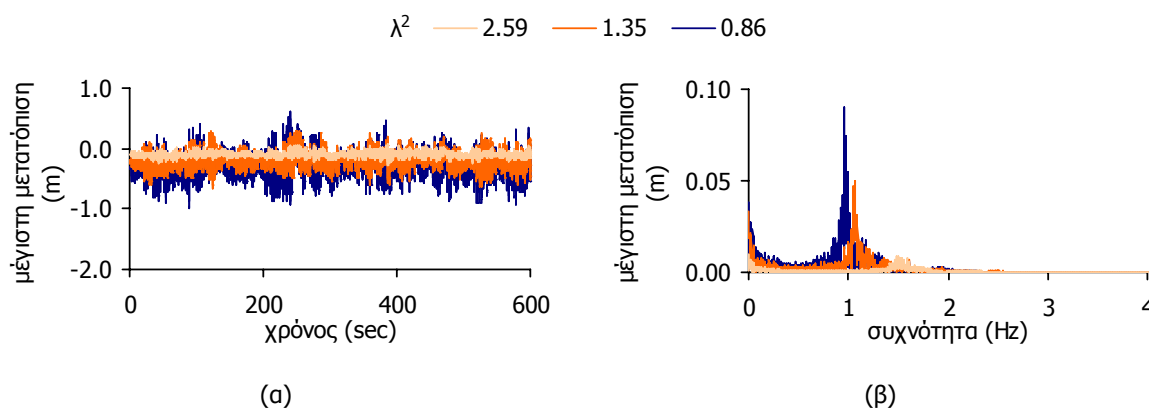
A.9.5.2. Επιρροή παραμέτρου λ^2

Η αρχική τάση καλωδίων του συστήματος που περιγράφηκε στην παράγραφο A.9.1 είναι ίση με 19% του ορίου διαρροής σ_y , που θεωρείται μία συνήθης τιμή για τέτοιες κατασκευές. Στην παράγραφο αυτή θεωρείται διάμετρος καλωδίων $D=80\text{mm}$ και αρχική προένταση $N_0=800\text{kN}$, αντιστοιχώντας σε αρχική τάση καλωδίων $10\%\sigma_y$, καθώς επίσης και διάμετρος καλωδίων $D=40\text{mm}$ και αρχική προένταση $N_0=600\text{kN}$, οδηγώντας σε αρχική τάση καλωδίων $30\%\sigma_y$. Υπολογίζοντας την παράμετρο λ^2 των συστημάτων με τα τρία διαφορετικά ποσοστά αρχικής τάσης (Πίνακας 6) παρατηρείται ότι το πρώτο δίκτυο καλωδίων με τη μικρότερη αρχική τάση αντιστοιχεί στη μεγαλύτερη παράμετρο λ^2 .

Πίνακας 6: Χαρακτηριστικά δικτύων καλωδίων με διαφορετικές διαμέτρους και αρχικές τάσεις καλωδίων

Δίκτυο καλωδίων	D [mm]	N_0 [kN]	$N_0/(A\sigma_y)$ [%]	λ^2	$\omega_{1S}[\text{sec}^{-1}]$	$f_{1S}[\text{Hz}]$
1	80	800	10	2.59	7.696	1.225
2	50	600	19	1.35	6.654	1.059
3	40	400	30	0.86	6.085	0.968

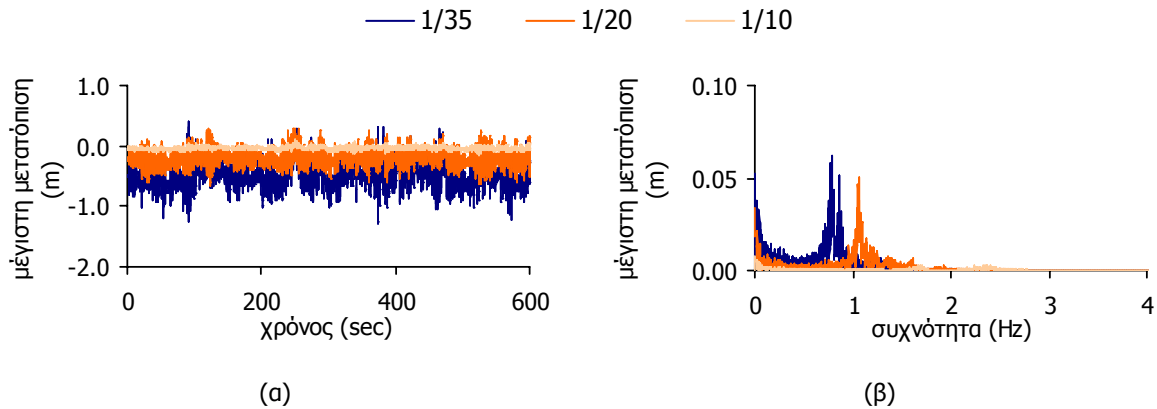
Το δίκτυο καλωδίων με τη μικρότερη αρχική τάση παρουσιάζει μικρότερα πλάτη ταλάντωσης από τα άλλα δίκτυα καλωδίων, όπως φαίνεται στο Σχήμα 45. Επίσης, καθώς αυξάνεται η παράμετρος λ^2 μειώνεται το πλάτος της ταλάντωσης.

Σχήμα 45: Μέγιστη παραμόρφωση δικτύων καλωδίων ανάλογα με την παράμετρο λ^2 : (α) χρονιοίστοιες, (β) φάσματα απόκρισηςA.9.5.3. Επιρροή λόγου βέλους προς άνοιγμα f/L

Διατηρώντας τα χαρακτηριστικά του δικτύου καλωδίων της παραγράφου A.9.1, δύο ακόμα συστήματα μελετώνται με λόγους βέλους προς άνοιγμα $f/L=1/35$ και $f/L=1/10$, αντιστοιχώντας σε ένα ρηχό και σε ένα βαθύ δίκτυο καλωδίων, αντίστοιχα. Οι συντελεστές ανεμοπίεσης c_{pe} για τα δύο αυτά συστήματα δίνονται στο Σχήμα 40. Ο Πίνακας 7 περιλαμβάνει τα χαρακτηριστικά των δύο δικτύων καλωδίων και αυτού που περιγράφηκε στην παράγραφο A.9.1, όπου φαίνεται ότι για το ρηχό δίκτυο καλωδίων προκύπτει η μεγαλύτερη παράμετρος λ^2 (Πίνακας 7). Μεγάλες καμπυλότητες οδηγούν σε μεγάλες δυσκαμψίες και συνεπώς σε μικρά πλάτη ταλάντωσης (Σχήμα 46). Επίσης, επιβεβαιώνεται άλλη μια φορά ότι καθώς αυξάνεται η τιμή της παραμέτρου λ^2 μειώνεται το πλάτος της ταλάντωσης.

Πίνακας 7: Χαρακτηριστικά δικτύων με διαφορετικά f/L

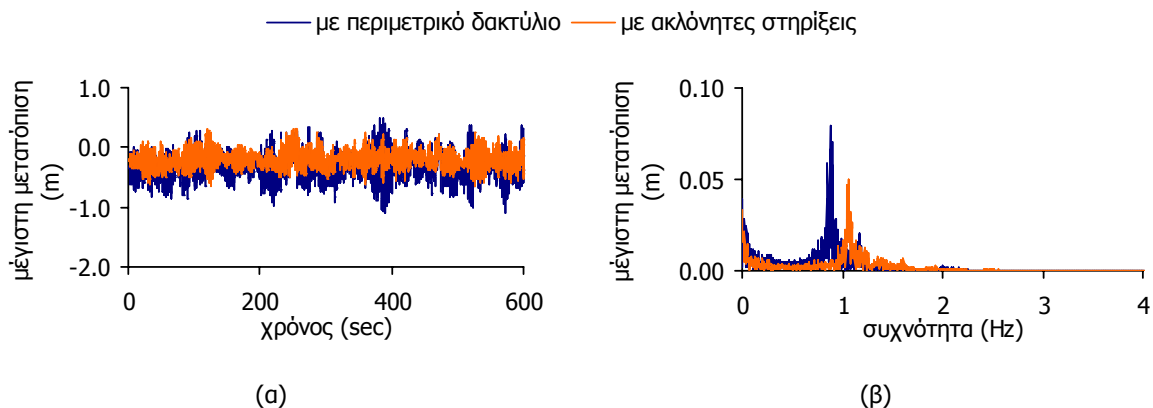
Δίκτυο καλωδίων	f/L	λ^2	$\omega_{1S}[\text{sec}^{-1}]$	$f_{1S}[\text{Hz}]$	$\omega_{1A}[\text{sec}^{-1}]$	$f_{1A}[\text{Hz}]$
1	1/35	0.44	-	-	5.253	0.836
2	1/20	1.35	6.654	1.059	-	-
3	1/10	5.40	8.205	1.306	-	-



Σχήμα 46: Μέγιστη παραμόρφωση δικτύων καλωδίων ανάλογα με το λόγο βέλους προς άνοιγμα f/L : (α) χρονοϊστορίες, (β) φάσματα απόκρισης

A.9.5.4. Επιρροή συνοριακών συνθηκών

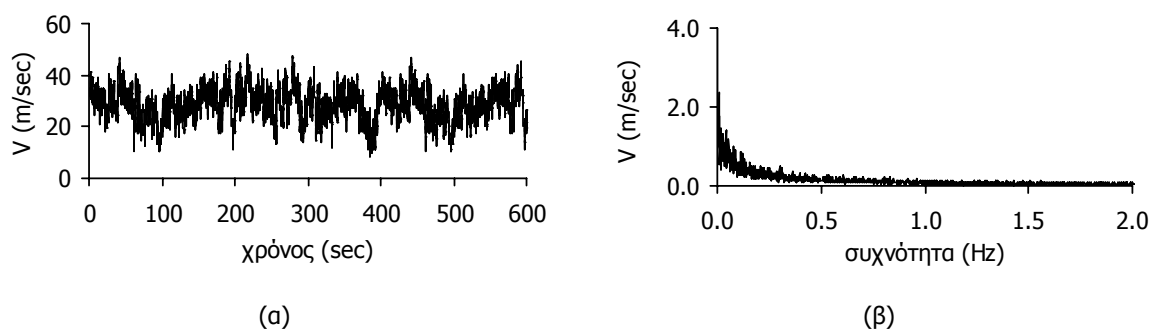
Στη συνέχεια προσομοιώνεται ο περιμετρικός δακτύλιος με τετραγωνική κοίλη διατομή πλάτους $b=6.0\text{m}$ και πάχους 0.6m , ειδικό βάρος $\rho_r=25\text{kN/m}^3$ και μέτρο ελαστικότητας $E_r=37\text{GPa}$. Η εντός επιπέδου ιδιομορφή του δακτυλίου έχει συχνότητα $\omega_r=5.54\text{sec}^{-1}$ (0.882Hz), που είναι πολύ πιο κοντά στις συχνότητες του ανέμου, ενώ η πρώτη συμμετρική ιδιομορφή του δικτύου καλωδίων έχει συχνότητα $\omega_{1S}=7.358\text{sec}^{-1}$ (1.171Hz). Η δυναμική απόκριση του δικτύου καλωδίων με τον περιμετρικό δακτύλιο είναι μεγαλύτερη σε σχέση με αυτήν του συστήματος με ακλόνητες στηρίξεις. Στο Σχήμα 47 δίνονται τα διαγράμματα της μέγιστης μετατόπισης για τα δύο δίκτυα καλωδίων. Το φάσμα απόκρισης δείχνει ότι για το δίκτυο με τον δακτύλιο ενεργοποιείται η ιδιομορφή του δακτυλίου, η οποία προκαλεί τις μεγαλύτερες ταλαντώσεις.



Σχήμα 47: Μέγιστη παραμόρφωση δικτύων καλωδίων ανάλογα με τις συνοριακές συνθήκες: (α) χρονοϊστορίες, (β) φάσματα απόκρισης

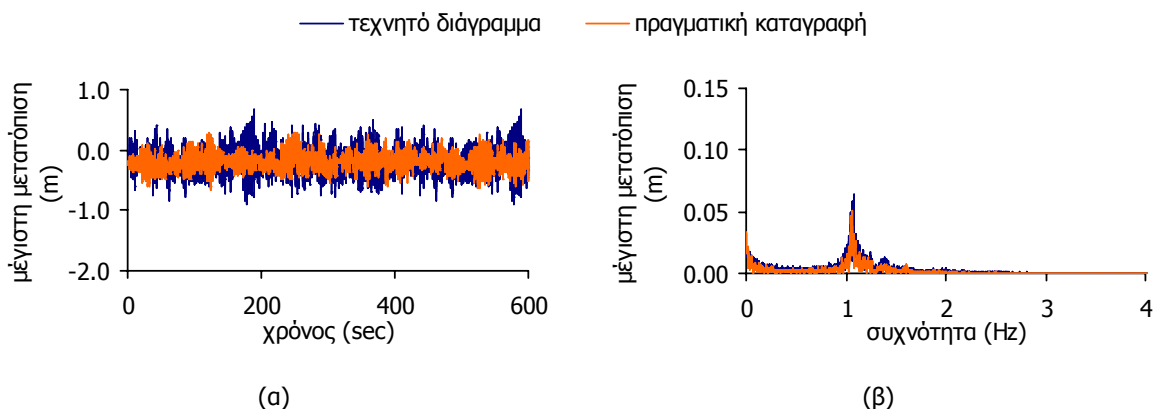
A.9.5.5. Τεχνητό διάγραμμα ταχύτητας ανέμου

Στην περίπτωση που δεν διατίθεται μία πραγματική καταγραφή ανέμου, μπορεί να δημιουργηθεί ένα τεχνητό διάγραμμα βασισμένο στη διαδικασία που προτείνεται στο [9-14]. Στην παρούσα εργασία, το διάγραμμα που χρησιμοποιείται δίνεται στο Σχήμα 48, λαμβάνοντας υπόψη το φάσμα ανέμου που περιέχεται στον Ευρωκώδικα 1 [8-1] και μέση τιμή ταχύτητας ανέμου ίση με 28.58m/sec , όπως υπολογίστηκε από την Εξ. (63).



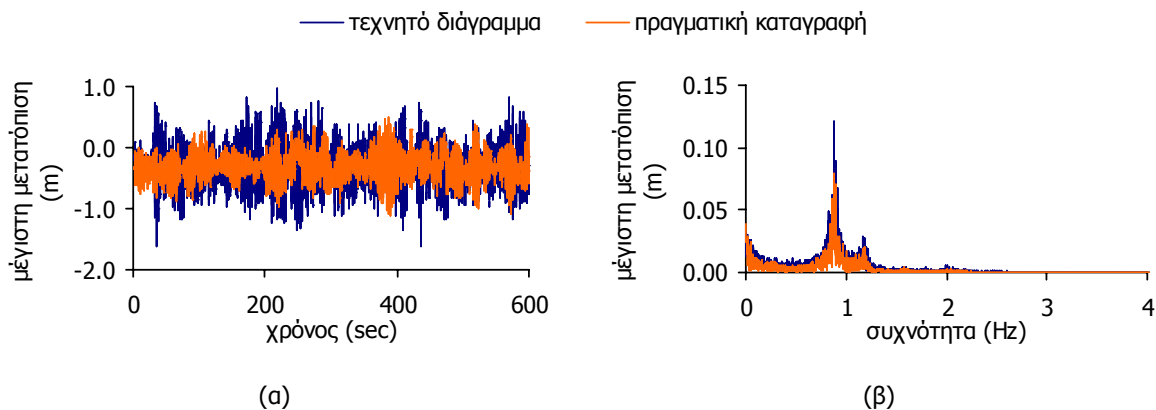
Σχήμα 48: Τεχνητό διάγραμμα ταχύτητας ανέμου: (α) διάγραμμα χρονοϊστορίας, (β) διάγραμμα Fourier

Το τεχνητό διάγραμμα είναι παρόμοιο με την πραγματική καταγραφή της ταχύτητας του ανέμου που δίνεται στο Σχήμα 41. Η μέγιστη και η ελάχιστη τιμή του διαγράμματος είναι 48.01m/sec και 8.47m/sec, αντίστοιχα. Η μέγιστη τιμή είναι πολύ κοντά στην αντίστοιχη του διαγράμματος που δίνεται στο Σχήμα 41a, ενώ η ελάχιστη τιμή είναι μικρότερη από την αντίστοιχη του ίδιου διαγράμματος οδηγώντας σε μεγαλύτερη διακύμανση. Οι κύριες συχνότητες του ανέμου είναι πολύ μικρότερες από 1Hz, όπως και στο Σχήμα 41β. Το φορτίο του ανέμου που προκύπτει από το διάγραμμα αυτό εφαρμόζεται στο δίκτυο καλωδίων με ακλόνητες στηρίξεις που περιγράφηκε στην παράγραφο A.9.1 και σε αυτό με τον περιμετρικό δακτύλιο της παραγράφου A.9.5.4. Στο Σχήμα 49 φαίνεται ότι η απόκριση είναι λίγο μεγαλύτερη για το τεχνητό διάγραμμα ταχύτητας ανέμου. Ωστόσο, οι συχνότητες ταλάντωσης και για τα δύο διαγράμματα είναι ίδιες.



Σχήμα 49: Μέγιστη παραμόρφωση δικτύων καλωδίων με ακλόνητες στηρίξεις ανάλογα με το διάγραμμα ανέμου: (α) χρονοϊστορίες, (β) φάσματα απόκρισης

Ανάλογα συμπεράσματα προκύπτουν και για το σύστημα με τον περιμετρικό δακτύλιο (Σχήμα 50). Επομένως σε περίπτωση που δεν διατίθεται ένα διάγραμμα πραγματικής καταγραφής ανέμου, ένα τεχνητό διάγραμμα ανέμου, όπως περιγράφεται στο [9-14], μπορεί να δώσει αξιόπιστα αποτελέσματα.



Σχήμα 50: Μέγιστη παραμόρφωση δικτύων καλωδίων με περιμετρικό δακτύλιο ανάλογα με το διάγραμμα ανέμου: (α) χρονοϊστορίες, (β) φάσματα απόκρισης

A.9.6. Συμπεράσματα

Η διερεύνηση της απόκρισης δικτύων καλωδίων σε δυναμικό φορτίο ανέμου αποδεικνύει ότι οι ισοδύναμες στατικές μέθοδοι που προτείνονται από τον Ευρωκώδικα 1 δεν μπορούν να δώσουν αξιόπιστα αποτελέσματα εφόσον δεν μπορούν να λάβουν υπόψη τους μη γραμμικά δυναμικά φαινόμενα όπως είναι οι υπεραρμονικοί συντονισμοί που αυξάνουν το πλάτος της ταλάντωσης. Όσο αυξάνεται η παράμετρος λ^2 τόσο μικραίνει το πλάτος της ταλάντωσης των δικτύων καλωδίων. Η προσομοίωση του περιμετρικού δακτυλίου επηρεάζει σημαντικά την απόκριση του δικτύου καλωδίων, γιατί ενεργοποιείται η εντός επιπέδου ιδιομορφή του δακτυλίου προκαλώντας μεγάλες ταλαντώσεις στο δίκτυο καλωδίων.

Μέρος της ενότητας αυτής έχει παρουσιαστεί στα συνέδρια [9-15] και [9-16].

A.10. ΣΥΝΟΨΗ ΚΑΙ ΣΥΜΠΕΡΑΣΜΑΤΑ

Σκοπός της εργασίας αυτής είναι η διερεύνηση της απόκρισης δικτύων καλωδίων υπό δυναμικά φορτία, εστιάζοντας την προσοχή στα δυναμικά φαινόμενα που χαρακτηρίζουν τα μη γραμμικά συστήματα. Αρχικώς μορφώνεται η εξίσωση κίνησης ενός απλού δικτύου καλωδίων που αποτελείται από δύο καθέτως διασταυρούμενα καλώδια με ίσο και αντίθετο αρχικό βέλος. Αναπτύσσοντας σε σειρά Taylor και αμελώντας μικρούς όρους, η εξίσωση κίνησης προκύπτει παρόμοια με αυτή του ταλαντωτή Duffing. Η αναλυτική λύση της μόνιμης απόκρισης της εξίσωσης Duffing διατίθεται στη βιβλιογραφία και υιοθετείται σε αυτήν την εργασία για την περίπτωση του ανωτέρω δικτύου καλωδίων. Επιβεβαιώνονται κύριοι και δευτερεύοντες συντονισμοί, όπως είναι ο υπεραρμονικός και ο υποαρμονικός συντονισμός. Η σχέση της μόνιμης παραμόρφωσης με τη συχνότητα της ταλάντωσης απεικονίζεται γραφικά για διάφορες συνθήκες συντονισμού, παρουσιάζοντας καμπύλωση του διαγράμματος της απόκρισης και εξάρτηση της απόκρισης από τις αρχικές συνθήκες. Αυτό επιβεβαιώνεται επιλύοντας αριθμητικά την εξίσωση κίνησης καθώς και χρησιμοποιώντας το λογισμικό ADINA, με το οποίο πραγματοποιούνται μη γραμμικές δυναμικές αναλύσεις. Με τη διερεύνηση αυτού του απλού δικτύου, επιτυγχάνεται ένα πολύ σημαντικό βήμα προς την κατανόηση των δυναμικών φαινομένων που διέπουν τη συμπεριφορά των δικτύων καλωδίων.

Στη συνέχεια, θεωρείται ένα πολυβάθμιο δίκτυο καλωδίων σχήματος υπερβολικού παραβολοειδούς με κυκλική κάτοψη, παρόμοιο με τη στέγη του Σταδίου Ειρήνης και Φιλίας στο Φάληρο. Τα άκρα των καλωδίων θεωρείται ότι αγκυρώνονται είτε σε ακλόνητες στηρίξεις είτε σε έναν παραμορφώσιμο περιμετρικό δακτύλιο, πολύ πιο δύσκαμπτο από το δίκτυο καλωδίων. Υπολογίζονται οι πρώτες συμμετρικές και αντισυμμετρικές ιδιομορφές με τις αντίστοιχες ιδιοσυχνότητες. Παραμετρικές

αναλύσεις δείχνουν ότι μεταβάλλοντας το λόγο βέλους προς άνοιγμα και τα μηχανικά χαρακτηριστικά των καλωδίων, η σειρά των πρώτων ιδιομορφών αλλάζει. Μία αδιαστατοποιημένη παράμετρος λ^2 , ανάλογη με αυτήν που είναι γνωστή από τη θεωρία των απλών καλωδίων, προτείνεται και για τα δίκτυα καλωδίων σε αυτή την εργασία, η οποία εξαρτάται από το λόγο βέλους προς άνοιγμα και την αρχική ανηγμένη επιμήκυνση των καλωδίων και καθορίζει τη σειρά εμφάνισης των ιδιομορφών. Για διάφορες τιμές αυτής της παραμέτρου, δύο ή περισσότερες ιδιομορφές με διαφορετικό σχήμα έχουν ίσες συχνότητες, φαινόμενο που χαρακτηρίζεται ως εσωτερικός συντονισμός. Γνωρίζοντας το σημαντικό ρόλο που παίζει αυτή η παράμετρος στη δυναμική απόκριση των μη γραμμικών συστημάτων, είναι εύκολο να επιλεγούν κατάλληλα τα μηχανικά και γεωμετρικά χαρακτηριστικά των δικτύων καλωδίων, έτσι ώστε να αποφευχθούν τέτοιου είδους συντονισμοί. Βάσει των αποτελεσμάτων των παραμετρικών αναλύσεων προτείνονται ημι-εμπειρικές σχέσεις για τον υπολογισμό των πρώτων ιδιοσυχνοτήτων του συστήματος, ενώ η σύγκριση αυτών με αποτελέσματα ιδιομορφικών αναλύσεων είναι πολύ ικανοποιητική. Αποδεικνύεται επίσης ότι η προσομοίωση του περιμετρικού δακτυλίου επηρεάζει σημαντικά τη συμμετρική ιδιομορφή του δικτύου καλωδίων και την αντίστοιχη ιδιοσυχνότητα, λόγω της ύπαρξης μιας εντός επιπέδου ιδιομορφής του δακτυλίου. Αντιθέτως, οι αντισυμμετρικές ιδιομορφές παραμένουν ανεπηρέαστες από την παρουσία του δακτυλίου.

Η δυναμική απόκριση ενός πολυβάθμιου συστήματος δικτύου καλωδίων προσεγγίζεται αρχικώς χρησιμοποιώντας ένα ισοδύναμο μονοβάθμιο σύστημα. Η μετατροπή των γεωμετρικών και μηχανικών χαρακτηριστικών από το ένα σύστημα στο άλλο βασίζεται σε μια μέθοδο που χρησιμοποιήθηκε στα αρχικά στάδια της έρευνας αυτής και παρέχει κατάλληλες σχέσεις μετασχηματισμού. Λαμβάνοντας υπόψη διαφορετικές γεωμετρικές δικτύων καλωδίων και διαφορετικές αρχικές τάσεις στα καλώδια δημιουργούνται διαγράμματα μόνιμης απόκρισης για το μονοβάθμιο σύστημα βάσει των αναλυτικών λύσεων, ενώ πραγματοποιούνται μη γραμμικές δυναμικές αναλύσεις για το πολυβάθμιο. Η σύγκριση των διαγραμμάτων των δύο συστημάτων οδηγεί στο συμπέρασμα ότι η μέθοδος αυτή μπορεί να δώσει μία ικανοποιητική εκτίμηση της συμπεριφοράς του πολυβάθμιου συστήματος, με κυριότερο πλεονέκτημα ότι μπορεί να προσδιορίσει το μέγεθος και τη συχνότητα του φορτίου που μπορεί να προκαλέσει μη γραμμικά φαινόμενα με μικρό σφάλμα και σε ελάχιστο υπολογιστικό χρόνο. Παρατηρείται επίσης ότι προκειμένου να πραγματοποιηθούν υπεραρμονικοί ή υποαρμονικοί συντονισμοί απαιτούνται μεγάλα φορτία. Ειδικά για τους υποαρμονικούς συντονισμούς, απαιτούνται και μεγάλα μεγέθη αρχικών παραμορφώσεων και ταχυτήτων. Ο συνδυασμός αυτών των δύο συνθηκών οδηγεί σε αστοχία καλωδίου στην αρχή της ανάλυσης, δηλαδή κατά την παροδική απόκριση, οδηγώντας στο συμπέρασμα ότι ένα πολυβάθμιο δίκτυο καλωδίων δύσκολα μπορεί να συντονιστεί υποαρμονικά.

Η εργασία περιλαμβάνει επίσης μία διερεύνηση της επιρροής της χωρικής κατανομής ενός αρμονικού φορτίου στην απόκριση των δικτύων καλωδίων. Θεωρούνται τρεις διαφορετικές χωρικές κατανομές: μία συμμετρική, μία αντισυμμετρική περί τον έναν οριζόντιο άξονα και μία αντισυμμετρική περί τους δύο οριζόντιους άξονες. Η μόνιμη απόκριση παριστάνεται γραφικά για συχνότητες φορτίου είτε κοντά στην ιδιοσυχνότητα του συστήματος, αποσκοπώντας σε φαινόμενα κύριου συντονισμού, είτε μικρότερες από την ιδιοσυχνότητα, επιδιώκοντας την ενεργοποίηση υπεραρμονικών συντονισμών. Παρατηρείται ότι η καμπύλωση των διαγραμμάτων είναι εντονότερη στην περίπτωση αντισυμμετρικής φόρτισης, και επομένως, για ένα μεγάλο εύρος συχνοτήτων του φορτίου, οι αρχικές συνθήκες καθορίζουν το πλάτος της μόνιμης απόκρισης του συστήματος. Παράλληλα, όταν το δίκτυο καλωδίων φορτίζεται ομοιόμορφα, η παραμορφωσιμότητα του δακτυλίου επηρεάζει σημαντικά το πλάτος της απόκρισης, κάτι που δεν συμβαίνει στην περίπτωση της αντισυμμετρικής φόρτισης.

Τέλος, προκειμένου να μελετηθεί η συμπεριφορά τέτοιων κατασκευών υπό πραγματικά δυναμικά φορτία όπως ο άνεμος, προσδιορίζεται η κατανομή των ανεμοπιέσεων σε τέτοιου είδους επιφάνειες, βασιζόμενη στις συστάσεις του Ευρωκώδικα 1. Η στέγη σχήματος υπερβολικού παραβολοειδούς

χωρίζεται σε ζώνες και δίνονται οι συντελεστές πίεσης για κάθε ζώνη ξεχωριστά, ανάλογα με την διεύθυνση του ανέμου. Συγκρίνοντας την προτεινόμενη κατανομή ανεμοπιέσεων με αποτελέσματα πειραμάτων στεγών σχήματος υπερβολικού παραβολοειδούς σε αεροδυναμική σήραγγα, επιβεβαιώνεται ότι η προσέγγιση που ακολουθείται σε αυτήν την εργασία οδηγεί σε λίγο μεγαλύτερες τιμές συντελεστών ανεμοπίεσης, ενώ η κατανομή των πιέσεων είναι πολύ ικανοποιητική. Στη συνέχεια πραγματοποιούνται μη γραμμικές δυναμικές αναλύσεις χρησιμοποιώντας την προτεινόμενη χωρική κατανομή πιέσεων και μία πραγματική καταγραφή καθώς και μία τεχνητή χρονοϊστορία ανέμου, προκειμένου να εντοπιστούν μη γραμμικά φαινόμενα συντονισμού. Το πλάτος της δυναμικής απόκρισης των δικτύων συγκρίνεται με αυτό που προκύπτει από την ισοδύναμη στατική ανάλυση που προτείνει ο Ευρωκώδικας 1. Παρατηρούνται μεγάλες ταλαντώσεις με συχνότητες ίσες με τις ιδιοσυχνότητες του συστήματος. Το διάγραμμα του ανέμου παρουσιάζει συχνότητες πολύ μικρότερες, ωστόσο προκαλεί υπεραρμονικούς συντονισμούς, ενώ μία μικρή διέγερση, με συχνότητα κοντά στην ιδιοσυχνότητα, προκαλεί κύριο συντονισμό, παρά την ύπαρξη απόσβεσης. Ως αποτέλεσμα παρατηρούνται μεγάλες διαφορές μεταξύ στατικών και δυναμικών αναλύσεων, ενώ καθώς αυξάνεται η τιμή της παραμέτρου λ^2 μειώνεται το πλάτος της ταλάντωσης. Κατόπιν αυτών των αποτελεσμάτων, οι ισοδύναμες στατικές μέθοδοι που λαμβάνουν μόνον έμμεσα υπόψη τα μη γραμμικά δυναμικά φαινόμενα, δεν θεωρούνται ακριβείς για την ανάλυση και διαστασιολόγηση τέτοιων κατασκευών.

A.11. ΠΡΩΤΟΤΥΠΗ ΣΥΜΒΟΛΗ ΤΗΣ ΔΙΑΤΡΙΒΗΣ

Στην εργασία αυτή αποδεικνύεται ότι τα δίκτυα καλωδίων, παρ' όλο που θεωρούνται πολύ πιο δύσκαμπτες κατασκευές από τα απλά καλώδια λόγω των αντίθετων καμπυλοτήτων τους στις δύο διευθύνσεις, παρουσιάζουν παρόμοια συμπεριφορά με αυτά, η οποία, υπό ορισμένες προϋποθέσεις, χαρακτηρίζεται από έντονα μη γραμμικά δυναμικά φαινόμενα. Η απόκριση των δικτύων καλωδίων σε στατικά φορτία μπορεί να υπολογιστεί με ακρίβεια εκτελώντας μη γραμμικές στατικές αναλύσεις που λαμβάνουν υπόψη τη γεωμετρική μη γραμμικότητα, αλλά η καθολική τους δυναμική απόκριση δεν μπορεί να προσεγγιστεί από μεμονωμένες αριθμητικές αναλύσεις. Η διερεύνηση της εξίσωσης κίνησης ενός απλού δικτύου καλωδίων, ως πρώτη προσέγγιση των φαινομένων που διέπουν τη δυναμική συμπεριφορά μη γραμμικών συστημάτων, παρέχει χρήσιμες πληροφορίες για τα δίκτυα καλωδίων.

Η γνώση των ιδιοσυχνοτήτων ενός πολυβάθμιου συστήματος, πριν από το στάδιο της οριστικής μελέτης της κατασκευής, παρέχει πολύτιμες πληροφορίες για τη δυναμική απόκριση του συστήματος, παρ' όλο που αυτές υπολογίζονται με γραμμικές μεθόδους. Η σχέση των ιδιοσυχνοτήτων μεταξύ τους και ο λόγος της συχνότητας της εξωτερικής φόρτισης προς την ιδιοσυχνότητα του συστήματος προμηνύει την εμφάνιση μη γραμμικών συντονισμών. Οι ημι-εμπειρικές σχέσεις που προτείνονται για την εκτίμηση των πρώτων ιδιοσυχνοτήτων ενός δικτύου καλωδίων με ή χωρίς περιμετρικό δακτύλιο μπορούν να χρησιμοποιηθούν σε στάδιο προκαταρκτικής μελέτης ή προμελέτης. Με αυτές μπορούν να επιλεγούν τα γεωμετρικά και μηχανικά χαρακτηριστικά ενός δικτύου καλωδίων με στόχο την αποφυγή εσωτερικών συντονισμών που ενδέχεται να αυξήσουν το πλάτος της ταλάντωσης σε μία δυναμική φόρτιση.

Η μέθοδος του ισοδύναμου μονοβάθμιου συστήματος, που βασίζεται στην εξίσωση κίνησης ενός απλού δικτύου καλωδίων, αποτελεί ένα σημαντικό εργαλείο που οδηγεί στον εντοπισμό των συνθηκών για τις οποίες μπορούν να συμβούν μη γραμμικά φαινόμενα. Διαφορετικά, σε πολυβάθμια συστήματα, η αναζήτηση των συνθηκών αυτών απαιτεί ένα μεγάλο πλήθος μη γραμμικών δυναμικών αναλύσεων μεταβάλλοντας με πολύ μικρά βήματα τη μέγιστη τιμή του φορτίου και τη συχνότητά του θεωρώντας διάφορες αρχικές συνθήκες. Γνωρίζοντας την ακριβή συχνότητα του φορτίου καθώς και το μέγεθος αυτού είναι δυνατόν να γίνει βαθύτερη διερεύνηση της συμπεριφοράς του πολυβάθμιου συστήματος στην περιοχή της συχνότητας αυτής, με σκοπό την καλύτερη διαστασιολόγηση τέτοιων κατασκευών.

Ισοδύναμες στατικές μέθοδοι, που χρησιμοποιούν δυναμικούς αυξητικούς συντελεστές, μπορούν να εκτιμήσουν με ικανοποιητική ακρίβεια τη συμπεριφορά ασθενώς μη γραμμικών συστημάτων που υπόκεινται σε δυναμικά φορτία, αλλά για συστήματα με έντονη μη γραμμική συμπεριφορά, η αριθμητική ανάλυση με χρονική ολοκλήρωση είναι η μόνη αξιόπιστη μέθοδος.

Ο/Η μελετητής/τρια που ασχολείται με συμβατικές κατασκευές που παρουσιάζουν γραμμική συμπεριφορά δεν είναι εξοικωμένος/η με μη γραμμικά δυναμικά φαινόμενα. Γνωρίζοντας τη φύση τέτοιων φαινομένων μπορεί να τα εντοπίσει και να τα ερμηνεύσει. Μεταβάλλοντας τις παραμέτρους που επηρεάζουν τη δυναμική απόκριση ενός μη γραμμικού συστήματος μπορεί να μορφώσει και να διαστασιολογήσει τέτοιες κατασκευές, γνωρίζοντας τι να περιμένει από ένα δίκτυο καλωδίων που υπόκειται σε δυναμικά φορτία, τι να αναζητήσει, και τι να αποφύγει.

1 INTRODUCTION

1.1 HISTORICAL SURVEY

Nature has always granted to the humanity examples to solve problems of covering spans. The vaulted caves were used as shelters, the trunks of the fallen trees formed bridges to cross streamlets or even rivers at the narrow passages and the interlaced vines constituted a sort of suspended roof, while the trees, standing upright, represented the necessary masts to support these roofs. These images, among many others, stimulated the human imagination and triggered structural engineering. The need for progress and evolution, along with the development of technology, which brought new, more efficient materials, generated the opportunity to elaborate new concepts, find new solutions, overcome the existing limits and always set new ones. The examples are numerous, still standing over the centuries, testifying the course of the human inventiveness.

Since the ancient Roman years, curves dominated in the field of engineering and architecture, substituting straight lines, made of stones or wood, which were proved to be inadequate in some cases. Arcades, arches, and domes were the best solution to cover large spans, such as aqueducts, bridges, churches, etc. Later, thin shells, made of concrete, gained the interest of architects, giving a different aspect to their creations with their lightness and captivating elegance. The function of these structures was to carry loads in pure compression, thus avoiding bending of the members.

The reverse solution was realised by structures with members that operate in pure tension, which belong to the family of tensile structures. The sails of ships were among the first membrane structures ever used, providing resistance to wind, developing only tension and moving the ship over the seas. The first suspended bridges, made of ropes, were used to cross canyons, while the first suspended roof was the "velarium" of the Coliseum, built in 70 b.C. in Rome (Photo 1-1), protected the spectators from rain and sun. During the last six centuries, many suspended bridges were constructed, but only in the second half of the twentieth century, tensile structures became a pioneer in the field of structural engineering, opening new frontiers.

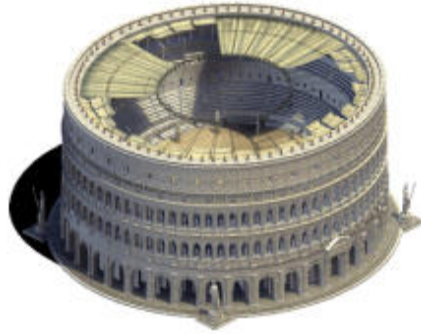


Photo 1-1: Schematic representation of the “velarium” of the Coliseum in Rome, Italy

1.2 TENSILE STRUCTURES

The term “tensile structure” is attributed to structures, which, while guiding the applied loads to the supports, remain constantly in tension. There are two groups of tensile structure: in the first one, the main tension elements are ropes or strands and cables, which operate as uniaxially stressed members, while in the second one, the tension is developed in biaxially stressed members, the tents or membranes. The shear and flexural rigidities of these elements, as well as their buckling resistance are negligible. Such structures are prestressed membrane or cable roofs, air-supported or inflated structures made also of membranes, tensegrity structures combining beams and cables, suspended or stayed bridges, antennae or guyed masts, sea-based applications, or even smaller structures such as snow avalanche nets, sailboats, mooring lines, trawl lines and nets, floating or submerged breakwaters, or aerostats. In most cases the tension elements are anchored to very stiff elements, which work mostly in compression, such as masts, columns, pylons, beams, trusses or arches ([1-1], [1-2]).

1.3 CABLE NETS

Cable nets belong to the family of tensile structures. They are characterised by their capacity to cover long spans without intermediate supports and to carry loads much heavier than their own weight. They are structures that always stimulate the interest and the imagination of both structural engineers and architects, demanding their collaboration, as their structural behaviour and geometry are closely related. The shape of the final surface depends on the geometry of their boundaries, the curvatures, the levels of cable pretension and the eventual internal supports. The most common shape of cable nets is the hyperbolic paraboloid with a surface that is convex with respect to one axis and concave with respect to the other, with a rectangular, rhomboid, circular or elliptical plan. The net consists of two families of prestressed cables, the main or carrying cables, which are suspended from the highest points of the boundary and the secondary or stabilising ones, which are anchored at the lowest points of the boundary. The difference of height between the highest or lowest points and the central node is called sag of the roof in the direction of the main or stabilising cables, respectively. The boundary is usually a prestressed reinforced concrete ring with a box cross-section.

These structures are very efficient, because the loads are transmitted through tension of the cables, usually made of high-strength steel, having thus the best exploitation of the material. In addition, with their unusual forms they differ from all other, conventional structures, something that makes them extremely elegant. These characteristics render them one of the most attractive alternatives for covering hangars, stadiums, swimming pools, ice rinks, exhibition halls, theatres, concert halls, churches and other long-span structures. On the other hand, these structures experience large

deformations, mainly because, due to their lack of shear rigidity, the cables change their shape in order to equilibrate the loads without shear. The large deflections can be alleviated by appropriate level of pretension. The design of such structures aims at maintaining all cables in tension under any load combination; in case of cable slackening, the net may exhibit large deformations. Opposite curvatures enable pretension in both directions, providing bearing capacity for loads directed downwards, such as snow and wind pressure and upwards, such as wind suction. Flat or nearly flat regions of the cable net surface should be avoided, because their stiffness is insufficient and they may easily flutter. In general, however, the suspended roofs cannot be calculated on the basis of linear theory, due to the large difference between their undeformed and their deformed shape. Thus, their analysis should be geometrical nonlinear. The principle of superposition does not apply and separate nonlinear analyses must be performed for each loading combination [1-3].

1.4 STRUCTURAL EXAMPLES

The first modern saddle-form cable net was the Raleigh Arena in North Carolina, built in 1953, which for many years after its completion, constituted an important exemplar for such structures. The saddle-shaped hyperbolic paraboloid roof form is created by a network of crosswise cables suspended between two opposing intersecting parabolic reinforced concrete arches, which reach a maximum height of 27.4m. They are inclined at approximately 21° and they cross each other at about 7.9m above the ground. They are supported by columns of composite cross-section while they extend into a tunnel below the surface at the east and west ends (Photo 1-2).



(a)



(b)



(c)



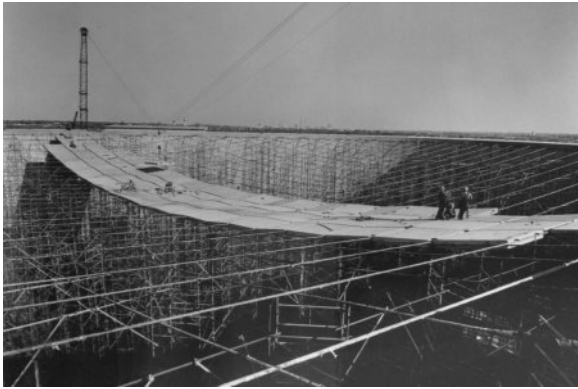
(d)

Photo 1-2: Raleigh Arena in North Carolina (a) construction of the arches (b) the cable net (c) internal view (d) the Arena today

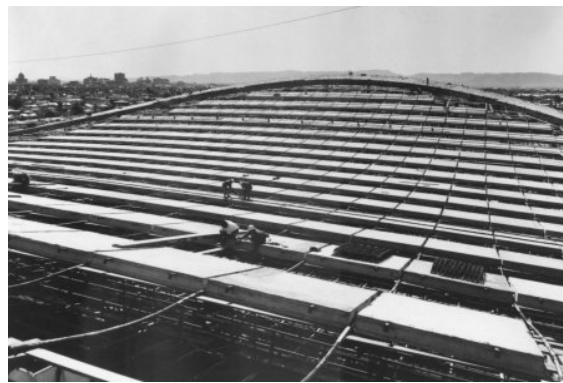
The cable net consists of 47 main cables of diameters that vary between 19mm to 33mm, while the stabilising cables are smaller with diameters between 13mm and 19mm. The dimensions of this structure are 92m×97m, covering an area of 10,000m², while the interior is column-free [1-4]. When this structure was completed, the cables were just anchored to the border, and no pretension was

applied. The roof soon began to flutter and oscillate violently, due to the turbulent wind. Inclined cables were added, connecting the net with the columns, in order to stiffen the roof ([1-5]).

The Arizona Veterans Memorial Coliseum in Phoenix, Arizona, U.S.A. was built in 1965 (Photo 1-3). The building has circular shape with 112m diameter. The edge ring, which is supported by steel columns, has 30.5m maximum height and 19.2m minimum height. The cable network is a square mesh with hyperbolic paraboloid shape. The roof carries over 1000 precast concrete panels [1-6].



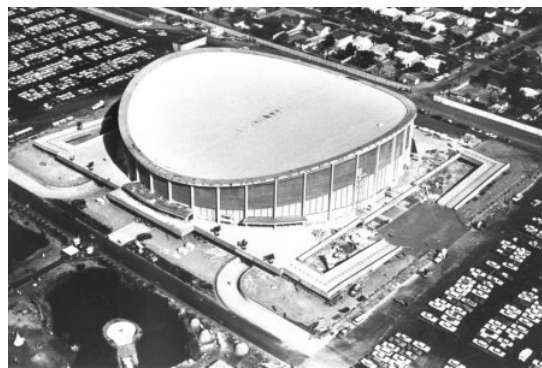
(a)



(b)



(c)



(d)

Photo 1-3: Arizona Veterans Memorial Coliseum in Phoenix, Arizona, U.S.A. (a), (b) placement of the concrete panels on the cable net, (c) the completed stadium, (d) aerial view of the stadium

Another pretensioned cable net, creating the surface of a hyperbolic paraboloid, is the roof of the Scandinavium Arena in Gothenburg, Sweden, constructed in May 1971 (Photo 1-4). The sag of the roof in the direction of the main cables is 10m and that in the direction of the stabilising ones is 4m. The grid of the network is orthogonal of 4m×4m. The ring beam has a rectangular cross-section with a width of 3.5m and a height of 1.2m. An alternative solution with a ring beam with a cross-section of a hollow steel box was investigated during design, but it was found to be too expensive. The contour ring is supported by four stiff pylons and 40 circular columns. The pylons are designed to take large horizontal forces. They are concrete walls, arranged radially, with a side length of 3.5m. The circular columns instead are designed to undertake mainly axial forces. Therefore, the ring beam is discontinuous at the top of the pylons, which influences the prestressing forces in the cable in the areas between the pylons and the top of the ring beam. The forces in the stabilising cables are significantly smaller than in other parts of the roof [1-7].



(a)



(b)



(c)



(d)

Photo 1-4: Scandinavien Arena in Gothenburg, Sweden (a) the stadium under construction, (b) placement of the cladding, (c) the completed stadium, (d) the stadium today

A different cable structure was built in Largo, Maryland, U.S.A., the US Air Arena (Photo 1-5). The roof consists of a warped circular ring of 122m diameter with square cross-section of 2.4m×2.4m and two groups of cables, which do not form a cable net. One set of cables is high and outside and the other low and inside, running straight across the building [1-8]. In 2002 the Arena was demolished (Photo 1-6).



(c)



(d)

Photo 1-5: US Air Arena in Largo, Maryland, U.S.A. (a) the stadium under construction, (b) plan view



Photo 1-6: US Air Arena in Largo, Maryland, U.S.A. during its demolition in 2002

Another saddle-form cable structure, now demolished, was the Sport Centre of San Siro in Milan, which was inaugurated in 1976 (Photo 1-7 and Photo 1-8). It had an elliptical plan view with axes of 144m and 146m. The cables were arranged in a quadratic grid of dimensions 2m×2m. The ring, made of steel, had a box cross-section with dimensions 2.5m×6.5m. The maximum height difference of the ring was 18.4m [1-9]. On January 17, 1985, one of the largest snowfalls of the 20th century in Milan caused large deflections of the net and severe damage to the cables. Three years later it was demolished [1-10].



(a)



(b)

Photo 1-7: Palasport of San Siro in Milan, Italy (a) the cable net, (b) the cable interconnections



(a)



(b)

Photo 1-8: Palasport of San Siro in Milan, Italy (a) aerial view during construction (b) the completed stadium

The saddle-shaped roof of Pengrowth Saddledome in Calgary, Alberta, Canada, is also a hyperbolic paraboloid (Photo 1-9). When it was inaugurated on October 15, 1983, it was known as the Olympic Saddledome as it would host the indoor ice events for the 1988 Winter Olympics. The horizontal projection of the suspended roof is a circle with a radius of 67.65m, covering 13,900m². From the centre point of the roof the carrying cables rise 14m to the top and the stabilising cables fall 6m to the valley of the ring. The bearing capacity of the main cables arises at 735kN, except of the four ones situated at the centre of the roof, which have a bearing capacity of 1235kN. The breaking load of the stabilising cables is 306kN. The edge ring consists of 16 precast elements of prestressed concrete and its dimensions are 1.5m×4.3m×27.4m [1-11].



(a)



(b)

Photo 1-9: Pengrowth Saddledome in Calgary, Alberta, Canada (a) the stadium under construction, (b) the completed stadium

The Stadium of Peace and Friendship in Greece, is another example of a saddle-shaped cable net. It was constructed in 1983 and it was used, among other stadiums, for the Olympic Games of 2004 (Photo 1-10). Its circular plan view has a diameter of 114m, and the sag of the roof is 6.15m, equal in both directions. The net consists of 27 cables in each direction and the cable spacing is constant and equal to 4m in both directions. The main cables have a diameter of 60mm and a breaking load of 3000kN, while the diameter of the stabilising cables is 46mm and their breaking load is 1850kN. The edge ring is made of prestressed concrete, with a box cross-section of dimensions 6.40m×8.15m. The thickness of its horizontal walls is 20cm and of the vertical ones 50cm. The ring seats on bearings, which are placed on 32 pylons. These pylons consist of radially oriented concrete walls. The bearings

allow small radial translations of the ring, but in case of violent horizontal forces, for example during a seismic event, the ring is restrained in the radial direction of the roof [1-12].



(a)



(b)



(c)



(d)



(e)



(f)

Photo 1-10: Stadium of Peace and Friendship in Athens, Greece (a) the stadium under construction, (b), (c) placement of the cables, (d) the cable interconnections (e) placement of the cladding, (f) the completed stadium

The Velodrome in London (Photos 1-11), which will host the Olympic track cycling events in 2012, is under construction. Steel cables form a huge cable net roof, which has a span of 136.5m at its widest point. The lightweight cable-net roof structure weighs only 30kg/m². 16km of cables have been used for the construction of the roof, weighing 100 tonnes alone. The cables were first laid out on the floor

of the building, with the nodes that join them also affixed. The inner side of the roof is clad in timber, while an aluminium cover is placed over the top of the timber cassettes to make the roof waterproof [1-13].



(a)



(b)



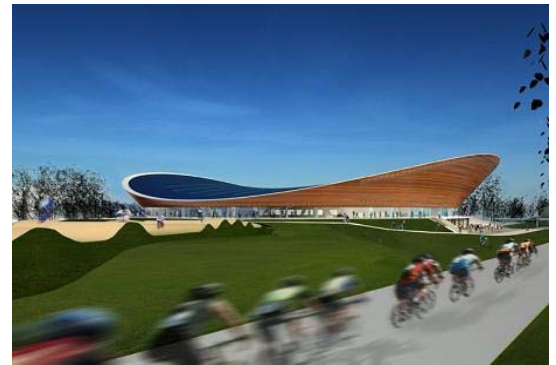
(c)



(d)



(e)



(f)

Photos 1-11: Velodrome in London, Great Britain (a) the stadium under construction, (b) the cable net, (c), (d) placement of the cladding, (e) internal view, (f) virtual representation of the completed stadium

Another example of a suspended roof is a small cable net, in the shape of a hyperbolic paraboloid surface, which forms the stage covering of the open theatre at Sao Jose do Rio Pardo, Brazil (Photo 1-12). The plan view of this structure is an ellipse, with the major axis equal to 20m and the minor one 13m. An orthogonal mesh of 10×6 cables, parallel to the axis of the ellipse, forms the cable net. The cables are anchored in a reinforced concrete ring, which has a rectangular cross-section

measuring 1.00m×0.45m. The axis of the edge ring follows the shape of the hyperbolic paraboloid surface. Four reinforced concrete pillars, of 3.70m height, sustain the edge ring [1-14].



Photo 1-12: The stage covering of the theatre at Sao Jose do Rio Pardo, Brazil

1.5 OBJECTIVE AND STRUCTURE OF THE THESIS

This thesis focuses on suspended roofs as the ones described above. These structures, being nonlinear and lightweight, exhibit large deformations and fatigue problems, especially when they are excited by dynamic loads, such as wind pressures. The geometric nonlinearity of cable structures produces nonlinear dynamic phenomena and secondary resonances, unknown in common linear structures, which may render their response unpredictable. The purpose of this research is to investigate the dynamic behaviour of such structures and to provide useful guidelines for their design. Beginning by their natural frequencies and vibration modes, which give insightful information about their overall nonlinear dynamic response, proceeding with exploring cable nets under simple harmonic loads with frequencies appropriately chosen to detect nonlinear resonant phenomena, and finally applying wind loads with realistic amplitudes, spatial distributions and time variation, the intensity of nonlinearity in their dynamic response and eventual problems of cable slackening or tensile failure are evaluated, in order to conclude with valuable suggestions for future design.

Following the general introduction on tensile structures and cable nets in particular, presented in this first chapter, chapter 2 contains a literature review on simple cables and cable nets, nonlinear dynamic phenomena, as well as recommendations of the pertinent codes regarding the calculation of the wind loads. In chapter 3, the dynamic behaviour of a simple cable net model is studied in detail and its equation of motion is solved analytically. Nonlinear phenomena are detected and similarities with a simple suspended cable are identified. Chapter 4 contains the validation of the finite element software, which will be used in the next chapters for analysing multi-degree-of-freedom models. Static and dynamic analyses of simple cable nets are conducted and the numerical results are compared with analytical ones. Chapter 5 presents a thorough investigation on the dynamic analysis of multi-degree-of-freedom cable nets, regarding their natural frequencies and vibration modes. The cable ends are considered either as fixed or flexible, taking into account the deformability of the boundary ring. Similarities with simple suspended cables are again underlined and semi-empirical formulae for the estimation of the first eigenfrequencies are provided and proposed to be used for preliminary design purposes. In chapter 6, the dynamic response of a MDOF cable net model is estimated using an equivalent single-degree-of-freedom model, consisting of two crossing cables and considering the vertical displacement of the central node as the only degree of freedom. Chapter 7 includes numerical

analyses of cable nets subjected to harmonic loads, considering several spatial distributions and frequencies, accounting for resonant conditions. Their dynamic behaviour is investigated, regarding the cable net maximum deflection and the cable maximum or minimum tension. The results are discussed and compared between cable nets with different boundary conditions. In chapter 8, the wind pressure spatial distribution is defined for different wind directions according to Eurocode 1, which is the current loading code in Europe, specifying wind pressure coefficients on structures. The accuracy of the assumptions made for the shape of a hyperbolic paraboloid is verified by comparing the pressure coefficients with the ones obtained by experimental results in wind tunnel tests reported in the literature. In chapter 9, actual wind records or artificial time histories of wind velocity are used to excite the cable nets, in order to compare their nonlinear dynamic response with respect to the one resulting by quasi-static procedures. Chapter 10 includes a summary of this thesis, the basic conclusions and contributions obtained from this research as well as suggestions for future research.

1.6 REFERENCES

- [1-1] J. W. Leonard, "Tension structures, behavior & analysis", McGraw-Hill, Inc., U.S.A., 1988.
- [1-2] P. Krishna, "Tension roofs and bridges", Journal of Constructional Steel Research, Vol. 57, pp. 1123-1140, 2001.
- [1-3] R. Levy and W. R. Spillers, "Analysis of geometrically nonlinear systems", Kluwer Academic Publishers, 2nd Edition, The Netherlands, 2003.
- [1-4] <http://www.arcaro.org/tension/album/dorton.htm>
- [1-5] H. A. Buchholdt, "An introduction to cable roof structures", Thomas Telford, 2nd Edition, Great Britain, 1999.
- [1-6] <http://www.arcaro.org/tension/album/arizona.htm>
- [1-7] <http://www.arcaro.org/tension/album/scandinaviu.htm>
- [1-8] <http://www.arcaro.org/tension/album/usair.htm>
- [1-9] <http://www.studioromaro.it/it/opere/stadi-e-grandi-coperture/palasport-a-milano,2,123>
- [1-10] http://it.wikipedia.org/wiki/Palasport_di_San_Siro
- [1-11] <http://www.arcaro.org/tension/album/saddledome.htm>
- [1-12] M. Majowiecki, "Tensostrutture Progetto e Verifica" Edizioni CREA, Italy, 1994, (in italian).
- [1-13] www.london2012.com
- [1-14] <http://www.arcaro.org/epidauro/>

2 THEORETICAL BACKGROUND AND LITERATURE REVIEW

2.1 INTRODUCTION

The response of simple suspended cables subjected to static or dynamic loads is studied extensively and many publications can be found in the literature. Analyses of larger cable structures, such as cable nets, are also conducted by several researchers for specific geometries and loading conditions, regarding the spatial distribution, the load amplitude and the load frequency. In this chapter, the main notions describing the behaviour of nonlinear systems are provided in order to understand qualitative features of the response of cable structures. Differences between linear and nonlinear systems are also highlighted. The equation of motion and the analytical expressions of the eigenfrequencies for a simple suspended cable and a simple cable net are reported from the literature, being the base of this investigation. The geometry of saddle-shaped cable nets is delineated, while important conclusions of publications regarding their static and dynamic response are also included. Design rules for cable structures, technical requirements and mechanical characteristics of cables are reported from the current codes, in order to use realistic values for the material of the cables in the analyses that will follow. Emphasis is given on the wind action, being the main dynamic load affecting suspended roofs. The wind spatial distribution referring to common shapes of roofs is retrieved from Eurocode. The calculation of the static wind load is based on equivalent static procedures, while the dynamic one on time-history diagrams produced by actual records of the wind velocity or by stochastic procedures.

2.2 NONLINEAR SYSTEMS

2.2.1 Behaviour of nonlinear systems

Cable structures have negligible bending, shear and buckling resistance. Because they cannot sustain any compression, they transmit the applied loads to the foundations by changing their shape and by developing only tension in their members. Thus, the deformed state of such structures is characterised by large displacements. The deformed shape differs significantly from the initial geometry of the unloaded structure, with remarkable change in stiffness as the deformation evolves. This interaction between the stiffness of the system and its deformed state is known as geometric

nonlinearity and it is the principal characteristic of such structures and their main difference from conventional ones [2-1].

According to Nayfeh and Pai [2-2], the modelling of nonlinear structural systems may be linear, pseudo nonlinear or nonlinear. In the first case, linear models describe both static and dynamic response and the solutions are unique. In the second case, a nonlinear model describes the static behaviour, but the dynamic one may be analysed by a linear model. The third case refers to a nonlinear static and dynamic model, which can be used for calculating the overall response of a nonlinear system. Only in the latter case is it possible to detect several dynamic equilibria and each one can be examined for a set of initial conditions and system parameters.

2.2.2 Nonlinear static analysis

As already mentioned, because of the geometric nonlinearity, the stiffness of nonlinear systems is related to the deformation. Thus, cable structures cannot be analysed on the basis of their original geometry, but it is necessary to take into account the deformed state at every step of the applied load, performing nonlinear structural analyses considering large displacements. This means that the internal forces do not vary linearly with the applied load, rendering the principle of superposition invalid [2-3].

For simple problems, such as SDOF cable systems, the analytical solution in static equilibrium can be easily obtained. For a given displacement, the stiffness of the system and the external load is calculated for the deformed geometry. For a given external load a trial and error procedure is required, until convergence is achieved. For complicated problems of nonlinear systems such as MDOF cable structures, numerical simulations are necessary, taking into account geometric nonlinearities. The Full Newton-Raphson method is one of them [2-4]. According to this method, the load is applied in steps, and the stiffness matrix is calculated in each iteration of every loading step, until convergence is obtained. The Modified Newton-Raphson method follows a similar procedure. The only difference from the Full Newton-Raphson method is that the stiffness matrix is not calculated in each iteration, but for every iteration of the same load step keeps the initial stiffness matrix. This assumption makes the method faster, but convergence is slower [2-4].

Several other procedures were also developed to solve large nonlinear problems, based on Newton's methods, such as the ones described in [2-5] – [2-8].

2.2.3 Nonlinear dynamic analysis

The dynamic response of a system is described by the following equation of motion [2-9]:

$$[M]\{\ddot{x}\} + [C]\{\dot{x}\} + [K]\{x\} = \{P(t)\} \quad (2-1)$$

where $[M]$ is the mass matrix, $[C]$ is the damping matrix, $[K]$ is the stiffness matrix, $\{P(t)\}$ is the vector of the external dynamic load, while $\{x\}$, $\{\dot{x}\}$ and $\{\ddot{x}\}$ the displacement, the velocity and the acceleration vectors, respectively. For linear systems exact solutions of Eq. (2-1) can be obtained, but for nonlinear systems, for which the stiffness depends on the displacement, that is $[K]=[K(x)]$, numerical techniques are required for analysing them, because the solution of the nonlinear ordinary differential equations becomes too complicated. However the results of single numerical analyses are unable to present all the features of the system's response.

During the last decades, the nonlinear behaviour of structures stimulated the scientists' interest in many fields. New terms were defined to describe nonlinear phenomena, unknown to the engineers dealing with conventional structures exhibiting linear response, such as attractors, limit cycles or closed paths, spirals, nodes and saddle points of equilibrium, stable and unstable equilibrium points,

superharmonic and subharmonic resonances, jump phenomena, bifurcations, etc. [2-10]. New methods were also found to identify and solve such problems ([2-11] – [2-13]). Many researchers have studied the occurrence of such nonlinear phenomena, addressing several applications in mechanical and structural engineering. Some representative examples are included in ([2-14] – [2-18]). In [2-19] a survey of recent developments in the field of nonlinear dynamic response of structures is presented.

Two types of analysis are available for solving dynamic problems: the frequency domain analysis and the time domain analysis [2-20]. The frequency domain analysis is based on the principle of superposition and is not appropriate for nonlinear structures. However, if the structure is considered as weakly nonlinear, it could be applied, but at first, it is necessary to carry out an eigenvalue analysis taking into account the stiffness in the deformed state due to the mean value of the dynamic load and any gravitational load and then adding the response of the fluctuating component of the dynamic load. On the other hand, the only reliable method to calculate the dynamic response of nonlinear structures is the time-domain method [2-21] in combination with the Full or Modified Newton-Raphson methods.

The three important requirements for a numerical procedure are 1) convergence – as the time step decreases, the numerical solution should approach the exact solution, 2) stability – the numerical solution should be stable in the presence of numerical round-off errors and 3) accuracy – the numerical procedure should provide results that are close enough to the exact solution. There are several types of time-stepping procedures, as the methods based on interpolation of excitation (i.e. piecewise exact method), methods based on finite difference expressions of velocity and acceleration (i.e. central difference method) and methods based on assumed variation of acceleration (i.e. Newmark method, Wilson θ) ([2-22], [2-23]). These methods are generally stable if the time step is small enough, i.e. $\Delta t < 1/2T_{\min}$, where T_{\min} is the smallest period of the structure and tends to become unstable if $\Delta t > T_{\min}$. On the other hand, a very small time step, smaller than required, is not necessary because it only increases the computational time. However, the time step should always describe the dynamic load.

The Composite method, introduced by Bathe [2-24] is a time integration method for solving nonlinear dynamic problems in time domain analysis, which is recommended for nonlinear systems. While, according to the standard Newmark method, the displacements, velocities, and accelerations are calculated for every time step Δt , the Composite one calculates them for every $0.5\Delta t$. For large deformation problems, the Newmark method can become unstable, while the composite scheme remains stable. However, for a given time step size, the scheme is about twice as expensive computationally as the Newmark method, due to the extra solution step at time $t+0.5\Delta t$ [2-25].

2.2.3.1 Phase portrait

In what follows, the phase portrait is described, which is one of the main tools that gives us the possibility to study a nonlinear system and identify properties of its motion, such as equilibrium, periodicity, unlimited growth, stability, instability, etc. The phase portrait construction is based on the transformation of the equation of motion in a function of one less unknown variables, and the representation of this function on a diagram of Cartesian axes x and y , called phase plane [2-10]. For a SDOF dynamical system, its motion may be expressed as:

$$M\ddot{x} + C\dot{x} + Kx = P(t) \Rightarrow \ddot{x} = \frac{P(t)}{M} - \frac{C}{M}\dot{x} - \frac{K}{M}x \Rightarrow \ddot{x} = g(x, \dot{x}, t) \quad (2-2)$$

A system is in equilibrium if its state does not change with time, which leads to $\dot{x} = \ddot{x} = 0$ and consequently to $g(x, 0, t) = 0$. Two types of equations are distinguished:

- the autonomous type, in which time t does not appear on the right hand side, and
- the non-autonomous type or forced equation in which g depends explicitly on time t .

The non-autonomous equations represent systems subjected to loads varying with time. For an autonomous system, adopting the transformation $\dot{x} = y$, Eq. (2-2) becomes:

$$\ddot{x} = g(x, \dot{x}) \xrightarrow{y=\dot{x}} \dot{y} = g(x, y) \tag{2-3}$$

A state at a time t_0 is described by a pair of numbers consisting of the displacement $x(t_0)$ and the velocity $\dot{x}(t_0)$, which can be considered also as the initial conditions. In such a system, the initial conditions determine all following states in a free motion. In the phase plane, with axes x and y , every state of the motion, at every time t , is represented by a point, having the coordinates $(x(t), y(t))$. The succession of states creates a curve, passing through the initial point for an undamped system, which is called a phase path, or trajectory or orbit. Figure 2-1 shows a closed path, where a point P leaves the initial state $(x(t_0), y(t_0))$ and after a time T returns to it, leaving again and returning to the same point an infinite number of times. Every circuit lasts the same time T , which does not depend on the initial conditions. Hence, the closed path defines a periodic motion, with period T and amplitude equal to the maximum value of x encountered by the curve. The time t does not appear on the phase portrait, but it determines the direction of the path, which is obtained from the relation $\dot{x} = y$. When $y > 0$, then also $\dot{x} > 0$, which means that x is increasing with time and when $y < 0$, $\dot{x} < 0$, meaning that x is decreasing with time. Therefore, the direction of the path is from left to right in the upper half-plane and from the right to the left in the lower half-plane as the arrow of Figure 2-1 shows.

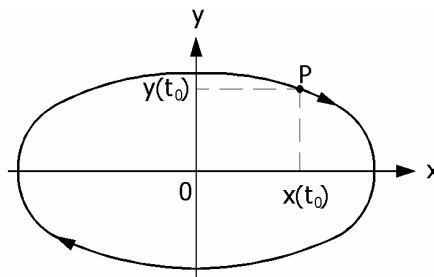


Figure 2-1: A closed path defining periodic motion

Equilibrium points correspond to constant solutions with constant displacement and zero velocity and acceleration. They are situated at points $(x, 0)$ where $g(x, 0) = 0$ and they can be regarded as degenerate phase paths. An equilibrium point surrounded by closed paths is called centre (Figure 2-2a). Figure 2-2b shows an unstable equilibrium point called saddle. This equilibrium point can never be reached in a finite time. In this case, the paths are hyperbolas, leading away from the equilibrium state to infinity and the asymptotic lines are called separatrices.

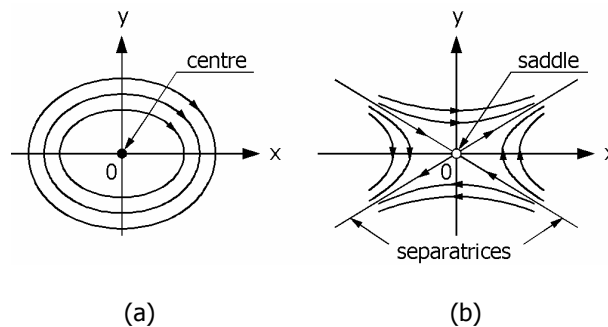


Figure 2-2: (a) Centre point, (b) Saddle point

If damping is included in the system, two cases are distinguished. In the first case, the damping is strong and no oscillation occurs. The paths start at infinity and lead very quickly to the origin, which is called stable node. Such a system is called dead beat (Figure 2-3a,b). In the second case, the damping is weak and the system performs oscillations with decreasing amplitudes. The paths have the form of a spiral and the origin is called a stable spiral or a stable focus (Figure 2-3c,d).

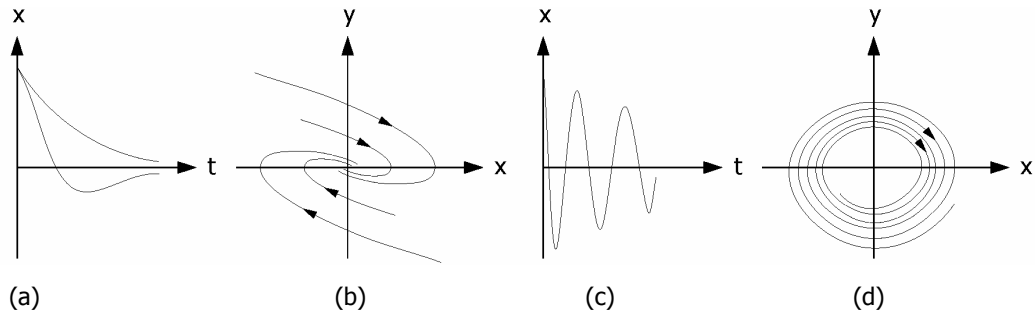


Figure 2-3: (a) Damped time solution for strong damping, (b) Phase portrait for strong damping, (c) Damped time solution for weak damping, (d) Phase portrait for weak damping

2.2.3.2 Nonlinear resonances

In nonlinear dynamics there are three main types of resonances. The first one is the external resonance, depending on the frequency of the external excitation Ω and its relation with the eigenfrequencies of the system ω . It consists of the primary resonance as well as the subharmonic and superharmonic resonances, called secondary resonances. The second one is the internal resonance, depending on the characteristics of the system and specifically on the relation between its natural frequencies. The third one is the parametric resonance ([2-26] – [2-27]).

In a harmonic-forced system, the external excitation tries to force the system at oscillations of frequency Ω , against its natural tendency to perform free vibrations with frequency ω . In undamped or lightly damped linear or nonlinear systems, when the loading frequency is equal to the eigenfrequency, that is $\Omega=\omega$, even a weak excitation forces the system to unbounded vibrations, with a continuously increasing amplitude and the system is said to be in the state of fundamental (primary) resonance. In nonlinear systems, superharmonic resonance may occur when the loading frequency may be expressed as:

$$\Omega=(1/n)\cdot\omega \quad (2-4)$$

where n is an integer. When the loading frequency is larger than the frequency of the system, related to it with the expression

$$\Omega=n\omega \quad (2-5)$$

where n is again an integer, phenomena of subharmonic resonance may occur. In both cases, the system responds in such a way that the free oscillation term does not decay to zero in spite of presence of damping and in contrast to the linear solution. Subharmonic oscillations can have potentially catastrophic effects [2-28].

In contrast to SDOF systems, which have only a single linearised natural frequency and a single mode of motion, an n -DOF system has n linearised natural frequencies and n corresponding mode shapes (some of which can be generalised modes corresponding to repeated eigenvalues). When two or more linearised natural frequencies are commensurable or nearly commensurable, for example $\omega_2\approx\omega_1$, $\omega_2\approx 2\omega_1$, $\omega_2\approx 3\omega_1$, $\omega_3\approx\omega_2\pm\omega_1$, $\omega_3\approx 2\omega_2\pm\omega_1$, $\omega_4\approx\omega_3\pm\omega_2\pm\omega_1$ and so on, the corresponding modes may be strongly nonlinearly coupled leading to internal resonances. If an internal resonance exists in a free

system, energy imparted initially to one of the modes involved in internal resonance, will be continuously exchanged among all the modes involved in that internal resonance. Moreover, if a harmonic external excitation of frequency Ω acts on a MDOF system, then, in addition to all primary and secondary resonances, resonant combinations of frequencies might exist. Finally, it should be mentioned that, during the internal resonances, the beat phenomenon characterises the response of the system, due to the combination of frequencies very close to each other.

In parametrically excited systems, the excitation appears as coefficient in the governing differential equations, simulating the time-dependent boundary conditions. In contrast to the case of external excitations, a small periodic parametric excitation can produce a large response when the frequency of the excitation is close to twice one of the natural frequencies of the system (principal parametric resonance).

The relation between oscillation amplitude and frequency is described by the response diagram in which the steady-state amplitude, denoted as a , is plotted on the vertical axis and the frequency ratio Ω/ω on the horizontal axis. For a free vibration of an undamped and unforced oscillator, the response is represented by one curve, called the backbone curve. For the forced system, the response is represented by different curves depending on the amplitude of the external force. These curves can be interpreted as perturbations out of the equilibrium state. In linear systems, the backbone curve is a straight vertical line and the response curves for the forced systems approach asymptotically this line, as the forcing frequency Ω approaches the system's frequency ω . This indicates the phenomenon of the primary resonance, in which the vibration amplitude increases infinitely when the force has the same frequency with the system. In nonlinear systems instead, the backbone curve is a bending curve representing either the softening or the hardening behaviour of the system (Figure 2-4). The softening behaviour means that the stiffness of the system decreases as the oscillation amplitude increases and the hardening behaviour means that the system's stiffness becomes progressively stronger for large amplitudes [2-19].

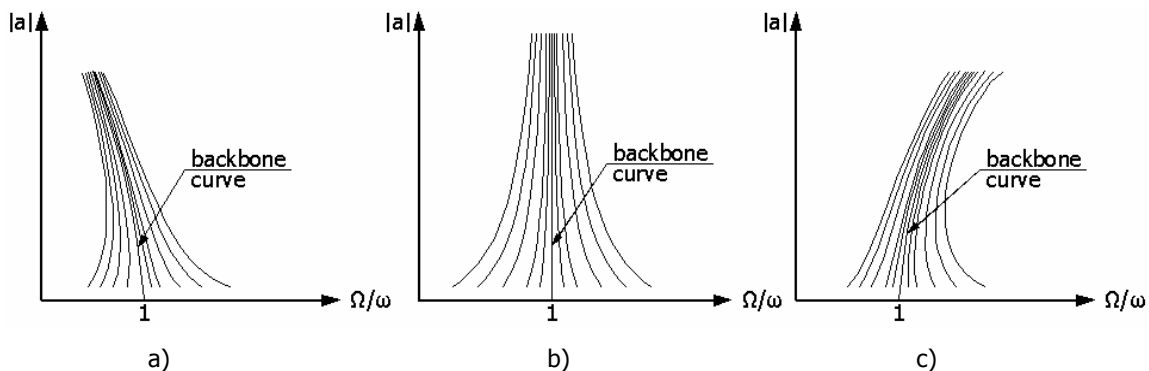


Figure 2-4: Amplitude-frequency curves for undamped systems with (a) softening nonlinear behaviour, (b) linear behaviour, (c) hardening nonlinear behaviour

Looking into the diagrams of Figure 2-4, important observations are made [2-10]:

- The bending of the response curves proves the bounded oscillations of the nonlinear systems for sufficiently small forces with frequencies close to the system's frequency, even if the system is undamped. In linear systems, even a small force, having the frequency of the system produces vibrations of infinitely increasing amplitudes, due to the fundamental resonance. In nonlinear systems instead, the nonlinearity controls the oscillation amplitude. As the amplitude increases (or decreases) the system becomes more (or less) stiff, changing its natural frequency, and the forcing term does not remain in step with the natural oscillation.

- Observing the response curves of the hardening (or softening) system, for $\Omega/\omega < 1$ (or $\Omega/\omega > 1$) a single response is expected, while for ratios $\Omega/\omega > 1$ (or $\Omega/\omega < 1$), there might be three different amplitudes of the system for the same forcing level. The initial conditions determine which of these responses is the actual response of the system. When only one response exists, this response is stable. When three different responses exist, only the oscillations with largest and smallest amplitudes are stable, while the remaining intermediate one is unstable.
- The multivaluedness of response curves due to nonlinearity leads to jump phenomena and consequently to hysteresis loops. If a force is applied to a nonlinear system with a hardening behaviour, described by the diagram of Figure 2-5, with an increasing frequency from Ω_1 to Ω_2 , the response point will move on the upper curve as far as point C, but then it will drop to point D on the lower curve and continue to point E. If the force has a decreasing frequency from Ω_2 to Ω_1 , it will follow the curve EDF, but at point F it will jump to the upper curve at point B, and continue until point A. This is in contrast to linear systems, where no hysteresis loops exist in frequency response functions, and the eventual steady states do not depend on the choice of initial conditions.

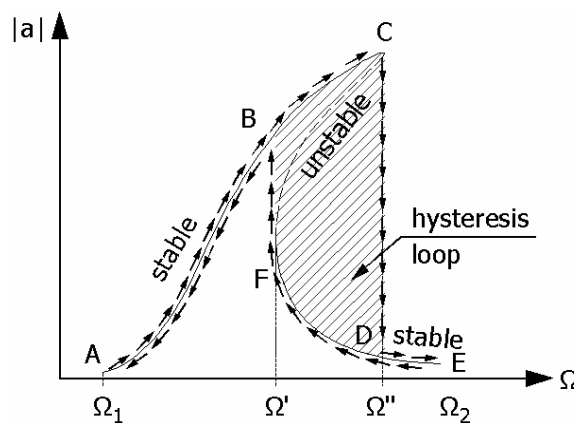


Figure 2-5: The jump phenomenon and hysteresis loop for a system with hardening behaviour

2.3 SIMPLE SUSPENDED CABLE

2.3.1 General

A sagged cable is considered, subjected to its self-weight, spanning a distance L . The two supports are at the same level. The sag of the cable at midpoint is f , its diameter is A and its mass density is m . The self-weight causes the deflection of the cable, while tension develops in the cable, tangential to the cable profile. No longitudinal loads are acting on the cable; thus, the horizontal equilibrium of a cable segment requires that the horizontal component of cable tension is constant along the cable and equal to H (Figure 2-6).

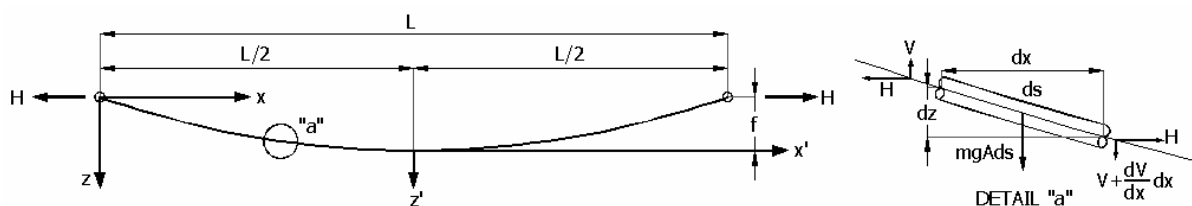


Figure 2-6: Sagged cable under its self-weight

As described in [2-29], the geometry of an inextensible suspended cable is expressed as:

$$z(x) = \frac{H}{mgA} \left\{ \cosh\left(\frac{mgAL}{2H}\right) - \cosh\left[\frac{mgA}{H}\left(\frac{L}{2} - x\right)\right] \right\} \quad (2-6)$$

where mgA is the self-weight of the cable per unit length. Given that the length of the cable segment is calculated as:

$$ds^2 = dz^2 + dx^2 \Rightarrow \frac{ds}{dx} = \sqrt{1 + \left(\frac{dz}{dx}\right)^2} \quad (2-7)$$

the horizontal component of the cable tension is defined as:

$$H \frac{d^2z}{dx^2} = -mgA \frac{ds}{dx} = -mgA \sqrt{1 + \left(\frac{dz}{dx}\right)^2} \quad (2-8)$$

An equivalent simply supported beam loaded by its self-weight could simulate the cable. Hence, moment equilibrium at the central point yields:

$$Hf = \frac{mgAL^2}{8} \Rightarrow H = \frac{mgAL^2}{8f} \quad (2-9)$$

Eq. (2-9) expresses also the horizontal component of the cable tension. For cables with sag-to-span ratio smaller than $1/8$, the profile adopted by the cable can be described with accuracy by the parabola:

$$z(x) = \frac{mgAL^2}{2H} \left[\frac{x}{L} - \left(\frac{x}{L}\right)^2 \right] = 4f \left[\frac{x}{L} - \left(\frac{x}{L}\right)^2 \right] \quad (2-10)$$

In case the origin of the coordinates is set at the mid-point of the cable curve, as shown in Figure 2-6, Eq. (2-10) becomes:

$$z'(x') = \frac{mgL^2}{2H} \left(\frac{x'}{L}\right)^2 = 4f \left(\frac{x'}{L}\right)^2 \quad (2-11)$$

The arc length of the cable, described by Eq. (2-7), can be rewritten as:

$$S = \int_0^L \sqrt{1 + \left(\frac{dz}{dx}\right)^2} dx \quad (2-12)$$

Differentiating Eq. (2-10) we obtain:

$$\frac{dz}{dx} = \frac{4f}{L} \left(1 - 2\frac{x}{L}\right) \text{ and } \frac{d^2z}{dx^2} = -\frac{8f}{L^2} \quad (2-13)$$

If the series expansion is considered [2-30]:

$$\sqrt{1+x} = 1 + \frac{1}{2}x - \frac{1}{2 \cdot 4}x^2 + \frac{1 \cdot 3}{2 \cdot 4 \cdot 6}x^3 \dots \approx 1 + \frac{1}{2}x \quad (2-14)$$

taking into account the first two terms, neglecting second order terms because the sag-to-span ratio is small with respect to 1, Eq. (2-12), which expresses the length of the cable, becomes:

$$\begin{aligned}
S &= \int_0^L \sqrt{1+z'^2} dx = \int_0^L \left[1 + \frac{1}{2} \left(\frac{4f}{L} \right)^2 \left(1 - 2 \frac{x}{L} \right)^2 \right] dx \Rightarrow \\
\Rightarrow S &= x + 8 \left(\frac{d}{L} \right)^2 x - \frac{8f^2}{L^3} \frac{x^2}{2} + \frac{32f^2}{L^4} \frac{x^3}{3} \Big|_0^L \approx x + 8 \left(\frac{f}{L} \right)^2 x \Big|_0^L \Rightarrow S = L \left(1 + \frac{8f^2}{L^2} \right)
\end{aligned} \tag{2-15}$$

The straight cable segment AB of Figure 2-7 is assumed with initial unstressed length equal to $ds_0=dx$. Considering an elongation at the cable, the deformed segment is A'B' with length ds .

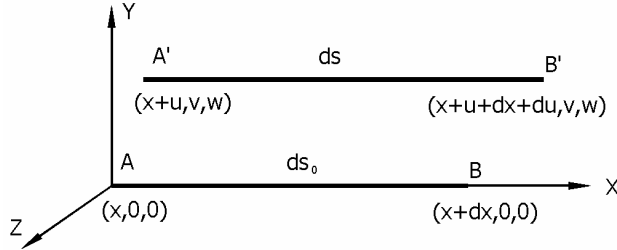


Figure 2-7: Elongation of cable segment AB

The Green-Lagrange strain (large strain) is defined as [2-31]:

$$\varepsilon_{x,GL} = \frac{du}{dx} + \frac{1}{2} \left(\frac{du}{dx} \right)^2 \tag{2-16}$$

The stretched length ds is:

$$ds = \sqrt{(dx + du)^2} = dx \sqrt{1 + 2 \frac{du}{dx} + \frac{du^2}{dx^2}} = dx \sqrt{1 + 2\varepsilon_{x,GL}} \tag{2-17}$$

and the elongation of the segment over the initial length is:

$$\frac{ds - ds_0}{ds_0} = \frac{dx \sqrt{1 + 2\varepsilon_{x,GL}} - dx}{dx} = \sqrt{1 + 2\varepsilon_{x,GL}} - 1 \Rightarrow \varepsilon_{x,GL} = \frac{ds^2 - ds_0^2}{2ds_0^2} \tag{2-18}$$

The engineering strain (small strain) is described by a simpler expression, neglecting the second order term:

$$\varepsilon_{x,e} = \frac{du}{dx} \tag{2-19}$$

The stretched length ds is expressed as:

$$ds = dx + du = dx(1 + \varepsilon_{x,e}) \tag{2-20}$$

and the elongation of the segment over the initial length is:

$$\frac{ds - ds_0}{s_0} = \frac{dx(1 + \varepsilon_{x,e}) - dx}{dx} = \varepsilon_{x,e} \tag{2-21}$$

According to the Hooke's law, the cable tension n on a cable segment due to an elongation ε_x is:

$$n = EA\epsilon_x \quad (2-22)$$

Assuming Green-Lagrange or large strains Eq. (2-22) becomes:

$$\frac{n}{EA} = \frac{ds^2 - ds_0^2}{2ds_0^2} \quad (2-23)$$

while, for engineering or small strains, it is:

$$\frac{n}{EA} = \frac{ds - ds_0}{ds_0} \quad (2-24)$$

For a small difference between the deformed and the undeformed length, the difference between the Green-Lagrange and the engineering strain is also small. This is confirmed by the chart of Figure 2-8, where the ratio of the deformed length over the unstressed one is plotted with respect to the strain ϵ .

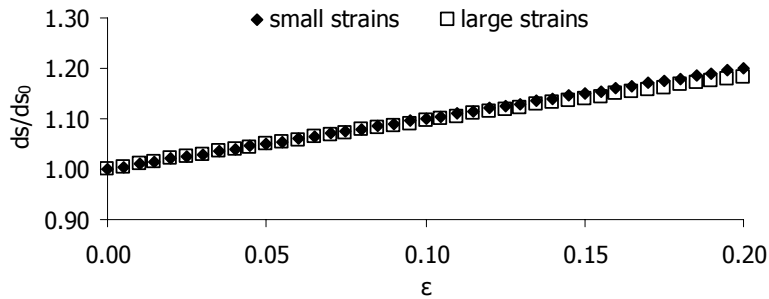


Figure 2-8: Difference between small and large strains

Consider now the suspended cable of Figure 2-9. If ds_0 is the original length of an infinitesimal segment at point P and ds is its deformed length, then:

$$ds_0^2 = dx^2 + dz^2 \quad (2-25)$$

$$ds^2 = (dx + du)^2 + (dz + dw)^2 \quad (2-26)$$

where u and w are the longitudinal and the vertical components of the displacement, respectively [2-29].

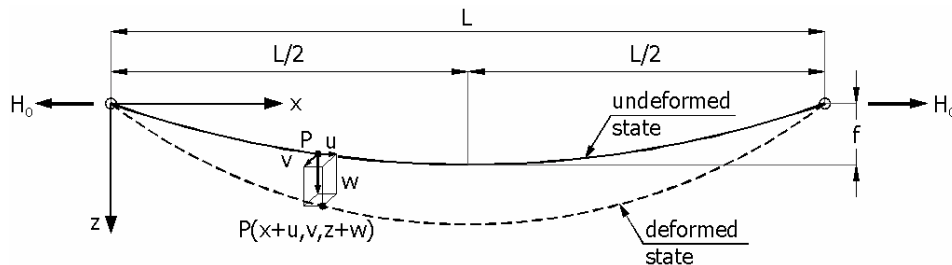


Figure 2-9: Deformed cable

Subtracting Eq. (2-25) from Eq. (2-26) and dividing by $2ds_0^2$:

$$\frac{ds^2 - ds_0^2}{2ds_0^2} = \frac{1}{2} \frac{du^2}{ds_0^2} + \frac{dx}{ds_0} \frac{du}{ds_0} + \frac{1}{2} \frac{dw^2}{ds_0^2} + \frac{dz}{ds_0} \frac{dw}{ds_0} \quad (2-27)$$

The left hand side of Eq. (2-27) can be written:

$$\begin{aligned} \frac{ds^2 - ds_0^2}{2ds_0^2} &= \frac{ds - ds_0}{ds_0} \cdot \frac{ds + ds_0}{2ds_0} = \frac{ds - ds_0}{ds_0} \left(1 + \frac{ds - ds_0}{2ds_0} \right) = \\ &= \frac{ds - ds_0}{ds_0} + \frac{1}{2} \left(\frac{ds - ds_0}{ds_0} \right)^2 \end{aligned} \quad (2-28)$$

This is the assumption of large displacements and large strains. However, neglecting the second term, which is very small, Eq. (2-28) results in the assumption of large displacements and small strains and Eq. (2-27) becomes:

$$\frac{ds^2 - ds_0^2}{2ds_0^2} = \frac{1}{2} \frac{du^2}{ds_0^2} + \frac{dx}{ds_0} \frac{du}{ds_0} + \frac{1}{2} \frac{dw^2}{ds_0^2} + \frac{dz}{ds_0} \frac{dw}{ds_0} \approx \frac{ds - ds_0}{ds_0} \quad (2-29)$$

Assuming that for flat cables the longitudinal change in length is small and neglecting this second order term, Eq. (2-29) results in:

$$\frac{ds - ds_0}{ds_0} = \frac{dx}{ds_0} \frac{du}{ds_0} + \frac{dz}{ds_0} \frac{dw}{ds_0} + \frac{1}{2} \left(\frac{dw}{ds_0} \right)^2 \quad (2-30)$$

2.3.2 Static response of simple cables

A simple cable with initial unstressed length S_0 , spanning a distance L , is studied next. A concentrated load P is applied at middle span and the cable stretches until an equilibrium position is obtained with a deflection at the midpoint equal to z_1 from the chord connecting points A and B, as shown in Figure 2-10. The self-weight of the cable is neglected and the material is assumed as linearly elastic. The equation of static equilibrium is reported from [2-32].

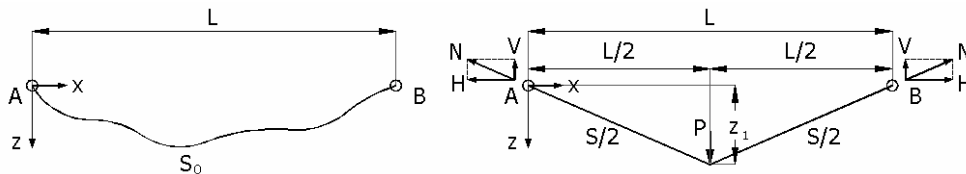


Figure 2-10: Cable with concentrated load at middle span

The vertical component V of tension N is:

$$V = P/2 \quad (2-31)$$

The sums of moments about points A and B give:

$$H = \frac{P}{2} \cdot \frac{L}{2z_1} \quad (2-32)$$

and the tension of the cable is:

$$N = \sqrt{V^2 + H^2} = \frac{P}{2} \sqrt{1 + \left(\frac{L}{2z_1} \right)^2} \quad (2-33)$$

while the stretched length S is:

$$S = 2\sqrt{\left(\frac{L}{2}\right)^2 + z_1^2} \quad (2-34)$$

which is related to the tension and the deflection by Hooke's law:

$$\sigma = E\varepsilon \Rightarrow \frac{N}{A} = E \frac{(S - S_0)}{S_0} \Rightarrow S = S_0 \left(1 + \frac{N}{AE}\right) \quad (2-35)$$

Combining Eqs. (2-33), (2-34) and (2-35), we obtain:

$$P = 2AE \frac{2z_1}{L} \left(\frac{L}{S_0} - \frac{1}{\sqrt{1 + (2z_1/L)^2}} \right) \quad (2-36)$$

Eq. (2-36) shows the nonlinear relationship between the load P and the deflection of the cable z_1 . It is difficult to obtain an explicit expression for z_1 as a function of P , without using numerical methods. Differentiating Eq. (2-36) the linearised stiffness of the cable can be evaluated:

$$K = \frac{\partial P}{\partial z} = \frac{4AE}{L} \left(\frac{L}{S_0} - \frac{1}{[1 + (2z_1/L)^2]^{3/2}} \right) \quad (2-37)$$

which depends on the deflection of the cable. In Figure 2-11 the non-dimensional load is plotted as function of z_1/L for two different cases of initial lengths, $S_0=L$ and $S_0=1.05L$. In the first case, the unloaded cable without pretension has a stiffness equal to zero (represented by the tangent angle of the curve at $z_1=0$). In the second case, in which the cable's initial length is larger than the span, the cable at first is slack, without any tension and without any stiffness, until the deflection becomes equal to:

$$z_1 = \frac{L}{2} \sqrt{\left(\frac{S_0}{L}\right)^2 - 1} \quad (2-38)$$

which for $S_0=1.05L$ results in $z_1=0.16L$. In both cases, as P and z_1 increase, the stiffness of the cable also increases and the response tends to become linear, in other words the system becomes stiffer.

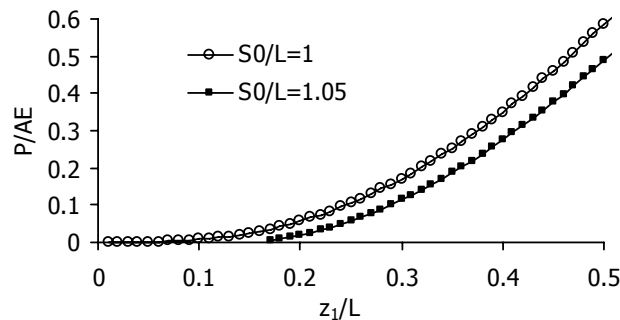


Figure 2-11: Load-deflection curve for central concentrated load

Following the same procedure for the cable of Figure 2-12, the expressions for the tension, the deformed length and the deflection of the cable are derived.

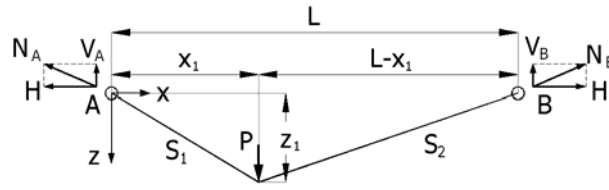


Figure 2-12: Cable with a concentrated load at an arbitrary location

The tensions of the cable are:

$$N_A = \frac{Pab}{\gamma c_1} \text{ and } N_B = \frac{Pab}{\gamma c_2} \quad (2-39)$$

where

$$a=x_1/L, b=1-a, \gamma=z_1/L, c_1 = \frac{1}{\sqrt{1+(\gamma/a)^2}} \text{ and } c_2 = \frac{1}{\sqrt{1+(\gamma/b)^2}} \quad (2-40)$$

The stretched lengths S_1 and S_2 are:

$$S_1 = \sqrt{x_1^2 + z_1^2} = L \frac{a}{c_1} \text{ and } S_2 = \sqrt{(L-x_1)^2 + z_1^2} = L \frac{b}{c_2} \quad (2-41)$$

and the unstressed lengths S_{01} , S_{02} and S_0 are:

$$S_{01} = \frac{L}{\frac{c_1}{a} + \frac{P}{AE} \frac{b}{\gamma}} \quad (2-42)$$

$$S_{02} = \frac{L}{\frac{c_2}{b} + \frac{P}{AE} \frac{a}{\gamma}} \quad (2-43)$$

$$S_0 = S_{01} + S_{02} = \frac{L}{\frac{c_1}{a} + \frac{P}{AE} \frac{b}{\gamma}} + \frac{L}{\frac{c_2}{b} + \frac{P}{AE} \frac{a}{\gamma}} \quad (2-44)$$

The load is expressed as:

$$\frac{P}{AE} = \frac{\gamma}{2ab} \left(\frac{L}{S_0} - c_1 - c_2 + \sqrt{\left(\frac{L}{S_0} + c_1 - c_2 \right)^2 + 4a \frac{L}{S_0} (c_2 - c_1)} \right) \quad (2-45)$$

The horizontal component of tension is constant along the cable, since no horizontal loads are applied. Simulating the cable by a simply supported beam, loaded in the same way as the cable, the deflected shape is the shape of the moment diagram of the equivalent beam:

$$M = Hz_1 = \frac{Px_1(L-x_1)}{x_1} \Rightarrow H = \frac{Px_1(L-x_1)}{x_1 z_1} \quad (2-46)$$

The analogy of the deflected cable to the moment diagram of a simply supported beam is useful in order to obtain the prestressed configuration of cables subjected to multiple loads. This moment

analogy method can be used for the generalised problem with multiple loads P_i applied at points x_i along the horizontal projection of the span, either if the horizontal component of tension is known, or the deflected profile at a specific point is known [2-32]. The chord connecting the endpoints of the cable makes an angle θ with the x -axis as illustrated in Figure 2-13.

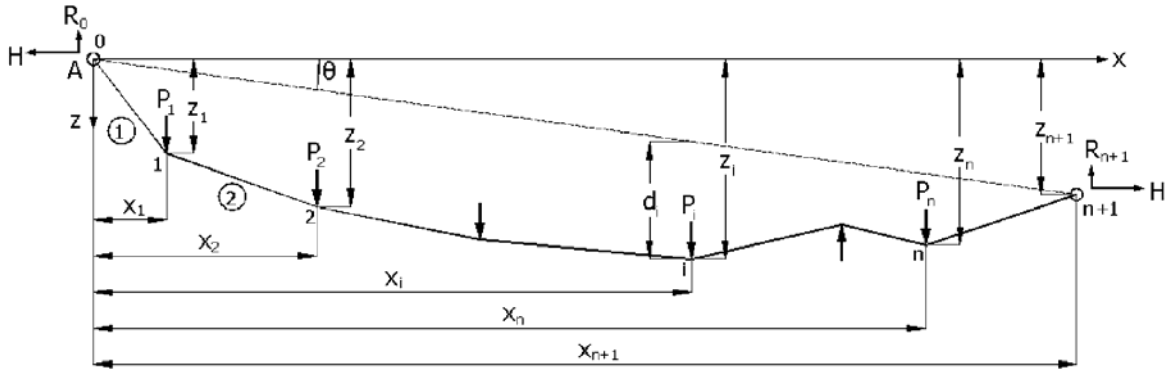


Figure 2-13: Cable with multiple concentrated loads

The vertical reactions are:

$$R_0 = \frac{1}{x_{n+1}} \left[\sum_{i=1}^n (x_{n+1} - x_i) P_i + H z_{n+1} \right] \quad (2-47)$$

$$R_{n+1} = \frac{1}{x_{n+1}} \left[\sum_{i=1}^n x_i P_i + H z_{n+1} \right] \quad (2-48)$$

If a simply supported beam directed along the chord is considered instead, the moment at any point i is:

$$m_i = \frac{1}{x_{n+1}} \left[\sum_{j=1}^i x_j (x_{n+1} - x_i) P_j + \sum_{j=i+1}^n x_i (x_{n+1} - x_j) P_j \right] \quad (2-49)$$

while the moments M_i in the cable must be zero at every point:

$$M_i = \frac{1}{x_{n+1}} \left[\sum_{j=1}^i x_j (x_{n+1} - x_i) P_j + \sum_{j=i+1}^n x_i (x_{n+1} - x_j) P_j + H z_{n+1} \right] - H z_i = 0 \Rightarrow \quad (2-50)$$

$$m_i + H(x_i \tan \theta - z_i) = 0 \Rightarrow m_i - H d_i = 0 \Rightarrow d_i = \frac{m_i}{H}$$

where d_i is the distance of the cable from the chord at point i . Eq. (2-50) shows that if the horizontal component of the cable tension is known, all d_i can be calculated. If, on the other hand, a distance d_I at point I is known, the distance d_i at any point i can be also calculated by:

$$d_i = \frac{m_i}{m_I} d_I \quad (2-51)$$

The vertical component of tension in each segment is equal to the tension of the equivalent beam:

$$V_i = -R_0 + \sum_{j=1}^i P_j \quad (2-52)$$

and the tension in each cable segment is:

$$N_i = \sqrt{V_i^2 + H^2} \quad (2-53)$$

The undeformed length of each segment is calculated by Hooke's law:

$$N_i = EA \frac{S_i - S_{0i}}{S_{0i}} \Rightarrow S_{0i} = \frac{\sqrt{(x_i - x_{i-1})^2 + (z_i - z_{i-1})^2}}{1 + \frac{T_i}{EA}} \quad (2-54)$$

The horizontal component of tension is not constant along the cable if horizontal loads are applied. In such a case the following expressions are used (Figure 2-14):

$$N_i = \sqrt{V_i^2 + H_i^2} \quad (2-55)$$

$$V_{i+1} = V_i - P_i \quad (2-56)$$

$$H_{i+1} = H_i - Q_i \quad (2-57)$$

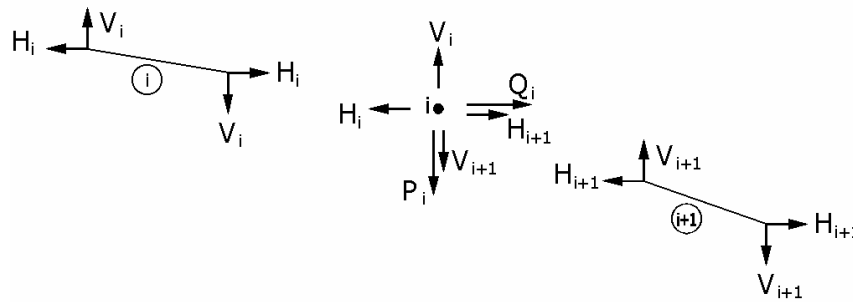


Figure 2-14: Equilibrium at the point i

If H_1 and V_1 are known, it is possible to calculate H_i , V_i and N_i at every point i of the cable, using Eqs. (2-55) – (2-57). If, in addition, the unstressed lengths S_{0i} and the coordinates at point 0 are known, the coordinates of all points can be calculated:

$$S_i = \left(1 + \frac{N_i}{EA}\right) \cdot S_{0i} \quad (2-58)$$

$$\Delta x_i = \frac{H_i}{N_i} \cdot S_i \quad (2-59)$$

$$\Delta z_i = \frac{V_i}{N_i} \cdot S_i \quad (2-60)$$

$$x_{i+1} = x_i + \Delta x_i \quad (2-61)$$

$$z_{i+1} = z_i + \Delta z_i \quad (2-62)$$

If only the horizontal distances Δx_i are known, the vertical distance Δz_i and the stressed lengths S_i are calculated as:

$$\Delta z_i = \frac{V_i}{H_i} \cdot \Delta x_i \tag{2-63}$$

$$S_i = \frac{N_i}{H_i} \cdot \Delta x_i \tag{2-64}$$

In case H_1 and V_1 are not known, the solution to the problem can be obtained only by iteration methods consisting of the following steps:

- Assume H_1 and V_1
- Calculate V_i , H_i and N_i [Eqs. (2-55), (2-56) and (2-57)]
- Calculate x_i , z_i and S_i [Eqs. (2-58) – (2-64)]
- Compare the computed x_{n+1} , z_{n+1} and S_{n+1} to the exact values at the end point $n+1$ and if they are different, assume new H_1 and V_1 and repeat from the first step.

A cable subjected to a uniformly distributed vertical load is also assumed. Two cases of loading are taken into account: a) loads distributed uniformly along the horizontal span of the segment, e.g. permanent suspended loads, snow etc. and b) loads distributed uniformly along the arc length of the segment e.g. self-weight of the cable [2-32]. In the first case, with a uniform load over the horizontal span of the cable segment (Figure 2-15), the vertical reaction at point A is obtained by the sum of moments about point B:

$$V_A = H \tan \theta + \frac{pL}{2} \tag{2-65}$$

The equilibrium of forces on the differential length is expressed as:

$$\frac{dH}{dx} = 0 \Rightarrow H = H_A = H_B \tag{2-66}$$

$$\frac{dV}{dx} dx = -p dx \Rightarrow V = V_A - px \tag{2-67}$$

and using Eq. (2-65), the vertical reaction V_B is calculated:

$$V_B = H \tan \theta - \frac{pL}{2} \tag{2-68}$$

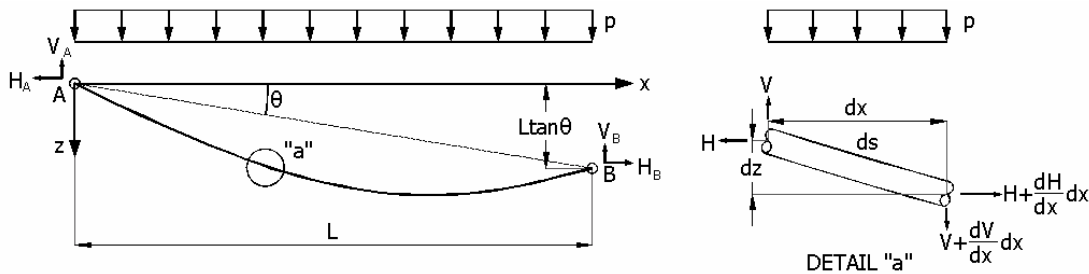


Figure 2-15: Uniform distributed load over horizontal span

The cable tension at point P, located at distance x from the end A, is calculated as:

$$N = \sqrt{H^2 + (V_A - px)^2} = H \sqrt{1 + \left[\tan \theta + \frac{PL}{2H} \left(1 - \frac{2x}{L} \right) \right]^2} \tag{2-69}$$

The vertical distance z of point P, shown in Figure 2-16, is:

$$z = x \tan \theta + d \quad (2-70)$$

where d is the distance from the chord to the cable, expressed as an expression of the moment m_x at point P in the equivalent simply supported beam:

$$d = \frac{m_x}{H} = \frac{px}{2H}(L - x) \quad (2-71)$$

If the sag of the cable at midpoint is defined as f , the horizontal component of the cable tension is calculated as:

$$f = \frac{pL^2}{8H} \Rightarrow H = \frac{pL^2}{8f} \quad (2-72)$$

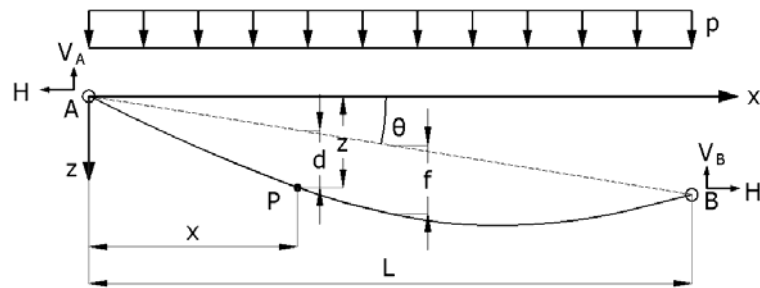


Figure 2-16: Point P at distance x

The unstressed length of the cable segment AP is determined as:

$$\frac{ds}{dx} = \left(1 + \frac{N}{EA}\right) \frac{ds_0}{dx} \Rightarrow \frac{ds_0}{dx} = \frac{ds}{dx} \frac{1}{\left(1 + \frac{N}{EA}\right)} \quad (2-73)$$

Expanding to series according to [2-30]:

$$\frac{1}{1 + x} = 1 - x + x^2 - x^3 + \dots \quad (2-74)$$

assuming that $N/AE \ll 1$, and neglecting the terms N/AE of higher order, Eq. (2-73) becomes:

$$\frac{ds_0}{dx} = \left(1 - \frac{N}{AE}\right) \frac{ds}{dx} = \left(1 - \frac{N}{AE}\right) \frac{N}{H} \quad (2-75)$$

If the unstressed length of the cable is known, the sag f can be determined combining Eqs. (2-69)(2-72) and (2-75). It is convenient to define the non-dimensional variables:

$$u = \tan \theta + 4 \frac{f}{L} \left(1 - 2 \frac{x}{L}\right) \quad (2-76)$$

$$\rho = \frac{pL}{2AE} \quad (2-77)$$

with:

$$u_0 = \tan\theta + 4f/L \text{ and } u_1 = \tan\theta - 4f/L \quad (2-78)$$

The total unstressed length is:

$$\begin{aligned} \frac{S_0}{L} = \frac{L}{16f} & \left\{ \left[u_0 \sqrt{1+u_0^2} - u_1 \sqrt{1+u_1^2} + \log \left(\frac{u_0 + \sqrt{1+u_0^2}}{u_1 + \sqrt{1+u_1^2}} \right) \right] + \right. \\ & \left. + \frac{\rho L}{2f} \left[u_1 - u_0 + \frac{1}{3}(u_1^3 - u_0^3) \right] \right\} \end{aligned} \quad (2-79)$$

Using various numerical procedures to determine the roots of Eq. (2-79), the sag f could be calculated. If the cable is considered as inextensible, with $\rho=0$, the expression defining the sag f is:

$$f = L \sqrt{\frac{3}{8} \left(\frac{S_0}{L} - 1 - \frac{1}{2} \tan^2 \theta \right)} \quad (2-80)$$

while the unstressed length becomes:

$$S_0 = L \left(1 + \frac{8f^2}{3L^2} + \frac{1}{2} \tan^2 \theta \right) \quad (2-81)$$

and if $\theta=0$:

$$f = L \sqrt{\frac{3}{8} \left(\frac{S_0}{L} - 1 \right)} \quad (2-82)$$

$$S_0 = L \left(1 + \frac{8f^2}{3L^2} \right) \quad (2-83)$$

In case a uniformly load q along the arc length of the cable segment is considered, as shown in Figure 2-17, a different solution is obtained.

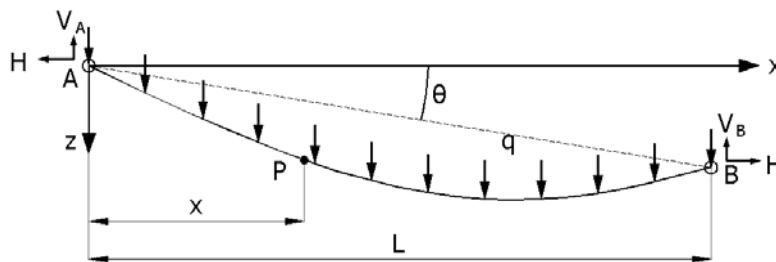


Figure 2-17: Cable with uniform load along the arc length of the cable

The equilibrium of forces on the differential length yields:

$$\frac{dH}{dx} = 0 \Rightarrow H = H_A = H_B \quad (2-84)$$

$$\frac{dV}{dx} dx = -q ds \Rightarrow \frac{dV}{dx} = -q \frac{ds}{dx} \quad (2-85)$$

Since the tension must be directed along the tangent to the arc:

$$V = H \frac{dz}{dx} \quad (2-86)$$

while, taking into account the arc's length given by Eq. (2-7), the cable tension is defined:

$$N = H \frac{ds}{dx} = H \sqrt{1 + \left(\frac{dz}{dx}\right)^2} \quad (2-87)$$

Substituting Eq. (2-86) into Eq. (2-85) the classic catenary's equation for the deflected profile of the arc arises:

$$\frac{d}{dx} \left(H \frac{dz}{dx} \right) = -q \frac{ds}{dx} \Rightarrow \frac{d^2z}{dx^2} + \frac{q}{H} \sqrt{1 + \left(\frac{dz}{dx}\right)^2} = 0 \quad (2-88)$$

and applying the boundary conditions $z=0$ at $x=0$ and $z=L \tan \theta$ at $x=L$, the solution is:

$$z(x) = \frac{H}{q} \left\{ \cosh(\gamma + \beta) - \cosh \left[\gamma + \beta \left(1 - 2 \frac{x}{L} \right) \right] \right\} \quad (2-89)$$

where

$$\beta = \frac{qL}{2H} \text{ and } \gamma = \sinh^{-1} \left(\tan \theta \frac{\beta}{\sinh \beta} \right) \quad (2-90)$$

Thus, the vertical component V and the tension N of the cable at a point x on the horizontal span are, respectively:

$$V = H \sinh \left[\gamma + \beta \left(1 - 2 \frac{x}{L} \right) \right] \quad (2-91)$$

$$N = H \cosh \left[\gamma + \beta \left(1 - 2 \frac{x}{L} \right) \right] \quad (2-92)$$

The total stretched length is obtained by integration of Eq. (2-85):

$$\frac{dV}{dx} = -q \frac{ds}{dx} \Rightarrow \frac{S}{L} = \frac{V_A - V_B}{qL} \quad (2-93)$$

and the unstressed length is calculated by integration of Eq. (2-75), applying the boundary conditions at the ends of the cable $s_0=0$ at $x=0$ and $s_0=S_0$ at $x=L$:

$$\frac{ds_0}{dx} = \left(1 - \frac{N}{AE} \right) \frac{ds}{dx} \Rightarrow \frac{S_0}{L} = \frac{V_A - V_B}{qL} - \frac{1}{2AE} \left[H + \frac{V_A N_A - V_B N_B}{qL} \right] \quad (2-94)$$

2.3.3 Dynamic response of simple cables

A simple cable is first treated as a single-degree-of-freedom (SDOF) undamped system, with supports at the same horizontal level [2-32]. The mass of the system is concentrated at the central node. This node is assumed to move only vertically. The cable is loaded by a concentrated load in the middle. The undeformed length of the cable is s_0 . The initial deflection of the cable is considered to be equal to z_0 . Due to the weight of the concentrated mass M , a static load P is assumed causing a static

deflection z^* . Then, a load $\Delta P(t)$, varying with time is also applied, or an initial displacement Δz_0 (Figure 2-18).

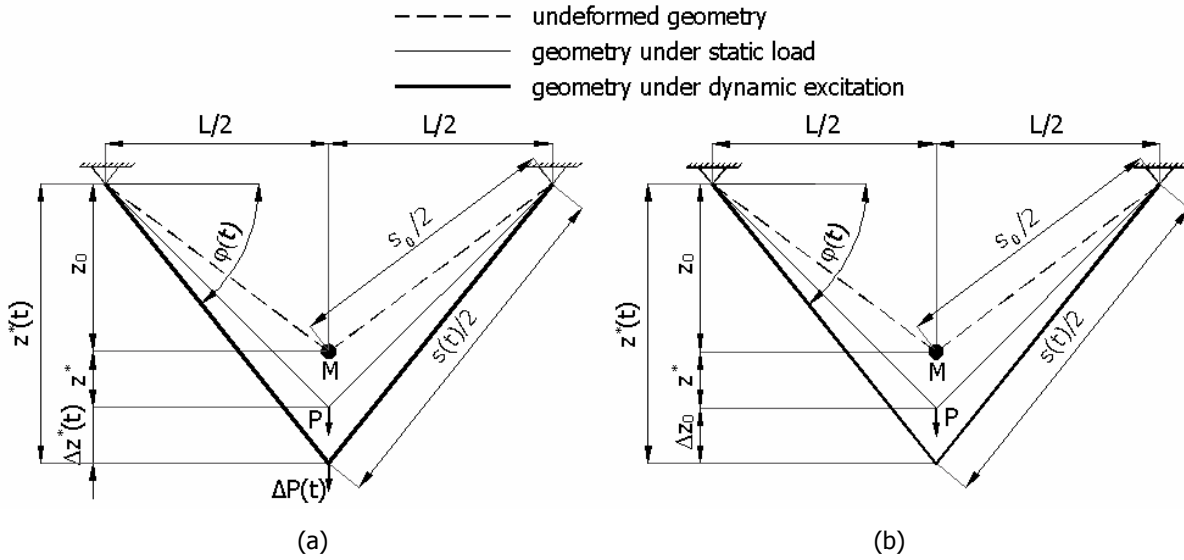


Figure 2-18: Single-degree-of-freedom cable (a) with time-dependent load, (b) with initial displacement

The equation of motion at any time t , as described in Figure 2-19, is:

$$M\ddot{z}^* = P(t) - 2N(t)\sin(\varphi(t)) \tag{2-95}$$

where $M\ddot{z}$ is the inertia force, $P(t)$ the external excitation and $2N(t)\sin\varphi(t)$ the vertical component of the cable tension. The dot denotes differentiation with respect to time. The deformed length of the cable at time t is $s(t)$, defined as:

$$\frac{s(t)}{2} = \sqrt{(z^*(t))^2 + \left(\frac{L}{2}\right)^2} \Rightarrow \frac{s(t)}{L} = \sqrt{\left(\frac{2z^*(t)}{L}\right)^2 + 1} \tag{2-96}$$

and the angle of inclination $\varphi(t)$ of each section is expressed as:

$$\sin \varphi(t) = \frac{2z^*(t)}{s(t)} = \frac{2z^*(t)}{L\sqrt{\left(\frac{2z^*(t)}{L}\right)^2 + 1}} = \frac{\tan \varphi(t)}{\sqrt{\tan^2 \varphi(t) + 1}} \tag{2-97}$$

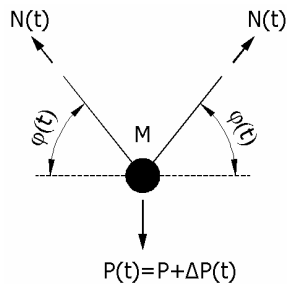


Figure 2-19: Equilibrium of the central node

If the material is considered as linearly elastic, the cable tension is:

$$N(t) = AE\varepsilon = AE \frac{s(t) - s_0}{s_0} \Rightarrow N(t) = AE\varepsilon = AE \left(\frac{L}{s_0} \sqrt{\tan^2 \varphi(t) + 1} - 1 \right) \quad (2-98)$$

where

$$\tan \varphi(t) = \frac{2z^*(t)}{L} = q(t) \quad (2-99)$$

Substituting Eqs. (2-97), (2-98) and (2-99) in Eq. (2-95), the nonlinear equation of motion of the mass M is obtained as a function of the forcing term P(t):

$$\frac{ML}{2} \ddot{q}(t) = P(t) - 2AE \left(\frac{L}{s_0} - \frac{1}{\sqrt{q^2(t) + 1}} \right) q(t) \quad (2-100)$$

The load consists of a steady prestressing force P and a time varying one $\Delta P(t)$, while the non-dimensional deflection $q(t)$ consists of a static deflection q and a transient one $\Delta q(t)$:

$$P(t) = P + \Delta P(t) \quad (2-101)$$

$$q(t) = q + \Delta q(t) \Rightarrow \ddot{q}(t) = \ddot{q} + \Delta \ddot{q}(t) = 0 + \Delta \ddot{q}(t) = \Delta \ddot{q}(t) \quad (2-102)$$

Thus, Eq. (2-100) becomes:

$$\frac{ML}{2} \Delta \ddot{q}(t) = (P + \Delta P(t)) - 2AE \left(\frac{L}{s_0} - \frac{1}{\sqrt{(q + \Delta q(t))^2 + 1}} \right) (q + \Delta q(t)) \quad (2-103)$$

In case of static equilibrium, the load P is expressed as:

$$P = 2AE \left(\frac{L}{s_0} - \frac{1}{\sqrt{q^2 + 1}} \right) q \quad (2-104)$$

and Eq. (2-103) becomes:

$$\frac{ML}{2} \Delta \ddot{q}(t) = \Delta P(t) - 2AE \left(\frac{L}{s_0} \Delta q(t) - \left(\frac{q + \Delta q(t)}{\sqrt{(q + \Delta q(t))^2 + 1}} - \frac{q}{\sqrt{q^2 + 1}} \right) \right) \quad (2-105)$$

Taylor expansion implies [2-30]:

$$f(z + \Delta z) = f(z) + \frac{f'(z)}{1!} \Delta z + \dots + \frac{f^{(n)}(z)}{n!} \Delta z^n \quad (2-106)$$

where $\Delta z \rightarrow 0$. Retaining only the first order term, Eq. (2-106) becomes:

$$f(z + \Delta z) - f(z) = f'(z) \cdot \Delta z \quad (2-107)$$

If we consider the function:

$$f(q) = \frac{q}{\sqrt{q^2 + 1}} \quad \text{and} \quad \Delta q(t) \ll 1 \quad (2-108)$$

taking into account Eq. (2-107), we obtain:

$$\frac{q + \Delta q(t)}{\sqrt{(q + \Delta q(t))^2 + 1}} - \frac{q}{\sqrt{q^2 + 1}} = \left(\frac{q}{\sqrt{q^2 + 1}} \right)' \Delta q = \left(\frac{1}{(q^2 + 1)^{3/2}} \right) \Delta q \quad (2-109)$$

Substituting Eq. (2-109) into Eq. (2-105) yields:

$$M\Delta\ddot{q}(t) + K\Delta q(t) = \frac{2\Delta P(t)}{L} \quad (2-110)$$

where K is the stiffness of the cable in the static equilibrium, obtained by Eq. (2-37):

$$K = \frac{4AE}{L} \left(\frac{L}{s_0} - \frac{1}{(q^2 + 1)^{3/2}} \right) \quad (2-111)$$

In free vibration the equation of motion is:

$$M\Delta\ddot{q}(t) + K\Delta q(t) = 0 \quad (2-112)$$

having the solution:

$$\Delta q(t) = a\sin(\omega t) + b\cos(\omega t) \quad (2-113)$$

where ω is the natural frequency of the system in the static equilibrium:

$$\omega = \sqrt{\frac{K}{M}} = \sqrt{\frac{4AE}{ML} \left(\frac{L}{s_0} - \frac{1}{(q^2 + 1)^{3/2}} \right)} \quad (2-114)$$

and the amplitudes a and b are defined by the initial conditions:

$$(a, b) = \left(\frac{\Delta\dot{q}(0)}{\omega}, \Delta q(0) \right) \quad (2-115)$$

where $\Delta\dot{q}(0)$ and $\Delta q(0)$ are the initial velocity and displacement, respectively.

In free damped vibration the equation of motion becomes [2-33]:

$$\begin{aligned} M\Delta\ddot{q}(t) + C\Delta\dot{q}(t) + K\Delta q(t) &= 0 \Rightarrow \\ \Rightarrow \Delta\ddot{q}(t) + \frac{C}{M}\Delta\dot{q}(t) + \frac{K}{M}\Delta q(t) &= 0 \Rightarrow \Delta\ddot{q}(t) + 2\zeta\omega\Delta\dot{q}(t) + \omega^2\Delta q(t) = 0 \end{aligned} \quad (2-116)$$

where ζ is the damping ratio. For $\zeta < 1$ the solution is:

$$\Delta q(t) = [A\sin(\omega_d t) + B\cos(\omega_d t)]e^{-\zeta\omega t} \quad (2-117)$$

where

$$\omega_d = \omega\sqrt{1 - \zeta^2} \quad (2-118)$$

The amplitudes A and B are defined again by the initial conditions:

$$(A, B) = \left(\frac{\Delta\dot{q}(0) + \Delta q(0)\zeta\omega}{\omega_d}, \Delta q(0) \right) \quad (2-119)$$

In forced vibration, in which $\Delta P(t)$ is a non-zero oscillatory load, expressed as $\Delta P(t) = aP \sin \Omega t$, the equation of motion of a damped system is:

$$M\Delta\ddot{q}(t) + C\Delta\dot{q}(t) + K\Delta q(t) = \frac{2\Delta P(t)}{L} \Rightarrow \Delta\ddot{q}(t) + 2\zeta\omega\Delta\dot{q}(t) + \omega^2\Delta q(t) = \frac{2\Delta P(t)}{ML} \quad (2-120)$$

having the solution:

$$\Delta q(t) = \frac{2aP}{ML[(1-\beta^2)^2 + (2\zeta\beta)^2]} \left\{ (1-\beta^2) \sin \Omega t - 2\zeta\beta \cos \Omega t + e^{-\zeta\omega t} \left[\Delta q(0) \cos \omega_D t + \frac{\Delta\dot{q}(0) + \Delta q(0)\zeta\omega}{\omega_d} \sin \omega_D t \right] \right\} \quad (2-121)$$

where $\beta = \Omega/\omega$ and

$$\omega_D = \omega\sqrt{1-\zeta^2} \quad (2-122)$$

The vibration modes and natural frequencies of a nonlinear system can be calculated conducting a linear modal analysis. Although it is not appropriate to perform any kind of linear analysis for nonlinear systems, it is important to know their linearised frequencies, in order to detect nonlinear dynamic phenomena, depending on the natural frequencies of the system, as it will be proved further on. Pugsley [2-34] gave some semi-empirical expressions for the first three in-plane modes of a sagged suspended chain, which could represent a hanging inextensible cable without pretension. He demonstrated the applicability of the results by conducting experiments on cables, in which the sag-to-span ratio ranged from 1:10 up to about 1:4. He used the expression:

$$\omega_n = \alpha_n \sqrt{\frac{g}{f}} \left[1 - \beta_n \left(\frac{f}{S} \right)^2 \right] \quad \text{where } n=1,2,3 \quad (2-123)$$

where f is the sag, g is the acceleration due to the gravity, S is the length of the chain and the coefficients α_n and β_n were obtained from experimental results. For the first three natural frequencies of the chain, from which the first and the third are related to antisymmetric modes and the second is related to the symmetric mode, the equations expressing the natural frequencies, based on Eq. (2-123), were:

$$\omega_1 = \frac{2\pi}{2\sqrt{2}} \sqrt{\frac{g}{f}} \left[1 - 3.0 \left(\frac{f}{S} \right)^2 \right] \quad (2-124)$$

$$\omega_2 = \frac{2\pi \cdot 1.4}{2\sqrt{2}} \sqrt{\frac{g}{f}} \left[1 - 1.5 \left(\frac{f}{S} \right)^2 \right] \quad (2-125)$$

$$\omega_3 = \frac{2\pi \cdot 2}{2\sqrt{2}} \sqrt{\frac{g}{f}} \left[1 - 0.7 \left(\frac{f}{S} \right)^2 \right] \quad (2-126)$$

From these formulae, it is interesting to note that the mass density m do not influence the frequencies of the hanging chain. These frequencies are similar to the natural frequency of the simple pendulum, which is:

$$\omega = \sqrt{\frac{g}{L}} \quad (2-127)$$

where L is its length (Figure 2-20), confirming that the hanging chain or the suspended inextensible slack cable swing in the vertical plane like a pendulum and the only force that tends to bring it back to the equilibrium state is gravity.

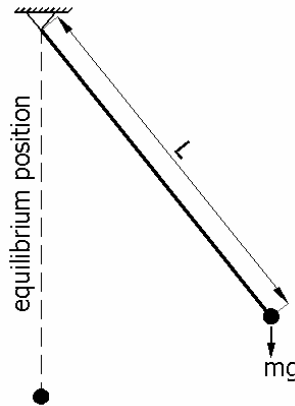


Figure 2-20: Simple pendulum

Ahmadi-Kashani [2-35] compared the semi-empirical formulae of Pugsley with numerical results for the entire range of sag-to-span ratio and slope angles θ (Figure 2-21). It was shown that Eq. (2-124) provided good approximations for the first frequency for slope angles $0^\circ < \theta < 65^\circ$. For the second mode the formula of Eq. (2-125) was applicable to larger values of θ i.e. $15^\circ < \theta < 85^\circ$ and for the third mode Eq. (2-126) did not yield as accurate results for angles $\theta > 35^\circ$. The reason may be due to the fact that, as the mode numbers increase, the experimental results become less and less accurate.

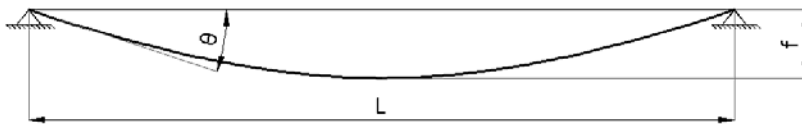


Figure 2-21: Geometry of the hanging cable assumed by Ahmadi-Kashani [2-35]

Improving the coefficients α_n and β_n for the expressions of the second and third natural frequencies, new approximate formulae were provided, for the first four in-plane and out-of-plane natural frequencies, applicable to a wide range of sag/span ratios and inclination angles. Thus, denoting the length of the cable as S , the in-plane natural frequencies of a hanging inextensible cable were expressed as:

$$\omega_1 = \frac{2\pi}{2\sqrt{2}} \sqrt{\frac{g}{f}} \left[1 - 3.00 \left(\frac{f}{S} \right)^2 \right] \quad (2-128)$$

$$\omega_2 = \frac{2\pi \cdot 1.43}{2\sqrt{2}} \sqrt{\frac{g}{f}} \left[1 - 1.44 \left(\frac{f}{S} \right)^2 \right] \quad (2-129)$$

$$\omega_3 = \frac{2\pi \cdot 2}{2\sqrt{2}} \sqrt{\frac{g}{f}} \left[1 - 1.30 \left(\frac{f}{S} \right)^2 \right] \quad (2-130)$$

$$\omega_4 = \frac{2\pi \cdot 2.45}{2\sqrt{2}} \sqrt{\frac{g}{f}} \left[1 - 0.90 \left(\frac{f}{S} \right)^2 \right] \quad (2-131)$$

while its out-of-plane natural frequencies were:

$$\omega_1 = \frac{2\pi}{4\sqrt{2}} \sqrt{\frac{g}{f}} \left[1 + 0.25 \left(\frac{f}{S} \right)^2 \right] \quad (2-132)$$

$$\omega_2 = \frac{2\pi \cdot 2}{4\sqrt{2}} \sqrt{\frac{g}{f}} \left[1 - 0.77 \left(\frac{f}{S} \right)^2 \right] \quad (2-133)$$

$$\omega_3 = \frac{2\pi \cdot 3}{4\sqrt{2}} \sqrt{\frac{g}{f}} \left[1 - 0.07 \left(\frac{f}{S} \right)^2 \right] \quad (2-134)$$

$$\omega_4 = \frac{2\pi \cdot 4}{4\sqrt{2}} \sqrt{\frac{g}{f}} \left[1 - 0.77 \left(\frac{f}{S} \right)^2 \right] \quad (2-135)$$

Irvine and Caughey [2-36] developed a linear theory for the free vibrations of a suspended cable, in which the sag-to-span ratio f/L is about 1:8 or less. They derived specific formulae for the frequencies of the in-plane and out-of-plane vibrations, introducing also the horizontal component of the pretension. They also compared their numerical results with experimental ones. The out-of-plane modes of a sagged cable were the swinging ones with frequencies:

$$\omega_n = \frac{n\pi}{L} \sqrt{\frac{H}{m}} \quad \text{where } n=1,2,3\dots \quad (2-136)$$

where H is the horizontal component of the initial pretension and m the cable mass density. The in-plane motion could be distinguished in antisymmetric in-plane modes, consisting of antisymmetric vertical components and symmetric longitudinal components and in symmetric ones, consisting of symmetric vertical components and antisymmetric longitudinal components. The frequencies of the antisymmetric in-plane modes of a sagged cable were described by:

$$\omega_n = \frac{2n\pi}{L} \sqrt{\frac{H}{m}} \quad \text{where } n=1,2,3\dots \quad (2-137)$$

The natural frequencies ω of the symmetric in-plane modes could be calculated by solving the following equation:

$$\tan\left(\frac{\tilde{\omega}}{2}\right) = \frac{\tilde{\omega}}{2} - \frac{4}{\lambda^2} \left(\frac{\tilde{\omega}}{2}\right)^3 \quad (2-138)$$

where:

$$\tilde{\omega} = \omega L \sqrt{\frac{m}{H}} \quad (2-139)$$

and

$$\lambda^2 = \left(\frac{8f}{L}\right)^2 \frac{LEA}{HL_e} \quad (2-140)$$

where L_e is the cable length defined as:

$$L_e = L \left[1 + 8 \left(\frac{f}{L} \right)^2 \right] \quad (2-141)$$

The length L_e is usually only a little larger than the span itself. Assuming $L \approx L_e$ for small sag-to-span ratios, Eq. (2-140) becomes:

$$\lambda^2 = 64 \left(\frac{f}{L} \right)^2 \frac{EA}{H} \quad (2-142)$$

The parameter λ^2 , which involves the cable geometry and elasticity, plays an important role in the cable's symmetric vibrations. The values of the frequencies for the in-plane symmetric modes depend on this parameter. Several cases were explored in [2-36] for different values of this parameter:

a) For large values of λ^2 the cable is considered as inextensible and Eq. (2-138) becomes:

$$\tan\left(\frac{\tilde{\omega}}{2}\right) = \frac{\tilde{\omega}}{2} \quad (2-143)$$

with the first two roots at:

$$(\tilde{\omega})_1 = 2.86\pi \text{ and } (\tilde{\omega})_2 = 4.92\pi \quad (2-144)$$

while the higher roots are quite accurately expressed as:

$$(\tilde{\omega})_n = (2n+1)\pi, \text{ where } n=3,4,5,\dots \quad (2-145)$$

b) For low values of λ^2 the cable is considered as a taut string with negligible sag and Eq. (2-138) becomes:

$$\tan\left(\frac{\tilde{\omega}}{2}\right) = -\infty \quad (2-146)$$

with roots:

$$(\tilde{\omega})_n = (2n-1)\pi, \text{ where } n=1,2,3,\dots \quad (2-147)$$

c) The roots of Eq. (2-138) depend on the value of the parameter λ^2 .

The first root lies between $1/2\pi$ and 1.43π , the second root lies between $3/2\pi$ and 2.46π , the third root lies between $5/2\pi$ and $7/2\pi$ and so on. In particular for:

- $\lambda^2 < 4\pi^2$ the frequency of the first symmetric in-plane mode is smaller than the frequency of the first antisymmetric in-plane mode and the vertical modal component of the first symmetric mode has no internal nodes with zero displacements along the span (Figure 2-22).

- $\lambda^2=4\pi^2$ the frequency of the first symmetric in-plane mode is equal to the frequency of the first antisymmetric in-plane mode. This phenomenon is called crossover of modes and this value of λ^2 designates the first crossover point. The vertical modal component of the first symmetric mode is tangential to the profile of the cable at each support (Figure 2-22).
- $\lambda^2>4\pi^2$ the frequency of the first symmetric in-plane mode is larger than the frequency of the first antisymmetric in-plane mode and the vertical modal component of the first symmetric mode has two internal nodes with zero displacements along the span (Figure 2-22).
- $\lambda^2=16\pi^2$ the second crossover point occurs and the frequency of the second symmetric in-plane mode is equal to the frequency of the second antisymmetric in-plane mode.
- In general, the parameter λ^2 takes the value $(\lambda_n)^2=(2n\pi)^2$ at the n^{th} crossover point.

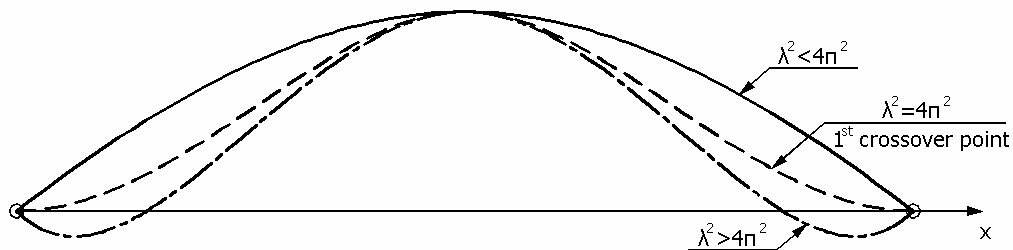


Figure 2-22: First symmetric mode for different values of the parameter λ^2

In addition, it was observed that the frequencies of the antisymmetric modes remain constant as λ^2 changes, while the frequencies of the symmetric modes change and at the crossover points become larger than the corresponding antisymmetric ones. This was also confirmed by conducting several experiments changing the sag of the cable and observing the first symmetric and the first antisymmetric in-plane vibration mode. As shown in Figure 2-23 the shape of the first symmetric mode changed before and after the first crossover point, while the one of the first antisymmetric mode remained unaltered.

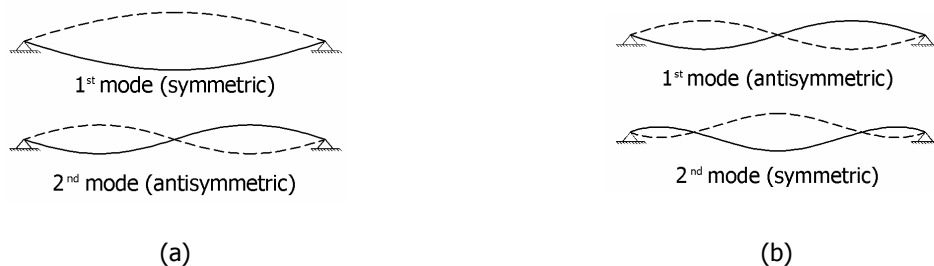


Figure 2-23: First two vibration modes of a simple suspended cable (a) before crossover, (b) after crossover

It should be mentioned that if an inextensible cable is investigated the phenomenon of modal transition does not occur, since λ^2 assumes a large value and the frequencies of the symmetric modes are no longer dependent on this parameter. The formulae provided by Irvine and Caughey, taking into account the pretension, are not comparable with the previous ones of Pugsley and Ahmadi-Kashani, which do not consider the pretension.

Rega and Luongo [2-37] explored an inextensible cable with flexible supports. Although an inextensible cable was assumed, the dynamic behaviour of the cable with the flexible supports was similar to the one of the elastic cable with fixed ends. The authors also investigated an elastic cable with flexible supports and they concluded that the cable extensibility plays a more important role than that of the supports in the system's dynamic behaviour. The former is sufficient by itself to cause crossover of all modes, while the latter causes transitions only under certain conditions.

The natural frequencies of an inclined cable do not present points of frequency crossover as proved in [2-38]. The points of frequency crossover are replaced by regions of frequency avoidance, in which the frequencies of the symmetric and the corresponding antisymmetric mode are close but distinct and their relative separation increases as the inclination angle of the cable increases. Due to the cable inclination, there is no longer symmetry of the static cable profile, which prohibits the formation of two separable sets of mode shapes. Near the frequency avoidance, the modes become hybrid, with mixture of symmetric and antisymmetric shapes and this has an important effect on the cable tension [2-39].

Hagedorn and Schäfer [2-40] investigated the effect of the nonlinear terms in the equations of motion on the first normal modes of the oscillations of an elastic flexible cable under the action of gravity. In [2-41] a nonlinear finite element approach was provided in order to calculate the static deflection and natural frequency for small oscillations about the nonlinear equilibrium position for single-span cables.

Zhang and Peil [2-42] studied the dynamic behaviour of an inclined cable in parametrically unstable zones for eleven cases of loading amplitude P_0 and for four cases of frequency ratios ω/ω_0 , where ω is the loading frequency and ω_0 the cable's frequency. They showed that the deformation modes of the cable depend on the loading amplitude and the frequency ratio. For frequency ratio $n=1.0$ the cable vibrates according to the first mode, while for $n>1.0$, modal transition takes place between the first mode and the modes of higher order, with the increase in the excitation strength. The change of the deformation mode indicates parametric instability of the cable. Therefore, the nonlinear parametric instability of the cable depends on both the frequency and the strength of excitation. Once the parametric instability occurs, the amplitudes of the cable will increase greatly, with vibration amplitudes larger than the ones caused by the fundamental resonance.

In [2-43] the equation of motion of an elastic cable as a continuous system was developed, having a quadratic and a cubic nonlinear term. The authors used the parameter λ^2 , defined by Eq. (2-142), as a parameter that determines the dynamic response of the cable. The frequency-amplitude relationship was obtained, proving that the behaviour of the cable is initially hardening for low λ^2 values. As λ^2 increases the behaviour is softening at low vibration amplitudes and becomes hardening again as the amplitude increases. In [2-44] the frequency-response curves for two prestressed cables were drawn, for a taut cable and a suspended sagged one. It was proved that the quadratic nonlinearity is responsible for the softening behaviour and the cubic nonlinearity for the hardening one. The shallower the cable is, the lower the effect of the quadratic nonlinearity becomes. Thus, the taut string presents a hardening response for every amplitude value, due to the prevailing cubic nonlinearity in the equation of motion. Instead, the response of the sagged suspended cable is softening at low vibration amplitudes, due to the large value of the coefficient of quadratic term, and becomes hardening as the amplitude increases. The same conclusions were derived in [2-45] where superharmonic resonance conditions of a simple cable were studied. In [2-46] the equation of motion of suspended elastic cables was studied under subharmonic resonances, detecting stable and unstable solutions. In [2-47] – [2-49] it was proved that internal resonance conditions of a suspended cable at crossover points lead to bifurcation mechanisms. A study for bifurcation and chaos mechanisms of simple cables, associated with the nonlinearity of the system, was also included in [2-50].

Srinil et al. [2-51] studied the free vibrations of sagged flexible horizontal or inclined cables in three-dimensional motion, conducting time-history analyses. It was shown that not only the 1:1 internal resonance between symmetric and antisymmetric modes – which corresponds to the crossover or avoidance points, respectively – but mostly the 2:1 internal resonances produce hybrid profiles of the cable's vibration and enhancement of the cable tension in some time intervals.

In [2-52] the free vibrations in three-dimensional motion of four undamped cables with different parameter λ^2 were explored, by means of time-history analyses. The cables were: a) one with small sag, considered as taut, b) one with λ^2 corresponding to the first crossover point, c) one corresponding to the 2nd crossover point and d) one with large sag. The ends of the cables were at the same level. Each cable was subjected to an initial displacement, having the spatial shape of a vibration mode at a time. No initial velocity and acceleration were taken into consideration. The cable nonlinear dynamic response was depicted in displacement diagrams versus time and diagrams of the maximum and minimum tension versus time, as well as Fourier amplitude spectra of the cable vertical displacements, in order to distinguish the frequencies of the oscillation. The interest was focused on two cables, which corresponded to the 1st and 2nd crossover point. 1:1 and 2:1 internal resonances produced beat phenomena in the time-history diagrams and transition of the vibration profile, exciting the modes involved in these internal resonances.

A review on nonlinear vibrations of simple suspended cables, regarding the mathematical modelling of the system, the methods of analysis, nonlinear dynamic phenomena, was included in [2-53]. Bifurcations and chaos phenomena of simple cables were also discussed in [2-54].

The dynamic response of a structure definitely depends on its stiffness and mass, but also on its damping. Damping is a characteristic of the structure associated with its capacity to dissipate the kinetic energy during the induced vibrations. It plays the most important role in the control of the oscillations caused by dynamic loads [2-55]. It is usually expressed as a percentage of the critical damping C_{cr} . For example, in a SDOF system the damping is calculated as [2-22]:

$$C = \zeta \cdot C_{cr} = 2 \cdot \zeta \cdot M \cdot \omega \quad (2-148)$$

where ζ is the damping ratio, M is the mass and ω is the circular natural frequency of the structure. In order to estimate the damping ratio in a system, experimental work is required in models or prototypes. That is why it is very difficult to estimate percentages of damping [2-22]. There are three sources of damping in cables: a) the material damping, due to the friction forces developed between the separated strands laid into a cable rope, which is usually small, b) the connection damping, due to the loss of energy from friction in joints and support connections and c) the environmental damping, due to the friction between the cables and the medium in which it is embedded, usually air or water [2-32]. Damping ratios for transmission lines, approximating the value of 2%, are suggested in [2-56]. Measurements of damping ratios for cable stays of a bridge, varying between 0.1%-0.3%, are reported in [2-57] and [2-58]. According to experiments, it was found that damping ratio is much higher for a slack cable, i.e. 4%, compared to a taut cable in which the damping ratio could arise at 0.4% [2-59].

2.4 CABLE NETWORKS

2.4.1 General

Prestressed cable net roofs can produce a wide range of shapes. The most frequent shape is the hyperbolic paraboloid. This kind of cable net is also called saddle roof, because the form resembles the shape of a saddle [2-60]. The surface of a hyperbolic paraboloid follows a convex curve with respect to one axis and a concave curve with respect to the other (Figure 2-24).

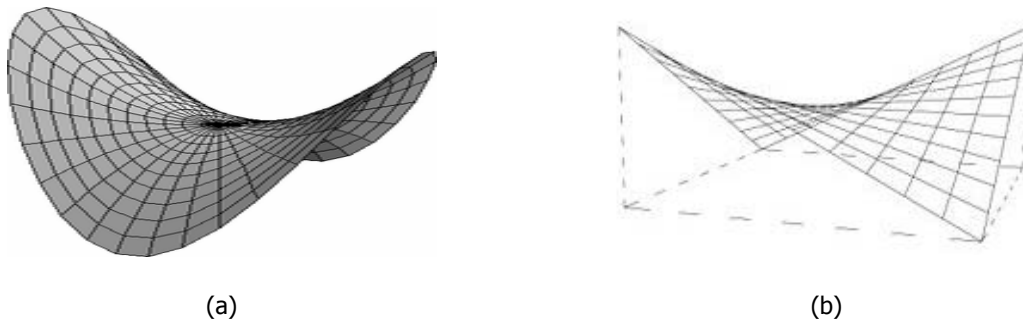


Figure 2-24: (a) Hyperbolic paraboloid, (b) Saddle roof

Mathematically, the hyperbolic paraboloid is a doubly ruled surface, and when it opens up along the x-axis and down along the y-axis, it can be described by:

$$z = \frac{x^2}{a^2} - \frac{y^2}{b^2} \tag{2-149}$$

For constant values of z, which correspond to a horizontal plane, the section is a hyperbola. For constant x or y values, corresponding to a vertical plane, the section is a parabola. If f_x/L_x and f_y/L_y are the sag-to-span ratios of a cable net forming a hyperbolic paraboloid surface, in x and y direction, respectively, Eq. (2-149) becomes:

$$z = \frac{4f_x}{L_x^2} x^2 - \frac{4f_y}{L_y^2} y^2 \tag{2-150}$$

with f_x, f_y taking always positive values. In case the sags are equal in both directions and the boundary is a circle, with $L_x=L_y=L$, the expressions giving the geometry of the structure (Figure 2-25) are:

$$z = \frac{4f}{L^2}(x^2 - y^2) \tag{2-151}$$

$$4x^2+4y^2=L^2 \tag{2-152}$$

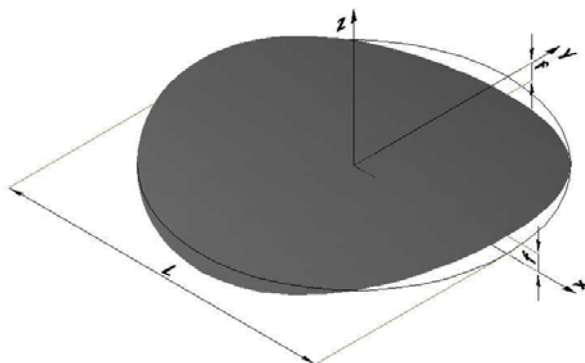


Figure 2-25: Saddle roof with circular plan view

A saddle-form cable network consists of two families of prestressed cables, which projected in plan create an orthogonal grid. The cables that are suspended from the highest points of the boundary are called carrying or main cables, while the stabilising or secondary cables are anchored at the lowest points of the boundary (Figure 2-26).

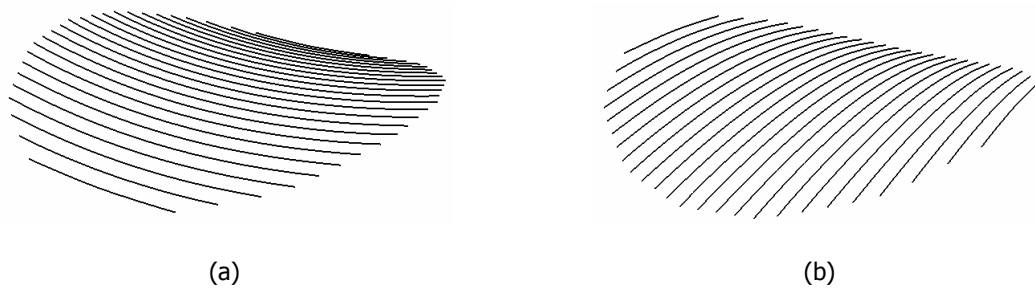


Figure 2-26: Components of a cable net: (a) main cables, (b) secondary cables

The cables are anchored to a boundary ring usually made of prestressed concrete with a closed box cross-section. It is supported by columns arranged radially and it is either rigidly connected with the columns or it seats on bearings placed on the top of the columns.

2.4.2 Static response of cable nets

Leonard in [2-32] gave an analytical solution for a simple cable net, consisting of two crossing cables, prestressing one another (Figure 2-27). The main features of that study are reported next. For the solution process, the prestressed state was considered to be the reference state. The origin of the coordinate system was placed at the central node and each segment was directed away from that node. The cross-sectional area at the unstressed state was A_0 and the instantaneous value of the elastic modulus at the reference state is E_R , conventionally based on the unstressed area A_0 , but assuming that it remained the same at the additionally deformed state. The span l and the sag ratio f_R for the two cables were equal. The initial pretension N_R with a horizontal component H_R , the elongation ratio λ_R and the length L of each segment in the prestressed reference configuration were the same for both cables.

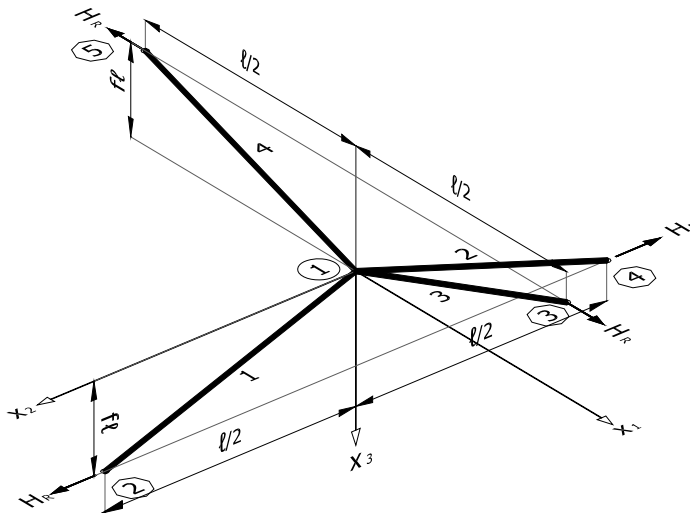


Figure 2-27: Simple cable net

Let S_0 be the initial unstressed length of the cables and ϵ the small initial strain, which, according to Hooke's law, will be:

$$\epsilon = \frac{L - S_0}{S_0} = \frac{N_R}{E_R A_0} \quad (2-153)$$

If p is defined as:

$$\rho = \sqrt{1 + 4f_R^2} \quad (2-154)$$

then

$$L = \frac{\ell}{2} \sqrt{1 + 4f_R^2} = \frac{\ell \rho}{2} \quad (2-155)$$

$$\frac{N_R}{H_R} = \frac{2L}{\ell} \Rightarrow N_R = H_R \rho \quad (2-156)$$

$$\lambda_R = \frac{L}{S_0} = \frac{S_0}{S_0} + \frac{L}{S_0} - \frac{S_0}{S_0} = 1 + \varepsilon = 1 + \frac{N_R}{E_R A_0} = 1 + \frac{H_R \rho}{E_R A_0} \quad (2-157)$$

The segment stiffness matrix is:

$$[{}^e K] = \frac{1}{L} \begin{bmatrix} B & -B \\ -B & B \end{bmatrix} \quad (2-158)$$

where

$$[B_i] = N_R [I] + (E_R A_0 \lambda_R - N_R) [\theta_{Ri}] [\theta_{Ri}]^T \quad (2-159)$$

and θ_{Ri} are the direction cosines for segment i in the prestressed reference state:

$$\begin{aligned} [\theta_{R1}]^T &= [0 \quad 1/\rho \quad 2f_R/\rho], \quad [\theta_{R2}]^T = [0 \quad -1/\rho \quad 2f_R/\rho] \\ [\theta_{R3}]^T &= [1/\rho \quad 0 \quad -2f_R/\rho], \quad [\theta_{R4}]^T = [-1/\rho \quad 0 \quad -2f_R/\rho] \end{aligned} \quad (2-160)$$

Substituting Eqs. (2-156) and (2-157) into Eq. (2-159):

$$[B_i] = H_R \rho [I] + \left(E_R A_0 \left(1 + \frac{H_R \rho}{E_R A_0} \right) - H_R \rho \right) [\theta_{Ri}] [\theta_{Ri}]^T = H_R \rho [I] + E_R A_0 [\theta_{Ri}] [\theta_{Ri}]^T \quad (2-161)$$

The system stiffness matrix is:

$$[K] = \frac{1}{L} \begin{bmatrix} [B_1] + [B_2] + [B_3] + [B_4] & -[B_1] & -[B_2] & -[B_3] & -[B_4] \\ -[B_1] & [B_1] & [0] & [0] & [0] \\ -[B_2] & [0] & [B_2] & [0] & [0] \\ -[B_3] & [0] & [0] & [B_3] & [0] \\ -[B_4] & [0] & [0] & [0] & [B_4] \end{bmatrix} \quad (2-162)$$

where $[0]$ denotes a 3x3 null matrix. The equation of equilibrium for the system to be solved is:

$$[K][D] = [P] \Rightarrow \frac{1}{L} \begin{bmatrix} [B_1] + [B_2] + [B_3] + [B_4] & -[B_1] & -[B_2] & -[B_3] & -[B_4] \\ -[B_1] & [B_1] & [0] & [0] & [0] \\ -[B_2] & [0] & [B_2] & [0] & [0] \\ -[B_3] & [0] & [0] & [B_3] & [0] \\ -[B_4] & [0] & [0] & [0] & [B_4] \end{bmatrix} \begin{bmatrix} D_1 \\ D_2 \\ D_3 \\ D_4 \\ D_5 \end{bmatrix} = \begin{bmatrix} P_1 \\ P_2 \\ P_3 \\ P_4 \\ P_5 \end{bmatrix} \quad (2-163)$$

Applying the boundary conditions, the displacements $\{D_2\}$, $\{D_3\}$, $\{D_4\}$ and $\{D_5\}$ of the support nodes 2 to 5 are zero, and the external loads $\{P_2\}$, $\{P_3\}$, $\{P_4\}$ and $\{P_5\}$ are unknown changes in reactions, the matrix is partitioned as shown by dashed lines. Thus, the equation of equilibrium becomes:

$$\{[B_1] + [B_2] + [B_3] + [B_4]\}[D_1] = [P_1] \quad (2-164)$$

For the system of Figure 2-27 Eq. (2-164) becomes:

$$\begin{bmatrix} 4\left(\frac{2H_R\rho^3 + E_R A_0}{\ell\rho^3}\right) & 0 & 0 \\ 0 & 4\left(\frac{2H_R\rho^3 + E_R A_0}{\ell\rho^3}\right) & 0 \\ 0 & 0 & 8\left(\frac{H_R\rho^3 + 4E_R A_0 f_R^2}{\ell\rho^3}\right) \end{bmatrix} \begin{bmatrix} d_{11} \\ d_{12} \\ d_{13} \end{bmatrix} = \begin{bmatrix} P_x \\ P_y \\ P_z \end{bmatrix} \quad (2-165)$$

where d_{1i} is the displacement of node 1 in the x_i direction. The solution of Eq. (2-165) is:

$$d_{11} = d_{12} = 0$$

$$d_{13} = \frac{P_z \ell \rho^3}{8(H_R \rho^3 + 4E_R A_0 f_R^2)} \quad (2-166)$$

In the chart of Figure 2-28 the nondimensionalised deflections w are plotted with respect to the sag ratio f_R , for three values of the ratio $E_R A_0 / H_R$, where w is defined as:

$$w = 8d_{13} \frac{E_R A_0}{P_z \ell} \quad (2-167)$$

It is noted that as the sag ratio increases the system becomes stiffer and the deflection of the central node decreases. As the ratio $E_R A_0 / H_R$ increases corresponding to smaller horizontal component of pretension H_R , the stiffness of the system also decreases and for the same sag ratio f_R the deflection increases. However, the effect of the sag ratio to the deflection of the central node is more important than the one of the modulus of rigidity. For $f_R > 0.20$ the three curves practically coincide, while values of sag ratio larger than 0.45 do not influence the deflection significantly.

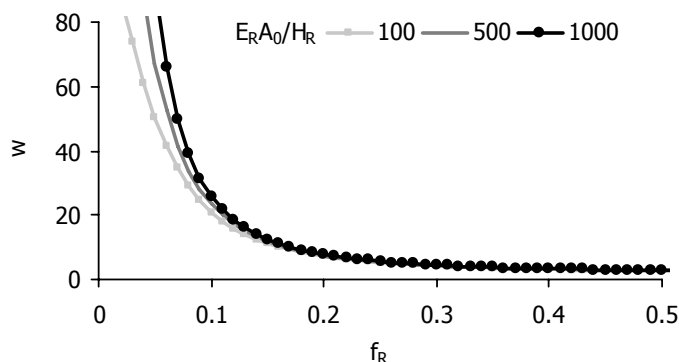


Figure 2-28: Deflections vs. sag ratio of cable net

Gero in [2-61] and [2-62] introduced a method for the scaling of a large network to a smaller one, both having fixed cable edges. The method is based on the Buckingham Pi theorem, which is a key theorem in dimensional analysis ([2-63], [2-64]). The Buckingham Pi theorem states that the

functional dependence between a certain number (e.g.: n) of variables can be reduced by the number (e.g. k) of independent dimensions occurring in those variables to give a set of $p=n-k$ independent, dimensionless numbers. It provides a method for computing sets of dimensionless parameters from the given variables. However, the choice of dimensionless parameters is not unique.

The method proposed the transformation of a network with large number of cables, called prototype, to a smaller network, that had a geometry similar to the prototype, referred to as model, using transformation relations and design charts that were produced with geometrically nonlinear analyses. The two networks, the prototype and the model, should have similar geometries, so that their corresponding quantities could also be similar. All cables were arranged in equal distances and had the same material, which was assumed to be linearly elastic. The nets were uniformly prestressed and loaded with nodal loads. The charts described the behaviour of the model, namely the maximum cable tension and the maximum net deflection, for different loads and axial cable stiffness. A typical chart for a flat cable net is shown in Figure 2-29. Using the transverse transformation relations, it was possible to evaluate the behaviour of the prototype. The charts produced were dimensionless and could be used for every system of units.

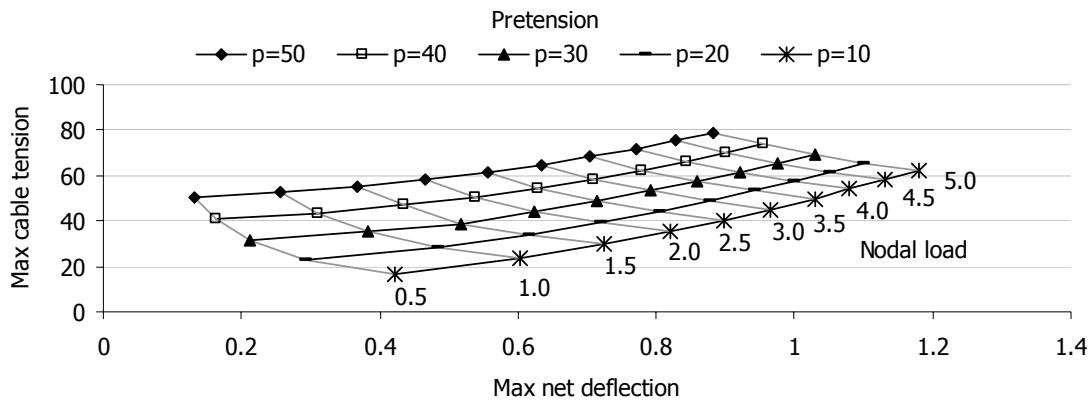


Figure 2-29: A typical design chart for a flat cable net with axial cable stiffness $EA=20000$

The proposed transformation relations are the following:

$$W_m = W_p \left(\frac{E_m}{E_p} \right) \left(\frac{L_m}{L_p} \right)^2 \left(\frac{N_p}{N_m} \right)^2 \quad : \text{nodal loads} \quad (2-168)$$

$$A_m = A_p \left(\frac{L_m}{L_p} \right)^2 \left(\frac{N_p}{N_m} \right) \quad : \text{cable cross-sectional area} \quad (2-169)$$

$$(EA)_m = (EA)_p \left(\frac{E_m}{E_p} \right) \left(\frac{L_m}{L_p} \right)^2 \left(\frac{N_p}{N_m} \right) \quad : \text{cable axial stiffness} \quad (2-170)$$

$$P_m = P_p \left(\frac{E_m}{E_p} \right) \left(\frac{L_m}{L_p} \right)^2 \left(\frac{N_p}{N_m} \right) \quad : \text{cable pretension} \quad (2-171)$$

$$T_m = T_p \left(\frac{E_m}{E_p} \right) \left(\frac{L_m}{L_p} \right)^2 \left(\frac{N_p}{N_m} \right) \quad : \text{cable tension} \quad (2-172)$$

$$d_m = d_p \frac{L_m}{L_p} \quad : \text{ nodal deflections} \quad (2-173)$$

where N is the number of the cables per direction, L is the maximum length of the cables, E the elastic modulus of the cables, while m and p are subscripts referring to model and prototype, respectively.

However, the deformability of the edge ring caused a variation in the tension of the cables and in the deflection of the net. Szabó et al. [2-65] proposed a method of preliminary analysis of cable nets with elliptical plan view, which considers the effect of the closed edge ring on the response of the net. This method was developed in two steps: a) the edge ring was presumed infinitely rigid and consequently undeformed, and the problem was solved only for the cable force distribution that caused compression to the ring, b) the edge ring was presumed deformable and the problem was solved only for the cable force distribution that developed bending to the ring. However, that method did not take into account the change of the cable geometry, thus the calculation was based on the undeformed structure. The influence of the deformations could be taken into consideration by repeating the process, taking the changed shape as a basis for the next iteration.

In [2-66] some mathematical techniques were described, in order to determine the initial shape of cable structures and compute their displacements resulting from static loads, considering the geometric nonlinearity. In [2-67], cable nets with elasto-plastic behaviour were assumed and the equilibrium equations were derived, considering the history of loading and the slackening of cables. A numerical method to calculate the static response of cable nets was presented in [2-68]. The numerical results were compared with experimental ones, resulting in good agreement.

A mathematical model for the analysis of such systems was presented by Talvik [2-69], in which the cable net and the flexural boundary structure were treated as two separate substructures, the former as a nonlinear structure and the latter as a linear one. At first, 1) the equilibrium position of the cable network was determined, using the dynamic relaxation method, 2) the cable forces of the segments adjacent to the contour were transformed to nodal loads applied to the contour, 3) the displacements of the elastic contour beam were calculated and 4) transformed to the displacements of the cable net supports. These displacements were compared with the ones calculated at step (1) and used for the second iteration, beginning again from step (1). The significance of the edge ring modelling to the static response of the cable net was also underlined in [2-70].

Majowiecki and Zoulas [2-71] investigated the influence of the mesh net and the bending stiffness of the contour ring on the structure's response. They showed that the number of cables did not influence significantly neither the net's vertical displacement in the centre of the rope net, nor the horizontal displacement of the ring, but instead the internal forces of the ring depended on the mesh density. As the ring's moments of inertia increased the vertical and horizontal deformation of the net and the ring, respectively, decreased, the axial force of the ring and the cable forces decreased also, while the ring's moment increased. They concluded that the interaction between the cable net and the flexible boundary ring should be taken into account in the analysis and that the fixed end hypothesis did not give any useful design information for actual structures, even for a preliminary design phase.

2.4.3 Dynamic response of cable nets

In tension structures, the dynamic loads are more significant than static loads and they may lead to large amplitude vibrations, overstressing of cables and fatigue problems. In cable structures, the stiffness is relatively small compared to other structural types while the mass may be large because of attached components or cladding. The natural frequencies of such structures are expected to be

smaller than most other structural components, since they are proportional to the square root of the stiffness to mass ratio.

In [2-72] the author derived a formula for the first frequency of a simple flat cable net, consisting of two cables, having the same pretension and cross-section. Leonard in [2-32], considering lumped or consistent masses [2-9], provides an analytical solution for the frequencies of a simple cable net with initial sag, having the shape of a cross as described in section 2.4.2. Reporting from [2-32], the Rayleigh-Ritz procedure [2-73] is applied and the displacement u_i of cable segment i of length L , is written as a linear combination of two shape functions:

$$u_i(x) = \psi_1(x)d_{i1} + \psi_2(x)d_{i2} \quad (2-174)$$

where the shape functions are:

$$\psi_1(x) = 1 - x/L = 1 - \xi \text{ and } \psi_2(x) = x/L = \xi \quad (2-175)$$

and d_{i1} , d_{i2} are nodal values of u_i at $x=0$ ($\xi=0$) and $x=L$ ($\xi=1$), respectively.

If m is the mass density per unit volume in the prestressed state, the consistent mass matrix for segment i will be:

$$M_i = \begin{bmatrix} m_{11} & m_{12} \\ m_{21} & m_{22} \end{bmatrix} \quad (2-176)$$

where

$$m_{ij} = \int_0^L A m \psi_i(x) \psi_j(x) dx \text{ with } i, j = 1, 2 \quad (2-177)$$

and A is the cross-sectional area in the prestressed state. If m_0 and A_0 are the mass density per unit volume and the cross-sectional area of the cable segment in the unstressed state, respectively, then, applying the principle of conservation of mass, the total mass of the segment is:

$$mAL = m_0 A_0 S_0 = m_0 A_0 L / \lambda_R \quad (2-178)$$

where λ_R is expressed by Eq. (2-157). Hence, the consistent mass matrix for the segment i is expressed as:

$$M_i = \frac{mAL}{6} \begin{bmatrix} 2 & 1 \\ 1 & 2 \end{bmatrix} = \frac{m_0 A_0 L}{6 \lambda_R} \begin{bmatrix} 2 & 1 \\ 1 & 2 \end{bmatrix} \quad (2-179)$$

If the mass matrix is considered as lumped, then:

$$M_i = \begin{bmatrix} m_{11} & 0 \\ 0 & m_{22} \end{bmatrix} = \frac{mAL}{2} \begin{bmatrix} 1 & 0 \\ 0 & 1 \end{bmatrix} = \frac{m_0 A_0 L}{2 \lambda_R} \begin{bmatrix} 1 & 0 \\ 0 & 1 \end{bmatrix} \quad (2-180)$$

where

$$m_{ii} = \int_0^L A m \psi_i(x) dx \quad i = 1, 2 \quad (2-181)$$

The assembled mass matrix of the cross cable system is therefore:

$$M = \frac{m_0 A_0 L}{6\lambda_R} a \begin{bmatrix} 4 & b & b & b & b \\ b & 1 & 0 & 0 & 0 \\ b & 0 & 1 & 0 & 0 \\ b & 0 & 0 & 1 & 0 \\ b & 0 & 0 & 0 & 1 \end{bmatrix} \quad (2-182)$$

where $a=3$ and $b=0$ for lumped mass matrix and $a=2$, $b=0.5$ for consistent mass matrix. Applying the boundary conditions, the displacements $\{D_2\}$, $\{D_3\}$, $\{D_4\}$ and $\{D_5\}$ of the support nodes 2 to 5 are zero, thus the equations of free vibration of node 1 are:

$$\left[-\frac{2m_0 A_0 L^2 \omega^2}{3\lambda_R} a [I] + \{[B_1] + [B_2] + [B_3] + [B_4]\} \right] [d] = [0] \quad (2-183)$$

and the three eigenfrequencies of the system are:

$$\begin{aligned} \omega_1 &= \left[\frac{3\lambda_R}{2am_0 A_0 \ell \rho} \frac{2}{\ell \rho} \left(4H_R \rho + \frac{16E_R A_0 f_R^2}{\rho^2} \right) \right]^{1/2} \Rightarrow \\ \omega_1 &= \left[\frac{24E_R}{am_0 \ell^2} \frac{\lambda_R}{\rho^4} \left(\frac{H_R}{E_R A_0} \rho^3 + 4f_R^2 \right) \right]^{1/2} \Rightarrow \\ \omega_1 &= \left[\frac{24E_R}{am_0 \ell^2} \left(\frac{1}{1+4f_R^2} \right)^2 \left(1 + \frac{H_R}{E_R A_0} \sqrt{1+4f_R^2} \right) \left(\frac{H_R}{E_R A_0} (1+4f_R^2)^{3/2} + 4f_R^2 \right) \right]^{1/2} \Rightarrow \\ \omega_1 &= \left[\frac{1}{a} \frac{24E_R}{m_0 \ell^2} \left(\frac{1}{1+4f_R^2} \right)^2 \left(1 + \frac{T_R}{E_R A_0} \right) \left(\frac{T_R}{E_R A_0} (1+4f_R^2) + 4f_R^2 \right) \right]^{1/2} \end{aligned} \quad (2-184)$$

$$\begin{aligned} \omega_2 = \omega_3 &= \left[\frac{3\lambda_R}{2am_0 A_0 \ell \rho} \frac{2}{\ell \rho} \left(4H_R \rho + \frac{2E_R A_0}{\rho^2} \right) \right]^{1/2} \Rightarrow \\ \omega_2 = \omega_3 &= \left[\frac{12}{am_0 \ell^2} \frac{\lambda_R}{\rho^4} \left(\frac{2H_R}{E_R A_0} \rho^3 + 1 \right) \right]^{1/2} \Rightarrow \\ \omega_2 = \omega_3 &= \left[\frac{12E_R}{am_0 \ell^2} \left(\frac{1}{1+4f_R^2} \right)^2 \left(1 + \frac{H_R}{E_R A_0} \sqrt{1+4f_R^2} \right) \left(\frac{2H_R}{E_R A_0} (1+4f_R^2)^{3/2} + 1 \right) \right]^{1/2} \Rightarrow \\ \omega_2 = \omega_3 &= \left[\frac{12E_R}{am_0 \ell^2} \left(\frac{1}{1+4f_R^2} \right)^2 \left(1 + \frac{T_R}{E_R A_0} \right) \left(\frac{2T_R}{E_R A_0} (1+4f_R^2) + 1 \right) \right]^{1/2} \end{aligned} \quad (2-185)$$

with eigenvectors:

$$V_1 = \begin{bmatrix} 0 \\ 0 \\ 1 \end{bmatrix}, V_2 = \begin{bmatrix} 0 \\ 1 \\ 0 \end{bmatrix}, V_3 = \begin{bmatrix} 1 \\ 0 \\ 0 \end{bmatrix} \quad (2-186)$$

For multi-degree-of-freedom models numerical analyses have been conducted in order to investigate the dynamic behaviour of the system regarding the natural frequencies. In [2-74] a transfer matrix

method was presented for calculating the natural frequencies of orthogonal flat cable nets. Examples with up to six cables in each direction were compared with a finite element method and their results for the first four frequencies showed good agreement. This method resulted in frequencies of the net, which were independent of the number of the cables in each direction. A boundary element approach was included in [2-75] in order to calculate the eigenfrequencies and the mode shapes of the free vibrations of flexible membranes with arbitrary shape. In [2-76] the authors presented a computational scheme for vibration analysis of flat cable nets consisting of highly tensioned cables and having orthogonal projections in plan. They were assumed to be subject to inertial forces concentrated at the cable intersections. The technique was based on decomposing the n dimensional vector space of a problem with n degrees of freedom, into a number of independent subspaces each of dimension r , where $r \leq n$ and then solving for the r eigenvalues.

Gambhir and Batchelor, in [2-77], developed a finite element method for the analysis of cable nets, flat or with initial sag, modelling the prestressed cable net as a series of finite length curved elements. Several boundary shapes were applied in order to evaluate their method. The numerical results giving the fundamental frequency of the cable net were compared with experimental ones resulting in sufficient accuracy. In [2-78], they investigated the influence of various parameters, such as the cable cross-sectional area, the initial pretension and the sag-to-span ratio, on the natural frequencies of 3D cable nets of two different types: type A, a hyperbolic paraboloid, bounded by straight line generators with cables parallel to these generators (Figure 2-30), and type B, being a hyper cable net with curved boundaries (Figure 2-31). It was shown that the natural frequencies a) were inversely proportional to span or linear dimension for both types of cable networks, b) were proportional to \sqrt{N} , where N is the pretension in each cable, for both types, c) were linearly related to the surface curvature, denoted as $8h_x/L_x^2$, d) were closely related to those of a taut cable if the rise/span ratio was zero, and as the ratio increased modal transition occurred. The modal shapes were not influenced by the change in cable span and pretension. In addition, an increase in the cable rigidity, resulting from an increase of the cross-sectional area of the cables, which also yielded to an increase of the mass per unit length, kept unaltered the natural frequencies.

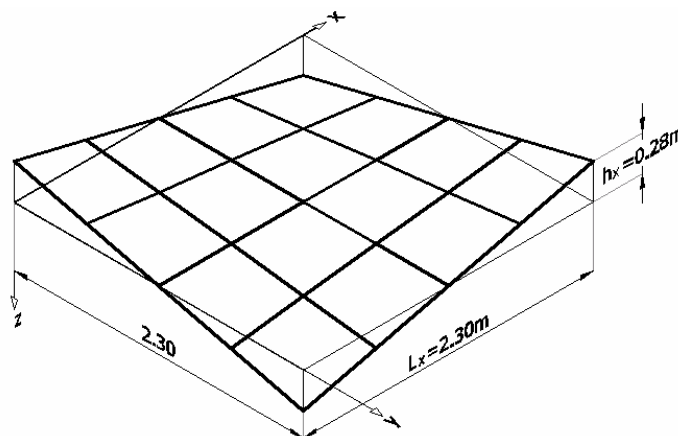


Figure 2-30: Cable net of type A (from [2-78])

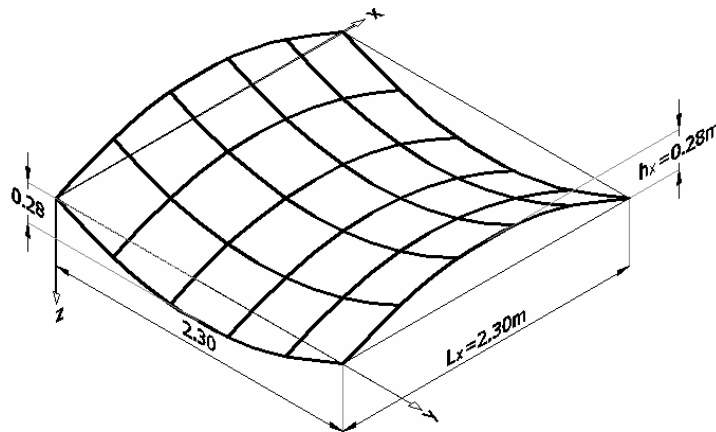


Figure 2-31: Cable net of type B (from [2-78])

Seeley et al. [2-79] studied the natural frequencies and modal shapes of a cable network with a circular plan view, forming a concave surface. The nets consisted of circular and radial cables with sag-to-span ratios between 1/9 and 1/15. The fundamental frequency of the net was described by an approximate formula, by means of the sag and the sag-to-span ratio. The value of this natural frequency was proved to be close to an average of the frequencies of the first in-plane and out-plane modes of a simple sagged cable with the same sag-to-span ratio.

Talvik [2-69] noticed that, in a cable network with an elliptical flexible contour ring (Figure 2-32), the first vibration mode involved mostly the contour ring, while the next four modes were determined only by cable net deformations. In the case of forced vibration, the motion of the contour ring dominated, while the cable net executed coupled motion.

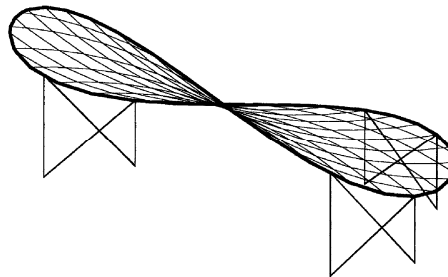


Figure 2-32: Saddle-shaped cable network with elliptical boundary structure (from [2-69])

Most of the pertinent publications, referring to the dynamic behaviour of cable nets, present new computerised methods of analysis and other numerical techniques to calculate the nonlinear dynamic response of cable networks and membranes, by solving the governing equations of motion ([2-80] – [2-87]), several of them compared with experimental results. In [2-88] a modified modal superposition method is used, appropriate for nonlinear systems, considering their geometrical nonlinearities by changing the geometry under load.

Geschwindner and West [2-89] studied the dynamic behaviour of the Aden Airways Network, having the shape of a rhomboid hyperbolic paraboloid. They conducted nonlinear dynamic analyses of a cable network oscillation for symmetric or antisymmetric spatial distributions of the dynamic load. They concluded that a uniform loading produced an almost linear dynamic response, whilst antisymmetric loads rendered the behaviour of the system more nonlinear.

Fan et al. [2-90] investigated the nonlinear dynamic response of a cable suspended roof during a strong earthquake. They concluded that, although the cable suspended roofs were not damaged as

other stiffer structures during strong earthquakes, since their natural frequencies were low in relation to the earthquake frequencies, they might lose their bearing capacity to resist vertical seismic effect, due to the nonlinear vibration of the system, which procured jump phenomena detected in the diagrams of the backbone curves.

Lazzari et al. [2-91] proposed a numerical analysis of the response of wind-induced flexible structures, offering the advantage to capture the effects of nonlinearities of both structural and aerodynamic origins of the problem. They also studied the free vibrations of a real saddle-form cable net, its resonant behaviour and its dynamic response under wind action. They interpreted the beat phenomenon of the displacement time-history diagram, in case of primary resonance, as the change of stiffness due to increase of deformation, producing also a change of the resonance frequency and avoiding the well-known continuously increasing amplitude of vibration, which occurs in linear systems.

Damping results from energy loss mechanisms and can be explained as material structural and aerodynamic. The damping sources are the structural system and its material, the roof cladding, the nodal point joints, the pre-stressing, the influence of air and external loads and the supporting structure. The damping ratio depends on the vibrating modes. Damping ratios, obtained by model tests for a rhomboid saddle-shaped roof, vary between 1% and 3%, if the structure is made of a cable net, 5%-10% if the cable net is combined with membrane and 7%-12% if the structure consists only of a membrane [2-92]. In [2-21], the damping ratio of an opened cable net roof was referred equal to 0.78%. The cable net had a surface of a hyperbolic paraboloid, with a circular plan view of diameter $L=120\text{m}$ and a sag-to-span ratio equal to $f/L=3\%$ for both main and secondary cables. The self-weight of the roof, including the net and the cladding was equal to 0.6kN/m^2 , and an additional air mass was assumed to be vibrating with the roof, only in resonant conditions, equal to 60kg/m^2 . In addition, the measured frequencies and damping ratios were mentioned, for the first four vibration modes of the saddle-shaped net roof over the Palais de sport in Milan, Italy, having a diameter of 125m (Table 2-1) and for the first two vibration modes of an experimental $20\text{m}\times 20\text{m}$ saddle-shaped net with edge cables and roofing membrane (Table 2-2).

Table 2-1: Measured frequencies and damping ratios for the roof of the Palais de sport in Milan

Mode	f (Hz)	ζ
1	0.7407	0.0188
2	0.8197	0.0218
3	1.0526	0.0164
4	1.1236	0.0110

Table 2-2: Measured frequencies and damping ratios for the experimental net

Mode	f (Hz)	ζ
1	1.59	0.0179
2	1.74	0.0175

The damping of a MDOF system is introduced as Rayleigh damping, which is expressed as [2-22]:

$$[C]=\alpha_0[M]+\alpha_1[K] \quad (2-187)$$

where $[C]$ is the damping matrix, $[M]$ is the mass matrix of the system and $[K]$ is the stiffness matrix corresponding to the zero initial displacements. The constants α_0 and α_1 have units of sec^{-1} and sec , respectively. The damping ratio for the n^{th} mode of a system is:

$$\zeta_n = \frac{\alpha_0}{2\omega_n} + \frac{\alpha_1\omega_n}{2} \quad (2-188)$$

The coefficients α_0 and α_1 can be determined from specified damping ratios ζ_i and ζ_j for the i^{th} and j^{th} modes, respectively, which leads to the following expression:

$$\frac{1}{2} \begin{bmatrix} \frac{1}{\omega_i} & \omega_i \\ \frac{1}{\omega_j} & \omega_j \end{bmatrix} \begin{Bmatrix} \alpha_0 \\ \alpha_1 \end{Bmatrix} = \begin{Bmatrix} \zeta_i \\ \zeta_j \end{Bmatrix} \quad (2-189)$$

If both modes have the same damping ratio ζ , then:

$$\alpha_0 = \zeta \frac{2\omega_i\omega_j}{\omega_i + \omega_j} \quad (2-190)$$

$$\alpha_1 = \zeta \frac{2}{\omega_i + \omega_j} \quad (2-191)$$

The modes i and j , chosen to define the coefficients α_0 and α_1 , must ensure that the damping ratio will be reasonable for all the modes contributing to the response. If, for example, five modes are included in the dynamic analysis and have almost the same damping ratio, the coefficients α_0 and α_1 should be calculated taking into account the eigenfrequencies of the first and the fourth mode. In this way, the damping ratio of the second and the third mode is slightly larger than ζ , while for modes higher than the fifth one it increases monotonically with frequency [2-22].

2.5 CABLE PROPERTIES

The basic element for cables is the steel wire with a tensile strength larger than that of ordinary structural steel. The steel wire has a cylindrical shape with a diameter of between 3 and 7 mm. A single straight wire, surrounded by a single layer of six wires with the same pitch and direction of helix, makes up the seven-wire strand [2-93], as shown in Figure 2-33.



Figure 2-33: Seven-wire strand

A straight wire core surrounded by successive spinning of layers, generally with opposite direction of helix, creates the multi wire helical strands, called spiral strands. Due to the twisting of the layers, the helical strand becomes self-compacting and thus there is no need to wrap or apply bands around the strand to hold the wires together. Typical values of the elastic modulus for a spiral strand are $E=145-170\text{GPa}$, depending on the size, almost 15-25% lower than the one for the single wire. In addition, the strength of the helical strand is approximately 10% lower than the sum of the breaking strengths of the individual wires. The way of winding defines the type of the strand. The main types of strands are those with one layer of wires (single layer strand), with two layers consisting of the same number of wires for each layer (seale strand), with two layers of wires having the same diameter for each layer (filler wire strand), with two layers of wires having different diameters in the outer layer (Warrington strand) and the multi-layer strands (combined patterns strand), as illustrated in Figure 2-34. Alternatively, the wire rope is composed by a number of steel wires spun together to form six strands, which in turn are spun together around a fiber core to form a rope (Figure 2-35).

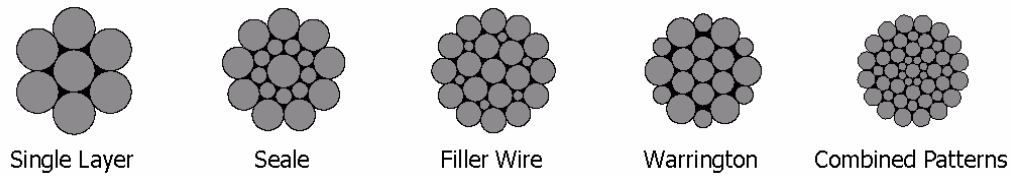


Figure 2-34: Basic strand construction

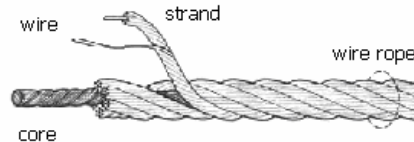


Figure 2-35: Wire rope

Locked coil strands are composed of two types of twisted wire: in the core normal round wires arranged as in a normal helical strand, and in the outer layers wires of a special Z-shape. This Z-shape is chosen so that the wires interlock which, in combination with the self-compacting effect from the spiral arrangement, ensures a tight surface (Figure 2-36). The locked-coil strands are more compact than any other type of strand. The elastic modulus is approximately $E=160-180\text{MPa}$.

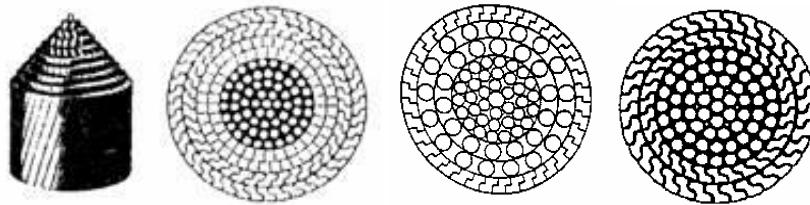


Figure 2-36: Typical cross-sections of locked coil strands

The term lay refers to the direction of the twist of the wires in a strand and to the direction that the strands are laid in the rope. In some cases, both wires in the strand and strands in the rope are laid in the same direction; otherwise, the wires are laid in one direction and the strands are laid in the opposite direction, depending on the intended use of the rope. The six types of lays used in wire ropes are as follows: 1) Right Regular Lay (RRL): The strands are laid in clockwise direction around the core and the wires in the strand are laid in a counter clockwise direction. 2) Left Regular Lay (LRL): The strands are laid in a counter clockwise direction around the core and the wires in the strand are laid in a clockwise direction. In this lay, each step of fabrication is exactly opposite from the right regular lay. In these two ways, the wires are parallel to the longitudinal axis of the strand. 3) Right Lang Lay (RLL): The strands are laid in a clockwise direction around the core and the wires in the strands are laid in clockwise direction. 4) Left Lang Lay (LLL): The strands are laid in a counter clockwise direction around the core and the wires in the strand are laid in a counter clockwise direction. These two lays are more resistant to the bending fatigue and to the abrasion than the previous two. 5) Right Alternate Lay (RAL): The strands are laid in clockwise direction. The wire in the strands are laid in a clockwise and counter clockwise direction in alternating strands and 6) Left Alternate Lay (LAL): The strands are laid in a counter clockwise direction, while the wire in the strands are laid in a counter clockwise direction in alternating strands [2-94]. These six different lays of wire rope are shown in Figure 2-37.

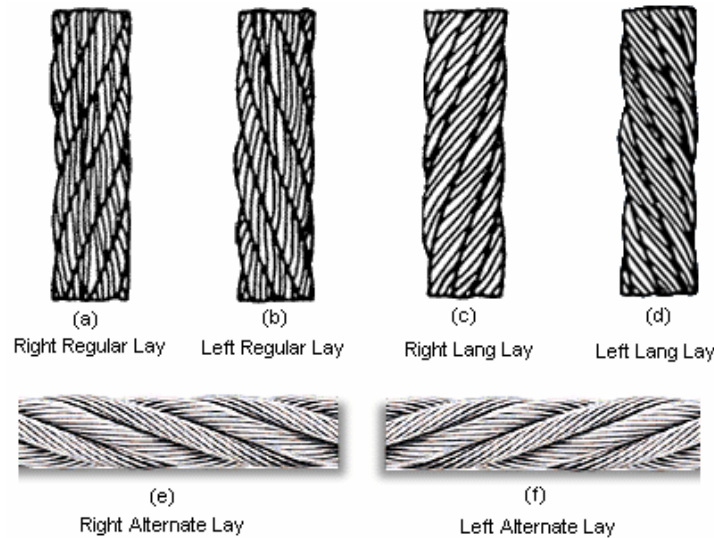


Figure 2-37: Lays of wire rope

The length of a rope lay is the distance measured parallel to the centre line of a wire rope in which a strand makes one complete spiral or turn around the rope. The length of a strand lay is the distance measured parallel to the centre line of the strand in which one wire makes one complete spiral or turnaround the strand. The lay length of a rope is the basic factor controlling the breaking load and extension characteristics of the finished cable. The breaking load is relatively low for short lay lengths and greater for longer lay lengths. Spiral strand constructions normally have lay lengths in the range 9-12 times the cable diameter, depending on the size of the finished strand and the number of the layers of wires. A small size strand may have long lay length, and thus large values of modulus and breaking loads. As the spiral becomes larger and more complex, the lay has to be shortened in order to produce a good, tight strand, which leads to low values of modulus and breaking load. On the other hand, the locked coil construction may have longer lays, not depending on the size of the cable, due to the interlocking of the outer wires [2-21].

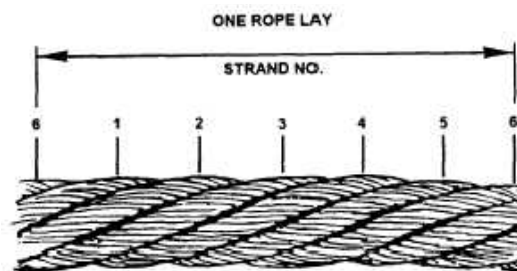


Figure 2-38: Lay length measurement

Eurocode 3, Part 1.11 [2-95] provides design rules for structures with tension components made of steel, which are adjustable and replaceable. These products are prefabricated, and installed into the structure on-site. For cable nets, two types of cables are recommended: the spiral strand ropes (having the characteristics of Table 2-3) and the full-locked coil ropes (with characteristics listed in Table 2-4).

Table 2-3: Spiral strand ropes (from [2-95])

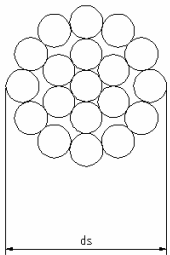
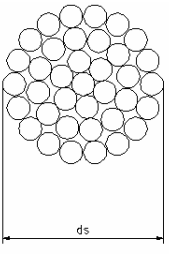
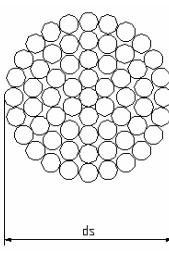
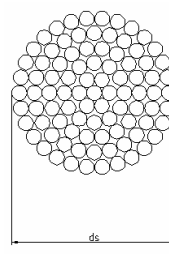
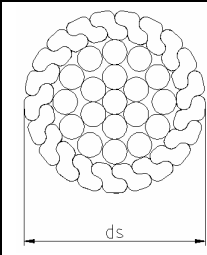
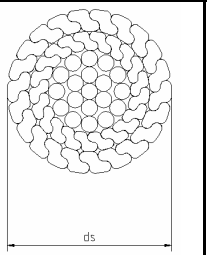
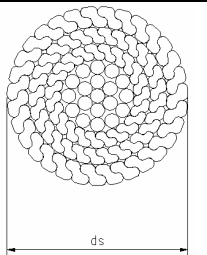
				
Construction	1 × 19	1 × 37	1 × 61	1 × 91
Diameter d_s [mm]	3 to 14	6 to 36	20 to 40	30 to 52
Wires per strand	19	37	61	91
Outer wire per strand	12	18	24	30
Breaking force factor K	0.525	0.52	0.51	0.51

Table 2-4: Full-locked coil ropes (from [2-95])

			
Construction	1 layer Z-wires	2 layer Z-wires	≥ 3 layer Z-wires
Diameter d_s [mm]	20 to 40	25 to 50	40 to 180
Tolerance d	+5%	+5%	+5%
Breaking force factor K	0.585	0.607	0.643

The value of the rope self-weight is related to the metallic cross-section and the unit length, taking account of the weight densities of steel and the corrosion protection system. For spiral strands or locked coil strands the following approximate expression for the nominal self-weight may be used:

$$g_k = wA_m \quad (2-192)$$

where w is the unit weight in $\text{kN}/(\text{m}\cdot\text{mm}^2)$, given in Table 2-5 and A_m is the metallic cross-sectional area in mm^2 , calculated as:

$$A_m = \frac{\pi d^2}{4} f \quad (2-193)$$

where d is the external diameter of the rope or strand, including sheathing for corrosion protection if used. The fill-factor f is defined as the ratio of the sum of the nominal metallic cross-sectional areas of all the wires in a rope (A) and the circumscribed area (A_u) of the rope based on its nominal diameter (d), also given in Table 2-5.

Table 2-5: Unit weight w and fill-factors f (from [2-95])

Ropes	Fill factor f							Unit weight $w \times 10^{-4}$ $\text{kN}/(\text{m}\cdot\text{mm}^2)$
	Core wires + 1 layer z-wires	Core wires + 2 layer z-wires	Core wires + >2 layer z-wires	number of wire layers around core wire				
				1	2	3-6	>6	
1 Spiral strand				0.77	0.76	0.75	0.73	0.830
2 Full-locked coil	0.81	0.84	0.88					0.830

Regarding the modulus of elasticity, the exact values should be derived from tests. Notional values of elastic moduli, for first estimations, when test results are not available, are tabulated in Table 2-6 for locked coil strands and bundles of strands.

Table 2-6: Notional values for the modulus of elasticity E_0 in the range of variable loads Q (from [2-95])

	High strength tension component	E_0 [kN/mm ²]	
		Steel wires	Stainless steel wires
1	Spiral strand ropes	150 ± 10	130 ± 10
2	Full locked coil ropes	160 ± 10	–

The characteristic values of the yield stress f_y and the ultimate tensile strength f_u shall be taken from the relevant technical specifications. The following values f_u are recommended:

Table 2-7: Recommended nominal tensile strength values f_u for steel and stainless steel wires (from [2-95])

		f_u [N/mm ²]
steel wires	round wires	1770
	Z-wires	1570
stainless steel wires	round wires	1450

The minimum breaking load of the cable is obtained as follows:

$$F_{\min} = \frac{d^2 R_r K}{1000} \text{ [kN]} \quad (2-194)$$

Where d is the diameter of the rope in mm, K is the breaking force factor and R_r is the rope grade in N/mm², which is designated by a number (e.g. 1770 [N/mm²]).

2.6 WIND ACTION ON STRUCTURES

The main dynamic loads affecting structures are the seismic load and the wind action. Cable structures, belonging to the family of lightweight structures, are more susceptible to wind loads, rather than to seismic ones. Eurocode 1, Part 1.4 [2-96], which is the current code in Europe, provides guidance regarding the determination of the wind load acting on structures, including the whole structure, parts of it or elements attached to the structure, e. g. components, cladding units and their fixings, safety and noise barriers. However, it is addressed to engineers dealing with structures having typical shapes, such as vertical walls of rectangular buildings, free-standing walls, parapets and fences, flat, monopitch, duopitch, hipped or multispans roofs, canopies, vaulted roofs or domes. For unusual shapes of structures, wind tunnel experiments are recommended as the only reliable method to evaluate the wind pressure on the structure's components.

2.6.1 Wind nature

The wind is the motion of the air with respect to the ground, caused by the differences of pressure between two points of the earth's atmosphere. The sun provides the energy necessary for this motion, by heating the earth. The atmosphere, which is quite transparent to the solar radiated heat, absorbs the heat from the earth and re-emits part of it to the ground and part of it to the higher layers of the air. The atmospheric pressure is produced by the weight of the overlying air. As the air moves vertically, it experiences a change of pressure and a change of temperature. On the other hand, the difference of temperature between the poles and the equator of the earth produces the horizontal motion of the air.

As the air moves horizontally, the surface of the earth exerts a drag force, produced by the roughness of the terrain and the friction developed between the earth and the air. This force reduces the velocity

of the flow near the ground, and decreases as the height above ground increases, up to the end of the boundary layer, where the free atmosphere begins. There, this force is considered as negligible and the wind flow has a gradient velocity along the isobars. The depth of the boundary layer depends on the wind intensity, the roughness of terrain, and the angle of latitude and ranges from a few hundred meters to several kilometres [2-97]. The roughness of the earth's surface, induced either by mountains, hills and forests, or by man-made obstructions, such as buildings, bridges and dams, not only decreases the wind velocity but also changes the wind direction causing the turbulence of the flow.

2.6.2 Wind velocity

2.6.2.1 Wind velocity records

The wind velocity can be divided in two parts; the mean wind velocity, described as a static part in the wind direction at a certain height and the time dependent velocity (gust) described as the dynamic part, having three different components in the along-wind, the horizontal cross-wind and the vertical cross-wind directions at a certain height. However, the main fluctuations occur in the longitudinal direction, which is also the mean direction of the flow. Close to the ground, the mean velocity decreases and the flow becomes more turbulent. Both phenomena occur due to the roughness of the earth's surface [2-98]. Generally, it is assumed that the mean wind velocity does not change with time over periods of 10min to 1 hour [2-99].

Structures, designed to sustain strong winds, may carry anemometers that measure the wind velocity and direction at specific time steps. For example, cable stayed or suspended bridges are equipped with such devices, in order to select the appropriate positions to place dampers to suppress cable vibrations of large amplitudes. Wind turbines, guyed masts, towers and chimneys are also wind-sensitive structures [2-100] – [2-109]. Wind velocity records are provided in [2-21], [2-97], [2-110] – [2-112]. Typical wind velocity records are shown in Figure 2-39, retrieved from the Department of Water Resources and Environmental Engineering of the School of Civil Engineering of the National Technical University of Athens [2-113].

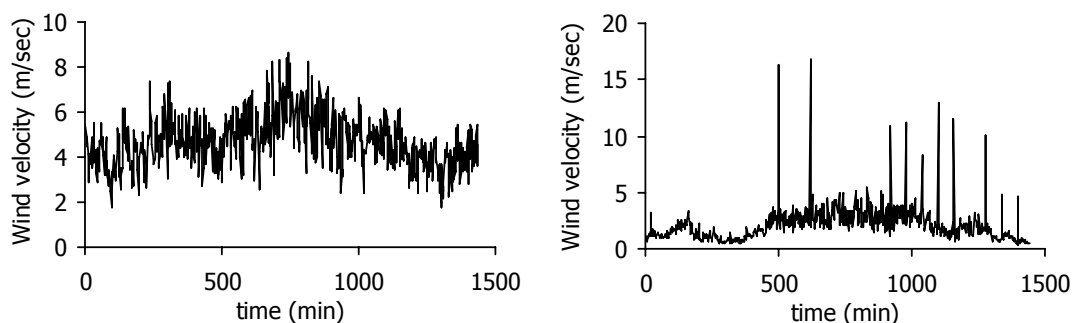


Figure 2-39: Typical wind velocity records

2.6.2.2 Basic wind velocity

According to Eurocode 1 [2-96], the fundamental value of the basic wind velocity, denoted as $v_{b,0}$, is the characteristic 10 minutes mean wind velocity, irrespective of the wind direction and time of year, at 10m above ground level in open country terrain with low vegetation. The basic wind velocity, referring to a height of 10m above ground of terrain with low vegetation, is expressed as:

$$V_b = V_{b,0} \cdot C_{dir} \cdot C_{season} \quad (2-195)$$

where c_{dir} and c_{season} are the direction and season factor, respectively. The recommended value for both factors is 1. Thus, Eq. (2-195) becomes:

$$V_b = V_{b,0} \quad (2-196)$$

2.6.2.3 Mean wind velocity

The mean wind profile in horizontally homogeneous terrain was first represented by the power law in [2-114] and expressed as:

$$V_H = V_{ref} \left(\frac{z_H}{z_{ref}} \right)^\alpha \quad (2-197)$$

where V_H is the mean velocity at a height z_H and V_{ref} is the mean velocity at a reference height z_{ref} , while the exponent α depends on the terrain roughness. Assuming that at some height above ground, called gradient height z_G , the air movement is not influenced by the ground obstruction and consequently, the wind velocity above that height is constant [2-115], Eq. (2-197) becomes:

$$V_H = V_G \left(\frac{z_H}{z_G} \right)^\alpha \quad (2-198)$$

where V_G is the velocity at gradient height. The parameters z_G and α depend on the ground roughness. Typical values for the gradient height are listed in Table 2-8.

Table 2-8: Typical values of parameters in wind profiles (from [2-112])

Terrain description	z_G (m)	α
1 Open sea, ice, tundra, desert	250	0.11
2 Open country with low scrub or scattered trees	300	0.15
3 Suburban areas, small towns, well wooded areas	400	0.25
4 Numerous tall buildings, cities, well developed industrial areas	500	0.36

If the wind velocity V_{ref} at height z_{ref} is known, the velocity V_G is calculated as:

$$V_G = V_{ref} \left(\frac{z_G}{z_{ref}} \right)^\alpha \quad (2-199)$$

Nowadays, the logarithmic law is used widely to represent the wind velocity profile. It is applicable to heights in excess of 10m. Below this height the velocity is assumed to be constant and equal to $V(10m)$ [2-116]. According to the logarithmic law the wind velocity at height z is expressed as:

$$V(z) = 2.5u_* \ln \left(\frac{z}{z_o} \right) \quad (2-200)$$

where z is the height above the surface, $V(z)$ is the mean wind velocity at height z and z_o is the roughness length. The shear velocity or friction velocity is calculated, taking into account the reference mean velocity 10m above ground level:

$$u_* = \frac{V(10m)}{2.5 \ln \left(\frac{10m}{z_o} \right)} = V(10m) \sqrt{k} \quad (2-201)$$

where k is the surface drag coefficient. If k is known the corresponding value for z_0 can be calculated from Eq. (2-200):

$$z_0 = z \cdot e^{-\left(\frac{V(z)}{2.5u_*}\right)} \quad (2-202)$$

Typical values of the roughness length z_0 and the surface drag coefficient k are listed in Table 2-9.

Table 2-9: Typical values of k and z_0 (from [2-116])

Terrain description	k	z_0 (m)
Sand	1.2-1.9	0.0001-0.001
Sea surface	0.7-2.6	0.005
Grass	3.4-7.6	0.01-0.10
Pine forest	28.0-30.0	0.90-1.00
Suburban area	10.5-15.4	0.20-0.40
Cities	14.2-16.6	0.35-0.45
Large cities	20.2-25.1	0.20-0.80

According to Eurocode 1 [2-96], the mean wind velocity $V_m(z)$ at a height z above the terrain, depends on the terrain roughness and orography and on the basic wind velocity v_b , and it is expressed as:

$$V_m(z) = c_o(z) c_r(z) v_b \quad (2-203)$$

where $c_o(z)$ is the orography factor, taken as 1.00, $c_r(z)$ is the roughness factor, which is equal to:

$$c_r(z) = k_r \ln(z/z_0) \text{ for } z_{\min} \leq z \leq z_{\max} \quad (2-204)$$

$$c_r(z) = k_r \ln(z_{\min}/z_0) \text{ for } z \leq z_{\min}$$

k_r is the terrain factor depending on the roughness length z_0 :

$$k_r = 0.19(z_0/z_{0,II})^{0.07} \quad (2-205)$$

z_{\max} is the maximum height equal to 200m, z_{\min} is the minimum height, z_0 is the roughness length, $z_{0,II}$ is the roughness length for terrain category II, equal to 0.05m. The heights z_0 , $z_{0,II}$ and z_{\min} are defined in Table 2-10.

Table 2-10: Terrain categories and terrain parameters (from [2-96])

Terrain category	z_0 (m)	z_{\min} (m)
0 Sea or coastal area exposed to the open sea	0.003	1
I Lakes or flat horizontal area with negligible vegetation and without obstacles	0.01	1
II Area with low vegetation such as grass and isolated obstacles (trees, buildings) with separations of at least 20 obstacle heights	0.05	2
III Area with regular cover of vegetation or buildings or isolated obstacles with separations of maximum 20 obstacle heights (such as villages, suburban terrain, permanent forest)	0.3	5
IV Area in which at least 15% of the surface is covered with buildings and their average height exceeds 15m	1.0	10

In order to compare the power law, the logarithmic one and the mean velocity based on Eurocode 1, a basic wind velocity is assumed equal to 30m/sec, referring to a height of 10m for a country terrain with low vegetation. The wind velocity profiles for the three considerations are shown in Figure 2-40, where it is shown that the logarithmic law results in conservative values of the wind velocities with respect to the power law and Eurocode 1.

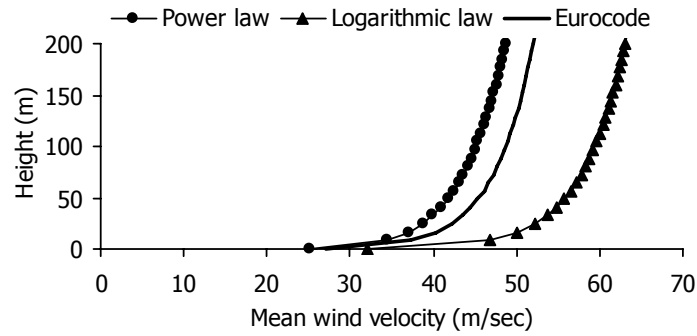


Figure 2-40: Wind velocity profiles

2.6.2.4 Turbulence intensity

The fluctuation of the wind velocity is known as turbulence, which depends on the height and on the roughness of the terrain. It is higher in rougher terrains than in smoother ones and it decreases as the height increases [2-112]. The turbulence intensity $I(z)$ is a parameter measuring the turbulence at height z and it is defined as the standard deviation of the turbulence $\sigma(z)$ divided by the mean velocity $V(z)$:

$$I(z) = \sigma(z)/V(z) \quad (2-206)$$

The variance varies with height dependent also on the ground roughness and mean wind velocity. In [2-116] the variance is expressed as:

$$\sigma(z) = 2.63u * \eta(0.538 + z/z_o)^{\eta^{16}} \quad (2-207)$$

with

$$\eta = 1 - z/H \quad (2-208)$$

H is the gradient height, given as:

$$H = u_* / (2\beta\omega \sin\phi) \quad (2-209)$$

where β is a constant equal to 6, ω is the angular rotation of the earth equal to $7.2722 \cdot 10^{-5}$ rad/sec and ϕ is the local angle of latitude.

In Eurocode 1 [2-96], the turbulence intensity is defined as:

$$I_v(z) = \sigma_v/V_m(z) = k_I / \{\ln(z/z_o) \cdot c_o(z)\} \text{ for } z_{\min} \leq z \leq z_{\max} \quad (2-210)$$

$$I_v(z) = I_v(z_{\min}) \text{ for } z \leq z_{\min} \quad (2-211)$$

where z_{\max} is the maximum height equal to 200m

z_{\min} is defined in Table 2-10

$V_m(z)$ is the mean wind velocity at height z

σ_v is the standard deviation of the turbulence:

$$\sigma_v = k_r \cdot v_b \cdot k_I \quad (2-212)$$

k_I is the turbulence factor with recommended value 1.00, k_r is calculated from Eq. (2-205) and v_b from Eq. (2-196).

2.6.2.5 Wind velocity power spectra

In statistical signal processing and physics, the properties of a time function are specified by the power spectral density, which is a positive real function of a frequency variable. It is often called simply the spectrum of the signal. It describes how the power of a signal or time series is distributed with frequency. In case of the wind, most countries have their own wind velocity spectrum, according to the weather conditions of the area, providing information about the main frequencies of the wind velocity. Several wind velocity power spectra are reported from the literature in [2-99]. Davenport [2-117] suggested that the wind velocity spectrum could be calculated as:

$$S_u(n) = \frac{4 \cdot (u^*)^2 \cdot (f(n))^2}{n \cdot \sqrt[3]{[1 + (f(n))^2]^4}} \quad (2-213)$$

where $f(n)$ is the non-dimensional frequency, expressed as:

$$f(n) = \frac{1200n}{V(10m)} \quad (2-214)$$

n is the velocity frequency, $V(10m)$ is the mean wind velocity at 10m and the friction velocity u^* is defined by Eq. (2-201).

Kaimal [2-118] introduced the height above the ground z :

$$S_u(z,n) = \frac{200 \cdot (u^*)^2 \cdot f(z,n)}{n \cdot \sqrt[3]{[1 + 50 \cdot f(z,n)]^5}} \quad (2-215)$$

with

$$f(z,n) = \frac{n \cdot z}{V(z)} \quad (2-216)$$

where $V(z)$ is the mean wind velocity at height z , which can be calculated according to the logarithmic law (Eq. (2-200)).

The spectrum suggested by Eurocode 1 [2-96] is calculated as:

$$S_v(z,n) = \frac{6.8 \cdot \sigma_v^2 \cdot f_L(z,n)}{n \sqrt[3]{[1 + 10.2 \cdot f_L(z,n)]^5}} \quad (2-217)$$

where σ_v is the standard deviation of the turbulence, defined by Eq. (2-212), and

$$f_L(z,n) = \frac{n \cdot L(z)}{V_m(z)} \quad (2-218)$$

$$L(z) = L_t \cdot \left(\frac{z}{z_t} \right)^\alpha \quad \text{for } z \geq z_{\min}$$

$$L(z) = L(z_{\min}) \quad \text{for } z < z_{\min} \quad (2-219)$$

where $L(z)$ is the turbulent length scale representing the average gust size for natural winds, with a reference height of $z_t=200m$, a reference length scale of $L_t=300m$, and $\alpha=0.67+0.05\ln(z_o)$. The mean velocity is calculated according to Eq. (2-203), while the roughness length z_o and the minimum height z_{\min} are taken from Table 2-10.

In order to compare the different wind velocity spectra, the basic wind velocity is assumed again equal to 30m/sec, referring to a height of 10m for a country terrain with low vegetation and the spectra of Kaimal and Eurocode 1 are calculated for $z=25\text{m}$. The non-dimensional spectral densities, according to the three considerations, defined as:

$$s(z,n) = \frac{n \cdot S(z,n)}{(V(10\text{m}))^2} \quad (2-220)$$

are plotted in Figure 2-41. In this chart it is shown that the spectrum calculated according to Eurocode 1 approaches the one of Kaimal.

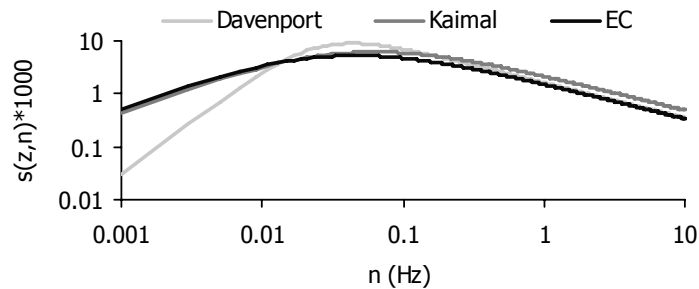


Figure 2-41: Wind velocity spectra

2.6.3 Wind artificial functions

In order to perform a nonlinear dynamic analysis for the wind action a wind velocity time-history diagram is required. In case no wind velocity records are available, it is convenient to create wind artificial functions giving the wind velocity fluctuations. In [2-119] efficient methods were presented to simulate random processes as a series of cosine functions with random phase angles and almost evenly spaced frequencies. It was suggested that the random process could be simulated as:

$$f(t) = \sqrt{2} \sum_{k=1}^N \sqrt{S_o(\omega_k) \Delta\omega} \cos(\omega'_k t + \phi_k) \quad (2-221)$$

where $S_o(\omega_k)$ is the spectral density function of $f_o(t)$ at frequency ω_k , ϕ_k is an independent random phase uniformly distributed between 0 and 2π , and

$$\Delta\omega = \frac{\omega_{\max}}{N} \quad (2-222)$$

$$\omega'_k = \omega_k + \delta\omega \quad (2-223)$$

where $\delta\omega$ is a small random frequency introduced. The frequency band, which is divided in N parts, must contain all the significant natural frequencies of the structure. For nonlinear structures the frequency step $\Delta\omega$ should be small, in order to take into consideration the fact that the natural frequencies of such structures vary with the amplitude of response.

In [2-21], Eq. (2-221) took the form of the wind velocity and was rewritten as:

$$v(z,t) = \sqrt{2} \sum_{i=1}^N \sqrt{S_v(z,n_i) \Delta n} \cos(2\pi n_i t + \phi_i) \quad (2-224)$$

with

$$\Delta n = \frac{n_{\max}}{N} \quad (2-225)$$

$$n_i = n_o + i \cdot \Delta n \quad (2-226)$$

where $n=2\pi/\omega$. In [2-120], Eq. (2-224) was combined with the recommendations of Eurocode 1 [2-96], in order to use an artificial time-history diagram of the wind velocity to calculate the dynamic response of a structure. Based on the Fourier transform of Eq. (2-221), a simulation algorithm is proposed in [2-121] to generate sample functions of stochastic process with three components in space, giving as an example a simulation of turbulent wind velocity fluctuations.

Taking into account the wind velocity spectrum of Eurocode 1 [2-96] and assuming a mean wind velocity equal to 30m/sec, a time-history diagram of the wind velocity, calculated from Eq. (2-224), is plotted in Figure 2-42.

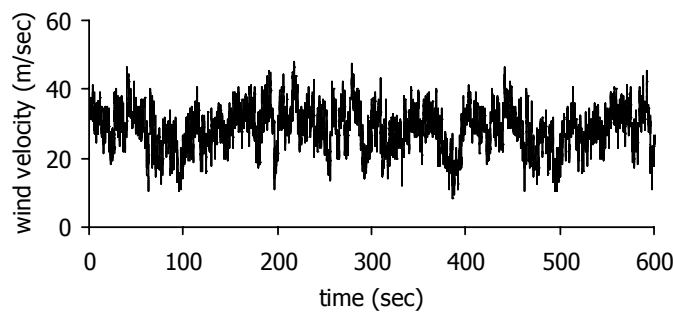


Figure 2-42: Artificial wind velocity time-history diagram

2.6.4 Wind pressure on structures

According to Bernoulli's theorem a horizontal airflow velocity V produces a pressure P as:

$$P + \frac{1}{2} \rho V^2 = \text{constant} \quad (2-227)$$

where the second term has dimensions of pressure and is called dynamic pressure, while ρ is the air density. This expression cannot be used in the case of turbulent flows around structures [2-112]. Pressures are expressed in a non-dimensional form, independent of the wind velocity:

$$C_p = \frac{\Delta P}{1/2 \rho V^2} \quad (2-228)$$

where C_p is called the pressure coefficient and ΔP is the pressure above or below the atmospheric pressure, induced by the wind over the surface. Thus, if P_o is the atmospheric pressure, ΔP can be written as:

$$\Delta P = P - P_o \quad (2-229)$$

Values of the pressure coefficient are provided in [2-97]. According to Eurocode 1 [2-96] the wind pressure on a structure's surface is calculated, taking also into account the velocity fluctuations. In what follows the methodology suggested by this code is described.

2.6.4.1 Peak velocity pressure

The peak velocity pressure $q_p(z)$ at height z , including the mean velocity and the short-term velocity fluctuations is:

$$q_p(z) = [1 + 7 \cdot I_v(z)] \cdot \frac{1}{2} \cdot \rho \cdot V_m^2(z) = c_e(z) \cdot q_b \quad (2-230)$$

where ρ is the air density, which depends on the altitude, the temperature and the barometric pressure, with recommended value 1.25 kg/m^3 , $I_v(z)$ the turbulence intensity obtained by Eqs. (2-210) and (2-211), q_b the basic velocity pressure and $c_e(z)$ the exposure factor:

$$q_b = 1/2 \rho (v_b)^2 \quad (2-231)$$

$$c_e(z) = [1 + 7I_v(z)] c_r^2(z) c_o^2(z) \quad (2-232)$$

2.6.4.2 Wind pressure on surfaces

The wind pressure on external surfaces is:

$$W_e = c_{pe} q_p(z) = c_{pe} c_e(z) q_b = c_{pe} [1 + 7I_v(z)] c_r^2(z) c_o^2(z) \frac{1}{2} \rho v_b^2 \quad (2-233)$$

and the wind pressure on internal surfaces, called suction is:

$$W_i = c_{pi} q_p(z) = c_{pi} c_e(z) q_b = c_{pi} [1 + 7I_v(z)] c_r^2(z) c_o^2(z) \frac{1}{2} \rho v_b^2 \quad (2-234)$$

where $q_p(z)$ the peak velocity pressure, q_b the basic velocity pressure, $c_e(z)$ the exposure factor, c_{pe} and c_{pi} the pressure coefficient for the external and internal pressure, respectively. Pressure, directed towards the surface is taken as positive, and suction, directed away from the surface as negative, as shown in Figure 2-43.

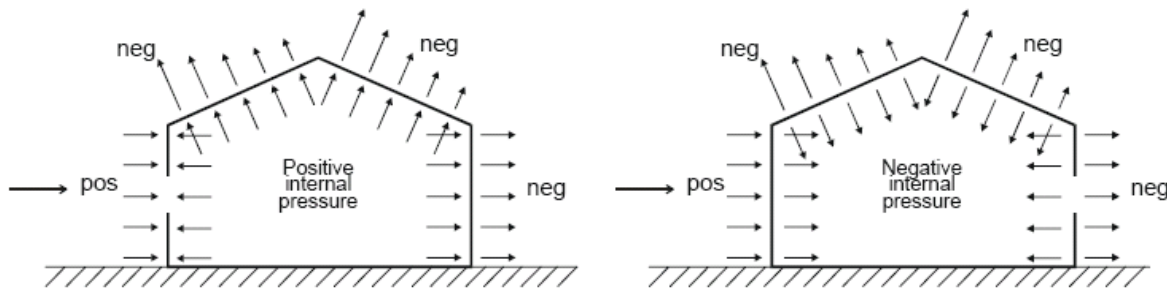


Figure 2-43: Pressure on surfaces (from [2-96])

2.6.4.3 External pressure coefficient c_{pe}

The external pressure coefficient c_{pe} depends on the size of the loaded surface A and it is provided in tables for loaded areas A of 1 m^2 and 10 m^2 . Values for the local coefficients $c_{pe,1}$ may be used for the small elements design, with an area per element of 1 m^2 , while values for the overall coefficients $c_{pe,10}$ may be used for the overall loaded structure. For $1 \text{ m}^2 < A < 10 \text{ m}^2$, the pressure coefficient is calculated as:

$$C_{pe} = c_{pe,1} - (c_{pe,1} - c_{pe,10}) \log_{10} A \quad (2-235)$$

The recommended procedure for loaded areas between 1m^2 and 10m^2 is shown in the diagram of Figure 2-44.

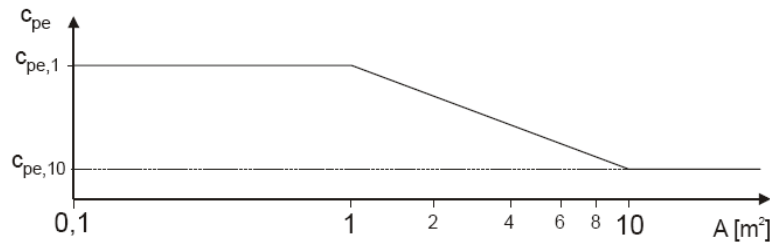


Figure 2-44: External pressure coefficient for building with a loaded area A between 1m^2 and 10m^2 (from [2-96])

The value of the pressure coefficient c_{pe} also depends on the shape and the dimensions of the roof, as well as the wind direction. The ones for vaulted, duopitch or flat roofs are reported next, as recommended in [2-96].

2.6.4.4 Vaulted roofs

The vaulted roof is divided into zones as shown in Figure 2-45 and the reference height is taken equal to $z_e = h + f$. The pressure coefficients, which can be used for such roofs, are shown in the diagram of Figure 2-45. For $0 < h/d < 0.5$, the coefficient $c_{pe,10}$ is obtained by linear interpolation, while for $0.2 \leq f/d \leq 0.3$ and $h/d \geq 0.5$, two values of $c_{pe,10}$ have to be considered.

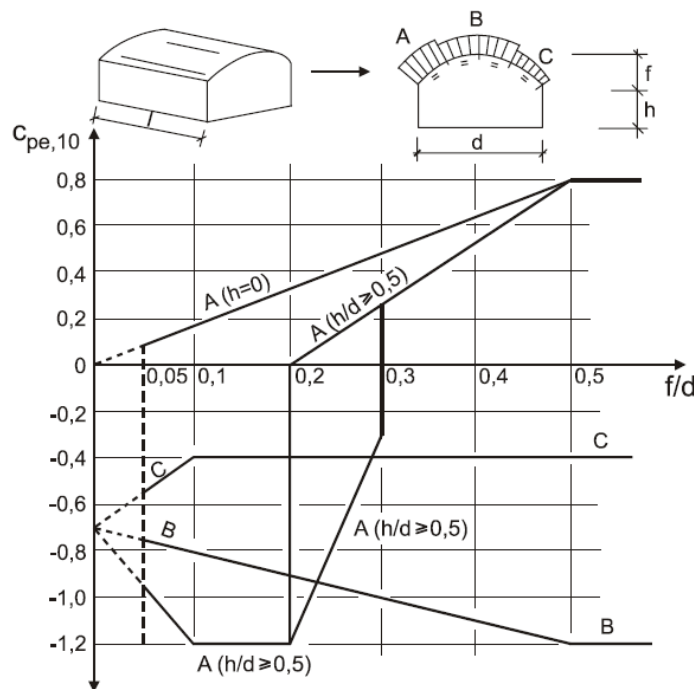


Figure 2-45: External pressure coefficients $c_{pe,10}$ for vaulted roofs with rectangular base (from [2-96])

2.6.4.5 Duopitch roofs

The zones of duopitch roofs are illustrated in Figure 2-46 with positive or negative pitch angle. The pressure coefficients $c_{pe,1}$ and $c_{pe,10}$ are provided for orthogonal wind directions $\theta = 0^\circ$ (Table 2-11) and $\theta = 90^\circ$ (Table 2-12). For pitch angles between $\alpha = -5^\circ$ and $\alpha = +5^\circ$ the roof should be considered as flat. The positive values of these coefficients correspond to overpressure and the negative ones to underpressure. In case positive and negative values are proposed, both values should be considered

but without mixing positive and negative values on the same face. The reference height z_e should be taken as h .

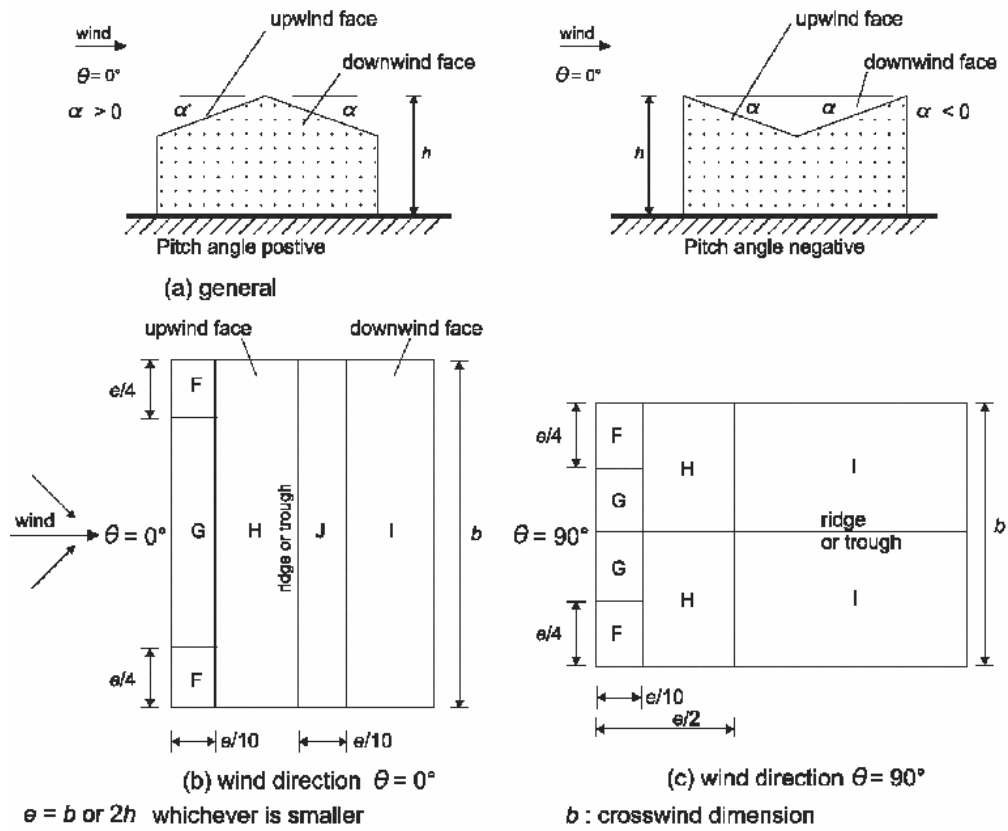


Figure 2-46: Key for duopitch roofs (from [2-96])

Table 2-11: External pressure coefficient for duopitch roofs for wind direction $\theta=0^\circ$ (from [2-96])

pitch angle α	Zone for wind direction $\theta = 0^\circ$									
	F		G		H		I		J	
	$C_{pe,10}$	$C_{pe,1}$	$C_{pe,10}$	$C_{pe,1}$	$C_{pe,10}$	$C_{pe,1}$	$C_{pe,10}$	$C_{pe,1}$	$C_{pe,10}$	$C_{pe,1}$
-45°	-0.6		-0.6		-0.8		-0.7		-1.0	-1.5
-30°	-1.1	-2.0	-0.8	-1.5	-0.8		-0.6		-0.8	-1.4
-15°	-2.5	-2.8	-1.3	-2.0	-0.9	-1.2	-0.5		-0.7	-1.2
-5°	-2.3	-2.5	-1.2	-2.0	-0.8	-1.2	+0.2		+0.2	
							-0.6		-0.6	
$+5^\circ$	-1.7	-2.5	-1.2	-2.0	-0.6	-1.2	-0.6		+0.2	
	0.0		0.0		0.0				-0.6	
$+15^\circ$	-0.9	-2.0	-0.8	-1.5	-0.3		-0.4		-1.0	-1.5
	+0.2		+0.2		+0.2		0.0		0.0	0.0
$+30^\circ$	-0.5	-1.5	-0.5	-1.5	-0.2		-0.4		-0.5	
	+0.7		+0.7		+0.4		0.0		0.0	
$+45^\circ$	0.0		0.0		0.0		-0.2		-0.3	
	+0.7		+0.7		+0.6		0.0		0.0	
$+60^\circ$	+0.7		+0.7		+0.7		-0.2		-0.3	
$+75^\circ$	+0.8		+0.8		+0.8		-0.2		-0.3	

Table 2-12: External pressure coefficient for duopitch roofs for wind direction $\theta=90^\circ$ (from [2-96])

Pitch angle α	Zone for wind direction $\theta=90^\circ$							
	F		G		H		I	
	$C_{pe,10}$	$C_{pe,1}$	$C_{pe,10}$	$C_{pe,1}$	$C_{pe,10}$	$C_{pe,1}$	$C_{pe,10}$	$C_{pe,1}$
-45°	-1.4	-2.0	-1.2	-2.0	-1.0	-1.3	-0.9	-1.2
-30°	-1.5	-2.1	-1.2	-2.0	-1.0	-1.3	-0.9	-1.2
-15°	-1.9	-2.5	-1.2	-2.0	-0.8	-1.2	-0.8	-1.2
-5°	-1.8	-2.5	-1.2	-2.0	-0.7	-1.2	-0.6	-1.2
5°	-1.6	-2.2	-1.3	-2.0	-0.7	-1.2	-0.6	
15°	-1.3	-2.0	-1.3	-2.0	-0.6	-1.2	-0.5	
30°	-1.1	-1.5	-1.4	-2.0	-0.8	-1.2	-0.5	
45°	-1.1	-1.5	-1.4	-2.0	-0.9	-1.2	-0.5	
60°	-1.1	-1.5	-1.2	-2.0	-0.8	-1.0	-0.5	
75°	-1.1	-1.5	-1.2	-2.0	-0.8	-1.0	-0.5	

2.6.4.6 Flat roofs

The surfaces of flat roofs are divided in zones according to the dimensions and the height of the building, depending on the wind direction. The pressure coefficients are provided for each zone of the surface. In Figure 2-47 the zones of flat roofs with parapets, sharp, curved or mansard eaves are defined and the corresponding pressure coefficients $C_{pe,1}$ and $C_{pe,10}$ are listed in Table 2-13. The reference height for flat roof and roofs with curved or mansard eaves should be taken as $z_e=h$, while for parapets it should be taken as $z_e=h+h_p$ (Figure 2-47).

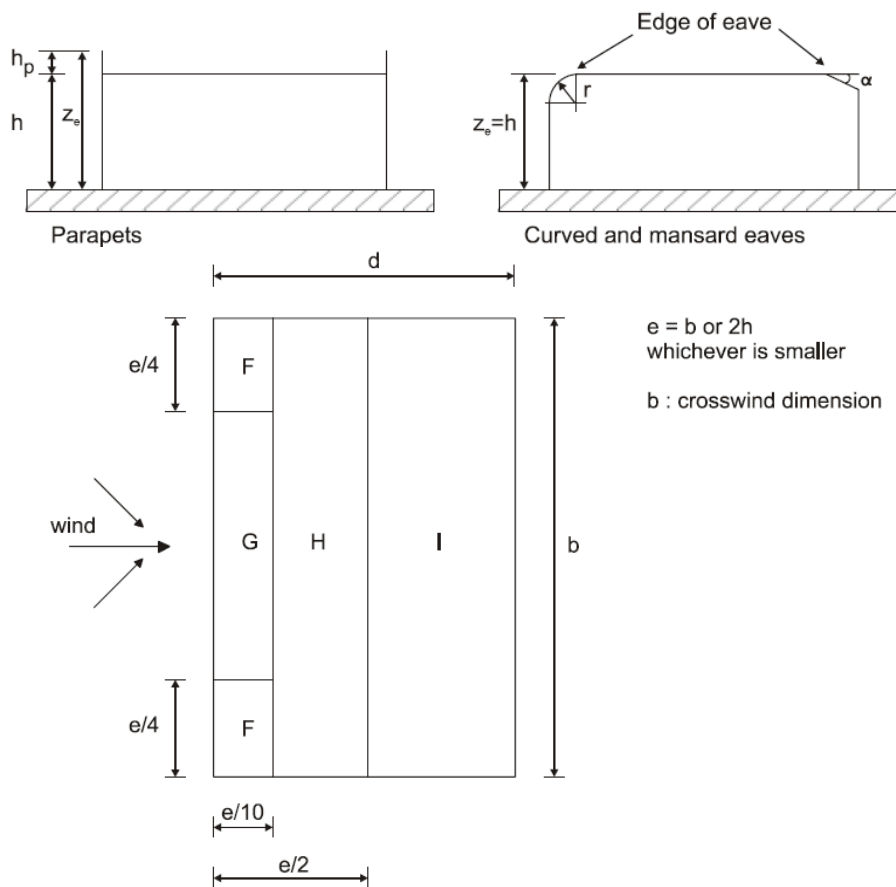


Figure 2-47: Key for flat roofs (from [2-96])

Table 2-13: External pressure coefficient for flat roofs (from [2-96])

Roof type		Zone							
		F		G		H		I	
		$C_{pe,10}$	$C_{pe,1}$	$C_{pe,10}$	$C_{pe,1}$	$C_{pe,10}$	$C_{pe,1}$	$C_{pe,10}$	$C_{pe,1}$
Sharp eaves		-1.8	-2.5	-1.2	-2.0	-0.7	-1.2	+0.2	-0.2
With parapets	$h_p/h=0.025$	-1.6	-2.2	-1.1	-1.8	-0.7	-1.2	+0.2	-0.2
	$h_p/h=0.05$	-1.4	-2.0	-0.9	-1.6	-0.7	-1.2	+0.2	-0.2
	$h_p/h=0.10$	-1.2	-1.8	-0.8	-1.4	-0.7	-1.2	+0.2	-0.2
Curved eaves	$r/h = 0.05$	-1.0	-1.5	-1.2	-1.8	-0.4		+0.2	-0.2
	$r/h = 0.10$	-0.7	-1.2	-0.8	-1.4	-0.3		+0.2	-0.2
	$r/h = 0.20$	-0.5	-0.8	-0.5	-0.8	-0.3		+0.2	-0.2
Mansard eaves	$\alpha = 30^\circ$	-1.0	-1.5	-1.0	-1.5	-0.3		+0.2	-0.2
	$\alpha = 45^\circ$	-1.2	-1.8	-1.3	-1.9	-0.4		+0.2	-0.2
	$\alpha = 60^\circ$	-1.3	-1.9	-1.3	-1.9	-0.5		+0.2	-0.2

2.6.4.7 Internal pressure coefficient c_{pi}

Internal and external pressures should be considered to act at the same time. The internal pressure coefficient, c_{pi} , depends on the size and distribution of the openings in the building envelope. Open windows, ventilators, chimneys, etc. as well as background permeability, such as air leakage around doors, windows, services and through the building envelope are considered openings of a building. A face of a building is regarded as dominant when the area of openings at that face is at least twice the area of openings and leakages in the remaining faces of the building.

When the area of the openings at the dominant face of a building is twice the area of the openings in the remaining faces, the internal pressure coefficient should be calculated as:

$$c_{pi}=0.75c_{pe} \quad (2-236)$$

In case the area of the openings at the dominant face is at least 3 times the area of the openings in the remaining faces, then:

$$c_{pi}=0.90c_{pe} \quad (2-237)$$

where c_{pe} is the value for the external pressure coefficient at the openings in the dominant face. When these openings are located in zones with different values of external pressures an area weighted average value of c_{pe} should be used. When the area of the openings at the dominant face is between 2 and 3 times the area of the openings in the remaining faces linear interpolation for calculating c_{pi} may be used. For buildings without a dominant face, the internal pressure coefficient c_{pi} should be determined from the diagram of Figure 2-48, and is a function of the ratio of the height and the depth of the building, h/d , and the opening ratio μ for each wind direction θ , which should be determined as:

$$\mu = \frac{\sum \text{area of openings where } c_{pe} \text{ is negative or } 0.0}{\sum \text{area of all openings}} \quad (2-238)$$

If it is not possible to estimate μ for a particular case, c_{pi} should be taken as the more onerous of +0.2 and -0.3.

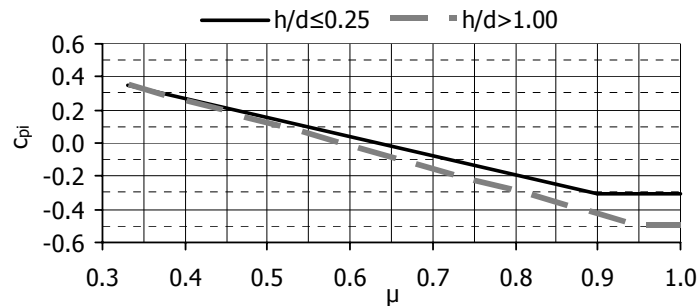


Figure 2-48: Internal pressure coefficients for uniformly distributed openings

In case there are no openings in the surfaces of the building, the internal pressure can be neglected, i.e. $c_{pi}=0.0$ [2-122].

2.6.4.8 Canopy roofs

A canopy roof is defined as the roof of a structure that does not have permanent walls. The degree of blockage under a canopy roof, shown in Figure 2-49, depends on the coefficient φ , which is the ratio of the area of feasible, actual obstructions under the canopy divided by the cross-sectional area under the canopy, both areas being normal to the wind direction.

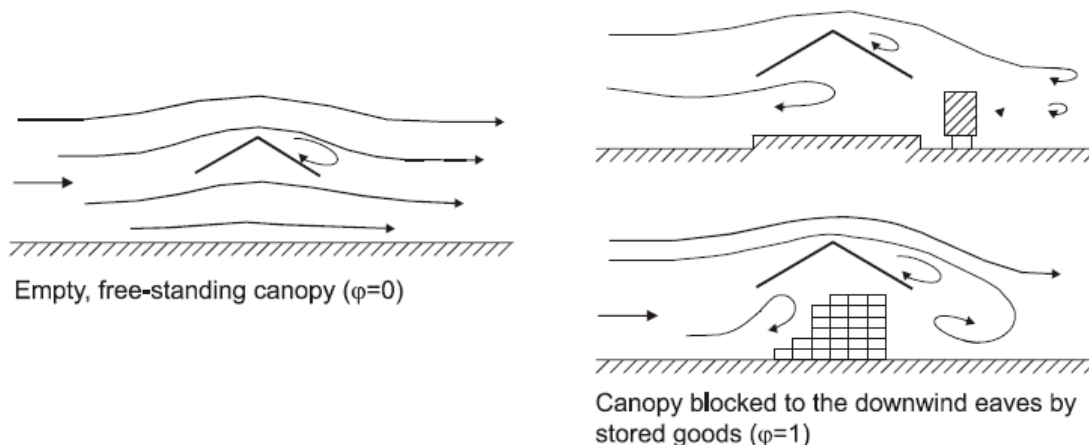


Figure 2-49: Airflow over canopy roofs (from [2-96])

The value $\varphi=0$ represents an empty canopy, and $\varphi=1$ represents the canopy fully blocked with contents to the down wind eaves only (this is not a closed building). The maximum and minimum values of the overall force coefficients, c_f , and the net pressure coefficients $c_{p,net}$ are provided for flat and monopitch canopies, listed in Table 2-14 and for dupitch canopies in Table 2-15, for $\varphi=0$ and $\varphi=1$, taking account of the combined effect of wind acting on both the upper and lower surfaces of the canopies for all wind directions. Intermediate values may be found by linear interpolation. Downwind of the position of maximum blockage, $c_{p,net}$ values for $\varphi=0$ should be used. The overall force coefficient c_f represents the resulting force, while the net pressure coefficient represents the maximum local pressure for all wind directions. It should be used in the design of roofing elements and fixings.

Table 2-14: Values of the coefficients $c_{p,net}$ and c_f for monopitch canopies (from [2-96])

Roof angle α	Blockage ϕ	Overall force coefficient c_f	Zone A	Zone B	Zone C
0°	Max all ϕ Min $\phi = 0$ Min $\phi = 1$	+ 0.2 - 0.5 - 1.3	+0.5 - 0.6 - 1.5	+1.8 - 1.3 - 1.8	+1.1 - 1.4 - 2.2
5°	Max all ϕ Min $\phi = 0$ Min $\phi = 1$	+ 0.4 - 0.7 - 1.4	+ 0.8 - 1.1 - 1.6	+2.1 - 1.7 - 2.2	+1.3 - 1.8 - 2.5
10°	Max all ϕ Min $\phi = 0$ Min $\phi = 1$	+ 0.5 - 0.9 - 1.4	+ 1.2 - 1.5 - 2.1	+ 2.4 - 2.0 - 2.6	+1.6 - 2.1 - 2.7
15°	Max all ϕ Min $\phi = 0$ Min $\phi = 1$	+ 0.7 - 1.1 - 1.4	+ 1.4 - 1.8 - 1.6	+ 2.7 - 2.4 - 2.9	+ 1.8 - 2.5 - 3.0
20°	Max all ϕ Min $\phi = 0$ Min $\phi = 1$	+ 0.8 - 1.3 - 1.4	+ 1.7 - 2.2 - 1.6	+ 2.9 - 2.8 - 2.9	+ 2.1 - 2.9 - 3.0
25°	Max all ϕ Min $\phi = 0$ Min $\phi = 1$	+ 1.0 - 1.6 - 1.4	+ 2.0 - 2.6 - 1.5	+ 3.1 - 3.2 - 2.5	+ 2.3 - 3.2 - 2.8
30°	Max all ϕ Min $\phi = 0$ Min $\phi = 1$	+ 1.2 - 1.8 - 1.4	+ 2.2 - 3.0 - 1.5	+ 3.2 - 3.8 - 2.2	+ 2.4 - 3.6 - 2.7

Table 2-15: Values of the coefficients $c_{p,net}$ and c_f for duopitch canopies (from [2-96])

			Net pressure coefficient $c_{p,net}$			
Roof angle α	Blockage ϕ	Overall force coefficient c_f	Zone A	Zone B	Zone C	Zone D
- 20	Max all ϕ Min $\phi = 0$ Min $\phi = 1$	+ 0.7 - 0.7 - 1.3	+ 0.8 - 0.9 - 1.5	+ 1.6 - 1.3 - 2.4	+ 0.6 - 1.6 - 2.4	+ 1.7 - 0.6 - 0.6
- 15	Max all ϕ Min $\phi = 0$ Min $\phi = 1$	+ 0.5 - 0.6 - 1.4	+ 0.6 - 0.8 - 1.6	+ 1.5 - 1.3 - 2.7	+ 0.7 - 1.6 - 2.6	+ 1.4 - 0.6 - 0.6
- 10	Max all ϕ Min $\phi = 0$ Min $\phi = 1$	+ 0.4 - 0.6 - 1.4	+ 0.6 - 0.8 - 1.6	+ 1.4 - 1.3 - 2.7	+ 0.8 - 1.5 - 2.6	+ 1.1 - 0.6 - 0.6
- 5	Max all ϕ Min $\phi = 0$ Min $\phi = 1$	+ 0.3 - 0.5 - 1.3	+ 0.5 - 0.7 - 1.5	+ 1.5 - 1.3 - 2.4	+ 0.8 - 1.6 - 2.4	+ 0.8 - 0.6 - 0.6
+ 5	Max all ϕ Min $\phi = 0$ Min $\phi = 1$	+ 0.3 - 0.6 - 1.3	+ 0.6 - 0.6 - 1.3	+ 1.8 - 1.4 - 2.0	+ 1.3 - 1.4 - 1.8	+ 0.4 - 1.1 - 1.5
+ 10	Max all ϕ Min $\phi = 0$ Min $\phi = 1$	+ 0.4 - 0.7 - 1.3	+ 0.7 - 0.7 - 1.3	+ 1.8 - 1.5 - 2.0	+ 1.4 - 1.4 - 1.8	+ 0.4 - 1.4 - 1.8
+ 15	Max all ϕ Min $\phi = 0$ Min $\phi = 1$	+ 0.4 - 0.8 - 1.3	+ 0.9 - 0.9 - 1.3	+ 1.9 - 1.7 - 2.2	+ 1.4 - 1.4 - 1.6	+ 0.4 - 1.8 - 2.1
+ 20	Max all ϕ Min $\phi = 0$ Min $\phi = 1$	+ 0.6 - 0.9 - 1.3	+ 1.1 - 1.2 - 1.4	+ 1.9 - 1.8 - 2.2	+ 1.5 - 1.4 - 1.6	+ 0.4 - 2.0 - 2.1
+ 25	Max all ϕ Min $\phi = 0$ Min $\phi = 1$	+ 0.7 - 1.0 - 1.3	+ 1.2 - 1.4 - 1.4	+ 1.9 - 1.9 - 2.0	+ 1.6 - 1.4 - 1.5	+ 0.5 - 2.0 - 2.0
+ 30	Max all ϕ Min $\phi = 0$ Min $\phi = 1$	+ 0.9 - 1.0 - 1.3	+ 1.3 - 1.4 - 1.4	+ 1.9 - 1.9 - 1.8	+ 1.6 - 1.4 - 1.4	+ 0.7 - 2.0 - 2.0
NOTE + values indicate a net downward acting wind action - values represent a net upward acting wind action						

2.6.5 Wind tunnel experiments

The most reliable method to calculate the wind pressure on a surface of a particular shape is the method of physical simulation, in which a scaled model of the construction is immersed in a turbulent atmospheric flow, simulated in a wind tunnel. Many publications referred to such experiments, regarding simple suspended cables, ([2-123], [2-124]), or real design projects concerning structures with unaccustomed geometries, such as the roofs of the Olympic stadium in Rome [2-125], the "Stadio delle Alpi" in Turin ([2-126], [2-127]), the "Karaiskaki" stadium in Athens ([2-127], [2-128]), "le grand Stade" in Paris [2-129], and the hangar at the airport in Riga (Latvia) [2-130], or roofs with normal shapes, such as canopy roofs ([2-131] – [2-134]), hip roofs [2-135], cantilevered roofs ([2-136] – [2-137]), duopitch roofs [2-138], curved roofs ([2-139], [2-140]) or flat roofs with circular plan view ([2-141] – [2-142]). In some of these publications, only the dynamic response of the structure was discussed. In others, pressure coefficient maps were also suggested, referring though to specific geometries. The results of the tests on models with common shapes can be compared and probably provide amendments to the approach of Eurocode 1.

Concerning the tensile structures, such as membranes or cable nets, some researchers performed a numerical simulation with the aid of suitable Computational Fluid Dynamics (CFD) programs ([2-143] – [2-144]), while others invented approximate procedures to estimate the wind pressure distribution on their models ([2-145], [2-146]). Few publications report the results of wind tunnel experiments of saddle roofs. In [2-147] the Calgary Olympic Coliseum in Canada was scaled for a wind tunnel test, in order to measure the maximum deflection of the net. Wind tunnel studies were carried out by Beutler [2-148], giving diagrams of the wind pressure distribution over a rhomboid saddle-form roof and for three different directions of the wind. Other results of wind tunnel test, using as models saddle-shaped suspended roofs with a rhomboid plan view, were also published in [2-149] – [2-151]. Buchholdt [2-21] gave a diagram of the pressure coefficient for an opened cable roof having the geometry of a hyperbolic paraboloid. In ([2-152] – [2-155]) a series of wind tunnel experiments was conducted on saddle-form roofs with rectangular, square and circular plan view and maps of wind pressure coefficients on the roof and the lateral walls for three different wind directions were provided.

2.6.6 Wind force

According to Eurocode 1 [2-96], the wind force, F_w acting on a structure or a structural element may be determined by vectorial summation of the forces $F_{w,e}$, $F_{w,i}$ and F_{fr} . For roofs or walls, the wind force becomes equal to the difference between the external and internal resulting forces, while friction forces F_{fr} act in the direction of the wind components parallel to external surfaces. These forces are expressed as:

$$F_{w,e} = c_s c_d \sum_{\text{surfaces}} w_e \cdot A_{ref} \quad (2-239)$$

$$F_{w,i} = \sum_{\text{surfaces}} w_i \cdot A_{ref} \quad (2-240)$$

$$F_{fr} = c_{fr} \cdot q_p(z_e) \cdot A_{fr} \quad (2-241)$$

where w_e and w_i are the wind pressure on external and internal surfaces, respectively, A_{ref} is the reference area of the structure or structural element and A_{fr} is the area of external surface parallel to the wind. The structural factor, defined as $c_s c_d$, consists of the size factor c_s , accounting for the effect on wind actions from the non-simultaneous occurrence of peak wind pressures on the surface, and the dynamic one c_d , which considers the effect of the vibrations of the structure due to turbulence.

The friction coefficient c_{fr} takes values between 0.01 (very smooth surface) and 0.04 (very rough surface).

The size factor is defined as:

$$c_s = \frac{1 + 7 \cdot I_v(z_e) \cdot \sqrt{B^2}}{1 + 7 \cdot I_v(z_e)} \quad (2-242)$$

and the dynamic one, as:

$$c_d = \frac{1 + 2 \cdot k_p \cdot I_v(z_e) \cdot \sqrt{B^2 + R^2}}{1 + 7 \cdot I_v(z_e) \cdot \sqrt{B^2}} \quad (2-243)$$

where z_e is the reference height, k_p is the peak factor defined as the ratio of the maximum value of the fluctuating part of the response to its standard deviation, I_v is the turbulence intensity defined in section 2.6.2.4, B^2 is the background factor, allowing for the lack of full correlation of the pressure on the structure surface and R^2 is the resonance response factor, allowing for turbulence in resonance with the vibration mode.

The background factor is expressed as:

$$B^2 = \frac{1}{1 + 0.9 \cdot \left(\frac{b+h}{L(z_e)} \right)^{0.63}} \quad (2-244)$$

where b and h is the width and height of the structure and $L(z_e)$ is the turbulent length scale at the reference height, defined by section 2.6.2.5. It is on the safe side to use $B^2=1$, leading to $c_s=1$. The peak factor k_p , defined as the ratio of the maximum value of the fluctuating part of the response to its standard deviation, is obtained by:

$$k_p = \sqrt{2 \cdot \ln(v \cdot T)} + \frac{0.6}{\sqrt{2 \cdot \ln(v \cdot T)}} \quad (2-245)$$

where T is the averaging time for the mean wind velocity and is equal to $T=600$ seconds, while the up-crossing frequency v should be expressed as:

$$v = n_{1,x} \sqrt{\frac{R^2}{B^2 + R^2}} \quad \text{with } v \geq 0.08 \text{ Hz} \quad (2-246)$$

where $n_{1,x}$ is the natural frequency of the structure and R^2 is:

$$R^2 = \frac{n^2}{2 \cdot \delta} \cdot S_L(z_e, n_{1,x}) \cdot R_h(\eta_h) \cdot R_b(\eta_b) \quad (2-247)$$

where δ is the total logarithmic decrement of damping, with recommended values for cables between 0.006 and 0.02, S_L is the non-dimensional power spectral density function, and R_h , R_b are the aerodynamic admittance functions. The non-dimensional power spectral density function is:

$$S_L(z, n) = \frac{n \cdot S_v(z, n)}{(\sigma_v)^2} \quad (2-248)$$

where σ_v is the standard deviation of the turbulence, defined by Eq. (2-212), and $S_v(z,n)$ is the one-sided variance spectrum according to Eq. (2-217) in section 2.6.2.5. The aerodynamic admittance functions are calculated as:

$$R_h = \frac{1}{\eta_h} - \frac{1}{2 \cdot \eta_h^2} (1 - e^{-2 \cdot \eta_h}) \quad (2-249)$$

$$R_b = \frac{1}{\eta_b} - \frac{1}{2 \cdot \eta_b^2} (1 - e^{-2 \cdot \eta_b}) \quad (2-250)$$

with

$$\eta_h = \frac{4.6 \cdot h}{L(z_e)} \cdot f_L(z_e, n_{1,x}) \quad (2-251)$$

$$\eta_b = \frac{4.6 \cdot b}{L(z_e)} \cdot f_L(z_e, n_{1,x}) \quad (2-252)$$

where $f_L(z_e, n_{1,x})$ is defined by Eq. (2-218) in section 2.6.2.5.

2.7 SUMMARY AND CONCLUSIONS

In this chapter, the main concepts regarding the nonlinear static and dynamic behaviour of structures are summarised, focusing on cable structures and specifically on simple suspended cables and cable networks. The dynamic response of cable nets is investigated in this work and the principal dynamic load affecting the lightweight structures is the wind, which, in some cases, causes cable failure due to fatigue. Hence, the calculation of the wind load on the surfaces of a structure is reported from the literature and the standing codes.

2.8 REFERENCES

- [2-1] R. Levy and W. R. Spillers, "Analysis of geometrically nonlinear systems", Kluwer Academic Publishers, 2nd Edition, The Netherlands, 2003.
- [2-2] A. H. Nayfeh and P. F. Pai, "Linear and nonlinear structural mechanics", John Wiley & Sons, Inc., U.S.A., 2004.
- [2-3] S. A. Raz, "Analytical methods in structural engineering", New Age International Publishers, 2nd Edition, New Delhi, India, 2001.
- [2-4] O. P. Gupta, "Finite and boundary element methods in engineering", A. A. Balkema Publishers, India, 1999.
- [2-5] M. Papadrakakis and C. J. Gantes, "Truncated Newton methods for nonlinear finite element analysis", Computers and Structures, Vol. 30, No. 3, pp. 705-714, 1988.
- [2-6] M. Papadrakakis and C. J. Gantes, "Preconditioned conjugate and secant-Newton methods for non-linear problems", International Journal for Numerical Methods in Engineering, Vol. 28, pp. 1299-1316, 1989.
- [2-7] M. Papadrakakis and V. Balopoulos, "Improved quasi-Newton methods for large nonlinear problems", Journal of Engineering Mechanics, Vol. 117, No. 6, pp. 1201-1219, 1991.

- [2-8] M. Y. Waziri , W. J. Leong, M. A. Hassan and M. Monsi, " Jacobian computation-free Newton's method for systems of nonlinear equations ", Journal of Numerical Mathematics and Stochastics, Vol. 2, No. 1, pp. 54-63, 2003.
- [2-9] Ι. Θ. Κατσικαδέλης, "Δυναμική των Κατασκευών", Εκδόσεις Συμμετρία, Αθήνα, Ελλάδα, Τόμος ΙΙ, 2004, (in greek).
- [2-10] D. W. Jordan and P. Smith, "Nonlinear ordinary differential equations – an introduction to dynamical systems", Oxford University Press Inc., U.S.A., 3rd Edition, 1999.
- [2-11] J. Kevorkian and J. D. Cole "Multiple scale and singular perturbation methods", Springer-Verlag, U.S.A., 1996.
- [2-12] E. M. de Jager and J. Furu, "The theory of singular perturbations", Elsevier Science B.V., The Netherlands, 1996.
- [2-13] R. H. Rand, "Lecture notes on nonlinear vibrations", v.52, Cornell University, U.S.A. 2005.
- [2-14] A. N. Kounadis, "Chaoslike phenomena in the non-linear dynamic stability of discrete damped or undamped systems under step loading", International Journal of Nonlinear Mechanics, Vol. 26, No. 3/4, pp. 301-311, 1991.
- [2-15] D. S. Sophianopoulos, A. N. Kounadis and A. F. Vakakis, "Complex dynamics of perfect discrete systems under partial follower forces", International Journal of Nonlinear Mechanics, Vol. 37, pp. 1121-1138, 2002.
- [2-16] A. N. Kounadis, C. J. Gantes and I. G. Raftoyiannis, "A geometric approach for establishing dynamic buckling loads of autonomous potential N-degree-of-freedom systems", International Journal of Nonlinear Mechanics, Vol. 39, pp. 1635-1646, 2004.
- [2-17] S. Vishnubhotla, J. Falzarano and A. Vakakis, "Large amplitude nonlinear dynamics of the mobile offshore base (MOB) at transit draft in a random seaway", Proceeding of the 9th International Offshore and Polar Engineering Conference, Brest, France, 1999.
- [2-18] A. F. Vakakis and D. J. Ewins "Effects of weak non-linearities on modal analysis", Mechanical Systems and Signal Processing, Vol. 8, No. 2, pp. 175-198, 1994.
- [2-19] G. Kerschen, K. Worden, A. F. Vakakis and J. C. Golinval, "Past, present and future of nonlinear system identification in structural dynamics", Mechanical Systems and Signal Processing, Vol. 20, pp. 505-592, 2006.
- [2-20] M. Paz, "Structural dynamics, theory and computation", 3rd Edition, Van Nostrand Reinhold, U.S.A., 1985.
- [2-21] H. A. Buchholdt, "An introduction to cable roof structures", Thomas Telford, 2nd Edition, Great Britain, 1999.
- [2-22] A. K. Chopra, "Dynamics of structures, theory and applications to earthquake engineering", Prentice Hall International, Inc., U.S.A., 1995.
- [2-23] E. L. Wilson, "Three-dimensional static and dynamic analysis of structures – A Physical Approach with Emphasis on Earthquake Engineering", Computers and Structures, Inc., California, U.S.A., 3rd Edition, 2002.
- [2-24] K. J. Bathe and M. M. I. Baig, "On the composite implicit time integration procedure for nonlinear dynamics", Computers and Structures, Vol. 83, pp. 2513-2524, 2005.

- [2-25] K. J. Bathe, "Conserving energy and momentum in nonlinear dynamics: A Simple Implicit Time Integration Scheme", *Computers and Structures*, Vol. 85, pp. 437-435, 2007.
- [2-26] A. Nayfeh and D. T. Mook, "Nonlinear oscillations", John Wiley & Sons, Inc., U.S.A., 1979.
- [2-27] J. Guckenheimer and P. Holmes, "Nonlinear oscillations, dynamical systems, and bifurcations of vector fields", *Applied Mathematical Sciences* Vol. 42, Springer-Verlag, U.S.A. 1983.
- [2-28] A. Vakakis, "Introduction to dynamical systems", Lecture Notes, National Technical University of Athens, Greece, 2002.
- [2-29] H. M. Irvine, "Cable structures", Dover Publications, Inc., U.S.A., 1981.
- [2-30] E. Kreyszig, "Advanced engineering mathematics", 8th Edition, John Wiley & Sons, Inc., U.S.A., 1999.
- [2-31] A. E. Armenakas, "Advanced mechanics of materials and applied elasticity", CRC Taylor & Francis, U.S.A., 2006.
- [2-32] J. W. Leonard, "Tension structures, behavior & analysis", McGraw-Hill, Inc., U.S.A., 1988.
- [2-33] R. W. Clough and J. Penzien, "Dynamics of structures", McGraw-Hill, Inc., U.S.A., 1993.
- [2-34] A. G. Pugsley, "On the natural frequencies of suspension chains", *Quarterly Journal of Mechanics and Applied Mathematics*, Vol. 2, Part 4, pp. 412-418, 1949.
- [2-35] K. Ahmadi-Kashani, "Vibration of hanging cables", *Computers and Structures*, Vol. 31, No. 5, pp. 699-715, 1989.
- [2-36] H. M. Irvine and T. K. Caughey, "The linear theory of free vibrations of a suspended cable", *Proceedings of the Royal Society of London. Series A, Mathematical and Physical Sciences*, London, Great Britain, Vol. 341, No. 1626, pp. 299-315, 1974.
- [2-37] G. Rega and A. Luongo, "Natural vibrations of suspended cables with flexible supports", *Computers and Structures*, Vol. 12, pp. 65-75, 1980.
- [2-38] J. J. Burgess and M. S. Triantafyllou, "The elastic frequencies of cables", *Journal of Sound and Vibration*, Vol. 120, No. 1, pp. 153-165, 1987.
- [2-39] M. S. Triantafyllou and L. Grinfolgel, "Natural frequencies and modes of inclined cables", *Journal of Structural Engineering*, Vol. 112, No. 1, pp. 139-148, 1986.
- [2-40] P. Hagedorn and B. Schäfer, "On non-linear free vibrations of an elastic cable", *International Journal of Non-Linear Mechanics*, Vol. 15, pp. 39-52, 1984.
- [2-41] W. M. Henghold and J. J. Russell, "Equilibrium and natural frequencies of cable structures (a nonlinear finite element approach)", *Computers and Structures*, Vol. 6, pp. 267-271, 1976.
- [2-42] Q. L. Zhang and U. Peil, "Dynamic behaviours of cables in parametrically unstable zones", *Computers and Structures*, Vol. 73, pp. 437-443, 1999.
- [2-43] A. Luongo, G. Rega, F. Vestroni, "Planar non-linear free vibrations of an elastic cable", *International Journal of Non-Linear Mechanics*, Vol. 19, No. 1, pp. 39-52, 1984.
- [2-44] F. Benedettini and G. Rega, "Non-linear dynamics of an elastic cable under planar excitation", *International Journal of Non-Linear Mechanics*, Vol. 22, No. 6, pp. 497-509, 1987.
- [2-45] F. Benedettini and G. Rega, "Planar non-linear oscillations of elastic cables under superharmonic resonance conditions", *Journal of Sound and Vibration*, Vol. 132, No. 3, pp. 353-366, 1989.

- [2-46] G. Rega and F. Benedettini, "Planar non-linear oscillations of elastic cables under subharmonic resonance conditions", *Journal of Sound and Vibration*, Vol. 132, No. 3, pp. 367-381, 1989.
- [2-47] F. Benedettini, G. Rega and R. Alaggio, "Non-linear oscillations of a four-degree-of-freedom model of a suspended cable under multiple internal resonance conditions", *Journal of Sound and Vibration*, Vol. 182, No. 4, pp. 775-798, 1995.
- [2-48] N. Srinil and G. Rega, "The effects of kinematic condensation on internally resonant forced vibrations of shallow horizontal cables", *International Journal of Non-Linear Mechanics*, Vol. 42, pp. 180-195, 2007.
- [2-49] N. Srinil and G. Rega, "Nonlinear longitudinal/transversal modal interactions in highly extensible suspended cables", *Journal of Sound and Vibration*, Vol. 310, pp. 230-242, 2008.
- [2-50] G. Rega, "Non-linearity, bifurcation and chaos in the finite dynamics of different cable models", *Chaos, Solitons and Fractals*, Vol. 7, No. 10, pp. 1507-1536, 1996.
- [2-51] N. Srinil, G. Rega and S. Chucheepsakul, "Nonlinear interactions in the 3D free vibrations of horizontal and inclined sagged cables", *Proceedings of the 5th International Symposium on cable dynamics*, Santa Margherita Ligure, Italy, pp. 77-84, 2003.
- [2-52] N. Srinil, G. Rega and S. Chucheepsakul, "Three-dimensional non-linear coupling and dynamic tension in the large-amplitude free vibrations of arbitrarily sagged cables", *Journal of Sound and Vibration*, Vol. 269, No. 3-5, pp. 823-852, 2004.
- [2-53] G. Rega, "Nonlinear vibrations of suspended cables—Part I: Modeling and analysis", *Applied Mechanics Review*, Vol. 57, No. 6, pp. 443-478, 2004.
- [2-54] G. Rega, "Nonlinear vibrations of suspended cables—Part II: Deterministic phenomena", *Applied Mechanics Review*, Vol. 57, No. 6, pp. 479-514, 2004.
- [2-55] K. C. S. Kwok, "Damping and control of structures subjected to dynamic loading", in: *Structures subjected to dynamic loading – Stability and Strength*, Editors: R. Narayanan and T. M. Roberts, Elsevier Science Publishers Ltd, Great Britain, pp. 303-334, 1991.
- [2-56] A. T. Yu, "Vibration damping of stranded cable", *Proceedings of the Society for Experimental Stress Analysis*, Vol. 9, pp. 141-158, 1952.
- [2-57] S. Kumarasena, N. P. Jones, P. Irwin and P. Taylor, "Wind-induced vibration of stay cables", Publication No. FHWA-HRT-05-083, U.S. Department of Transportation, Federal Highway Administration, U.S.A., 2007.
- [2-58] Y. Li, B. Wang, W. Lu, Q. Tao and H. Liao, "Wind tunnel test for rain-wind induced vibration of cables in cable-stayed bridges" *Proceedings of the 7th Asia-Pacific Conference on wind Engineering*, Taipei, Taiwan, 2009.
- [2-59] S. E. Ramberg and O. M. Griffin, "Free vibration of taut and slack marine cables", *Journal of the Structural Division, ASCE*, Vol. 103, pp. 2079-2092, 1977.
- [2-60] M. Majowiecki, "Tensostrutture progetto e verifica", Edizioni CREA, Italy, 1994, (in italian).
- [2-61] J. S. Gero, "The behaviour of cable network structures", *Structures Report SR8*, University of Sydney, Australia, 1975.
- [2-62] J. S. Gero, "The preliminary design of cable network structures", *Structures Report SR9*, University of Sydney, Australia, 1975.

- [2-63] E. Buckingham, "On physically similar systems; Illustrations of the use of dimensional equations", *Physical Review*, Vol. 4, pp. 345-376, 1914.
- [2-64] R. V. Giles, "Schaum's outline of theory and problems of fluid mechanics and hydraulics", McGraw-Hill, U.S.A., 1977.
- [2-65] J. Szabó, L. Kollár and M. N. Pavlović, "Structural design of cable-suspended roofs", Akadémiai Kiadó and Ellis Horwood Limited, Hungary and Great Britain, 1984.
- [2-66] C. Birnstiel, "Analysis and design of cable structures", *Computers and Structures*, Vol. 2, pp. 817-831, 1972.
- [2-67] A. A. Atai and A. Mioduchowski, "Equilibrium analysis of elasto-plastic cable nets", *Computers and Structures*, Vol. 66, No. 2-3, pp. 163-171, 1998.
- [2-68] G. D. Stefanou, E. Moossavi, S. Bishop and P. Koliopoulos, "Conjugate gradients method for calculating the response of large cable nets to static loads", *Computers and Structures*, Vol. 49, No. 5, pp. 843-848, 1993.
- [2-69] I. Talvik, "Finite element modelling of cable networks with flexible supports", *Computers and Structures*, Vol. 79, pp. 2443-2450, 2001.
- [2-70] D. S. Porter Jr. and D. W. Fowler, "The analysis of nonlinear cable net systems and their supporting structures", *Computers and Structures*, Vol. 3, pp. 1109-1123, 1973.
- [2-71] M. Majowiecki and F. Zoulas, "On the elastic interaction between rope net and space frame anchorage structures", *Proceedings of the 3rd International Conference on Space Structures*, University of Surrey, Guildford, Great Britain, pp. 778-84, 1984.
- [2-72] A. Chisalita, "Finite deformation analysis of cable networks", *Journal of Engineering Mechanics – ASCE*, Vol. 110, No. 2, pp. 207-223, 1984.
- [2-73] M. Παπαδρακάκης, "Ανάλυση φορέων με τη μέθοδο των πεπερασμένων στοιχείων", Εκδόσεις Παπασωτηρίου, Αθήνα, Ελλάδα, 2001, (in greek).
- [2-74] B. L. Dhoopar, P. C. Gupta and B. P. Singh, "Vibration analysis of orthogonal cable networks by transfer matrix method", *Journal of Sound and Vibration*, Vol. 101, No. 4, pp. 575-584, 1985.
- [2-75] J. T. Katsikadelis and E. J. Sapountzakis, "An Approach to the vibration problem of homogeneous, non-homogeneous and composite membranes based on the boundary element method", *International Journal for Numerical Methods in Engineering*, Vol. 26, No. 11, pp. 2439-2455, 1988.
- [2-76] A. Zingoni, "An efficient computational scheme for the vibration analysis of high tension cable nets", *Journal of the Sound and Vibration*, Vol. 189, No. 1, pp. 55-79, 1996.
- [2-77] M. L. Gambhir and B. deV. Batchelor, "A finite element for 3-D prestressed cablenets", *International Journal for Numerical Methods in Engineering*, Vol. 11, pp. 1699-1718, 1977.
- [2-78] M. L. Gambhir and B. deV. Batchelor, "Finite element study of the free vibration of 3D cable networks", *International Journal of Solids and Structures*, Vol. 15, pp. 127-136, 1979.
- [2-79] G. R. Seeley, P. Christiano and H. Stefan, "Natural frequencies of circular cable networks", *Journal of the Structural Division*, Vol. 101, No. ST5, pp. 1171-1177, 1975.
- [2-80] N. F. Morris, "Dynamic response of cable networks", *Journal of the Structural Division*, Vol. 100, No. ST10, pp. 2091-2108, 1973.

- [2-81] N. F. Morris, "Modal analysis of cable networks", *Journal of the Structural Division*, Vol. 101, No. ST1, pp. 97-108, 1975.
- [2-82] H. Ozdemir, "A finite element approach for cable problems", *Computers and Structures*, Vol. 15, pp. 427-437, 1979.
- [2-83] G. R. Monforton and N. M. El-Hakim, "Analysis of truss-cable structures", *Computers and Structures*, Vol. 11, pp. 327-335, 1980.
- [2-84] M. Papadrakakis, "Inelastic dynamic response of cable networks", *Journal of Structural Engineering*, Vol. 109, No. 5, pp. 1139-1154, 1983.
- [2-85] O. Vilnay and P. Rogers, "Statical and dynamical response of cable nets", *International Journal of Solids and Structures*, Vol. 26, No. 3, pp. 229-312, 1990.
- [2-86] S. Swaddiwudhipong, C. M. Wang, K. M. Liew and S. L. Lee, "Optimal pretensioned forces for cable networks", *Computers and Structures*, Vol. 33, No. 6, pp. 1349-1354, 1989.
- [2-87] G. D. Stefanou, "The response of large cable nets to general dynamic loads based on step-by-step time integration techniques", *Journal of the International Association for Shell and Spatial Structures*, IASS, Vol. 38, No. 123, pp. 53-64, 1997.
- [2-88] L. F. Geschwindner, "Nonlinear dynamic analysis by modal superposition", *Journal of the Structural Division*, Vol. 107, No. ST12, pp. 2325-2336, 1981.
- [2-89] L. F. Geschwindner and H. H. West, "Forced vibrations of cable networks", *Journal of the Structural Division*, Vol. 106, ST9, pp. 1885-1898, 1980.
- [2-90] J. Fan, F. He and Z. Liu, "Chaotic oscillation of saddle form cable-suspended roofs under vertical excitation action", *Nonlinear Dynamics*, Vol. 12, pp. 57-68, 1997.
- [2-91] M. Lazzari, A. V. Saetta and R. V. Vitaliani, "Non-linear dynamic analysis of cable-suspended structures subjected to wind actions", *Computers and Structures*, Vol. 79, pp. 953-969, 2001.
- [2-92] G. D. Stefanou, "Dynamic response of tension cable structures due to wind loads", *Computers and Structures*, Vol. 43, No. 2, pp. 365-372, 1992.
- [2-93] N. J. Gimsing, "Cable supported bridges – concept & design", John Wiley & Sons, 2nd Edition, Great Britain, 1998.
- [2-94] www.transpacifichardware.com
- [2-95] EUROCODE 3, PART 1.11, "Design of structures with tension components", 2003.
- [2-96] EUROCODE 1, PART 1.4, "General actions – wind actions", 2003.
- [2-97] E. Simiu and R. H. Scanlan, "Wind effects on structures", John Wiley & Sons, Inc., U.S.A., 2nd Edition, 1986.
- [2-98] D. Ghiocel and D. Lungu, "Wind, snow and temperature effects on structures based on probability", Abacus Press, Tunbridge Wells, Kent, 1975.
- [2-99] J. J. Jang and Y. L. Lee, "A study of along wind speed power spectrum for Taiwan area", *Journal of Marine Science and Technology*, Vol. 6, No.1, pp. 71-77, 1998.
- [2-100] C. C. Baniotopoulos, "Design of wind-sensitive structures", in: "Wind effects on buildings and design of wind-sensitive structures", CISM courses and lectures, No. 493, International Centre for Mechanical Sciences, Editors: T. Stathopoulos and C. C. Baniotopoulos, Springer Wien New York, Udine, Italy, pp. 201-227, 2007.

- [2-101] I. Lavassas, G. Nikolaidis, P. Zervas, E. Efthimiou, I.N. Doudoumis and C. C. Baniotopoulos, "Analysis and design of the prototype of a steel 1-MW wind turbine tower", *Engineering Structures*, Vol. 25, No. 8, pp. 1097-1106, 2003.
- [2-102] Α. Τσιπλακίδου, Α. Φανούλη, Ε. Κολτσάκης και Χ. Μπανιωτόπουλος, "Σχεδιασμός χαλύβδινων δικτυωτών ιστών για φόρτιση ανέμου και πάγου", Πρακτικά 5^{ου} Εθνικού Συνεδρίου Μεταλλικών Κατασκευών, Χάνθη, Ελλάδα, Τόμος Ι, σελ. 207-214, 2005 (in greek).
- [2-103] Ε. Ευθυμίου και Χ. Κ. Μπανιωτόπουλος, "Διερεύνηση της απόκρισης χαλύβδινων δικτυωτών ιστών τηλεπικοινωνιών υπό ανεμοφόρτιση και σεισμική δράση", Πρακτικά 6^{ου} Εθνικού Συνεδρίου Μεταλλικών Κατασκευών, Ιωάννινα, Ελλάδα, Τόμος ΙΙ, σελ. 102-108, 2008 (in greek).
- [2-104] EUROCODE 3, PART 7.1, "Towers, masts and chimneys – Towers and masts", 2002.
- [2-105] EUROCODE 3, PART 7.2, "Towers, masts and chimneys - Chimneys", 2003.
- [2-106] M. M. Hand, N. D. Kelley and M. J. Balas, "Identification of wind turbine response to turbulent inflow structures", *Proceedings of the 4th ASME/JSME Joint Fluids Engineering Conference*, Honolulu, Hawaii, 2003.
- [2-107] U. Peil and H. Nölle, "Guyed masts under wind load", *Journal of Wind Engineering and Industrial Aerodynamics*, Vol. 41-44, pp. 2129-2140-525, 1992.
- [2-108] C. Gantes, R. Khoury, J. J. Connor and C. Pouangare, "Modeling, loading and preliminary design considerations for tall guyed towers", *Computers and Structures*, Vol. 49, pp. 797-805, 1993.
- [2-109] H. Yan-li, M. Xing and W. Zhao-min, "Nonlinear discrete analysis method for random vibration of guyed masts under wind load", *Journal of Wind Engineering and Industrial Aerodynamics*, Vol. 91, pp. 513-525, 2003.
- [2-110] H. J. Sutherland, P. L. Jones and B. A. Neal, "The long-term inflow and structural test program", *Proceeding of the Wind Energy Symposium 2001*, ASME, AIAA-2001-0039, pp. 1-11, 2001.
- [2-111] H. J. Sutherland, "Preliminary analysis of the structural and inflow data from the LIST turbine", *Proceeding of the Wind Energy Symposium 2001*, ASME, AIAA-2001-0041, pp. 1-11, 2001.
- [2-112] T. Stathopoulos, "Introduction to wind engineering, wind structure, wind-building interaction", in: "Wind effects on buildings and design of wind-sensitive structures", CISM courses and lectures, No. 493, International Centre for Mechanical Sciences, Editors: T. Stathopoulos and C. C. Baniotopoulos, Springer Wien New York, Udine, Italy, pp. 1-30, 2007.
- [2-113] <http://meteo.chi.civil.ntua.gr>
- [2-114] G. Hellman, "Über die Bewegung der Luft in den untersten Schichten der Atmosphäre", *Meteorologische Zeitschrift*, Vol. 34, pp. 915-929, 1916.
- [2-115] T. Gibbs, "Windstorms" in: "International perspectives on natural disasters, occurrence, mitigation and consequences", Editors: J. P. Stoltman, J. Lidstone and L. M. DeChano, Kluwer Academic Publishers, The Netherlands, 2004.
- [2-116] H. Buchholdt, "Structural dynamics for engineers", Thomas Telford, Great Britain, 1997.
- [2-117] A. G. Davenport, "The spectrum of horizontal gustiness near the ground in high winds", *Quarterly Journal of the Royal Meteorological Society*, Vol. 87, pp. 194-211, 1961.

- [2-118] J. C. Kaimal, J. C. Wyngaard, Y. Izumi and O. R. Coté, "Spectral characteristics of surface layer turbulence", *Quarterly Journal of the Royal Meteorological Society*, Vol. 98, pp. 563-589, 1972.
- [2-119] M. Shinozuka and C. M. Jan, "Digital simulation of random processes and its applications", *Journal of Sound and Vibration*, Vol. 25, No. 1, pp. 111-128, 1972.
- [2-120] J. Györgyi and G. Szabó, "Dynamic analysis of wind effects by using an artificial wind function", *Slovak Journal of Civil Engineering*, Vol. 3, pp. 21-33, 2008.
- [2-121] G. Deodatis, "Simulation of ergodic multivariate stochastic processes", *Journal of Engineering Mechanics*, Vol. 122, No. 8, pp. 778-787, 1996.
- [2-122] Leonardo da Vinci Pilot Project CZ/02/B/F/PP-134007, "Handbook 3: Action effects for buildings", Development of skills facilitating implementation of eurocodes, Aachen, Germany, 2005, <http://eurocodes.jrc.ec.europa.eu/showpublication.php?id=64>.
- [2-123] S. Cheng, H. Tanaka, P. A. Irwin, J. B. Jakobsen, "Aerodynamic instability of inclined cables", *Proceedings of the 5th International Symposium on cable dynamics*, Santa Margherita Ligure, Italy, pp. 69-76, 2003.
- [2-124] G. Bartoli, F. Cluni, V. Gusella and L. Procino, "Dynamics of cable under wind action: Wind tunnel experimental analysis", *Journal of Wind Engineering and Industrial Aerodynamics*, Vol. 94, pp. 259-273, 2006.
- [2-125] C. Borri, M. Majowiecki and P. Spinelli, "Wind response of a large tensile structure: the new roof of the Olympic stadium in Rome", *Journal of Wind Engineering and Industrial Aerodynamics*, Vol. 41-44, pp. 1435-1446, 1992.
- [2-126] B. J. Vickery and M. Majowiecki, "Wind induced response of a cable supported stadium roof", *Journal of Wind Engineering and Industrial Aerodynamics*, Vol. 41-44, pp. 1447-1458, 1992.
- [2-127] P. Biagini, C. Borri and L. Facchini, "Wind response of large roofs of stadions and arena", *Journal of Wind Engineering and Industrial Aerodynamics*, Vol. 95, pp. 871-887, 2007.
- [2-128] C. Borri and C. Costa, "Bridge aerodynamics and aeroelastic phenomena", in: "Wind effects on buildings and design of wind-sensitive structures", CISM courses and lectures, No. 493, International Centre for Mechanical Sciences, Editors: T. Stathopoulos and C. C. Baniotopoulos, Springer Wien New York, Udine, Italy, pp. 167-200, 2007.
- [2-129] O. Flamand, J. Biétry, C. Barré, E. Germain and P. Bourcier, "Fatigue calculation on the roof sustaining cables of a large stadium in Paris", *Journal of Wind Engineering and Industrial Aerodynamics*, Vol. 64, pp. 127-134, 1996.
- [2-130] M. Kazakevitch, "The aerodynamics of a hangar membrane roof", *Journal of Wind Engineering and Industrial Aerodynamics*, Vol. 77-78, pp. 157-169, 1998.
- [2-131] B. Natalini, J. O. Marighetti and M. B. Natalini, "Wind tunnel modeling of mean pressures on planar canopy roof", *Journal of Wind Engineering and Industrial Aerodynamics*, Vol. 90, pp. 427-439, 2002.
- [2-132] Y. Uematsu, E. Izumi and T. Stathopoulos, "Wind force coefficients for designing free-standing canopy roofs", *Journal of Wind Engineering and Industrial Aerodynamics*, Vol. 95, pp. 1486-1510, 2007.

- [2-133] Y. Uematsu, T. Stathopoulos and E. Iizumi, "Wind loads on free-standing canopy roofs: Part 1 local wind pressures", *Journal of Wind Engineering and Industrial Aerodynamics*, Vol. 96, pp. 1015-1028, 2008.
- [2-134] Y. Uematsu, T. Stathopoulos and E. Iizumi, "Wind loads on free-standing canopy roofs: Part 2 overall wind forces", *Journal of Wind Engineering and Industrial Aerodynamics*, Vol. 96, pp. 1029-1042, 2008.
- [2-135] Y. L. Xu and G. F. Reardon, "Variations of wind pressure on hip roofs with roof pitch", *Journal of Wind Engineering and Industrial Aerodynamics*, Vol. 73, pp. 267-284, 1998.
- [2-136] J. G. Zhao and K. M. Lam, "Characteristics of wind pressures on large cantilevered roofs: effect of roof inclination", *Journal of Wind Engineering and Industrial Aerodynamics*, Vol. 90, pp. 1867-1880, 2002.
- [2-137] A. Katsumura, Y. Tamura and O. Nakamura, "Universal wind load distribution simultaneously reproducing largest load effects in all subject members on large-span cantilevered roof", *Journal of Wind Engineering and Industrial Aerodynamics*, Vol. 95, pp. 1145-1165, 2007.
- [2-138] A. D. Cope, K. R. Gurley, M. Gioffre and T. A. Reinhold, "Low-rise gable roof wind loads: Characterization and stochastic simulation", *Journal of Wind Engineering and Industrial Aerodynamics*, Vol. 93, pp. 719-728, 2005.
- [2-139] S. Franchini, S. Pindado, J. Meseguer and A. Sanz-Andrés, "A parametric, experimental analysis of conical vortices on curved roofs of low-rise buildings", *Journal of Wind Engineering and Industrial Aerodynamics*, Vol. 93, pp. 639-650, 2005.
- [2-140] P. A. Blackmore and E. Tsokri, "Wind loads on curved roofs", *Journal of Wind Engineering and Industrial Aerodynamics*, Vol. 94, pp. 833-844, 2006.
- [2-141] Y. Uematsu, k. Watanabe, A. Sasaki, M. Yamada and T. Hongo, "Wind-induced dynamic response and resultant load estimation of a circular flat roof", *Journal of Wind Engineering and Industrial Aerodynamics*, Vol. 83, pp. 251-261, 1999.
- [2-142] Y. Uematsu, T. Moteki and T. Hongo, "Model of wind pressure field on circular flat roofs and its application to load estimation", *Journal of Wind Engineering and Industrial Aerodynamics*, Vol. 96, pp. 1003-1014, 2008.
- [2-143] M. Glück, M. Breuer, F. Durst, A. Halfmann and E. Rank, "Computation of fluid-structure interaction on lightweight structures", *Journal of Wind Engineering and Industrial Aerodynamics*, Vol. 89, pp. 1351-1368, 2001.
- [2-144] Y. Wu, X. Sun and S. Shen, "Computation of wind-structure interaction on tension structures", *Journal of Wind Engineering and Industrial Aerodynamics*, Vol. 96, pp. 2019-2032, 2008.
- [2-145] B. Tabarrok and Z. Qin, "Nonlinear analysis of tension structures", *Computers and Structures*, Vol. 45, No. 5/6, pp. 973-984, 1992.
- [2-146] B. Tabarrok and Z. Qin, "Dynamic analysis of tension structures", *Computers and Structures*, Vol. 62, No. 3, pp. 467-474, 1997.
- [2-147] I. Elashkar and M. Novak, "Wind tunnel studies of cable roofs", *Journal of Wind Engineering and Industrial Aerodynamics*, Vol. 13, pp. 407-419, 1983.

- [2-148] N. Esquillan and Y. Saillard (Editors), "Proceedings of the IASS Colloquium on Hanging Roofs, Continuous Metallic Shell Roofs and Superficial Lattice Roofs, Paris, France, 1962", North Holland Publishing Company, Amsterdam, 1963.
- [2-149] X. Y. Sun, Y. Wu, Q. S. Yang and S. Z. Shen, "Wind tunnel tests on the aeroelastic behaviors of pretensioned saddle-shaped suspended roofs", Proceedings of the BBAA VI International Colloquium on Bluff Bodies Aerodynamics and Applications, Milan, Italy, 2008.
- [2-150] Y. Uematsu, F. Arakatsu, S. Matsumoto and F. Tekeda, "Wind force coefficients for the design of a hyperbolic paraboloid free roof", Proceedings of the 7th Asia-Pacific Conference on Wind Engineering, Taipei, Taiwan, 2009.
- [2-151] F. Li, M. Gu and J. Pan, "Practical wind-resistant design of large space flexible cable net", Proceedings of the 7th Asia-Pacific Conference on Wind Engineering, Taipei, Taiwan, 2009.
- [2-152] F. Rizzo, P. D'Asdia and L. Procino, "Wind action evaluation on tension roofs of hyperbolic paraboloid shape", Proceedings of the BBAA VI International Colloquium on Bluff Bodies Aerodynamics and Applications, Milan, Italy, 2008.
- [2-153] F. Rizzo, P. D'Asdia and M. Lazzari, "Aerodynamic behaviour of hyperbolic paraboloid shaped roofs: wind tunnel tests", Proceedings of the EACWE 5, Florence, Italy, 2009.
- [2-154] F. Rizzo, P. D'Asdia, M. Lazzari and G. Olivato, "Aerodynamic behaviour of hyperbolic paraboloid shaped roofs: POD and CFD analysis", Proceedings of the EACWE 5, Florence, Italy, 2009.
- [2-155] F. Rizzo, P. D'Asdia, M. Lazzari and L. Procino, "Wind action evaluation on tension roofs of hyperbolic paraboloid shape", Engineering Structures, Vol. 23, pp. 445-461, 2011.

3 ANALYTICAL SOLUTIONS FOR SIMPLE CABLE NETS

3.1 INTRODUCTION

During the last decades, the attention of several researchers has been focused on cable vibrations. Due to its geometric nonlinearity, the cable response under dynamic loading is very complicated, dominated by phenomena that do not appear in a linear structure. The field of nonlinear dynamics has been developed introducing several methods that detect this kind of nonlinear phenomena [3-1].

A first approach to cables' dynamic response has been oriented towards calculating the frequencies of a simple cable. Pugsley [3-2] introduced semi-empirical formulae for the three in-plane frequencies of a suspended sagged chain. Ahmadi-Kashani [3-3] obtained closed formulae for the frequencies of an inclined hanging inextensible cable, while in [3-4] the authors derived formulae for the natural frequencies and mode shapes of taut, inclined cables. Burgess and Triantafyllou [3-5] explored and compared the elastic frequencies of a horizontal sagged cable and an inclined one. Irvine and Caughey [3-6] derived formulae for the frequencies of the in-plane and out-of-plane vibrations of a horizontal suspended cable. Rega and Luongo [3-7] studied the natural frequencies of an inextensible cable with flexible supports. Rega et al. [3-8] instead, explored the effect of nonlinear terms on the crossover frequencies of a prestressed or slack cable. The nonlinear dynamic response of a simple cable is studied in many works. In [3-9] the equation of motion of a simple cable as a continuum system is presented, having quadratic and cubic nonlinear terms. In [3-10] the response curves of a taut cable and a suspended sagged one are plotted, exploring the influence of nonlinear terms on the steady-state response of the cable. In [3-11] and [3-12] the authors studied the motion of a suspended elastic cable under nonlinear resonances.

In more recent works the analytical equations of motion are solved numerically giving the dynamic response of a simple cable. Takahashi et al. [3-13] showed that the in-plane antisymmetric response of a cable under a symmetric harmonic load occurs through bifurcation, the frequency for this bifurcation depends on the sag-to-span ratio and within the unstable regions a strong coupling between symmetric and antisymmetric responses is observed. In [3-14] the authors evaluated numerically the analytical solution of the equation, describing the motion of sagged flexible horizontal or inclined cables, detecting nonlinear phenomena, such as internal resonances, crossover or avoidance points, through the time-history diagrams of the cable's dynamic response. An investigation

of a simple cable vibration is presented in [3-15], taking into account higher order terms of longitudinal dynamic deformation, capturing thus nonlinear coupling of longitudinal/vertical displacements.

Very few publications provide analytical solutions for the equation of motion of cable nets or their natural frequencies. Chisalita in [3-16] provided a formula for the first frequency of a simple flat cable net, consisting of two crossing cables, having the same cross-section and pretension. Leonard [3-17] referred to a similar cable net including the initial sag of the cables. He presented expressions of its three natural frequencies, considering lumped or consistent mass. Seeley et al. [3-18] gave a formula for the fundamental frequency of a circular cable network, with cables arranged radially and ring-wise, for a limited range of the sag-to-span ratio, showing that the first frequency of the net depends solely on the sag. For multi-degree-of-freedom models numerical analyses have been conducted, in order to investigate the dynamic behaviour of the system, regarding the natural frequencies ([3-19], [3-20]) or its dynamic oscillation ([3-21], [3-22]). In [3-23] the author presented a simple approach to calculate natural frequencies of geometrically nonlinear cable structures, using straight axial elements. He analysed two different flat nets consisting of two or four cables and a saddle-shaped cable net of an actual structure. The frequencies of these models were compared with the results referred by other sources and found to be in good agreement. Talvik in [3-24] presented and verified a mathematical model for the analysis of prestressed cable networks with flexible contour ring. The equations were solved by iterative methods and explicit time integration.

In this chapter, the simplest cable net is taken into consideration, aiming at deriving the analytical equations in static and dynamic equilibrium. It is a symmetric system of two crossing cables having the same geometrical and mechanical characteristics. The motion of the central node is investigated, allowing for all three translational degrees of freedom. Expressions of the three natural frequencies of the system are also provided, referring to the prestressed but unforced state. However, deriving an exact analytical solution of this equation of motion is proved to be very difficult due to the complexity of the nonlinear terms. In addition, detecting the conditions that cause resonant phenomena by solving numerically the equation of motion is a time consuming procedure requiring a trial and error iterative process. Thus, several simplifications are made which lead to the analogy of a Duffing oscillator, the analytical solution of which can be found in the literature ([3-25] – [3-27]) and several applications are provided in [3-1]. On the basis of this simplification, expressions of the steady-state response regarding the deflection of the net are reported in this work and dynamic phenomena that characterise nonlinear systems are delineated, such as nonlinear resonances, bending of the response curves, hysteresis loops and instability regions, leading to unexpected large amplitudes of oscillation. An example is presented in order to confirm the theoretical conclusions and to compare the exact model with the simplified one.

3.2 CABLE NET WITH TWO CABLES (EXACT MODEL)

3.2.1 Geometry

The simplest possible cable net model is studied, which is a structure consisting of two crossing perpendicular cables (Figure 3-1). The ends of the cables are fixed while the central node is free. The span of each cable between the supports is equal to L and the cable sags are f .

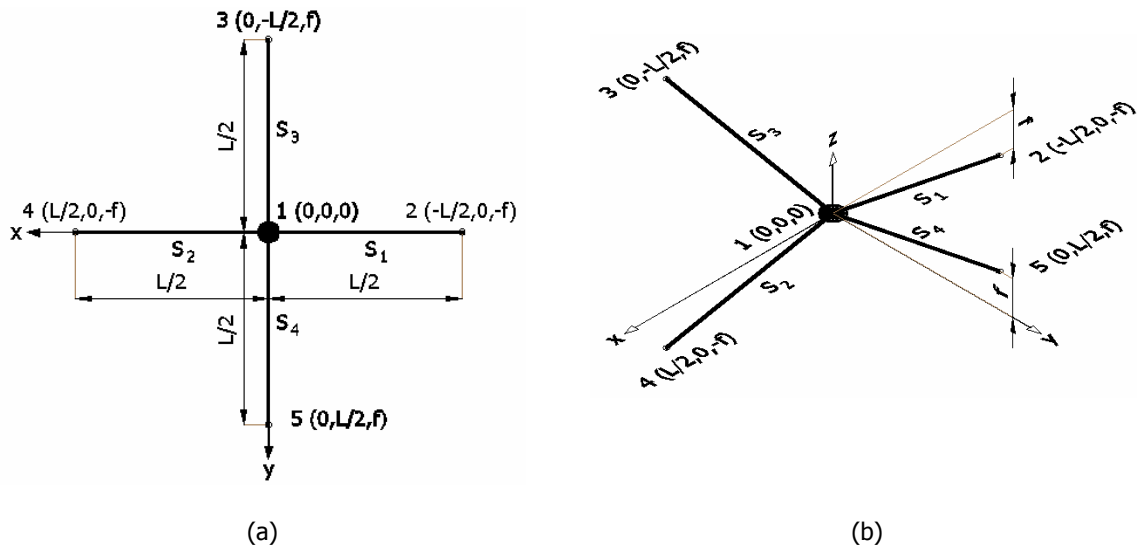


Figure 3-1: Geometry of cable net: (a) plan view, (b) perspective view

The uniformly distributed mass of the cables is considered as lumped. Additional concentrated mass can be taken into account. The total mass is attached to the central node. No local sag is produced between two adjacent nodes, as no self-weight is taken into account. Both cables have the same cross-section, material and initial pretension N_0 , with horizontal component H_0 . The initial pretension is introduced as initial strain ϵ_0 to all cable segments, which, according to Hooke's law, is equal to:

$$N_0 = EA\epsilon_0 = H_0 \frac{2S_N}{L} \quad (3-1)$$

where S_N is the length of each segment at the equilibrium state under pretension expressed as:

$$S_N = \sqrt{(L/2)^2 + f^2} \quad (3-2)$$

Assuming small strains, the initial length S_0 for all segments is equal to:

$$\epsilon_0 = \frac{S_N - S_0}{S_0} \Rightarrow S_0 = \frac{S_N}{1 + \epsilon_0} = \frac{S_N}{1 + \frac{N_0}{EA}} \quad (3-3)$$

Considering instead large strains, the initial length S_0 for all segments is equal to:

$$\epsilon_0 = \frac{S_N^2 - S_0^2}{2S_0^2} \Rightarrow S_0 = \frac{S_N}{\sqrt{1 + 2\epsilon_0}} = \frac{S_N}{\sqrt{1 + 2\frac{N_0}{EA}}} \quad (3-4)$$

3.2.2 Equilibrium of the central node

If we define as u , v and w the displacements of the central node, referring to the global axes x , y , z , respectively, the deformed structure is shown in Figure 3-2.

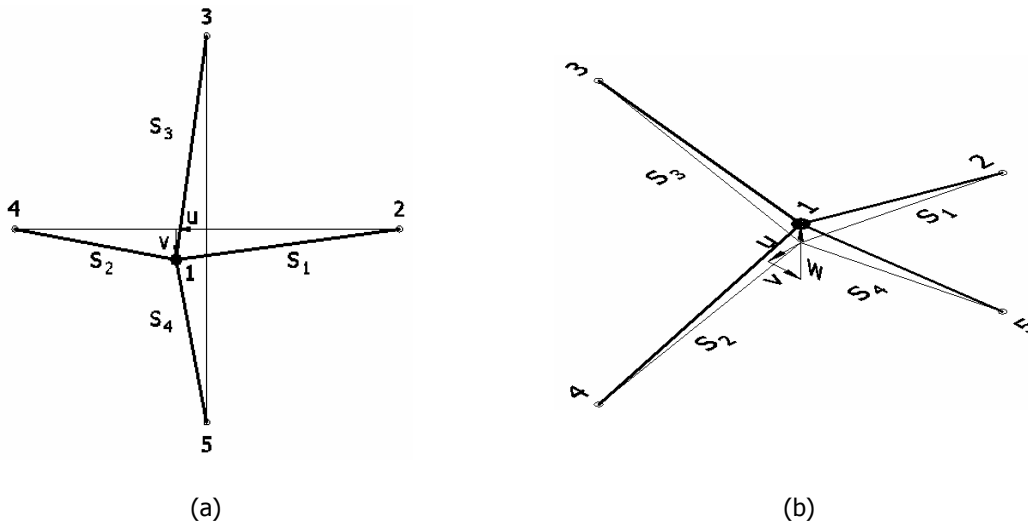


Figure 3-2: Deformed cable net: (a) plan view, (b) perspective view

The deformed lengths of the cable segments are calculated as:

$$S_1 = \sqrt{(L/2 + u)^2 + v^2 + (f + w)^2} \quad (3-5)$$

$$S_2 = \sqrt{(L/2 - u)^2 + v^2 + (f + w)^2} \quad (3-6)$$

$$S_3 = \sqrt{u^2 + (L/2 + v)^2 + (f - w)^2} \quad (3-7)$$

$$S_4 = \sqrt{u^2 + (L/2 - v)^2 + (f - w)^2} \quad (3-8)$$

The cable tension for each deformed segment, with the assumption of large displacements – small strains, is expressed as:

$$N_i = EA \left(\frac{S_i - S_0}{S_0} \right) = EA \left(\frac{S_N - S_0}{S_0} \right) + EA \left(\frac{S_i - S_N}{S_0} \right) = N_0 + EA \left(\frac{S_i - S_N}{S_0} \right) \quad (3-9)$$

while for large displacements – large strains:

$$N_i = EA \left(\frac{S_i^2 - S_0^2}{2S_0^2} \right) = EA \left(\frac{S_N^2 - S_0^2}{2S_0^2} \right) + EA \left(\frac{S_i^2 - S_N^2}{2S_0^2} \right) = N_0 + EA \left(\frac{S_i^2 - S_N^2}{2S_0^2} \right) \quad (3-10)$$

where $i=1,2,3,4$, and their components, referring to the global axes, are calculated by the following expressions:

$$N_{1x} = N_1 \cdot (L/2 + u) / (S_1) \quad (3-11)$$

$$N_{1y} = N_1 \cdot v / (S_1) \quad (3-12)$$

$$N_{1z} = N_1 \cdot (f + w) / (S_1) \quad (3-13)$$

$$N_{2x} = N_2 \cdot (L/2 - u) / (S_2) \quad (3-14)$$

$$N_{2y} = -N_2 \cdot v / (S_2) \quad (3-15)$$

$$N_{2z} = -N_2 \cdot (f+w) / (S_2) \quad (3-16)$$

$$N_{3x} = N_3 \cdot u / (S_3) \quad (3-17)$$

$$N_{3y} = N_3 \cdot (L/2+v) / (S_3) \quad (3-18)$$

$$N_{3z} = -N_3 \cdot (f-w) / (S_3) \quad (3-19)$$

$$N_{4x} = -N_4 \cdot u / (S_4) \quad (3-20)$$

$$N_{4y} = N_4 \cdot (L/2-v) / (S_4) \quad (3-21)$$

$$N_{4z} = N_4 \cdot (f-w) / (S_4) \quad (3-22)$$

The sum of forces at the central node, referring to the x, y, z global axes, are:

$$N_x = N_{1x} - N_{2x} + N_{3x} - N_{4x} \quad (3-23)$$

$$N_y = N_{1y} - N_{2y} + N_{3y} - N_{4y} \quad (3-24)$$

$$N_z = N_{1z} - N_{2z} + N_{3z} - N_{4z} \quad (3-25)$$

3.2.3 Stiffness and eigenfrequencies of the system

Assuming large displacements but small strains, differentiating equations (3-23)-(3-25) with respect to u, v and w, respectively, the stiffness coefficients of the cable system are obtained:

$$K_x = \frac{\partial N_x}{\partial u}, \quad K_y = \frac{\partial N_y}{\partial v}, \quad K_z = \frac{\partial N_z}{\partial w} \quad (3-26)$$

and the three corresponding natural frequencies of the system, dependent on the displacements u, v and w, are:

$$\omega_x = \sqrt{\frac{K_x}{M}}, \quad \omega_y = \sqrt{\frac{K_y}{M}}, \quad \omega_z = \sqrt{\frac{K_z}{M}} \quad (3-27)$$

The frequencies ω_x and ω_y refer to a horizontal vibration of the central node with respect to x and y axes, while the ω_z frequency refers to a vertical vibration of the central node. Considering zero displacement ($u=v=w=0$) for the unforced and undeformed state, the stiffness coefficients at the prestressed equilibrium states are:

$$K_{x0} = \frac{4 \cdot (EAL^2 + 2N_0L^2 + 8N_0f^2)}{\sqrt{(L^2 + 4f^2)^3}} = \frac{4EA}{L} \cdot \frac{\left(1 + 2\frac{N_0}{EA} + 8\frac{N_0f^2}{EA L^2}\right)}{\sqrt{\left(1 + 4\frac{f^2}{L^2}\right)^3}} \quad (3-28)$$

$$K_{y0} = \frac{4 \cdot (EAL^2 + 2N_0L^2 + 8N_0f^2)}{\sqrt{(L^2 + 4f^2)^3}} = \frac{4EA}{L} \cdot \frac{\left(1 + 2\frac{N_0}{EA} + 8\frac{N_0}{EA} \frac{f^2}{L^2}\right)}{\sqrt{\left(1 + 4\frac{f^2}{L^2}\right)^3}} = K_{x0} \quad (3-29)$$

$$K_{z0} = \frac{4 \cdot (8EAf^2 + 2N_0L^2 + 8N_0f^2)}{\sqrt{(L^2 + 4f^2)^3}} = \frac{4EA}{L} \cdot \frac{\left(8\frac{f^2}{L^2} + 2\frac{N_0}{EA} + 8\frac{N_0}{EA} \frac{f^2}{L^2}\right)}{\sqrt{\left(1 + 4\frac{f^2}{L^2}\right)^3}} \quad (3-30)$$

while the three corresponding natural frequencies of the system can be expressed by:

$$\omega_{x0} = \omega_{y0} = \sqrt{\frac{K_{x0}}{M}} = \sqrt{\frac{K_{y0}}{M}} = \sqrt{\frac{4EA}{ML} \cdot \frac{\left(1 + 2\frac{N_0}{EA} + 8\frac{N_0}{EA} \frac{f^2}{L^2}\right)}{\sqrt{\left(1 + 4\frac{f^2}{L^2}\right)^3}}} \quad (3-31)$$

$$\omega_{z0} = \sqrt{\frac{K_{z0}}{M}} = \sqrt{\frac{4EA}{ML} \cdot \frac{\left(8\frac{f^2}{L^2} + 2\frac{N_0}{EA} + 8\frac{N_0}{EA} \frac{f^2}{L^2}\right)}{\sqrt{\left(1 + 4\frac{f^2}{L^2}\right)^3}}} \quad (3-32)$$

which are exactly the same as the ones reported by Leonard [3-17] for the same cable system.

In [3-17] and in chapter 2 the stiffness coefficient of a simple cable is provided, in the prestressed configuration due to a load P , applied at middle span and causing a deflection z :

$$K(z) = \frac{4AE}{L} \left(\frac{L}{S_0} - \frac{1}{\sqrt{\left(1 + 4\frac{z_1^2}{L^2}\right)^3}} \right) = \frac{4EA}{L} \cdot \frac{\left(4\frac{z_1^2}{L^2} + \frac{N_0}{EA} + 4\frac{N_0}{EA} \frac{z_1^2}{L^2}\right)}{\sqrt{\left(1 + 4\frac{z_1^2}{L^2}\right)^3}} \quad (3-33)$$

where

$$S_0 = \frac{2\sqrt{\left(\frac{L}{2}\right)^2 + z_1^2}}{\left(1 + \frac{N_0}{AE}\right)} \quad (3-34)$$

Comparing the stiffness coefficient K_{z0} of Eq. (3-30) with the one of Eq. (3-33), it is noted that for $z_1=f$ the second cable of the cable net doubles the stiffness of the system. Thus, the cable net is stiffer than a simple cable with the same geometry and the same mechanical characteristics. This is an additional effect of the stabilising cable, besides offering stiffness for both upward and downward

loads and enabling pretension. As the cable net deforms, one of its cables becomes stiffer and the other softer. If one of the two cables becomes slack, its stiffness vanishes and the cable net response becomes similar to the one of a simple cable.

Assuming instead large displacements and large strains, the stiffness coefficients of the cable system at the prestressed, unforced and undeformed equilibrium state are:

$$K_{x0} = K_{y0} = \frac{4 \cdot (EAL^2 + 3N_0L^2 + 8N_0f^2)}{\sqrt{(L^2 + 4f^2)^3}} = \frac{4EA}{L} \cdot \frac{\left(1 + 3\frac{N_0}{EA} + 8\frac{N_0}{EA} \frac{f^2}{L^2}\right)}{\sqrt{\left(1 + 4\frac{f^2}{L^2}\right)^3}} \quad (3-35)$$

$$K_{z0} = \frac{4 \cdot (8EAf^2 + 2N_0L^2 + 16N_0f^2)}{\sqrt{(L^2 + 4f^2)^3}} = \frac{4EA}{L} \cdot \frac{\left(8\frac{f^2}{L^2} + 2\frac{N_0}{EA} + 16\frac{N_0}{EA} \frac{f^2}{L^2}\right)}{\sqrt{\left(1 + 4\frac{f^2}{L^2}\right)^3}} \quad (3-36)$$

and the three corresponding natural frequencies of the system:

$$\omega_{x0} = \omega_{y0} = \sqrt{\frac{K_{x0}}{M}} = \sqrt{\frac{K_{y0}}{M}} = \sqrt{\frac{4EA}{ML} \cdot \frac{\left(1 + 3\frac{N_0}{EA} + 8\frac{N_0}{EA} \frac{f^2}{L^2}\right)}{\sqrt{\left(1 + 4\frac{f^2}{L^2}\right)^3}}} \quad (3-37)$$

$$\omega_{z0} = \sqrt{\frac{K_{z0}}{M}} = \sqrt{\frac{4EA}{ML} \cdot \frac{\left(8\frac{f^2}{L^2} + 2\frac{N_0}{EA} + 16\frac{N_0}{EA} \frac{f^2}{L^2}\right)}{\sqrt{\left(1 + 4\frac{f^2}{L^2}\right)^3}}} \quad (3-38)$$

The corresponding eigenvectors are:

$$V_x = \begin{bmatrix} 1 \\ 0 \\ 0 \end{bmatrix}, V_y = \begin{bmatrix} 0 \\ 1 \\ 0 \end{bmatrix}, V_z = \begin{bmatrix} 0 \\ 0 \\ 1 \end{bmatrix} \quad (3-39)$$

For common levels of initial cable stress, at about 20% of the yield stress and for modulus of elasticity 165GPa, which is a common value for materials used in such structures, the difference between the two assumptions arises at maximum 0.09% for all three eigenfrequencies, independently of the sag-to-span ratio, as illustrated in Figure 3-3. The difference is small if a sag-to-span ratio equal to $f/L=1/20$ is assumed, for initial cable stress varying between 10% and 35% of the yield stress, as shown in Figure 3-4. Thus, computing the eigenfrequencies with the assumption of small strains, gives results that are considered as sufficiently accurate for all practical purposes.

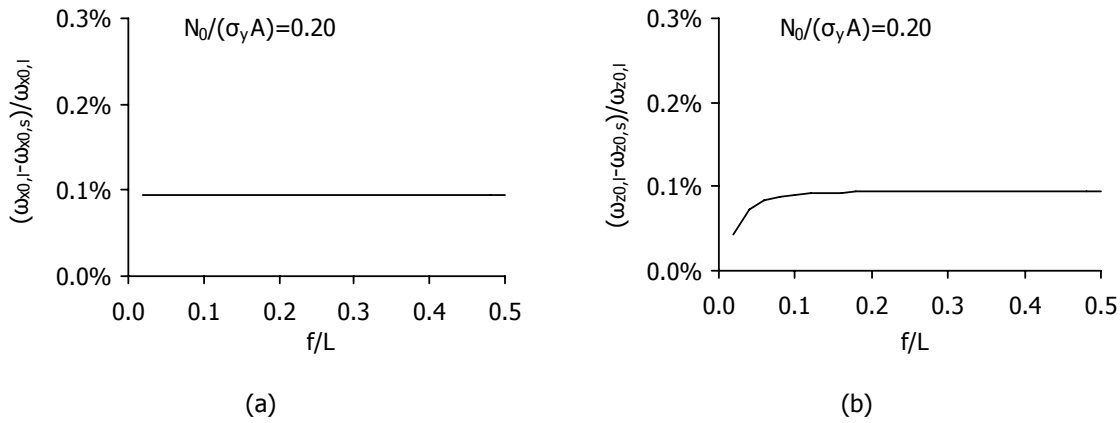


Figure 3-3: Difference of eigenfrequencies: (a) ω_{x0} and ω_{y0} , (b) ω_{z0} , for initial cable stress 20% of the yield stress (s: small strains, l: large strains)

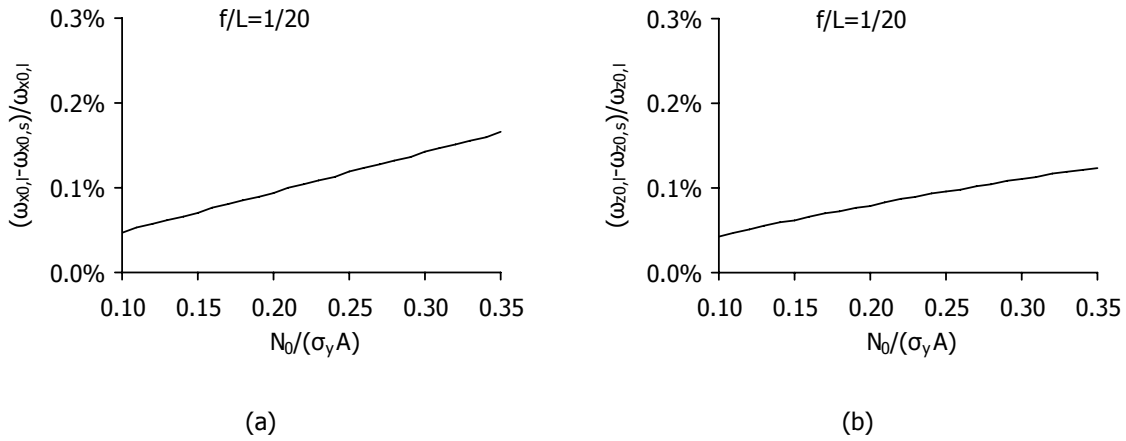


Figure 3-4: Difference of eigenfrequencies: (a) ω_{x0} and ω_{y0} , (b) ω_{z0} , for sag-to-span ratio $f/L=1/20$ (s: small strains, l: large strains)

In both cases, if $L^2=8f^2$, then $\omega_{x0}=\omega_{y0}=\omega_{z0}$, which means that a crossover between the three vibration modes occurs. Crossover points occur when two or more eigenfrequencies with different modal shapes are equal. Cable structures are characterised by such crossover points [3-28]. For $L^2<8f^2$, $K_{x0,y0}<K_{z0}$ and $\omega_{x0,y0}<\omega_{z0}$, meaning that the first vibration modes of the cable net are defined by the horizontal motion of the central node, regarding the x and y axes. For $L^2>8f^2$ instead, $K_{x0,y0}>K_{z0}$ and $\omega_{x0,y0}>\omega_{z0}$, meaning that the first vibration mode of the cable net is defined by the vertical motion of the central node. The variation of the ratio $K_{x0,y0}/K_{z0}$ with respect to the sag-to-span ratio, considering large and small displacements, is plotted in Figure 3-5, for Young modulus $E=165\text{GPa}$, yield stress $\sigma_y=1570\text{MPa}$, considering one of the most common categories of cable steel St 1570/1770. The pretension is equal to 20% of the yield stress. In this chart, it is shown that independently of the f/L ratio, the difference between the two assumptions of large or small strains is negligible. It is also noted, that the coefficients K_{x0} and K_{y0} become larger than K_{z0} , as the sag-to-span ratio becomes smaller than $1/\sqrt{8}=0.354$, which would never be the case for an actual cable net.

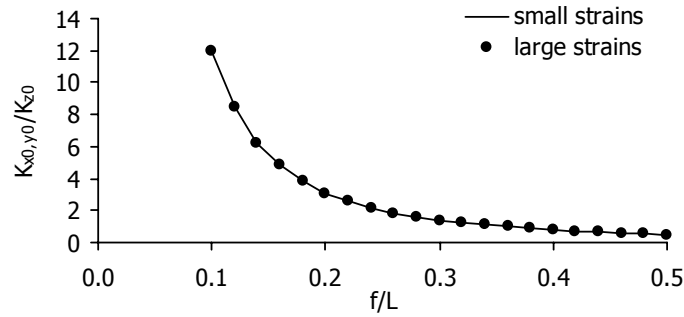


Figure 3-5: Variation of the ratio $K_{x_0,y_0}/K_{z_0}$ with respect to the sag-to-span ratio f/L

In Figure 3-6 the variation of the ratio $K_{x_0,y_0}/K_{z_0}$ with respect to the level of pretension is illustrated, considering large and small displacements, for Young modulus $E=165\text{GPa}$, yield stress $\sigma_y=1570\text{MPa}$ and sag-to-span ratio equal to 0.2 and a level of initial stress between 10% and 35% of the yield stress. The level of pretension does not change significantly the ratio of the stiffness coefficients, while the difference between the two assumptions is again negligible.

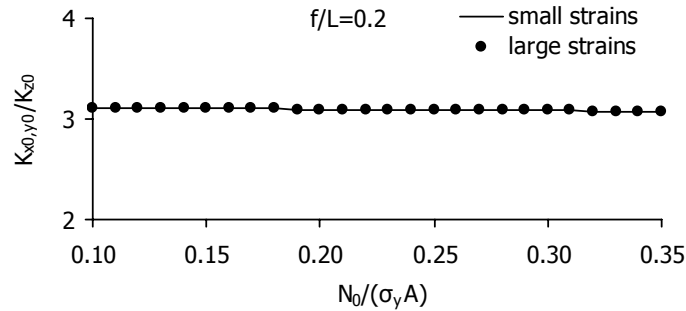


Figure 3-6: Variation of the ratio $K_{x_0,y_0}/K_{z_0}$ with respect to the pretension level

3.2.4 Equations of static equilibrium

The equilibrium for static loads is described by the following equations:

$$N_x = N_{1x} - N_{2x} + N_{3x} - N_{4x} = P_x \quad (3-40)$$

$$N_y = N_{1y} - N_{2y} + N_{3y} - N_{4y} = P_y \quad (3-41)$$

$$N_z = N_{1z} - N_{2z} + N_{3z} - N_{4z} = P_z \quad (3-42)$$

where P_x , P_y and P_z are the three components of the external static load, applied on the central node, with respect to the global axes.

The maximum permissible deflection, caused by a vertical load exerted on the central node, can be defined with respect to the maximum allowable stress of the cables, which is considered equal to the yield stress σ_y . According to Hooke's law, at the ultimate stage, the cable stress is expressed as:

$$\sigma_y = E \left(\frac{S_i - S_0}{S_0} \right), \quad i=1,2,3,4 \quad (3-43)$$

Substituting the initial length of the cable segments, expressed by Eq. (3-3), taking into account Eq. (3-2), Eq. (3-43) becomes:

$$S_i = \frac{\frac{\sigma_y}{E} + 1}{1 + \frac{N_0}{EA}} \cdot \sqrt{(L/2)^2 + f^2}, \quad i=1,2,3,4 \quad (3-44)$$

Substituting the deformed lengths of the cables, defined by Eqs. (3-5)-(3-8), Eq. (3-44) becomes:

$$\begin{aligned} (L/2)^2 + (f \pm w)^2 &= \frac{\left(\frac{\sigma_y}{E} + 1\right)^2}{\left(1 + \frac{N_0}{EA}\right)^2} \cdot [(L/2)^2 + f^2] \Rightarrow \\ w^2 \pm 2fw &= \frac{\left(\frac{\sigma_y}{E} + 1\right)^2}{\left(1 + \frac{N_0}{EA}\right)^2} \cdot [(L/2)^2 + f^2] - [(L/2)^2 + f^2] \end{aligned} \quad (3-45)$$

The four solutions of Eq. (3-45) are:

$$w = \pm f \pm \sqrt{f^2 - Q} \quad (3-46)$$

where

$$Q = \left[1 - \frac{\left(\frac{\sigma_y}{E} + 1\right)^2}{\left(1 + \frac{N_0}{EA}\right)^2} \right] \cdot [(L/2)^2 + f^2] \quad (3-47)$$

The minimum absolute values of these four solutions constitute the maximum permissible deflection, which is defined as:

$$|w_{\max}| = \left| f - \sqrt{f^2 - Q} \right| \quad (3-48)$$

The maximum permissible deflection depends on the sag and the span, the yield stress σ_y , the initial pretension in terms of initial strain and the Young modulus E. The diagram of Figure 3-7 shows the variation of the ratio w_{\max}/L with respect to f/L , for yield stress $\sigma_y=1570\text{MPa}$, Young modulus $E=165\text{GPa}$ and initial stress equal to 20% of the yield stress, which are common values for cable nets. For values of the sag-to-span ratio between 1/35 and 1/2, the values of the ratio w_{\max}/L are smaller than 0.05, and as the ratio f/L increases, w_{\max}/L decreases. The maximum load causing the maximum deflection is shown in Figure 3-8, as a ratio of the load over the initial pretension, with respect to the sag-to-span ratio. In this chart an eventual cable slackening is taken into consideration, by setting the stiffness of the slackened cable equal to zero. As the net becomes stiffer and the ratio f/L increases, the maximum permissible load also increases.

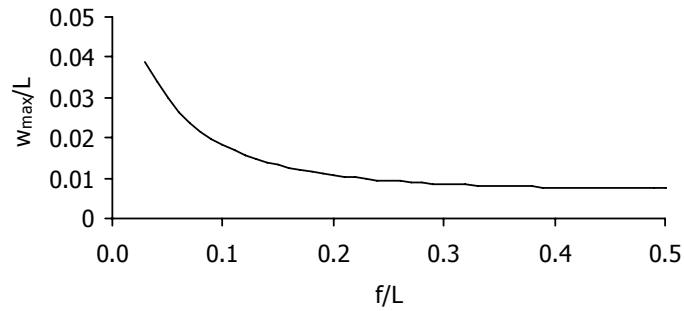
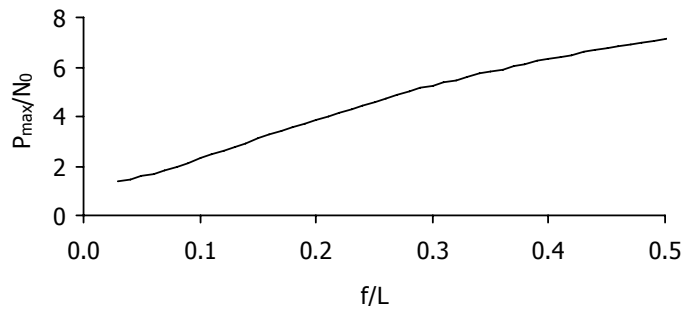


Figure 3-7: Maximum deflection variation with respect to the sag-to-span ratio

Figure 3-8: Variation of the ratio of the maximum static load P_{max} over the initial pretension N_0 , with respect to the sag-to-span ratio

3.2.5 Equations of motion

In case a dynamic load is applied on the central node, the equations of motion of this node for the three directions of the global axes are expressed in the equilibrium state:

$$M\ddot{u} + C\dot{u} + N_x = P_x(t) \Rightarrow M\ddot{u} + C\dot{u} + N_{1x} - N_{2x} + N_{3x} - N_{4x} = P_x(t) \quad (3-49)$$

$$M\ddot{v} + C\dot{v} + N_y = P_y(t) \Rightarrow M\ddot{v} + C\dot{v} + N_{1y} - N_{2y} + N_{3y} - N_{4y} = P_y(t) \quad (3-50)$$

$$M\ddot{w} + C\dot{w} + N_z = P_z(t) \Rightarrow M\ddot{w} + C\dot{w} + N_{1z} - N_{2z} + N_{3z} - N_{4z} = P_z(t) \quad (3-51)$$

where $P_x(t)$, $P_y(t)$ and $P_z(t)$ are the three components of the external dynamic load, varying with time, referring to the global axes. The damping C is a function of the damping ratio ζ , expressed as [3-29]:

$$C = \zeta C_{cr} = 2\zeta M \omega_{z0} \quad (3-52)$$

3.2.6 Numerical example

3.2.6.1. Geometry and prestressing

A numerical example is considered of a cable net consisting of two cables having a diameter $D=10\text{mm}$ and cross-sectional area $A=7.85 \cdot 10^{-5}\text{m}^2$. The span of the cables is $L=50.00\text{m}$ and their sag $f=2.50\text{m}$. The cable material is treated as nonlinear, having no compression branch, and linear elastic tension branch, with Young modulus $E=165000\text{MPa}$ (Figure 3-9a). The initial strain of the cables is $\epsilon_0=0.001$, which is interpreted as an initial pretension $N_0=EA\epsilon_0=12.959\text{kN}$. If a maximum cable stress is taken into account, it is set equal to the yield stress 1570MPa (Figure 3-9b), which corresponds to a strain $\epsilon_{max}=0.0095152$ and a maximum cable tension $N_{max}=123.31\text{kN}$.

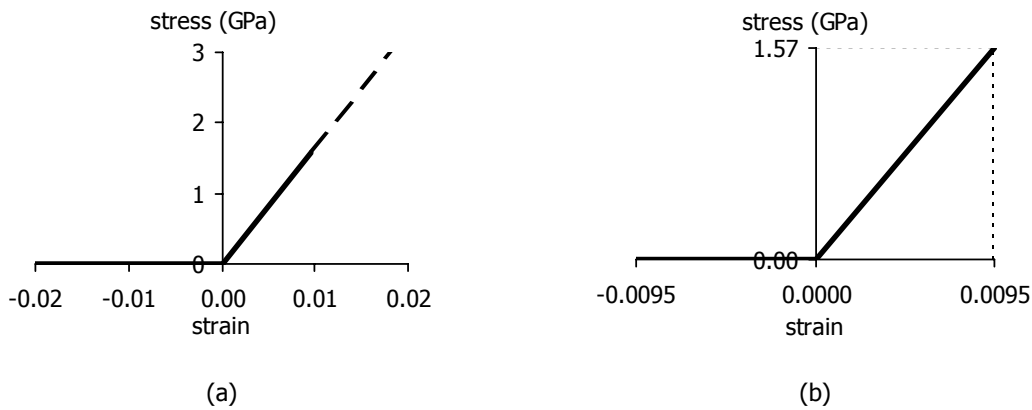


Figure 3-9: Material constitutive law with zero compression branch and: (a) infinitely linear elastic tension branch, (b) linear elastic tension branch limited by the yield stress

3.2.6.2. Static response

A vertical displacement towards +z is enforced at the central node, in steps of 0.05m. The length of each segment at the equilibrium state under pretension is calculated from Eq. (3-2):

$$S_N = \sqrt{(L/2)^2 + f^2} = \sqrt{25^2 + 2.5^2} = 25.12\text{m} \quad (3-53)$$

while the initial length S_0 for all segments, according to Eq. (3-3), is:

$$S_0 = \frac{S_N}{1 + \varepsilon_0} = \frac{25.12}{1 + 0.001} = 25.10\text{m} \quad (3-54)$$

The deformed lengths of the cable segments are obtained by Eqs. (3-5)-(3-8) and the cable tensions by Eq. (3-9). The static load P_z , which counterpoises the imposed deflection w , is calculated from Eq. (3-42), taking into consideration Eqs. (3-11)-(3-22). For a nonlinear material with infinitely elastic tension branch, the load – displacement curve is plotted in Figure 3-10 and the cable tension variation with respect to the central node deflection, in Figure 3-11. The curved diagrams show the intense nonlinearity of the system.

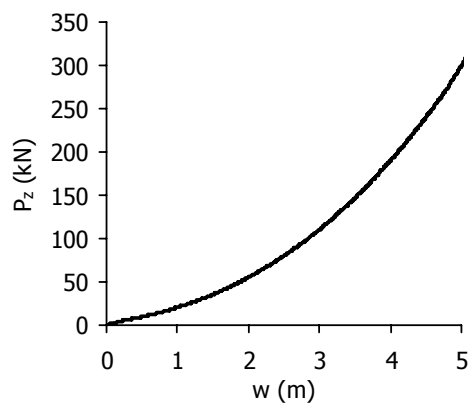


Figure 3-10: Load – displacement curve for nonlinear material with infinitely elastic tension branch

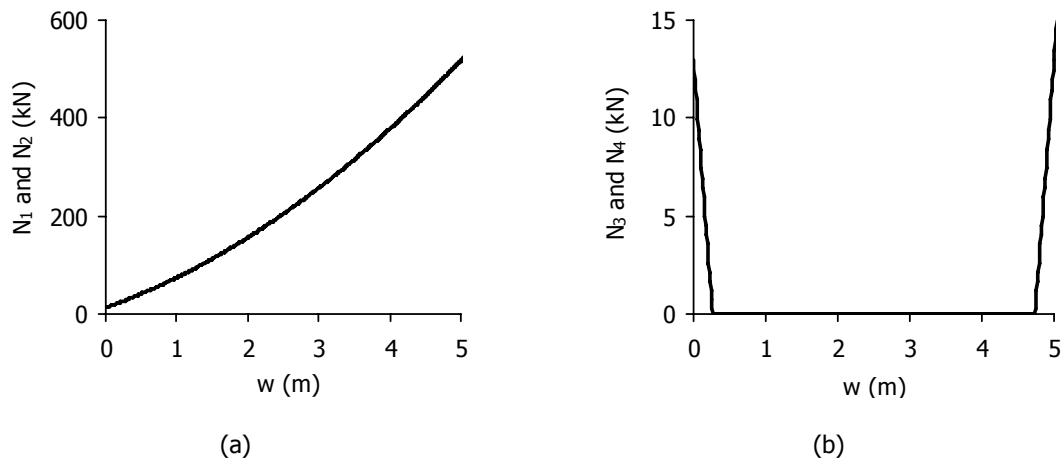


Figure 3-11: Cable tension variation with respect to the central node deflection for nonlinear material with infinitely elastic tension branch: (a) segments 1 and 2, (b) segments 3 and 4

When the vertical displacement becomes equal to $w=0.27\text{m}$, the length of segments 3 and 4 is calculated from Eq. (3-7):

$$S_3 = \sqrt{(L/2)^2 + (f - w)^2} = \sqrt{25^2 + (2.5 - 0.27)^2} = 25.10\text{m} \tag{3-55}$$

which is equal to the initial unstressed length S_0 . This means that, for this imposed vertical displacement, segments 3 and 4 become slack. As the displacement increases, the distance between the central node 1 and nodes 3 and 4 further decreases, until $w=f=2.50\text{m}$ and then it increases again. When $w=4.73\text{m}$ the length of these two segments becomes again equal to S_0 :

$$S_3 = \sqrt{(L/2)^2 + (f - w)^2} = \sqrt{25^2 + (2.5 - 4.73)^2} = 25.10\text{m} \tag{3-56}$$

and as the displacement w continues to increase, tension develops again and the cables stop being slack. The length of segments 1 and 2 always increases as the displacement w increases. The diagrams of the distance between the central node and the anchorages of segments 1 and 3 are illustrated in Figure 3-12.

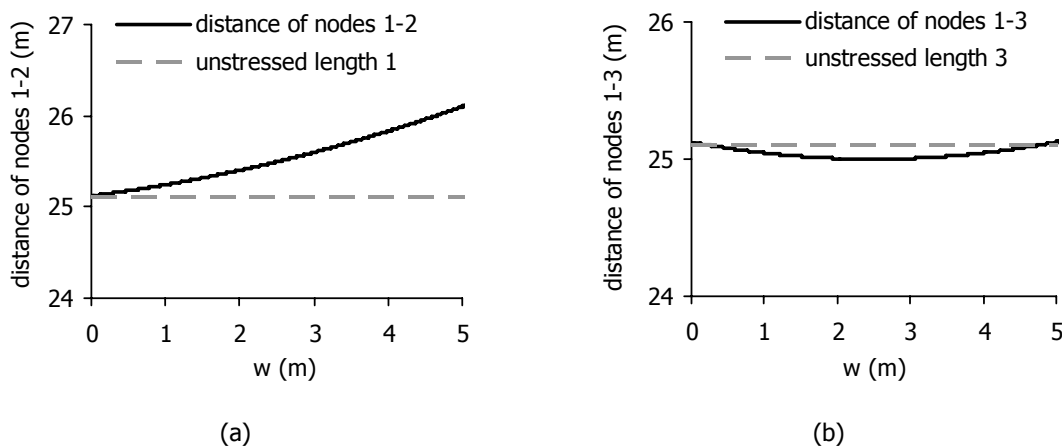


Figure 3-12: Distance between node 1 and (a) node 2, (b) node 3, with respect to the central node deflection for nonlinear material with infinitely elastic tension branch

If a nonlinear material is considered with null compression branch and a limit for tension stress equal to the yield stress, the load – displacement curve is plotted in Figure 3-13 and the cable tension

variation with respect to the central node deflection in Figure 3-14. The change of stiffness, represented by the abrupt change of the slope of the load – displacement curve in Figure 3-13, occurs when the imposed displacement becomes $w=0.27\text{m}$ and cable segments 3 and 4 become slack, as shown in Figure 3-14b. Up to this level of imposed displacement the response appears to be practically linear, while beyond that level it exhibits the well-known nonlinearity of single cables.

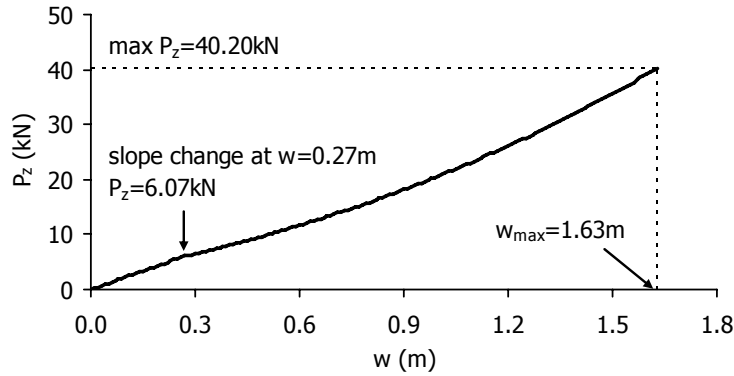


Figure 3-13: Load – displacement curve for nonlinear material with linear elastic tension branch limited by the yield stress

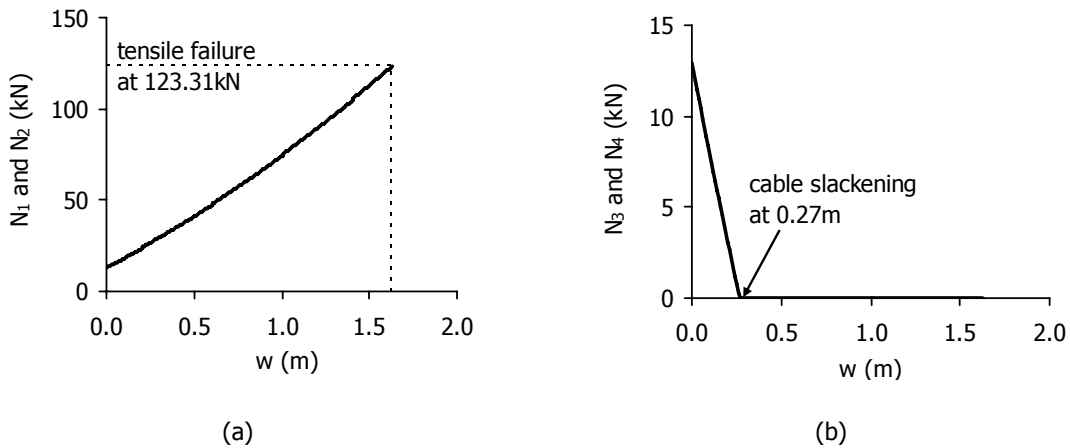


Figure 3-14: Cable tension variation with respect to the central node deflection for nonlinear material with linear elastic tension branch limited by the yield stress: (a) segments 1 and 2, (b) segments 3 and 4

The behaviour of the system is the same as described before, until the imposed displacement becomes $w=1.63\text{m}$, which corresponds to a static load $P_0=40.20\text{kN}$. Then, the stress of segments 1 and 2 becomes equal to the yield stress, a limit which represents the maximum allowable cable stress, causing failure of the cables. The tension of these cable segments is equal to the maximum tension $N_{\text{max}}=123.31\text{kN}$, while cable segments 3 and 4 are slack at the end of the calculation. The maximum allowable displacement is also verified by Eq. (3-48), using Eq. (3-47):

$$Q = \left[1 - \frac{\left(\frac{\sigma_y}{E} + 1 \right)^2}{\left(1 + \frac{N_0}{EA} \right)^2} \right] \cdot \left[(L/2)^2 + f^2 \right] = -10.79\text{m}^2 \tag{3-57}$$

$$|w_{\max}| = \left| f - \sqrt{f^2 - Q} \right| = \left| 2.5 - \sqrt{2.5^2 + 10.79} \right| = 1.63\text{m} \quad (3-58)$$

3.2.6.3. Eigenfrequencies

The distributed mass of the cables is considered equal to $m=7.85\text{kN}\cdot\text{sec}^2\cdot\text{m}^{-4}$, while an additional concentrated mass is applied on the central node, equal to $M_c=0.1\text{t}=0.1\text{kN}\cdot\text{sec}^2\cdot\text{m}^{-1}$. The masses are considered as lumped, so that the total mass at the central node is equal to $M=m\cdot 4S_0/2\cdot A+M_c=0.131\text{kN}\cdot\text{sec}^2\cdot\text{m}^{-1}$. Assuming large displacements and small strains, the stiffness coefficients are obtained by Eqs. (3-28)-(3-30):

$$K_{x0} = K_{y0} = \frac{4EA}{L} \cdot \frac{\left(1 + 2 \frac{N_0}{EA} + 8 \frac{N_0}{EA} \frac{f^2}{L^2} \right)}{\sqrt{\left(1 + 4 \frac{f^2}{L^2} \right)^3}} = 1023.43\text{kN/m}$$

$$K_{z0} = \frac{4EA}{L} \cdot \frac{\left(8 \frac{f^2}{L^2} + 2 \frac{N_0}{EA} + 8 \frac{N_0}{EA} \frac{f^2}{L^2} \right)}{\sqrt{\left(1 + 4 \frac{f^2}{L^2} \right)^3}} = 22.49\text{kN/m}$$

and the corresponding natural frequencies, at the prestressed, unforced and undeformed equilibrium state from Eqs. (3-31) and (3-32):

$$\omega_{x0} = \omega_{y0} = \sqrt{\frac{K_{x0}}{M}} = \sqrt{\frac{K_{y0}}{M}} = \sqrt{\frac{1023.43}{0.131}} \text{sec}^{-1} = 88.39 \text{sec}^{-1}$$

$$\omega_{z0} = \sqrt{\frac{K_{z0}}{M}} = \sqrt{\frac{22.49}{0.131}} \text{sec}^{-1} = 13.10 \text{sec}^{-1}$$

while, assuming large displacements and large strains, the stiffness coefficients are calculated according to Eqs. (3-35) and (3-36):

$$K_{x0} = K_{y0} = \frac{4EA}{L} \cdot \frac{\left(1 + 3 \frac{N_0}{EA} + 8 \frac{N_0}{EA} \frac{f^2}{L^2} \right)}{\sqrt{\left(1 + 4 \frac{f^2}{L^2} \right)^3}} = 1024.45\text{kN/m}$$

$$K_{z0} = \frac{4EA}{L} \cdot \frac{\left(8 \frac{f^2}{L^2} + 2 \frac{N_0}{EA} + 16 \frac{N_0}{EA} \frac{f^2}{L^2} \right)}{\sqrt{\left(1 + 4 \frac{f^2}{L^2} \right)^3}} = 22.51\text{kN/m}$$

and the corresponding natural frequencies:

$$\omega_{x0} = \omega_{y0} = \sqrt{\frac{K_{x0}}{M}} = \sqrt{\frac{K_{y0}}{M}} = \sqrt{\frac{1024.45}{0.131}} \text{ sec}^{-1} = 88.44 \text{ sec}^{-1}$$

$$\omega_{z0} = \sqrt{\frac{K_{z0}}{M}} = \sqrt{\frac{22.51}{0.131}} \text{ sec}^{-1} = 13.11 \text{ sec}^{-1}$$

The difference between the two approaches of both stiffness coefficients and frequencies calculation is insignificant. The variation of the natural frequency ω_z , calculated from Eq. (3-27), taking into account Eq. (3-26), is plotted in Figure 3-15, in which it is evident that the increase of the deflection results in increase of the stiffness and consequently the natural frequency. When the system exhibits the maximum deflection $w_{\max}=1.63\text{m}$, the natural frequency is $\omega_z=16.27\text{sec}^{-1}$, being 24% larger than the natural frequency at the unforced and undeformed state, $\omega_{z0}=13.10\text{sec}^{-1}$.

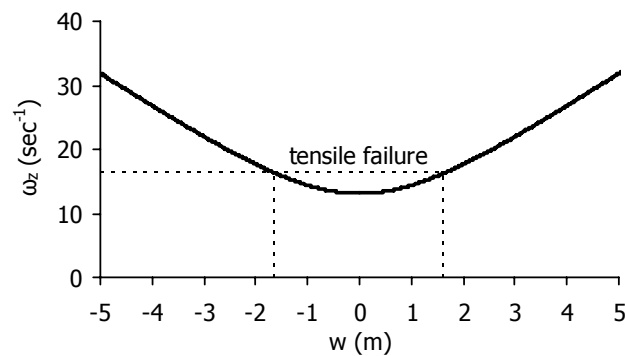


Figure 3-15: Variation of the natural frequency with respect to the deflection

3.2.6.4. Dynamic response

In order to investigate the dynamic response of the system, the equation of motion is solved using the program MATLAB [3-30]. This program allows the user to solve many technical computing problems, especially those with matrix and vector formulations. Typical uses include math and computation, algorithm development, data acquisition, modelling, simulation, and prototyping, data analysis, exploration, and visualisation, scientific and engineering graphics, application development including graphical user interface building. With this program the time-history response of the system is calculated, solving numerically the analytical equations of motion. In order to solve numerically ordinary differential equations, it employs the Runge-Kutta integration method [3-31].

Firstly, an undamped system is analysed, in order to detect large-scale oscillations for different loading frequencies. The cable material is treated as nonlinear with linear elastic tension branch limited by the yield stress and zero compression branch. A harmonic load is applied on the central node, equal to $P_z=P_0 \cdot \cos \Omega t$. The loading frequency is chosen to be equal to $\Omega=\omega_{z0}=13.10\text{sec}^{-1}$ (2.08Hz), aiming at fundamental resonance phenomena, while the load amplitude is $P_0=1.30\text{kN}$, which, after several trials, is proved to be the minimum load causing failure of the cables. The time-history diagrams of the central node deflection and the tension of cable segment 3, which arrives first at failure, are illustrated in Figure 3-16.

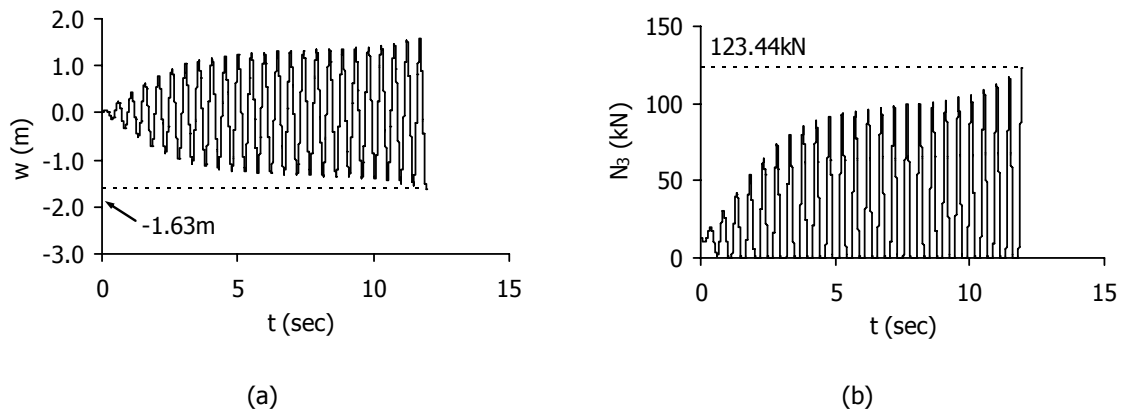


Figure 3-16: Fundamental resonance with $P_z=(1.30\text{kN})\cos(\omega_{z0}t)$. Time-history diagrams of (a) the central node vertical displacement, (b) the tension of cable segment 3

The failure occurs at time 11.926sec and the analysis stops. At that time, the displacement at the central node is 1.63m, equal to the maximum allowable deflection. The tension developed in cable segments 3 and 4 is 123.44kN, which is slightly larger than the permissible tension, exceeding thus the yield stress threshold and causing the termination of the analysis. The phase plane plot and the response spectrum of the central node deflection are plotted in Figure 3-17. In these charts, it is noted that the maximum (absolute) velocity of the central node is 21.11m/sec, while the main frequency of the oscillation is equal to the loading frequency, being also the frequency of the system.

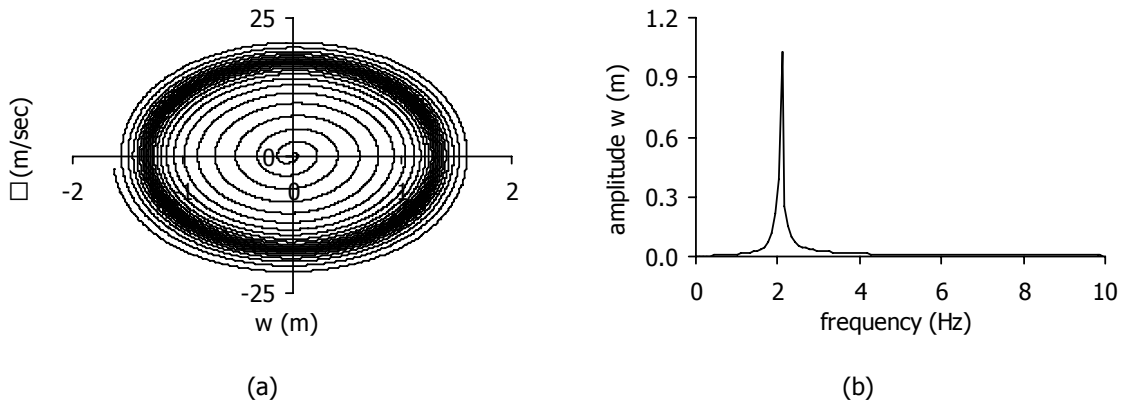


Figure 3-17: Fundamental resonance with $P_z=(1.30\text{kN})\cos(\omega_{z0}t)$, (a) phase plane plot of the central node motion, (b) deflection response spectrum of the central node

The ratio of the maximum velocity over the maximum deflection, compared with the natural frequency and the loading frequency, is:

$$\frac{\dot{w}_{\max}}{w_{\max}} = \frac{21.11\text{ m/sec}}{1.63\text{ m}} = 12.95\text{ sec}^{-1} = 0.99\omega_{z0} \approx \Omega \quad (3-59)$$

This information will be used in the next section.

Comparing the dynamic response of the cable net with the static one, analysed in section 3.2.6.2, it is worth mentioning that the static load causing failure of the cables is 40.20kN, while the dynamic one is only 1.30kN. Hence, the maximum dynamic load that this cable net can sustain is thirty times smaller than the static one. Nevertheless, in nonlinear systems, the maximum steady-state response occurs for $\Omega=\omega+\sigma$, where ω is the eigenfrequency and σ is a non-zero frequency detuning. In order

to find numerically which frequency detuning causes the maximum response, a parametric analysis is required, changing the frequency of the load by small steps.

Next, a loading frequency $\Omega = \omega_{z0}/3 = 4.37 \text{sec}^{-1}$ (0.69Hz) is selected, aiming at superharmonic resonant conditions. The amplitude of the dynamic load that is proved to cause cable failure in this case is equal to $P_0 = 19.97 \text{kN}$, which is half of the static one. The time-history diagrams of the central node deflection and the tension of cable segment 1, which arrives at failure, are plotted in Figure 3-18. Failure occurs at time 1.631sec and the analysis stops. At that time, the displacement at the central node is 1.63m, while the tension of cable segments 1 and 2 is 123.32kN, almost equal to the permissible tension. The phase plane plot and the response spectrum of the central node deflection are illustrated in Figure 3-19. The central node oscillates with two dominant frequencies, one equal to 0.61Hz, being close to the loading frequency and one equal to 1.84Hz, which is close to the system's frequency.

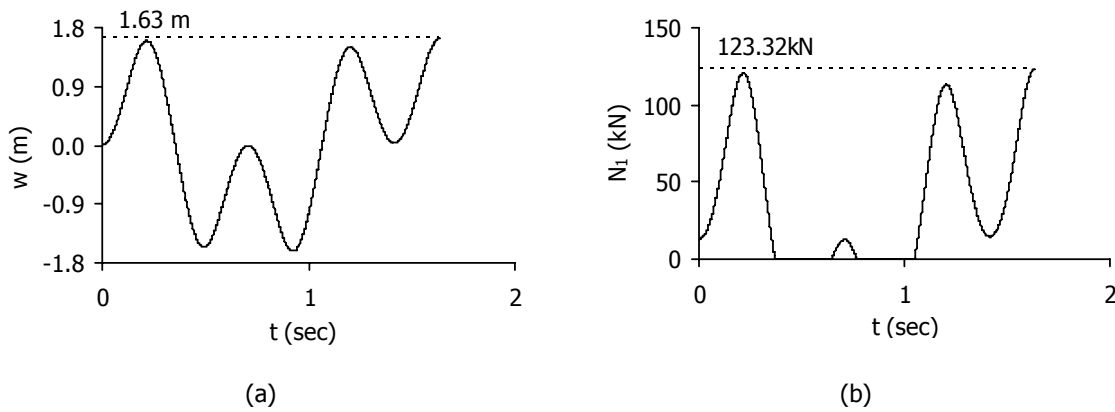


Figure 3-18: Superharmonic resonance with $P_z = (19.97 \text{kN}) \cos(0.33 \omega_{z0} t)$. Time-history diagrams of (a) the central node vertical displacement, (b) the tension of cable segment 1

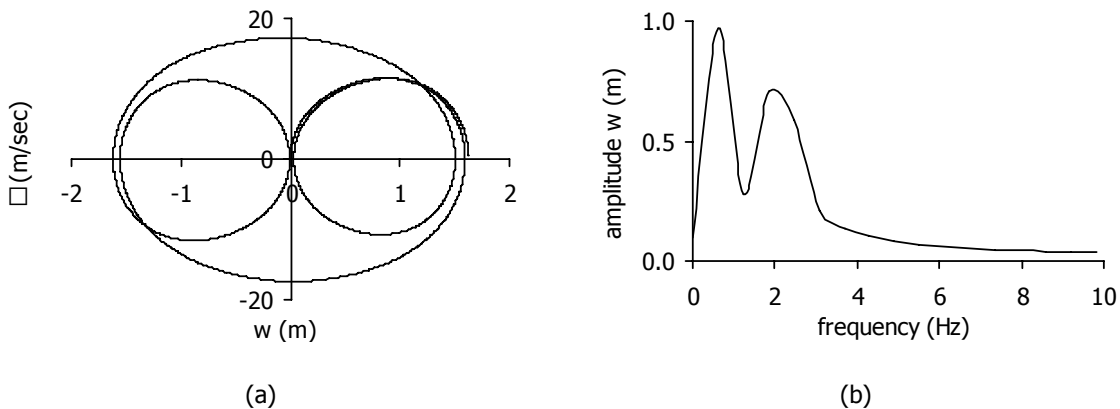


Figure 3-19: Superharmonic resonance with $P_z = (19.97 \text{kN}) \cos(0.33 \omega_{z0} t)$, (a) phase plane plot of the central node motion, (b) deflection response spectrum of the central node

In this case, the maximum (absolute) velocity of the central node is 17.23m/sec. The ratio of the maximum velocity over the maximum deflection, compared with the natural frequency and the loading frequency, is:

$$\frac{\dot{w}_{\max}}{w_{\max}} = \frac{17.23 \text{m/sec}}{1.63 \text{m}} = 10.57 \text{sec}^{-1} = 0.80 \omega_{z0} \approx 2.40 \Omega \tag{3-60}$$

Subsequently, aiming at subharmonic resonance, the loading frequency is chosen equal to $\Omega=3\omega_{z0}=39.30\text{sec}^{-1}$ (6.25Hz). The amplitude of the dynamic load equals to the maximum static one, $P_0=40.20\text{kN}$, without causing cable failure. The time-history diagrams of the central node deflection and the tension of cable segment 1 are plotted in Figure 3-20. The phase plane plot and the response spectrum of the central node deflection are illustrated in Figure 3-21. In this case, the maximum (absolute) velocity of the central node is 11.62m/sec and the maximum deflection is 0.36m. The ratio of the maximum velocity over the maximum deflection, compared with the natural frequency and the loading frequency, is:

$$\frac{\dot{w}_{\max}}{w_{\max}} = \frac{11.62\text{m/sec}}{0.36\text{m}} = 32.30\text{sec}^{-1} = 2.46\omega_{z0} = 0.82\Omega \quad (3-61)$$

The central node oscillates with a frequency (6.25Hz) equal to the loading frequency and another one (2.05Hz), very close to the system's frequency.

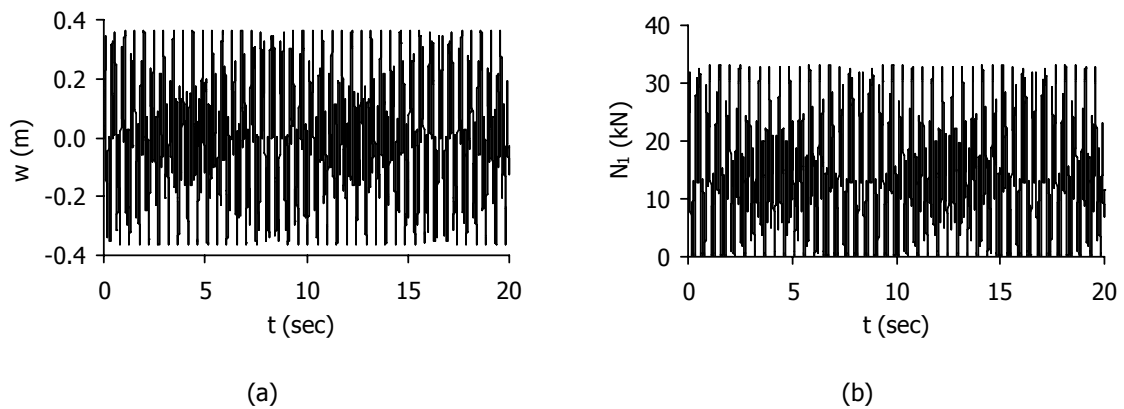


Figure 3-20: Subharmonic resonance with $P_z=(40.20\text{kN})\cos(3\omega_{z0}t)$. Time-history diagrams of (a) the central node vertical displacement, (b) the tension of cable segment 1

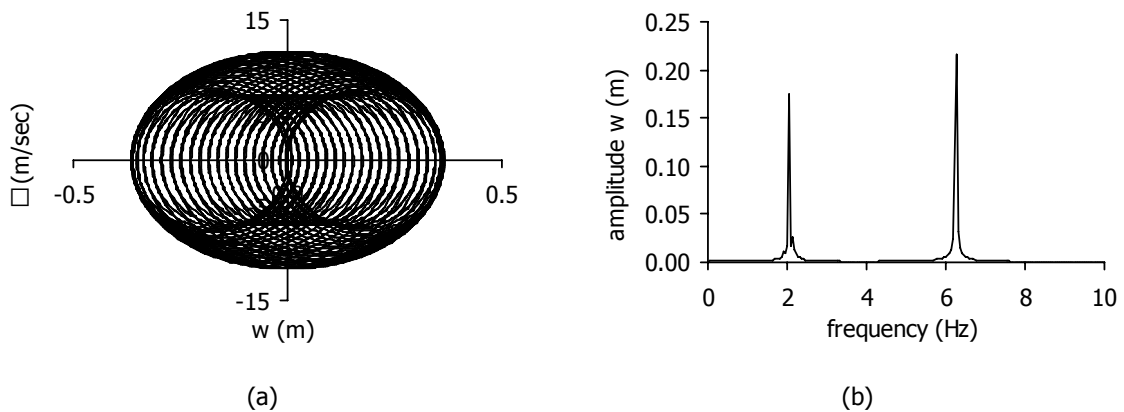


Figure 3-21: Subharmonic resonance with $P_z=(40.20\text{kN})\cos(3\omega_{z0}t)$, (a) phase plane plot of the central node motion, (b) deflection response spectrum of the central node

In these last two cases, although the loading frequency is away from the natural frequency, the eigenmode is activated, due to the relation between these two frequencies. Hence, the system vibrates not only with the loading frequency but also with the natural frequency, but this information is not sufficient to confirm the superharmonic and subharmonic resonances. Occurrence of these nonlinear resonances signifies large oscillation amplitudes, even though the loading frequency is away from the eigenfrequency of the system, as well as sudden changes of the response amplitude for small changes of the loading frequency. Especially in case of subharmonic resonance, the initial

conditions play an important role along with the frequency detuning for specific load amplitude and damping ratio. In order to include these parameters and to detect nonlinear phenomena, a damped system is analysed next. The cable material is now assumed to be nonlinear with infinitely elastic tension branch and zero compression branch, in order to detect nonlinear phenomena without cable tensile failure, which leads to the analysis termination. A vertical dynamic load is applied on the central node described as $P=P_0 \cdot \cos \Omega t$. Two damping ratios are chosen, equal to $\zeta=0.5\%$, being a common value for simple cables [3-28] and $\zeta=2\%$, corresponding to the damping ratio for cable nets [3-32]. The steady-state deflection w_{ss} is calculated for a wide range of loading frequencies and the response diagrams are plotted, either for zero initial conditions, or for initial deflection 1m and velocity 20m/sec. The parameter R_d is defined as the ratio of the steady-state deflection w_{ss} , over the static one w_{st} :

$$R_d = \frac{w_{ss}}{w_{st}} \quad (3-62)$$

Firstly, the parameter R_d is calculated for values of frequency ratio (Ω/ω_{z0}) between 0.80 and 1.20 increasing in steps of 0.01. A load amplitude equal to $P_0=1\text{kN}$ is considered, which applied statically causes a deflection $w_{st}=0.045\text{m}$. The variation of the parameter R_d with respect to the frequency ratio is shown in Figure 3-22. The maximum value of the ratio R_d for damping ratio $\zeta=0.5\%$ is 50.876 occurring for $\Omega/\omega_{z0}=1.09$, while for $\zeta=2\%$ and $\Omega/\omega_{z0}=0.96$ R_d becomes equal to 26.067, thus indicating the importance of the dynamic nature of the response. The bending of the response curve is noted as the frequency ratio increases, resulting in a sudden decrease of the steady-state response amplitude, named as jump phenomenon. Moreover, for frequency ratios close to 1 two responses are observed, one with small deflection amplitude, for zero initial conditions, and one with large amplitude which is obtained taking into account the initial deflection and velocity. The dependence of the response of the system on the initial conditions and the jump of the oscillation amplitude are phenomena that occur only in nonlinear systems.

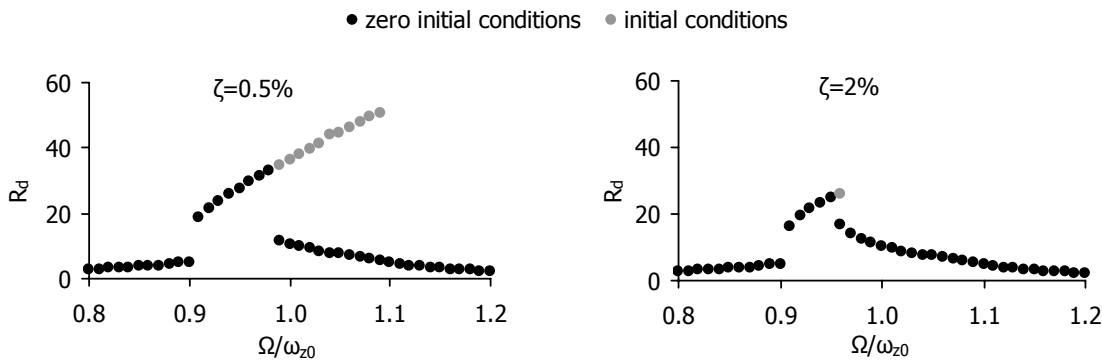


Figure 3-22: Steady-state deflection under fundamental resonance for $P_0=1\text{kN}$

For frequency ratios (Ω/ω_{z0}) between 0.25 and 0.60 the load amplitude is assumed to be equal to $P_0=5\text{kN}$, which, applied as a static load, causes a deflection equal to $w_{st}=0.022\text{m}$. The variation of R_d with respect to the ratio (Ω/ω_{z0}) is illustrated in Figure 3-23 for both values of damping ratio. Considering $\zeta=0.5\%$, three peaks are observed, for frequency ratios 0.32, 0.48 and 0.56, while for $\zeta=2\%$, only one peak of the response is noted for frequency ratio 0.48. These peaks of the response diagram, for loading frequencies smaller than the natural frequency of the system, appear only in nonlinear systems and indicate the occurrence of superharmonic resonances. As the damping decreases, superharmonic resonances occur for more frequency ratios. On the other hand, for frequency ratios away of the aforementioned values, the response amplitude of the central node does

not depend on the damping ratio. In this case, the initial conditions do not influence the steady-state response of the net.

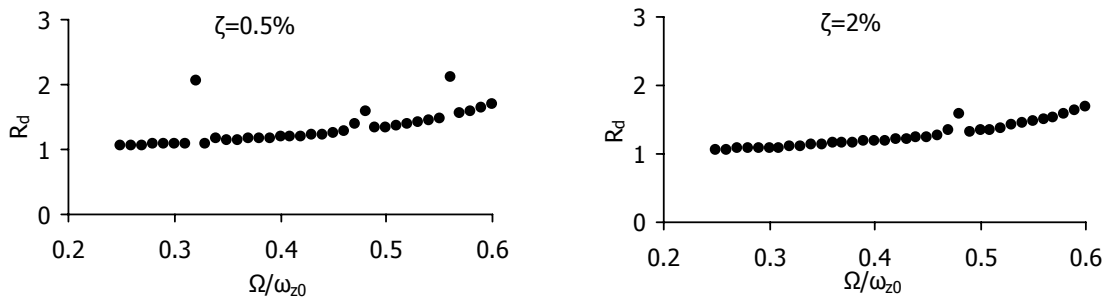


Figure 3-23: Steady-state deflection under superharmonic resonance for $P_0=5\text{kN}$

For a loading amplitude equal to $P_0=15\text{kN}$ and a frequency ratio varying between 2.80 and 3.50, the corresponding response diagrams are illustrated in Figure 3-24. For this load, the static deflection is $w_{st}=0.76\text{m}$. If zero initial conditions are considered, the oscillation amplitudes are very small for both damping ratios. If the initial deflection and velocity are taken into consideration, large amplitudes are noted for damping ratio $\zeta=0.5\%$ and for frequency ratios close to 3. This means that subharmonic resonance phenomena take place during the vibration of the cable net, resulting in sudden increase of the deflection, delineating the intense nonlinear dynamic behaviour of the cable net.

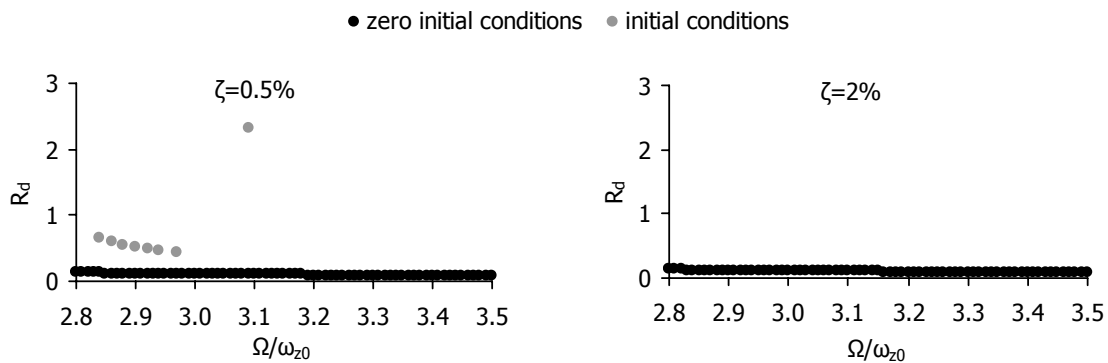


Figure 3-24: Steady-state deflection under subharmonic resonance for $P_0=15\text{kN}$

It should be mentioned that subharmonic resonances occur for a specific load frequency, load amplitude and initial conditions. A small change of the load frequency results in smaller oscillation amplitudes than the ones corresponding to the nonlinear phenomena. Finding the exact loading frequency for which the system exhibits the maximum response amplitude under fundamental, superharmonic, or subharmonic resonance, requires a parametric analysis, for different load amplitudes, initial conditions, damping ratios and a very small step of variation of loading frequency. In what follows, an attempt to simplify the problem is presented, in order to provide analytical solutions and important information about the conditions under which these nonlinear phenomena occur.

3.3 A SDOF CABLE NET SYSTEM (SIMPLIFIED MODEL)

3.3.1 Forced vibration of the system – Non-resonant excitations

A single-degree-of-freedom system is assumed, similar to the one described before, allowing only for vertical displacements. An external excitation $P_z(t)=P_0\cos\Omega t$ is applied on the central node, with a

loading frequency Ω away from the only eigenfrequency ω_{z0} of the system at the unforced, undeformed and prestressed equilibrium state. Substituting the expressions of the tension of the cables (Eq. (3-9)) and the prestressed, initial and deformed lengths of Eqs. (3-2), (3-3), (3-5) - (3-8), respectively, into the vertical components of the cable tensions (Eqs. (3-13), (3-16), (3-19) and (3-22)), the differential equation (3-51) becomes:

$$M\ddot{w} + C\dot{w} + N_z = P_z(t) \Rightarrow$$

$$M\ddot{w} + C\dot{w} - \frac{4EA(f+w)}{L\sqrt{1+4\frac{(f+w)^2}{L^2}}} + \frac{4EA(f-w)}{L\sqrt{1+4\frac{(f-w)^2}{L^2}}} + \frac{4w(EA+N_0)}{L\sqrt{1+4\frac{f^2}{L^2}}} = P_z(t) \quad (3-63)$$

A function of type:

$$g(z) = \frac{1}{(1+z)^m} \quad (3-64)$$

can be expanded in Taylor series [3-31], with respect to the variable z , around $z_0=0$, as follows:

$$g(z) = \frac{1}{(1+z)^m} = (1+z)^{-m} = 1 - mz + \frac{m(m+1)}{2!}z^2 - \frac{m(m+1)(m+2)}{3!}z^3 + \dots \quad (3-65)$$

Taking into account that the sag-to-span ratio f/L is usually very small for actual cable nets, allowing thus to neglect its third or higher powers, Eq. (3-63), developed in Taylor series, becomes:

$$M\ddot{w} + C\dot{w} - \frac{4EA(f+w)}{L} \left(1 - 2\frac{(f+w)^2}{L^2} \right) +$$

$$+ \frac{4EA(f-w)}{L} \left(1 - 2\frac{(f-w)^2}{L^2} \right) + \frac{4w(EA+N_0)}{L} \left(1 - 2\frac{f^2}{L^2} \right) = P_z(t) \Rightarrow \quad (3-66)$$

$$M\ddot{w} + C\dot{w} + \frac{16EAw^3}{L^3} + \frac{32EAf^2w}{L^3} + \frac{8N_0w}{L} - \frac{16N_0f^2w}{L^3} = P_z(t) \Rightarrow$$

$$M\ddot{w} + C\dot{w} + \frac{16EAw^3}{L^3} + \frac{4EA}{L} \cdot \left(8\frac{f^2}{L^2} + 2\frac{N_0}{EA} - 4\frac{N_0}{EA}\frac{f^2}{L^2} \right) w = P_z(t)$$

Expanding the expression of the stiffness K_{z0} of the undeformed system of Eq. (3-30) in Taylor series with respect to the term f/L , according to Eq. (3-65), and neglecting terms of order $(f/L)^4$, it reduces to:

$$K_{z0} = \frac{4EA}{L} \cdot \frac{\left(8\frac{f^2}{L^2} + 2\frac{N_0}{EA} + 8\frac{N_0}{EA}\frac{f^2}{L^2} \right)}{\sqrt{\left(1 + 4\frac{f^2}{L^2} \right)^3}} \Rightarrow \quad (3-67)$$

$$\Rightarrow K_{z0} = \frac{4EA}{L} \left(8\frac{f^2}{L^2} + 2\frac{N_0}{EA} + 8\frac{N_0}{EA}\frac{f^2}{L^2} \right) \left(1 - 6\frac{f^2}{L^2} \right) \Rightarrow$$

$$\Rightarrow K_{z0} = \frac{4EA}{L} \cdot \left(8\frac{f^2}{L^2} + 2\frac{N_0}{EA} - 4\frac{N_0}{EA}\frac{f^2}{L^2} \right)$$

Eq. (3-66) can be written as:

$$M\ddot{w} + C\dot{w} + K_{z0}w + \frac{16EAw^3}{L^3} = P_z(t) \Rightarrow \ddot{w} + \frac{C}{M}\dot{w} + \omega_{z0}^2w + \frac{16EA}{ML^3}w^3 = \frac{P_0}{M}\cos(\Omega t) \quad (3-68)$$

where a nonlinear cubic term appears with a coefficient depending on the modulus of elasticity of the cable material, the cable cross-sectional area and the span of the cables. The ratio of the linear term over the nonlinear term is defined as R:

$$R = \frac{4EA \cdot \left(8 \frac{f^2}{L^2} + 2 \frac{N_0}{EA} - 4 \frac{N_0}{EA} \frac{f^2}{L^2} \right) \cdot w/L}{16EAw^3/L^3} = \left(2 \frac{f^2}{L^2} + \frac{N_0}{2EA} - \frac{N_0}{EA} \frac{f^2}{L^2} \right) \cdot \frac{L^2}{w^2} \quad (3-69)$$

The ratio R is plotted in Figure 3-25 with respect to f/L , taking into consideration the maximum permissible deflection shown in Figure 3-7 for yield stress $\sigma_y=1570\text{MPa}$, Young modulus $E=165\text{GPa}$ and initial stress equal to 20% of the yield stress. As the sag-to-span ratio increases, the ratio R increases as well, taking large values. Hence, as the sag-to-span ratio increases, and the system becomes stiffer due to the large opposite curvatures, the contribution of the nonlinear term in the dynamic motion of the net could be considered as very small with respect to the one of the linear term, concluding that the system's behaviour becomes quasi linear.

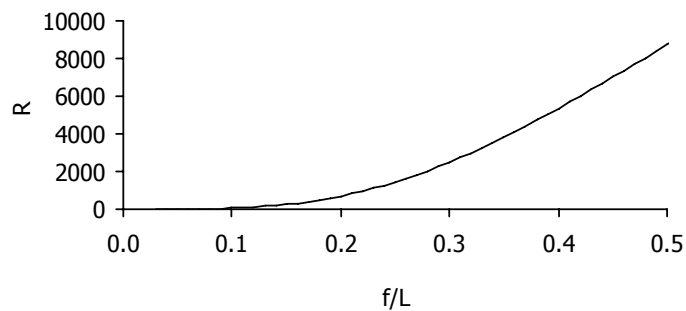


Figure 3-25: Ratio R with respect to the sag-to-span ratio

For sag-to-span ratios between $1/35$ and $1/10$, the above ratio takes values between 1.6 and 57 (Figure 3-26). For common values of the ratio f/L , the nonlinear term of the displacement is smaller than the linear term and its contribution could be presumed as considerable only for very shallow cable nets. However, as will be shown further on, the effect of this small nonlinear term on the system's dynamic response is not negligible, even for sag-to-span ratios larger than $1/35$, producing large-scale phenomena, which do not occur for linear systems.

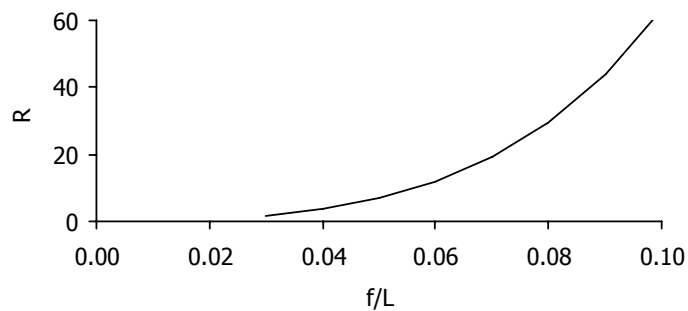


Figure 3-26: Ratio R with respect to the sag-to-span ratio between $f/L=1/35$ and $f/L=1/10$

The ratio of the linear term over the velocity term is defined as RV:

$$RV = \frac{K_{z0}W}{C\dot{W}} = \frac{K_{z0}W}{2\zeta M\omega_{z0}\dot{W}} = \frac{\omega_{z0}}{2\zeta} \cdot \frac{W}{\dot{W}} \quad (3-70)$$

The maximum damping ratio ζ , measured for cable nets, is 2% [3-32]. Taking into account the results of the example in section 3.2.6.4, the minimum ratio of the deflection over the velocity can be considered equal to $1/(2.46\omega_{z0})$. In this case, the parameter RV is equal to:

$$RV = \frac{1}{2 \cdot 2.46 \cdot 0.02} = 10.16 \quad (3-71)$$

The change of the parameter RV with respect to the ratio rw, defined as:

$$rw = \frac{\dot{W}}{W\omega_{z0}} \quad (3-72)$$

for damping ratio $\zeta=2\%$, is plotted in Figure 3-27. It is noted that even for much larger values of the ratio rw than the ones calculated in section 3.2.6.4, the ratio RV is larger than 1, which means that the velocity term can be considered as small with respect to the linear term of the displacement.

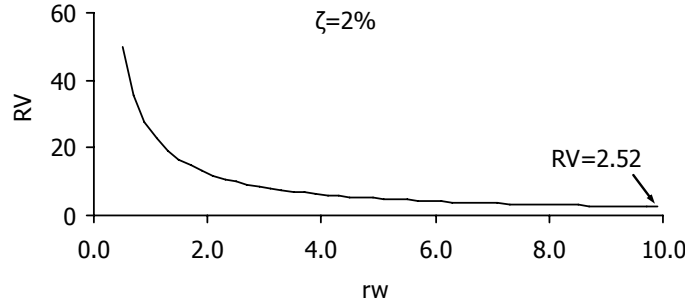


Figure 3-27: Ratio RV with respect to ratio rw for damping ratio $\zeta=2\%$

Nayfeh and Mook [3-25] thoroughly explored the equation:

$$\ddot{W} + 2\epsilon\mu\dot{W} + \omega_0^2 W + \epsilon\alpha W^3 = K \cos(\Omega t) \quad (3-73)$$

known as the equation of motion referring to a forced damped Duffing oscillator, with μ being positive, and the coefficient of the nonlinear term α being either positive (hardening spring) or negative (softening spring). Here the main features of this investigation are reported. The equation of motion of the simple cable net, described by Eq. (3-68), can take the form of Eq. (3-73), with positive coefficient of the nonlinear term and become:

$$\ddot{W} + 2\epsilon\mu\dot{W} + \omega_{z0}^2 W + \epsilon\alpha W^3 = P \cos(\Omega t) \quad (3-74)$$

where:

$$2\epsilon\mu = \frac{C}{M} = 2\zeta\omega_{z0} \quad (3-75)$$

$$\epsilon\alpha = \frac{16EA}{ML^3} \quad (3-76)$$

$$P = \frac{P_0}{M} \quad (3-77)$$

$$\omega_{z0} = \sqrt{\frac{K_{z0}}{M}} = \sqrt{\frac{4EA}{ML} \cdot \left(8 \frac{f^2}{L^2} + 2 \frac{N_0}{EA} - 4 \frac{N_0}{EA} \frac{f^2}{L^2} \right)} \quad (3-78)$$

The parameter ε is assumed to be small and dimensionless, with $\varepsilon < 1$, defining the small scale of the coefficients of the velocity and the cubic term in the equation of motion with respect to the one of the linear term. The exact value of this parameter is not important, because the solution of the problem is independent of ε . It depends only on the parameters $\varepsilon\mu$ and $\varepsilon\alpha$, as defined in Eqs. (3-75) and (3-76), respectively, meaning that the parameter ε never appears alone in the solution. For $\varepsilon=0$ a linear, undamped system is described by the equation of motion. In order to find a solution of nonlinear equations of motions, several methods are used, named as perturbation techniques, such as Lindstedt's method, the method of multiple scales, the method of averaging, the method of harmonic balance, etc. ([3-25], [3-27], [3-33], [3-34], [3-35]). In this case, the method of multiple scales is applied. The main idea of this method is to consider the expansion representing the response to be a function of multiple independent variables, called scales. The introduced independent variables will be time intervals, referring to "slow" or "fast" vibrations, named as time scales. A "slow" vibration is produced by an excitation having a frequency near the eigenfrequency of the system, while a "fast" vibration is produced by a high frequency excitation with a time period smaller than the natural period of the system. In linear systems the amplitude of "fast" vibrations is small; in nonlinear systems, instead, the high frequency excitation alters the "slow properties" of a system, such as the natural frequencies, the location and stability of equilibrium points and the response to resonant excitations, having thus a significant effect on its dynamics at a time scale comparable to the natural time period of the system. Hence, the time scales are defined as:

$$T_n = \varepsilon^n t \quad (3-79)$$

with $n=0,1,2,\dots$, $T_0 > T_1 > T_2 > \dots > T_n$ and $T_0=t$ being the "slow" time while $T_1, T_2 \dots T_n$ being the variables of the "fast" time. In order to understand the meaning of "slow" and "fast" vibrations, two typical dynamic response diagrams are shown in Figure 3-28, where the "slow" and "fast" components of the response are shown. In case the dynamic response of a system consists of "slow" and "fast" components, the "fast" oscillation is embounded by a "slow" envelope.

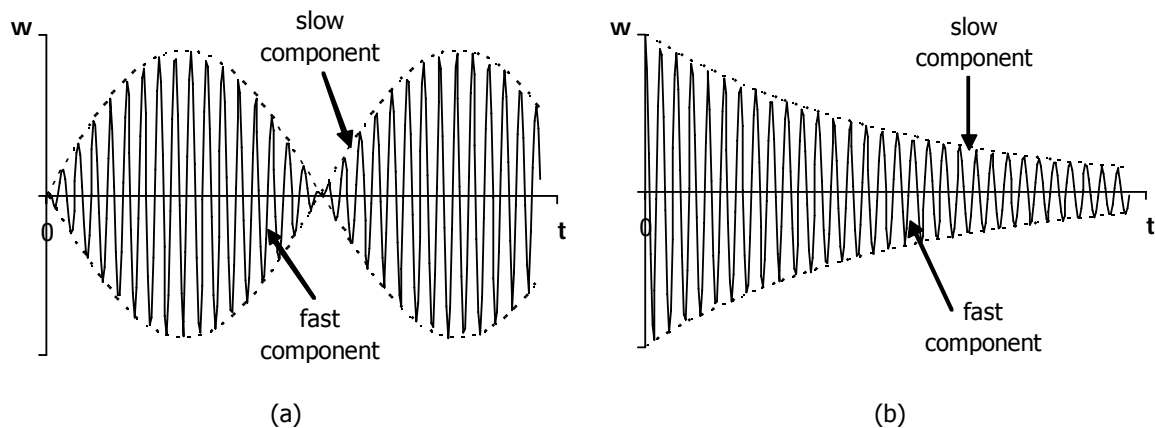


Figure 3-28: "Slow" and "fast" oscillations: (a) dynamic response consisting of two different frequencies, (b) dynamic response of a damped system

It is assumed that the solution of the equation of motion, described by Eq. (3-74), can be expressed as:

$$w(t,\varepsilon)=w_0(T_0,T_1,T_2,\dots)+\varepsilon w_1(T_0,T_1,T_2,\dots)+\varepsilon^2 w_2(T_0,T_1,T_2,\dots)+\dots \quad (3-80)$$

For this investigation, the analysis will be carried out to $O(\varepsilon^2)$, thus only the time scales T_0 and T_1 are introduced. The solution is separated into "slow" components referring to the time T_0 and "fast" components referring to the time T_1 .

$$w(t,\varepsilon)=w_0(T_0,T_1,\dots)+\varepsilon w_1(T_0,T_1,\dots)+\dots \text{ where } T_0=t, T_1=\varepsilon t, \dots \quad (3-81)$$

The time derivatives are expressed as:

$$\begin{aligned} \frac{d}{dt} &= \frac{dT_0}{dt} \frac{d}{dT_0} + \frac{dT_1}{dt} \frac{d}{dT_1} + \dots = D_0 + \varepsilon D_1 + \dots \\ \frac{d^2}{dt^2} &= D_0^2 + \varepsilon D_0 D_1 + \varepsilon^2 (D_1^2 + \varepsilon D_0 D_2) + \dots \end{aligned} \quad (3-82)$$

where

$$D_k(\bullet) = \frac{\partial(\bullet)}{\partial T_k}, \quad k=0,1,\dots \quad (3-83)$$

Substituting the series expression into Eq. (3-74) yields:

$$\begin{aligned} &\frac{d^2}{dt^2} [w_0(T_0, T_1, \dots) + \varepsilon w_1(T_0, T_1, \dots) + \dots] + \\ &+ 2\varepsilon\mu \frac{d}{dt} [w_0(T_0, T_1, \dots) + \varepsilon w_1(T_0, T_1, \dots) + \dots] + \\ &+ \omega_{z0}^2 [w_0(T_0, T_1, \dots) + \varepsilon w_1(T_0, T_1, \dots) + \dots] + \\ &+ \varepsilon \alpha [w_0(T_0, T_1, \dots) + \varepsilon w_1(T_0, T_1, \dots) + \dots]^3 = P \cos(\Omega t) \Rightarrow \\ &\Rightarrow D_0^2 (w_0 + \varepsilon w_1 + \dots) + 2\varepsilon D_0 D_1 (w_0 + \dots) + 2\varepsilon\mu D_0 (w_0 + \dots) + \dots + \\ &+ \omega_{z0}^2 (w_0 + \varepsilon w_1 + \dots) + \varepsilon \alpha w_0^3 + \dots = P \cos(\Omega t) \end{aligned} \quad (3-84)$$

Equating coefficients of like powers of ε , one obtains:

$$O(\varepsilon^0): D_0^2 w_0 + \omega_{z0}^2 w_0 = P \cos(\Omega t) \quad (3-85)$$

$$O(\varepsilon^1): D_0^2 w_1 + \omega_{z0}^2 w_1 = -2D_0 D_1 w_0 - 2\mu D_0 w_0 - \alpha w_0^3 \quad (3-86)$$

The first equation has the following solution ([3-36] and [3-37]):

$$w_0(T_0, T_1) = A(T_1) e^{j\omega_{z0} T_0} + \bar{A}(T_1) e^{-j\omega_{z0} T_0} + \Lambda e^{j\Omega T_0} + \Lambda e^{-j\Omega T_0} + cc \quad (3-87)$$

where $A(T_1)$ is an undetermined function for now and:

$$\Lambda = \frac{1}{2} P \left(\frac{1}{\omega_{z0}^2 - \Omega^2} \right) \quad (3-88)$$

Substituting the expression of the solution, Eq. (3-86) becomes:

$$\begin{aligned}
& D_0^2 w_1 + \omega_{z0}^2 w_1 = \\
& = -[2j\omega_{z0}(D_1 A + \mu A) + 3aA^2 \bar{A} + 6aA\Lambda^2] e^{j\omega_{z0} T_0} \\
& - (2j\Omega\mu\Lambda + 3a\Lambda^3 + 6aA\bar{A}\Lambda) e^{j\Omega T_0} \\
& - a \left\{ A^3 e^{3j\omega_{z0} T_0} + \Lambda^3 e^{3j\Omega T_0} + 3A^2 \Lambda e^{j(2\omega_{z0} + \Omega) T_0} + 3\bar{A}^2 \Lambda e^{j(\Omega - 2\omega_{z0}) T_0} + \right. \\
& \left. + 3\Lambda^2 A e^{j(2\Omega + \omega_{z0}) T_0} + 3\Lambda^2 A e^{j(-2\Omega + \omega_{z0}) T_0} \right\} + cc
\end{aligned} \tag{3-89}$$

The first term, which has the exponent $j\omega_{z0}T_0$, increases with time without bounds. Terms that grow indefinitely with time are referred to as secular terms. In the above equation there are terms that can be secular when the loading frequency is very small $\Omega=O(\epsilon)$ or when there is a secondary resonance, $\omega_{z0} \approx (m\omega_{z0} + n\Omega)$, with $|m| + |n| = 3$. In the case of non-resonant conditions, when the loading frequency Ω is away from 0, $3\omega_{z0}$, $\omega_{z0}/3$, the first term is the only secular term and it must be eliminated because the exact solution remains bounded at all times ([3-38] and [3-39]), due to the damping and the nonlinearity. Thus, we set:

$$2j\omega_{z0}(D_1 A + \mu A) + 3aA^2 \bar{A} + 6aA\Lambda^2 = 0 \tag{3-90}$$

Assuming that the function $A(T_1)$ is expressed as:

$$A(T_1) = \frac{a(T_1)}{2} e^{j\beta(T_1)} \quad \text{and} \quad \bar{A}(T_1) = \frac{a(T_1)}{2} e^{-j\beta(T_1)} \tag{3-91}$$

where a , β are real amplitude and phase of the displacement, respectively. If the above expressions are substituted into Eq. (3-90), the following equation is obtained:

$$\begin{aligned}
& 2j\omega_{z0} \left(\frac{a'}{2} e^{j\beta} + j\beta' \frac{a}{2} e^{j\beta} + \mu \frac{a}{2} e^{j\beta} \right) + 3a \left(\frac{a}{2} \right)^3 e^{j\beta} + 3aa\Lambda^2 e^{j\beta} = 0 \Rightarrow \\
& \Rightarrow \left(j\omega_{z0} a' - \omega_{z0} \beta' a + j\omega_{z0} \mu a + 3a \left(\frac{a}{2} \right)^3 + 3aa\Lambda^2 \right) e^{j\beta} = 0 \Rightarrow \\
& \Rightarrow j\omega_{z0} a' - \omega_{z0} \beta' a + j\omega_{z0} \mu a + 3a \left(\frac{a}{2} \right)^3 + 3aa\Lambda^2 = 0
\end{aligned} \tag{3-92}$$

Separating the real and imaginary parts gives the following set of differential equations:

$$\begin{aligned}
& \text{(a): } a' = -\mu a \Rightarrow a = a_0 e^{-\mu T_1} \\
& \text{(b): } \frac{3aa^3}{8} - a\omega_{z0}\beta' + 3aa\Lambda^2 = 0 \Rightarrow \beta' = \left(\frac{3aa_0^2 e^{-2\mu T_1}}{8\omega_{z0}} + \frac{3a\Lambda^2}{\omega_{z0}} \right) \Rightarrow \\
& \Rightarrow \beta = \beta_0 + \frac{3a\Lambda^2}{\omega_{z0}} T_1 + \frac{3aa_0^2 e^{-2\mu T_1}}{8\omega_{z0}} \cdot \frac{1}{(-2\mu)} \Rightarrow \\
& \Rightarrow \beta = \beta_0 + \frac{3a\Lambda^2}{\omega_{z0}} T_1 - \frac{3aa_0^2 e^{-2\mu T_1}}{16\mu\omega_{z0}}
\end{aligned} \tag{3-93}$$

Substituting the above expressions, the response of the nonlinear system, defined by Eq. (3-87), is expressed as:

$$\begin{aligned}
w(t) &= A(T_1)e^{j\omega_{z0}T_0} + \Lambda e^{j\Omega T_0} + cc = \frac{a_0}{2} e^{-\varepsilon\mu T_0} e^{j\beta(T_1)} e^{j\omega_{z0}T_0} + \Lambda e^{j\Omega T_0} + cc = \\
&= a_0 e^{-\varepsilon\mu t} \cos\left(\omega_{z0}t + \frac{3\varepsilon a \Lambda^2}{\omega_{z0}}t - \frac{3a}{16\mu\omega_{z0}} a_0^2 e^{-2\mu\varepsilon t} + \beta_0 + O(\varepsilon^2)\right) + \\
&+ P\left(\frac{1}{\omega_{z0}^2 - \Omega^2}\right) \cos \Omega t + O(\varepsilon)
\end{aligned} \tag{3-94}$$

where a_0 and β_0 are the initial amplitude and phase of the displacement, respectively. Using the Maclaurin series [3-31] for the exponential function $e^{-2\mu\varepsilon t} = 1 - 2\mu\varepsilon t$, keeping only the first term, because the parameter ε and the damping coefficient μ are very small, the above equation becomes:

$$\begin{aligned}
w(t) &= a_0 e^{-\varepsilon\mu t} \cos\left[\left(\omega_{z0} + \frac{3\varepsilon a \Lambda^2}{\omega_{z0}} + \frac{3\varepsilon a a_0^2}{8\omega_{z0}}\right)t - \frac{3a}{16\mu\omega_{z0}} a_0^2 + \beta_0 + O(\varepsilon^2)\right] + \\
&+ P\left(\frac{1}{\omega_{z0}^2 - \Omega^2}\right) \cos \Omega t + O(\varepsilon)
\end{aligned} \tag{3-95}$$

3.3.2 Forced vibration of the system – Fundamental resonance

In case of fundamental resonance the excitation is assumed to be weak, in order to prove that a weak excitation produces large-scale oscillations. The parameter ε is introduced again, defining the small amplitude of the load:

$$P_0 = \varepsilon p_0, P = P_0/M = \varepsilon p_0/M = \varepsilon p \quad \text{with } p = O(1) \tag{3-96}$$

The loading frequency is close to the eigenfrequency, $\Omega \approx \omega_{z0}$. A small detuning parameter σ is introduced to express the proximity of the loading frequency to ω_{z0} , such that:

$$\Omega = \omega_{z0} + \varepsilon\sigma \tag{3-97}$$

with $\sigma = O(1)$. Hence, the equation of motion, based on Eq. (3-74), will be:

$$\ddot{w} + 2\varepsilon\mu\dot{w} + \omega_{z0}^2 w + \varepsilon\alpha w^3 = \varepsilon p \cos(\omega_{z0}t + \varepsilon\sigma t) \tag{3-98}$$

Expressing the solution as before:

$$w(t, \varepsilon) = w_0(T_0, T_1) + \varepsilon w_1(T_0, T_1) + \dots \tag{3-99}$$

where $T_0 = t$, $T_1 = \varepsilon t$, ..., applying the method of multiple scales and collecting like-terms in ε , one obtains:

$$O(\varepsilon^0): D_0^2 w_0 + \omega_{z0}^2 w_0 = 0 \tag{3-100}$$

$$O(\varepsilon^1): D_0^2 w_1 + \omega_{z0}^2 w_1 = -2D_0 D_1 w_0 - 2\mu D_0 w_0 - \alpha w_0^3 + \frac{p}{2} e^{j(\omega_{z0} T_0 + \sigma T_1)} \tag{3-101}$$

The solution of the Eq. (3-100), is:

$$w_0(T_0, T_1) = A(T_1) e^{j\omega_{z0} T_0} + \bar{A}(T_1) e^{-j\omega_{z0} T_0} \tag{3-102}$$

Substituting the above solution into Eq. (3-101), it becomes:

$$\begin{aligned}
D_0^2 w_1 + \omega_{z0}^2 w_1 &= \\
&= -2j\omega_{z0} (D_1 A + \mu A) e^{j\omega_{z0} T_0} - a \left(A^3 e^{3j\omega_{z0} T_0} + 3A^2 e^{2j\omega_{z0} T_0} \bar{A} e^{-j\omega_{z0} T_0} \right) + \frac{p}{2} e^{j(\omega_{z0} T_0 + \sigma T_1)} = \\
&= - \left(2j\omega_{z0} (D_1 A + \mu A) + 3a A^2 \bar{A} + \frac{p}{2} e^{j\sigma T_1} \right) e^{j\omega_{z0} T_0} - a A^3 e^{3j\omega_{z0} T_0}
\end{aligned} \quad (3-103)$$

To eliminate the first term, which is a secular term, requires that:

$$2j\omega_{z0} (D_1 A + \mu A) + 3a A^2 \bar{A} - \frac{p}{2} e^{j\sigma T_1} = 0 \quad (3-104)$$

The function $A(T_1)$ is assumed to be expressed as:

$$A(T_1) = \frac{a(T_1)}{2} e^{j\beta(T_1)} \quad \text{and} \quad \bar{A}(T_1) = \frac{a(T_1)}{2} e^{-j\beta(T_1)} \quad (3-105)$$

where a , β are real amplitude and phase of the displacement, respectively. Substituting into Eq. (3-104) and using the Euler formula [3-31] for the exponential function $e^{ix} = \cos x + j \sin x$, the following equation is obtained:

$$\begin{aligned}
2j\omega_{z0} \left(\frac{a'}{2} e^{j\beta} + j\beta' \frac{a}{2} e^{j\beta} + \mu \frac{a}{2} e^{j\beta} \right) + 3a \left(\frac{a}{2} \right)^3 e^{j\beta} - \frac{p}{2} e^{j\sigma T_1} &= 0 \Rightarrow \\
\Rightarrow (j\omega_{z0} a' - \omega_{z0} \beta' a + j\omega_{z0} \mu a) e^{j\beta} + 3a \left(\frac{a}{2} \right)^3 e^{j\beta} - \frac{p}{2} e^{j\sigma T_1} &= 0 \Rightarrow \\
\Rightarrow \left(j\omega_{z0} a' - \omega_{z0} \beta' a + j\omega_{z0} \mu a + 3a \left(\frac{a}{2} \right)^3 - \frac{p}{2} e^{j(\sigma T_1 - \beta)} \right) e^{j\beta} &= 0 \Rightarrow \\
\Rightarrow j\omega_{z0} a' - \omega_{z0} \beta' a + j\omega_{z0} \mu a + 3a \left(\frac{a}{2} \right)^3 - \frac{p}{2} (\cos(\sigma T_1 - \beta) + j \sin(\sigma T_1 - \beta)) &= 0
\end{aligned} \quad (3-106)$$

Separating the real and imaginary parts, a new set of differential equations can be provided:

$$\begin{aligned}
\text{(a): } a' &= -\mu a + \frac{p}{2\omega_{z0}} \sin(\sigma T_1 - \beta) \\
\text{(b): } 3a \left(\frac{a}{2} \right)^3 - a\omega_{z0} \beta' - \frac{p}{2} \cos(\sigma T_1 - \beta) &= 0 \Rightarrow a\beta' = \frac{3aa^3}{8\omega_{z0}} - \frac{p}{2\omega_{z0}} \cos(\sigma T_1 - \beta)
\end{aligned} \quad (3-107)$$

Setting:

$$\gamma = \sigma T_1 - \beta \quad (3-108)$$

the above equations are transformed into an autonomous set of ordinary differential equations:

$$\text{(a): } a' = -\mu a + \frac{p}{2\omega_{z0}} \sin \gamma, \quad \text{(b): } a\gamma' = a\sigma - \frac{3aa^3}{8\omega_{z0}} + \frac{p}{2\omega_{z0}} \cos \gamma \quad (3-109)$$

Steady-state motions require that:

$$a' = \gamma' = 0 \quad (3-110)$$

and Eqs. (3-109) become:

$$(a): \frac{p}{2\omega_{z0}} \sin \gamma = \mu a, (b): a\sigma - \frac{3aa^3}{8\omega_{z0}} = -\frac{p}{2\omega_{z0}} \cos \gamma \quad (3-111)$$

The peak amplitude of the free oscillation term is given for $\sin \gamma = 1$:

$$a_p = \frac{p}{2\mu\omega_{z0}} \quad (3-112)$$

and the corresponding value of the detuning σ is calculated for $\cos \gamma = 0$:

$$\sigma_p = \frac{3aa_p^2}{8\omega_{z0}} = \frac{3ap^2}{32\mu^2\omega_{z0}^3} \quad (3-113)$$

If the peak amplitude of the free oscillation is set to be equal to the maximum permissible deflection w_{max} , expressed by Eq. (3-48) and plotted in Figure 3-7, the maximum permissible dynamic load P_0 , which causes the maximum deflection, can be calculated from Eq. (3-112), taking into account Eq. (3-96). The ratio of the dynamic load P_0 , which causes the maximum deflection, over the corresponding static one P_{max} illustrated in Figure 3-8, with respect to the sag-to-span ratio, for damping ratios $\zeta=0.5\%$ and $\zeta=2\%$, is shown in Figure 3-29. This ratio is very small for both damping ratios. As the damping ratio ζ decreases, the maximum permissible dynamic load also decreases. As the sag-to-span ratio becomes larger and the system becomes stiffer the maximum permissible dynamic load increases.

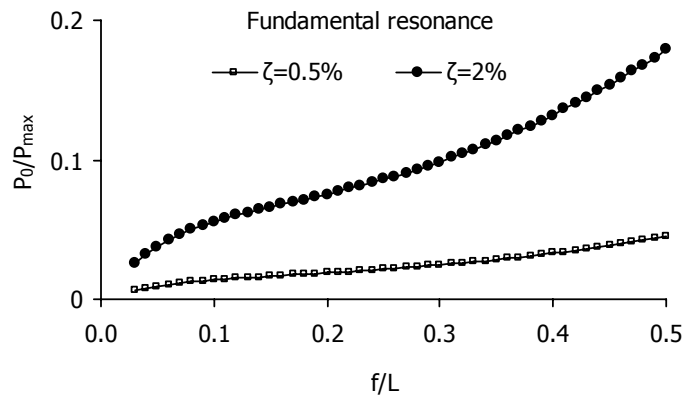


Figure 3-29: Variation of the ratio of the maximum dynamic load P_0 over the static one (P_{max}), with respect to the sag-to-span ratio, for the case of fundamental resonance

The frequency-amplitude relation for fundamental resonance is expressed as:

$$\left(a\sigma - \frac{3aa^3}{8\omega_{z0}} \right)^2 + (\mu a)^2 = \frac{p^2}{4\omega_{z0}^2} \Rightarrow \left[\left(\sigma - \frac{3aa^2}{8\omega_{z0}} \right)^2 + \mu^2 \right] a^2 = \frac{p^2}{4\omega_{z0}^2} \quad (3-114)$$

The phase of the periodic solution is computed as:

$$\sin \gamma = \frac{2\mu a\omega_{z0}}{p} \quad \text{and} \quad \tan \gamma = -\frac{\mu}{\left(\sigma - \frac{3aa^2}{8\omega_{z0}} \right)} \quad (3-115)$$

From the above formulae it can be noted that the phase depends not only on the loading frequency, the damping and the frequency of the system, as in linear systems, but also on the response

amplitude. If $\mu=p=0$, one obtains the amplitude-frequency relation for free oscillation of undamped, unforced oscillator, which represents the backbone curve of the system:

$$a=0 \text{ or } \sigma - \frac{3\alpha a^2}{8\omega_{z0}} = 0 \Rightarrow a = \pm \sqrt{\frac{8\sigma\omega_{z0}}{3\alpha}} \quad (3-116)$$

If $\mu, p \neq 0$ the frequency – response curves are obtained in the form:

$$\sigma = \frac{3\alpha a^2}{8\omega_{z0}} \pm \sqrt{\frac{p^2}{4\omega_{z0}^2 a^2} - \mu^2} \quad (3-117)$$

The backbone curve represents either the equilibrium state ($a=0$) or the free vibrations of the undamped system about the equilibrium state ($a \neq 0, \mu=p=0$), while any other response curve ($a, \mu, p \neq 0$) represents perturbations from the unforced state. It should be noted that there exist frequency ranges for which only one solution is possible and other frequency ranges where three solutions exist. This occurs due to the bending of the response curve. In this case, the initial conditions determine which of these three responses actually develops. Only two of them are stable solutions and the third is an unstable one. The multiple co-existing solutions lead to jump phenomena [3-40], creating nonlinear hysteresis loops. In linear systems, there are no hysteresis loops and the response does not depend on the initial conditions. Hence, only one solution exists for a given loading frequency. Typical frequency – response curves and phase diagrams for linear and nonlinear systems are shown in Figure 3-30 and Figure 3-31, respectively. The definition of the hysteresis loop due to the jump phenomenon is shown in Figure 3-32.

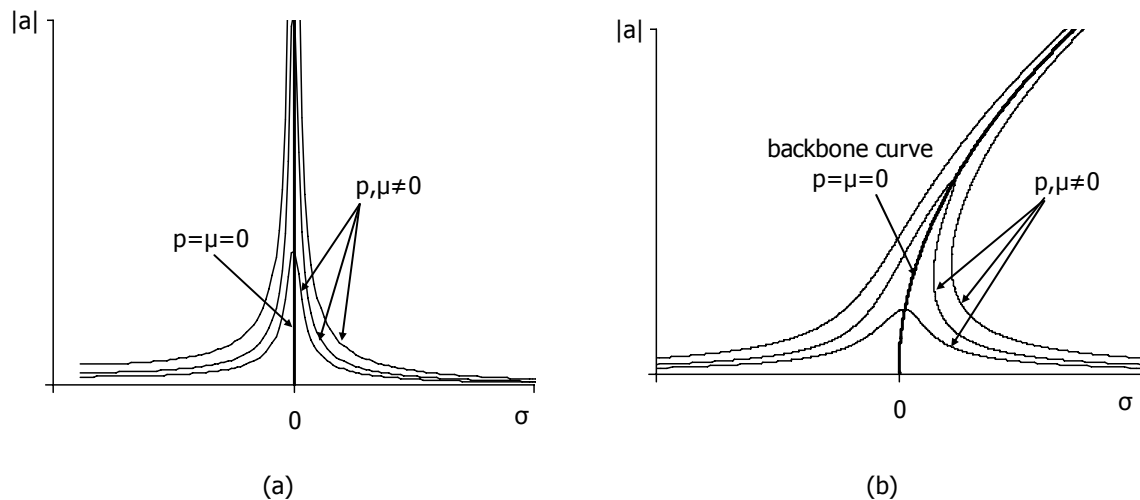


Figure 3-30: Fundamental resonance: Amplitude $|a|$ vs. frequency detuning σ for (a) linear system, (b) nonlinear system

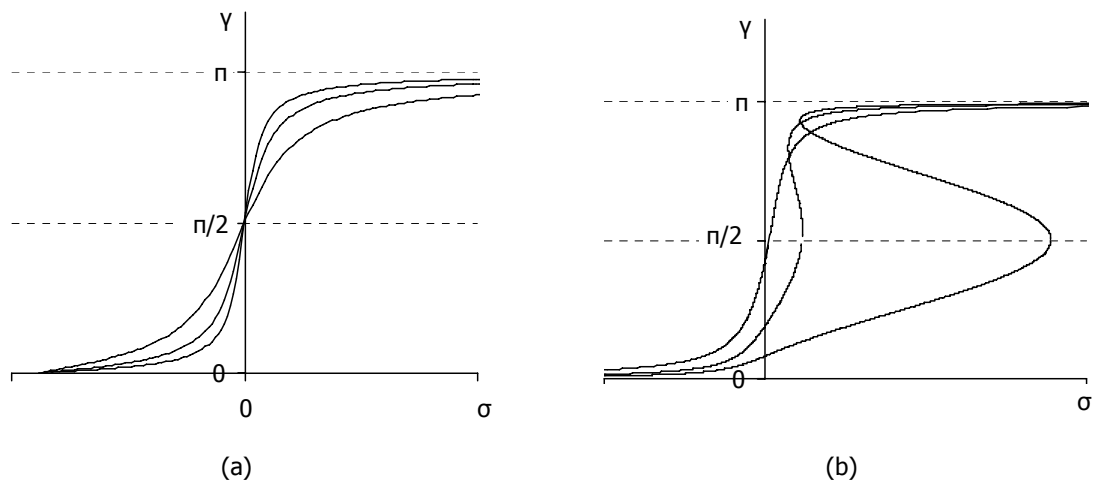


Figure 3-31: Fundamental resonance: Phase γ vs. frequency detuning σ for (a) linear system, (b) nonlinear system

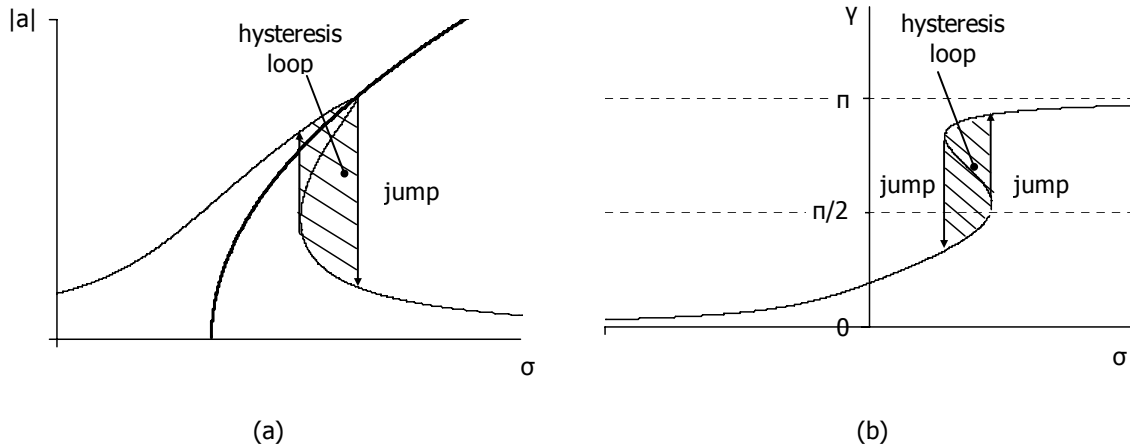


Figure 3-32: Jump phenomenon (a) amplitude $|a|$ vs. frequency detuning σ , (b) phase γ vs. frequency detuning σ

The influence of the sag-to-span ratio on the response curve of the simple cable net is shown in Figure 3-33a for three different ratios, $f/L=1/10$, $f/L=1/20$ and $f/L=1/35$ for the same damping ratio and load amplitude. In this case, the cable span L , the Young modulus E , the cable diameter, the concentrated mass of the central node and the initial strain are considered the same for all three sag-to-span ratios, meaning that only the eigenfrequency changes (Eq. (3-78)) and not the coefficient ϵa of the nonlinear term, expressed by Eq. (3-76). As the sag-to-span ratio increases, the eigenfrequency increases, representing deeper and stiffer cable nets, the backbone curve tends to be linear and the response curves approach the backbone, predicting a more linear behaviour. Keeping constant the damping ratio, the load amplitude, the Young modulus, the sag-to-span ratio, equal to $1/20$, the concentrated mass and the initial strain and changing the cable span L and the cable diameter so that the eigenfrequency remains the same and only the coefficient of the nonlinear term ϵa changes, the diagrams of the response curves are illustrated in Figure 3-33b for three different cable spans, $L=50\text{m}$, $L=100\text{m}$ and $L=200\text{m}$. As the cable span increases, the coefficient ϵa decreases, reducing the influence of the nonlinear term on the response of the net and leading to a more linear behaviour. For values of the frequency detuning σ away from zero, the response does not depend on the coefficient ϵa , but only on the eigenfrequency.

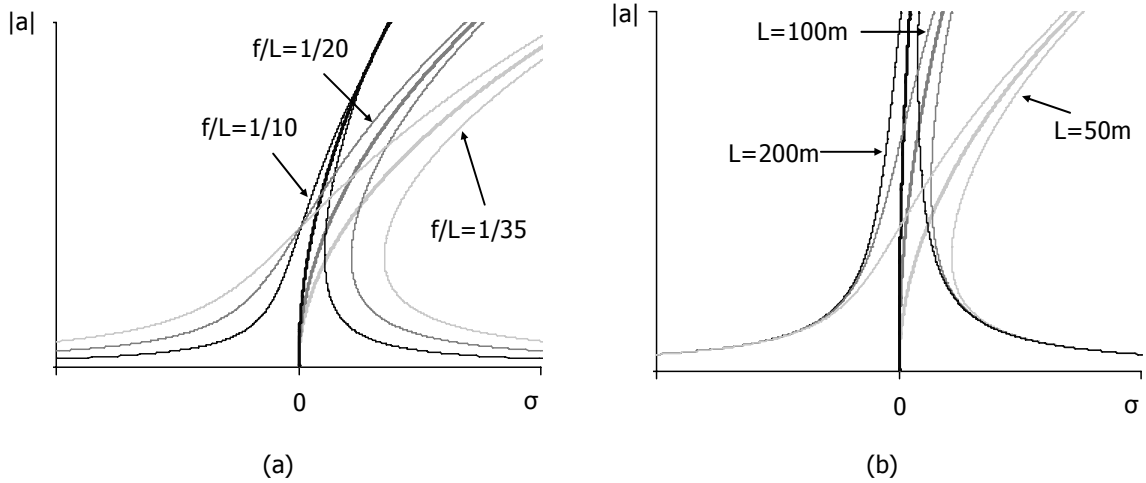


Figure 3-33: Fundamental resonance: Amplitude $|a|$ vs. frequency detuning σ for (a) different sag-to-span ratios f/L , (b) different spans L

The response of the nonlinear system at steady state is obtained by Eq. (3-99) taking into account Eqs. (3-102), (3-105) and (3-108):

$$\begin{aligned}
 w(t) &= w_0 + O(\epsilon) = Ae^{j\omega_{z0}T_0} + O(\epsilon) = \frac{a(T_1)}{2} e^{j\beta(T_1)} e^{j\omega_{z0}T_0} + O(\epsilon) = \\
 &= a \cos(\omega_{z0}T_0 + \sigma T_1 - \gamma) + O(\epsilon) = a \cos(\omega_{z0}t + \epsilon\sigma t - \gamma) + O(\epsilon) = \\
 &= a \cos(\Omega t - \gamma) + O(\epsilon)
 \end{aligned} \tag{3-118}$$

The phase γ can be calculated from Eq. (3-115) and the amplitude of the oscillation a by Eq. (3-117). The response has the same frequency with the excitation, which means that the term "fundamental resonance" can be used.

3.3.3 Forced vibration of the system – Superharmonic resonance

Considering a loading frequency $\Omega \approx \omega_{z0}/3$, a detuning parameter σ , such that:

$$3\Omega = \omega_{z0} + \epsilon\sigma, \quad \text{with } \sigma = O(1) \tag{3-119}$$

and taking into consideration that in Eq. (3-89) the term proportional to $e^{j3\Omega t}$ is another secular term, we eliminate all secular terms by setting:

$$2j\omega_{z0}(D_1A + \mu A) + 3aA^2\bar{A} + 6aA\Lambda^2 + a\Lambda^3 e^{j\epsilon\sigma T_0} = 0 \tag{3-120}$$

Setting:

$$A(T_1) = \frac{a(T_1)}{2} e^{j\beta(T_1)} \quad \text{and} \quad \bar{A}(T_1) = \frac{a(T_1)}{2} e^{-j\beta(T_1)} \tag{3-121}$$

and substituting into (3-120), the following equation is obtained:

$$\begin{aligned}
& 2j\omega_{z0} \left(\frac{a'}{2} e^{j\beta} + j\beta' \frac{a}{2} e^{j\beta} + \mu \frac{a}{2} e^{j\beta} \right) + 3a \left(\frac{a}{2} \right)^3 e^{j\beta} + 3aa\Lambda^2 e^{j\beta} + a\Lambda^3 e^{j\sigma T_1} = 0 \Rightarrow \\
& \Rightarrow \left(j\omega_{z0} a' - \omega_{z0} \beta' a + j\omega_{z0} \mu a + 3a \left(\frac{a}{2} \right)^3 + 3aa\Lambda^2 \right) e^{j\beta} + a\Lambda^3 e^{j\sigma T_1} = 0 \Rightarrow \\
& \Rightarrow j\omega_{z0} a' - \omega_{z0} \beta' a + j\omega_{z0} \mu a + 3a \left(\frac{a}{2} \right)^3 + 3aa\Lambda^2 + \\
& + a\Lambda^3 (\cos(\sigma T_1 - \beta) + j \sin(\sigma T_1 - \beta)) = 0
\end{aligned} \tag{3-122}$$

Separating the real and imaginary parts of the above equation and setting $\gamma = \sigma T_1 - \beta$, a system of differential equations is derived:

$$(a): a' = -\mu a - \frac{a\Lambda^3}{\omega_{z0}} \sin \gamma \tag{3-123}$$

$$\begin{aligned}
(b): \frac{3aa^3}{8} - a\omega_{z0}\beta' + 3aa\Lambda^2 + a\Lambda^3 \cos \gamma &= 0 \Rightarrow \\
\Rightarrow a(\sigma - \gamma') &= \frac{3aa^3}{8\omega_{z0}} + \frac{3aa\Lambda^2}{\omega_{z0}} + \frac{a\Lambda^3}{\omega_{z0}} \cos \gamma \Rightarrow \\
\Rightarrow a\gamma' &= a \left(\sigma - \frac{3a\Lambda^2}{\omega_{z0}} \right) - \frac{3aa^3}{8\omega_{z0}} - \frac{a\Lambda^3}{\omega_{z0}} \cos \gamma
\end{aligned} \tag{3-124}$$

Steady-state motions require that $a' = \gamma' = 0$, and Eqs. (3-123) and (3-124) become:

$$(a): -\mu a = \frac{a\Lambda^3}{\omega_{z0}} \sin \gamma \tag{3-125}$$

$$(b): \left(\sigma - \frac{3a\Lambda^2}{\omega_{z0}} - \frac{3aa^2}{8\omega_{z0}} \right) a = \frac{a\Lambda^3}{\omega_{z0}} \cos \gamma \tag{3-126}$$

The phase of the periodic solution is computed as:

$$\tan \gamma = - \frac{\mu}{\sigma - \frac{3a\Lambda^2}{\omega_{z0}} - \frac{3aa^2}{8\omega_{z0}}} \tag{3-127}$$

The peak amplitude of the free oscillation term is calculated from Eq. (3-125), for $\sin \gamma = -1$:

$$a_p = \frac{a\Lambda^3}{\mu\omega_{z0}} \tag{3-128}$$

which depends on the cubic term coefficient a . The corresponding value of the frequency detuning σ is obtained by Eq. (3-126) for $\cos \gamma = 0$:

$$\sigma_p = \frac{3a\Lambda^2}{\omega_{z0}} \left(1 + \frac{a^2\Lambda^4}{8\mu^2\omega_{z0}^2} \right) \tag{3-129}$$

The frequency-amplitude relation for the superharmonic resonance is expressed as:

$$\left[\left(\sigma - \frac{3a\Lambda^2}{\omega_{z0}} - \frac{3aa^2}{8\omega_{z0}} \right)^2 + \mu^2 \right] a^2 = \frac{a^2\Lambda^6}{\omega_{z0}^2} \Rightarrow \sigma = \frac{3a\Lambda^2}{\omega_{z0}} + \frac{3aa^2}{8\omega_{z0}} \pm \sqrt{\frac{a^2\Lambda^6}{\omega_{z0}^2 a^2} - \mu^2} \quad (3-130)$$

A typical frequency – response curve for the case of superharmonic resonance is illustrated in Figure 3-34. When conditions for superharmonic resonance hold, for excitations of large amplitude and loading frequency approximately equal to $\omega_{z0}/3$, the amplitude of the oscillation does not decay to zero, in spite of the presence of damping, in contrast to linear systems. In addition, a hardening response of the system leads to the bending of the response curve, hysteresis loops and jump phenomena.

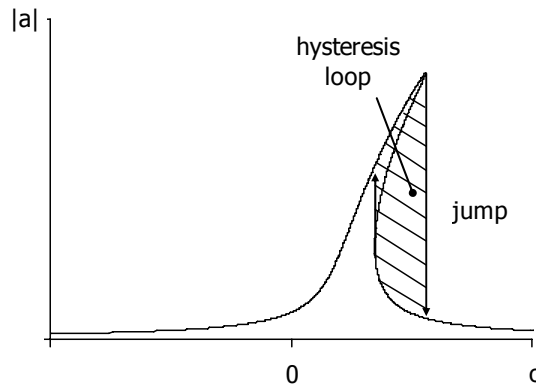


Figure 3-34: Superharmonic resonance: Amplitude $|a|$ vs. frequency detuning σ

The response of the nonlinear system at steady state, defined by Eq. (3-87), is expressed as:

$$\begin{aligned} w(t) &= a \cos(\omega_{z0}t + \beta_0) + P \left(\frac{1}{\omega_{z0}^2 - \Omega^2} \right) \cos \Omega t + O(\varepsilon) \Rightarrow \\ \Rightarrow w(t) &= a \cos(\omega_{z0}t + \varepsilon\sigma t - \gamma_0) + P \left(\frac{1}{\omega_{z0}^2 - \Omega^2} \right) \cos \Omega t + O(\varepsilon) \Rightarrow \\ \Rightarrow w(t) &= a \cos(3\Omega t - \gamma_0) + P \left(\frac{1}{\omega_{z0}^2 - \Omega^2} \right) \cos \Omega t + O(\varepsilon) \end{aligned} \quad (3-131)$$

having a term with the same frequency as the excitation and a free oscillation term whose frequency is exactly three times the frequency of the excitation. The amplitude of the oscillation a can be calculated from Eq. (3-130). The maximum amplitude is equal to:

$$\max w = a_p + P \left(\frac{1}{\omega_{z0}^2 - \Omega^2} \right) = \frac{a\Lambda^3}{\mu\omega_{z0}} + 2\Lambda \quad (3-132)$$

where Λ is expressed by Eq. (3-88). Setting the maximum amplitude equal to the maximum permissible deflection w_{\max} , as defined by Eq. (3-48) and illustrated in Figure 3-7, Eq. (3-132) becomes:

$$\frac{a\Lambda^3}{\mu\omega_{z0}} + 2\Lambda = w_{\max} \quad (3-133)$$

which has one real root and two non real complex conjugate roots for Λ . The real root is:

$$\Lambda_0 = \frac{G}{6a} - \frac{4\mu\omega_{z0}}{G} \quad (3-134)$$

where

$$G = \left[\mu a^2 \omega_{z0} \left(108w_{\max} + 12 \sqrt{\frac{96\mu\omega_{z0} + 81aw_{\max}^2}{a}} \right) \right]^{1/3} \quad (3-135)$$

The load amplitude, corresponding to Λ_0 according to Eq. (3-88), is:

$$P_0 = 2M \cdot \Lambda_0 \cdot (\omega_{z0}^2 - \Omega^2) \quad (3-136)$$

with

$$\Omega = \frac{1}{3} \cdot (\omega_{z0} + \sigma_p) = \frac{1}{3} \cdot \left[\omega_{z0} + \frac{3a\Lambda_0^2}{\omega_{z0}} \left(1 + \frac{a^2\Lambda_0^4}{8\mu^2\omega_{z0}^2} \right) \right] \quad (3-137)$$

The ratio of the dynamic load P_0 , which causes the maximum deflection, over the corresponding static one P_{\max} , illustrated in Figure 3-8, with respect to the sag-to-span ratio, for damping ratios $\zeta=0.5\%$ and $\zeta=2\%$, is shown in Figure 3-35.

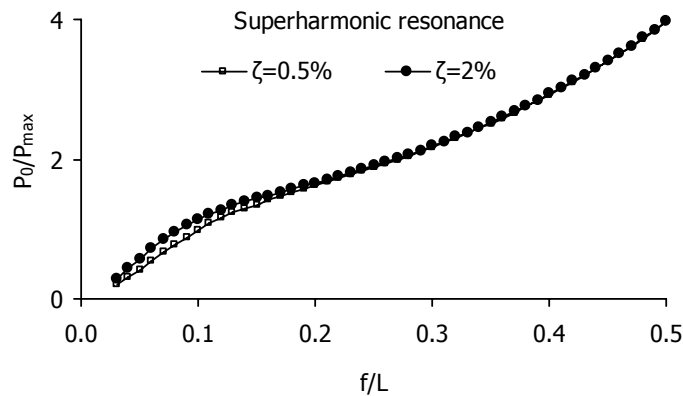


Figure 3-35: Variation of the ratio of the maximum permissible dynamic load P_0 over the maximum permissible static load P_{\max} , with respect to the sag-to-span ratio, for the case of superharmonic resonance

In this case, the maximum permissible dynamic load, for sag/span ratios larger than $f/L=0.08$ for $\zeta=2\%$ and $f/L=0.10$ for $\zeta=0.5\%$, is larger than the static one (Figure 3-36), meaning that only for small sag-to-span ratios and for dynamic load amplitudes smaller but near the maximum permissible static loads, the superharmonic resonance may cause cable failure. This means that for large sag-to-span ratios, corresponding to very deep cable nets, static loading is more crucial than dynamic one under superharmonic resonance.

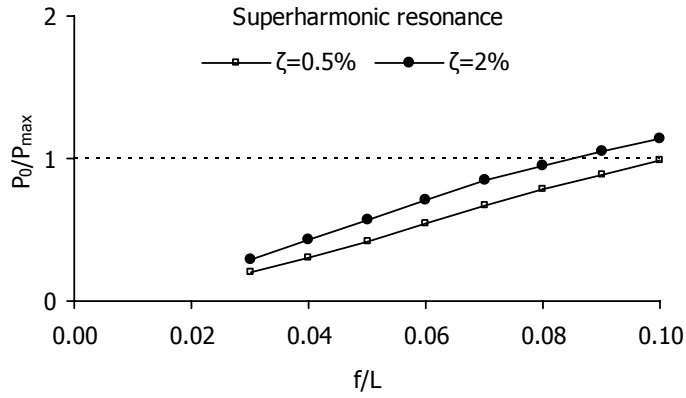


Figure 3-36: Variation of the ratio of the maximum dynamic load P_0 over the maximum static load P_{max} , with respect to the sag-to-span ratio between the range of 0.03 and 0.10, for the case of superharmonic resonance

3.3.4 Forced vibration of the system – Subharmonic resonance

Considering now a loading frequency $\Omega \approx 3\omega_{z0}$ and a detuning parameter σ , such that:

$$\Omega = 3\omega_{z0} + \varepsilon\sigma, \quad \text{with } \sigma = O(1) \quad (3-138)$$

in Eq. (3-89) the term proportional to $e^{j(\Omega - 2\omega_{z0})T_0}$ is another secular term, which can be written as $e^{j(\omega_{z0}T_0 + \sigma T_1)} = e^{j\omega_{z0}T_0} e^{j\sigma T_1}$. Hence, eliminating all secular terms:

$$2j\omega_{z0}(D_1A + \mu A) + 3aA^2\bar{A} + 6aA\Lambda^2 + 3a\bar{A}^2\Lambda e^{j\sigma T_1} = 0 \quad (3-139)$$

and setting:

$$A(T_1) = \frac{a(T_1)}{2} e^{j\beta(T_1)} \quad \text{and} \quad \bar{A}(T_1) = \frac{a(T_1)}{2} e^{-j\beta(T_1)} \quad (3-140)$$

Eq. (3-139) gives the following expression:

$$\begin{aligned} & 2j\omega_{z0} \left(\frac{a'}{2} e^{j\beta} + j\beta' \frac{a}{2} e^{j\beta} + \mu \frac{a}{2} e^{j\beta} \right) + 3a \left(\frac{a}{2} \right)^3 e^{j\beta} + 3aa\Lambda^2 e^{j\beta} + 3a\bar{A}^2\Lambda e^{j\sigma T_1} = 0 \Rightarrow \\ & \Rightarrow \left(j\omega_{z0}a' - \omega_{z0}\beta'a + j\omega_{z0}\mu a + 3a \left(\frac{a}{2} \right)^3 + 3aa\Lambda^2 \right) e^{j\beta} + \frac{3aa^2}{4} e^{-2j\beta} \Lambda e^{j\sigma T_1} = 0 \Rightarrow \\ & \Rightarrow j\omega_{z0}a' - \omega_{z0}\beta'a + j\omega_{z0}\mu a + 3a \left(\frac{a}{2} \right)^3 + 3aa\Lambda^2 + \\ & + \frac{3aa^2}{4} \Lambda (\cos(\sigma T_1 - 3\beta) + j \sin(\sigma T_1 - 3\beta)) = 0 \end{aligned} \quad (3-141)$$

Separating the real and imaginary parts and setting $\gamma = \sigma T_1 - 3\beta$, the following differential equations are obtained:

$$(a): a' = -\mu a - \frac{3aa^2\Lambda}{4\omega_{z0}} \sin \gamma \quad (3-142)$$

$$(b): \frac{3aa^3}{8} - a\omega_{z0}\beta' + 3aa\Lambda^2 + \frac{3aa^2}{4} \Lambda \cos \gamma = 0 \Rightarrow \quad (3-143)$$

$$\begin{aligned} \Rightarrow \frac{a}{3}(\sigma - \gamma') &= \frac{3aa^3}{8\omega_{z0}} + \frac{3aa\Lambda^2}{\omega_{z0}} + \frac{3aa^2\Lambda}{4\omega_{z0}} \cos \gamma \Rightarrow \\ \Rightarrow a\gamma' &= a \left(\sigma - \frac{9a\Lambda^2}{\omega_{z0}} \right) - \frac{9aa^3}{8\omega_{z0}} - \frac{9aa^2\Lambda}{4\omega_{z0}} \cos \gamma \end{aligned}$$

The steady-state motions correspond to $a'=\gamma'=0$, and Eq. (3-142) and (3-143) become:

$$(a): -\mu a = \frac{3aa^2\Lambda}{4\omega_{z0}} \sin \gamma, (b): \left(\sigma - \frac{9a\Lambda^2}{\omega_{z0}} - \frac{9aa^2}{8\omega_{z0}} \right) a = \frac{9aa^2\Lambda}{4\omega_{z0}} \cos \gamma \quad (3-144)$$

The frequency-amplitude relation for the subharmonic resonance is expressed as:

$$\left[\left(\sigma - \frac{9a\Lambda^2}{\omega_{z0}} - \frac{9aa^2}{8\omega_{z0}} \right)^2 + 9\mu^2 \right] a^2 = \frac{81a^2\Lambda^2}{16\omega_{z0}^2} a^4 \quad (3-145)$$

Eq. (3-145) has a double zero solution, called trivial solution ($a=0$) and two non-zero ones, denoted as nontrivial ones, defined as:

$$\begin{aligned} \left(\sigma - \frac{9a\Lambda^2}{\omega_{z0}} - \frac{9a}{8\omega_{z0}} a^2 \right)^2 + 9\mu^2 &= \frac{81a^2\Lambda^2}{16\omega_{z0}^2} a^2 \Rightarrow \\ \Rightarrow \left(\sigma - \frac{9a\Lambda^2}{\omega_{z0}} \right)^2 + \left(\frac{9a}{8\omega_{z0}} a^2 \right)^2 - 2 \left(\sigma - \frac{9a\Lambda^2}{\omega_{z0}} \right) \frac{9a}{8\omega_{z0}} a^2 + 9\mu^2 &= \frac{81a^2\Lambda^2}{16\omega_{z0}^2} a^2 \Rightarrow \\ \Rightarrow \left(\frac{9a}{8\omega_{z0}} \right)^2 a^4 - \left(\frac{81a^2\Lambda^2}{16\omega_{z0}^2} + \left(\sigma - \frac{9a\Lambda^2}{\omega_{z0}} \right) \frac{18a}{8\omega_{z0}} \right) a^2 + \left(\sigma - \frac{9a\Lambda^2}{\omega_{z0}} \right)^2 + 9\mu^2 &= 0 \Rightarrow \\ \Rightarrow a^2 = c \pm \sqrt{c^2 - s} \end{aligned} \quad (3-146)$$

where

$$s = \frac{64\omega_{z0}^2}{81a^2} \left[\left(\sigma - \frac{9a\Lambda^2}{\omega_{z0}} \right)^2 + 9\mu^2 \right] \text{ and } c = \left(\sigma \frac{8\omega_{z0}}{9a} - 6\Lambda^2 \right) \quad (3-147)$$

One of the two nontrivial solutions is stable and the other one is unstable. For nontrivial solutions, it is required that, $c>0$ and $c^2 \geq s$. Thus, it must be satisfied that:

$$\begin{aligned} a) \text{ for a given } \sigma \\ c^2 \geq s \Rightarrow \sigma \geq \frac{63a}{8\omega_{z0}} \Lambda^2 + \frac{2\omega_{z0}}{a} \frac{\mu^2}{\Lambda^2} \Rightarrow \frac{63a}{8\omega_{z0}} \Lambda^4 - \sigma \Lambda^2 + \frac{2\omega_{z0}}{a} \mu^2 \leq 0 \Rightarrow \\ \Rightarrow \frac{\sigma}{\mu} - \sqrt{\frac{\sigma^2}{\mu^2} - 63} \leq \frac{63a}{4\omega_{z0}\mu} \Lambda^2 \leq \frac{\sigma}{\mu} + \sqrt{\frac{\sigma^2}{\mu^2} - 63} \end{aligned} \quad (3-148)$$

b) for a given Λ

$$\begin{aligned}
 c^2 \geq s &\Rightarrow \left(\frac{8\omega_{z0}}{9a} \sigma - 6\Lambda^2 \right)^2 \geq \frac{64\omega_{z0}^2}{81a^2} \left[\left(\sigma - \frac{9a\Lambda^2}{\omega_{z0}} \right)^2 + 9\mu^2 \right] \Rightarrow \\
 &\Rightarrow -2 \frac{48\omega_{z0}}{9a} \sigma \Lambda^2 + 36\Lambda^4 \geq \frac{64\omega_{z0}^2}{81a^2} \left(-2\sigma \frac{9a\Lambda^2}{\omega_{z0}} + \left(\frac{9a\Lambda^2}{\omega_{z0}} \right)^2 \right) + \frac{64\omega_{z0}^2}{9a^2} \mu^2 \Rightarrow \quad (3-149) \\
 &\Rightarrow -\frac{32\omega_{z0}}{9a} \sigma \Lambda^2 + 36\Lambda^4 \geq \left(-2 \frac{64\omega_{z0}}{9a} \sigma \Lambda^2 + 64\Lambda^4 \right) + \frac{64\omega_{z0}^2}{9a^2} \mu^2 \Rightarrow \\
 &\Rightarrow \sigma \geq \frac{63a}{8\omega_{z0}} \Lambda^2 + \frac{2\omega_{z0}}{a} \frac{\mu^2}{\Lambda^2}
 \end{aligned}$$

The above conditions define a region in which subharmonic solutions appear. This region and a typical frequency – response curve for the case of subharmonic resonance are illustrated in Figure 3-37.

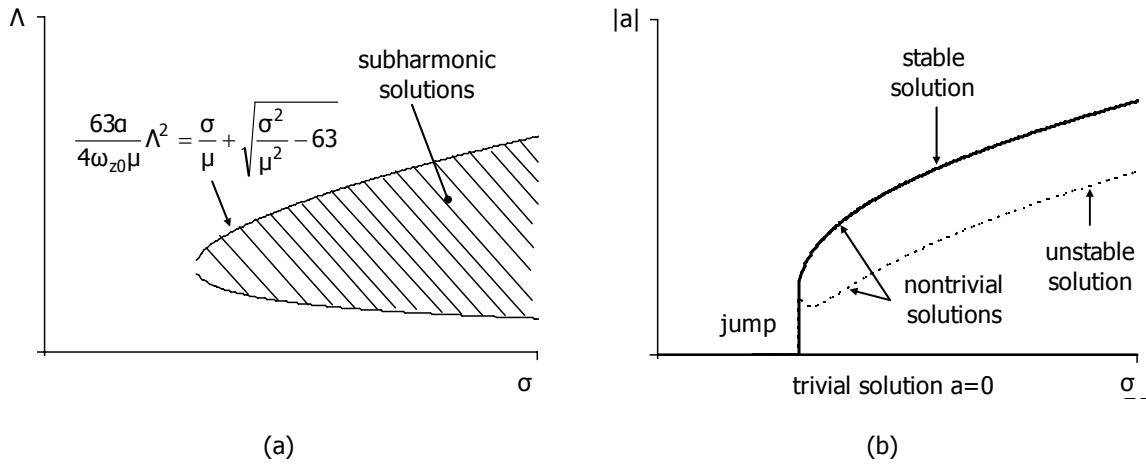


Figure 3-37: Subharmonic resonance: (a) region of subharmonic solutions, (b) Amplitude $|a|$ vs. frequency detuning σ

The initial conditions define the response amplitude of the system. For the trivial solution $a=0$, the steady-state response depends only on the external load:

$$w(t) = P \left(\frac{1}{\omega_{z0}^2 - \Omega^2} \right) \cos \Omega t + O(\varepsilon) \quad (3-150)$$

while for the non-trivial stable solution of a the response of the nonlinear system at steady state is:

$$\begin{aligned}
 w(t) &= a \cos(\omega_{z0}t + \beta_0) + P \left(\frac{1}{\omega_{z0}^2 - \Omega^2} \right) \cos \Omega t + O(\varepsilon) \Rightarrow \\
 &\Rightarrow w(t) = a \cos \left(\frac{3\omega_{z0}t + \varepsilon\sigma t - \gamma_0}{3} \right) + P \left(\frac{1}{\omega_{z0}^2 - \Omega^2} \right) \cos \Omega t + O(\varepsilon) \Rightarrow \quad (3-151) \\
 &\Rightarrow w(t) = a \cos \left(\frac{\Omega t - \gamma_0}{3} \right) + P \left(\frac{1}{\omega_{z0}^2 - \Omega^2} \right) \cos \Omega t + O(\varepsilon)
 \end{aligned}$$

having a term with the same frequency as the excitation and a free oscillation term whose frequency is exactly one-third the frequency of the excitation. The existence of multiple solutions, depending on

the initial conditions, renders the dynamic behaviour of the system unpredictable and in some cases with catastrophic results.

3.3.5 Free vibration of the system

If $\mu=p=0$ Eq. (3-107) becomes:

$$\begin{aligned} a' &= 0 \Rightarrow a = a_0 \\ 3a\left(\frac{a}{2}\right)^3 - a\omega_{z0}\beta' &= 0 \Rightarrow \beta' = \frac{3aa_0^2}{8\omega_{z0}} \Rightarrow \beta = \frac{3aa_0^2}{8\omega_{z0}} T_1 + \beta_0 \end{aligned} \quad (3-152)$$

where a_0 and β_0 are constants, defined by the initial conditions. Hence, the function $A(T_1)$, defined by Eq. (3-105), becomes:

$$A(T_1) = \frac{a_0}{2} \exp\left[j \frac{3aa_0^2}{8\omega_{z0}} T_1 + j\beta_0\right] \text{ and } \bar{A}(T_1) = \frac{a_0}{2} \exp\left[-j \frac{3aa_0^2}{8\omega_{z0}} T_1 - j\beta_0\right] \quad (3-153)$$

For $\mu=p=0$, from Eq. (3-117):

$$\sigma = \frac{3aa^2}{8\omega_{z0}} \quad (3-154)$$

thus:

$$\Omega = \omega_{z0} + \varepsilon \frac{3aa_0^2}{8\omega_{z0}} \quad (3-155)$$

and combining the previous results of Eqs. (3-99), (3-102), (3-105), (3-153) and (3-155), one obtains the periodic solution:

$$\begin{aligned} w(t, \varepsilon) &= \frac{a_0}{2} \exp\left[j \frac{3aa_0^2}{8\omega_{z0}} \varepsilon T_0 + j\beta_0 + j\omega_{z0} T_0\right] + \\ &+ \frac{a_0}{2} \exp\left[-j \frac{3aa_0^2}{8\omega_{z0}} \varepsilon T_0 - j\beta_0 - j\omega_{z0} T_0\right] + O(\varepsilon) \Rightarrow \\ w(t, \varepsilon) &= a_0 \cos(\Omega t + \beta_0) + O(\varepsilon) \end{aligned} \quad (3-156)$$

3.3.6 Stability of the system

In order to investigate the stability of the system, we set $a=a_0+a_1$ and $\gamma=\gamma_0+\gamma_1$ with $|a_1| \ll |a_0|$ and $|\gamma_1| \ll |\gamma_0|$. Assuming that $a_1\gamma_1 \approx 0$, $\sin\gamma_1 \approx \gamma_1$, $\cos\gamma_1 \approx 1$, Eqs. (3-109) will be:

$$\begin{aligned} \text{(a): } a'_0 + a'_1 &= -\mu(a_0 + a_1) + \frac{p}{2\omega_{z0}} \sin(\gamma_0 + \gamma_1) \Rightarrow \\ &\Rightarrow a'_0 + a'_1 = -\mu(a_0 + a_1) + \frac{p}{2\omega_{z0}} (\sin\gamma_0 + \gamma_1 \cos\gamma_0) \Rightarrow \\ &\Rightarrow a'_1 = -\mu a_1 + \frac{p}{2\omega_{z0}} \gamma_1 \cos\gamma_0 \end{aligned} \quad (3-157)$$

$$\begin{aligned}
\text{(b): } (\gamma'_0 + \gamma'_1) &= \sigma - \frac{3a(a_0 + a_1)^2}{8\omega_{z0}} + \frac{p}{2\omega_{z0}(a_0 + a_1)} \cos(\gamma_0 + \gamma_1) \\
\Rightarrow \gamma'_0 + \gamma'_1 &= \sigma - \frac{3a(a_0^2 + 2a_0a_1)}{8\omega_{z0}} + \frac{p}{2\omega_{z0}a_0 \left(1 + \frac{a_1}{a_0}\right)} (\cos \gamma_0 - \gamma_1 \sin \gamma_0) \Rightarrow \\
\Rightarrow \gamma'_0 + \gamma'_1 &= \sigma - \frac{3a(a_0^2 + 2a_0a_1)}{8\omega_{z0}} + \frac{p}{2\omega_{z0}a_0} \left(1 - \frac{a_1}{a_0}\right) (\cos \gamma_0 - \gamma_1 \sin \gamma_0) \Rightarrow \quad (3-158) \\
\Rightarrow \gamma'_1 &= -\frac{3aa_0a_1}{4\omega_{z0}} - \frac{p}{2\omega_{z0}a_0} \gamma_1 \sin \gamma_0 - \frac{pa_1}{2\omega_{z0}a_0^2} \cos \gamma_0 \Rightarrow \\
\Rightarrow \gamma'_1 &= -\left(\frac{3aa_0}{4\omega_{z0}} - \frac{p}{2\omega_{z0}a_0^2} \cos \gamma_0\right) a_1 - \frac{p}{2\omega_{z0}a_0} \gamma_1 \sin \gamma_0
\end{aligned}$$

Using Eqs. (3-111), the above expressions become:

$$\text{(a): } a'_1 = -\mu a_1 - \left(a_0\sigma - \frac{3aa_0^3}{8\omega_{z0}}\right) \gamma_1, \quad \text{(b): } \gamma'_1 = -\left(\frac{\sigma}{a_0} - \frac{9aa_0}{8\omega_{z0}}\right) a_1 - \mu \gamma_1 \quad (3-159)$$

The above linear system of first order differential equations can be written as:

$$(\dot{X}) = [A](X) \Rightarrow \begin{pmatrix} a'_1 \\ \gamma'_1 \end{pmatrix} = \begin{bmatrix} -\mu & -\left(a_0\sigma - \frac{3aa_0^3}{8\omega_{z0}}\right) \\ \left(\frac{\sigma}{a_0} - \frac{9aa_0}{8\omega_{z0}}\right) & -\mu \end{bmatrix} \begin{pmatrix} a_1 \\ \gamma_1 \end{pmatrix} \quad (3-160)$$

The homogeneous solutions can be determined as:

$$a_1 = A_1 e^{\lambda t} \text{ and } \gamma_1 = \Gamma_1 e^{\lambda t} \quad (3-161)$$

which have to satisfy Eq. (3-160):

$$\begin{aligned}
[A]e^{\lambda t} - \lambda[I]e^{\lambda t} &= 0 \Rightarrow \\
\Rightarrow \begin{bmatrix} a_{11} - \lambda & a_{12} \\ a_{21} & a_{22} - \lambda \end{bmatrix} &= \begin{bmatrix} -\mu - \lambda & -\left(a_0\sigma - \frac{3aa_0^3}{8\omega_{z0}}\right) \\ \left(\frac{\sigma}{a_0} - \frac{9aa_0}{8\omega_{z0}}\right) & -\mu - \lambda \end{bmatrix} = 0 \quad (3-162)
\end{aligned}$$

The above system has non-trivial solutions if and only if $\det([A]-\lambda[I])=0$, thus:

$$\begin{aligned}
\begin{vmatrix} -\mu - \lambda & -\left(a_0\sigma - \frac{3aa_0^3}{8\omega_{z0}}\right) \\ \left(\frac{\sigma}{a_0} - \frac{9aa_0}{8\omega_{z0}}\right) & -\mu - \lambda \end{vmatrix} &= 0 \Rightarrow \lambda^2 - (a_{11} + a_{22})\lambda + \det[A] = 0 \Rightarrow \\
\Rightarrow \lambda^2 + 2\lambda\mu + \mu^2 + \left(\sigma - \frac{3aa_0^2}{8\omega_{z0}}\right) \left(\sigma - \frac{9aa_0^2}{8\omega_{z0}}\right) &= 0 \quad (3-163)
\end{aligned}$$

The above expression can be written as:

$$\lambda^2 - r\lambda + q = 0 \text{ with } \Delta=r^2 - 4q \tag{3-164}$$

where:

$$r=(a_{11}+a_{22})=-2\mu \text{ and } q = \det[A] = \mu^2 + \left(\sigma - \frac{3\alpha a_0^2}{8\omega_{z0}} \right) \left(\sigma - \frac{9\alpha a_0^2}{8\omega_{z0}} \right) \tag{3-165}$$

If λ_1 and λ_2 are the eigenvalues of A, then Eq. (3-164) can be written as:

$$\lambda^2 - r\lambda + q = (\lambda - \lambda_1)(\lambda - \lambda_2) = \lambda^2 - (\lambda_1 + \lambda_2)\lambda + \lambda_1\lambda_2 \tag{3-166}$$

Hence, r is the sum of the eigenvalues, q is the product and Δ the discriminant. The following criteria can be set regarding critical points:

- Node: if $q>0$ and $\Delta\geq 0$
- Saddle: if $q<0$
- Centre: if $r=0$ and $q>0$
- Spiral: if $r\neq 0$ and $\Delta<0$

A point K_0 is called stable critical point if all trajectories that at some instant are sufficiently close to K_0 remain close to K_0 at all future times. It is called a stable and attractive critical point if it is stable and every trajectory approaches K_0 as $t \rightarrow \infty$. It is called unstable if it is not stable. A critical point K_0 is:

- Stable and attractive: if $r<0$ and $q>0$
- Stable: if $r\leq 0$ and $q>0$
- Unstable: if $r>0$ or $q<0$

according to the stability criteria for critical points ([3-31] and [3-40]). The above criteria are summarised in the chart of Figure 3-38:

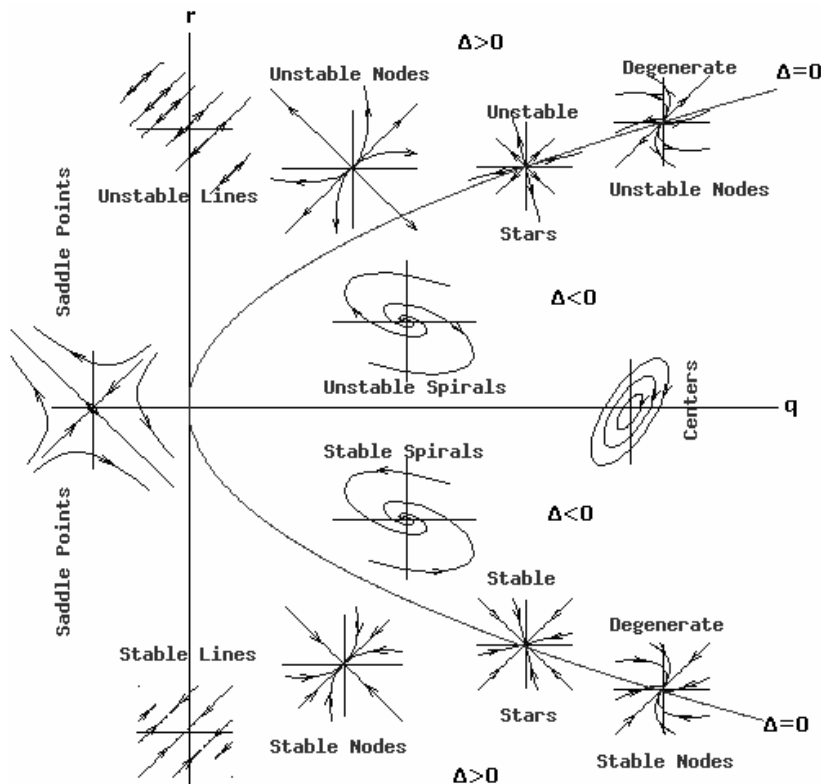


Figure 3-38: Stability chart (from [3-41])

Provided that $r=-2\mu$, which means that it is always $r \leq 0$ with $\lambda_1 + \lambda_2 < 0$, in order to have stability, both eigenvalues must have non-positive real parts, thus $q = \lambda_1 \lambda_2 > 0$. Thus, the steady-state motions will be unstable only if:

$$q = \mu^2 + \left(\sigma - \frac{3aa_0^2}{8\omega_{z0}} \right) \left(\sigma - \frac{9aa_0^2}{8\omega_{z0}} \right) < 0 \tag{3-167}$$

For $\mu=0$, the instability region is defined by two curves. The first one is the backbone curve, expressed as:

$$\sigma = \frac{3aa_0^2}{8\omega_{z0}} \tag{3-168}$$

and the second one is defined as:

$$\sigma = \frac{9aa_0^2}{8\omega_{z0}} \tag{3-169}$$

The unstable solutions are for values of frequency detuning σ :

$$\frac{3aa_0^2}{8\omega_{z0}} < \sigma < \frac{9aa_0^2}{8\omega_{z0}} \tag{3-170}$$

In this case, the diagram of the steady-state response is illustrated in Figure 3-39.

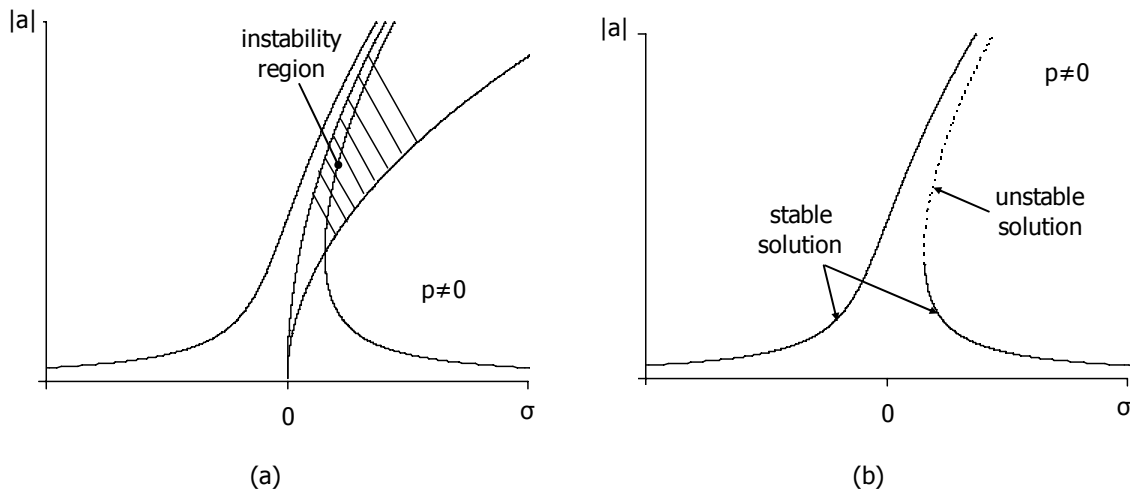


Figure 3-39: (a) Instability region, (b) Stable and unstable solutions without damping

For $\mu \neq 0$, the instability region is defined again by two curves. The first one is expressed as:

$$\sigma = \frac{6aa_0^2}{8\omega_{z0}} + \sqrt{\left(\frac{3aa_0^2}{8\omega_{z0}} \right)^2 - \mu^2} \tag{3-171}$$

while the second one is:

$$\sigma = \frac{6aa_0^2}{8\omega_{z0}} - \sqrt{\left(\frac{3aa_0^2}{8\omega_{z0}}\right)^2 - \mu^2} \quad (3-172)$$

Unstable solutions appear for values of frequency detuning σ :

$$\frac{6aa_0^2}{8\omega_{z0}} - \sqrt{\left(\frac{3aa_0^2}{8\omega_{z0}}\right)^2 - \mu^2} < \sigma < \frac{6aa_0^2}{8\omega_{z0}} + \sqrt{\left(\frac{3aa_0^2}{8\omega_{z0}}\right)^2 - \mu^2} \quad (3-173)$$

In this case, the diagram of the steady-state response is illustrated in Figure 3-40, in which it is shown how the damping influences the instability region, by restraining it.

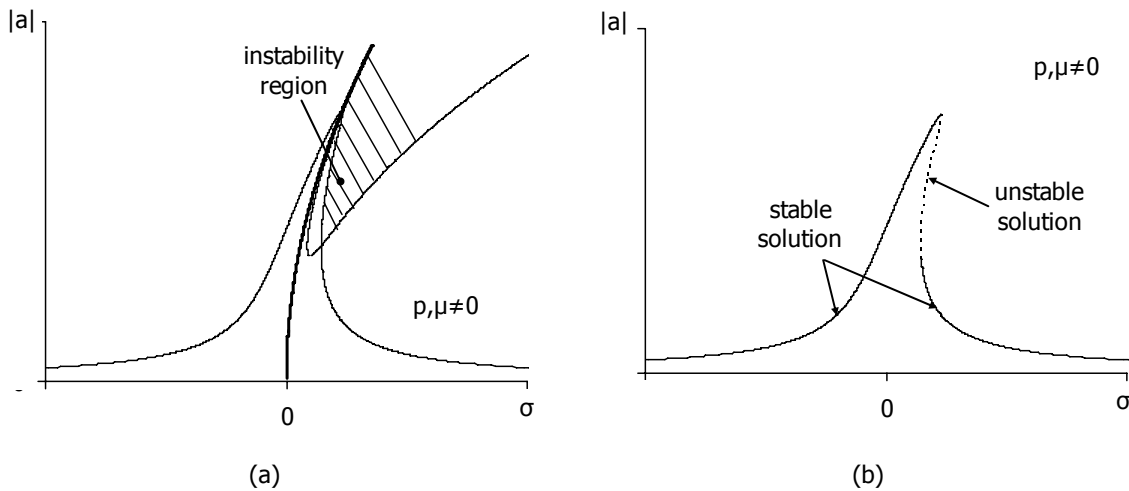


Figure 3-40: (a) Instability region, (b) Stable and unstable solutions with damping

3.3.7 Example of SDOF cable net

3.3.7.1. Eigenfrequency

In order to quantify the above conclusions, the same example described in section 3.2.6 is used. The stiffness coefficient K_{z0} , calculated according to Eq. (3-67), is:

$$K_{z0} = \frac{4EA}{L} \cdot \left(8 \frac{f^2}{L^2} + 2 \frac{N_0}{EA} - 4 \frac{N_0}{EA} \frac{f^2}{L^2} \right) = 22.51 \text{ kN/m}$$

and the corresponding natural frequency:

$$\omega_{z0} = \sqrt{\frac{K_{z0}}{M}} = \sqrt{\frac{23.20}{0.131}} = 13.19 \text{ sec}^{-1}$$

The coefficient of the nonlinear cubic term of the equation of motion of Eq. (3-76) is equal to:

$$\varepsilon a = \frac{16EA}{ML^3} = 12.66 \text{ m}^{-2} \text{ sec}^{-2} \quad (3-174)$$

3.3.7.2. Fundamental resonance

Three loading amplitudes are considered, equal to $P_0=0.1\text{kN}$, 0.3kN and 0.5kN . These loads are small with respect to the load that causes tensile failure of the cables of an undamped system in fundamental resonant conditions, equal to 1.30kN , as shown in section 3.2.6.4. The frequency-amplitude relation for the fundamental resonance ($\Omega \approx \omega_{z0}$), calculated from Eq. (3-114), and the phase of the periodic solution, computed according to Eq. (3-115), are plotted for two damping ratios, equal to $\zeta=0.5\%$ or $\epsilon\mu=0.066$ (Figure 3-41) and $\zeta=2\%$ or $\epsilon\mu=0.264$ (Figure 3-42), which are common values for cable structures. In these diagrams it can be noted that as the damping ratio decreases and the loading amplitude increases, not only the steady-state amplitude increases, but also the bending of the response curve. In addition, the phase γ depends on the loading amplitude, something that does not occur in linear systems.

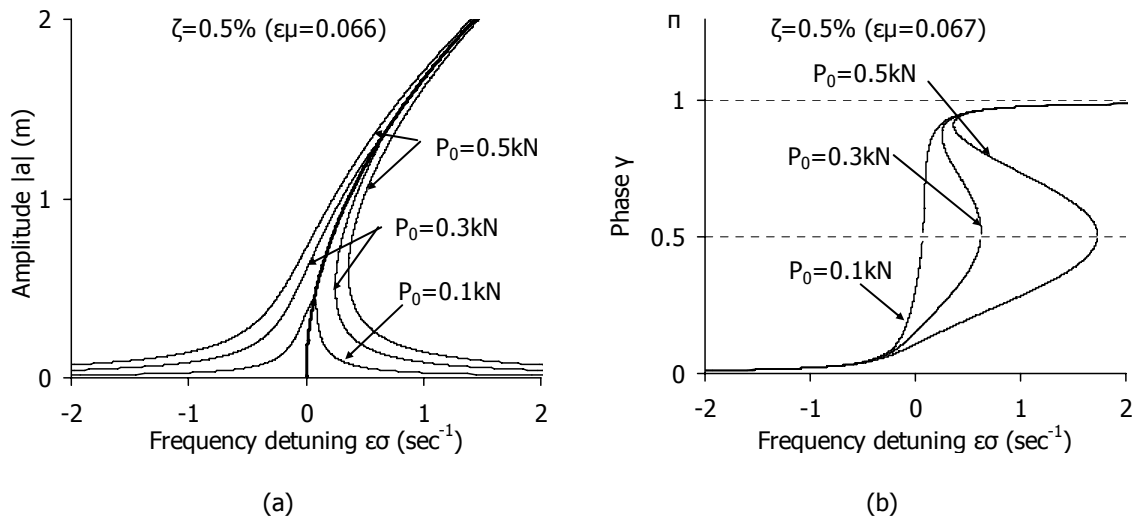


Figure 3-41: Fundamental resonance for damping ratio $\zeta=0.5\%$ (a) amplitude $|a|$ vs. frequency detuning $\epsilon\sigma$, (b) phase γ vs. frequency detuning $\epsilon\sigma$

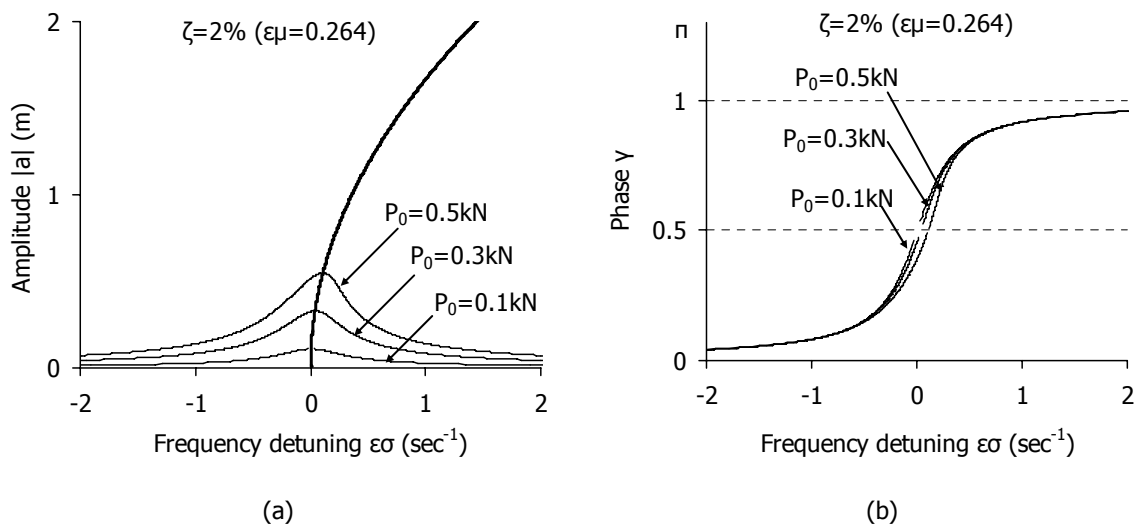


Figure 3-42: Fundamental resonance for damping ratio $\zeta=2\%$ (a) amplitude $|a|$ vs. frequency detuning $\epsilon\sigma$, (b) phase γ vs. frequency detuning $\epsilon\sigma$

Neglecting the nonlinear cubic term of the equation of motion, the corresponding frequency-amplitude diagrams of the equation of motion describing a linear system, are shown in Figure 3-43, while the phase of the periodic solution with respect of the frequency detuning is plotted in Figure 3-44, which

does not depend on the load amplitude. Comparing the two groups of diagrams, one can mention that, for large values of damping ratios, the nonlinear response of the cable net approaches the linear one.

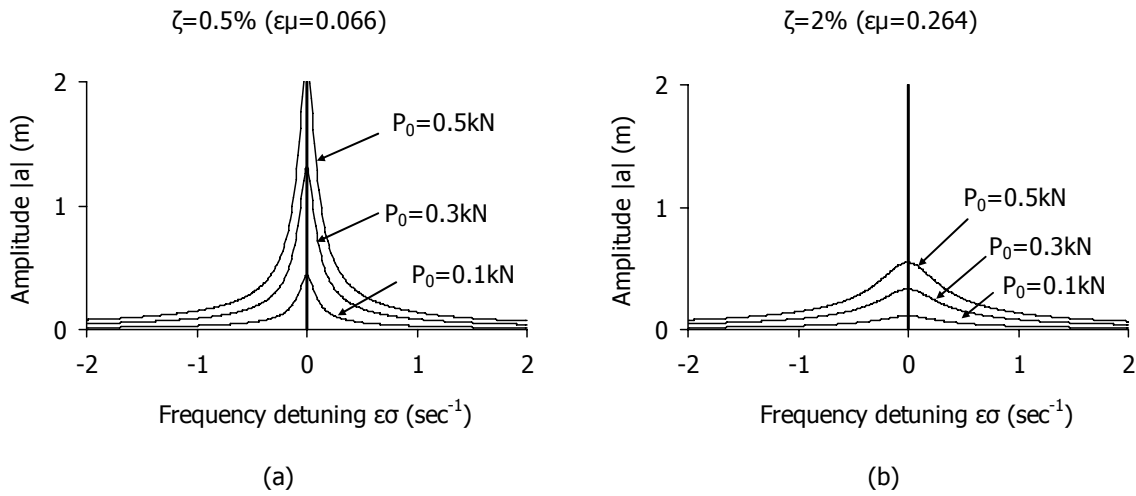


Figure 3-43: Fundamental resonance for the linear system: Amplitude $|a|$ vs. frequency detuning $\epsilon\sigma$, (a) for damping ratio $\zeta=0.5\%$, (b) for damping ratio $\zeta=2\%$

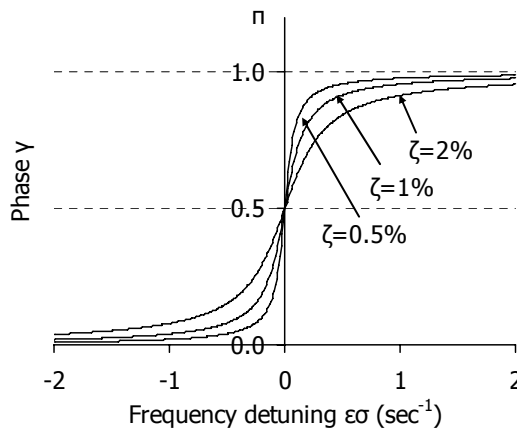


Figure 3-44: Fundamental resonance for the linear system: phase γ vs. frequency detuning $\epsilon\sigma$

If a damping ratio equal to $\zeta=0.5\%$ and a loading amplitude $P_0=0.5\text{kN}$ are considered, for a frequency detuning equal to $\epsilon\sigma=0.5\text{sec}^{-1}$, according to Eq. (3-117), one unstable steady-state response amplitude due to the cubic term is calculated as $a=1.02\text{m}$ as well as two stable ones, $a=0.31\text{m}$ (denoted as stable 1) and $a=1.28\text{m}$ (denoted as stable 2). Considering instead zero frequency detuning ($\epsilon\sigma=0.0\text{sec}^{-1}$), the steady-state response amplitude is equal to $a=0.72\text{m}$. The phase of the periodic solution for the stable solutions is $\gamma=0.11\pi$ for $\epsilon\sigma=0.0\text{sec}^{-1}$, $\gamma=0.20\pi$ for stable solution 1 and $\gamma=0.95\pi$ for stable solution 2 (Figure 3-45).

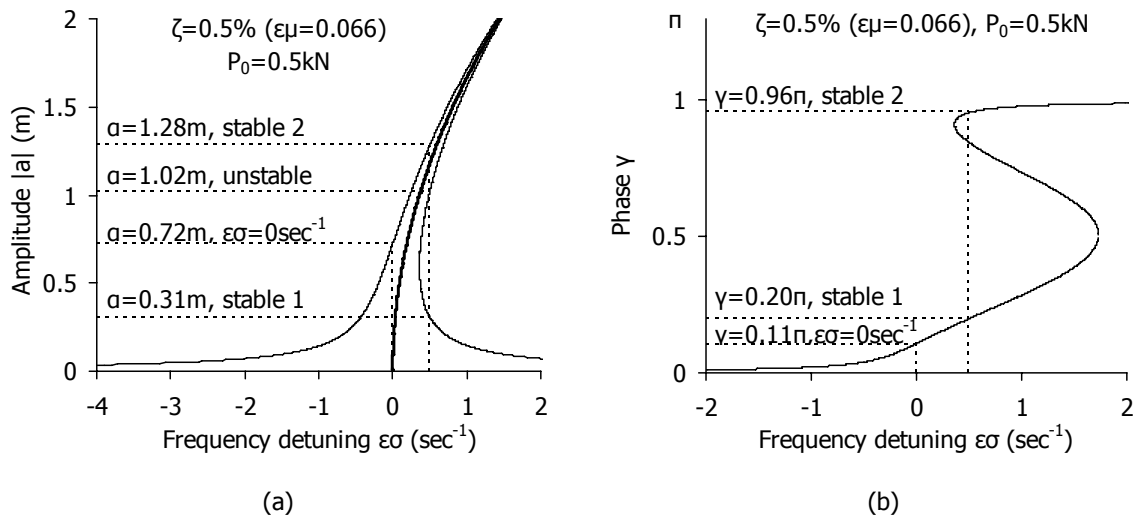


Figure 3-45: Fundamental resonance for damping ratio $\zeta=0.5\%$ and loading amplitude $P_0=0.5\text{kN}$ (a) amplitude $|a|$ vs. frequency detuning $\epsilon\sigma$, (b) phase γ vs. frequency detuning $\epsilon\sigma$

The solution of the equation of motion for the case of fundamental resonance is expressed by Eq. (3-118), where the maximum steady-state amplitude of the vertical displacement can be calculated for the above cases, as:

$$\epsilon\sigma=0.5\text{sec}^{-1}, a=0.31\text{m (stable 1)} \tag{3-175}$$

$$\epsilon\sigma=0.5\text{sec}^{-1}, a=1.28\text{m (stable 2)} \tag{3-176}$$

$$\epsilon\sigma=0.0\text{sec}^{-1}, a=0.72\text{m} \tag{3-177}$$

The time-history diagram of the steady-state vertical displacement, for both stable solutions with frequency detuning $\epsilon\sigma=0.5\text{sec}^{-1}$, is shown in Figure 3-46 and for zero frequency detuning in Figure 3-47.

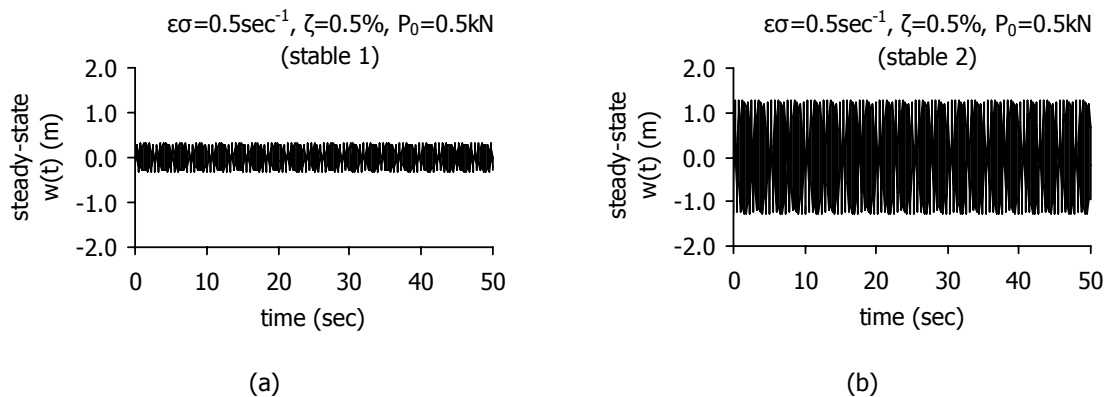


Figure 3-46: Fundamental resonance: Time-history diagram of the steady-state response for frequency detuning $\epsilon\sigma=0.5\text{sec}^{-1}$, damping ratio $\zeta=0.5\%$ and loading amplitude $P_0=0.5\text{kN}$: (a) stable solution 1, (b) stable solution 2

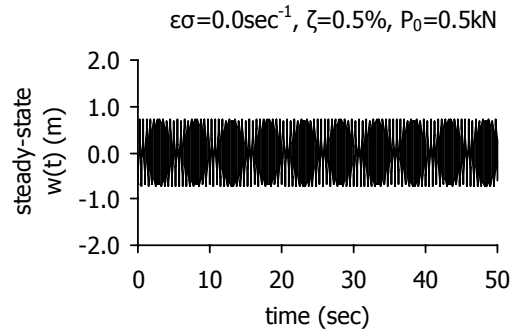


Figure 3-47: Fundamental resonance: Time-history diagram of the steady-state response for zero frequency detuning ($\varepsilon\sigma=0.0\text{sec}^{-1}$), damping ratio $\zeta=0.5\%$ and loading amplitude $P_0=0.5\text{kN}$

The minimum values of the steady-state displacements for these three stable solutions can be obtained by solving numerically the equation of motion, described by Eq. (3-74), using MATLAB. At the end of the calculation, the system vibrates with the steady-state amplitudes. In Figure 3-48 the time-history diagram of the central node vertical displacement is illustrated, for frequency detuning $\varepsilon\sigma=0.5\text{sec}^{-1}$, damping ratio $\zeta=0.5\%$ and loading amplitude $P_0=0.5\text{kN}$. For the stable solution 1, zero initial conditions are taken into account, while the stable solution 2 is realised considering initial velocity 20m/sec. In Figure 3-49, the time-history diagram of the vertical displacement is plotted, for zero frequency detuning, damping ratio $\zeta=0.5\%$, loading amplitude $P_0=0.5\text{kN}$ and zero initial conditions.

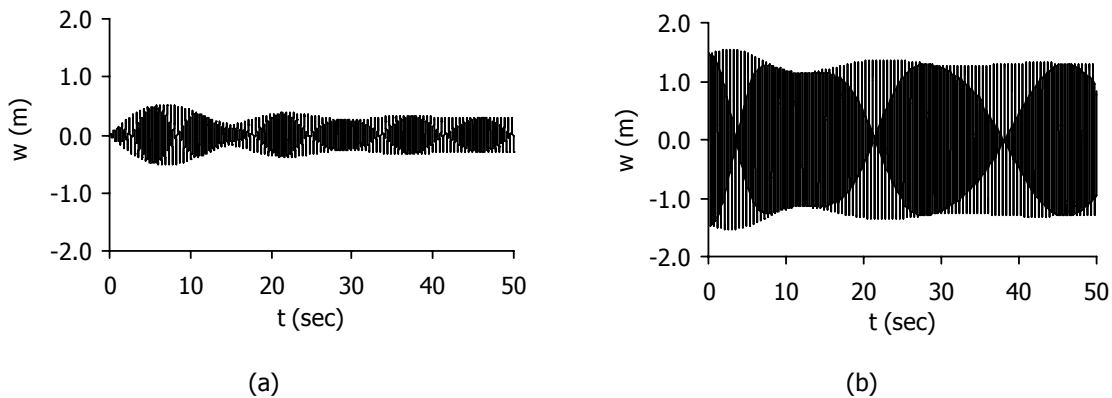


Figure 3-48: Fundamental resonance: Time-history diagram of the central node displacement for frequency detuning $\varepsilon\sigma=0.5\text{sec}^{-1}$, damping ratio $\zeta=0.5\%$ and loading amplitude $P_0=0.5\text{kN}$ for (a) zero initial conditions (stable solution 1), (b) initial velocity 20m/sec (stable solution 2)

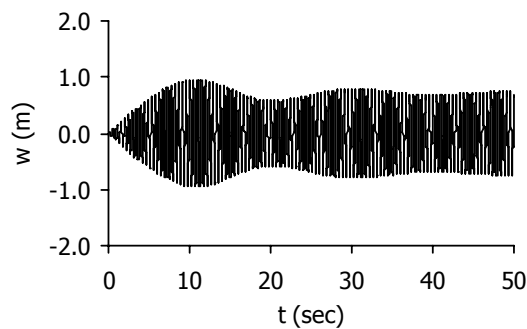


Figure 3-49: Fundamental resonance: Time-history diagram of the central node displacement for zero frequency detuning ($\varepsilon\sigma=0.0\text{sec}^{-1}$), damping ratio $\zeta=0.5\%$ and loading amplitude $P_0=0.5\text{kN}$

The dependence of the response amplitude on the initial conditions, the bending of the response curve and the jump phenomena, confirmed analytically and numerically, prove that the simple cable net, when subjected to a harmonic load with frequency close to the natural frequency of the system, exhibits an intense nonlinear dynamic behaviour.

3.3.7.3. Superharmonic resonance

For damping ratio equal to $\zeta=0.5\%$ ($\epsilon\mu=0.066$) and loading amplitudes $P_0=8\text{kN}$, 10kN and 12kN , the frequency-amplitude relation for the superharmonic resonance ($\Omega\approx\omega_{z0}/3$) calculated from Eq. (3-130) is shown in Figure 3-50. These loads are smaller than the one causing failure of the cables of an undamped system in superharmonic resonant conditions, equal to 19.97kN as shown in section 3.2.6.4 and much smaller than the maximum static load, which is equal to 40.20kN as shown in section 3.2.6.2. It can be noted that, in case the frequency detuning is small with respect to the frequency of the system, only large loads, close to the breaking loads, can produce superharmonic resonance with large response amplitudes. In addition, the larger the load amplitude, the more the response curve bends.

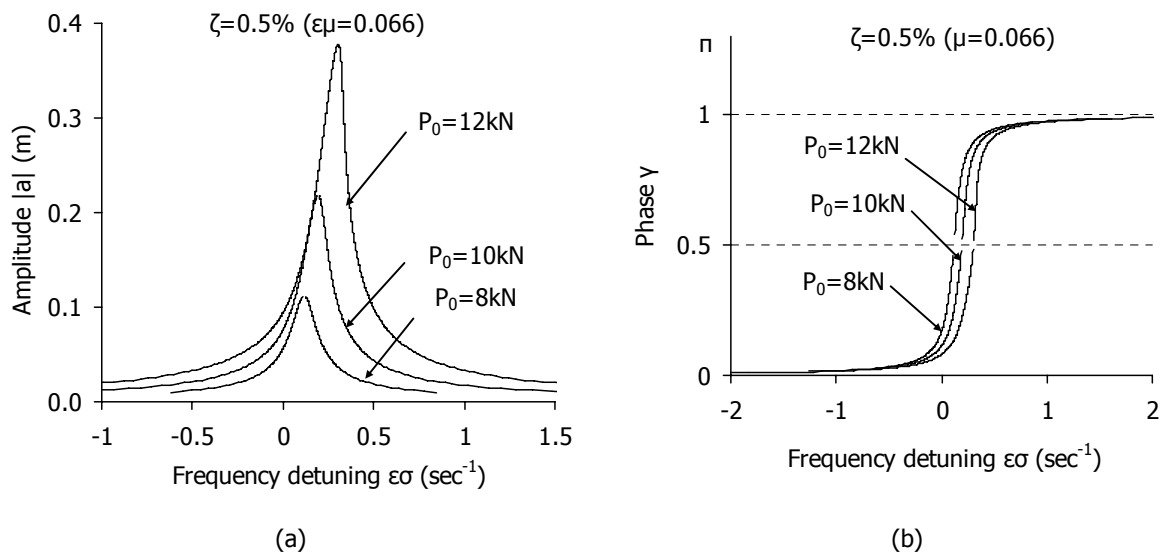


Figure 3-50: Superharmonic resonance for damping ratio $\zeta=0.5\%$: (a) amplitude $|a|$ vs. frequency detuning $\epsilon\sigma$, (b) phase γ vs. frequency detuning $\epsilon\sigma$

For loading amplitude $P_0=12\text{kN}$ and zero frequency detuning ($\epsilon\sigma=0.0\text{sec}^{-1}$), the steady-state response amplitude due to the cubic term, is equal to $a=0.095\text{m}$ and the phase $\gamma=0.08\pi$, while for frequency detuning $\epsilon\sigma=0.20\text{sec}^{-1}$ $a=0.25\text{m}$ and $\gamma=0.23\pi$ (Figure 3-51).

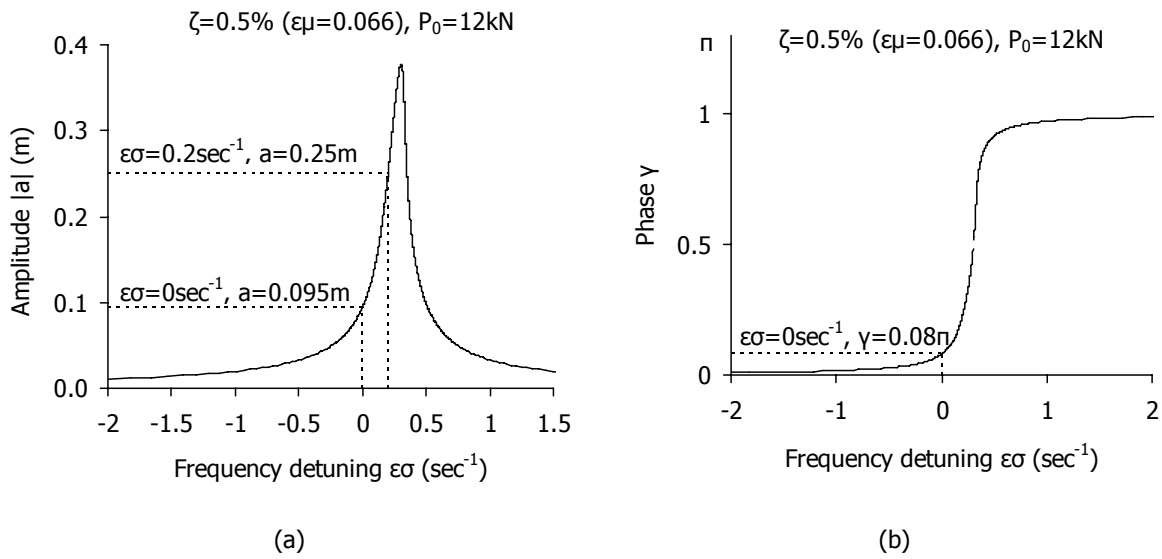


Figure 3-51: Superharmonic resonance for $\zeta=0.5\%$ and $P_0=12\text{kN}$: (a) amplitude $|a|$ vs. frequency detuning $\varepsilon\sigma$, (b) phase γ vs. frequency detuning $\varepsilon\sigma$

The solution of the equation of motion for the case of superharmonic resonance is obtained by Eq. (3-131), where $P=P_0/M=91.60\text{m/sec}^2$ and the maximum steady-state amplitude of the vertical displacement can be calculated as:

$$\begin{aligned} \varepsilon\sigma &= 0.0\text{sec}^{-1}, a = 0.095\text{m}, \Omega = (\omega_{z0} + \varepsilon\sigma)/3 = (13.19 + 0.0)/3 = 4.40\text{sec}^{-1} \\ \max w &= a + \frac{P}{\omega_{z0}^2 - \Omega^2} = 0.095 + 91.60 \left(\frac{1}{13.19^2 - 4.40^2} \right) = 0.69\text{m} \\ \varepsilon\sigma &= 0.20\text{sec}^{-1}, a = 0.25\text{m}, \Omega = (\omega_{z0} + \varepsilon\sigma)/3 = (13.19 + 0.20)/3 = 4.46\text{sec}^{-1} \\ \max w &= a + \frac{P}{\omega_{z0}^2 - \Omega^2} = 0.25 + 91.60 \left(\frac{1}{13.19^2 - 4.46^2} \right) = 0.84\text{m} \end{aligned} \tag{3-178}$$

The time-history diagram of the steady-state vertical displacement, calculated from Eq. (3-131) is plotted in Figure 3-52.

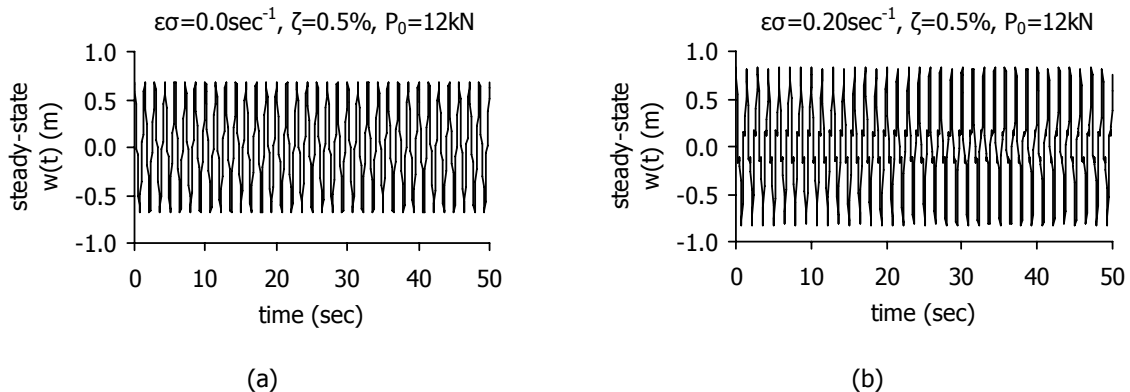


Figure 3-52: Superharmonic resonance: Time-history diagram of the steady-state response for damping ratio $\zeta=0.5\%$, loading amplitude $P_0=12\text{kN}$ and (a) zero frequency detuning ($\varepsilon\sigma=0.0\text{sec}^{-1}$), (b) $\varepsilon\sigma=0.20\text{sec}^{-1}$

This steady-state amplitude of the central node deflection is also obtained by solving numerically the equation of motion using MATLAB. The time-history diagrams of the central node vertical displacement are illustrated in Figure 3-53 for both frequency detuning values. Although a difference

is observed between the calculated steady-state amplitudes according to Eq. (3-178) and the ones of Figure 3-53, arising at 19% for $\epsilon\sigma=0.0\text{sec}^{-1}$ and at 15% for $\epsilon\sigma=0.20\text{sec}^{-1}$, the superharmonic resonance is verified by the significant increase of the response amplitude for this small increase of the loading frequency.

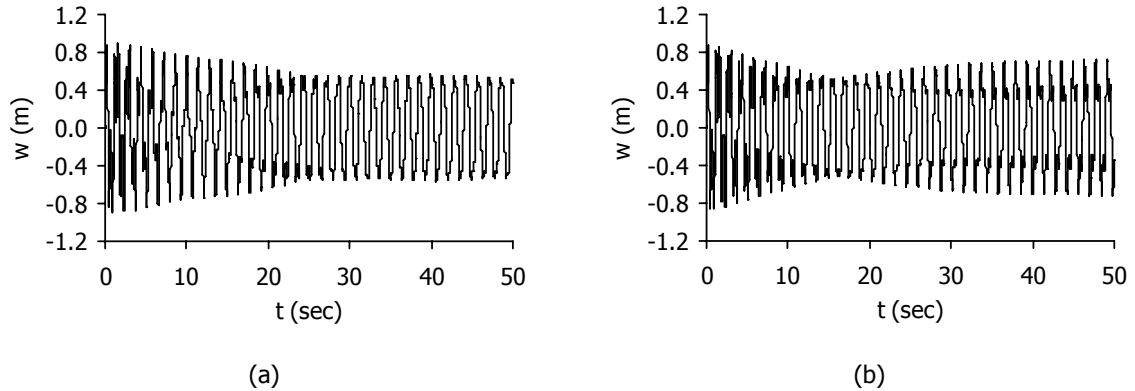


Figure 3-53: Superharmonic resonance: Time-history diagram of the central node displacement for damping ratio $\zeta=0.5\%$, loading amplitude $P_0=12\text{kN}$ and (a) zero frequency detuning ($\epsilon\sigma=0.0\text{sec}^{-1}$), (b) $\epsilon\sigma=0.20\text{sec}^{-1}$

3.3.7.4. Subharmonic resonance

In case $\Omega \approx 3\omega_{20}$, for damping ratio equal to $\zeta=0.5\%$ ($\epsilon\mu=0.066$) and $\zeta=2\%$ ($\epsilon\mu=0.264$), the region of the subharmonic solutions, defined by Eq. (3-148) or (3-149), is shown in Figure 3-54 by means of the amplitude Λ and the amplitude a . As the damping ratio increases, the subharmonic region moves towards larger values of the frequency detuning $\epsilon\sigma$. For larger values of damping ratios, the minimum load amplitude required for subharmonic conditions is larger, considering the frequency detuning $\epsilon\sigma$ constant. For the case of $\Omega=3\omega_{20}$ ($\epsilon\sigma=0.0\text{sec}^{-1}$), no subharmonic solutions can be detected.

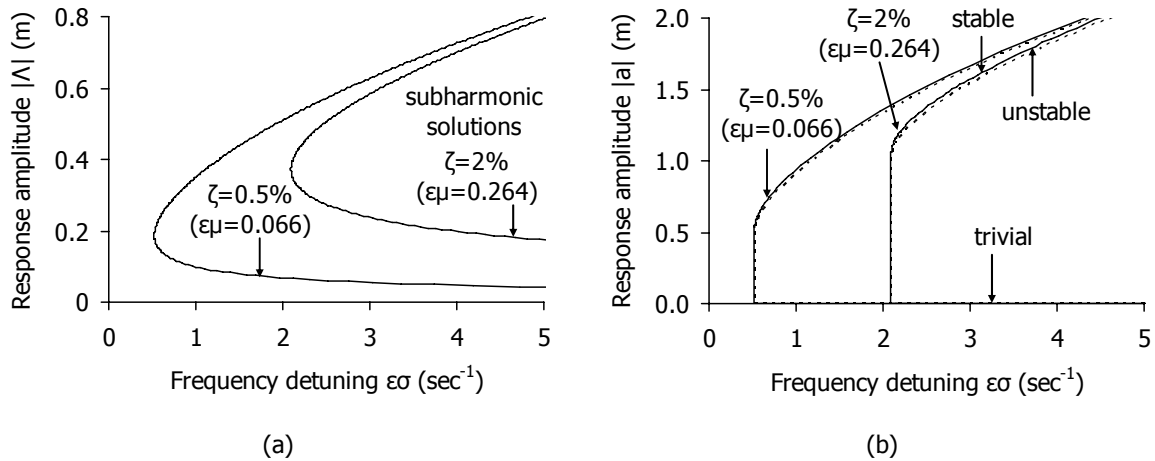


Figure 3-54: Subharmonic resonance with $\zeta=0.5\%$ and $\zeta=2\%$: (a) response amplitude Λ vs. frequency detuning $\epsilon\sigma$, (b) response amplitude a vs. frequency detuning $\epsilon\sigma$

Figure 3-55a illustrates the curve that defines the region of the subharmonic solutions, by means of the load amplitude P_0 that corresponds to the amplitude Λ of Figure 3-54a, according to Eq. (3-88) and taking into account Eq. (3-77). In Figure 3-55b the load P_0 is plotted with respect to the response amplitude a . It is worth mentioning that according to the chart of Figure 3-55b, in case a subharmonic resonance occurs, smaller load amplitudes cause larger response amplitudes. This occurs because, based on Figure 3-55a, as the load decreases a larger frequency detuning is required in order to have subharmonic solutions (Figure 3-54b). In addition, as the damping ratio increases the frequency

detuning that can cause subharmonic resonance increases for the same load amplitude (Figure 3-55a).

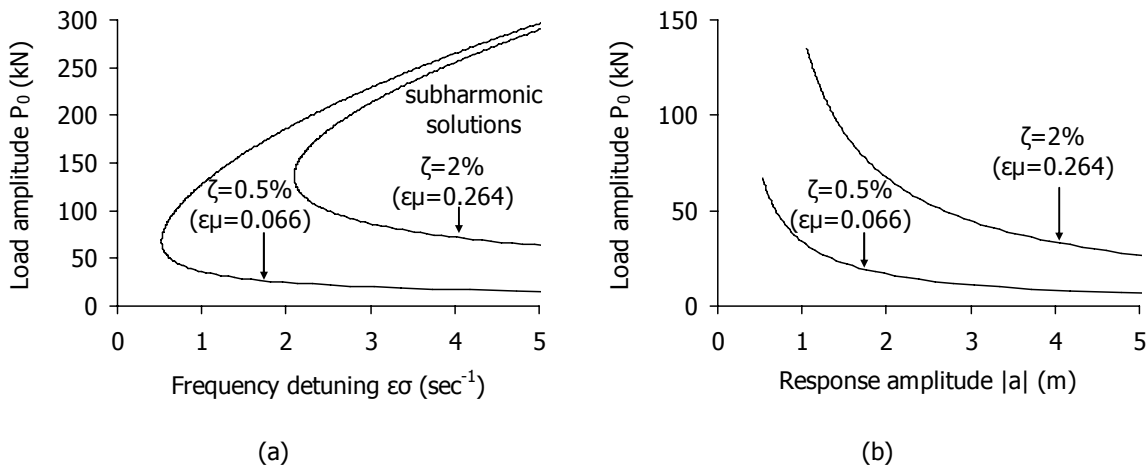


Figure 3-55: Subharmonic resonance with $\zeta=0.5\%$ and $\zeta=2\%$: (a) load amplitude P_0 vs. frequency detuning $\varepsilon\sigma$, (b) load amplitude P_0 vs. response amplitude a

Considering a loading amplitude $P_0=35\text{kN}$, damping ratio $\zeta=0.5\%$ and zero frequency detuning ($\varepsilon\sigma=0.0\text{sec}^{-1}$), the steady-state response amplitude due to the cubic term is equal to $a=0.0\text{m}$, as shown in Figure 3-56a. For frequency detuning larger than $\varepsilon\sigma=1.10\text{sec}^{-1}$, instead, there are subharmonic solutions. For example, for $\varepsilon\sigma=1.40\text{sec}^{-1}$ there are two stable solutions, a trivial one ($a=0.0\text{m}$) and a non-trivial one which is calculated equal to $a=1.13\text{m}$ (Eqs. (3-146) and (3-147)), as shown also in Figure 3-56b. In this case, the initial conditions determine which of the two stable solutions describe the actual response of the system.

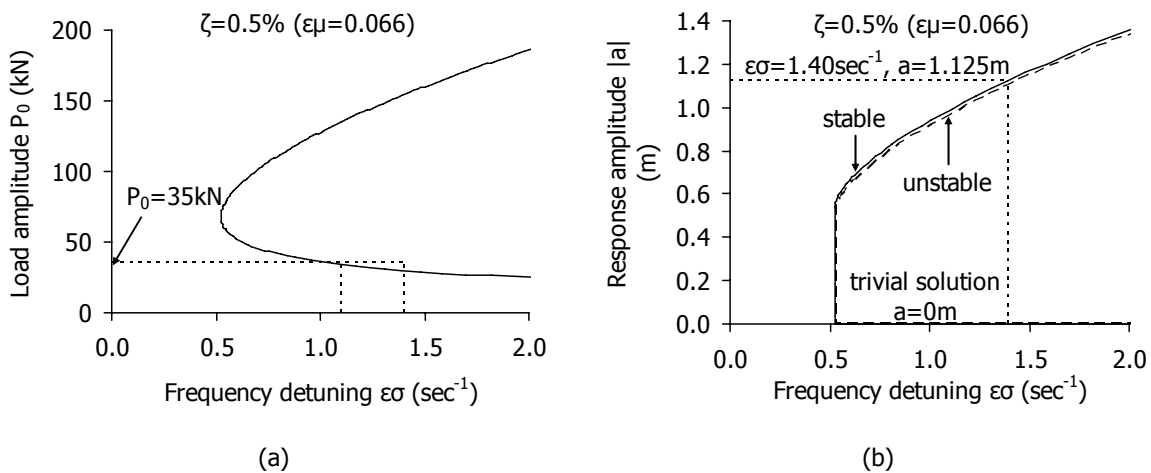


Figure 3-56: Subharmonic resonance with $\zeta=0.5\%$: (a) load amplitude P_0 vs. frequency detuning $\varepsilon\sigma$, (b) response amplitude a vs. frequency detuning $\varepsilon\sigma$

The solution of the equation of motion in case of trivial solution is expressed by Eq. (3-150), while for the case of subharmonic resonance in Eq. (3-151), with $P=P_0/M=267.18\text{m/sec}^2$, $\omega_{20}=13.19\text{sec}^{-1}$. Thus, for zero frequency detuning ($\Omega=3\omega_{20}=39.57\text{sec}^{-1}$), when no subharmonic resonance can occur, the maximum amplitude is calculated as:

$$\max w = \left| P \left(\frac{1}{\omega_{z0}^2 - \Omega^2} \right) \right| = \left| 267.18 \text{m/sec}^2 \left(\frac{1}{(13.19 \text{sec}^{-1})^2 - (39.57 \text{sec}^{-1})^2} \right) \right| \Rightarrow \quad (3-179)$$

$$\max w = 0.19 \text{m}$$

For frequency detuning $\varepsilon\sigma=1.4\text{sec}^{-1}$, the loading frequency is $\Omega=3\omega_{z0}+\varepsilon\sigma=40.97\text{sec}^{-1}$, and the trivial solution results in maximum oscillation amplitude:

$$\max w = \left| P \left(\frac{1}{\omega_{z0}^2 - \Omega^2} \right) \right| = \left| 267.18 \text{m/sec}^2 \left(\frac{1}{(13.19 \text{sec}^{-1})^2 - (40.97 \text{sec}^{-1})^2} \right) \right| \Rightarrow \quad (3-180)$$

$$\max w = 0.18 \text{m}$$

while the non-trivial solution with $a=1.13\text{m}$ results in maximum oscillation amplitude:

$$\max w = a + P \left(\frac{1}{\omega_{z0}^2 - \Omega^2} \right) = 1.13 \text{m} + 0.18 \text{m} = 1.31 \text{m} \quad (3-181)$$

The time-history diagrams of the total steady-state vertical displacement are illustrated in Figure 3-57 for zero frequency detuning ($\varepsilon\sigma=0.0\text{sec}^{-1}$) and for frequency detuning equal to $\varepsilon\sigma=1.40\text{sec}^{-1}$, taking also into account the component of the response due to the external load. The maximum response amplitude in the first diagram is equal to 0.19m and in the second 1.13m. Hence, a 3.5% increase of the loading frequency may produce an oscillation of 6 times larger response amplitude. These steady-state amplitudes of the central node deflection are also obtained by solving numerically the equation of motion, using MATLAB. The time-history diagram of the displacement for zero frequency detuning is shown in Figure 3-58. In Figure 3-59 two diagrams of the system's response are plotted for frequency detuning $\varepsilon\sigma=1.4\text{sec}^{-1}$. In the first diagram zero initial conditions are assumed and the steady-state response amplitude due to the cubic term is equal to the trivial solution $a=0.0\text{m}$. In the second chart, an initial deflection 0.80m and an initial velocity 10m/sec are assumed, in order to have the non-trivial solution. In this case the response amplitude is much larger. This investigation proves that the initial conditions influence significantly the response of the system. Changing the initial conditions subharmonic resonance may or may not occur for the specific frequency detuning and load amplitude. The exact initial conditions that can cause subharmonic resonances are not specified by the analytical solutions. They can be found only after several trials. The analytical solutions can only predict the possibility for the subharmonic resonance to take place.

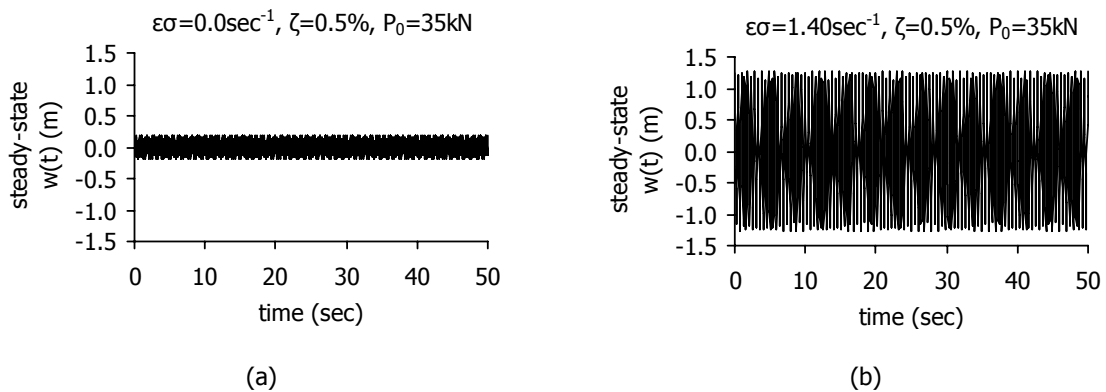


Figure 3-57: Subharmonic resonance: Time-history diagram of the steady-state response, damping ratio $\zeta=0.5\%$ loading amplitude $P_0=35\text{kN}$ and (a) zero frequency detuning ($\varepsilon\sigma=0.0\text{sec}^{-1}$), (b) $\varepsilon\sigma=1.40\text{sec}^{-1}$

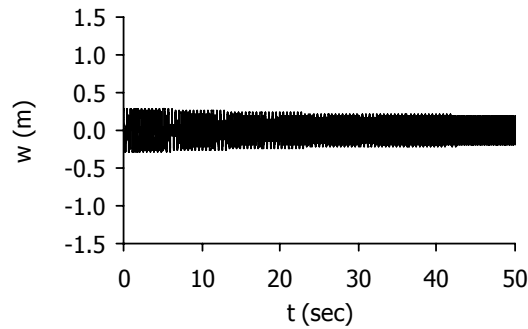


Figure 3-58: Subharmonic resonance: Time-history diagram of the central node displacement for zero frequency detuning ($\varepsilon\sigma=0.0\text{sec}^{-1}$), damping ratio $\zeta=0.5\%$, loading amplitude $P_0=35\text{kN}$

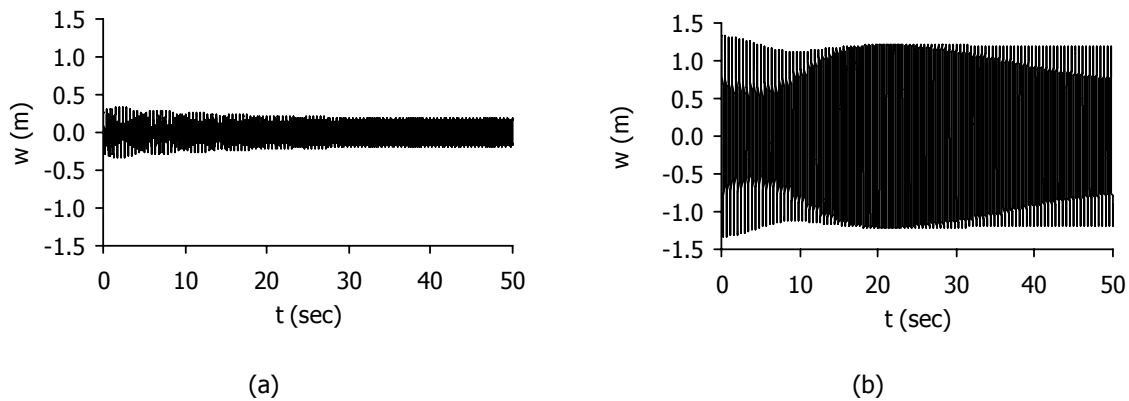


Figure 3-59: Subharmonic resonance: Time-history diagram of the central node displacement for frequency detuning $\varepsilon\sigma=1.4\text{sec}^{-1}$, damping ratio $\zeta=0.5\%$, loading amplitude $P_0=35\text{kN}$ (a) zero initial conditions, (b) initial displacement 0.8m and velocity 10m/sec

3.4 COMPARISON OF THE TWO MODELS

In this section the dynamic behaviour of the exact model of section 3.2, is compared with the simplified one of section 3.3. The numerical example already used for both models will be studied again in order to evaluate the accuracy of the assumed simplifications. It should be mentioned that the analytical solutions of the simplified model do not take into account an eventual cable slackening. This means that either the loads causing the nonlinear phenomena or the loading frequencies may be different for the exact model, with respect to the ones for the simplified model.

3.4.1 Eigenfrequencies

As calculated in section 3.2.6.3 and in section 3.3.7.1, the stiffness coefficient K_{z0} and the corresponding natural frequency for the two models are tabulated in Table 3-1. The difference for both magnitudes is negligible.

Table 3-1: Stiffness coefficient and natural frequencies

	Exact Model	Simplified Model	Difference
Stiffness coefficient K_{z0} (kN/m)	22.49	22.51	0.09%
Frequency ω_{z0} (rad/sec)	13.10	13.19	0.70%

3.4.2 Cable failure

In section 3.2.6.4 the dynamic load amplitude that causes cable failure is calculated for the exact model, solving numerically the equation of motion expressed by Eq. (3-51). Given that the analytical

solutions of the simplified model, do not consider cable slackening, and solving numerically the analytical equation of motion of Eq. (3-74), the corresponding load amplitudes are calculated for three loading frequencies. The results for both models are tabulated in Table 3-2 and compared. The difference of the maximum load amplitude between the two models is considered as very small. Regarding the case with $\Omega=3\omega_{z0}$, the maximum load is considered equal to the maximum static one, without causing cable failure.

Table 3-2: Maximum load amplitudes

	$(\Omega=\omega_{z0})$	$(\Omega=0.33\omega_{z0})$	$(\Omega=3\omega_{z0})$
Exact Model	1.30kN	19.97kN	(40.20kN)
Simplified Model	1.37kN	20.54kN	(40.20kN)
Difference	5%	3%	no failure

3.4.3 Fundamental resonance

The response diagrams described by the analytical solutions for the simplified model provide insightful information about the loading frequency for which the cable net exhibits the maximum steady-state amplitude, whether jump phenomena are expected, and dependence on the initial conditions. In Figure 3-60 the diagrams of Figure 3-22 are compared with the corresponding ones describing the response of the simplified model under fundamental resonance, calculated from Eq. (3-117), taking into consideration load amplitude $P_0=1\text{kN}$ ($\varepsilon\rho=114.50\text{m/sec}^2$) and damping ratio $\zeta=0.5\%$ ($\varepsilon\mu=0.066$) or $\zeta=2\%$ ($\varepsilon\mu=0.264$).

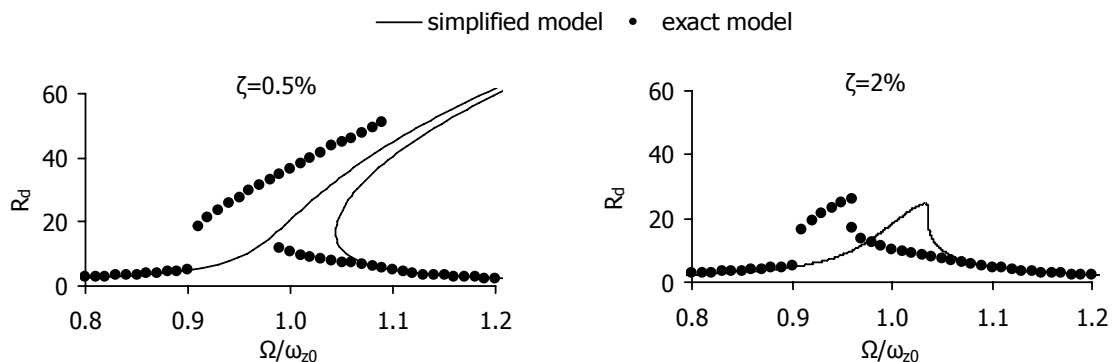


Figure 3-60: Steady-state deflection response factor R_d , with respect to the frequencies ratio for the exact and the simplified model under fundamental resonance for $P_0=1\text{kN}$

It is noted that the simplified model can predict with satisfactory accuracy the maximum steady-state amplitude, the slope of the response curve and the dependence on the initial conditions, but the diagrams of the exact model are shifted towards smaller frequency ratios. This occurs because during the oscillation the large amplitudes result in cable slackening and the stiffness of the system decreases. As a consequence, the natural frequency of the system decreases and thus the fundamental resonance occurs for smaller frequencies. The difference in the frequency ratio arises at 7% for both damping ratios, which is considered as sufficiently small. For frequency ratios smaller than 0.91 and larger than 1.07, for which no cable slackening occurs for this load amplitude, no difference between the responses of the two models is observed.

3.4.4 Superharmonic resonance

In Figure 3-61 the diagrams of Figure 3-23 are compared with the corresponding ones describing the response of the simplified model under superharmonic resonance, calculated from Eq. (3-130). In case of damping ratio equal to $\zeta=0.5\%$, the exact model oscillates with large amplitude when the frequency ratio is 0.32, causing cable slackening, while the corresponding solution of the simplified

model shows that the frequency ratio for the superharmonic resonance is 0.33, but the oscillation amplitude is not significant. For frequency ratios different from 0.32, the two responses are in good agreement except from the frequency ratios close to 0.50, indicating an order-two superharmonic resonance, which cannot be detected from the simplified model having only one cubic nonlinear term.

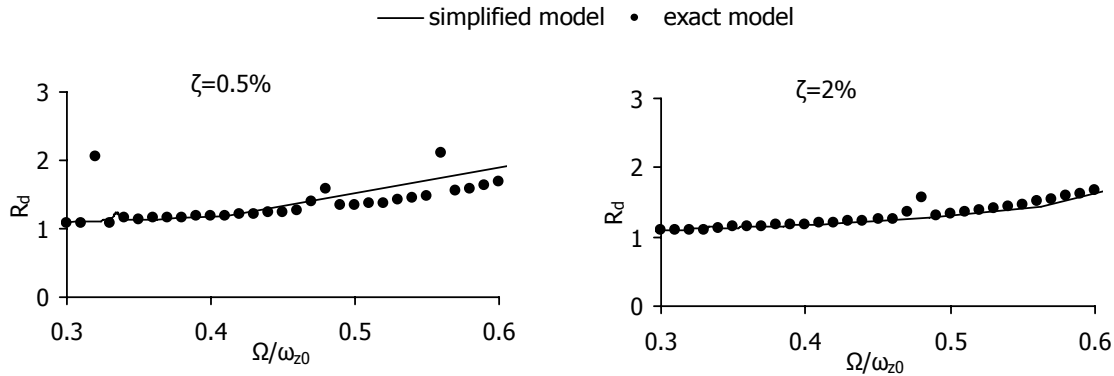


Figure 3-61: Steady-state deflection response factor R_d , with respect to the frequencies ratio for the exact and the simplified model under superharmonic resonance for $P_0=5kN$

3.4.5 Subharmonic resonance

The investigation of the simplified model in section 3.3.7.4 showed that, for load amplitude $P_0=35kN$, frequency detuning $\epsilon\sigma=1.40sec^{-1}$, initial deflection 0.80m and initial velocity 10m/sec, subharmonic resonance occurs. Retaining the same parameters, the steady-state response of the exact model is small, but keeping the same load amplitude and frequency detuning and changing only the initial deflection to 1.00m and the initial velocity to 16m/sec, subharmonic resonance takes place for the exact model too and the central node oscillates with large amplitudes, as illustrated in Figure 3-62, while for zero initial conditions the response amplitude is very small. It is worth mentioning that the deflection of the central node of Figure 3-62b is much larger than the maximum permissible one, which is equal to 1.63m. This response is calculated assuming an infinitely linear material in order to detect this nonlinear resonance without cable failure. If a maximum permissible cable stress is assumed instead, due to the initial conditions, which cause large response at the beginning of the calculation, the cable stress arrives at the yield stress within the first second and the analysis stops.

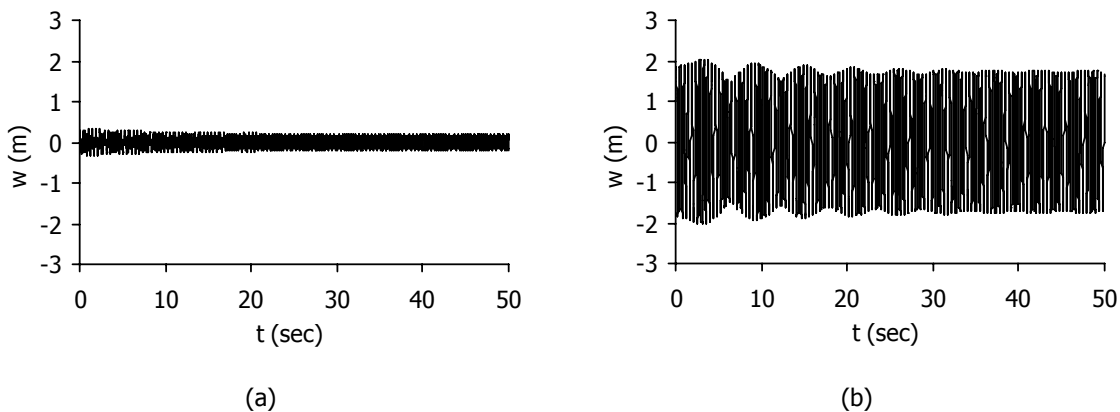


Figure 3-62: Exact model under subharmonic resonance with $\zeta=0.5\%$: Time-history diagram of the central node displacement for frequency detuning $\epsilon\sigma=1.40sec^{-1}$, damping ratio $\zeta=0.5\%$, loading amplitude $P_0=35kN$ (a) zero initial conditions, (b) initial displacement 1.0m and velocity 16m/sec

Thus, the simplified model can predict with sufficient accuracy the occurrence of subharmonic resonances regarding the frequency detuning and the load amplitude, but not the initial conditions

that can cause such phenomena, nor the possibility for the phenomenon to take place regarding the maximum permissible stress of the cables. In some cases the subharmonic resonance is impossible to evolve before cable failure, because, for small initial conditions, subharmonic solutions require large load amplitude, while for small load amplitudes large initial conditions are necessary. Such large loads or initial deflections, even if applied statically, lead to cable tensile failure.

3.5 SUMMARY AND CONCLUSIONS

The simplest cable net is considered, consisting of two crossing cables. The analytical equations of motion for the central free node are derived for all three translational degrees of freedom. The three natural frequencies are also calculated for the unforced, undeformed system. The maximum permissible deflection is calculated, setting the maximum permissible cable stress equal to the yield stress of the material. The equation of motion of a nonlinear system can be solved numerically for specific load amplitude, loading frequency and initial conditions. Nonlinear phenomena, such as subharmonic and superharmonic resonances, dependence on the initial conditions and bending of the response curves, producing unstable solutions and leading to jump phenomena and hysteresis loops, can be detected by a large number of numerical analyses, for different values of loading frequency and amplitude, as well as initial conditions that are changed in very small steps. This is proved to be a time consuming procedure.

This cable net is further investigated, assuming only the vertical displacement, thus constituting a single-degree-of-freedom system. The exact equation of motion is simplified by neglecting small terms, leading to a single-degree-of-freedom system with a cubic nonlinear term, similar to a Duffing oscillator. The analytical formulae for steady-state responses in different resonant cases are obtained for this system and the corresponding diagrams are plotted. Many features of nonlinear systems dynamic behaviour are detected for the cable net and its nonlinear behaviour, delineated by the analytical solution, is also verified by solving numerically the simplified equation of motion.

The numerical solutions of the exact cable net and the analytical ones of the simplified model are compared by means of a numerical example. The analytical solution of the Duffing oscillator does not include an eventual cable slackening. As a result, if one of the two cables of the exact model becomes slack, small differences are noted between the two models. These differences are focused on the exact loading frequency and amplitude or the initial conditions that are required for a nonlinear phenomenon to evolve. In addition, the analytical solution of the Duffing equation, having only a cubic term, cannot predict the order-two superharmonic resonances, which are proved to occur for the exact model. Nevertheless, the response diagrams, described by these analytical solutions, provide useful information about the loading frequency for which the cable net exhibits the maximum steady-state amplitude, whether jump phenomena or dependence on the initial conditions are expected.

The analytical solutions describe only the steady-state response, while cable failure may occur during the transient one. However, the information provided by the simplified model can be used to further investigate the response of the exact model during the transient response conducting numerical analyses.

Part of this work has been accepted for publication [3-42].

3.6 REFERENCES

- [3-1] G. Kerschen, K. Worden, A. F. Vakakis and J. C. Golinval, "Past, present and future of nonlinear system identification in structural dynamics", *Mechanical Systems and Signal Processing*, Vol. 20, pp. 505-592, 2006.

- [3-2] A. G. Pugsley, "On the natural frequencies of suspension chains", *Quarterly Journal of Mechanics and Applied Mathematics*, Vol. 2, Part 4, pp. 412-418, 1949.
- [3-3] K. Ahmadi-Kashani, "Vibration of hanging cables", *Computers and Structures*, Vol. 31, No. 5, pp. 699-715, 1989.
- [3-4] M. S. Triantafyllou and L. Grinfogel, "Natural frequencies and modes of inclined cables", *Journal of Structural Engineering*, Vol. 112, No. 1, pp. 139-148, 1986.
- [3-5] J. J. Burgess and M. S. Triantafyllou, "The elastic frequencies of cables", *Journal of Sound and Vibration*, Vol. 120, No. 1, pp. 153-165, 1987.
- [3-6] H. M. Irvine and T. K. Caughey, "The linear theory of free vibrations of a suspended cable", *Proceedings of the Royal Society of London. Series A, Mathematical and Physical Sciences*, London, Great Britain, Vol. 341, No. 1626, pp. 299-315, 1974.
- [3-7] G. Rega and A. Luongo, "Natural vibrations of suspended cables with flexible supports", *Computers and Structures*, Vol. 12, pp. 65-75, 1980.
- [3-8] G. Rega, F. Vestroni and F. Benedettini, "Parametric analysis of large amplitude free vibrations of a suspended cable", *International Journal of Solids and Structures*, Vol. 20, pp. 95-106, 1984.
- [3-9] A. Luongo, G. Rega, F. Vestroni, "Planar non-linear free vibrations of an elastic cable", *International Journal of Non-Linear Mechanics*, Vol. 19, No. 1, pp. 39-52, 1984.
- [3-10] F. Benedettini and G. Rega, "Non-linear dynamics of an elastic cable under planar excitation", *International Journal of Non-Linear Mechanics*, Vol. 22, No. 6, pp. 497-509, 1987.
- [3-11] G. Rega and F. Benedettini, "Planar non-linear oscillations of elastic cables under subharmonic resonance conditions", *Journal of Sound and Vibration*, Vol. 132, No. 3, pp. 367-381, 1989.
- [3-12] F. Benedettini and G. Rega, "Planar non-linear oscillations of elastic cables under superharmonic resonance conditions", *Journal of Sound and Vibration*, Vol. 132, No. 3, pp. 353-366, 1989.
- [3-13] K. Takahashi, Q. Wu and S. Nakamura, "In-plane antisymmetric response of cables through bifurcation under symmetric sinusoidally time-varying load", *Journal of Sound and Vibration*, Vol. 268, pp. 1-14, 2003.
- [3-14] N. Srinil, G. Rega and S. Chucheepsakul, "Nonlinear interactions in the 3D free vibrations of horizontal and inclined sagged cables", *Proceedings of the 5th International Symposium on cable dynamics*, Santa Margherita Ligure, Italy, pp. 77-84, 2003.
- [3-15] N. Srinil and G. Rega, "The effects of kinematic condensation on internally resonant forced vibrations of shallow horizontal cables", *International Journal of Non-Linear Mechanics*, Vol. 42, pp. 180-195, 2007.
- [3-16] A. Chisalita, "Finite deformation analysis of cable networks", *Journal of Engineering Mechanics*, Vol. 110, No. 2, pp. 207-223, 1984.
- [3-17] J. W. Leonard, "Tension structures, behavior & analysis", McGraw-Hill, Inc., U.S.A., 1988.
- [3-18] G. R. Seeley, P. Christiano and H. Stefan, "Natural frequencies of circular cable networks" *Journal of the Structural Division* Vol. 101, No. ST5, pp. 1171-1177, 1975.
- [3-19] M. L. Gambhir and B. deV. Batchelor, "Finite element study of the free vibration of 3D cable networks", *International Journal of Solids and Structures*, Vol. 15, pp. 127-136, 1978.

- [3-20] B. L. Dhoopar, P. C. Gupta and B. P. Singh, "Vibration analysis of orthogonal cable networks by transfer matrix method", *Journal of the Sound and Vibration*, Vol. 101, No. 4, pp. 575-584, 1985.
- [3-21] N. F. Morris, "Dynamic response of cable networks", *Journal of the Structural Division*, Vol. 100, No. ST10, pp. 2091-2108, 1973.
- [3-22] L. F. Geschwindner and H. H. West, "Forced vibrations of cable networks", *Journal of the Structural Division*, Vol. 106, ST9, pp. 1885-1898, 1980.
- [3-23] A. S. K. Kwan, "A simple technique for calculating natural frequencies of geometrically nonlinear prestressed cable structures", *Computers and Structures*, Vol. 74, pp. 41-50, 1998.
- [3-24] I. Talvik, "Finite element modelling of cable networks with flexible supports", *Computers and Structures*, Vol. 79, pp. 2443-2450, 2001.
- [3-25] A. Nayfeh and D. T. Mook, "Nonlinear oscillations", John Wiley & Sons, Inc., U.S.A., 1979.
- [3-26] J. Guckenheimer and P. Holmes, "Nonlinear oscillations, dynamical systems, and bifurcations of vector fields", *Applied Mathematical Sciences* Vol. 42, Springer-Verlag, U.S.A. 1983.
- [3-27] A. Vakakis, "Introduction to dynamical systems", *Lecture Notes*, National Technical University of Athens, Greece, 2002.
- [3-28] H. M. Irvine, "Cable structures", Dover Publications, Inc., U.S.A., 1981.
- [3-29] A. K. Chopra, "Dynamics of structures, theory and applications to earthquake engineering", Prentice Hall International, Inc., U.S.A., 1995.
- [3-30] MATLAB, "The language of technical computing", v.7.9.0.529 (R2009b), The MathWorks, Inc., U.S.A., 2009.
- [3-31] E. Kreyszig, "Advanced engineering mathematics", 8th Edition, John Wiley & Sons, Inc., U.S.A., 1999.
- [3-32] H. A. Buchholdt, "An introduction to cable roof structures", Thomas Telford, 2nd Edition, Great Britain, 1999.
- [3-33] J. Kevorkian and J. D. Cole, "Multiple scale and singular perturbation methods", Springer-Verlag, U.S.A., 1996.
- [3-34] E. M. de Jager and J. Furu, "The theory of singular perturbations", Elsevier Science B.V., The Netherlands, 1996.
- [3-35] R. H. Rand, "Lecture notes on nonlinear vibrations", v.52, Cornell University, U.S.A. 2005.
- [3-36] M. Paz, "Structural dynamics, theory and computation", *Library of Congress Cataloging in Publication Data*, U.S.A., 1991.
- [3-37] R. W. Clough and J. Penzien, "Dynamics of structures", McGraw-Hill, Inc., U.S.A., 1993.
- [3-38] C. M. Bender and S. A. Orszag, "Advanced mathematical methods for scientists and engineers, Asymptotic methods and perturbation theory", Springer-Verlag, U.S.A., 1999.
- [3-39] P. B. Kahn, "Mathematical methods for scientists and engineers, Linear and nonlinear systems", Dover Publications, Inc., U.S.A., 2004.
- [3-40] D. W. Jordan and P. Smith, "Nonlinear ordinary differential equations – an introduction to dynamical systems", Oxford University Press Inc., U.S.A., 3rd Edition, 1999.

-
- [3-41] E. G. Wiens, "Egwald mathematics – nonlinear dynamics: two dimensional flows and phase diagrams", Egwald Web-Services Ltd.
www.egwald.ca/nonlineardynamics/twodimensionaldynamics.php
- [3-42] I. Vassilopoulou and C. J. Gantes, "Nonlinear dynamic phenomena in a SDOF model of cable net", *Archive of Applied Mechanics*, 2011 (accepted for publication).

4 VALIDATION OF FINITE ELEMENT SOFTWARE

4.1 INTRODUCTION

As already discussed, suspended cable structures, subjected to either static or dynamic transverse loads, usually experience large displacements with respect to their span, belonging thus to the family of geometrically nonlinear structures. Their response cannot be calculated on the basis of their undeformed geometry, since their stiffness depends on the deformed state, increasing when the deflection increases. The internal forces do not vary linearly with load and the principle of superposition cannot be applied. It is thus necessary to perform nonlinear analyses, considering large displacements and taking into account the deformed geometry at every load step. In addition, as cables cannot sustain any compression, their material must be treated and modelled as nonlinear, having only tension branch.

In the previous chapter, analytical expressions for simple cable nets have been derived, describing their static equilibrium and dynamic equations of motion. A single-degree-of-freedom cable net model was thoroughly explored, detecting nonlinear phenomena, such as nonlinear resonances and instability regions, confirming the intense geometric nonlinearity of the system. However, in this investigation, an eventual cable slackening was not taken into account and many simplifications were made in order to overcome the difficulty of complex mathematics. Obtaining analytical solutions for three dimensional cable structures of many degrees of freedom, turns out to be practically impossible, due to their complex nonlinearity. Consequently, the investigation of the cable networks' dynamic response, performed in the following chapters, will be based on results of numerical analyses.

The scope of this chapter is to compare the results of the finite element software that will be used further on, with those derived from analytical solutions or results obtained from the literature, thus confirming its appropriateness and accuracy. The comparison is carried out for a simple suspended cable and for the simplest cable net with two cables, regarding the natural frequencies and the static and dynamic nonlinear response under resonant conditions, in terms of nodal deflection and cable tension variation diagrams. The cables are modelled to sustain only tension, taking thus into consideration an eventual cable slackening.

4.2 PRESENTATION AND ASSUMPTIONS OF THE FINITE ELEMENT SOFTWARE

The finite element analysis software that will be used for this work is ADINA [4-1], which can perform linear and nonlinear analyses of structures, including effects of material nonlinearities and large deformations. It offers versatile and generally applicable finite elements for solids, trusses, beams, pipes, plates, shells and gaps. Material models for metals, soils and rocks, plastics, rubber, fabrics, wood, ceramics and concrete are available. It also offers the option to consider the mass matrix as lumped or consistent. It can include element birth or death, initial strains or stresses and restart analysis in order to consider a deformed state from a previous analysis as an initial condition for the subsequent one. It provides the possibility for linear or nonlinear static or dynamic analyses, calculation of frequencies, modes, and modal participation factors, mode superposition, linearised buckling, collapse analysis. The results can be plotted in graphs, or listed in tables. Response spectra and Fourier analyses with amplitude – frequency diagrams or power spectral density are also available, following a time-history analysis. Videos or snapshots of the deformed state can also be provided.

The following assumptions are adopted in the analyses with ADINA ([4-2] and [4-3]):

- The cables are modelled as truss elements with initial strain, introducing thus the initial pretension.
- The cross-sectional area of the element is assumed to remain unchanged.
- The cable material can be considered in some specific cases as linear, with the same Young modulus for the compression and the tension branch, or in most cases as nonlinear, having null compression branch and being linear elastic regarding the tension branch with a constant modulus of elasticity. In most of the examples analysed in this chapter, the Young modulus is equal to $E=165\text{MPa}$ and the maximum cable stress is considered equal to the yield stress 1570MPa , corresponding to a strain equal to 0.009515.
- The mass matrix can be calculated as lumped or consistent. The lumped mass matrix is formed by dividing the elements mass among its nodes and the element has no rotational mass.
- The assumption of large displacements – small strains is adopted for nonlinear static or dynamic analysis.
- In all cases, the unstressed length of the cable segments is not taken into account and the form-finding procedure is not included. The geometry and stiffness of the equilibrium state under prestressing are considered as initial state, and the initial length of the cable elements is the one of the given geometry.
- The damping, if considered, is introduced as Rayleigh damping. For a SDOF system, with only one eigenfrequency the coefficients α_0 and α_1 are calculated as:

$$\alpha_0=2\zeta\omega \text{ and } \alpha_1=0 \quad (4-1)$$

- The nonlinear static analysis is performed using the Full Newton iteration method [4-4], in which a new stiffness matrix is always formed at the beginning of each new load step and iteration, taking into consideration large displacements.
- The eigenvalue problem for calculating the natural frequencies and modes is solved by linear modal analysis. If the structure is nonlinear and is preloaded or prestressed, the analysis is performed in two runs. In the first run, the preload is applied (gravity loads, initial strains, etc.) in a nonlinear static analysis. This run can contain one or more solution steps. In the second run, the analysis restarts from the last solution of the first run, in order to perform a frequency or time-history analysis based on the stiffness and mass matrix corresponding to the time of solution start; in this case the time of solution start is the time corresponding to the restart analysis. Therefore, the stiffness and mass matrices include all geometric and material nonlinearities corresponding to the end of the nonlinear static analysis.

- The Composite method [4-5], based on Newmark's method [4-6], is used as the time integration method for solving nonlinear dynamic problems in time domain analysis, which is recommended for nonlinear systems. In the composite method, the displacements, velocities, and accelerations are solved at a time $t + 0.5\Delta t$.

The results of this program regarding the natural frequencies of the system are compared with the ones obtained by MAPLE [4-7], using the analytical solutions provided in chapter 3 and solving the eigenvalue problem. The nonlinear dynamic results of ADINA are compared with the ones obtained by MATLAB [4-8]. The assumption that the cable cannot sustain any compression is realised by setting equal to zero the tension of the cables whenever it becomes negative, nullifying thus their stiffness. ADINA results will be denoted as "numerical" while MAPLE and MATLAB results as "analytical".

ADINA considers as initial geometry the one at the state in which it calculates the eigenfrequencies. If, for example the system is prestressed, the length of the cable segments at the equilibrium state under pretension S_N is considered to be the initial length of the segment. In addition, small strains are taken into account. Thus, the cable tension for each deformed segment is calculated as:

$$N_i = N_0 + EA \left(\frac{S_i - S_N}{S_N} \right) \text{ where } i=1,2,3,4 \quad (4-2)$$

and the linearised stiffnesses, at the equilibrium state under pretension, will be:

$$K_{x0} = K_{y0} = \frac{4 \cdot (EAL^2 + N_0L^2 + 8N_0f^2)}{\sqrt{(L^2 + 4f^2)^3}} = \frac{4EA}{L} \frac{\left(1 + \frac{N_0}{EA} + 8 \frac{N_0}{EA} \frac{f^2}{L^2} \right)}{\sqrt{\left(1 + 4 \frac{f^2}{L^2} \right)^3}} \quad (4-3)$$

$$K_{z0} = \frac{4 \cdot (8EAf^2 + 2N_0L^2)}{\sqrt{(L^2 + 4f^2)^3}} = \frac{4EA}{L} \frac{\left(8 \frac{f^2}{L^2} + 2 \frac{N_0}{EA} \right)}{\sqrt{\left(1 + 4 \frac{f^2}{L^2} \right)^3}} \quad (4-4)$$

The three natural frequencies of the system will be:

$$\omega_{x0} = \omega_{y0} = \sqrt{\frac{4EA}{ML} \frac{\left(1 + \frac{N_0}{EA} + 8 \frac{N_0}{EA} \frac{f^2}{L^2} \right)}{\sqrt{\left(1 + 4 \frac{f^2}{L^2} \right)^3}}} \quad (4-5)$$

$$\omega_{z0} = \sqrt{\frac{4EA}{ML} \frac{\left(8 \frac{f^2}{L^2} + 2 \frac{N_0}{EA} \right)}{\sqrt{\left(1 + 4 \frac{f^2}{L^2} \right)^3}}} \quad (4-6)$$

The difference is calculated between these expressions of eigenfrequencies with the ones obtained in the chapter 3, taking into consideration large displacements and small strains, defined as:

$$\omega_{x0} = \omega_{y0} = \sqrt{\frac{4EA}{ML} \cdot \frac{\left(1 + 2 \frac{N_0}{EA} + 8 \frac{N_0}{EA} \frac{f^2}{L^2}\right)}{\sqrt{\left(1 + 4 \frac{f^2}{L^2}\right)^3}}} \quad (4-7)$$

$$\omega_{z0} = \sqrt{\frac{4EA}{ML} \cdot \frac{\left(8 \frac{f^2}{L^2} + 2 \frac{N_0}{EA} + 8 \frac{N_0}{EA} \frac{f^2}{L^2}\right)}{\sqrt{\left(1 + 4 \frac{f^2}{L^2}\right)^3}}} \quad (4-8)$$

Thus, for initial cable stress 20% of the yield stress and E=165GPa, the difference between the numerical results and the analytical solution, expressed in the previous chapter assuming small strains, arises at maximum 0.09% for all three eigenfrequencies, independently of the sag-to-span ratio, as plotted in Figure 4-1. For a sag-to-span ratio equal to f/L=1/20 and initial cable stress varying between 10% and 35% of the yield stress, the difference is also small, as shown in Figure 4-2. Thus, the numerical calculation of the eigenfrequencies, can be considered as sufficiently accurate.

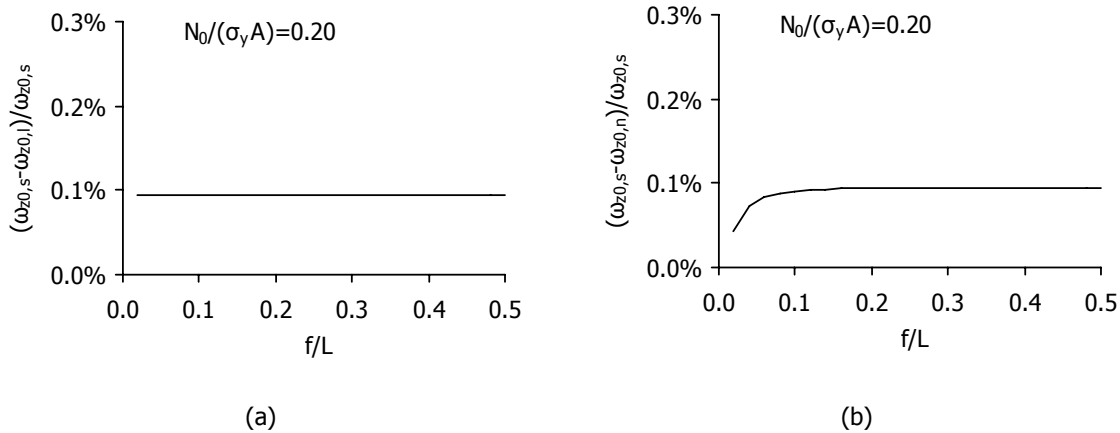


Figure 4-1: Difference of the eigenfrequencies: (a) ω_{x0} and ω_{y0} , (b) ω_{z0} , for initial cable stress 20% σ_y (s: small strains, n: numerical calculation)

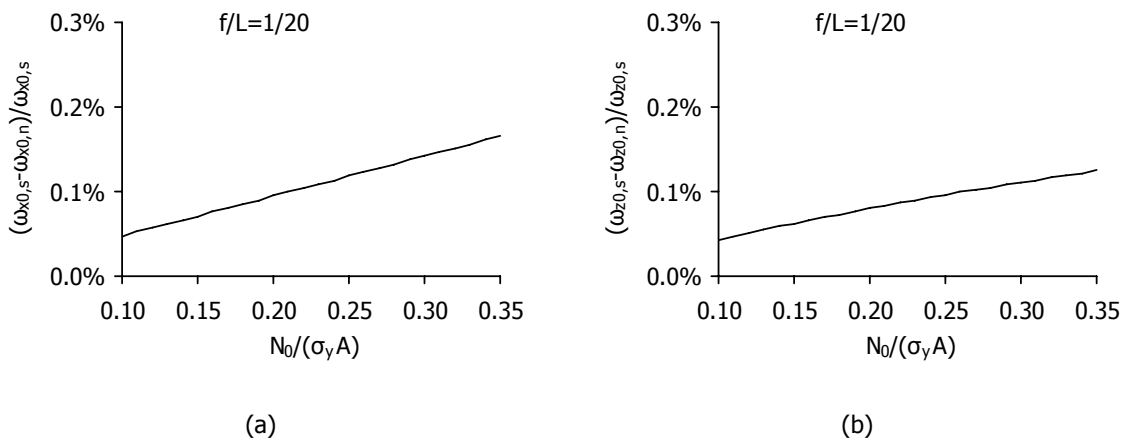


Figure 4-2: Difference of the eigenfrequencies: (a) ω_{x0} and ω_{y0} , (b) ω_{z0} , for sag-to-span ratio f/L=1/20 (s: small strains, n: numerical calculation)

4.3 NUMERICAL EXAMPLE

4.3.1 Geometry

A cable net is used as an example, as described in chapter 3, consisting of two cables having diameter $D=10\text{mm}$, cross-sectional area $A=7.85\cdot 10^{-5}\text{m}^2$ and Young modulus $E=165000\text{MPa}$. The initial strain of the cables is $\varepsilon_0=0.001$, which is interpreted as an initial pretension $N_0=EA\varepsilon_0=12.959\text{kN}$. The span of the cables is $L=50.00\text{m}$ and their sag $f=2.50\text{m}$. The distributed mass of the cables is $m=7.85\text{kN/m}^4\cdot\text{sec}^2$, while an additional concentrated mass is applied on the central node, equal to $M_c=0.1\text{t}=0.1\text{kN}\cdot\text{sec}^2\cdot\text{m}^{-1}$. The masses are considered as lumped, so that the total mass at the central node is equal to $M=m\cdot 4S_N/2\cdot A+M_c=0.131\text{kN}\cdot\text{sec}^2\cdot\text{m}^{-1}$.

4.3.2 Static response

A concentrated vertical static load is applied on the central node, towards $+z$, equal to $P=40\text{kN}$. The numerical results are compared with the analytical ones, regarding the deflection and the cable tension of two characteristic segments. The material is treated as nonlinear. The load – displacement curve is plotted in Figure 4-3 and the cable tension variation of segments 1 and 3, with respect to the central node deflection in Figure 4-4.

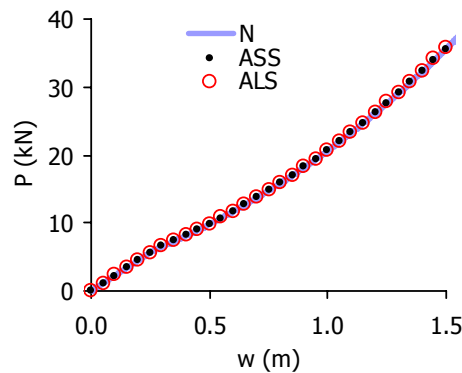


Figure 4-3: Load – displacement curve for the static load $P=40\text{kN}$ (numerically (N), analytically considering small strains (ASS) or large strains (ALS))

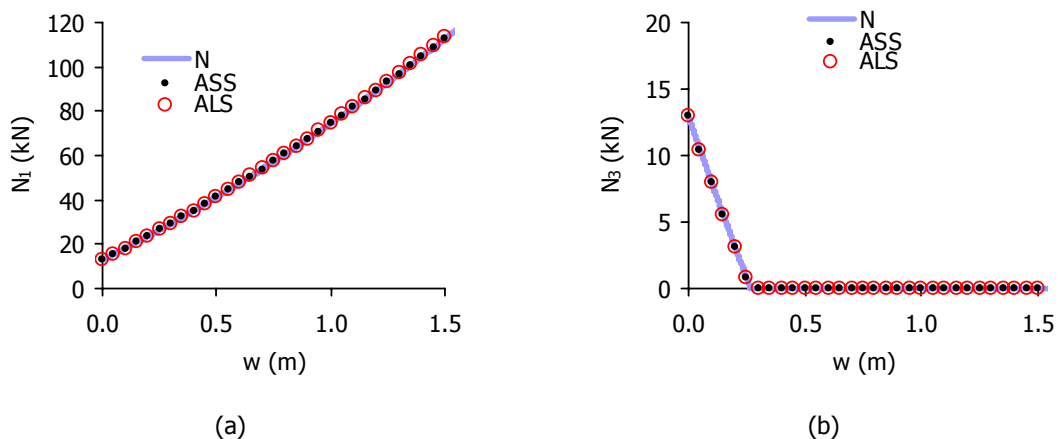


Figure 4-4: Cable tension variation with respect to the central node deflection (a) segment 1, (b) segment 3 (numerically (N), analytically considering small strains (ASS) or large strains (ALS))

It is obvious that the system's response is nonlinear due to the geometrically nonlinear behaviour of the cables and the loosening of the cable segments 3 and 4. The numerical solution, which takes into

account large displacements and small strains is compared with the analytical one, considering large displacements and either small or large strains. All results are in very good agreement.

4.3.3 Eigenfrequencies

The eigenfrequencies are calculated analytically, considering large displacements - small or large strains and numerically, taking into consideration only large displacement – small strains. The natural frequencies are tabulated in Table 4-1, while the difference between numerical and analytical solutions is listed in Table 4-2 and it is considered as insignificant.

Table 4-1: Calculated natural frequencies: numerically (N), analytically considering small strains (ASS) or large strains (ALS)

MODE	Frequency (sec ⁻¹)			Frequency (Hz)			Period (sec)		
	(N)	(ASS)	(ALS)	(N)	(ASS)	(ALS)	(N)	(ASS)	(ALS)
1	13.10	13.10	13.11	2.08	2.09	2.09	0.48	0.48	0.48
2	88.35	88.39	88.44	14.06	14.07	14.07	0.06	0.07	0.07
3	88.35	88.39	88.44	14.06	14.07	14.07	0.06	0.07	0.07

Table 4-2: Difference between the calculated natural frequencies: numerically (N), analytically considering small strains (ASS) or large strains (ALS)

MODE	Frequency (sec ⁻¹)	
	(ASS-N)/ASS	(ALS-N)/ALS
1	0%	0%
2	0%	0.1%
3	0%	0.1%

4.3.4 Dynamic response without damping

Subsequently, a vertical load is applied on the central node, varying with time as $P=P_0 \cdot \cos\Omega t$, with load amplitude $P_0=1\text{kN}$. The loading frequency equal to $\Omega=\omega_{20}$ is assigned, where $\omega_{20}=13.10\text{sec}^{-1}$. The response of the system is calculated numerically, as well as analytically, and presented by means of the time-history diagram of the deflection w of the central node, the corresponding phase plane plot, and the time-history of the cable tension of segments 1 and 3. Large displacements and small strains are considered for both numerical and analytical solutions, but for the former the initial length of the cables is assumed equal to the unstretched length S_0 and the cable tension is described by Eq. (3-9) while for the latter the initial length of the cables is considered to be equal to the prestressed length S_N , and the cable tension at each step is expressed by Eq. (4-2).

The integration time step has been varied for both approaches, in order to compare and evaluate the accuracy of the results. Thus, the response diagrams are plotted for three different time steps, with respect to the loading period $T_L=0.48\text{sec}$ being equal to the system's period T_S , which are $\Delta t_1 \approx T_L/10=0.05\text{sec}$ (Figure 4-5), $\Delta t_2 \approx T_L/50=0.01\text{sec}$ (Figure 4-6), and $\Delta t_3 \approx T_L/100=0.005\text{sec}$ (Figure 4-7). In Table 4-3 the maximum deflection of the central node, the maximum tension of the above cable segments and the difference between the two analyses are tabulated. It can be noted that the maximum magnitudes calculated analytically do not depend on the time step, while for the numerical analysis the time step Δt_1 gives wrong results with a difference of 20-22% with respect to the ones obtained analytically, while the other two analyses with time steps Δt_2 and Δt_3 provide results with differences of 0.9-1.1% and 0-0.4%, respectively, which can be both considered as satisfactory. Between the first and the second analysis the time step is decreasing 5 times and the accuracy is increasing significantly by 21 times. Between the second and the third analysis the time step is decreasing only by 2 times, and the difference between the analytical and the numerical solution is decreasing to one third. It is doubtful whether the additional gain in accuracy between Δt_2 and Δt_3 justifies the increase in computational time. Nevertheless, the third time step is chosen for the numerical analysis, when the loading frequency is close to the eigenfrequency of the system.

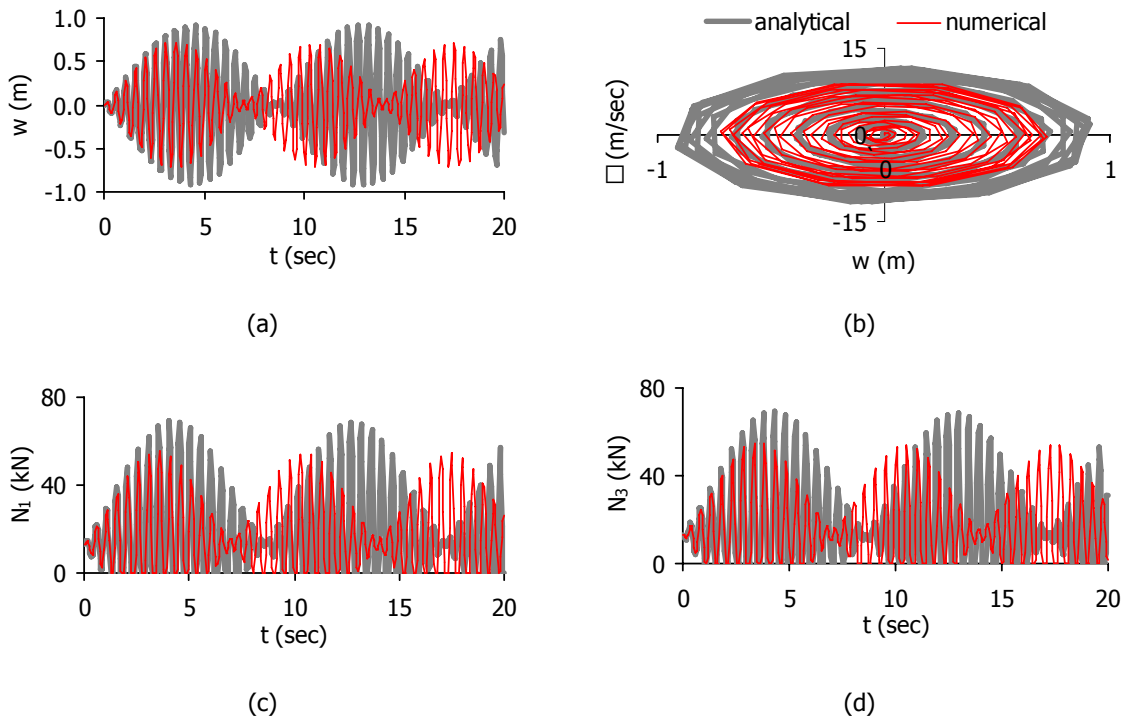


Figure 4-5: Dynamic response for $P=(1\text{kN})\cos(\omega_{20}t)$ and $\Delta t_1=0.05\text{sec}$, (a) central node deflection time-history diagram, (b) phase plane plot of the central node movement, (c) tension time-history diagram of segment 1, (d) tension time-history diagram of segment 3. Small strains are considered for the analytical solution.

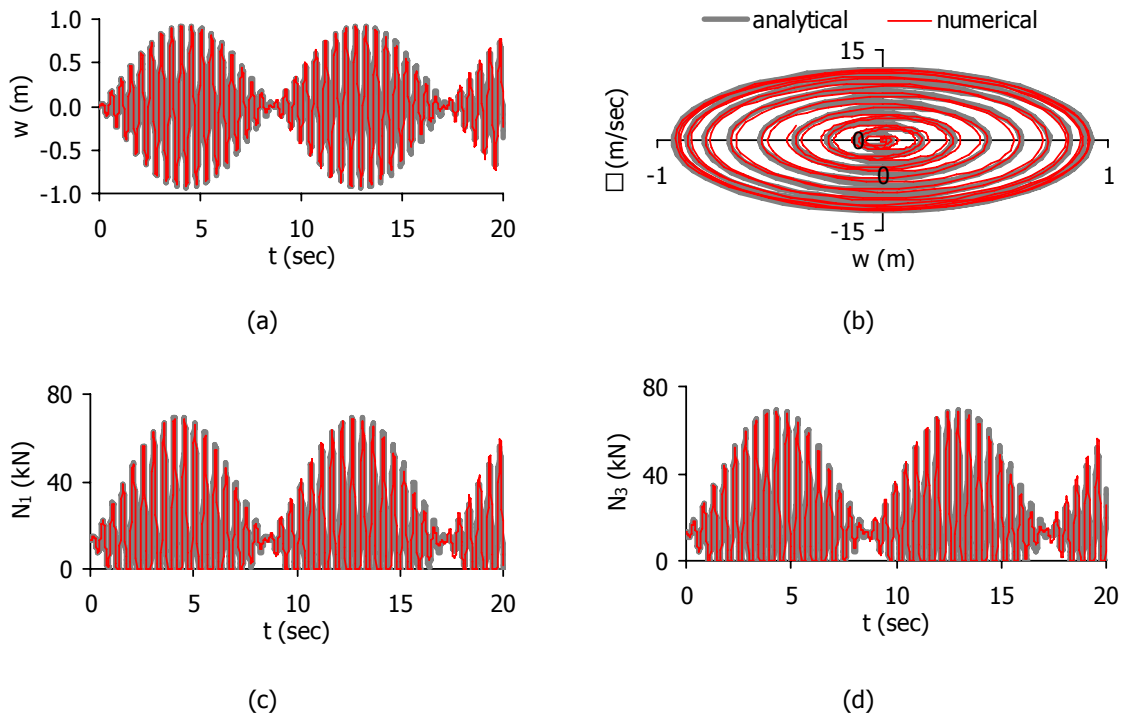


Figure 4-6: Dynamic response for $P=(1\text{kN})\cos(\omega_{20}t)$ and $\Delta t_2=0.01\text{sec}$, (a) central node deflection time-history diagram, (b) phase plane plot of the central node movement, (c) tension time-history diagram of segment 1, (d) tension time-history diagram of segment 3. Small strains are considered for the analytical solution.

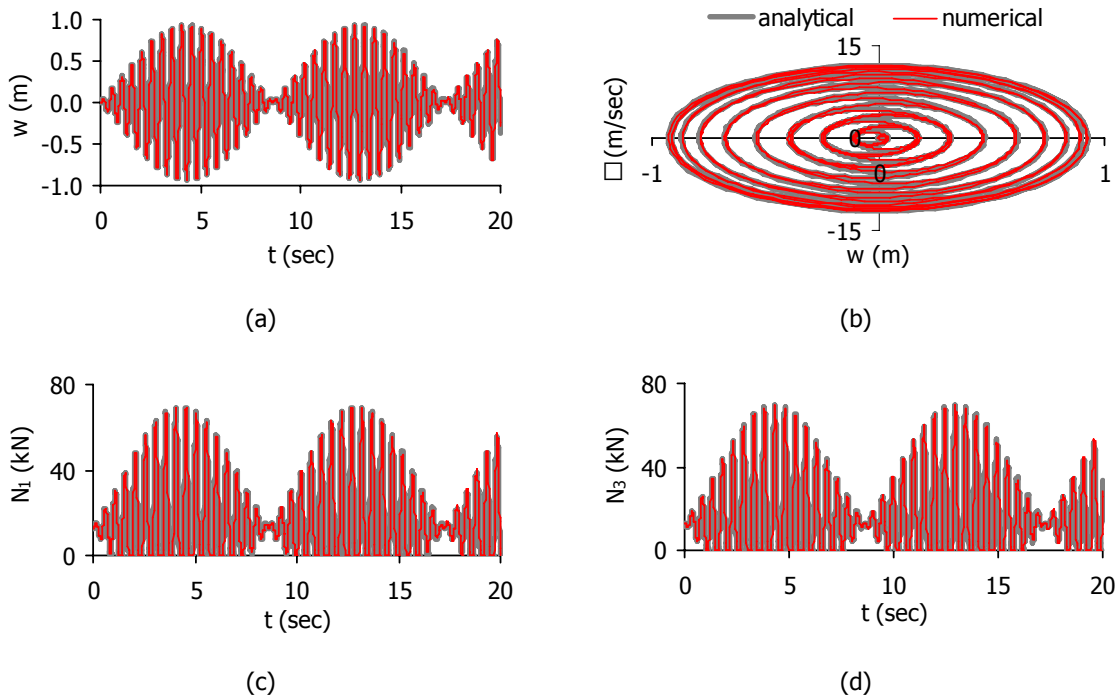


Figure 4-7: Dynamic response for $P=(1\text{kN})\cos(\omega_{20}t)$ and $\Delta t_3=0.005\text{sec}$, (a) central node deflection time-history diagram, (b) phase plane plot of the central node movement, (c) tension time-history diagram of segment 1, (d) tension time-history diagram of segment 3. Small strains are considered for the analytical solution.

Table 4-3: Maximum deflection and cable tension for $P=(1\text{kN})\cos(\omega_{20}t)$

Procedure	$\Delta t_1=0.05\text{sec}$			$\Delta t_2=0.01\text{sec}$			$\Delta t_3=0.005\text{sec}$		
	w (m)	tension of segment (kN)		w (m)	tension of segment (kN)		w (m)	tension of segment (kN)	
		1	3		1	3		1	3
analytical (A)	0.92	69.10	69.31	0.93	69.32	69.57	0.93	69.36	69.59
numerical (N)	0.72	55.20	55.09	0.92	68.71	68.73	0.93	69.09	69.27
(A-N)/A	22%	20%	21%	1.1%	1%	0.9%	0%	0.4%	0.4%

Choosing the appropriate time step depends not only on the accuracy of the results, but also on the computational time needed. In order to have more accuracy in the results, the computational time becomes extremely high. The difference between the two assumptions regarding the calculation of the cable tension at each step does not alter significantly the results.

Keeping only the third time step, $\Delta t_3=0.005\text{sec}$, and the load amplitude $P_0=1\text{kN}$, the assumption of "large displacements – large strains" is now adopted for the analytical approach and the cable tension is expressed by Eq. (3-10). The analytical results are compared again with the corresponding numerical ones, plotted in Figure 4-8 and tabulated in Table 4-4. Comparing the charts of Figure 4-8 with those of Figure 4-7, no significant difference is observed. The small difference between the two analyses is also shown in Table 4-4 for the maximum response, by means of nodal displacement and cable tension. It is increased with respect to the corresponding one of Table 4-3 for the same time step, but it is considered again very small. Based on these observations, the assumption of small strains will be adopted further on in the analytical solution, in order to compare the results with the ones obtained by the numerical analysis, which uses by default the assumption of "large displacement – small strains".

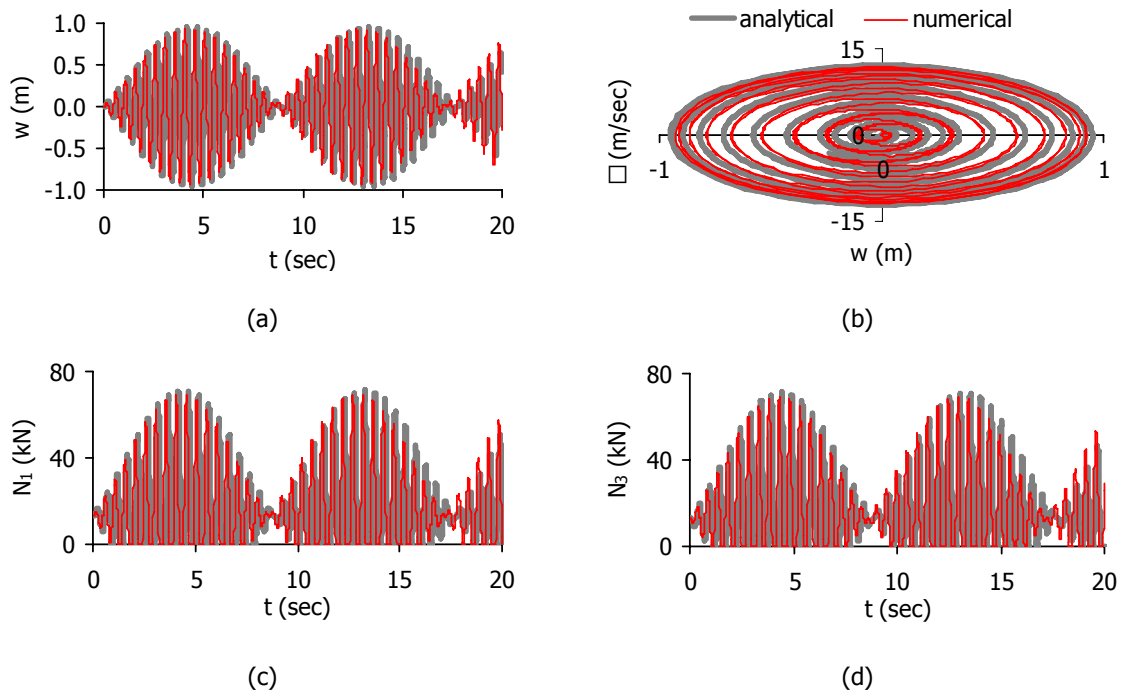


Figure 4-8: Dynamic response for $P=(1\text{kN})\cos(\omega_{20}t)$ and $\Delta t_3=0.005\text{sec}$, (a) central node deflection time-history diagram, (b) phase plane plot of the central node movement, (c) tension time-history diagram of segment 1, (d) tension time-history diagram of segment 3. Large strains are considered for the analytical solution.

Table 4-4: Maximum deflection and cable tension for $P=(1\text{kN})\cos(\omega_{20}t)$, considering large strains for the analytical solution

Procedure	$\Delta t_3=0.005\text{sec}$		
	w (m)	tension of segment (kN)	
		1	3
analytical (A)	0.95	71.32	71.31
numerical (N)	0.93	69.09	69.27
(A-N)/A	2%	3%	3%

Next, the loading amplitude equals to $P_0=1\text{kN}$ and a loading frequency smaller than the system's eigenfrequency is selected, $\Omega=\omega_{20}/3=4.37\text{rad/sec}$. The time step chosen, with respect to the loading period $T_L=1.44\text{sec}$ and the system's period $T_S=0.48\text{sec}$, is $\Delta t \approx T_L/300 \approx T_S/100=0.005\text{sec}$. In the charts of Figure 4-9, the comparison of the results between the analytical and numerical analyses is shown. In Table 4-5 the maximum deflection of the central node, the maximum tension of the cable segments 1 and 3 and the difference between the two analyses are tabulated, which is null.

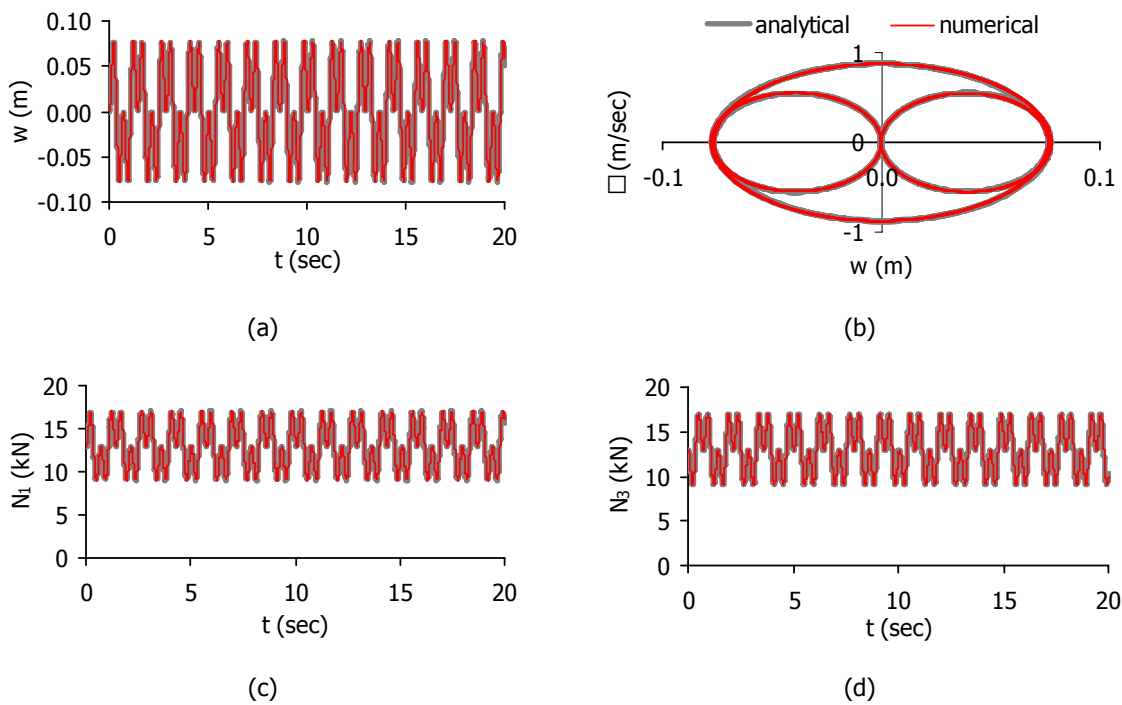


Figure 4-9: Dynamic response for $P=(1.0\text{kN})\cos(\omega_{20}t/3)$ and $\Delta t=0.005\text{sec}$, (a) central node deflection time-history diagram, (b) phase plane plot of the central node movement, (c) tension time-history diagram of segment 1, (d) tension time-history diagram of segment 3

Table 4-5: Maximum deflection and cable tension for $P=(1.0\text{kN})\cos(\omega_{20}t/3)$

Procedure	$\Delta t=0.005\text{sec}$		
	w (m)	tension of segment (kN)	
		1	3
analytical (A)	0.08	17.00	17.00
numerical (N)	0.08	17.02	17.02
(A-N)/A	0 %	-0.1%	-0.1%

From the above results it is obvious that the specific load amplitude results in small amplitudes of the displacement of the central node and the cable tension. If a dynamic load with larger amplitude is taken into consideration, such as $P=(10\text{kN})\cos(\omega_{20}t/3)$, the results for time step $\Delta t=0.005\text{sec}$ are shown in the charts of Figure 4-10 and in Table 4-6. Even for the larger load amplitude the difference between the numerical and the analytical results is very small. This means that the appropriate time step depends on the system's period and not on the loading amplitude.

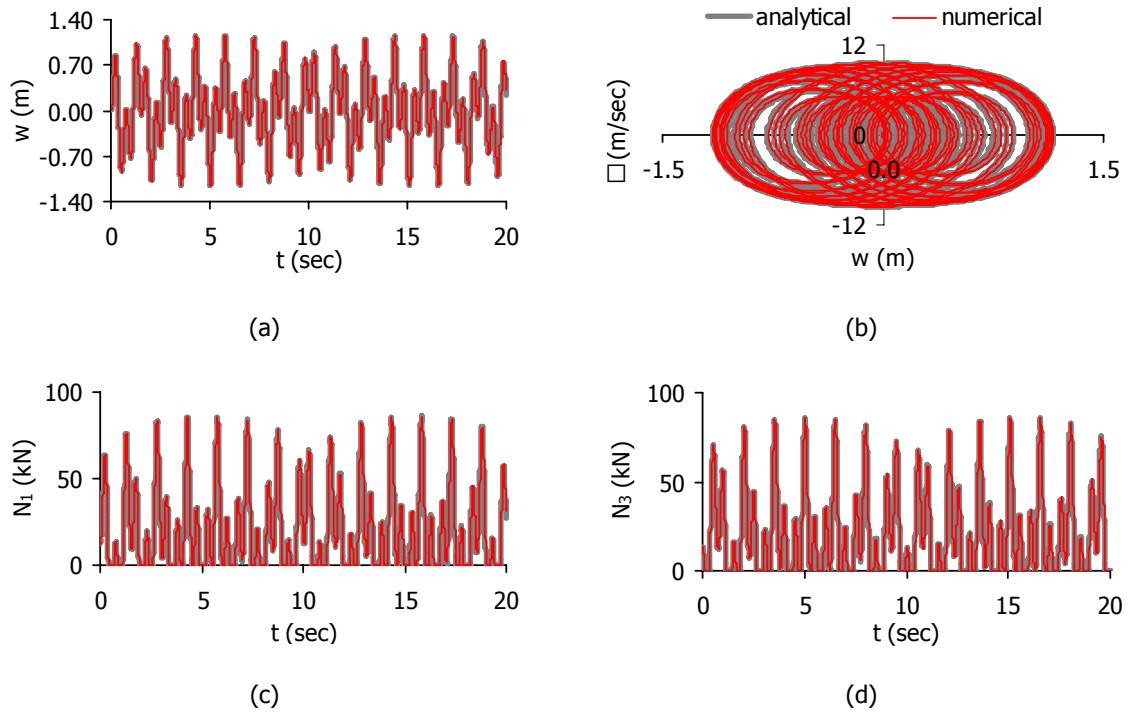


Figure 4-10: Dynamic response for $P=(10\text{kN})\cos(\omega_{z0}t/3)$ and $\Delta t=0.005\text{sec}$, (a) central node deflection time-history diagram, (b) phase plane plot of the central node movement, (c) tension time-history diagram of segment 1, (d) tension time-history diagram of segment 3

Table 4-6: Maximum deflection and cable tension for $P=(10\text{kN})\cos(\omega_{z0}t/3)$

Procedure	$\Delta t=0.005\text{sec}$		
	w (m)	tension of segment (kN)	
		1	3
analytical (A)	1.16	86.00	86.00
numerical (N)	1.16	85.91	85.98
(A-N)/A	0 %	0.1%	0 %

Subsequently, a loading frequency larger than the eigenfrequency is assumed, namely $\Omega=3\omega_{z0}=39.30\text{rad/sec}$, while the amplitude of the load remains equal to 10kN. The time step chosen, with respect to the loading period $T_L=0.16\text{sec}$ and the system's period $T_S=0.48\text{sec}$, is $\Delta t \approx 3T_L/100 \approx T_S/100 = 0.005\text{sec}$. In the charts of Figure 4-11, the comparison of the results between the analytical and numerical analyses is plotted. The difference is larger than the previous cases, especially regarding the phase plane plot of the central node movement. Thus, a smaller time step is chosen, equal to $\Delta t \approx T_L/100 \approx T_S/300 = 0.0015$. The results are plotted in Figure 4-12 and listed in Table 4-7, proving that this time step is more appropriate.

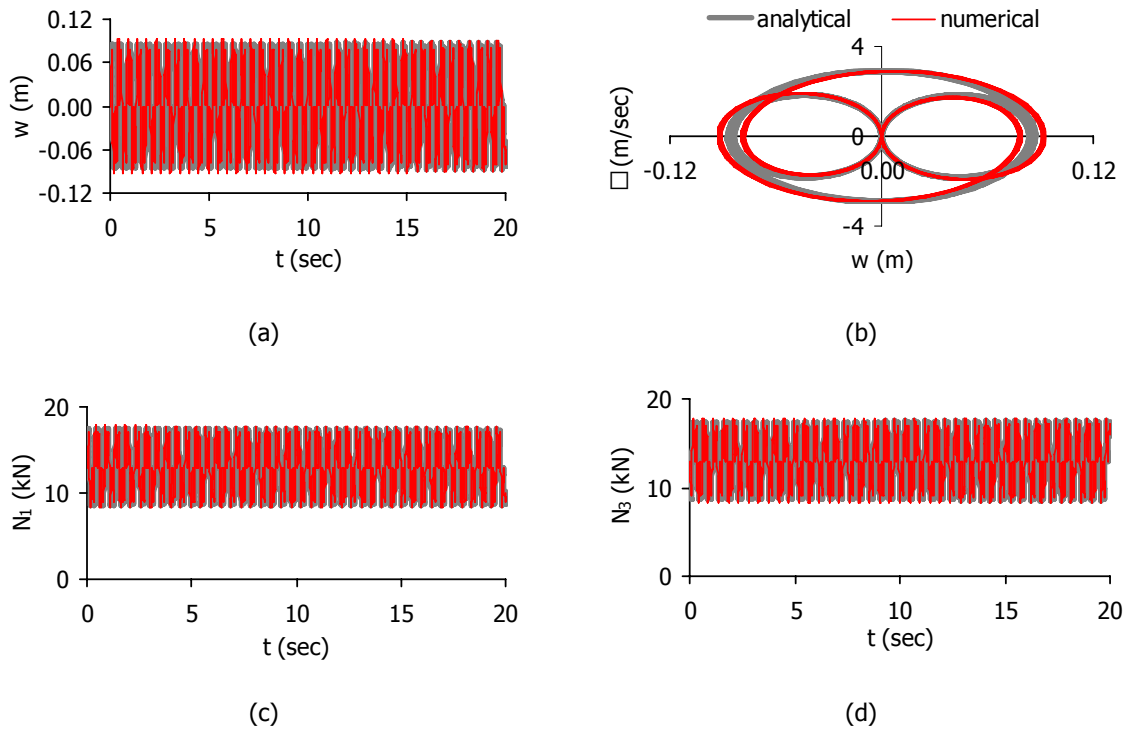


Figure 4-11: Dynamic response for $P=(10\text{kN})\cos(3\omega_{20}t)$ and $\Delta t=0.005\text{sec}$, (a) central node deflection time-history diagram, (b) phase plane plot of the central node movement, (c) tension time-history diagram of segment 1, (d) tension time-history diagram of segment 3

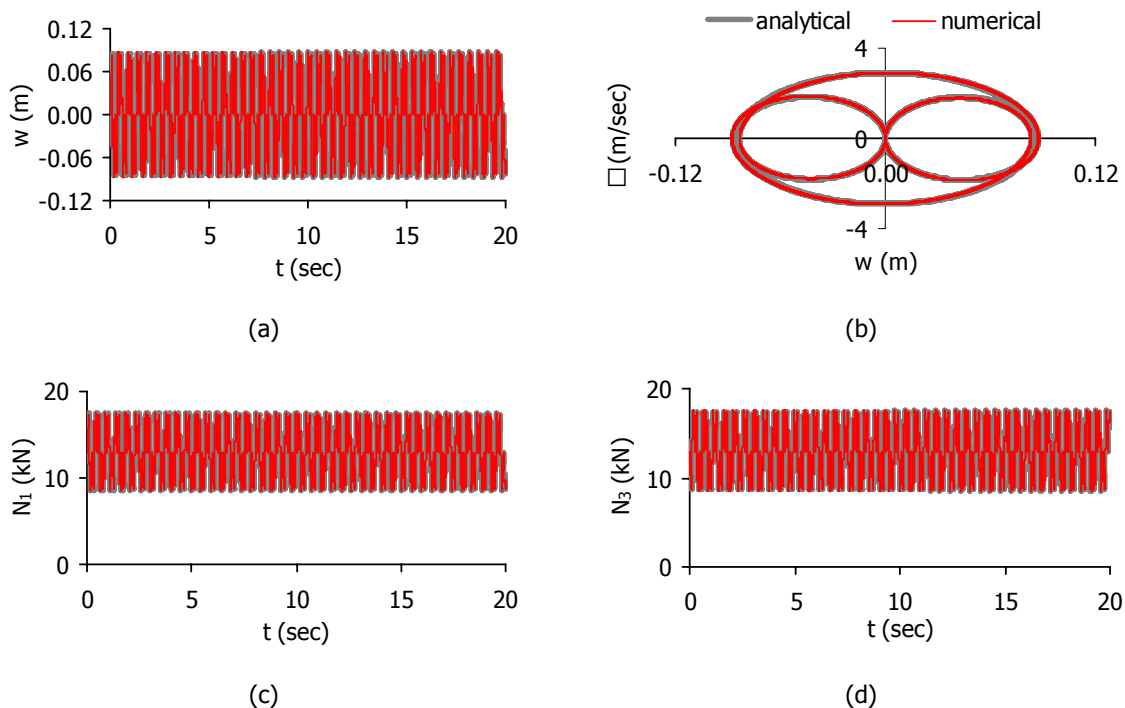


Figure 4-12: Dynamic response for $P=(10\text{kN})\cos(3\omega_{20}t)$ and $\Delta t=0.0015\text{sec}$, (a) central node deflection time-history diagram, (b) phase plane plot of the central node movement, (c) tension time-history diagram of segment 1, (d) tension time-history diagram of segment 3

Table 4-7: Maximum deflection and cable tension for $P=(10\text{kN})\cos(3\omega_{z0}t)$

Procedure	$\Delta t=0.0015\text{sec}$		
	w (m)	tension of segment (kN)	
	1	1	3
analytical (A)	0.09	17.52	17.52
numerical (N)	0.09	17.55	17.55
(A-N)/A	0 %	-0.2%	-0.2%

4.3.5 Dynamic response with damping

Adding damping in the system, the numerical results are compared with the analytical ones, using the same assumptions of section 4.3.4 regarding the loading frequencies. The time step remains equal to $\Delta t=0.005\text{sec}$. Two damping ratios are considered $\zeta=0.5\%$ and $\zeta=2\%$. For $\omega_{z0}=13.10\text{sec}^{-1}$, the Rayleigh damping coefficients α_0 and α_1 are calculated as:

- a) $\zeta=0.5\%$, $\alpha_0=2\zeta\omega=0.131$ and $\alpha_1=0$
- b) $\zeta=2\%$, $\alpha_0=2\zeta\omega=0.524$ and $\alpha_1=0$
- (4-9)

Thus, for $P_0=1\text{kN}$ and $\Omega=\omega_{z0}$, the response of the system is plotted for damping ratio $\zeta=0.5\%$ (Figure 4-13) and $\zeta=2\%$ (Figure 4-14). The maximum deflection of the central node and the maximum cable tension of segments 1 and 3 are tabulated in Table 4-8. Again, very small difference is observed between the analytical and the numerical solutions, for both damping ratios.

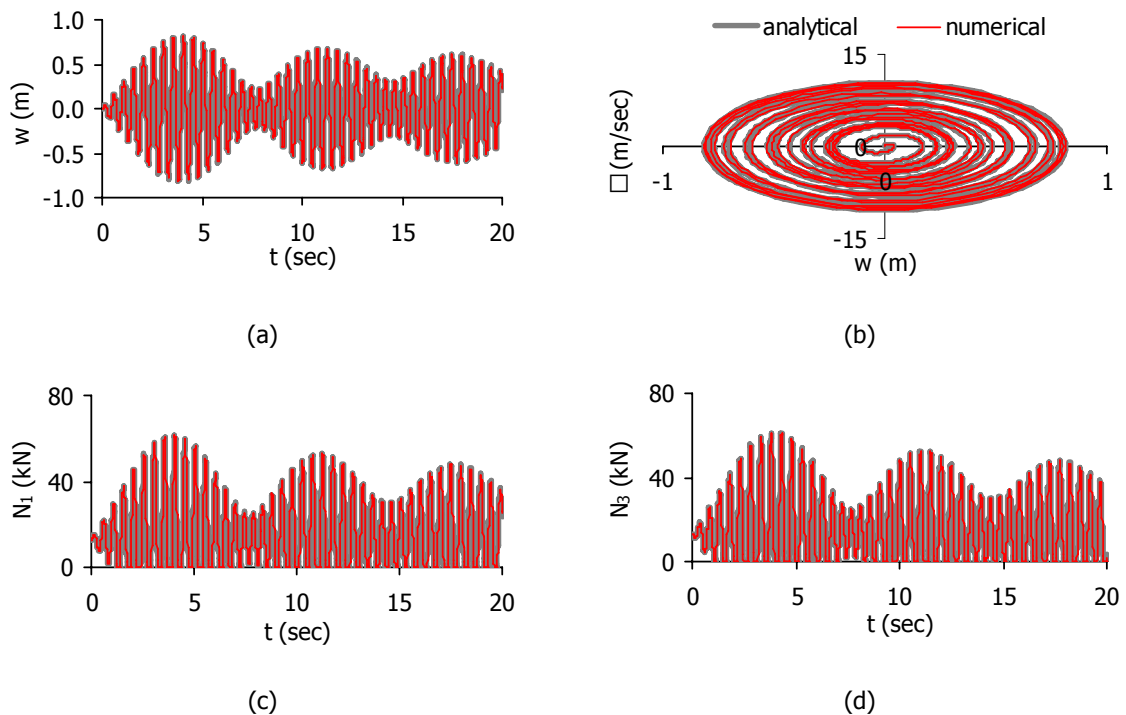


Figure 4-13: Dynamic response for $P=(1\text{kN})\cos(\omega_{z0}t)$, damping ratio $\zeta=0.5\%$ and $\Delta t=0.005\text{sec}$, (a) central node deflection time-history diagram, (b) phase plane plot of the central node movement, (c) tension time-history diagram of segment 1, (d) tension time-history diagram of segment 3

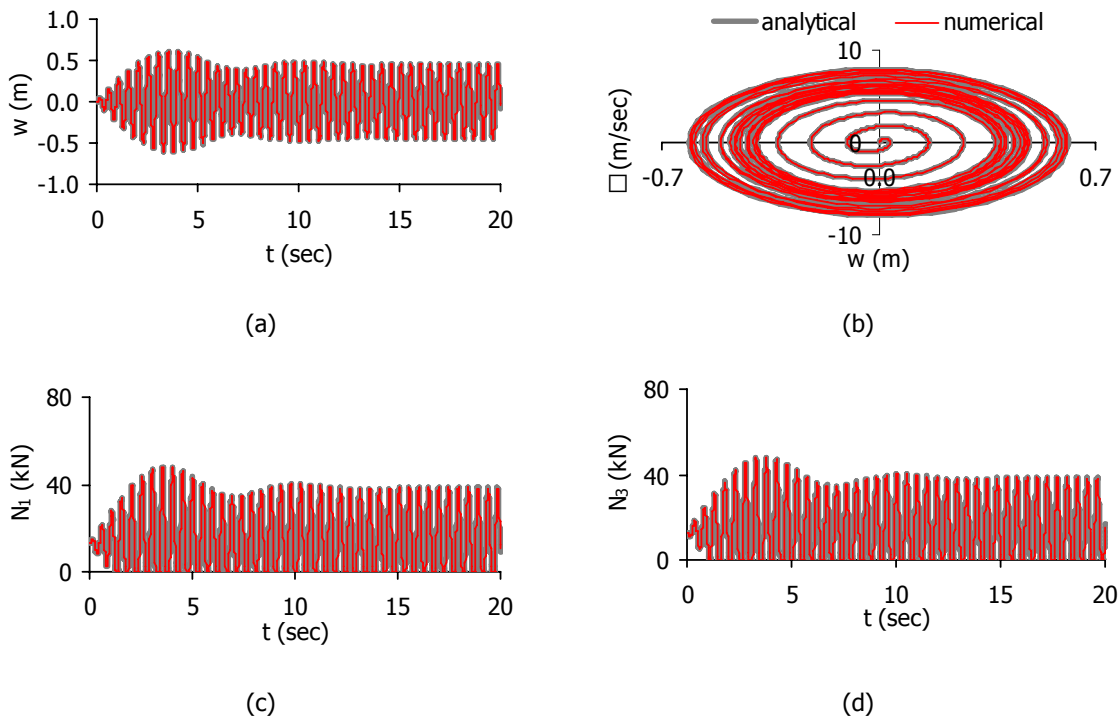


Figure 4-14: Dynamic response for $P=(1\text{kN})\cos(\omega_{z0}t)$, damping ratio $\zeta=2\%$ and $\Delta t=0.005\text{sec}$, (a) central node deflection time-history diagram, (b) phase plane plot of the central node movement, (c) tension time-history diagram of segment 1, (d) tension time-history diagram of segment 3

Table 4-8: Maximum deflection and cable tension for $P=(1\text{kN})\cos(\omega_{z0}t)$ and damping ratios $\zeta=0.5\%$ and $\zeta=2\%$

Procedure	$\Delta t=0.005\text{sec}$					
	$\zeta=0.5\%$			$\zeta=2\%$		
	w (m)	tension of segment (kN)		w (m)	tension of segment (kN)	
		1	3		1	3
analytical (A)	0.82	61.58	61.47	0.61	48.16	48.17
numerical (N)	0.81	61.38	61.29	0.61	48.07	48.07
(A-N)/A	1%	0.3%	0.3%	0%	0.2%	0.1%

For damping ratio $\zeta=0.5\%$, loading amplitude $P_0=10\text{kN}$, loading frequency equal to $\Omega=\omega_{z0}/3$ and time step $\Delta t=0.005\text{sec}$, the response of the system is illustrated in the charts of Figure 4-15, while the maximum response is listed in Table 4-9. The results do not show important differences between the analytical and the numerical procedures.

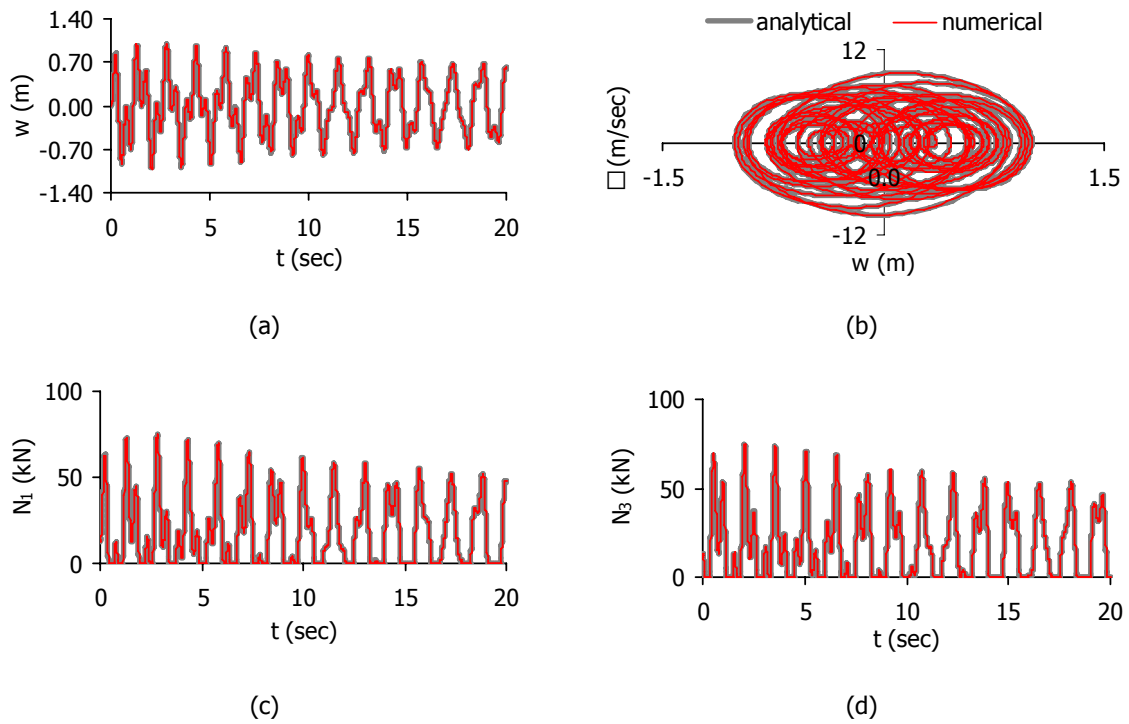


Figure 4-15: Dynamic response for $P=(10\text{kN})\cos(\omega_{z0}t/3)$, damping ratio $\zeta=0.5\%$ and $\Delta t=0.005\text{sec}$, (a) central node deflection time-history diagram, (b) phase plane plot of the central node movement, (c) tension time-history diagram of segment 1, (d) tension time-history diagram of segment 3

Table 4-9: Maximum deflection and cable tension for $P=(10\text{kN})\cos(\omega_{z0}t/3)$ and damping ratio $\zeta=0.5\%$

Procedure	$\Delta t=0.005\text{sec}$		
	w (m)	tension of segment (kN)	
		1	3
analytical (A)	1.01	74.97	75.10
numerical (N)	1.01	75.00	75.19
(A-N)/A	0%	0%	-0.1%

Keeping constant the loading amplitude and the damping ratio, while the loading frequency takes the value $\Omega=3\omega_{z0}$, the response of the net calculated by the two procedures for time step $\Delta t=0.0015\text{sec}$ is plotted in Figure 4-16 and the maximum magnitudes of the response are listed in Table 4-10. The difference between the numerical and the analytical results is insignificant.

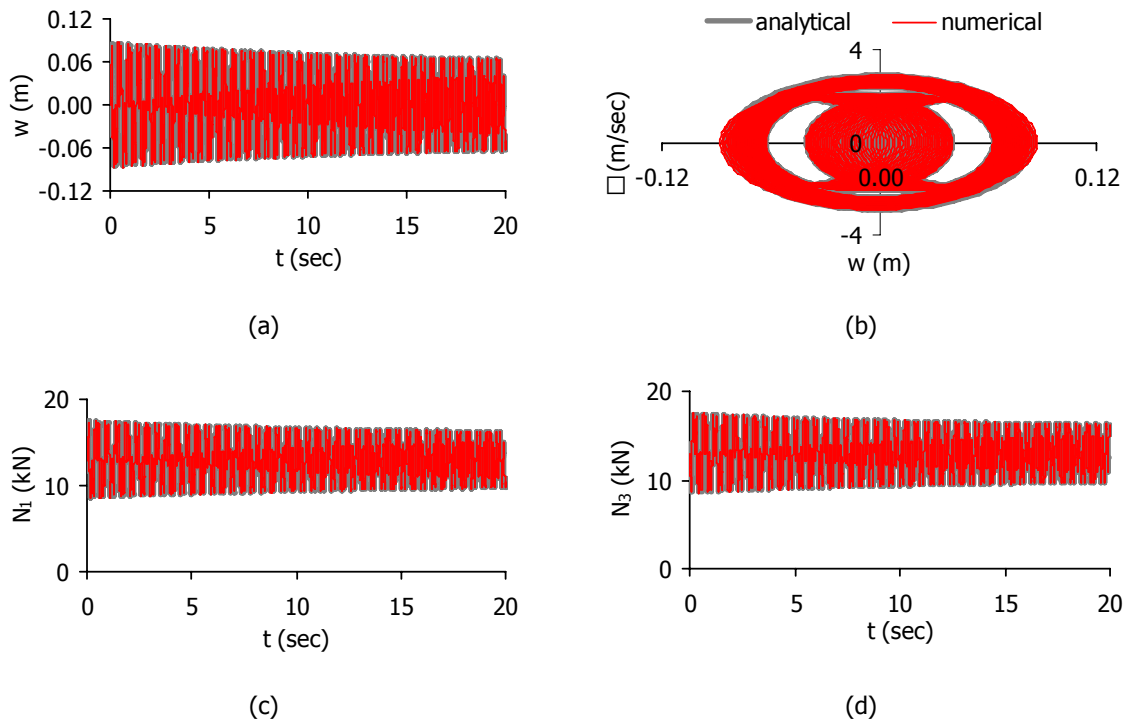


Figure 4-16: Dynamic response for $P=(10\text{kN})\cos(3\omega_{20}t)$, damping ratio $\zeta=0.5\%$ and $\Delta t=0.0015\text{sec}$, (a) central node deflection time-history diagram, (b) phase plane plot of the central node movement, (c) tension time-history diagram of segment 1, (d) tension time-history diagram of segment 3

Table 4-10: Maximum deflection and cable tension for $P=(10\text{kN})\cos(3\omega_{20}t)$ and damping ratio $\zeta=0.5\%$

Procedure	$\Delta t=0.0015\text{sec}$		
	w (m)	tension of segment (kN)	
		1	3
analytical (A)	0.09	17.41	17.42
numerical (N)	0.09	17.52	17.54
(A-N)/A	0%	-0.6%	-0.7%

4.3.6 Dynamic response under resonance

As shown in chapter 3, the maximum steady-state response for load amplitude $P_0=1\text{kN}$ and damping ratio $\zeta=0.5\%$ is observed for frequency ratio $\Omega/\omega_{20}=1.09$, considering initial deflection 1m and initial velocity 20m/sec, while for zero initial conditions the oscillation amplitude is small. The same problem is solved numerically, considering infinitely linear material regarding the tension branch. In Figure 4-17 the response for zero initial conditions is illustrated, while in Figure 4-18 the corresponding diagrams are plotted taking into account initial conditions. Aiming at superharmonic resonance, a numerical analysis is performed for loading amplitude $P_0=5\text{kN}$, damping ratio $\zeta=0.5\%$ and frequency ratio $\Omega/\omega_{20}=0.32$. The numerical results, compared with the analytical ones, are illustrated in Figure 4-19. Finally, as proved in the previous chapter, subharmonic resonance occurs for $\zeta=0.5\%$, $P_0=15\text{kN}$, $\Omega/\omega_{20}=3.09$ and initial conditions by means of deflection 1m and velocity 20m/sec. The numerical results for these assumptions are shown in Figure 4-20. In all cases the results obtained by the two approaches are compared, showing very good agreement.

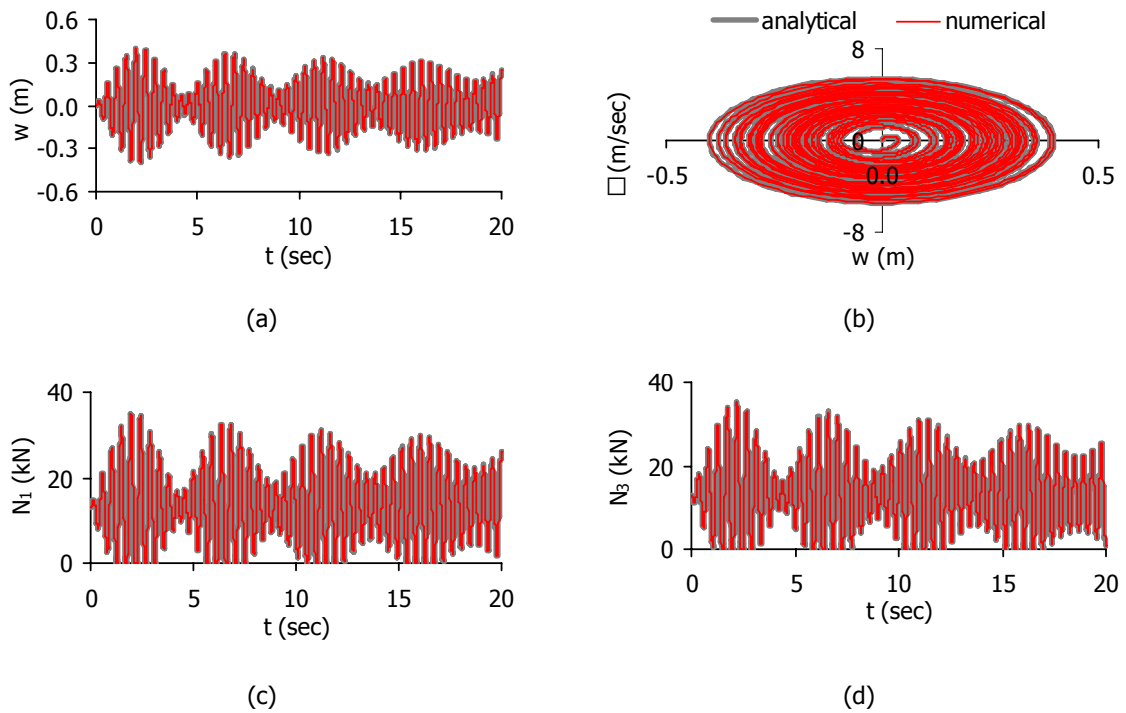


Figure 4-17: Dynamic response for $P=(1\text{kN})\cos(1.09\omega_{20}t)$, damping ratio $\zeta=0.5\%$, $\Delta t=0.004\text{sec}$ and zero initial conditions: (a) central node deflection time-history diagram, (b) phase plane plot of the central node movement, (c) tension time-history diagram of segment 1, (d) tension time-history diagram of segment 3

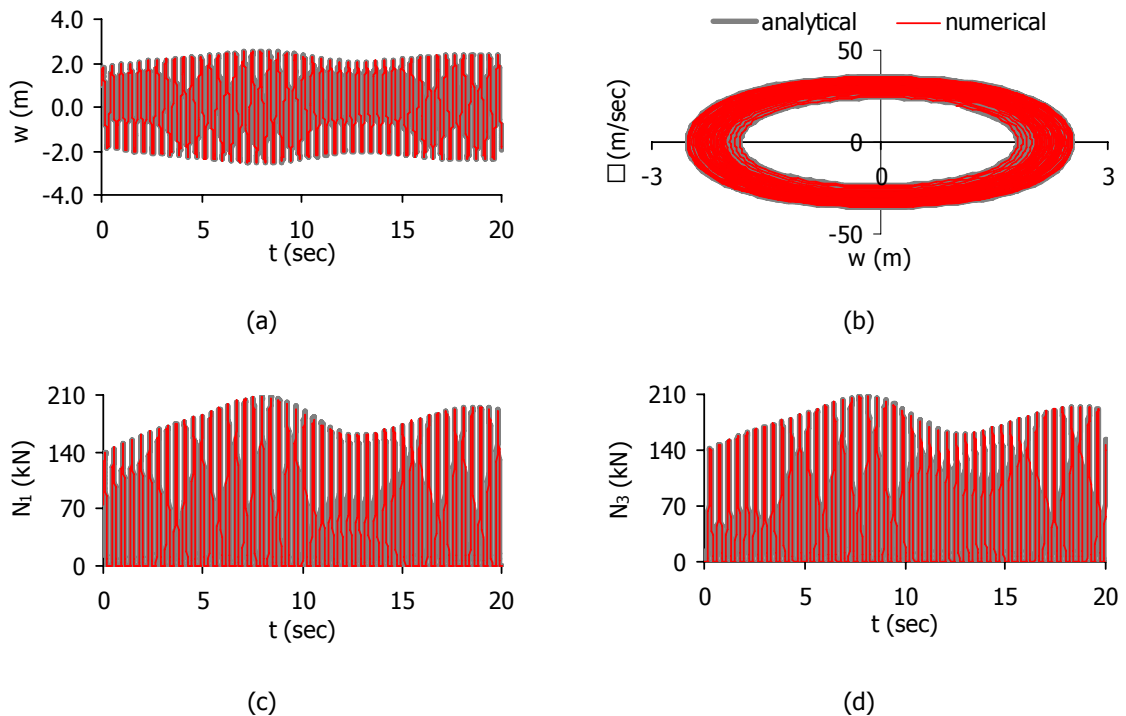


Figure 4-18: Dynamic response for $P=(1\text{kN})\cos(1.09\omega_{20}t)$, damping ratio $\zeta=0.5\%$, $\Delta t=0.004\text{sec}$ and initial conditions: (a) central node deflection time-history diagram, (b) phase plane plot of the central node movement, (c) tension time-history diagram of segment 1, (d) tension time-history diagram of segment 3

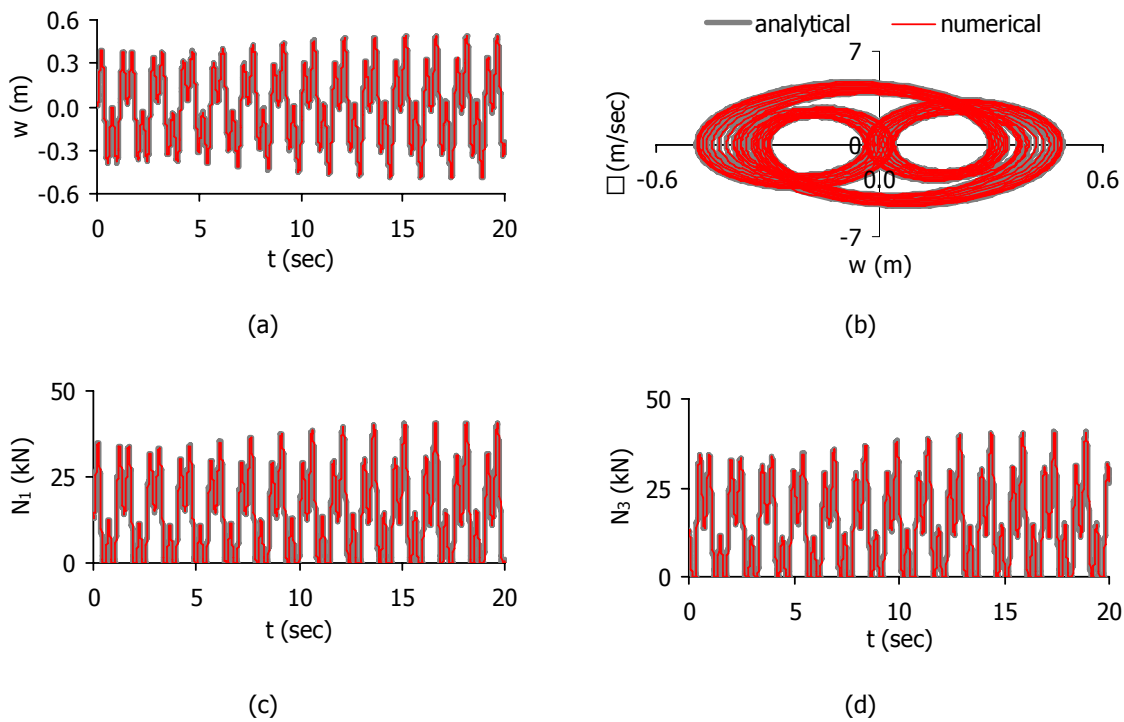


Figure 4-19: Dynamic response for $P=(5kN)\cos(0.32\omega_{20}t)$, damping ratio $\zeta=0.5\%$, $\Delta t=0.004\text{sec}$: (a) central node deflection time-history diagram, (b) phase plane plot of the central node movement, (c) tension time-history diagram of segment 1, (d) tension time-history diagram of segment 3

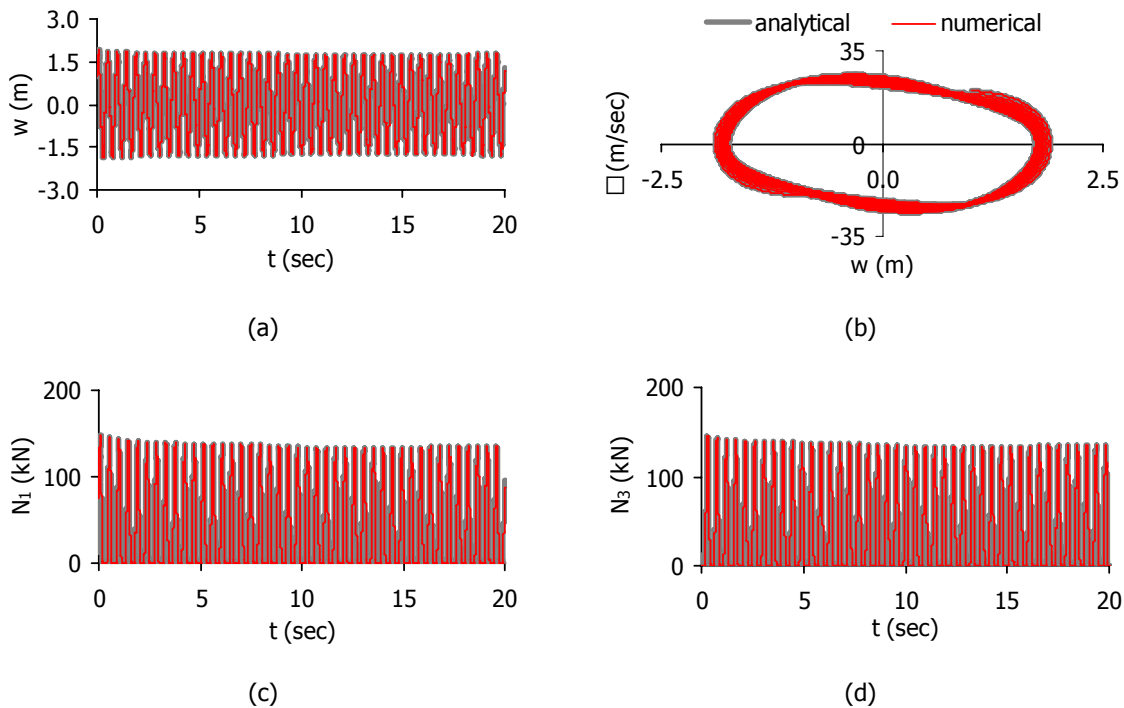


Figure 4-20: Dynamic response for $P=(15kN)\cos(3.09\omega_{20}t)$, damping ratio $\zeta=0.5\%$, $\Delta t=0.0015\text{sec}$ and initial conditions: (a) central node deflection time-history diagram, (b) phase plane plot of the central node movement, (c) tension time-history diagram of segment 1, (d) tension time-history diagram of segment 3

4.4 CONCLUSIONS

The finite element analysis software ADINA, which is chosen to be used for this work, gives results with minor differences compared with the analytical ones regarding the eigenfrequencies and the dynamic response to a harmonic load. The damping ratio introduced as Rayleigh damping, the nonlinear material, the distributed cable masses assumed as lumped and the initial conditions are proved to be taken into account correctly. Assuming small strains but large displacements, for common values of Young modulus of the cable material and for the permissible limits of cable stresses, the numerical solution does not differ substantially from the analytical one that takes into consideration large displacements and strains. Hence, the assumption of small strains adopted by the finite element software, gives sufficiently accurate results, for the allowable maximum values of the cable stresses. In addition, assuming as the initial length of the cables, the one under pretension and not the unstretched one, the results do not differ significantly. Concerning time-history analysis, the time step is an important parameter for the accuracy of the system's response. From the cases analysed in this chapter, the appropriate time step for accurate results is proved to be dependent on the system's period, but not on the loading amplitude. In order to achieve a compromise between the computational time required and a satisfactory accuracy of the results, the time step $T_{\min}/100$ is chosen, where T_{\min} is the smaller period between the system's period T_S and the loading period T_L .

4.5 REFERENCES

- [4-1] ADINA (Automatic Dynamic Incremental Nonlinear Analysis) v8.4, ADINA R & D, Inc., U.S.A., 2006.
- [4-2] ADINA (Automatic Dynamic Incremental Nonlinear Analysis) v8.4, ADINA User interface command reference manual, Vol. I: ADINA Solids & Structures model definition, ADINA R & D, Inc., U.S.A., 2006.
- [4-3] ADINA (Automatic Dynamic Incremental Nonlinear Analysis) v8.4, Theory and modeling guide, Vol. I: ADINA Solids & Structures, ADINA R & D, Inc., U.S.A., 2006.
- [4-4] E. Kreyszig, "Advanced engineering mathematics", 8th Edition, John Wiley & Sons, Inc., U.S.A., 1999.
- [4-5] K. J. Bathe and M. M. I. Baig, "On the composite implicit time integration procedure for nonlinear dynamics", Computers and Structures, Vol. 83, pp. 2513-2524, 2005.
- [4-6] A. K. Chopra, "Dynamics of structures, theory and applications to earthquake engineering", Prentice Hall International, Inc., U.S.A., 1995.
- [4-7] MAPLE, v.8.0, Waterloo Maple, Inc., Canada, 2002.
- [4-8] MATLAB, "The language of technical computing", v.7.9.0.529 (R2009b), The MathWorks, Inc., U.S.A., 2009.
- [4-9] H. M. Irvine, "Cable structures", Dover Publications, Inc., U.S.A., 1981.

5 EIGENFREQUENCIES AND EIGENMODES OF SADDLE-FORM CABLE NETS

5.1 INTRODUCTION

As shown in the previous chapters, the nonlinearity of cable structures may produce intense nonlinear phenomena, such as nonlinear resonances, bending of the response curve, hysteresis loops and jump phenomena. The natural frequencies of the cable system, although calculated by a modal analysis, which is a linear procedure, play an important role in the nonlinear dynamic behaviour, because they are used to define nonlinear resonances. The relation between the eigenfrequencies defines eventual internal resonances, which lead to a continuous exchange of energy among the corresponding vibration modes, even in free vibrations. The relation between the loading frequency and the natural frequencies defines fundamental, superharmonic and subharmonic resonances for a forced vibration. All these phenomena, related to the linear natural frequencies as well as the loading frequency, render the dynamic response of a nonlinear system unpredictable [5-1].

Many researchers have focused their interest on the vibration modes and natural frequencies of individual cables, starting from Pugsley [5-2] who gave semi-empirical formulae for the three in-plane frequencies of a suspended sagged chain. Gambhir and Batchelor [5-3] explored parametrically the influence of the cable mass, the sag, the span, and the vertical distance of the cable ends, on the natural frequencies of a sagged inclined cable. Irvine and Caughey [5-4] introduced an important parameter for simple cables. This parameter, named λ^2 , collects the geometrical and mechanical characteristics of a sagged suspended cable, defines crossover points, at which modal transition and internal resonances occur between the first symmetric and the first antisymmetric in-plane modes, and governs the symmetric in-plane modes. When this parameter is very large, the cable may be considered as inextensible, and when it is very small, the cable profile approaches that of a taut string. This parameter is defined as:

$$\lambda^2 = \left(\frac{mgAL}{H} \right)^2 \frac{LEA}{HL_e} \quad (5-1)$$

where mgA is the cable weight per unit length, E is the elastic modulus of the cable material, A is the cable cross-sectional area, L is the cable span, H is the horizontal component of the tension, and L_e is approximately equal to the cable length, defined as:

$$L_e = L \left[1 + 8 \left(\frac{f}{L} \right)^2 \right] \quad (5-2)$$

where f is the sag. Assuming that for small sag-to-span ratios, $L \approx L_e$ and taking into account the expression of the horizontal component of tension, constant along the cable, which is given from the static equilibrium as:

$$H = \frac{mgAL^2}{8f} \quad (5-3)$$

the above expression of Eq. (5-1) becomes:

$$\lambda^2 = 64 \left(\frac{f}{L} \right)^2 \frac{EA}{H} \quad (5-4)$$

In their study Irvine and Caughey considered the cable as extensible, with a sag-to-span ratio up to $1/8$ and they compared their results with experimental ones. They verified that the first symmetric mode has a natural frequency smaller than the one of the first antisymmetric mode for $\lambda^2 < 4\pi^2$. These two frequencies become equal when $\lambda^2 = 4\pi^2$, corresponding to a crossover point, while for larger values of this parameter the first antisymmetric mode becomes the first mode of the system, having the smallest natural frequency. The authors also reported that the shape of the cable's first symmetric mode changes with respect to this parameter. Thus, for $\lambda^2 < 4\pi^2$, the vertical component of this mode has no internal nodes with zero displacements, for $\lambda^2 = 4\pi^2$ the vertical component is tangential to the profile at the supports, while for $\lambda^2 > 4\pi^2$, two internal nodes with zero displacements appear (Figure 5-1).

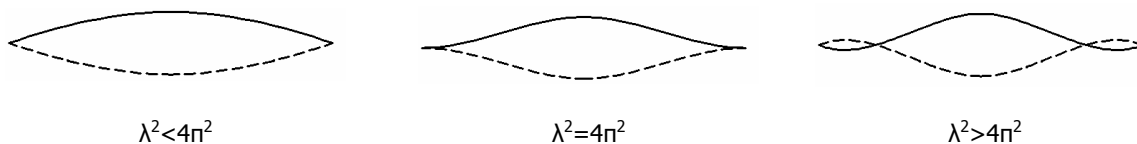


Figure 5-1: Profile of the deformed cable for the first symmetric mode

The parameter λ^2 was used by other researchers for further investigation of simple sagged cables ([5-5], [5-6], [5-7]), or inclined cables ([5-8], [5-9]). For the latter, instead of crossover points, avoidance points were detected, meaning that, while in frequency crossover two natural frequencies become close, in frequency avoidance they always remain apart and never coincide.

Regarding multi-degree-of-freedom cable networks, in [5-10] the authors presented a finite element method for the analysis of prestressed cable networks, based on Hamilton's principle and modelling the cables with curved elements. The fundamental frequency was calculated and compared with the results of other methods, as well as with experimental data, showing good agreement. In [5-11] they studied the natural frequencies of 3D saddle-form cable nets with respect to various parameters, such as the cable cross-sectional area, the initial pretension, the sag-to-span ratio, and the surface curvature. In [5-12] a transfer matrix method was presented in order to carry out vibration analyses of orthogonal cable nets without initial sag. They showed that the frequencies of the net are independent of the number of cables in each direction. A computational scheme for calculating the eigenvalues and eigenvectors of cable nets was presented in [5-13].

In [5-14] the influence of the boundary ring on the static response of the cable net was proved to be significant. Talvik [5-15] mentioned that, if the flexibility of the contour ring of a cable network is taken into consideration, the first vibration mode involves mostly the contour ring, while the next four modes are determined only by cable net deformations. Seeley et al. [5-16] investigated the eigenfrequencies and eigenmodes of a concave cable network with a circular plan view, consisting of circular and radial cables. The sag of the net was obtained by the static loading and the range of sag-to-span ratio was between 1/9 and 1/15. They noticed that only the higher order frequencies depend on the extensibility of the network, expressed by a parameter in terms of the elastic modulus of the cable material, the cable cross-sectional area, the number of radial cables, the diameter of the network and the uniformly distributed dead load. They derived an approximate formula of the fundamental circular frequency of the net, involving only the sag and the sag-to-span ratio, concluding that the first natural frequency of the concave cable net is close to the average of the uncoupled in-plane and out-plane fundamental frequencies of an individual cable with the same sag/span ratio. Buchholdt [5-17] mentioned that cable sags between 4% and 6% of the span results in satisfactory structural behaviour, if the level of pretension is high enough so that no cable slackening occurs under any combination of loading. He also suggested that in order to calculate with accuracy the eigenfrequencies of a cable roof, the deformed state under permanent loads and the wind load produced by the mean wind velocity should be taken into account. He reported measured frequencies of a saddle-shaped net roof, with a circular plan of 125m diameter, between 0.74Hz and 1.12Hz for the first seven modes.

In this chapter the dynamic behaviour of saddle-form cable networks is analysed, regarding the natural frequencies and vibration modes. The cable ends are considered either as fixed or anchored to a boundary ring. This ring is usually made of prestressed concrete, having a closed box cross-section. It is much stiffer than the cable net, but not stiff enough to neglect its elastic deformability, which influences significantly the net's behaviour, as proved in [5-18], during the early stages of this work.

5.2 MODELLING ISSUES AND ASSUMPTIONS

The model adopted is a three-dimensional symmetric cable net, having the geometry of a hyperbolic paraboloid surface and a circular plan view of diameter L . The network consists of N cables in each direction, arranged in a quadratic grid. The sag of the longest main and secondary cables is equal to f , which is also considered as the sag of the roof. In Figure 5-2 the geometry of the cable net is defined. In this Figure, an auxiliary coordinate system $x'y'$ is also shown, which will be used further on. All cables have a circular cross-section with diameter D and area A and their material is assumed infinitely linearly elastic with Young modulus E . They are simulated by truss elements that can sustain only tension. Each part of a cable between two adjacent net intersection points is modelled with one straight truss element, with no flexural stiffness. The initial cable pretension is N_0 , which is introduced as initial strain in all cables, equal to $\varepsilon_0 = N_0/EA$. The cable mass density is equal to m and an additional concentrated nodal mass M may also be considered. A lumped mass matrix is used for the analysis. All three translational degrees of freedom are considered as free for all internal nodes of the net. For the net with rigid supports, the cable ends are modelled as pinned (Figure 5-3).

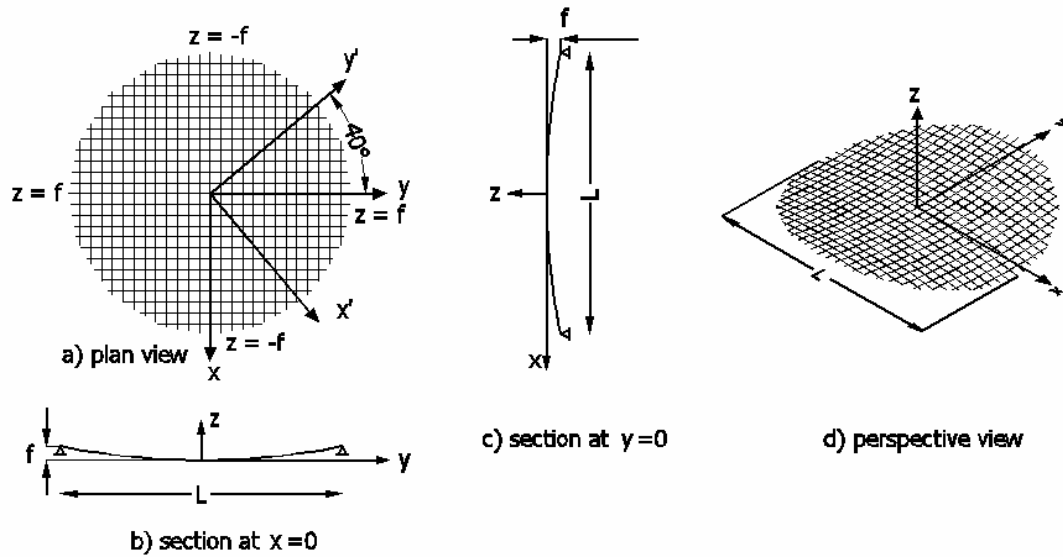


Figure 5-2: Geometry of the cable net with rigid supports

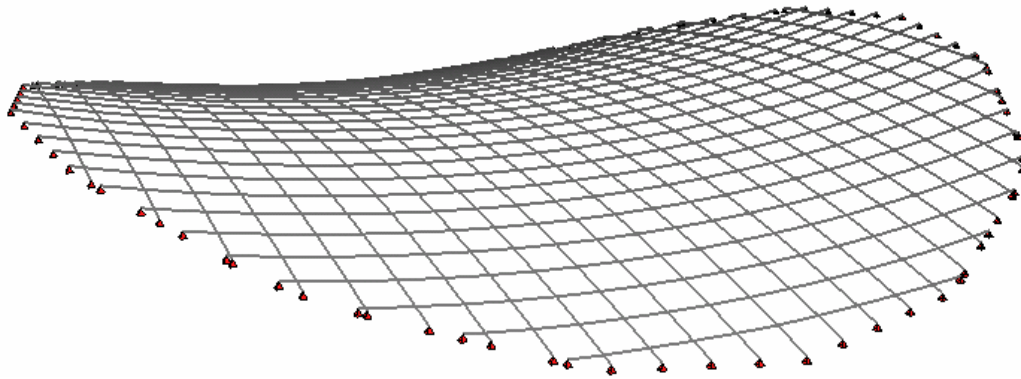


Figure 5-3: Model of the cable net with fixed ends

Without loss of generality, the edge ring, if considered, has a square box cross-section of width b , wall thickness $b/10$, with cross-sectional area A_r , moment of inertia I_r , unit weight ρ_r and elastic modulus E_r (Figure 5-4). The z -displacement of the ring's nodes is restrained. The displacement in the x -direction is not permitted for the two nodes of the ring with coordinate $x=0$, and, respectively, the y -displacement is not permitted for the two ring nodes with coordinate $y=0$, in order to avoid rigid body motion. Thus, the radial deformation of the ring is allowed, but not the overall rotation about the z global axis. The local y -axes of the beams modelling the boundary ring are oriented towards the central node of the net. The model of this cable net is shown in Figure 5-5.

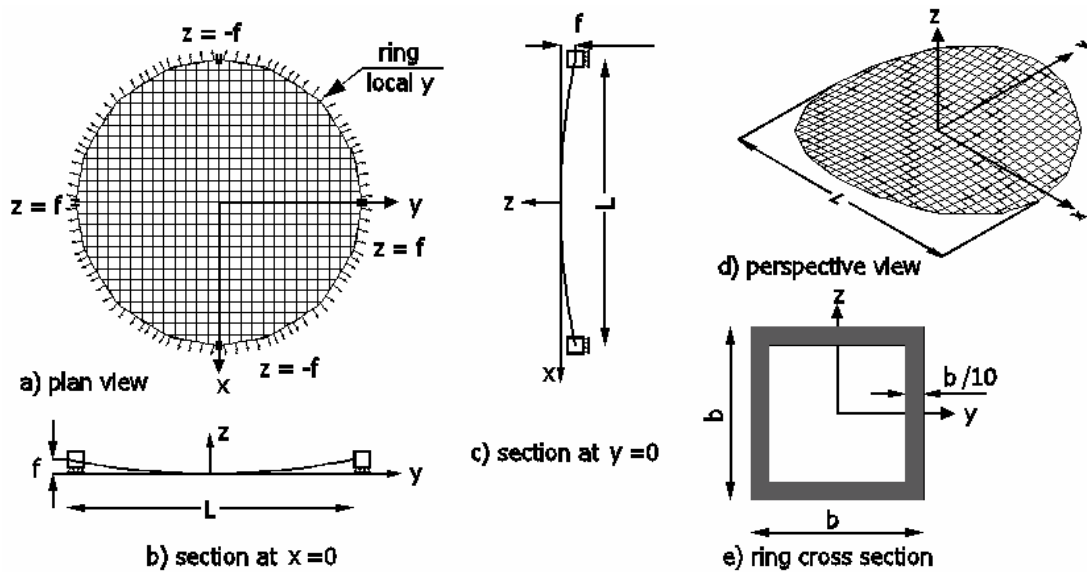


Figure 5-4: Geometry of the cable net with flexible edge ring

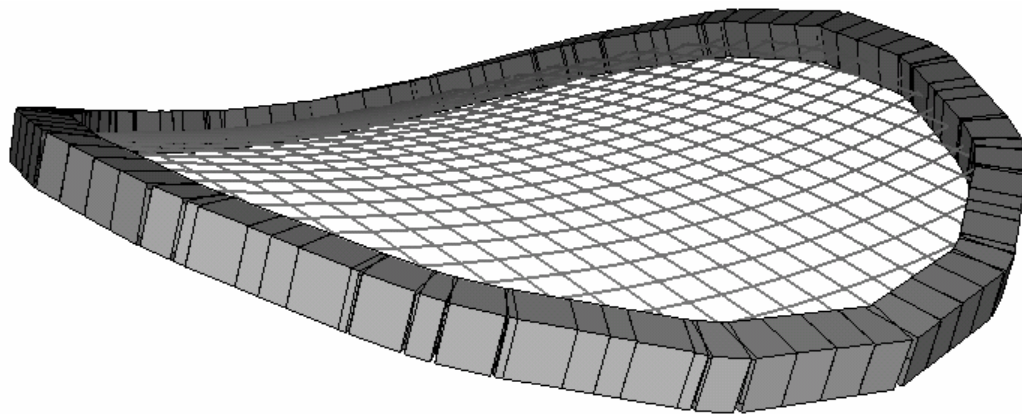


Figure 5-5: Model of the cable net with the boundary ring

The net is uniformly prestressed. Linear modal analyses are performed to calculate the eigenmodes and eigenfrequencies. It should be mentioned that the concentrated nodal masses, whenever they are taken into account, are applied only on the free nodes of the cable net and not on the ring nodes, because the ring's mass is already much larger and any additional mass is considered as negligible. For the calculation of the natural frequencies of the system, the geometry and stiffness of the state under prestressing are considered, as will be explained further on. All analyses have been carried out with the finite element software ADINA ([5-19] and [5-20]).

5.3 INITIAL STATE UNDER PRETENSION

Two typical cable nets are studied in the state of pretension, without a boundary ring. In these cable nets, there are 25 cables in each direction, their diameter in plan view is $L=100\text{m}$, the material of the cables has an elastic modulus $E=165\text{GPa}$ and the cable mass density is equal to $10.0\text{kN/m}^4\cdot\text{sec}^2$. The cables have a diameter $D=50\text{mm}$. The initial pretension is assumed to be equal to 500kN for all cable segments, introduced as initial strain. The sag-to-span ratio for the first cable net is equal to $1/20$ (Figure 5-6) while for the second one it is $1/10$ (Figure 5-7). In this case, the first four natural frequencies are tabulated in Table 5-1 for both nets.

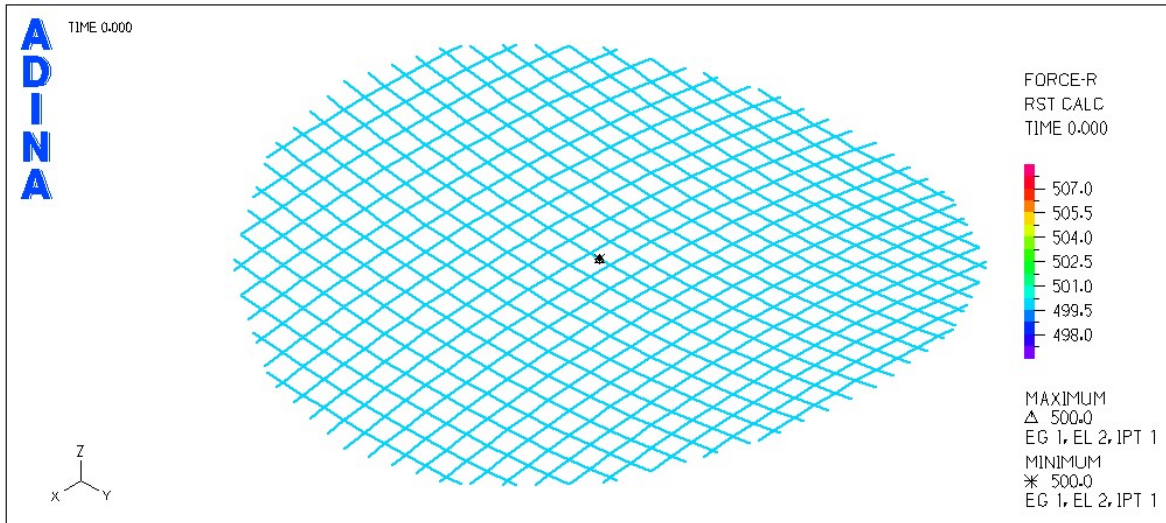


Figure 5-6: Cable tension for the cable net with $f/L=1/20$, considering initial pretension $N_0=500\text{kN}$

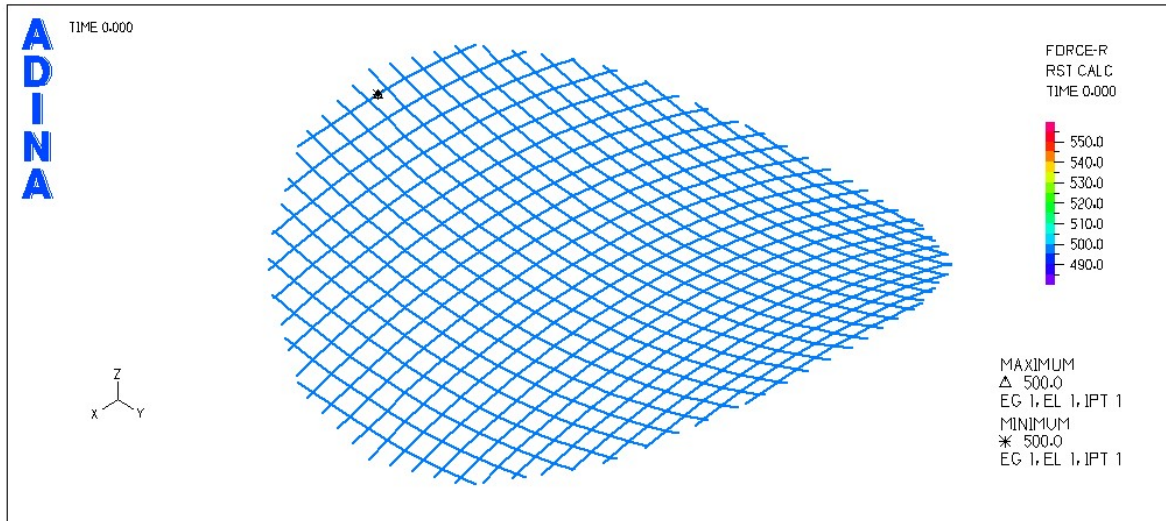
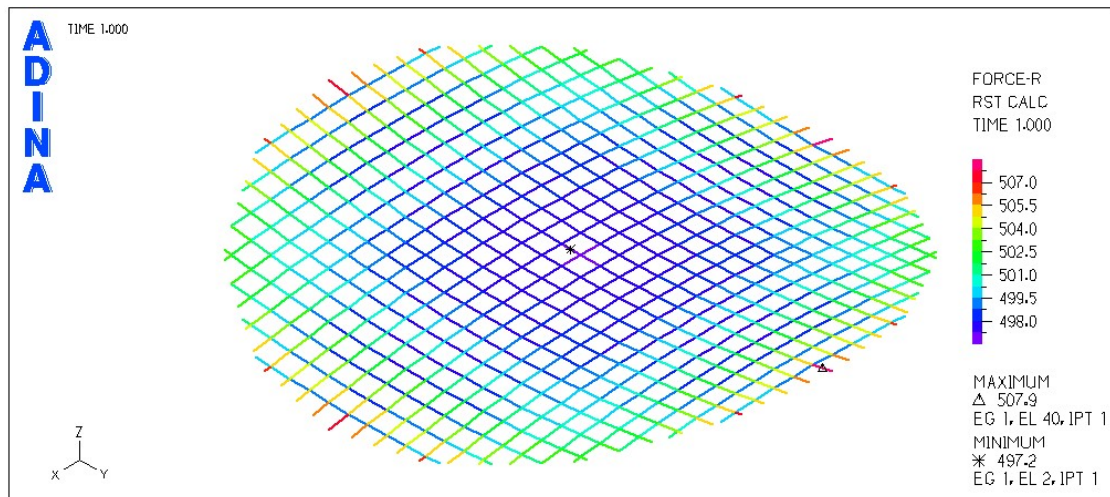
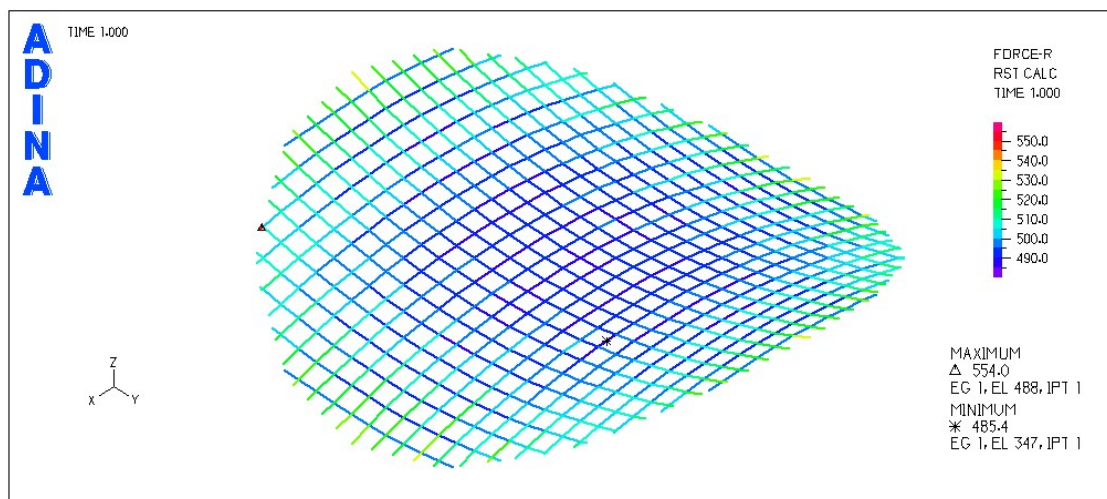


Figure 5-7: Cable tension for the cable net with $f/L=1/10$, considering initial pretension $N_0=500\text{kN}$

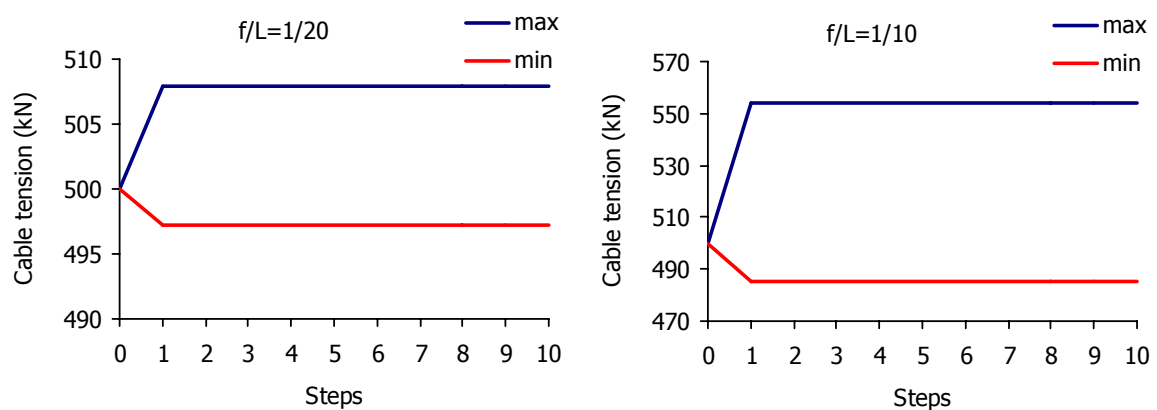
Table 5-1: Eigenfrequencies of the nets considering a uniform cable tension

	$f/L=1/20$	$f/L=1/10$
$\omega_1[\text{sec}^{-1}]$	11.57	11.22
$\omega_2[\text{sec}^{-1}]$	12.32	13.80
$\omega_3[\text{sec}^{-1}]$	12.32	13.80
$\omega_4[\text{sec}^{-1}]$	13.23	15.82

A nonlinear static analysis is performed next, considering only the pretension, in ten steps. The change of pretension, which corresponds to each cable segment when all nodes are in equilibrium, is illustrated in Figure 5-8 for the first cable net and in Figure 5-9 for the second one. This analysis is considered as equivalent to the stage of form-finding.

Figure 5-8: Cable tension at the static equilibrium state for the cable net with $f/L=1/20$ Figure 5-9: Cable tension at the static equilibrium state for the cable net with $f/L=1/10$

It is worth mentioning that the equilibrium is obtained already from the first step of the analysis, as shown in Figure 5-10. The maximum tensions are 508kN and 554kN and the minimum ones 497kN and 485kN for the two cable nets with $f/L=1/20$ and $f/L=1/10$, respectively. It is noted that as the curvature increases, the tension variation along the cable also increases.

Figure 5-10: Maximum and minimum cable tension for the cable net with $f/L=1/20$ and $f/L=1/10$

The level of pretension variance is compared with results obtained with the finite element software EASY [5-21], which is a program for the integrated analysis and design of lightweight surface structures. The cable tension distribution for the net with $f/L=1/20$ is shown in Figure 5-11 and for $f/L=1/10$ in Figure 5-12, as calculated with EASY at the stage of form-finding.

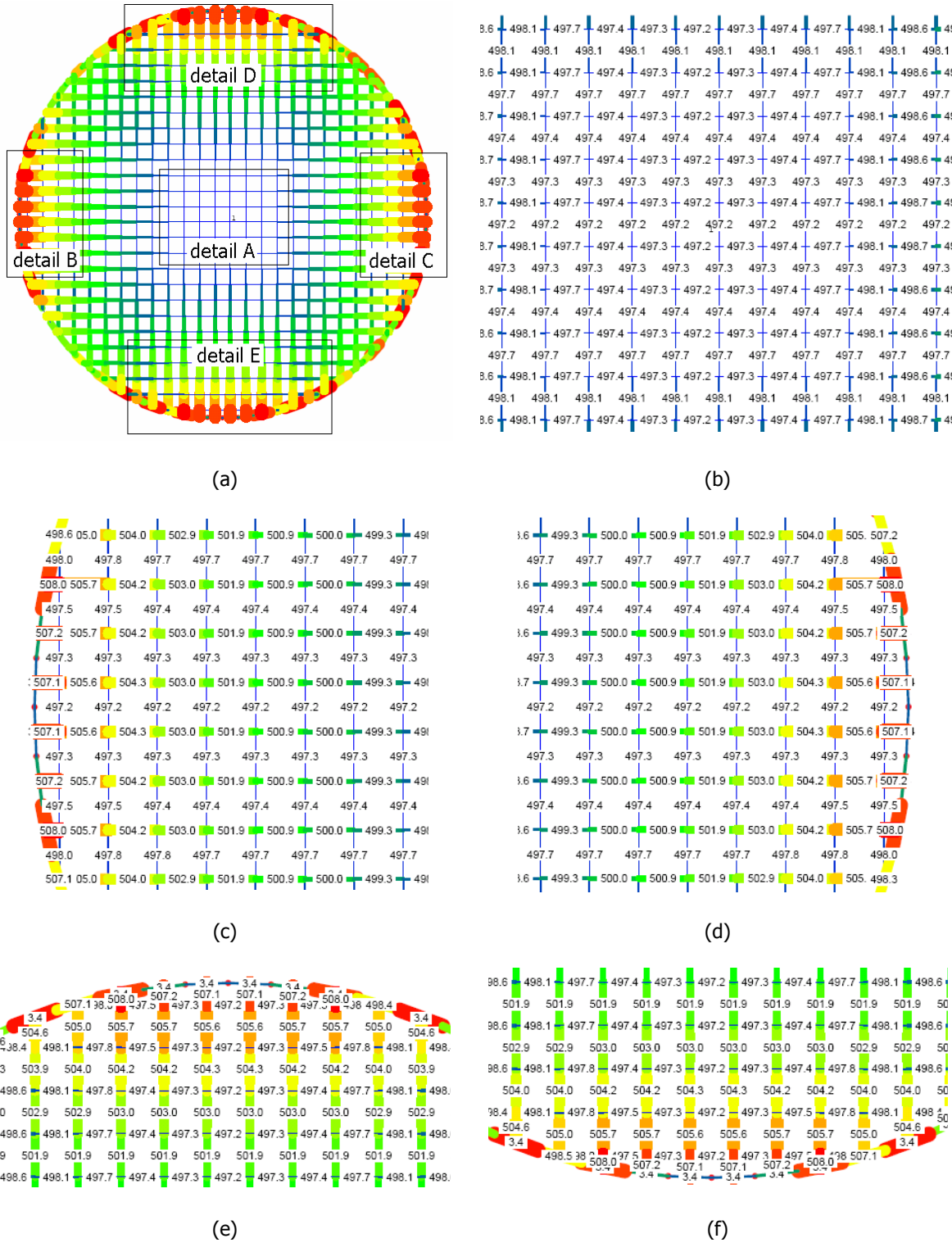


Figure 5-11: (a) Schematic diagram of cable tensions after form-finding obtained with EASY for the cable net with $f/L=1/20$, (b) detail A, (c) detail B, (d) detail C, (e) detail D, (f) detail E

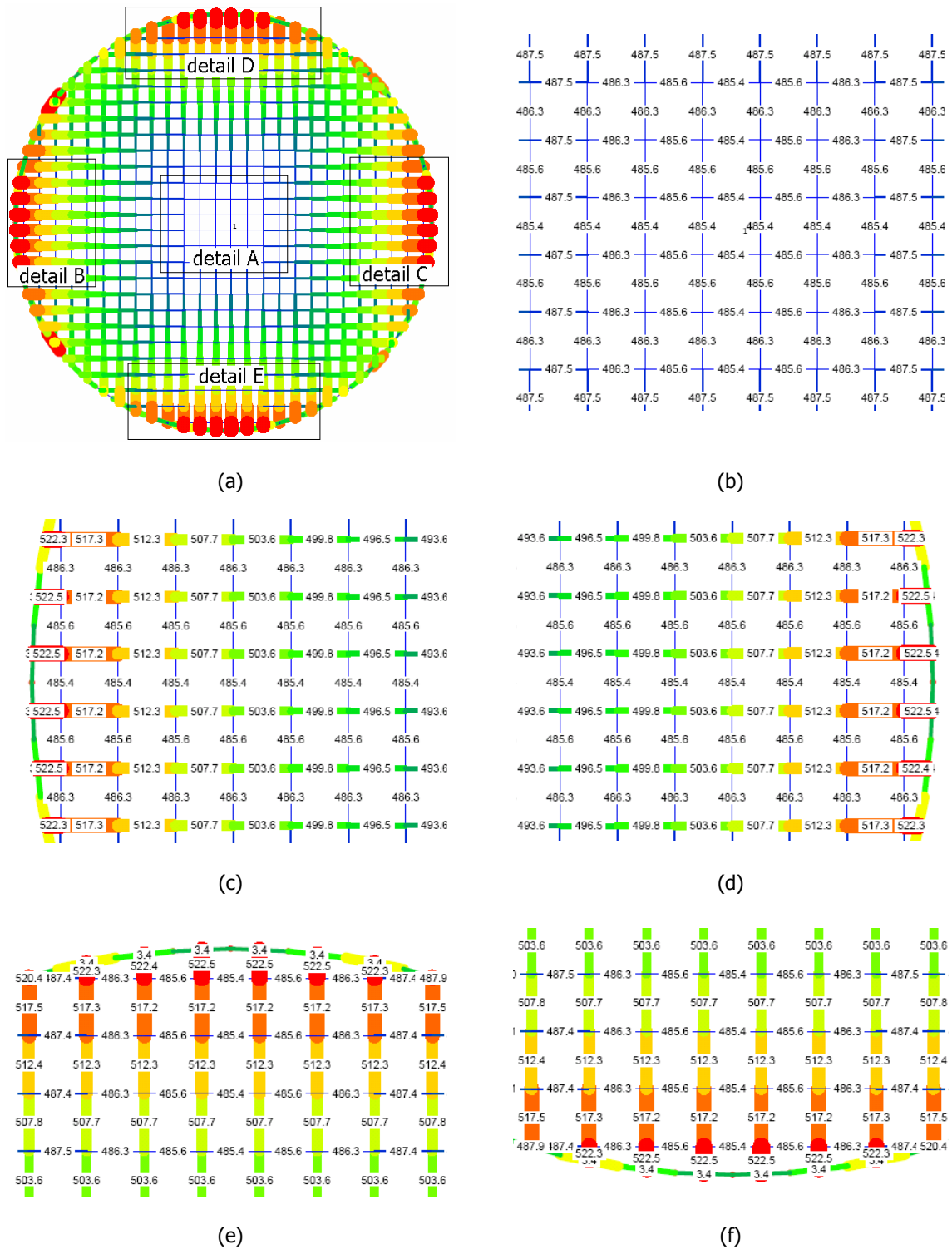


Figure 5-12: (a) Schematic diagram of cable tensions after form-finding obtained with EASY for the cable net with $f/L=1/10$, (b) detail A, (c) detail B, (d) detail C, (e) detail D, (f) detail E

Assuming a horizontal component of pretension equal to the minimum cable tension calculated by ADINA, that is 497kN for $f/L=1/20$ and 485kN for $f/L=1/10$, the form-finding obtained with EASY results in a maximum cable tension equal to 507kN and 523kN, respectively. For the cable net with $f/L=1/20$ the difference between the results of ADINA and EASY is almost 0.2%, while for the second

cable net with $f/L=1/10$, the difference arises to 6%. However, the difference is considered as small in both cases.

The new cable tensions, after equilibrium is obtained, are inserted in the ADINA model and the deformed state under pretension is considered as the initial state in order to calculate again the eigenfrequencies of the two cable nets. In this case the natural frequencies are tabulated in Table 5-2. Comparing them with the ones of Table 5-1, it is observed that the difference is larger for the deep cable net, but can be considered as negligible, for both cable networks. Hence, for simplicity, in what follows, a uniform strain will be inserted in all cable segments for the first step of the analysis.

Table 5-2: Eigenfrequencies of the nets considering the cable tension at the static equilibrium state

	$f/L=1/20$	$f/L=1/10$
ω_1 [sec ⁻¹]	11.57	11.21
ω_2 [sec ⁻¹]	12.31	13.77
ω_3 [sec ⁻¹]	12.31	13.77
ω_4 [sec ⁻¹]	13.22	15.78

5.4 CABLE NET WITH RIGID SUPPORTS

5.4.1 The vibration modes

In order to investigate the vibration modes of a cable net with rigid supports, parametric analyses were performed for a large number of cable net models with different geometrical and mechanical characteristics, regarding the number of cables in each direction N , the projected diameter L , the sag-to-span ratio f/L , the initial pretension N_0 , the elastic modulus of the cable material E , the cable mass density m , the nodal concentrated mass M , the cable diameter D and thus the cross-sectional area A .

The cable net's eigenmodes can be distinguished in symmetric and antisymmetric ones. The former ones consist of symmetric vertical components and antisymmetric horizontal components with respect to both horizontal axes x and y , while the latter ones consist of antisymmetric vertical components and symmetric horizontal components with reference to one, or to both horizontal axes. In this work, the first four modes are thoroughly studied, which are (i) the first symmetric mode of the net, denoted as 1S, (ii) the first antisymmetric modes with respect to x' or y' axis (Figure 5-2), respectively, which, due to the symmetry of the model, are similar, with equal eigenfrequencies and thus are treated as one mode, denoted, both of them, as 1A and finally (iii) the first antisymmetric mode with respect to both horizontal axes, which is denoted as 2A. In Figure 5-13 the z -eigenvector of the first four modes are shown, indicating the z -displacements of the net nodes, as well as the axes of symmetry, while in Figure 5-14 the deformed structure according to these four modes is illustrated.

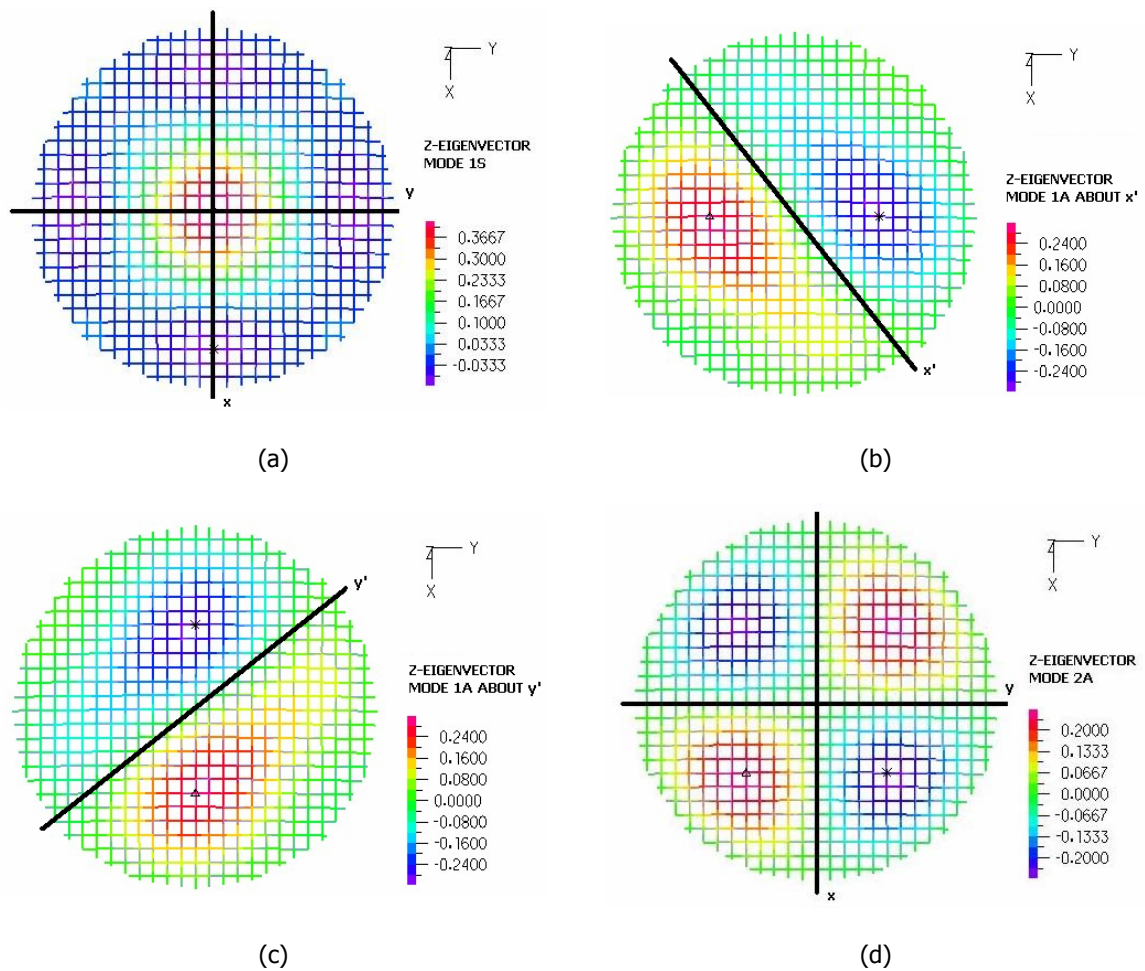


Figure 5-13: Z-eigenvectors of the first four vibration modes of a cable net with rigid supports, a) mode 1S, b) and c) modes 1A, d) mode 2A

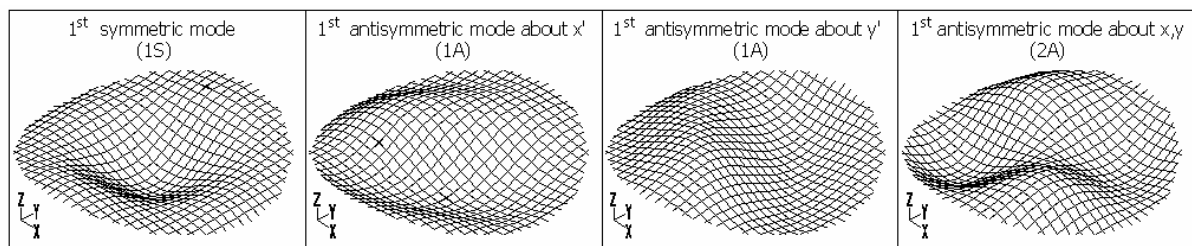


Figure 5-14: The first four vibration modes of a cable net with rigid supports

Looking into the eigenmodes and eigenfrequencies of the cable nets, frequency crossovers and modal transitions, similar to those occurred for the simple suspended cable, were also observed, meaning that the eigenmodes do not appear necessarily in a specific sequence. To describe these phenomena, a parameter λ^2 is herein introduced for cable nets, similar to that for a simple cable, which is expressed as:

$$\lambda^2 = \left(\frac{f}{L}\right)^2 \frac{EA}{N_0} \tag{5-5}$$

where N_0 is the mean value of the pretension of all cables. Small values of this parameter are noted for shallow cable nets, or deep cable nets with low levels of pretension. Accounting for realistic structures, with the Young modulus taking values between 140GPa and 170GPa, the initial cable stress varying between 0.10 and 0.35 of the yield stress, with a yield stress 1570MPa or 1670MPa, considering the two most common categories of steel for cables 1570/1770MPa and 1670/1860MPa, respectively, the minimum and maximum values of parameter λ^2 with respect to the sag-to-span ratio are shown in Figure 5-15.

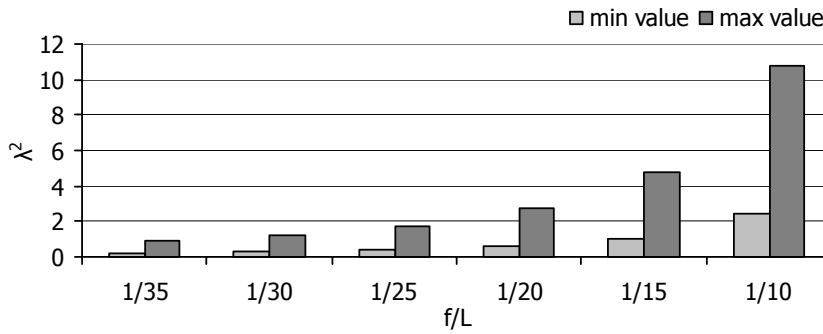


Figure 5-15: Variation of the parameter λ^2 with respect to sag/span ratio f/L

The modes of the cable net are found to depend on the parameter λ^2 , in a similar manner as for the simple cable. More specifically:

a) For $\lambda^2 \leq 0.80$ the first eigenmode of the system is mode 1S, while the second and third eigenmodes are modes 1A. The fourth eigenmode is mode 2A. Mode 1S has a natural frequency smaller than the one of modes 1A, which in turn, is smaller than the frequency of mode 2A, that is $\omega_{1S} < \omega_{1A} < \omega_{2A}$. For $\lambda^2 = 0.80$ the first three eigenmodes have equal natural frequencies, which means $\omega_{1S} = \omega_{1A}$, accounting for the first crossover point. The first four eigenmodes have the sequence shown in Figure 5-16.

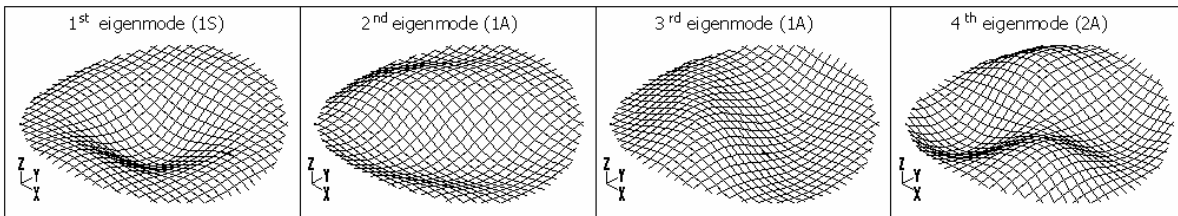


Figure 5-16: The first four eigenmodes of a cable net with rigid supports for $\lambda^2 \leq 0.80$

b) For $0.80 < \lambda^2 \leq 0.98$ the natural frequencies of the first two eigenmodes, which are modes 1A, are equal and smaller than that of mode 1S, which is the third cable net eigenmode, followed by mode 2A. This means $\omega_{1A} < \omega_{1S} < \omega_{2A}$. For $\lambda^2 = 0.98$ the natural frequencies of the 3rd eigenmode – which is mode 1S – and the fourth eigenmode – which is mode 2A – are equal, that is $\omega_{1S} = \omega_{2A}$ (second crossover point). The sequence of the first four eigenmodes is shown in Figure 5-17.

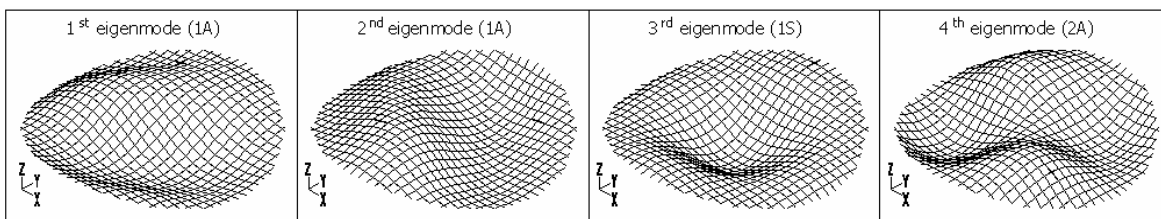


Figure 5-17: The first four eigenmodes of a cable net with rigid supports for $0.80 < \lambda^2 \leq 0.98$

c) For $0.98 < \lambda^2 \leq 1.17$ (Figure 5-18) a transition between the 3rd and 4th eigenmodes occurs. Thus, mode 1S becomes the 4th cable net eigenmode, while modes 1A remain the first two eigenmodes. This means $\omega_{1A} < \omega_{2A} < \omega_{1S}$. For $\lambda^2 = 1.17$ the natural frequencies of the 1st, 2nd and 3rd eigenmodes are equal, that is $\omega_{1A} = \omega_{2A}$ (third crossover point).

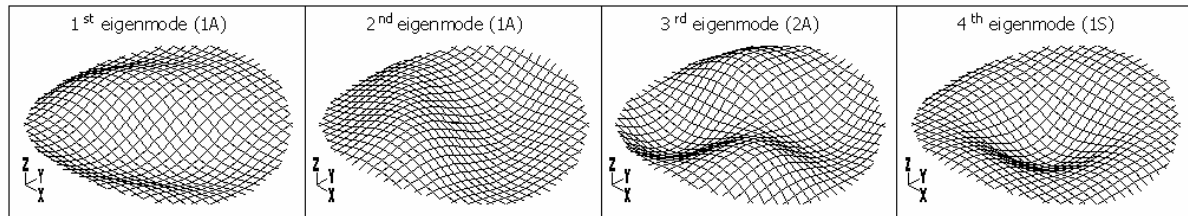


Figure 5-18: The first four eigenmodes of a cable net with rigid supports for $0.98 < \lambda^2 \leq 1.17$

d) For $1.17 < \lambda^2$ (Figure 5-19) a transition between the 3rd and the first two eigenmodes occurs. Mode 2A becomes the first mode of the system, modes 1A become second and third, while 1S remains the fourth mode. This means $\omega_{2A} < \omega_{1A} < \omega_{1S}$.

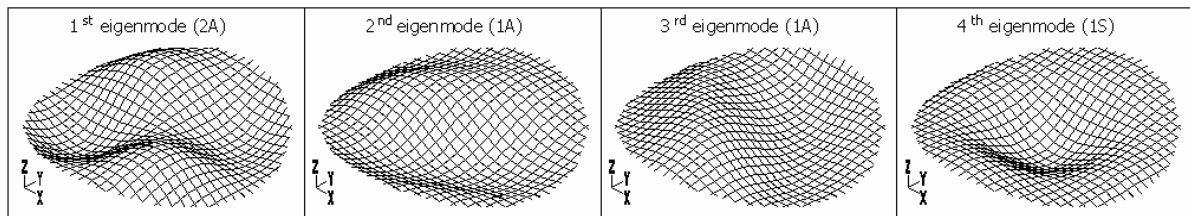


Figure 5-19: The first four eigenmodes of a cable net with rigid supports for $1.17 < \lambda^2$

The above limits of λ^2 refer to the first four eigenmodes of a cable net with rigid supports. Transitions among higher modes also occur for different values of λ^2 .

The shape of the first symmetric mode changes with respect to parameter λ^2 , as also occurs for simple suspended cables. Thus, for small values, smaller than 1.17, the vertical component of this mode has no internal nodes with zero displacements (Figure 5-20), for values near 1.17 the vertical modal component is tangential to the horizontal plane at the cable ends (Figure 5-21), while for large values, larger than 1.17, internal nodes with zero displacements are observed (Figure 5-22).

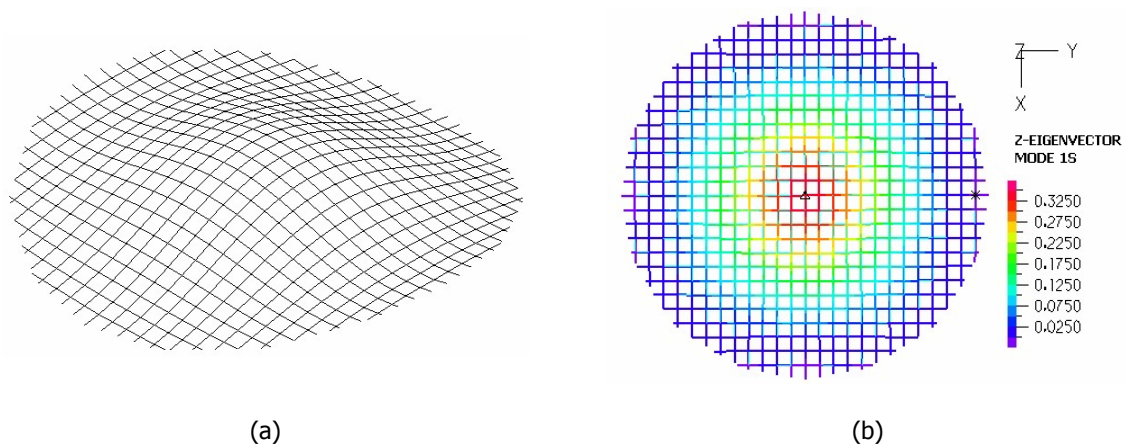


Figure 5-20: First symmetric mode of a cable net with rigid supports for $\lambda^2 = 0.70$ (< 1.17), a) perspective view, b) Z-eigenvector

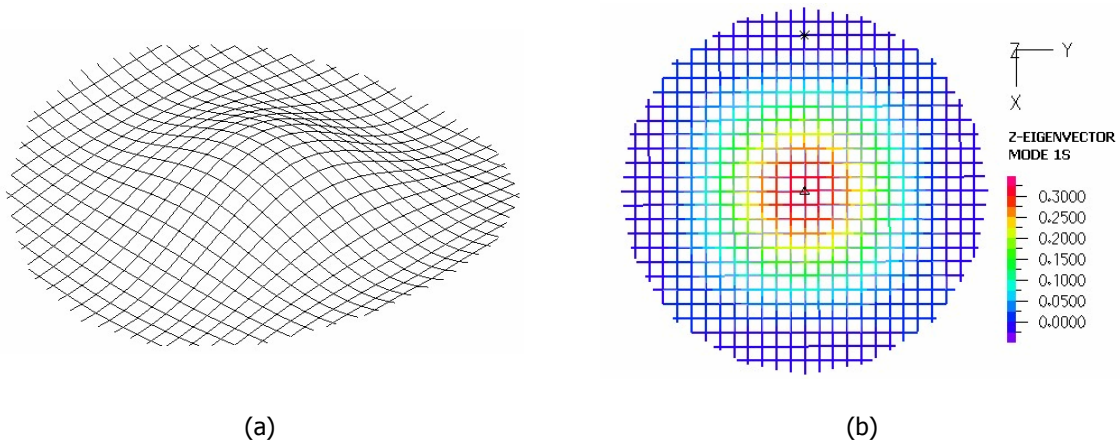


Figure 5-21: First symmetric mode of a cable net with rigid supports for $\lambda^2=1.17$, a) perspective view, b) Z-eigenvector

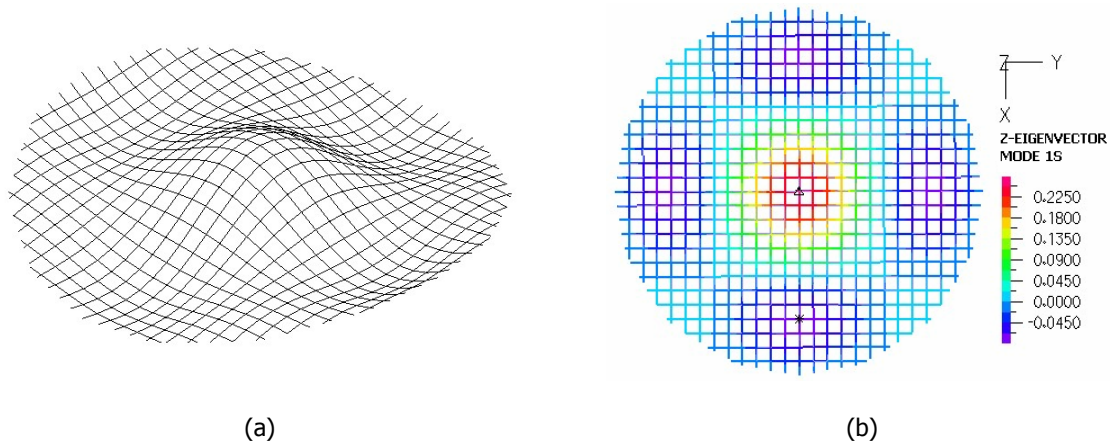


Figure 5-22: First symmetric mode of a cable net with rigid supports for $\lambda^2=2.60 (>>1.17)$, a) perspective view, b) Z-eigenvector

5.4.2 The natural frequencies

In this section parametric analyses are presented for the ten characteristic cases of Table 5-3, in order to illustrate the relation between the natural frequencies and the characteristics of the cable net, and especially parameter λ^2 . Keeping the characteristics of Table 5-3 constant and varying the cable cross-sectional area between 10mm and 80mm, parameter λ^2 changes. The 1S, 1A and 2A modes are considered again.

Table 5-3: Characteristic cases for eigenfrequency investigation

	Cases									
	1	2	3	4	5	6	7	8	9	10
N	25	25	25	25	25	25	25	35	25	11
L [m]	100	100	100	100	100	100	50	50	100	100
f/L	1/20	1/20	1/35	1/35	1/20	1/20	1/20	1/20	1/20	1/20
N_0 [kN]	400	600	400	400	400	400	400	400	400	400
E [GPa]	165	165	165	165	165	148.5	165	165	165	165
m [$kN \cdot sec^2 \cdot m^{-4}$]	10	10	8	10	8	9	10	10	0	0
M [$kN \cdot sec^2 \cdot m^{-1}$]	0	0	0	0	0	0	0	0	0.5	0.5

The analysis results are shown in the charts of Figure 5-23, where the parameter λ^2 is plotted on the horizontal axis and the normalised frequency $\omega/\sqrt{(g/L)}$ on the vertical axis for the ten cable nets of Table 5-3, where g is the gravitational constant, considered equal to 10m/sec^2 .

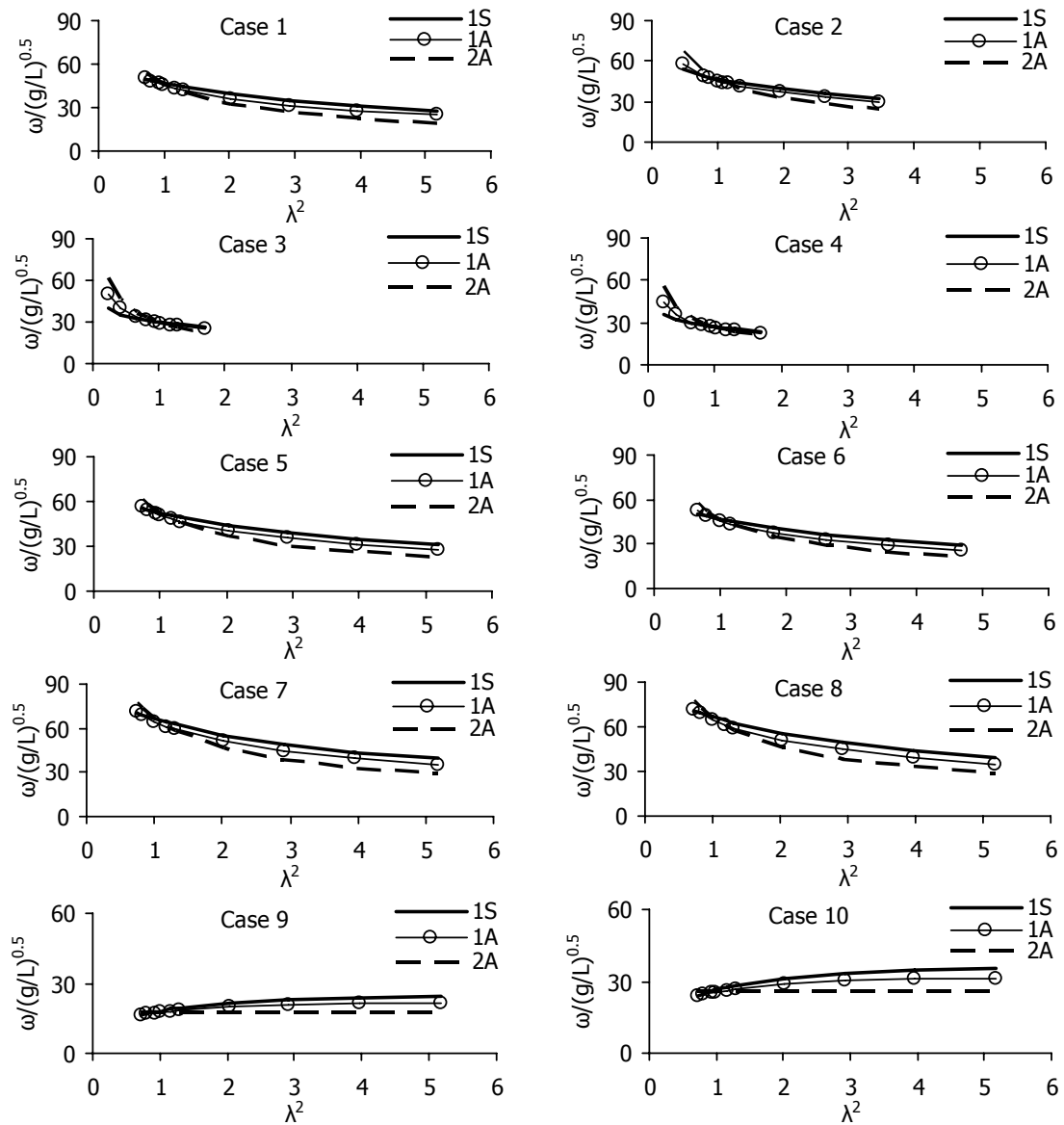


Figure 5-23: Normalised natural frequencies of a cable net with rigid supports vs. λ^2

From the charts some important remarks can be elicited:

- As λ^2 increases resulting in a stiffer net, the natural frequencies decrease when distributed mass is considered (cases 1-8).
- If λ^2 , m , E , L and f/L are kept constant, changing the level of pretension does not alter the natural frequencies (cases 1, 2).
- Keeping λ^2 , m , E , N_0 and L constant, the natural frequencies decrease as the sag-to-span ratio f/L decreases (cases 1, 4 and 3, 5).
- Keeping λ^2 , m , E , N_0 and f/L constant, the natural frequencies increase as L decreases (cases 1, 7).
- On the other hand, if λ^2 , N_0 and f/L remain constant, the natural frequencies increase with respect to $1/\sqrt{m}$ (cases 1, 5).

- Moreover, if λ^2 , N_0 and f/L remain constant, the natural frequencies do not change if the ratio $\sqrt{(E/m)}$ remains the same (cases 1, 6).
- When only the cable mass density m is taken into consideration and no concentrated mass M is considered, the number of cables in each direction has no effect on the natural frequencies and eigenmodes (cases 7, 8). Considering concentrated nodal masses M instead, the number of cables in each direction influences the frequencies significantly (cases 9, 10). In the latter case the eigenfrequencies increase with respect to $1/\sqrt{N+1}$.
- If only concentrated mass M is considered, but no cable mass density m , changing the cable cross-sectional area, the frequencies of modes 1S and 1A increase, but the one of mode 2A does not change (cases 9, 10).
- Finally, the frequency crossovers occur at the same values of the parameter λ^2 for all cable nets, as mentioned before.

5.4.3 Empirical formulae

In order to quantify the above observations and to elicit empirical formulae, which can be used to estimate the eigenfrequencies of the net, almost six hundred runs have been performed for the cable nets with geometrical and mechanical characteristics listed in Table 5-4. Considering cases that approximate realistic structures, the cable diameter was chosen in such a way as to keep the pretension level between 10% and 35% of the steel yield stress, taking into account the steel categories St 1570/1770 and St 1670/1860. Thus, the initial cable stress, introduced by the initial strain, meaning the pretension, is calculated between $0.10 \cdot 1570\text{MPa} = 157\text{MPa}$ and $0.35 \cdot 1670\text{MPa} = 585\text{MPa}$.

Table 5-4: Characteristics of the cable nets with rigid supports

N	L [m]	f/L	N_0 [kN]	E [GPa]	D [mm]	m [$\text{kN} \cdot \text{sec}^2 \cdot \text{m}^{-4}$]	M [$\text{kN} \cdot \text{sec}^2 \cdot \text{m}^{-1}$]
25	100	1/10-1/20-1/35	400	165	30-55	10	0-0.5-1
25	100	1/10-1/20-1/35	600	165	37-69	10	0-0.5-1
25	100	1/10-1/20-1/35	800	165	42-80	10	0-0.5-1
25	100	1/10-1/20-1/35	400	165	30-55	8	0-0.5-1
25	100	1/10-1/20-1/35	600	165	37-69	8	0-0.5-1
25	100	1/10-1/20-1/35	800	165	42-80	8	0-0.5-1
25	100	1/20	400	165	30-55	0	0.5-1
25	100	1/20	600	165	37-69	0	0.5-1
25	100	1/20	800	165	42-80	0	0.5-1
19	100	1/20	400	165	30-55	0-8	0-0.5-1
19	100	1/20	600	165	37-69	0-8	0-0.5-1
19	100	1/20	800	165	42-80	0-8	0-0.5-1
11	100	1/20	400	165	30-55	0-8	0-0.5-1
11	100	1/20	600	165	37-69	0-8	0-0.5-1
11	100	1/20	800	165	42-80	0-8	0-0.5-1
25	100	1/20	400	150	30-55	10	0-0.5-1
25	100	1/20	600	150	37-69	10	0-0.5-1
25	100	1/20	800	150	42-80	10	0-0.5-1
25	50	1/20	400	165	30-55	10	0-0.5-1
25	50	1/20	600	165	37-69	10	0-0.5-1
25	50	1/20	800	165	42-80	10	0-0.5-1
25	200	1/20	600	165	37-67	10	0-0.5-1
25	200	1/20	800	165	42-80	10	0-0.5-1
25	200	1/20	1000	165	47-90	10	0-0.5-1

A new non-dimensional parameter β is introduced, in order to include all the above information in one chart. This parameter represents the non-dimensional cable net frequencies.

$$\beta = \omega \sqrt{\frac{mAL + \frac{M(N+1)}{2}}{\frac{50EA}{L} \left(\frac{f}{L}\right)^2}} \quad (5-6)$$

In the charts of Figure 5-24, plotting on the horizontal axis the parameter λ^2 and on the vertical one the parameter β for each one of the frequencies of the net, it is noted that each natural frequency follows the same curve for all cable nets.

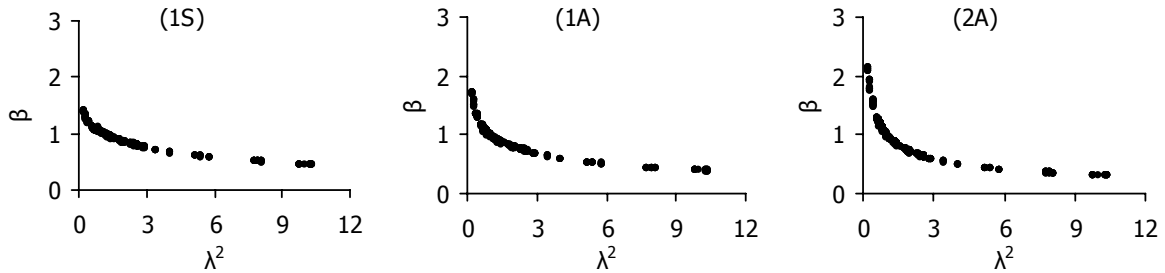


Figure 5-24: Parameter β for the 1S, 1A and 2A modes of a cable net with rigid supports vs. λ^2

Based on the results of the modal analyses, it is possible to produce approximate mathematical formulae estimating the natural frequencies of the cable nets. According to the above charts, there is a relation between the two non-dimensional parameters β and λ^2 , for each of the three modes, which can be expressed as follows:

$$\begin{aligned} \lambda^2 \cdot \beta^n &= 1 \Rightarrow \\ \Rightarrow \frac{EA}{N_0} \left(\frac{f}{L}\right)^2 \cdot \left[\omega \sqrt{\frac{mAL + \frac{M(N+1)}{2}}{\frac{50EA}{L} \left(\frac{f}{L}\right)^2}} \right]^n &= 1 \Rightarrow \\ \Rightarrow \omega_e &= \frac{f}{L} \cdot \sqrt[n]{\left(\frac{\frac{50EA}{L}}{mAL + \frac{M(N+1)}{2}} \right) \left[\frac{N_0}{EA} \left(\frac{L}{f}\right)^2 \right]} \end{aligned} \quad (5-7)$$

where the subscript e denotes that this is an empirical expression of the eigenfrequencies, $n=n_{1S}=3$ for mode 1S, $n=n_{1A}=2.5$ for modes 1A and $n=n_{2A}=2$ for mode 2A. Thus, Eq. (5-7) becomes, for the three modes, respectively:

$$\omega_{1S,e} = \frac{f}{L} \cdot \sqrt[3]{\left(\frac{\frac{50EA}{L}}{mAL + \frac{M(N+1)}{2}} \right) \left[\frac{N_0}{EA} \left(\frac{L}{f}\right)^2 \right]} \quad (5-8)$$

$$\omega_{1A,e} = \frac{f}{L} \cdot \sqrt[2.5]{\left(\frac{\frac{50EA}{L}}{mAL + \frac{M(N+1)}{2}} \right) \left[\frac{N_0}{EA} \left(\frac{L}{f}\right)^2 \right]} \quad (5-9)$$

$$\omega_{2A,e} = \sqrt{\left(\frac{\frac{50N_0}{L}}{mAL + \frac{M(N+1)}{2}} \right)} \tag{5-10}$$

In order to compare the numerical results with the ones provided by these formulae, the above charts are shown again in Figure 5-25, including the curves represented by Eqs. (5-8) – (5-10).

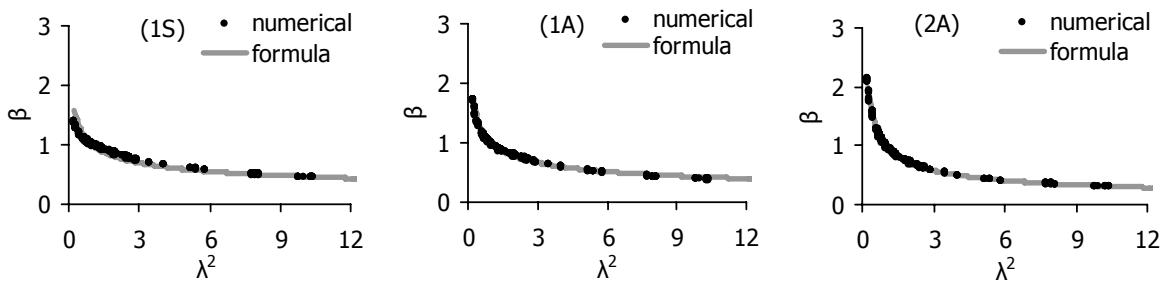


Figure 5-25: Parameter β vs. λ^2 (studied cases and empirical formulae)

The accuracy of the empirical formulae is also illustrated in Figure 5-26, where $\omega_{i,n}$ and $\omega_{i,e}$ are the net’s frequencies calculated by numerical methods and by Eqs. (5-8) – (5-10), respectively and i stands for 1S, 1A or 2A. The results are considered as satisfactory.

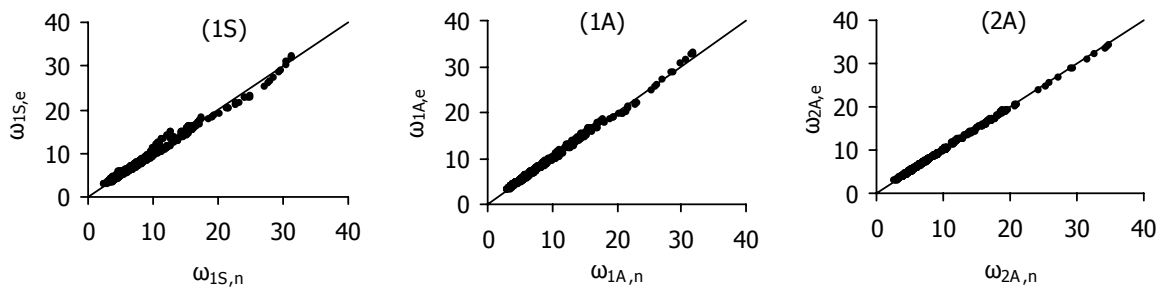


Figure 5-26: Empirical formulae for natural frequencies vs. numerical data

The error of the above formulae is calculated for all the results obtained from the parametric modal analyses performed, as the ratio $(\omega_{i,n}-\omega_{i,e})/\omega_{i,n}$. The charts of Figure 5-27 show the mean absolute value of the error for different values of the non-dimensional parameter λ^2 .

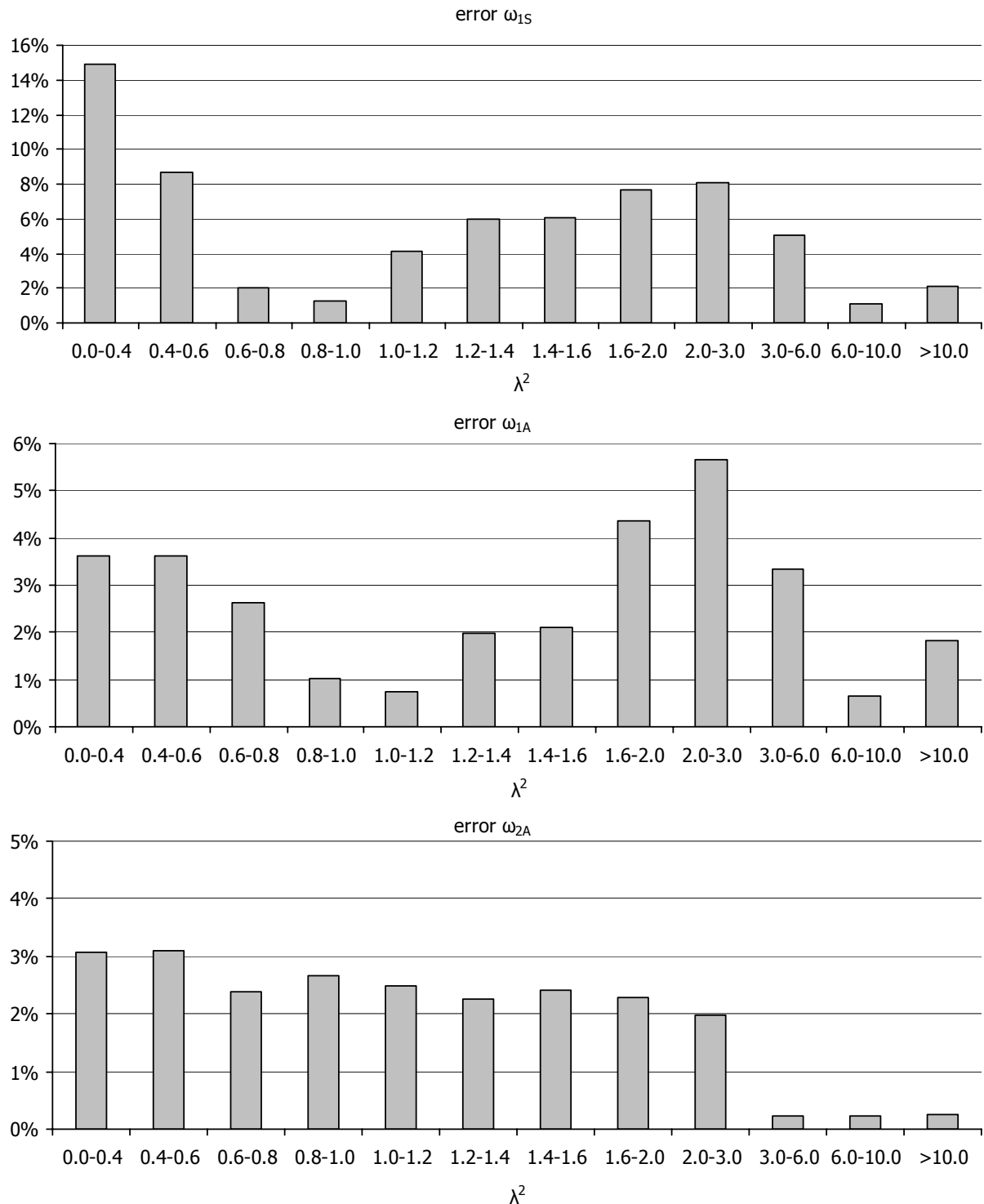


Figure 5-27: Error of the empirical formulae for natural frequencies with respect to λ^2

The error of the formula providing the frequency of the first symmetric mode (1S), arises at 16% for very low values of the parameter λ^2 . These values of λ^2 correspond to the shallowest cable net, with a sag/span ratio equal to 1/35 and to the highest levels of initial stress, up to 35% of the yield stress 1670MPa, considering a cable diameter 30mm for pretension 400kN, 37mm for 600kN and 42mm for 800kN. These cable diameters are very small for such spans, so these low values of the parameter λ^2 do not represent actual designs. The error of the same formula for values of λ^2 larger than 0.4, arises at maximum 10%, which is considered as satisfactory for preliminary design. The error of the

formulae giving the frequencies of the antisymmetric modes 1A and 2A is very small, not more than 5% for the former and 2.5% for the latter.

5.5 BOUNDARY RING

5.5.1 The natural mode

In order to extend the above investigation into the natural frequencies of a cable net anchored to a deformable edge ring, at first, the ring itself is analysed, without the cables. Conducting a parametric linear modal analysis, the fundamental frequency of such a structure is calculated, considering different geometrical and mechanical characteristics, regarding the projected diameter, the sag/span ratio, the elastic modulus of the ring's material, the geometry of its cross-section and its unit weight. The first vibration mode is characterised by an in-plane breathing motion of the ring (Figure 5-28).

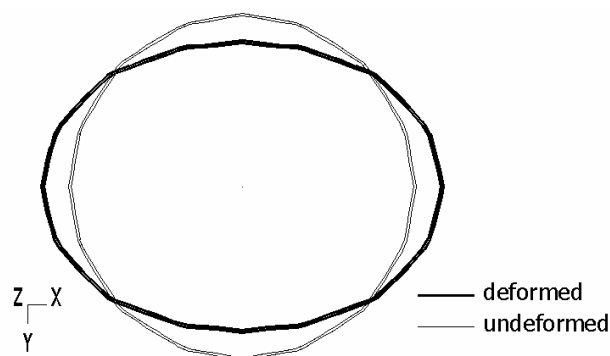


Figure 5-28: Ring's first vibration mode (in-plane mode)

5.5.2 The fundamental natural frequency

More than two hundred cases have been taken into consideration for the parametric analysis, in which the ring modulus of elasticity E_r varies between 30GPa, 34GPa, 37GPa and 39GPa, accounting for the concrete categories B25, B35, B45 and B55, respectively, according to DIN codes. The ring's cross-section has the shape of a square box, as shown in Figure 5-4, with width b taking the values $b=5.00\text{m}$, $b=6.50\text{m}$, $b=8.00\text{m}$ or $b=10.00\text{m}$ for the models with diameter $L=100\text{m}$, and, respectively $b=8.00\text{m}$, $b=10.0\text{m}$, $b=12.00\text{m}$ or $b=14.00\text{m}$ for the models with diameter $L=200\text{m}$, while for the model with diameter $L=50\text{m}$ the width b varies with values $b=2.00\text{m}$, $b=3.50\text{m}$, $b=5.00\text{m}$ or $b=7.00\text{m}$. In all cases, the unit weight of the ring ρ_r takes the values 25kN/m^3 , 35kN/m^3 or 45kN/m^3 , considering eventual electromechanical equipment. The geometrical and mechanical characteristics of the considered cases are listed in Table 5-5.

Table 5-5: Characteristics of the edge ring

L [m]	f/L	E_r [GPa]	b [m]	ρ_r [kN/m^3]
100	1/20	30-39	5-10	25-45
100	1/35	30-39	5-10	25-45
100	1/15	30-39	5-10	25-45
100	1/10	30-39	5-10	25-45
200	1/20	30-39	8-14	25-45
50	1/20	30-39	2-7	25-45

The calculated fundamental frequencies for all the above cases are plotted in Figure 5-29 where on the vertical axis the non-dimensional eigenfrequency $\omega_r/\sqrt{g/L}$ is represented and on the horizontal axis the non-dimensional parameter γ , defined as:

$$\gamma = \frac{E_r I_r}{\rho_r A_r L^3} \quad (5-11)$$

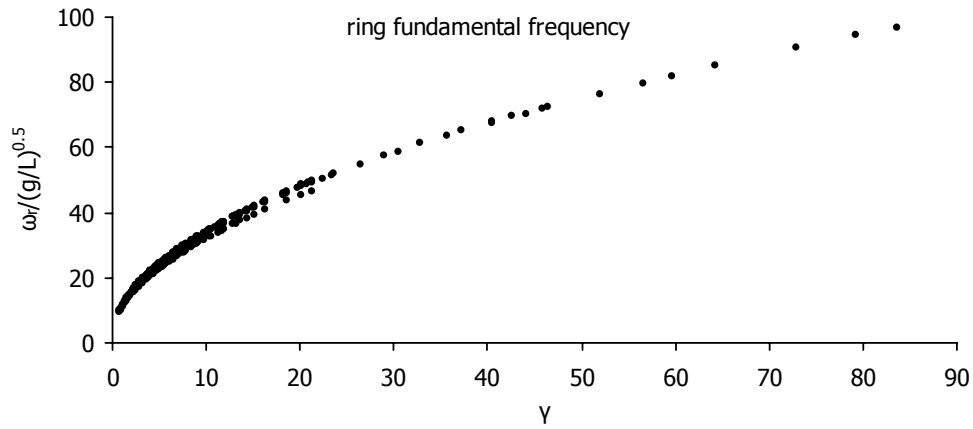


Figure 5-29: Normalised fundamental frequency of the ring without cables vs. non-dimensional parameter γ

From the above chart, one can conclude that the relation between the non-dimensional natural frequency of the edge ring without cables and the parameter γ is the same for all cases. In [5-22] the expression of the natural frequency for any mode of vibration is provided, concerning the flexural vibration of a plane circular ring:

$$\omega_r = \sqrt{\frac{E_r I_r g}{\rho_r A_r R^4} \frac{i^2(1-i^2)^2}{i^2+1}} = 4 \sqrt{\frac{E_r I_r g}{\rho_r A_r L^4} \frac{i^2(1-i^2)^2}{i^2+1}} \quad (5-12)$$

When $i=1$, $\omega_r=0$ and the ring moves as a rigid body. For $i=2$, the ring performs the fundamental mode of flexural vibration and Eq. (5-12) becomes:

$$\omega_r = 10.73 \sqrt{\frac{E_r I_r g}{\rho_r A_r L^4}} \quad (5-13)$$

When $i=3$, the calculated frequency corresponds to the ring's second mode, which is the first antisymmetric vibration mode, being 2.8 times larger than the first eigenfrequency of the ring. This mode is not taken into account, because it cannot influence the vibration of the net, as will be shown next.

Although, the above formula refers to a plane ring, it can also be used for the boundary ring of a hyperbolic paraboloid roof. The error of the above formula is calculated for all results obtained from the parametric modal analyses performed for each case, as the ratio $(\omega_{rn} - \omega_{re})/\omega_{rn}$, where ω_{rn} and ω_{re} are the ring's frequency calculated by numerical methods and by Eq. (5-13), respectively. The chart of Figure 5-30 shows the absolute value of the error for different values of the sag-to-span ratio. The error is very small for the shallow rings of small sag/span ratios, but as the ratio increases and the ring becomes deeper, with large curvatures, the error increases.

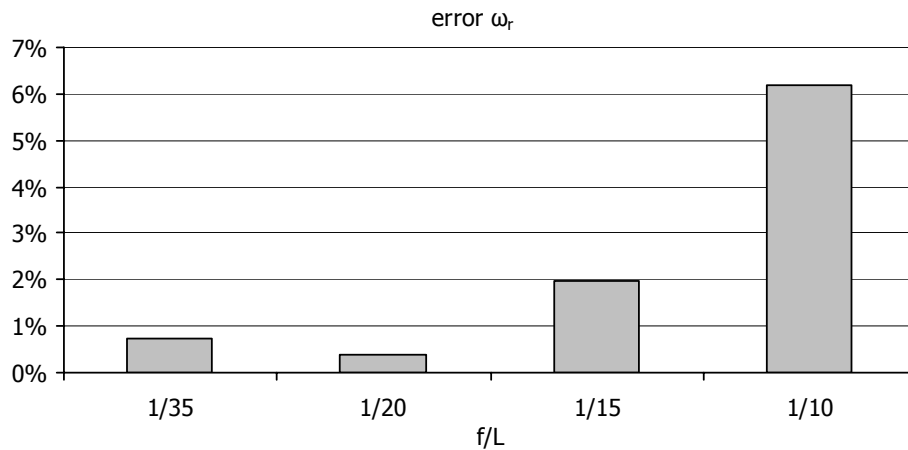


Figure 5-30: Error of the empirical formula for the fundamental frequency of the ring with respect to the sag-to-span ratio

5.5.3 Empirical formula

In order to calibrate this error, an improved formula is proposed for the estimation of the frequency of the ring's mode, considering also the sag-to-span ratio, as follows:

$$\omega_r = 10.73(1.04 - f/L) \sqrt{\frac{E_r I_r g}{\rho_r A_r L^4}} \quad (5-14)$$

In order to compare the numerical results with the ones estimated by the empirical formula, the chart of Figure 5-29 is plotted again in Figure 5-31, including the curve represented by Eq. (5-14).

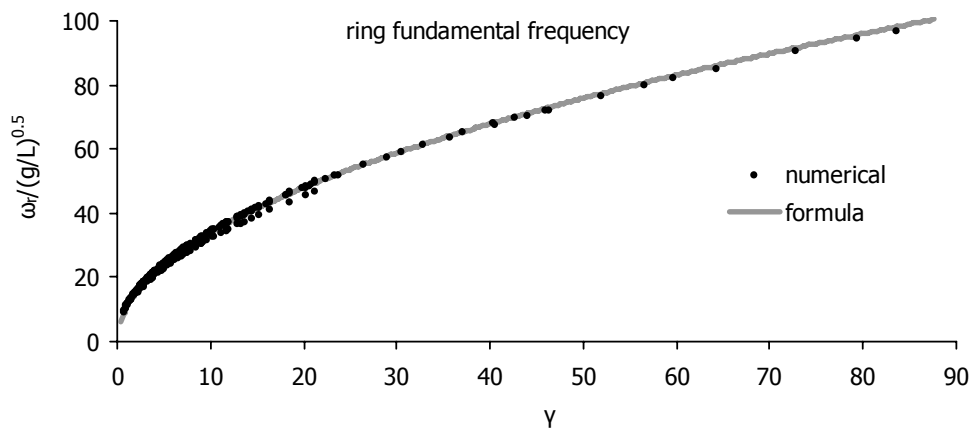


Figure 5-31: Normalised fundamental frequency of the ring vs. γ (studied cases and empirical formula)

The error of this improved formula with respect to the ratio $(\omega_m - \omega_{re})/\omega_m$ is illustrated in Figure 5-32, where ω_m and ω_{re} are the ring's frequency calculated by numerical methods and by Eq. (5-14), respectively, which shows that the mean absolute value of the error for all sag-to-span ratios is not more than 1%. The accuracy of the improved empirical formula is also illustrated in Figure 5-33, and is considered as sufficient for all practical purposes.

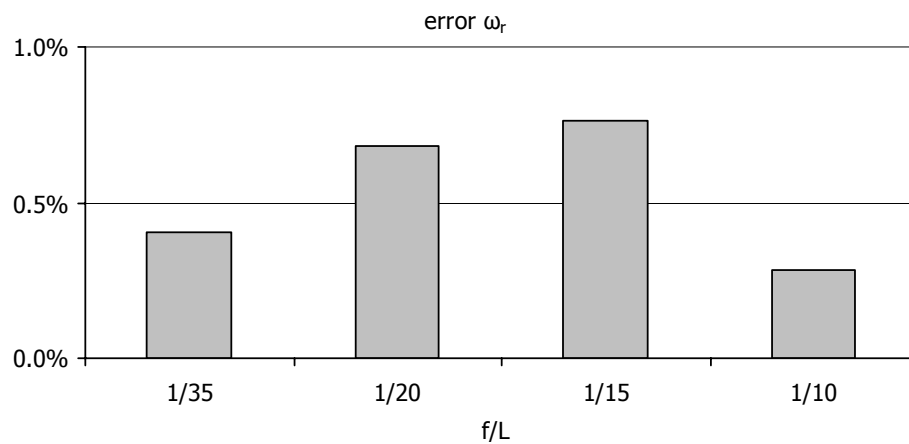


Figure 5-32: Error of the improved empirical formula for the fundamental frequency of the ring with respect to the sag-to-span ratio

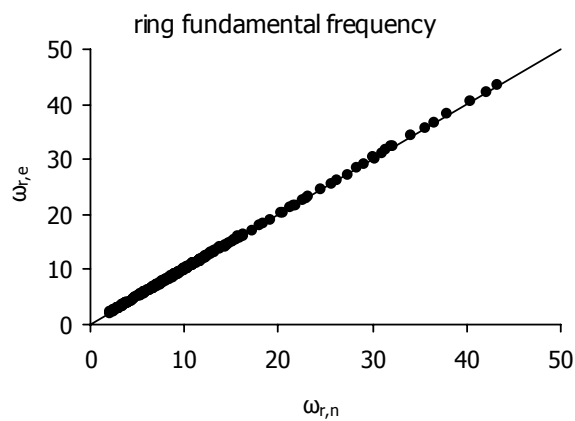


Figure 5-33: Formula for the ring's fundamental frequency vs. numerical data

5.6 CABLE NET WITH BOUNDARY RING

5.6.1 The natural modes

Continuing the investigation of cable networks regarding their natural frequencies, both components of the suspended roof are now considered, namely the cable net and the deformable edge ring. The remark of Talvik [5-15] is verified. He noticed that in case the flexibility of the boundary ring is taken into account, among the first natural modes there are the ones concerning the cable net, modes 1S, 1A and 2A as described before, but there is also the in-plane mode of the ring, which produces a symmetric vertical vibration of the cable net. These modes are shown in Figure 5-34.

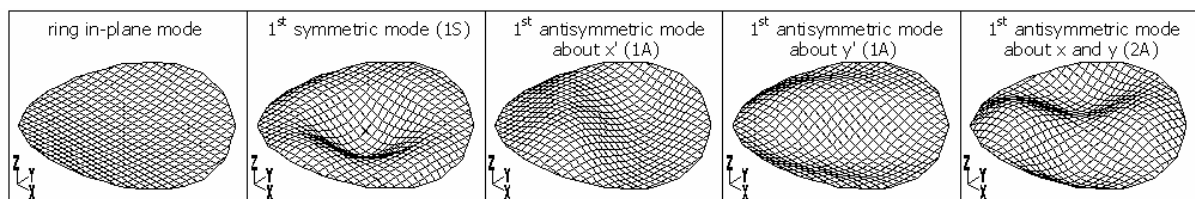


Figure 5-34: First five eigenmodes of the cable net with the flexible edge ring

For illustration purposes, two cable nets are considered with geometrical characteristics $L=50\text{m}$, $f/L=1/20$, cable characteristics $N_0=100\text{kN}$, $D=30\text{mm}$, $m=10\text{kN}\cdot\text{sec}^2\cdot\text{m}^{-4}$, $E=165\text{GPa}$, and ring characteristics $E_r=39\text{GPa}$, $\rho_r=25\text{kN/m}^3$, while the width b of the square box takes the values $b=2.00\text{m}$, for the first one, representing a flexible ring and $b=5.00\text{m}$, for the second one, representing a stiffer ring. The two models are illustrated in Figure 5-35 and Figure 5-36, respectively.

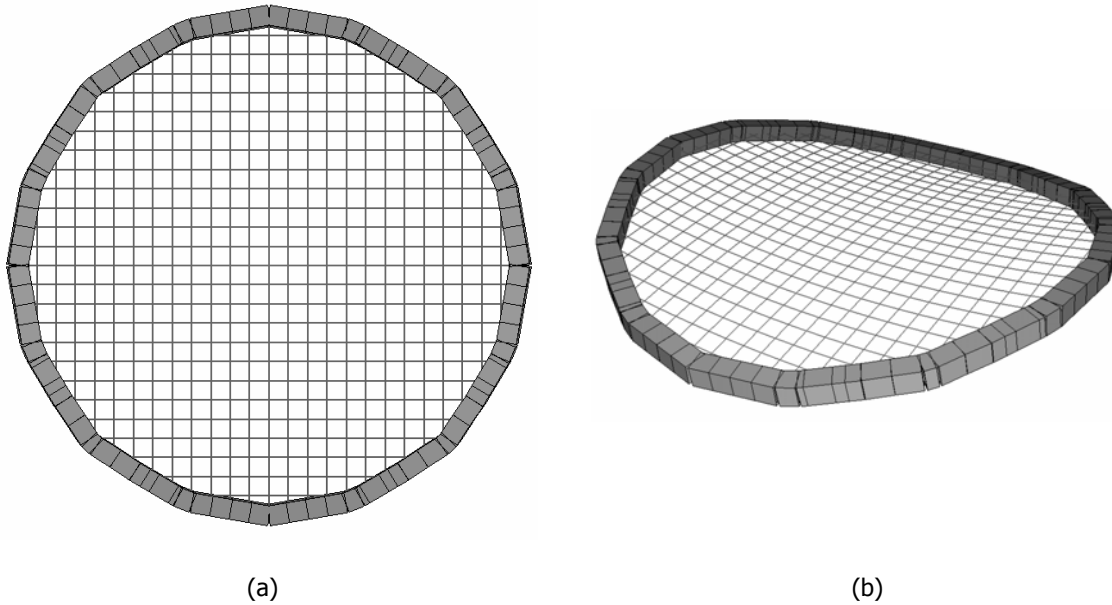


Figure 5-35: The cable net with ring cross-section width $b=2.00\text{m}$ (a) plan view, (b) perspective view

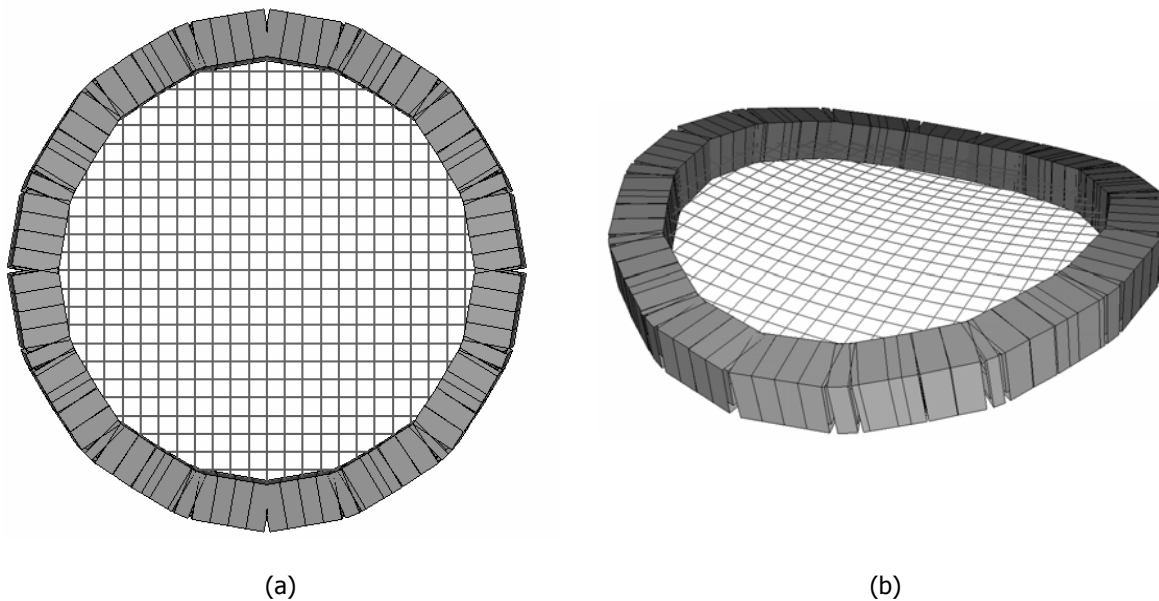
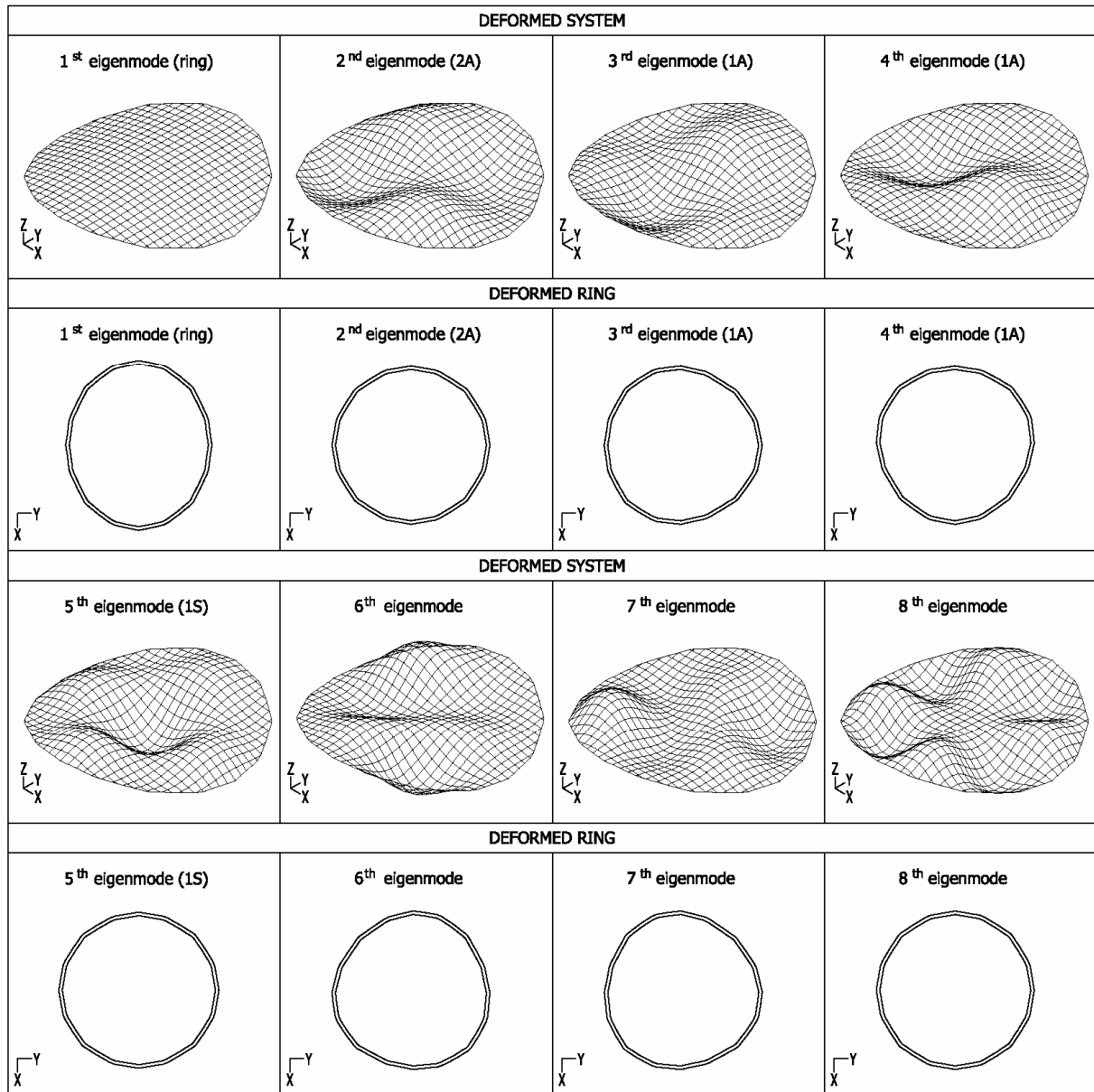


Figure 5-36: The cable net with ring cross-section width $b=5.00\text{m}$ (a) plan view, (b) perspective view

For the first structure, the first mode of the combined system is the ring in-plane mode and the vibration modes of the net follow (Figure 5-37), while for the second one, the ring in-plane mode is the eighth mode of the system and the net modes appear as the first ones (Figure 5-38).

Figure 5-37: The first eight eigenmodes of the cable net with ring cross-section width $b=2.00\text{m}$

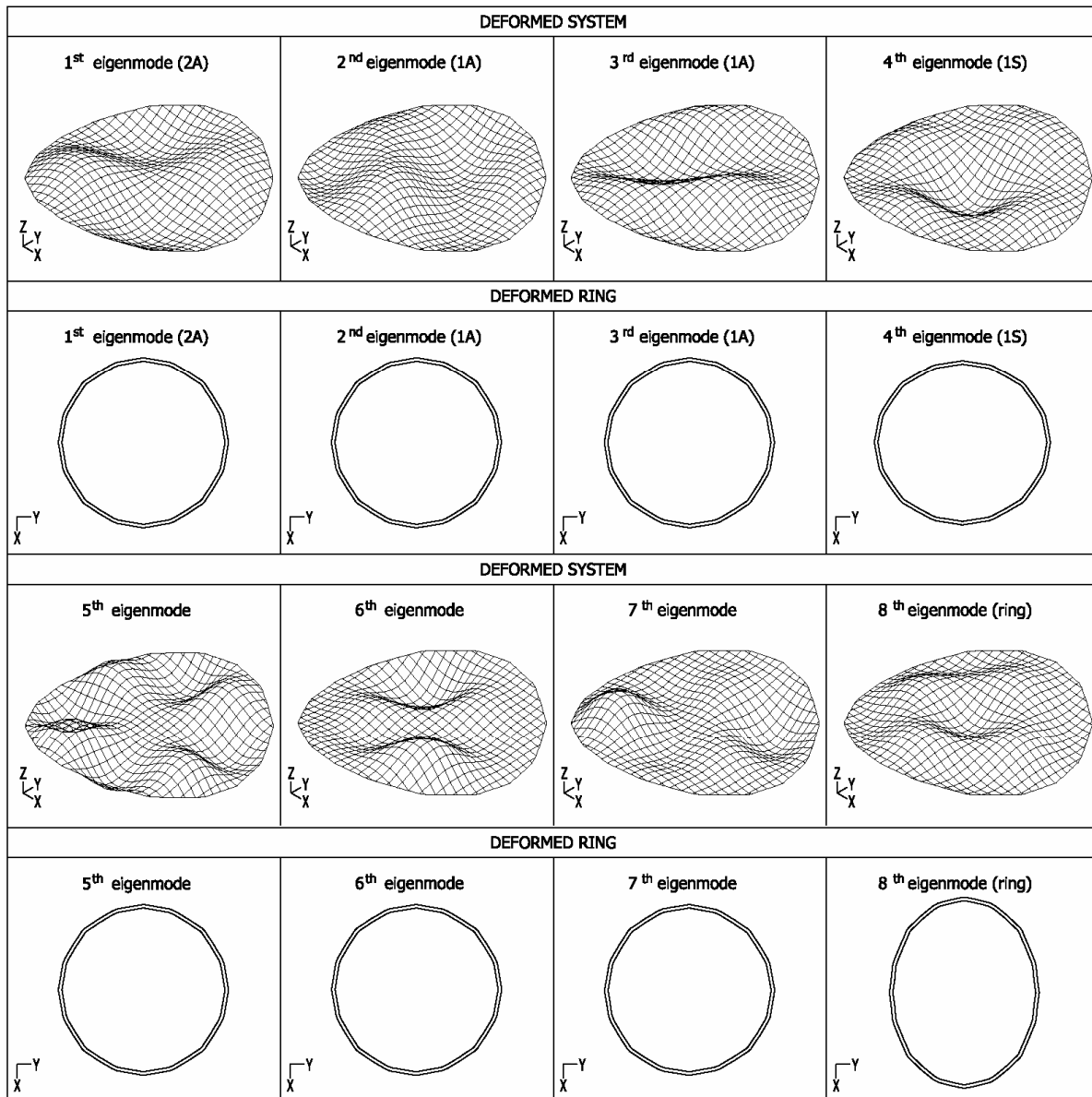


Figure 5-38: The first eight eigenmodes of the cable net with ring cross-section width $b=5.00\text{m}$

Hence, for common values of the ring's stiffness and cable net stiffness in terms of pretension and cable cross-sectional area, the ring's in-plane mode is the first eigenmode of the system and the corresponding frequency can be estimated by Eq. (5-14), with negligible influence of the cable net. In this case, the following four eigenmodes are the same vibration modes of the cable net analysed in section 5.4.1 with negligible influence of the ring, and their frequencies can be expressed by Eqs. (5-8) – (5-10) with small errors. For high values of the ring's stiffness, its in-plane mode becomes of higher order, while the corresponding eigenfrequency still follows the law of Eq. (5-14). In this case the first four modes of the system are the vibration modes of the net studied previously, with frequencies that still follow Eqs. (5-8) – (5-10). Between these first four modes and the ring's one, other vibration modes appear, most of them higher order net's modes, but also hybrid ones, involving the ring and the net into the vibration.

For intermediate values of the ring's stiffness, the symmetric vibration of the net and the in-plane one of the ring are not distinct; it is not possible to distinguish which mode represents a pure vibration of the net involving also the ring and which one is mainly a vibration of the ring that produces a

symmetric oscillation to the net. Consequently, in what follows, the 1st symmetric mode of the system is investigated, whether this is produced mainly due to a net symmetric vibration or a ring in-plane one. The corresponding frequency will be named as ω_{1SS} .

5.6.2 The natural frequencies

For the sake of simplicity, the frequencies of a sample of cable nets are calculated and discussed, with characteristics listed in Table 5-6. Parametric analyses are performed in order to evaluate the contribution of the edge ring deformability to the net's vibration modes, by varying the ring stiffness $E_r I_r$ and the ring mass $\rho_r A_r$. The frequencies of this system are compared with those of the cable net with rigid supports. In Table 5-7 the parameter λ^2 and the numerically calculated eigenfrequencies are listed for each net with rigid supports, which will be used to compare them with the corresponding ones of the combined system.

Table 5-6: Characteristics of the cable nets with the flexible edge ring

	Cases									
	1	2	3	4	5	6	7	8	9	10
N	25	25	25	25	25	25	25	35	25	11
L [m]	100	100	100	100	100	100	50	50	100	100
f/L	1/20	1/20	1/20	1/20	1/35	1/20	1/20	1/20	1/20	1/20
D [mm]	40	40	60	60	40	63.2	40	40	40	40
N_0 [kN]	400	600	600	600	400	600	400	400	400	400
E [GPa]	165	165	165	165	165	148.5	165	165	165	165
m [kN·sec ² ·m ⁻⁴]	10	10	10	8	10	9	10	10	0	0
M [kN·sec ² ·m ⁻¹]	0	0	0	0	0	0	0	0	0.5	0.5

Table 5-7: Eigenfrequencies of cable nets with rigid supports

	Cases									
	1	2	3	4	5	6	7	8	9	10
λ^2	1.30	0.86	1.94	1.94	0.42	1.94	1.30	1.30	1.30	1.30
ω_{1S} [sec ⁻¹]	14.01	15.85	12.54	14.02	9.98	12.54	28.02	28.05	6.16	9.00
ω_{1A} [sec ⁻¹]	13.21	15.02	11.61	12.90	11.16	11.61	26.41	26.42	5.81	8.48
ω_{2A} [sec ⁻¹]	12.94	15.22	10.57	11.81	13.01	10.57	25.88	25.87	5.70	8.25

Keeping the ring unit weight constant and equal to 25kN/m³, the ring's effect on the system's frequency of the first symmetric mode (ω_{1SS}) is studied, by varying the elastic modulus E_r and the ring cross-section width b as in section 5.5.2, accounting for realistic values of the ring's stiffness and cross-sectional area. The charts of Figure 5-39 show the variation of the non-dimensional first four natural frequencies of the system (including the double 1A frequency) with respect to the ring stiffness represented by the non-dimensional parameter γ , defined in Eq. (5-11). In these charts, ω_{1A} , ω_{2A} are the frequencies of 1A and 2A modes of the net, respectively, while ω_{1SS} is the frequency of the first symmetric mode of the system.

The change of the combined system's non-dimensional frequency ω_{1SS} of the first symmetric mode with respect to the ring stiffness is shown in the charts of Figure 5-40. In these charts, the frequencies of three systems are compared, the ring without the cables, the cable net without the ring (supported rigidly) and the cable net with the ring. In Figure 5-41 the change of the ratio of the ω_{1SS}/ω_{1S} , with respect to the ratio ω_r/ω_{1S} is depicted. In these two Figures, ω_r is the frequency of the ring without the cables, as calculated from Eq. (5-14), ω_{1S} is the frequency of the first symmetric mode for the cable net with rigid supports, and ω_{1SS} is the frequency of the first symmetric mode of the cable net with the elastic ring, both calculated numerically.

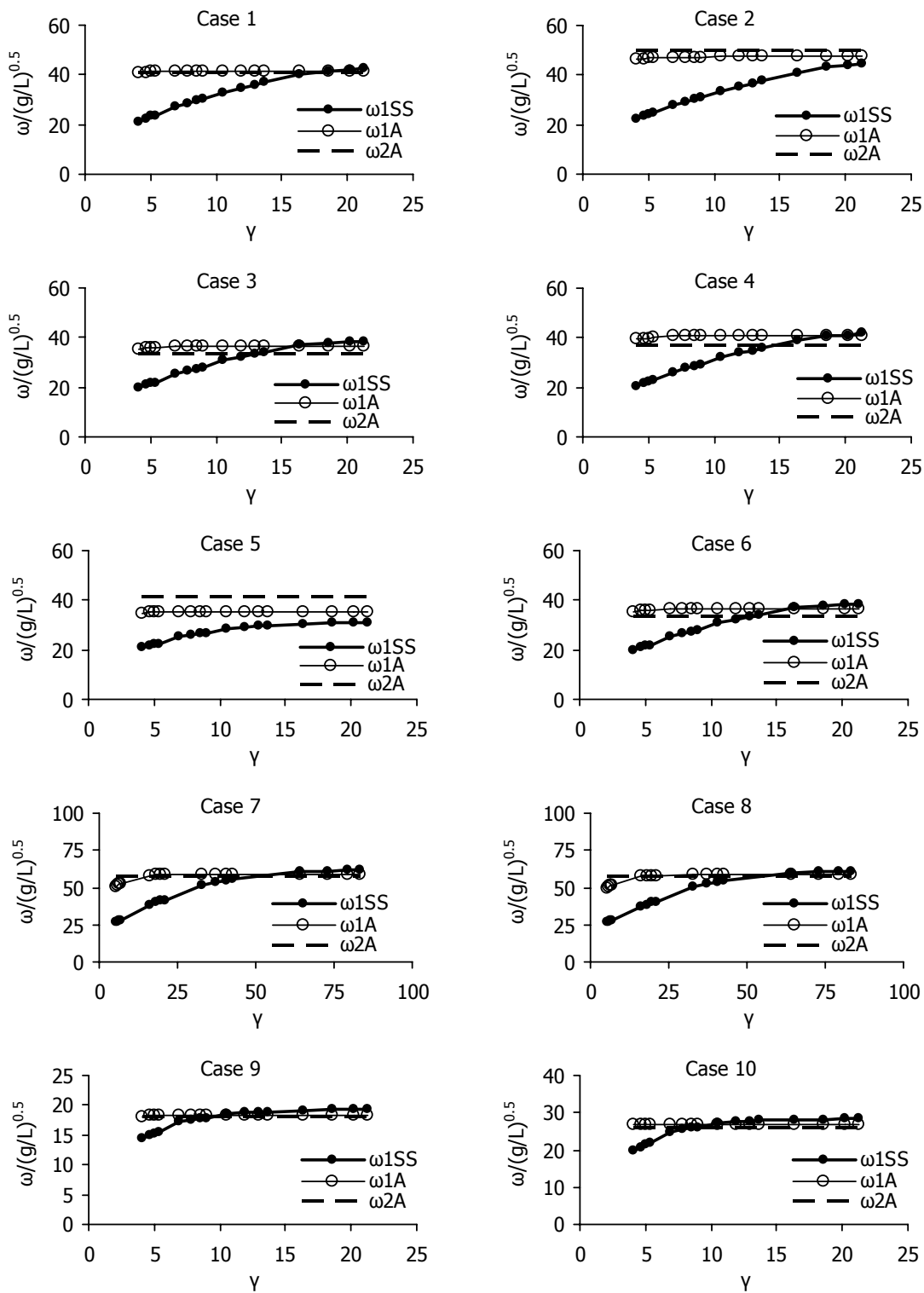
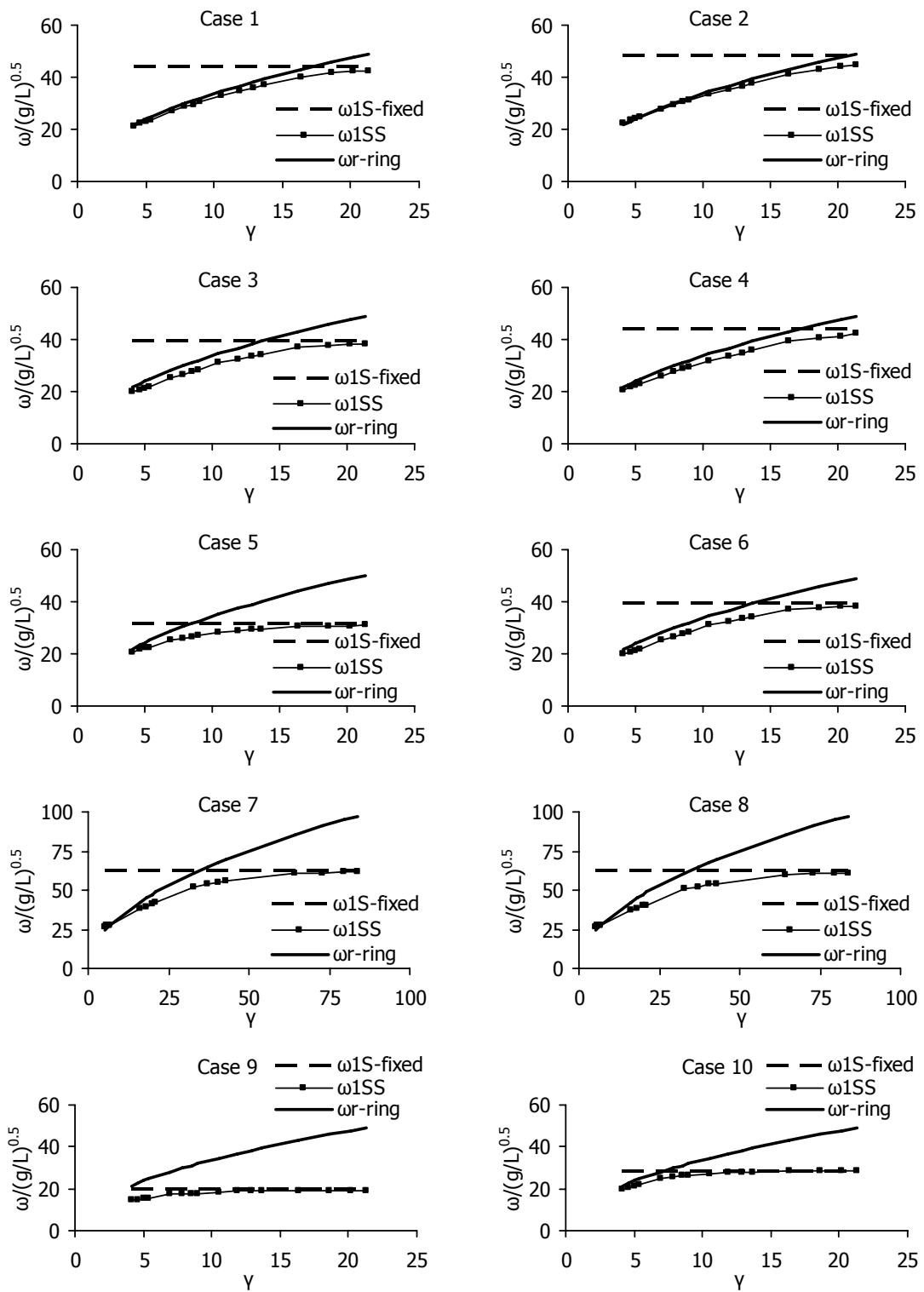


Figure 5-39: Normalised natural frequencies of the cable net with ring vs. γ

Figure 5-40: Normalised natural frequencies vs. γ of the combined system and its separated components

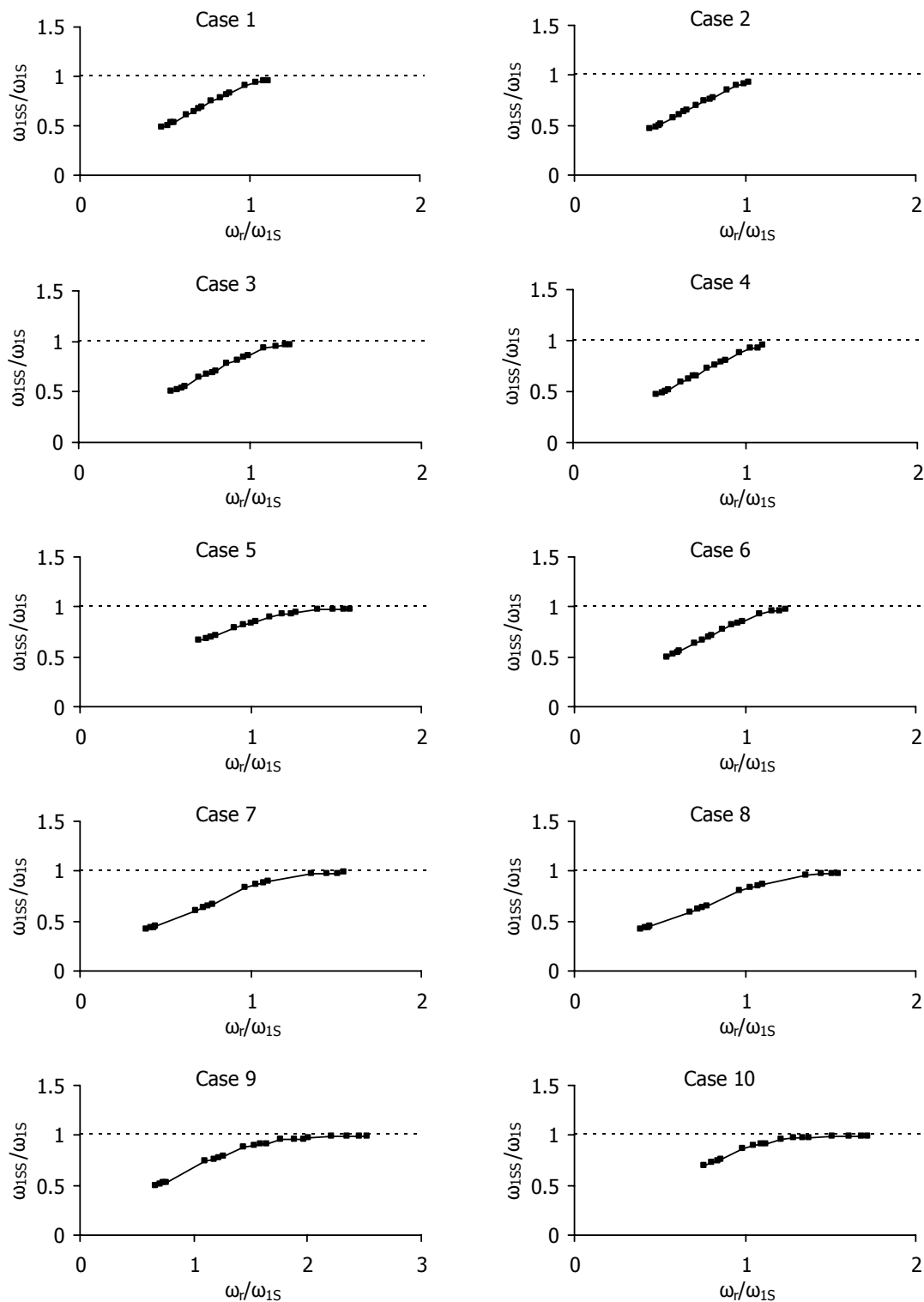


Figure 5-41: Change of the frequency of the combined system, with respect to the ratio of the frequencies of the separated components

For all cases, as the mass of the ring increases, the frequency ω_{1SS} , decreases, as expected. As a representative example, the variation of the non-dimensional frequency ω_{1SS} of the system with respect to the mass of the ring is shown in Figure 5-42, for the first case of Table 5-6. Keeping the

elastic modulus E_r and the cross-section width b constant and equal to 37GPa and 5.00m, respectively, the ring unit weight ρ_r varies between 25kN/m³~50kN/m³.

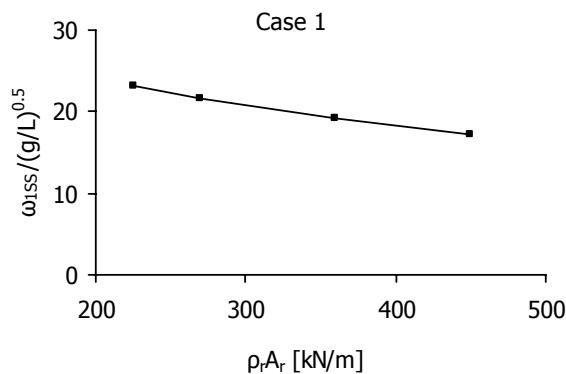


Figure 5-42: Normalised natural frequency ω_{1SS} vs. $\rho_r A_r$

From the above charts some important conclusions can be drawn:

- As the stiffness of the ring increases the frequency ω_{1SS} increases.
- If m , E , L , f/L and the stiffness of the ring are kept constant, an increase of the level of pretension increases slightly the frequency ω_{1SS} (cases 1, 2).
- Keeping m , E , N_0 , L , f/L and the ring stiffness constant, the frequency ω_{1SS} increases as the cable diameter D increases (cases 2, 3).
- Moreover, if λ^2 , N_0 and f/L remain constant, for the same levels of the ring's stiffness, the frequency ω_{1SS} does not change, if the ratio $\sqrt{E/m}$ remains the same (cases 3, 6).
- Keeping m , E , N_0 , L and the ring stiffness constant, the frequency ω_{1SS} slightly decreases as the sag-to-span ratio f/L decreases (cases 1, 5).
- For the same levels of the ring's stiffness and keeping f/L , N_0 , E , m constant, the frequency ω_{1SS} increases as L decreases (cases 1, 7)
- On the other hand, if the ring stiffness, E , N_0 , L , and f/L remain constant, the frequency ω_{1SS} increases slightly as the cable mass density m decreases (cases 3, 4).
- If only the cable mass density is taken into account, the frequency ω_{1SS} does not depend on the number of cables in each direction (cases 7, 8), but when concentrated nodal masses are considered instead, this frequency is influenced by the number of cables (cases 9, 10).
- The frequency ω_{1SS} , for low levels of the ring's stiffness, is the frequency of the in-plane mode of the ring and can be calculated using Eq. (5-13), but as the stiffness increases the frequency diverges from the curve of the above equation and tends to become equal to ω_{1S} of the net with rigid supports (Figure 5-40 and Figure 5-41).
- The frequency of mode 2A (ω_{2A}) remains unchanged in presence of the edge ring (Figure 5-39).
- The frequency of modes 1A (ω_{1A}) does not change more than 3.4% due to the deformability of the edge ring (Figure 5-39). This is the case because, for realistic values of ring flexural stiffness and cable axial stiffness, the antisymmetric vibration mode of the boundary ring is always much larger than the first four frequencies of the cable net. Thus, it cannot influence significantly the antisymmetric vibration mode of the net.
- If the stiffness of the ring is kept constant, and the mass of the edge ring increases, the frequency ω_{1SS} decreases (Figure 5-42).

5.6.3 Empirical formulae

Based on the aforementioned results, and on the charts of Figure 5-40 and those of Figure 5-41, it can be concluded that the first symmetric mode of a cable net with a flexible boundary ring, depends on the ratio of the stiffness of the ring and that of the cable net. If the ring is flexible enough with respect to the cable net, the first symmetric mode is the in-plane mode of the ring. On the other hand, when the ring is much stiffer than the cable net, it behaves as a rigid support to the cables, and its vibration mode is one of the higher order modes, while the first symmetric mode of the system is the one of the cable net. The stiffness ratio of the two components of such a system is expressed as the ratio of the natural frequencies of the two independent systems and constitutes the criterion that indicates whether the first symmetric mode of the system will be the in-plane mode of the ring or the first symmetric mode of the net.

In order to find an approximate empirical formula calculating the frequency of the first symmetric mode of the combined system, more than one thousand cases were considered, combining the characteristics of the ring listed in Table 5-8, with those of the cable nets tabulated in Table 5-9.

Table 5-8: Characteristics of the edge ring

L [m]	f/L	E _r [GPa]	b [m]	ρ _r [kN/m ³]
100	1/20	30-39	5-8	25-35
100	1/35	30-39	5-8	25-35
100	1/10	30-39	5-8	25-35
200	1/20	30-39	10-12	25-35
50	1/20	30-39	3.5-5	25-35

Table 5-9: Characteristics of the cable nets with edge ring

N	L [m]	f/L	N ₀ [kN]	E [GPa]	D [mm]	m [kN·sec ² ·m ⁻⁴]	M [kN·sec ² ·m ⁻¹]
25	100	1/10-1/20-1/35	400	165	30-50	0-10	0-0.5-1.0
25	100	1/10-1/20-1/35	600	165	40-60	0-10	0-0.5-1.0
25	100	1/10-1/20-1/35	800	165	50-80	0-10	0-0.5-1.0
19	100	1/20	400	165	30-50	0-10	0-0.5-1.0
19	100	1/20	600	165	40-60	0-10	0-0.5-1.0
19	100	1/20	800	165	50-80	0-10	0-0.5-1.0
25	100	1/20	400	165	30-50	8	0-0.5-1.0
25	100	1/20	600	165	40-60	8	0-0.5-1.0
25	100	1/20	800	165	50-80	8	0-0.5-1.0
25	100	1/20	400	150	30-50	0-10	0-0.5-1.0
25	100	1/20	600	150	40-60	0-10	0-0.5-1.0
25	100	1/20	800	150	50-80	0-10	0-0.5-1.0
25	50	1/20	400	165	30-50	0-10	0-0.5-1.0
25	50	1/20	600	165	40-60	0-10	0-0.5-1.0
25	50	1/20	800	165	50-80	0-10	0-0.5-1.0
25	200	1/20	600	165	37-67	10	0-0.5-1.0
25	200	1/20	800	165	42-80	10	0-0.5-1.0
25	200	1/20	1000	165	47-90	10	0-0.5-1.0

In the chart of Figure 5-43, plotting on the horizontal axis the ratio ω_r/ω_{1S} , and on the vertical one the ratio ω_{1SS}/ω_{1S} , where again ω_r is the frequency of the ring without the cables, as calculated from Eq. (5-14) and ω_{1S} is the frequency of the first symmetric mode for the cable net with rigid supports, a large dispersion can be noticed, when the ratio ω_r/ω_{1S} takes values between 1 and 3, which means that any empirical formula assessing the frequency ω_{1SS} will present large values of error. Nevertheless, it can be noticed that if the ring's frequency ω_r is less than, approximately, 65% of ω_{1S} , then the first natural frequency of the combined system is close to the ring's frequency and the first symmetric mode of the system is the in-plane mode of the ring. As the ring becomes stiffer and its frequency increases, the combined system's first natural frequency approaches asymptotically the

frequency (ω_{1S}) of the cable net with rigid supports and the first symmetric mode of the system is the symmetric mode of the net.

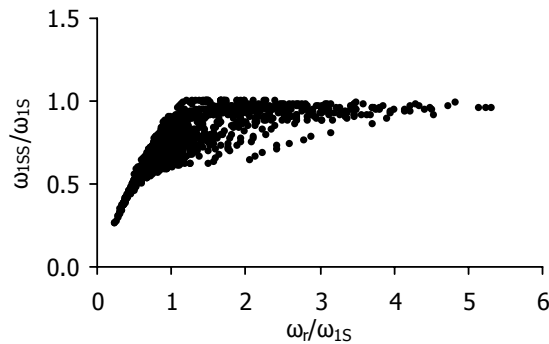


Figure 5-43: Change of the ratio ω_{1SS}/ω_{1S} with respect to the ratio ω_r/ω_{1S} (numerical data)

Hence, if the ring's frequency ω_r , according to Eq. (5-14) is computed less than approximately 65% of ω_{1S} , estimated by Eq. (5-8), then the frequency ω_{1SS} of the first symmetric mode of the cable net with edge ring can be evaluated from this equation. If, on the other hand, it results to more than 65% of ω_{1S} , the frequency ω_{1SS} depends on the value of ω_{1S} . This can be expressed as follows:

$$\begin{aligned} \text{if } \omega_r < 0.65 \omega_{1S}, \text{ then } \omega_{1SS} = \omega_r = 10.73(1.04 - f/L) \sqrt{\frac{E_r I_r g}{\rho_r A_r L^4}} \\ \text{if } \omega_r \geq 0.65 \omega_{1S}, \text{ then } \omega_{1SS} = \omega_{1S} \left[1 - 0.35 \cdot \left(0.65 \cdot \frac{\omega_{1S}}{\omega_r} \right)^2 \right] \end{aligned} \quad (5-15)$$

In order to evaluate the accuracy of the empirical formula calculating the frequency of the first symmetric mode of the combined system, a comparison of the numerical results with the ones of Eq. (5-15) is shown in Figure 5-44, which includes the chart of Figure 5-43 and the plot of the curve of the empirical formula.

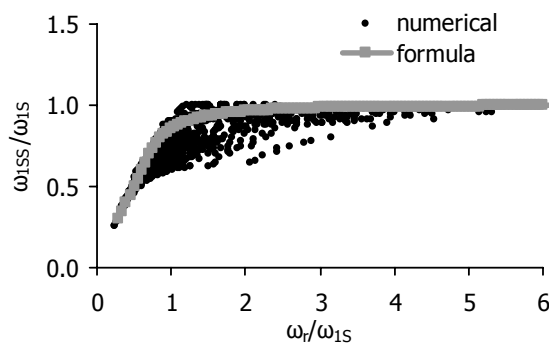


Figure 5-44: Change of the ratio ω_{1SS}/ω_{1S} with respect to the ratio ω_r/ω_{1S} (numerical data and empirical formula)

The error of the above formula is calculated for all results obtained from the parametric modal analyses performed, as the ratio $(\omega_{1SS,n} - \omega_{1SS,e})/\omega_{1SS,n}$, where $\omega_{1SS,n}$ and $\omega_{1SS,e}$ are the ring's frequency calculated by numerical methods and by Eq. (5-15), respectively. Figure 5-45 illustrates the mean absolute value of the calculated error by the empirical formula, with respect to the ratio ω_r/ω_{1S} , which represents the ratio of the stiffnesses for the two separated components. As already mentioned, the

maximum error is observed for values of this ratio between 0.65 and 2.0, arising at 13% for stiffness ratios between 1.0 and 1.5.

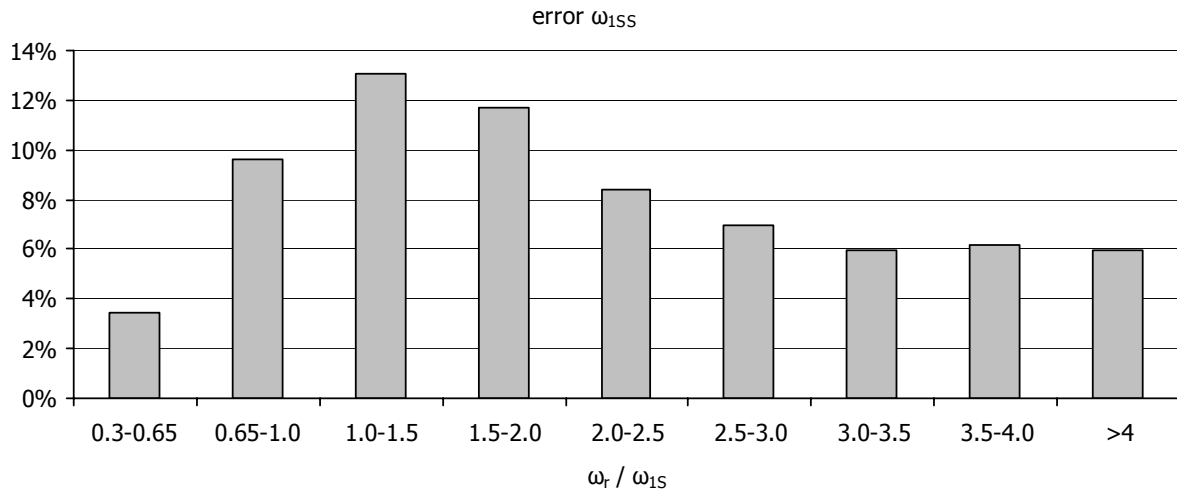


Figure 5-45: Error of the empirical formula for the natural frequency ω_{155} with respect to the ratio of the frequencies for the two separated systems

The chart of Figure 5-46 shows the mean absolute value of the error for the three sag-span ratios considered, in which it is shown that the error becomes smaller as this ratio increases, with maximum error for the shallowest net with $f/L=1/35$, equal to 18%. In Figure 5-47 the mean absolute value of the error is again calculated with respect to the concentrated nodal mass. The formula results in more accurate results if only distributed mass is considered along the cables. The concentrated mass instead influences more the vibration of the ring. In Figure 5-48 it is shown that the error is larger for small values of the non-dimensional parameter λ^2 , because, as shown in section 5.4.3, the error of the empirical formula for the symmetric mode of the cable net with rigid supports presents also larger error for small values of this parameter. Finally the error of the empirical formula for the frequency ω_{155} is larger for very small values of this frequency, between 2.0sec^{-1} and 5.0sec^{-1} , as shown in Figure 5-49.

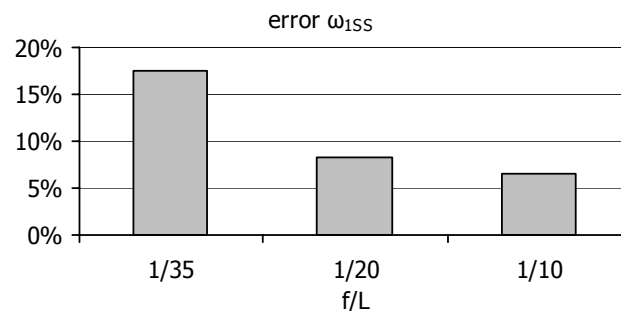


Figure 5-46: Error of the empirical formula for the natural frequency ω_{155} with respect to the sag-to-span ratio

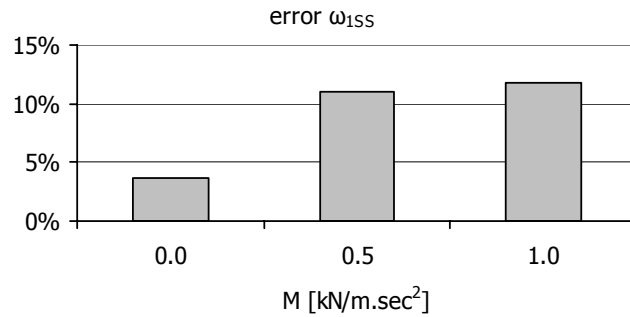


Figure 5-47: Error of the empirical formula for the natural frequency ω_{1SS} with respect to the concentrated nodal mass M

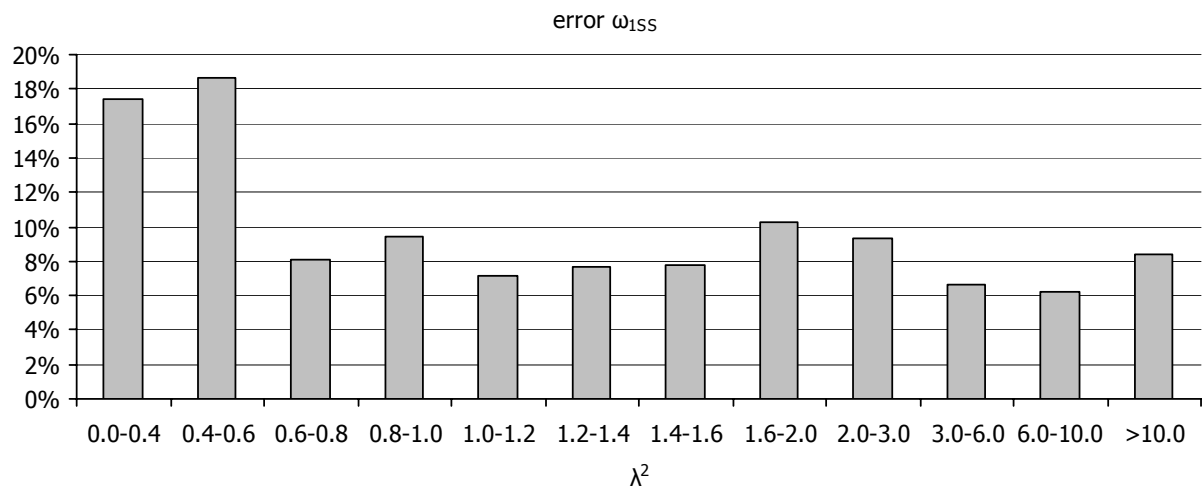


Figure 5-48: Error of the empirical formula for the natural frequency ω_{1SS} with respect to λ^2

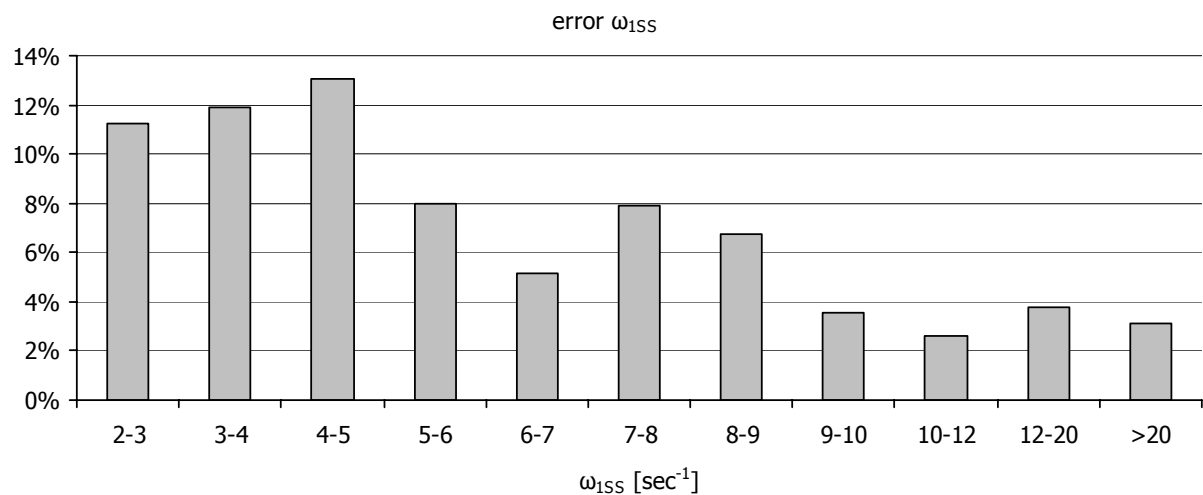


Figure 5-49: Error of the empirical formula for the natural frequency ω_{1SS} with respect to the numerically calculated natural frequency ω_{1SS}

The accuracy of the empirical formulae is also shown in Figure 5-50. In any case, it is considered as satisfactory for preliminary design purposes. Since the presence of the edge ring does not influence significantly the frequencies of the net's antisymmetric vibration modes, the empirical formulae of Eqs. (5-9) and (5-10) can also be used for the case of a cable net with cables anchored to a deformable edge ring.

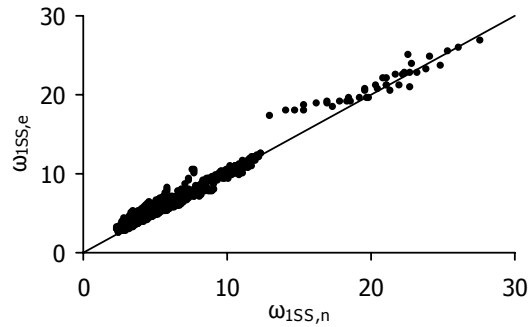


Figure 5-50: Empirical formula for natural frequency ω_{1SS} vs. numerical data

5.7 CONCLUSIONS

Symmetric saddle-shaped cable nets, having rigid supports, have been thoroughly investigated regarding the first natural frequencies and vibration modes. Many similarities with a simple suspended cable have been observed. The appearance sequence of the modes can be predicted by a non-dimensional parameter λ^2 for cable nets, similar to the one referring to simple suspended cables. Crossover points, at which modal transition occurs, depend also on this parameter. Semi-empirical formulae are proposed, which can assess the first four eigenfrequencies of such a structure, with satisfactory results.

If the cable ends are considered as flexible, taking into consideration the deformability of the contour ring, the dynamic response of the system, regarding its frequencies and modes, becomes more complicated. The existence of the ring negligibly influences the antisymmetric modes of the cable net, but an in-plane mode of the ring produces a symmetric vertical oscillation of the net, influencing significantly the motion of the net. Exploring this system, it was concluded that in some cases, two symmetric modes appear among the first five vibration modes of the system, but in some others, there is only one symmetric mode among the first eigenmodes. This depends on the stiffness of the ring with respect to the one of the cable net. Another semi-empirical formula is proposed for estimating the frequency of the system's 1st symmetric mode, either produced by the symmetric vibration of the net, involving the ring, or by the in-plane mode of the ring, involving also the net.

The knowledge of the natural frequencies of a nonlinear system and the relations between them provides the designer with important information about the eventual occurrence of internal resonances. It is possible to use the proposed formulae to calculate the natural frequencies of a cable net, with either rigid or flexible supports, at a preliminary design stage of analysis, in order to design the structure, aiming at avoiding internal resonances between the first vibration modes, which may lead to oscillations of large amplitude, provoking also an unpredictable dynamic response, with a continuous exchange of energy between the modes involved in resonance.

Part of the work developed in this chapter has been presented in [5-23], [5-24] and published in [5-25].

5.8 REFERENCES

- [5-1] A. Nayfeh and D. T. Mook, "Nonlinear oscillations", John Wiley & Sons, Inc., U.S.A., 1979.
- [5-2] A. G. Pugsley, "On the natural frequencies of suspension chains", Quarterly Journal of Mechanics and Applied Mathematics, Vol. 2, Part 4, pp. 412-418, 1949.

- [5-3] M. L. Gambhir and B. deV. Batchelor, "Parametric study of free vibration of sagged cables", *Computers and Structures*, Vol. 8, pp. 641-648, 1978.
- [5-4] H. M. Irvine and T. K. Caughey, "The linear theory of free vibrations of a suspended cable", *Proceedings of the Royal Society of London. Series A, Mathematical and Physical Sciences*, London, Great Britain, Vol. 341, No. 1626, pp. 299-315, 1974.
- [5-5] G. Rega and A. Luongo, "Natural vibrations of suspended cables with flexible supports", *Computers and Structures*, Vol.12, pp. 65-75, 1980.
- [5-6] M. S. Triantafyllou, "The dynamics of translating cables", *Journal of Sound and Vibration*, Vol. 103, No. 2, pp. 171-182, 1985.
- [5-7] J. W. Leonard, "Tension structures, behavior & analysis", McGraw-Hill, Inc., U.S.A., 1988.
- [5-8] J. J. Burgess and M. S. Triantafyllou, "The elastic frequencies of cables", *Journal of Sound and Vibration*, Vol. 120, No. 1, pp. 153-165, 1987.
- [5-9] M. S. Triantafyllou and L. Grinfogel, "Natural frequencies and modes of inclined cables", *Journal of Structural Engineering*, Vol. 112, No. 1, pp. 139-148, 1987.
- [5-10] M. L. Gambhir and B. deV. Batchelor, "A finite element for 3-D prestressed cablenets", *International Journal for Numerical Methods in Engineering*, Vol. 11, pp. 1699-1718, 1977.
- [5-11] M. L. Gambhir and B. deV. Batchelor, "Finite element study of the free vibration of 3D cable networks", *International Journal of Solids and Structures*, Vol. 15, pp. 127-136, 1979.
- [5-12] B. L. Dhoopar, P. C. Gupta and B. P. Singh, "Vibration analysis of orthogonal cable networks by transfer matrix method", *Journal of the Sound and Vibration*, Vol. 101, No. 4, pp. 575-584, 1985.
- [5-13] A. Zingoni, "An efficient computational scheme for the vibration analysis of high tension cable nets", *Journal of the Sound and Vibration*, Vol. 189, No. 1, pp. 55-79, 1996.
- [5-14] D. S. Porter Jr. and D. W. Fowler, "The analysis of nonlinear cable net systems and their supporting structures", *Computers and Structures*, Vol. 3, pp. 1109-1123, 1973.
- [5-15] I. Talvik, "Finite element modelling of cable networks with flexible supports", *Computers and Structures*, Vol. 79, pp. 2443-2450, 2001.
- [5-16] G. R. Seeley, P. Christiano and H. Stefan, "Natural frequencies of circular cable networks", *Journal of the Structural Division*, Vol. 101, No. ST5, pp. 1171-1177, 1975.
- [5-17] H. A. Buchholdt, "An introduction to cable roof structures", Thomas Telford, 2nd Edition, Great Britain, 1999.
- [5-18] I. Vassilopoulou and C. J. Gantes, "Cable nets with elastically deformable edge ring", *International Journal of Space Structures*, Vol. 20, No.1, pp. 15-34, 2005.
- [5-19] ADINA (Automatic Dynamic Incremental Nonlinear Analysis) v8.4, ADINA User interface command reference manual, Vol. I: ADINA Solids & Structures model definition, ADINA R & D, Inc., U.S.A., 2006.
- [5-20] ADINA (Automatic Dynamic Incremental Nonlinear Analysis) v8.4, Theory and modeling guide, Vol. I: ADINA Solids & Structures, ADINA R & D, Inc., U.S.A., 2006.
- [5-21] EASY v7.0, Technet GmbH, Germany, 2000.

-
- [5-22] S. Timoshenko, "Vibration problems in engineering", D. Van Nostrand Company, Inc., U.S.A., 1937.
- [5-23] I. Vassilopoulou and C. J. Gantes, "Modal transition and dynamic nonlinear response of cable nets under fundamental resonance", Proceedings of the 8th HSTAM International Congress on Mechanics, Patras, Greece, Vol. 2, pp. 787-794, 2007.
- [5-24] I. Vassilopoulou and C. J. Gantes, "Vibration modes and dynamic response of saddle form cable nets under sinusoidal excitation", Proceedings of the Euromech Colloquium 483, Geometrically Non-linear Vibrations of Structures, FEUP, Porto, Portugal, pp. 129-132, 2007.
- [5-25] I. Vassilopoulou and C. J. Gantes, "Vibration modes and natural frequencies of saddle form cable nets", Computers and Structures, Vol. 88, pp.105-119, 2010.

6 INVESTIGATION OF A MDOF CABLE NET USING AN EQUIVALENT SDOF CABLE NET

6.1 INTRODUCTION

Nonlinear phenomena, such as superharmonic or subharmonic resonances, bending of the response curve and jump phenomena, instability regions, as well as response amplitudes dependent on the initial conditions, can be detected in simple models by exploring their equation of motion. In a multi-degree-of-freedom system, for which no analytical solutions can be found, the only way to plot a response curve, which can show if the above phenomena may occur, is by conducting a large number of nonlinear time-history analyses, for different closely spaced load amplitudes and frequencies.

The idea of solving an equivalent SDOF system to estimate the dynamic response of a complex structure has been adopted by many researchers ([6-1] – [6-8]). This method is based on equating the energy of the real structure to the one of the SDOF system. Ensuring equal displacements and velocities in both systems, the kinematic similarity is maintained. This approach has the advantage that the equation of motion for a SDOF oscillator can be solved analytically. Hence, it is possible to determine the range of the parameters that influence the dynamic response of the system. On the other hand, using this method, it is impossible to assess the overall response of the MDOF system, because the simulation is obtained only in the main direction of motion, neglecting the other two dimensions of the large structure.

Another method of reducing the dimensions of a large-scale event, using a smaller one with similar characteristics, is a method based on the Buckingham Pi theorem [6-9]. This theorem states that if an equation involves a number of variables and n fundamental measurement units, then the equation can be expressed in terms of n fewer arguments that are non-dimensional ratios of the original variables. The concept is based on the notion that an equation must be dimensionally homogeneous, that is, its solution must be invariant to any change in the system of measurement units employed. This technique has been adopted to design small-scale experiments in order to simulate with accuracy large-scale phenomena.

This theorem was adopted by Gero ([6-10], [6-11]). He presented a method to estimate the static behaviour of a large cable net, referred to as prototype, using charts that describe the behaviour of a smaller one, referred to as model, by means of the maximum deflection and cable tension. The

transformation of the large structure to the smaller one was obtained by similarity relations. The proposed method was restricted to nets with fixed cable edges. The two networks should have similar geometries, with the same sag-to-span ratio, so that their corresponding quantities could also be similar.

During the first steps of this work, the preliminary design method developed by Gero was extended to elastically supported cable network structures, by taking into consideration the characteristics of the edge ring, and more specifically its flexural stiffness $E_r I_r$ ([6-12] - [6-14]). Thus, the ring was no longer considered as rigid, but elastically deformable, accounting for more realistic boundary conditions for the cables. Additional charts and similarity relations were provided for the preliminary design of the edge ring, including the sag-to-span ratio of the net as a variable in the transformation relations. This method was further developed for the case of dynamic response [6-15], providing additional similarity relations for the mass and the natural frequency of the system, for the case of fixed cable ends.

In this chapter, this preliminary design method transforms a MDOF cable net into an equivalent SDOF cable net, in order to solve the equation of motion, as described in chapter 3 and thus have the possibility to detect nonlinear phenomena and estimate the nonlinear dynamic response of the large structure. The analytical solution, depicting the steady-state amplitude of the equivalent SDOF model, is compared with the steady-state response of the MDOF system, obtained numerically, evaluating the accuracy of the method.

6.2 SIMILARITY RELATIONS

The relations that are used in this work for the transformation of the large cable net, called prototype, to the smaller one, called model, are based on the ones provided in [6-15], for a cable net with fixed cable ends and are the following:

$$(P_0)_m = (P_0)_p \left(\frac{E_m}{E_p} \right) \left(\frac{L_m}{L_p} \right)^2 \left(\frac{N_p + 1}{N_m + 1} \right)^2 \sqrt{\frac{f_m / L_m}{f_p / L_p}} \quad : \text{nodal load amplitude} \quad (6-1)$$

$$D_m = D_p \left(\frac{L_m}{L_p} \right) \sqrt{\left(\frac{N_p + 1}{N_m + 1} \right) \left(\frac{f_p / L_p}{f_m / L_m} \right)} \quad : \text{cable diameter} \quad (6-2)$$

$$A_m = A_p \left(\frac{L_m}{L_p} \right)^2 \left(\frac{N_p + 1}{N_m + 1} \right) \left(\frac{f_p / L_p}{f_m / L_m} \right)^2 \quad : \text{cable cross-sectional area} \quad (6-3)$$

$$(EA)_m = (EA)_p \left(\frac{E_m}{E_p} \right) \left(\frac{L_m}{L_p} \right)^2 \left(\frac{N_p + 1}{N_m + 1} \right) \left(\frac{f_p / L_p}{f_m / L_m} \right)^2 \quad : \text{cable axial stiffness} \quad (6-4)$$

$$(N_0)_m = (N_0)_p \left(\frac{E_m}{E_p} \right) \left(\frac{L_m}{L_p} \right)^2 \left(\frac{N_p + 1}{N_m + 1} \right) \quad : \text{cable initial pretension} \quad (6-5)$$

$$N_{c,m} = N_{c,p} \left(\frac{E_m}{E_p} \right) \left(\frac{L_m}{L_p} \right)^2 \left(\frac{N_p + 1}{N_m + 1} \right) \quad : \text{cable tension} \quad (6-6)$$

$$\rho_m = \rho_p \left(\frac{E_m}{E_p} \right) \left(\frac{L_p}{L_m} \right)^2 \left(\frac{f_m/L_m}{f_p/L_p} \right)^2 \quad : \text{cable unit weight} \quad (6-7)$$

$$M_m = M_p \left(\frac{E_m}{E_p} \right) \left(\frac{L_m}{L_p} \right) \left(\frac{N_p + 1}{N_m + 1} \right)^2 \quad : \text{nodal mass} \quad (6-8)$$

$$w_{d,m} = w_{d,p} \left(\frac{L_m}{L_p} \right) \left(\frac{f_m/L_m}{f_p/L_p} \right) \quad : \text{nodal dynamic deflection} \quad (6-9)$$

$$w_m = w_p \frac{L_m}{L_p} \quad : \text{nodal static deflection} \quad (6-10)$$

$$\omega_m = \omega_p \quad : \text{natural frequency} \quad (6-11)$$

where N is the number of cables per direction, L is the maximum length of the cables, meaning the diameter of the circular plan view, f/L is the sag-to-span ratio, E the elastic modulus of the cables, while the subscripts m and p refer to the model and the prototype, respectively. Two more relations are added, describing the loading frequency and the damping ratio:

$$\Omega_m = \Omega_p \quad : \text{loading frequency} \quad (6-12)$$

$$\zeta_m = \zeta_p \quad : \text{damping ratio} \quad (6-13)$$

6.3 PROTOTYPE AND MODEL

6.3.1 Assumptions

Two large cable nets are used as prototypes, having a diameter $L_p=100\text{m}$ and sag-to-span ratios equal to $f_p/L_p=1/35$ ($f_p=2.857\text{m}$) and $f_p/L_p=1/20$ ($f_p=5.00\text{m}$), while the number of cables in each direction is $N_p=25$ (Figure 6-1).

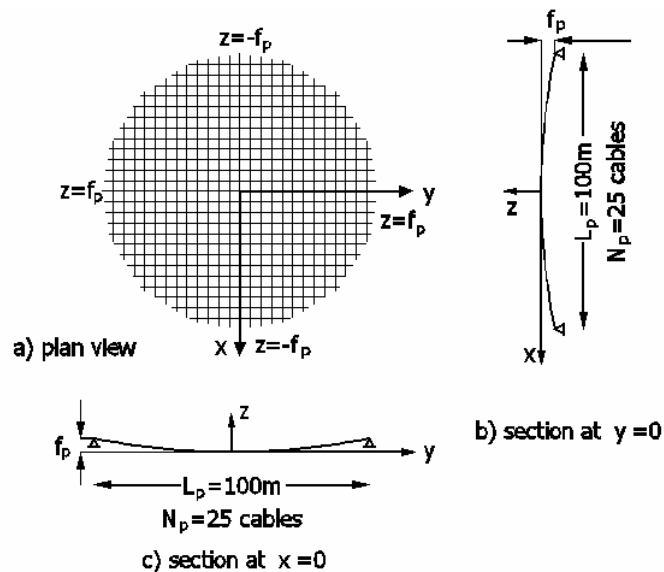


Figure 6-1: Geometry of the prototype

The Young modulus is assumed equal to $E_p=165\text{GPa}$. The unit weight of the cables is taken equal to $\rho_p=100\text{kN/m}^3$. For the nonlinear dynamic analyses of the prototype that are conducted, in order to compare the numerical results of the large structure with the analytical ones of the small structure, harmonic loads, expressed as $P_p(t)=(P_0)_p\cos\Omega_p t$, are exerted vertically on every node of the net, having the same amplitude and time variation. The oscillation of the central node of the net will describe the response of the net.

Rayleigh damping [6-16] is introduced, being mass-proportional and stiffness-proportional, expressed as:

$$[C]=\alpha_0[M]+\alpha_1[K] \quad (6-14)$$

where $[C]$ is the damping matrix, $[M]$ is the mass matrix of the system and $[K]$ is the stiffness matrix corresponding to zero initial displacements. If two modes i and j have the same damping ratio ζ , the coefficients α_0 and α_1 can be calculated as:

$$\alpha_0 = \zeta \frac{2\omega_i\omega_j}{\omega_i + \omega_j} \quad (6-15)$$

$$\alpha_1 = \zeta \frac{2}{\omega_i + \omega_j} \quad (6-16)$$

In this investigation the damping ratio is considered equal for the first symmetric mode (1S) and for the first antisymmetric mode with respect to both horizontal axes (2A). Two alternative values of this ratio are assumed, $\zeta_p=2\%$ and $\zeta_p=0.5\%$.

The parameter λ^2 , which characterises the dynamic response of the cable net, controls the sequence of the vibration modes, as well as the shape of the first symmetric mode of the system, as reported in chapter 5. For $\lambda^2 < 1.17$, the vertical component of this mode has no internal nodes with zero displacements, for $\lambda^2 = 1.17$ the vertical modal component is tangential to the profile at the cable ends, while for $\lambda^2 > 1.17$, two internal nodes with zero displacements are observed, on each horizontal axis.

This parameter is expressed as:

$$\lambda^2 = \left(\frac{f}{L}\right)^2 \frac{EA}{N_0} \quad (6-17)$$

Taking into account $E=165\text{GPa}$ and initial cable stress equal to $0.10\sigma_y$, with yield stress 1570MPa , the chart of Figure 6-2 shows that for sag-to-span ratio equal or larger than $1/30$, this parameter is equal or larger than 1.17 , respectively, meaning that internal nodes with zero displacements appear in the first symmetric mode. For levels of pretension higher than $0.20\sigma_y$, the parameter λ^2 is larger than 1.17 , for sag-to-span ratios equal or larger than $1/20$, while for deeper cable nets this parameter is larger than this limit for initial cable stress between $0.10\sigma_y$ and $0.35\sigma_y$. The same limits exist if a larger yield stress is assumed equal to 1670MPa , but in general, the parameter λ^2 takes slightly smaller values (Figure 6-3). It will be shown that this limit influences the accuracy of the proposed method.

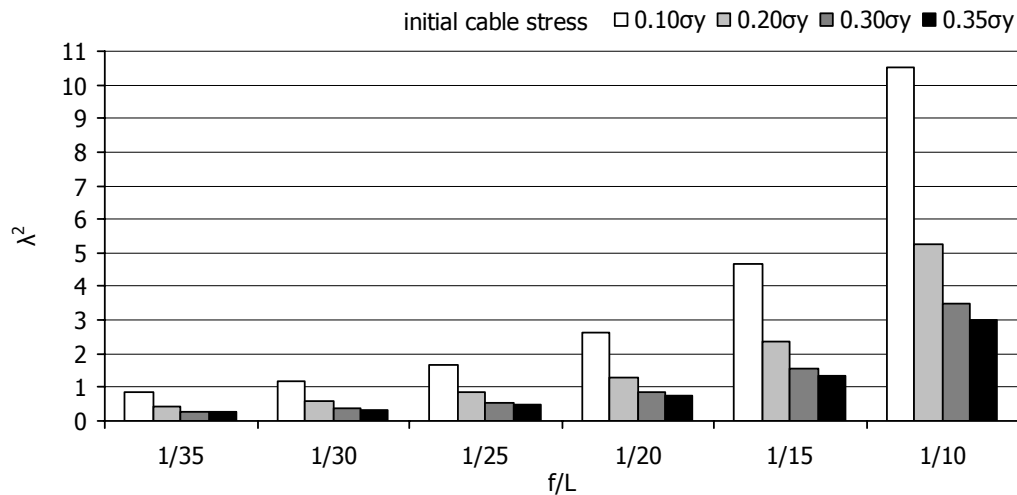


Figure 6-2: Variation of the parameter λ^2 with respect to the sag-to-span ratio ($E=165\text{GPa}$, $\sigma_y=1570\text{MPa}$)

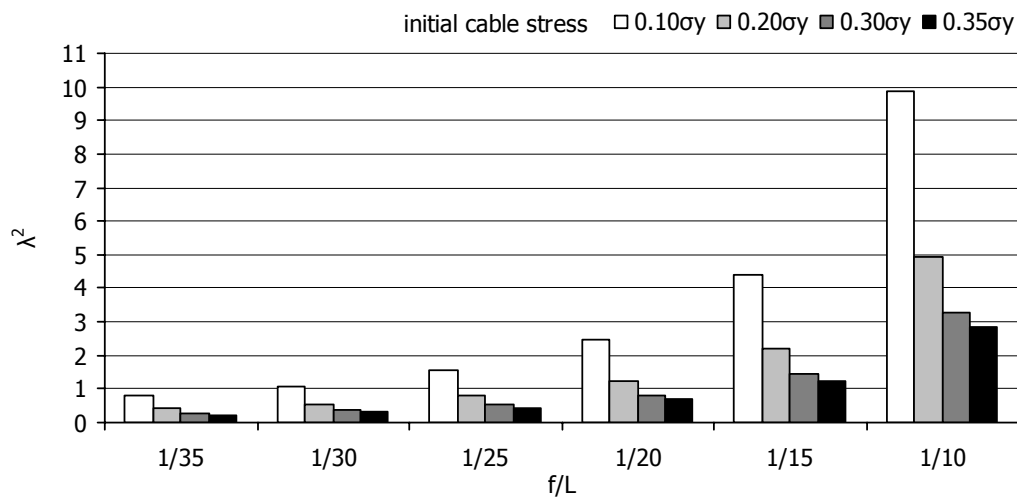


Figure 6-3: Variation of the parameter λ^2 with respect to the sag-to-span ratio ($E=165\text{GPa}$, $\sigma_y=1670\text{MPa}$)

The model utilised as the equivalent SDOF system is similar to the one described in chapter 3, consisting of two crossing cables ($N_m=1$), with a concentrated mass at the central node M_m . In order to minimise the scaling error, each model has the same sag-to-span ratio f_m/L_m , cable span L_m , and Young modulus E_m with the corresponding prototype (Figure 6-4a). A harmonic load, expressed as $P_m(t)=(P_0)_m \cos \Omega_m t$, is exerted vertically on the central node (Figure 6-4b).

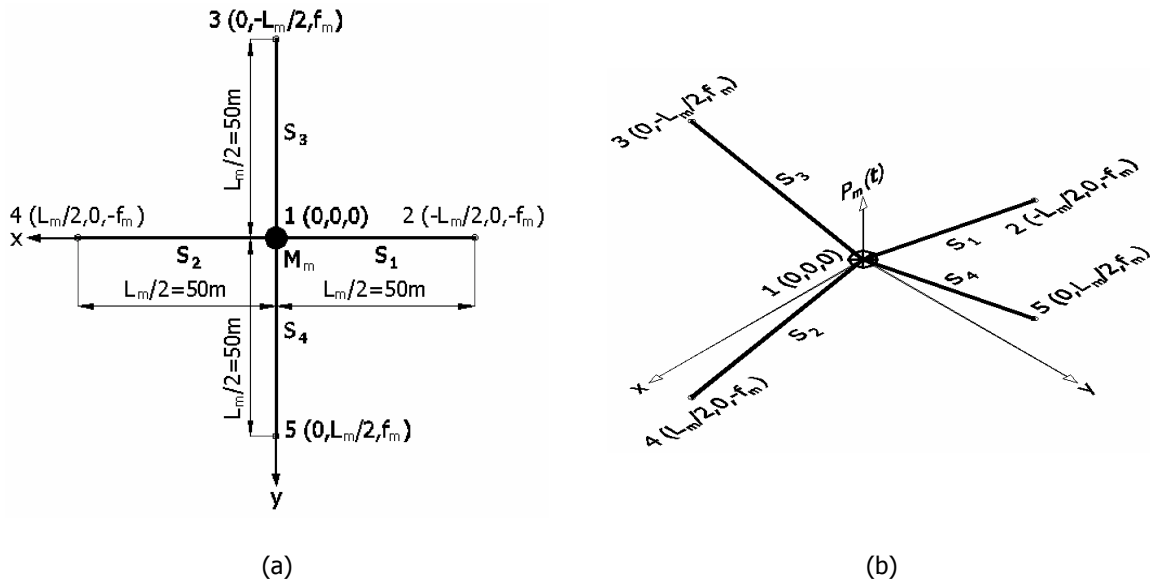


Figure 6-4: (a) Geometry of the model, (b) Load for the model

The similarity relations, expressed by Eqs. (6-1)-(6-13), are reduced to the following:

$$(P_0)_m = (P_0)_p \left(\frac{N_p + 1}{N_m + 1} \right)^2 \quad : \text{nodal load amplitude} \quad (6-18)$$

$$D_m = D_p \sqrt{\left(\frac{N_p + 1}{N_m + 1} \right)} \quad : \text{cable diameter} \quad (6-19)$$

$$A_m = A_p \left(\frac{N_p + 1}{N_m + 1} \right) \quad : \text{cable cross-sectional area} \quad (6-20)$$

$$(EA)_m = (EA)_p \left(\frac{N_p + 1}{N_m + 1} \right) \quad : \text{cable axial stiffness} \quad (6-21)$$

$$(N_0)_m = (N_0)_p \left(\frac{N_p + 1}{N_m + 1} \right) \quad : \text{cable initial pretension} \quad (6-22)$$

$$N_{c,m} = N_{c,p} \left(\frac{N_p + 1}{N_m + 1} \right) \quad : \text{cable tension} \quad (6-23)$$

$$M_m = M_p \left(\frac{N_p + 1}{N_m + 1} \right)^2 \quad : \text{nodal mass} \quad (6-24)$$

$$W_{d,m} = W_{d,p} \quad : \text{nodal dynamic deflection} \quad (6-25)$$

$$W_m = W_p \quad : \text{nodal static deflection} \quad (6-26)$$

$$\omega_m = \omega_p \quad : \text{ natural frequency} \quad (6-27)$$

$$\Omega_m = \Omega_p = \Omega \quad : \text{ loading frequency} \quad (6-28)$$

$$\zeta_m = \zeta_p = \zeta \quad : \text{ damping ratio} \quad (6-29)$$

6.3.2 Analytical solution for the model

The main expressions of the SDOF model, describing the dynamic response in resonant conditions, are reported and summarised here, based on the theory presented in chapter 3.

6.3.2.1 Equation of motion

The equation of motion of the SDOF cable net is:

$$\ddot{w} + 2\varepsilon\mu\dot{w} + \omega_m^2 w + \varepsilon\alpha w^3 = P_m \cos(\Omega t) \quad (6-30)$$

where the eigenfrequency is expressed as:

$$\omega_m = \sqrt{\frac{4(EA)_m}{M_m L_m} \cdot \left(8 \frac{f_m^2}{L_m^2} + 2 \frac{(N_0)_m}{(EA)_m} - 4 \frac{(N_0)_m}{(EA)_m} \frac{f_m^2}{L_m^2} \right)} \quad (6-31)$$

and

$$P_m = \frac{(P_0)_m}{M_m} \quad (6-32)$$

$$\varepsilon\mu = \zeta\omega_m \quad (6-33)$$

$$\varepsilon\alpha = \frac{16(EA)_m}{M_m L_m^3} \quad (6-34)$$

6.3.2.2 Fundamental resonance

For fundamental resonant conditions, the steady-state response is:

$$w(t) = a \cos(\Omega t - \gamma) + O(\varepsilon) \quad (6-35)$$

The loading frequency is expressed as:

$$\Omega = \omega_m + \varepsilon\sigma \quad (6-36)$$

where $\varepsilon\sigma$ is the detuning, which, for a given amplitude of the response, is calculated by the following equation:

$$\sigma = \frac{3\alpha a^2}{8\omega_m} \pm \sqrt{\frac{p^2}{4\omega_m^2 a^2} - \mu^2} \Rightarrow \varepsilon\sigma = \frac{3\varepsilon\alpha a^2}{8\omega_m} \pm \sqrt{\frac{(\varepsilon p)^2}{4\omega_m^2 a^2} - (\varepsilon\mu)^2} \quad (6-37)$$

Taking into account Eqs. (6-33) and (6-34) and substituting εp with:

$$\varepsilon p = P_m = \frac{(P_0)_m}{M_m} \quad (6-38)$$

Eq. (6-37) can be rewritten as:

$$\varepsilon\sigma = \frac{6a^2}{\omega_m} \cdot \frac{(EA)_m}{M_m L_m^3} \pm \sqrt{\frac{(P_0)_m^2}{4M_m^2 \omega_m^2 a^2} - (\zeta\omega_m)^2} \quad (6-39)$$

The peak amplitude of the free oscillation term is:

$$a_{\text{peak}} = \frac{\rho}{2\mu\omega_m} = \frac{\varepsilon\rho}{2\varepsilon\mu\omega_m} = \frac{(P_0)_m}{2M_m \zeta \omega_m^2} \quad (6-40)$$

and the corresponding value of the detuning σ :

$$\sigma_{\text{peak}} = \frac{3a\rho^2}{32\mu^2\omega_m^3} \Rightarrow \varepsilon\sigma_{\text{peak}} = \frac{3\varepsilon a(\varepsilon\rho)^2}{32(\varepsilon\mu)^2\omega_m^3} = \frac{3(P_0)_m^2 (EA)_m}{2M_m^3 \zeta^2 \omega_m^5 L_m^3} \quad (6-41)$$

The backbone curve of the system is described by:

$$\sigma = \frac{3a^2}{8\omega_m} \Rightarrow \varepsilon\sigma = \frac{3\varepsilon a^2}{8\omega_m} \Rightarrow \varepsilon\sigma = \frac{6a^2}{\omega_m} \cdot \frac{(EA)_m}{M_m L_m^3} \quad (6-42)$$

The unstable solutions are for values of frequency detuning σ :

$$\begin{aligned} \frac{6a^2}{8\omega_m} - \sqrt{\left(\frac{3a^2}{8\omega_m}\right)^2 - \mu^2} < \sigma < \frac{6a^2}{8\omega_m} + \sqrt{\left(\frac{3a^2}{8\omega_m}\right)^2 - \mu^2} \Rightarrow \\ \frac{6\varepsilon a^2}{8\omega_m} - \sqrt{\left(\frac{3\varepsilon a^2}{8\omega_m}\right)^2 - (\varepsilon\mu)^2} < \varepsilon\sigma < \frac{6\varepsilon a^2}{8\omega_m} + \sqrt{\left(\frac{3\varepsilon a^2}{8\omega_m}\right)^2 - (\varepsilon\mu)^2} \Rightarrow \\ 2B - \sqrt{B^2 - (\zeta\omega_m)^2} < \varepsilon\sigma < 2B + \sqrt{B^2 - (\zeta\omega_m)^2} \end{aligned} \quad (6-43)$$

where

$$B = \frac{6a^2 (EA)_m}{\omega_m M_m L_m^3} \quad (6-44)$$

6.3.2.3 Superharmonic resonance

For superharmonic resonant conditions, the steady-state response is:

$$w(t) = a \cos(3\Omega t - \gamma_0) + \frac{(P_0)_m}{M_m} \left(\frac{1}{\omega_m^2 - \Omega^2} \right) \cos \Omega t + O(\varepsilon) \quad (6-45)$$

The loading frequency is expressed as:

$$3\Omega = \omega_m + \varepsilon\sigma \quad (6-46)$$

For a given amplitude of the free oscillation term a , the frequency detuning is calculated by:

$$\begin{aligned}
\sigma &= \frac{3a\Lambda^2}{\omega_m} + \frac{3aa^2}{8\omega_m} \pm \sqrt{\frac{a^2\Lambda^6}{\omega_m^2 a^2} - \mu^2} \Rightarrow \\
\Rightarrow \varepsilon\sigma &= \frac{3\varepsilon a\Lambda^2}{\omega_m} + \frac{3\varepsilon aa^2}{8\omega_m} \pm \sqrt{\frac{(\varepsilon a)^2 \Lambda^6}{\omega_m^2 a^2} - (\varepsilon\mu)^2} \Rightarrow \\
\Rightarrow \varepsilon\sigma &= \frac{48\Lambda^2}{\omega_m} \cdot \frac{(EA)_m}{M_m L_m^3} + \frac{6a^2}{\omega_m} \cdot \frac{(EA)_m}{M_m L_m^3} \pm \sqrt{\frac{\Lambda^6}{\omega_m^2 a^2} \cdot \left(\frac{16(EA)_m}{M_m L_m^3}\right)^2 - (\zeta\omega_m)^2}
\end{aligned} \tag{6-47}$$

where

$$\Lambda = \frac{(P_0)_m}{2M_m} \left(\frac{1}{\omega_m^2 - \Omega^2} \right) \tag{6-48}$$

The peak amplitude of the free oscillation term is expressed as:

$$a_{\text{peak}} = \frac{a\Lambda^3}{\mu\omega_m} = \frac{\varepsilon a\Lambda^3}{\varepsilon\mu\omega_m} = \frac{16(EA)_m}{M_m L_m^3} \cdot \frac{1}{\zeta\omega_m^2} \Lambda^3 \tag{6-49}$$

and the corresponding value of the detuning $\varepsilon\sigma$:

$$\begin{aligned}
\sigma_{\text{peak}} &= \frac{3a\Lambda^2}{\omega_{z0}} \left(1 + \frac{a^2\Lambda^4}{8\mu^2\omega_m^2} \right) \Rightarrow \varepsilon\sigma_{\text{peak}} = \frac{3\varepsilon a\Lambda^2}{\omega_m} \left(1 + \frac{(\varepsilon a)^2 \Lambda^4}{8(\varepsilon\mu)^2 \omega_m^2} \right) \Rightarrow \\
\varepsilon\sigma_{\text{peak}} &= \frac{48(EA)_m}{\omega_m M_m L_m^3} \cdot \left[\frac{(P_0)_m}{2M_m} \left(\frac{1}{\omega_m^2 - \Omega^2} \right) \right]^2 \cdot \\
&\cdot \left(1 + \frac{1}{8\zeta^2\omega_m^4} \left(\frac{16(EA)_m}{M_m L_m^3} \right)^2 \cdot \left[\frac{(P_0)_m}{2M_m} \left(\frac{1}{\omega_m^2 - \Omega^2} \right) \right]^4 \right)
\end{aligned} \tag{6-50}$$

6.3.2.4 Subharmonic resonance

In case of subharmonic resonance, the loading frequency is expressed as:

$$\Omega = 3\omega_m + \varepsilon\sigma \tag{6-51}$$

For a given detuning $\varepsilon\sigma$, subharmonic solutions with non-trivial amplitudes exist only if:

$$\begin{aligned}
\frac{\sigma}{\mu} - \sqrt{\frac{\sigma^2}{\mu^2} - 63} &\leq \frac{63a}{4\omega_{z0}\mu} \Lambda^2 \leq \frac{\sigma}{\mu} + \sqrt{\frac{\sigma^2}{\mu^2} - 63} \Rightarrow \\
\frac{\varepsilon\sigma}{\varepsilon\mu} - \sqrt{\frac{(\varepsilon\sigma)^2}{(\varepsilon\mu)^2} - 63} &\leq \frac{63\varepsilon a}{4\omega_m\varepsilon\mu} \Lambda^2 \leq \frac{\varepsilon\sigma}{\varepsilon\mu} + \sqrt{\frac{(\varepsilon\sigma)^2}{(\varepsilon\mu)^2} - 63} \Rightarrow \\
\frac{\varepsilon\sigma}{\zeta\omega_m} - \sqrt{\frac{(\varepsilon\sigma)^2}{(\zeta\omega_m)^2} - 63} &\leq \frac{256\Lambda^2}{\zeta\omega_m^2} \cdot \frac{(EA)_m}{M_m L_m^3} \leq \frac{\varepsilon\sigma}{\zeta\omega_m} + \sqrt{\frac{(\varepsilon\sigma)^2}{(\zeta\omega_m)^2} - 63}
\end{aligned} \tag{6-52}$$

where Λ is defined by Eq. (6-48), while for a given Λ subharmonic solutions exist if:

$$\sigma \geq \frac{63a}{8\omega_m} \Lambda^2 + \frac{2\omega_m}{a} \frac{\mu^2}{\Lambda^2} \Rightarrow \varepsilon\sigma \geq \frac{63\varepsilon a}{8\omega_m} \Lambda^2 + \frac{2\omega_m}{\varepsilon a} \frac{(\varepsilon\mu)^2}{\Lambda^2} \Rightarrow$$

$$\varepsilon\sigma \geq \frac{126\Lambda^2}{\omega_m} \cdot \frac{(EA)_m}{M_m L_m^3} + \frac{M_m L_m^3}{8(EA)_m} \frac{\zeta^2 \omega_m^3}{\Lambda^2} \quad (6-53)$$

with amplitude calculated by:

$$a^2 = \left(\sigma \frac{8\omega_m}{9a} - 6\Lambda^2 \right) \pm \sqrt{\left(\sigma \frac{8\omega_m}{9a} - 6\Lambda^2 \right)^2 - \frac{64\omega_m^2}{81a^2} \left[\left(\sigma - \frac{9a\Lambda^2}{\omega_m} \right)^2 + 9\mu^2 \right]} =$$

$$= \left(\varepsilon\sigma \frac{8\omega_m}{9\varepsilon a} - 6\Lambda^2 \right) \pm \sqrt{\left(\varepsilon\sigma \frac{8\omega_m}{9\varepsilon a} - 6\Lambda^2 \right)^2 - \frac{64\omega_m^2}{81(\varepsilon a)^2} \left[\left(\varepsilon\sigma - \frac{9\varepsilon a\Lambda^2}{\omega_m} \right)^2 + 9(\varepsilon\mu)^2 \right]} \Rightarrow$$

$$a^2 = \left(\varepsilon\sigma \frac{\omega_m M_m L_m^3}{18(EA)_m} - 6\Lambda^2 \right) \pm$$

$$\pm \sqrt{\left(\varepsilon\sigma \frac{\omega_m M_m L_m^3}{18(EA)_m} - 6\Lambda^2 \right)^2 - \frac{M_m^2 L_m^6 \omega_m^2}{324(EA)_m^2} \left[\left(\varepsilon\sigma - \frac{9\Lambda^2}{\omega_m} \cdot \frac{16(EA)_m}{M_m L_m^3} \right)^2 + 9(\zeta\omega_m)^2 \right]} \quad (6-54)$$

In case no subharmonic resonant conditions exist, the response at steady state depends only on the external load:

$$w(t) = \frac{(P_0)_m}{M_m} \left(\frac{1}{\omega_m^2 - \Omega^2} \right) \cos \Omega t + O(\varepsilon) \quad (6-55)$$

while, for the non-trivial stable solution of response amplitude, the response of the nonlinear system at steady state is:

$$w(t) = a \cos\left(\frac{\Omega t - \gamma_0}{3}\right) + \frac{(P_0)_m}{M_m} \left(\frac{1}{\omega_m^2 - \Omega^2} \right) \cos \Omega t + O(\varepsilon) \quad (6-56)$$

6.4 EXAMPLE 1: CABLE NET WITH SAG-SPAN RATIO $f/L=1/35$

For this example, the cable diameter is assumed equal to $D_p=50\text{mm}$, with cross-sectional area $A_p=0.00196\text{m}^2$. The concentrated mass on every node is equal to:

$$M_p = \frac{2A_p \rho_p L_p}{g(N_p + 1)} = \frac{2 \cdot 0.00196\text{m}^2 \cdot 100\text{kN/m}^3 \cdot 100\text{m}}{10\text{m/sec}^2 (25 + 1)} = 0.151\text{kNsec}^2 \text{m}^{-1} \quad (6-57)$$

The pretension is $(N_0)_p=600\text{kN}$, corresponding to approximately 20% of the yield stress, which is considered equal to 1570MPa.

6.4.1 Transformation of the prototype to the model

The equivalent SDOF model for the cable net with sag-to-span ratio $f_p/L_p=1/35$, has the following characteristics:

$$D_m = D_p \sqrt{\left(\frac{N_p + 1}{N_m + 1}\right)} = 0.05m \sqrt{\left(\frac{26}{2}\right)} = 0.18m \quad (6-58)$$

$$A_m = A_p \left(\frac{N_p + 1}{N_m + 1}\right) = 0.00196m^2 \cdot \frac{26}{2} = 0.0255m^2 \quad (6-59)$$

$$(EA)_m = (EA)_p \left(\frac{N_p + 1}{N_m + 1}\right) = 165000000kN/m^2 \cdot 0.0255m^2 = 4211697.6kN \quad (6-60)$$

$$(N_0)_m = (N_0)_p \left(\frac{N_p + 1}{N_m + 1}\right) = 600kN \cdot \frac{26}{2} = 7800kN \quad (6-61)$$

$$M_m = M_p \left(\frac{N_p + 1}{N_m + 1}\right)^2 = 0.151kNsec^2 m^{-1} \cdot \left(\frac{26}{2}\right)^2 = 25.52kNsec^2 m^{-1} \quad (6-62)$$

6.4.2 Analytical solution for the SDOF model

6.4.2.1 Maximum static deflection

The maximum cable tension is calculated as:

$$N_{cmax,m} = A_m \sigma_y = 0.0255m^2 \cdot 157000kN/m^2 = 40035kN \quad (6-63)$$

The maximum permissible deflection is defined as:

$$|w_{max,m}| = \left| f_m - \sqrt{f_m^2 - Q} \right| = \left| 2.857m - \sqrt{(2.857m)^2 + 38.517m^2} \right| = 3.975m \quad (6-64)$$

where

$$Q = \left[1 - \frac{\left(\frac{\sigma_y}{E} + 1\right)^2}{\left(1 + \frac{(N_0)_m}{(EA)}\right)^2} \right] \cdot \left[(L_m/2)^2 + f_m^2 \right] \Rightarrow \quad (6-65)$$

$$Q = \left[1 - \frac{\left(\frac{1570000kN/m^2}{165000000kN/m^2} + 1\right)^2}{\left(1 + \frac{7800kN}{4211697.6kN}\right)^2} \right] \cdot \left[(100m/2)^2 + (2.857m)^2 \right] = -38.517m^2$$

6.4.2.2 Maximum static load

Based on the theory of chapter 3 regarding the static analysis of the simple cable net, the load that causes the maximum permissible deflection is equal to:

$$P_{max,m} = 10939kN \quad (6-66)$$

The diagram of the applied load with respect to the deflection of the central node is depicted in Figure 6-5:

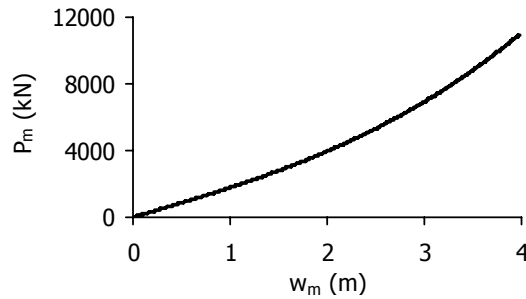


Figure 6-5: Load – displacement curve

6.4.2.3 Eigenfrequency of the model

The eigenfrequency of the SDOF model is calculated from Eq. (6-31):

$$\begin{aligned}\omega_m &= \sqrt{\frac{4(EA)_m}{M_m L_m} \cdot \left(8 \frac{f_m^2}{L_m^2} + 2 \frac{(N_0)_m}{(EA)_m} - 4 \frac{(N_0)_m}{(EA)_m} \frac{f_m^2}{L_m^2} \right)} \Rightarrow \\ \omega_m &= \sqrt{\frac{4 \cdot 4211697.6}{25.52 \cdot 100} \cdot \left(8 \frac{2.857^2}{100^2} + 2 \frac{7800}{4211697.6} - 4 \frac{7800}{4211697.6} \frac{2.857^2}{100^2} \right)} \Rightarrow \\ \omega_m &= 8.22 \text{ sec}^{-1}\end{aligned}\quad (6-67)$$

6.4.2.4 Fundamental resonance for damping ratio $\zeta=2\%$

The maximum amplitude of the steady-state response, defined by Eq. (6-40), cannot be larger than the maximum permissible deflection. Thus, the threshold of the load amplitude can be calculated:

$$\begin{aligned}a_{\text{peak}} \leq w_{\text{max},m} &\Rightarrow (P_0)_{m,\text{peak}} \leq 2M_m \zeta \omega_m^2 w_{\text{max},m} \Rightarrow \\ (P_0)_{m,\text{peak}} &\leq 2 \cdot 25.52 \text{ kN sec}^2 \text{ m}^{-1} \cdot 0.02 \cdot (8.22 \text{ sec}^{-1})^2 \cdot 3.975 \text{ m} = 274.17 \text{ kN}\end{aligned}\quad (6-68)$$

which corresponds to load amplitude for the MDOF cable net:

$$(P_0)_{p,\text{peak}} = (P_0)_{m,\text{peak}} \left(\frac{N_m + 1}{N_p + 1} \right)^2 = 274.17 \text{ kN} \cdot \left(\frac{2}{26} \right)^2 = 1.62 \text{ kN}\quad (6-69)$$

Taking into consideration that during the transient response the deflection of the net cannot exceed the maximum permissible one, a smaller load amplitude is chosen for the prototype equal to $(P_0)_p = 1.30 \text{ kN}$, corresponding to a nodal load for the SDOF model, equal to:

$$(P_0)_m = (P_0)_p \left(\frac{N_p + 1}{N_m + 1} \right)^2 = 1.30 \text{ kN} \cdot \left(\frac{26}{2} \right)^2 = 219.70 \text{ kN}\quad (6-70)$$

For this load amplitude the maximum amplitude of the steady-state response is:

$$a_{\text{peak}} = \frac{(P_0)_m}{2M_m \zeta \omega_m^2} = \frac{219.70 \text{ kN}}{2 \cdot 25.52 \text{ kN sec}^2 \text{ m}^{-1} \cdot 0.02 \cdot (8.22 \text{ sec}^{-1})^2} = 3.185 \text{ m}\quad (6-71)$$

and the corresponding value of the detuning σ :

$$\begin{aligned}\varepsilon\sigma_{\text{peak}} &= \frac{3(P_0)_m^2 (EA)_m}{2M_m^3 \zeta^2 \omega_m^5 L_m^3} \Rightarrow \\ \varepsilon\sigma_{\text{peak}} &= \frac{3 \cdot (219.70\text{kN})^2 \cdot 4211697.6\text{kN/m}^2}{2 \cdot (25.52\text{kN sec}^2 \text{ m}^{-1})^3 \cdot 0.02^2 \cdot (8.22 \text{ sec}^{-1})^5 \cdot (100\text{m})^3} = 1.22 \text{ sec}^{-1}\end{aligned}\quad (6-72)$$

Hence, the peak steady-state response amplitude occurs for loading frequency:

$$\Omega = \omega_m + \varepsilon\sigma = 8.22\text{sec}^{-1} + 1.22\text{sec}^{-1} = 9.44\text{sec}^{-1} = 1.15\omega_m \quad (6-73)$$

The response curve is based on Eq. (6-39):

$$\begin{aligned}\varepsilon\sigma &= \frac{6a^2}{\omega_m} \cdot \frac{(EA)_m}{M_m L_m^3} \pm \sqrt{\frac{(P_0)_m^2}{4M_m^2 \omega_m^2 a^2} - (\zeta\omega_m)^2} \Rightarrow \\ \varepsilon\sigma &= \frac{6a^2}{8.22 \text{ sec}^{-1}} \cdot \frac{4211697.6\text{kN}}{25.52\text{kN sec}^2 \text{ m}^{-1} \cdot (100\text{m})^3} \pm \\ &\pm \sqrt{\frac{(219.7\text{kN})^2}{4 \cdot (25.52\text{kN sec}^2 \text{ m}^{-1})^2 (8.22 \text{ sec}^{-1})^2 \cdot a^2} - (0.02 \cdot 8.22 \text{ sec}^{-1})^2} \Rightarrow \\ \varepsilon\sigma &= \left(0.12a^2 \pm \sqrt{\frac{0.27}{a^2} - 0.027} \right) \text{sec}^{-1}\end{aligned}\quad (6-74)$$

while the frequency ratio is calculated as:

$$\frac{\Omega}{\omega_m} = \frac{\omega_m + \varepsilon\sigma}{\omega_m} \quad (6-75)$$

The backbone curve of the system is calculated according to Eq. (6-42):

$$\varepsilon\sigma = \frac{6a^2}{\omega_m} \cdot \frac{(EA)_m}{M_m L_m^3} = \frac{6 \cdot 4211697.6\text{kN} \cdot a^2}{8.22 \text{ sec}^{-1} \cdot 25.52\text{kN sec}^2 \text{ m}^{-1} \cdot (100\text{m})^3} = 0.12a^2 (\text{sec}^{-1}) \quad (6-76)$$

The instability region is defined by the expression (6-43) taking into consideration Eqs. (6-44) and (6-76):

$$\begin{aligned}2B - \sqrt{B^2 - (\zeta\omega_m)^2} < \varepsilon\sigma < 2B + \sqrt{B^2 - (\zeta\omega_m)^2} \Rightarrow \\ 2B - \sqrt{B^2 - (0.02 \cdot 8.22 \text{ sec}^{-1})^2} < \varepsilon\sigma < 2B + \sqrt{B^2 - (0.02 \cdot 8.22 \text{ sec}^{-1})^2} \Rightarrow \\ 2B - \sqrt{B^2 - (0.1644 \text{ sec}^{-1})^2} < \varepsilon\sigma < 2B + \sqrt{B^2 - (0.1644 \text{ sec}^{-1})^2}\end{aligned}\quad (6-77)$$

where

$$B = \frac{6a^2 (EA)_m}{\omega_m M_m L_m^3} = \frac{6 \cdot 4211697.6\text{kN} \cdot a^2}{8.22 \text{ sec}^{-1} \cdot 25.52\text{kN sec}^2 \text{ m}^{-1} \cdot (100\text{m})^3} = 0.12a^2 (\text{sec}^{-1}) \quad (6-78)$$

The amplitude of the steady-state response with respect to the ratio of the loading frequency over the eigenfrequency is plotted in Figure 6-6. The bending of the curve indicates the intense nonlinearity of the system. This bending means that jump phenomena are expected to characterise the response of the prototype, multiple response amplitudes dependent on the initial conditions, existence of unstable solutions, while the maximum steady-state amplitude is predicted for frequency ratio larger than 1.

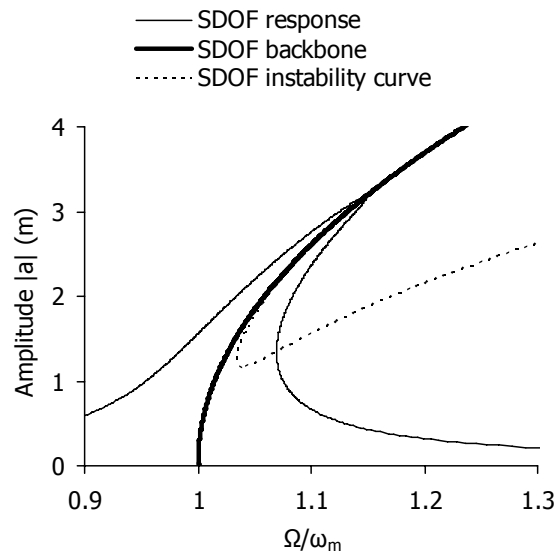


Figure 6-6: Fundamental resonance: response curve of the SDOF model for $\zeta=2\%$ and load amplitude $(P_0)_m=219.7\text{kN}$

6.4.2.5 Superharmonic resonance for damping ratio $\zeta=2\%$

In case of superharmonic resonant conditions, the peak amplitude of the free oscillation term is expressed by Eq. (6-49):

$$a_{\text{peak}} = \frac{16(EA)_m}{M_m L_m^3} \cdot \frac{\Lambda^3}{\zeta \omega_m^2} \Rightarrow \quad (6-79)$$

$$a_{\text{peak}} = \frac{16 \cdot 4211697.6\text{kN}}{25.52\text{kN sec}^2 \text{ m}^{-1} \cdot (100\text{m})^3} \cdot \frac{\Lambda^3}{0.02 \cdot (8.22 \text{ sec}^{-1})^2} = (1.954 \cdot \Lambda^3)(\text{m})$$

Assuming that the maximum steady-state amplitude must not exceed the maximum permissible deflection:

$$a + 2\Lambda = (1.954 \cdot \Lambda^3 + 2\Lambda)(\text{m}) = 3.975\text{m} \quad (6-80)$$

leads to the solution of Λ satisfying Eq. (6-80):

$$\Lambda_0 = \frac{\varepsilon G}{6\varepsilon\alpha} - \frac{4\varepsilon\mu\omega_m}{\varepsilon G} = \frac{\varepsilon G \cdot M_m L_m^3}{6 \cdot 16(EA)_m} - \frac{4\zeta\omega_m^2}{\varepsilon G} \Rightarrow \quad (6-81)$$

$$\Lambda_0 = \frac{20.14 \text{ sec}^{-2} \text{ m}^{-1} \cdot 25.52\text{kN sec}^2 \text{ m}^{-1} \cdot (100\text{m})^3}{6 \cdot 16 \cdot 4211697.6\text{kN}} - \frac{4 \cdot 0.02 \cdot (8.22 \text{ sec}^{-1})^2}{20.14 \text{ sec}^{-2} \text{ m}^{-1}} \Rightarrow$$

$$\Lambda_0 = 1.003\text{m}$$

where:

$$G = \left[\frac{\varepsilon \mu (\varepsilon \alpha)^2}{\varepsilon^3} \omega_m \left(108 w_{\max, m} + 12 \sqrt{\frac{96 \varepsilon \mu \omega_m + 81 \varepsilon \alpha w_{\max, m}^2}{\varepsilon \alpha}} \right) \right]^{1/3} \Rightarrow$$

$$G = \left[\frac{\zeta \omega_m^2}{\varepsilon^3} \left(\frac{16(EA)_m}{M_m L_m^3} \right)^2 \left(108 w_{\max, m} + 12 \sqrt{\frac{96 \zeta \omega_m^2 + 81 \cdot \frac{16(EA)_m}{M_m L_m^3} \cdot w_{\max, m}^2}{\frac{16(EA)_m}{M_m L_m^3}}} \right) \right]^{1/3} \Rightarrow \quad (6-82)$$

$$\varepsilon G = 20.14 \text{ sec}^{-2} \text{ m}^{-1}$$

Considering that the loading frequency is equal to:

$$\Omega = \omega_m / 3 = 8.22 / 3 = 2.74 \text{ sec}^{-1} \quad (6-83)$$

the threshold of the load amplitude can be obtained from Eq. (6-48), taking into account the expression of Eq. (6-81):

$$(P_0)_{m, \text{peak}} = 2M_m \Lambda_0 (\omega_m^2 - \Omega^2) \Rightarrow$$

$$(P_0)_{m, \text{peak}} = 2 \cdot 25.52 \text{ kN sec}^2 \text{ m}^{-1} \cdot 1.003 \text{ m} \cdot \left((8.22 \text{ sec}^{-1})^2 - (2.74 \text{ sec}^{-1})^2 \right) \Rightarrow \quad (6-84)$$

$$(P_0)_{m, \text{peak}} = 3074.70 \text{ kN}$$

which corresponds to load amplitude for the MDOF cable net:

$$(P_0)_{p, \text{peak}} = (P_0)_{m, \text{peak}} \left(\frac{N_m + 1}{N_p + 1} \right)^2 = 3074.70 \text{ kN} \cdot \left(\frac{2}{26} \right)^2 = 18.19 \text{ kN} \quad (6-85)$$

A smaller load amplitude is chosen for the prototype equal to $(P_0)_p = 14 \text{ kN}$, corresponding to a nodal load for the SDOF model, equal to:

$$(P_0)_m = (P_0)_p \left(\frac{N_p + 1}{N_m + 1} \right)^2 = 14 \text{ kN} \cdot \left(\frac{26}{2} \right)^2 = 2366 \text{ kN} \quad (6-86)$$

meaning:

$$\Lambda = \frac{(P_0)_m}{2 \cdot M_m} \left(\frac{1}{\omega_m^2 - \Omega^2} \right) \Rightarrow$$

$$\Lambda = \frac{2366 \text{ kN}}{2 \cdot 25.52 \text{ kN sec}^2 \text{ m}^{-1}} \cdot \frac{1}{(8.22 \text{ sec}^{-1})^2 - (2.74 \text{ sec}^{-1})^2} \Rightarrow \quad (6-87)$$

$$\Lambda = 0.772 \text{ m}$$

The amplitude of the free oscillation term for this nodal load is:

$$a_{\text{peak}} = (1.954 \cdot \Lambda^3) (\text{m}) = 1.954 \text{ m}^{-2} \cdot (0.772 \text{ m})^3 = 0.90 \text{ m} \quad (6-88)$$

occurring for frequency detuning:

$$\begin{aligned}\varepsilon\sigma_{\text{peak}} &= \frac{48(EA)_m}{\omega_m M_m L_m^3} \cdot \Lambda^2 \cdot \left(1 + \frac{1}{8\zeta^2 \omega_m^4} \left(\frac{16(EA)_m}{M_m L_m^3} \right)^2 \cdot \Lambda^4 \right) \Rightarrow \\ \varepsilon\sigma_{\text{peak}} &= \frac{48 \cdot 4211697.6\text{kN}}{8.22 \text{ sec}^{-1} \cdot 25.52\text{kN sec}^2 \text{ m}^{-1} \cdot (100\text{m})^3} \cdot (0.772\text{m})^2 \cdot \\ &\cdot \left(1 + \frac{1}{8 \cdot 0.02^2 \cdot (8.22 \text{ sec}^{-1})^4} \left(\frac{16 \cdot 4211697.6\text{kN}}{25.52\text{kN sec}^2 \text{ m}^{-1} \cdot (100\text{m})^3} \right)^2 \cdot (0.772\text{m})^4 \right) \Rightarrow \\ \varepsilon\sigma_{\text{peak}} &= 0.67 \text{ sec}^{-1}\end{aligned}\quad (6-89)$$

The maximum steady-state amplitude is:

$$w_{\text{max,super,m}} = a + 2\Lambda = (1.954 \cdot \Lambda^3 + 2\Lambda)(\text{m}) = 0.90\text{m} + 2 \cdot 0.772\text{m} = 2.44\text{m} \quad (6-90)$$

The diagram of the steady-state response is defined by Eq. (6-47):

$$\begin{aligned}\varepsilon\sigma &= \frac{48\Lambda^2}{\omega_m} \cdot \frac{(EA)_m}{M_m L_m^3} + \frac{6a^2}{\omega_m} \cdot \frac{(EA)_m}{M_m L_m^3} \pm \sqrt{\frac{\Lambda^6}{\omega_m^2 a^2} \cdot \left(\frac{16(EA)_m}{M_m L_m^3} \right)^2 - (\zeta\omega_m)^2} \Rightarrow \\ \varepsilon\sigma &= \frac{48 \cdot (0.772\text{m})^2}{(8.22 \text{ sec}^{-1})} \cdot \frac{4211697.6\text{kN}}{25.52\text{kN sec}^2 \text{ m}^{-1} \cdot (100\text{m})^3} + \\ &+ \frac{6a^2}{(8.22 \text{ sec}^{-1})} \cdot \frac{4211697.6\text{kN}}{25.52\text{kN sec}^2 \text{ m}^{-1} \cdot (100\text{m})^3} \pm \\ &\pm \sqrt{\frac{(0.772\text{m})^6}{(8.22 \text{ sec}^{-1})^2 a^2} \cdot \left(\frac{16 \cdot 4211697.6\text{kN}}{25.52\text{kN sec}^2 \text{ m}^{-1} \cdot (100\text{m})^3} \right)^2 - [0.02 \cdot (8.22 \text{ sec}^{-1})]^2} \Rightarrow \\ \varepsilon\sigma &= 0.574 \text{ sec}^{-1} + 0.12a^2(\text{sec}^{-1}) \pm \sqrt{\frac{0.022}{a^2}(\text{sec}^{-2}) - 0.027(\text{sec}^{-2})}\end{aligned}\quad (6-91)$$

and the frequency detuning is calculated for a given response amplitude. The total response amplitude is:

$$w_m = a + 2\Lambda \quad (6-92)$$

where Λ this time is calculated as:

$$\begin{aligned}\Lambda &= \frac{(P_0)_m}{2 \cdot M_m} \left(\frac{1}{\omega_m^2 - \Omega^2} \right) \Rightarrow \Lambda = \frac{2366\text{kN}}{2 \cdot 25.52\text{kN sec}^2 \text{ m}^{-1}} \cdot \frac{1}{(8.22 \text{ sec}^{-1})^2 - \Omega^2} \Rightarrow \\ \Lambda &= \frac{46.36\text{m} / \text{sec}^2}{(8.22 \text{ sec}^{-1})^2 - \Omega^2}\end{aligned}\quad (6-93)$$

with

$$\Omega = \frac{\omega_m + \varepsilon\sigma}{3} \quad (6-94)$$

The response diagram is plotted in Figure 6-7.

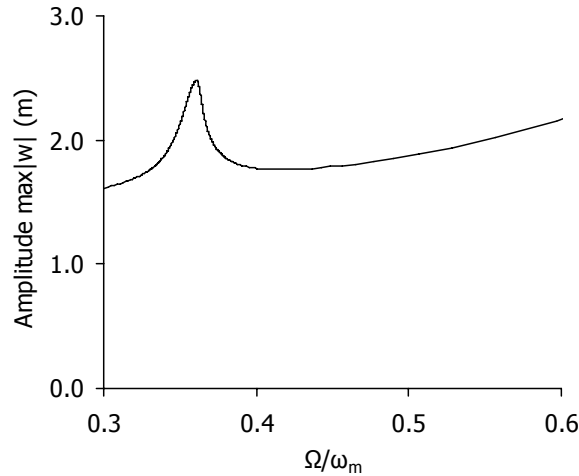


Figure 6-7: Superharmonic resonance: response curve of the SDOF model for $\zeta=2\%$ and load amplitude $(P_0)_m=2366\text{kN}$

6.4.2.6 Subharmonic resonance for damping ratio $\zeta=2\%$

Subharmonic solutions, with non-trivial amplitudes of the free oscillation term, exist only if:

$$\begin{aligned} \varepsilon\sigma &\geq \frac{126\Lambda^2}{\omega_m} \cdot \frac{(EA)_m}{M_m L_m^3} + \frac{M_m L_m^3}{8(EA)_m} \cdot \frac{\zeta^2 \omega_m^3}{\Lambda^2} \Rightarrow \\ \varepsilon\sigma &\geq \frac{126\Lambda^2}{8.22 \text{ sec}^{-1}} \cdot \frac{4211697.6\text{kN}}{25.52\text{kN sec}^2 \text{ m}^{-1} \cdot (100\text{m})^3} + \\ &+ \frac{25.52\text{kN sec}^2 \text{ m}^{-1} \cdot (100\text{m})^3}{8 \cdot 4211697.6\text{kN}} \cdot \frac{0.02^2 \cdot (8.22 \text{ sec}^{-1})^3}{\Lambda^2} \Rightarrow \\ \varepsilon\sigma &\geq 2.53\Lambda^2 (\text{sec}^{-1}) + \frac{0.168}{\Lambda^2} (\text{sec}^{-1}) \end{aligned} \quad (6-95)$$

for a given value of Λ . The load amplitude is calculated from Eq. (6-48):

$$(P_0)_m = 2M_m \Lambda (\omega_m^2 - \Omega^2) = 51.04\text{kN sec}^2 \text{ m}^{-1} \cdot \Lambda \cdot \left[(8.22 \text{ sec}^{-1})^2 - \Omega^2 \right] \quad (6-96)$$

where

$$\Omega = 3\omega_m + \varepsilon\sigma = 24.66\text{sec}^{-1} + \varepsilon\sigma \quad (6-97)$$

for a frequency detuning satisfying inequality (6-95), while the amplitude of the oscillation is obtained by Eq. (6-54):

$$\begin{aligned} a^2 &= \varepsilon\sigma \frac{\omega_m M_m L_m^3}{18(EA)_m} - 6\Lambda^2 \pm \\ &\pm \sqrt{\left(\varepsilon\sigma \frac{\omega_m M_m L_m^3}{18(EA)_m} - 6\Lambda^2 \right)^2 - \frac{\omega_m^2}{324(EA)_m^2} \left[\left(\varepsilon\sigma - \frac{9\Lambda^2}{\omega_m} \cdot \frac{16(EA)_m}{M_m L_m^3} \right)^2 + 9(\zeta\omega_m)^2 \right]} \Rightarrow \\ a^2 &= c \pm \sqrt{c^2 - D \cdot E} \end{aligned} \quad (6-98)$$

where

$$c = \varepsilon\sigma \cdot \frac{8.22 \text{ sec}^{-1} \cdot 25.52 \text{ kN sec}^2 \text{ m}^{-1} \cdot (100 \text{ m})^3}{18 \cdot 4211697.6 \text{ kN}} - 6\Lambda^2 = (2.77\varepsilon\sigma - 6\Lambda^2)(\text{m}^2) \quad (6-99)$$

$$D = \frac{(8.22 \text{ sec}^{-1})^2 \cdot (25.52 \text{ kN sec}^2 \text{ m}^{-1} \cdot (100 \text{ m})^3)^2}{324 \cdot (4211697.6 \text{ kN})^2} = 7.66 \text{ m}^4 \text{ sec}^2 \quad (6-100)$$

$$E = \left(\varepsilon\sigma - \frac{9\Lambda^2}{8.22 \text{ sec}^{-1}} \cdot \frac{16 \cdot 4211697.6 \text{ kN}}{25.52 \text{ kN sec}^2 \text{ m}^{-1} \cdot (100 \text{ m})^3} \right)^2 + 9 \cdot (0.02 \cdot 8.22 \text{ sec}^{-1})^2 \Rightarrow \quad (6-101)$$

$$\Rightarrow E = \left[(\varepsilon\sigma - 2.89\Lambda^2)^2 + 0.24 \right] (\text{sec}^{-2})$$

Thus, Eq. (6-98) becomes:

$$a^2 = (2.77\varepsilon\sigma - 6\Lambda^2)(\text{m}^2) \pm \sqrt{\left[(2.77\varepsilon\sigma - 6\Lambda^2)(\text{m}^2) \right]^2 - 7.66 \cdot \left[(\varepsilon\sigma - 2.89\Lambda^2)^2 + 0.24 \right] (\text{m}^4)} \quad (6-102)$$

Figure 6-8 illustrates the curve that defines the region of the subharmonic solutions, by means of Λ and $(P_0)_m$ with respect to the frequency ratio and to the response amplitude, according to Eq. (6-102). In Figure 6-9 the same charts are plotted for values of load amplitude up to the maximum permissible static one. In Figure 6-10 the response amplitude is plotted with respect to the frequency ratio and the loading amplitude. In Figure 6-11 the response amplitude is again plotted for values up to the maximum permissible one. It is noted that in Figure 6-9a the amplitude Λ is much smaller with respect to the one of the free oscillation term, shown in Figure 6-11a, confirming that subharmonic resonances can suddenly develop vibrations with very large amplitudes leading to catastrophic results. The frequency ratios that could cause subharmonic resonance without cable failure are between 3.18 and 3.70 (Figure 6-11a), resulting in oscillation amplitudes larger than 1.77m (Figure 6-11), while the load amplitude should be larger than 4732kN (Figure 6-9b and Figure 6-11b), corresponding to 28kN for the prototype.

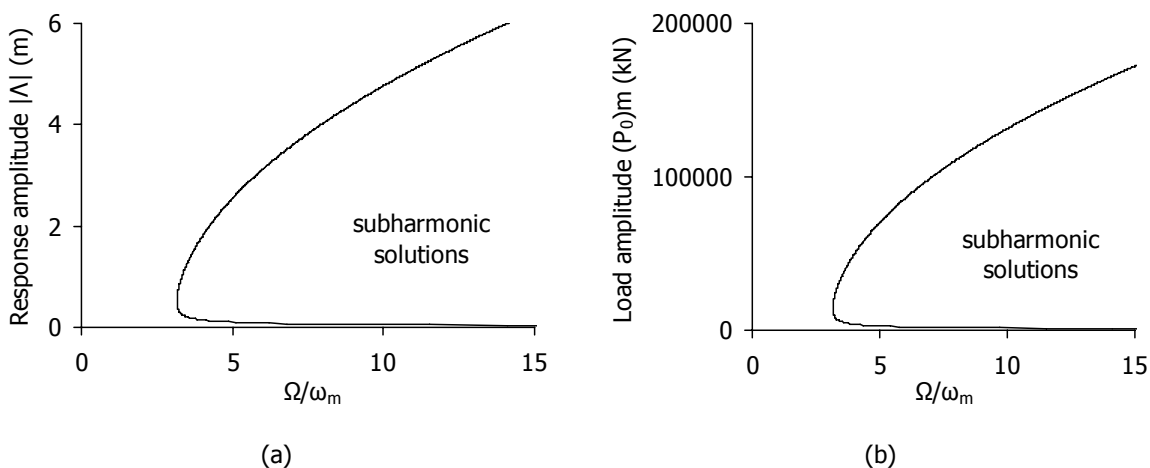


Figure 6-8: Subharmonic resonance of the SDOF model for $\zeta=2\%$: (a) Λ vs. frequency ratio, (b) $(P_0)_m$ vs. frequency ratio

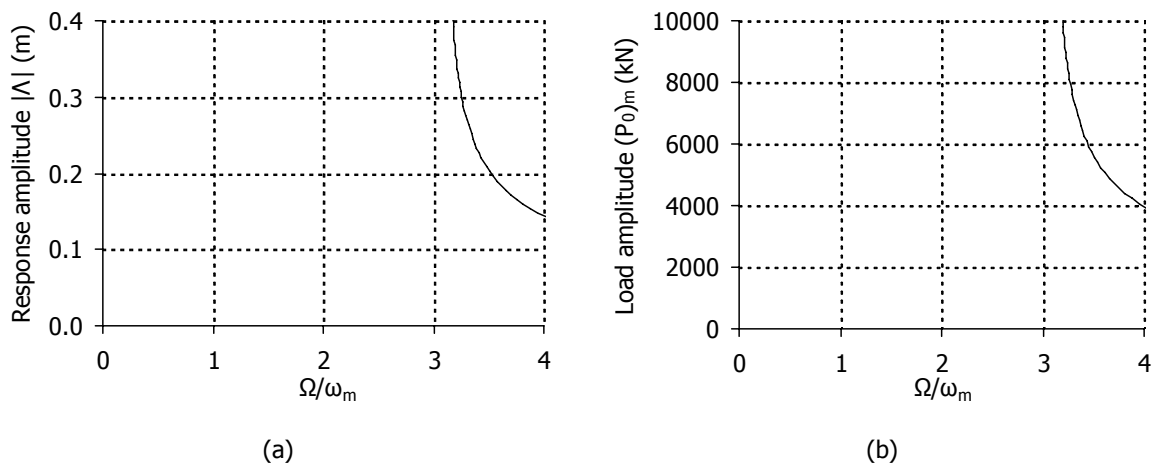


Figure 6-9: Subharmonic resonance of the SDOF model for $\zeta=2\%$ for loads up to the maximum permissible static one: (a) Λ vs. frequency ratio, (b) $(P_0)_m$ vs. frequency ratio

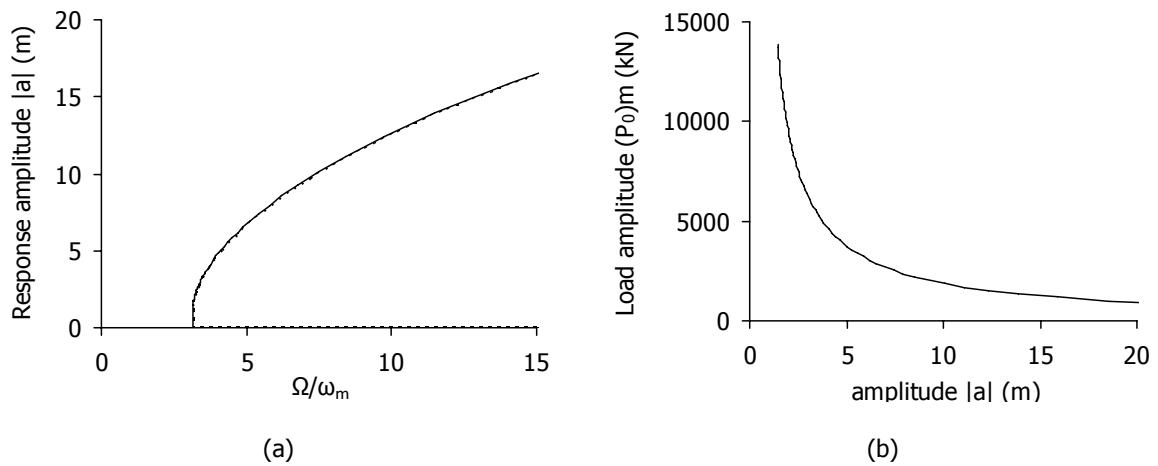


Figure 6-10: Subharmonic resonance of the SDOF model for $\zeta=2\%$: (a) response amplitude vs. frequency ratio, (b) load amplitude $(P_0)_m$ vs. response amplitude

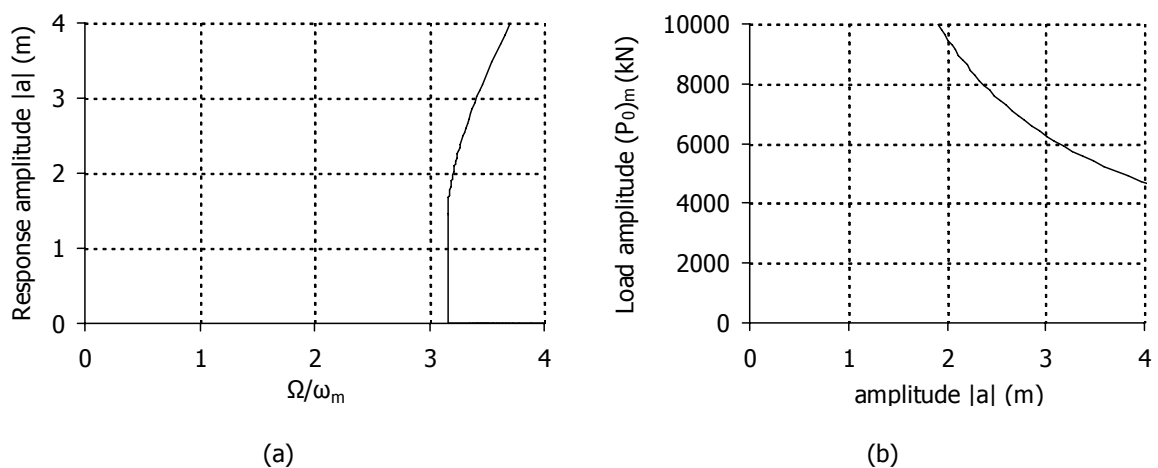


Figure 6-11: Subharmonic resonance of the SDOF model for $\zeta=2\%$ for loads up to the maximum permissible static one: (a) response amplitude vs. frequency ratio, (b) load amplitude $(P_0)_m$ vs. response amplitude

A parametric analysis, changing the load amplitude, the frequency ratio and the initial deflection, keeping the initial velocity of the central node equal to 16m/sec, shows that as the load amplitude

increases, the minimum initial deflection and the frequency ratio that can cause subharmonic resonance decrease (Figure 6-12).

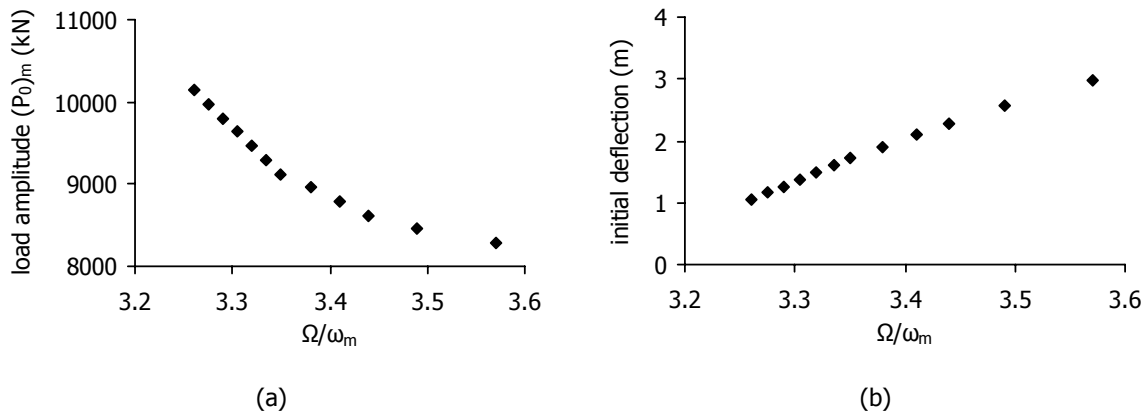


Figure 6-12: Subharmonic resonant conditions for the SDOF model with $\zeta=2\%$: (a) $(P_0)_m$ vs. frequency ratio, (b) initial deflection vs. frequency ratio

If, for example, the load amplitude is equal to $(P_0)_m=10140\text{kN}$, which corresponds to a load amplitude $(P_0)_p=60\text{kN}$ for the MDOF prototype, the minimum initial deflection required in order to have a subharmonic resonance is 1.06m with a loading frequency equal to $\Omega=3.26\omega_m$, assuming an initial velocity equal to 16m/sec . The time-history diagrams of the central node deflection, for these initial conditions and for zero initial conditions, are shown in Figure 6-13.

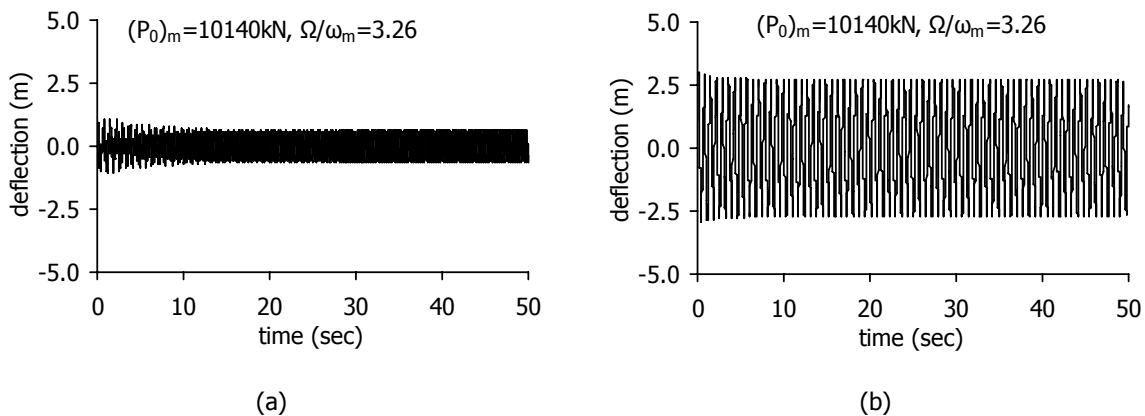


Figure 6-13: Time-history diagrams of the central node deflection for $\Omega/\omega_m=3.26$ and $(P_0)_m=10140\text{kN}$: (a) with zero initial conditions, (b) with initial displacement and velocity

If the load amplitude is equal to $(P_0)_m=9464\text{kN}$, corresponding to 56kN for the MDOF prototype, an initial velocity 16m/sec , a minimum initial deflection 1.49m and a loading frequency $\Omega=3.32\omega_m$ are required for subharmonic resonance. The deflection time-history diagrams, for these initial conditions and for zero initial conditions, are shown in Figure 6-14.

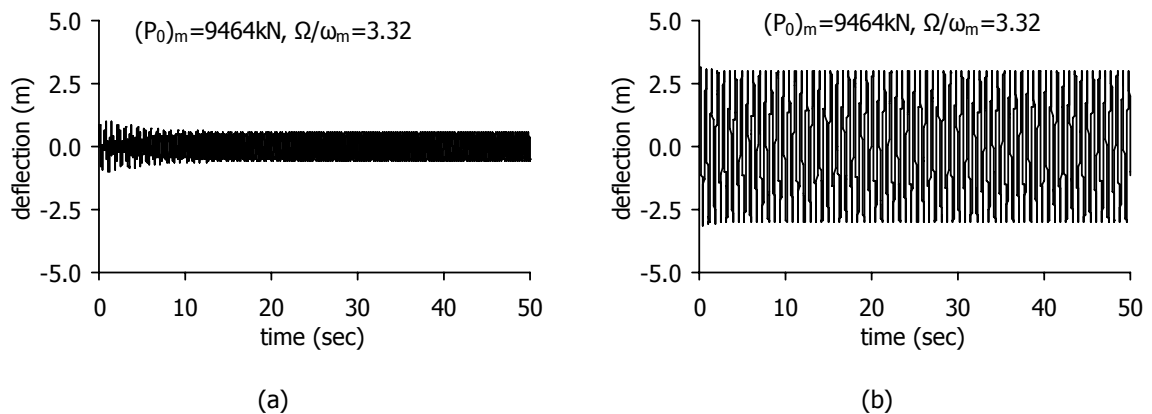


Figure 6-14: Time-history diagrams of the central node deflection for $\Omega/\omega_m=3.32$ and $(P_0)_m=9464\text{kN}$: (a) with zero initial conditions, (b) with initial displacement and velocity

For a load amplitude equal to $(P_0)_m=8619\text{kN}$, corresponding to 51kN for the MDOF prototype, an initial velocity 16m/sec, a minimum initial deflection 2.28m and a loading frequency $\Omega=3.44\omega_m$ constitute the conditions for subharmonic resonance. The time-history diagrams of the central node deflection, for these initial conditions and for zero initial conditions, are shown in Figure 6-15.

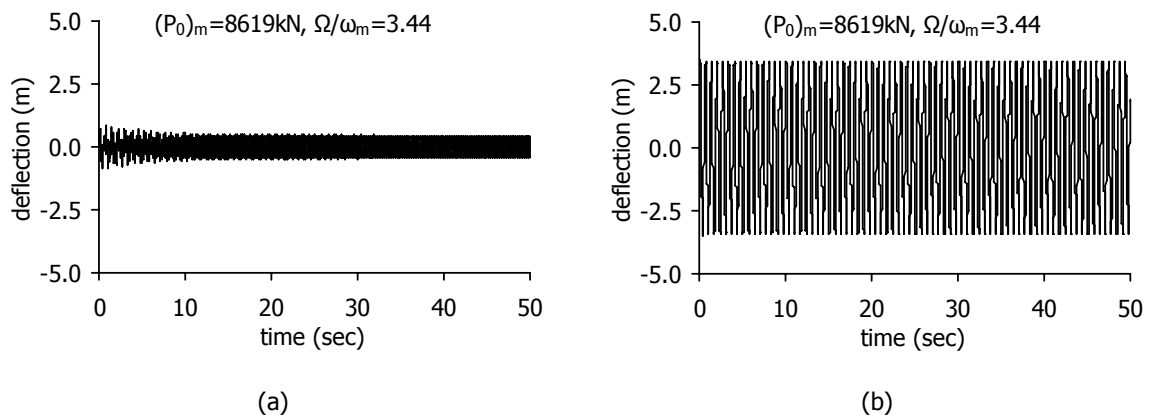


Figure 6-15: Time-history diagrams of the central node deflection for $\Omega/\omega_m=3.44$ and $(P_0)_m=8619\text{kN}$: (a) with zero initial conditions, (b) with initial displacement and velocity

If the load amplitude is equal to $(P_0)_m=8281\text{kN}$, (corresponding to $(P_0)_p=49\text{kN}$), subharmonic resonance occurs for an initial velocity equal to 16m/sec, a minimum initial deflection 2.99m and a loading frequency $\Omega=3.57\omega_m$. The time-history diagrams of the central node deflection, for these initial conditions and for zero initial conditions, are shown in Figure 6-16. In this case, the load amplitude is smaller, the initial deflection required in order to have subharmonic resonant conditions is larger and, during the resonant phenomenon, the dynamic deflection of the central node reaches almost the maximum permissible one.

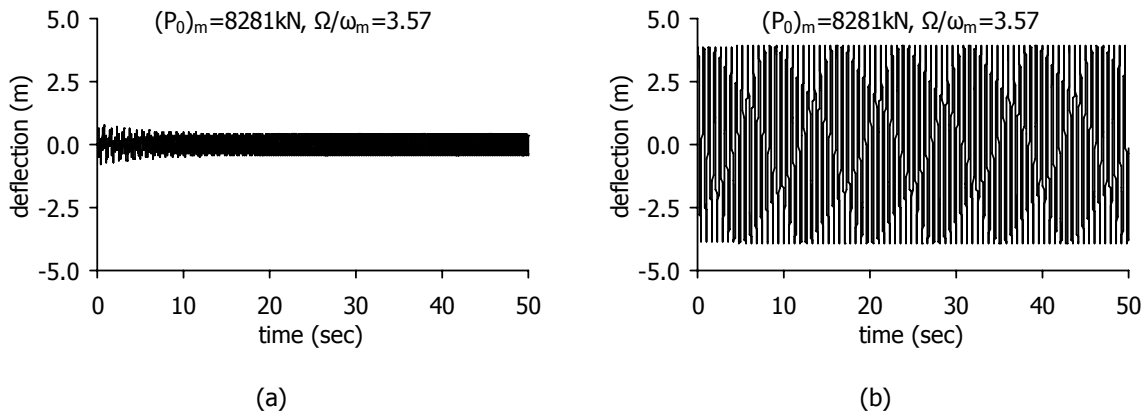


Figure 6-16: Time-history diagrams of the central node deflection for $\Omega/\omega_m=3.57$ and $(P_0)_m=8281\text{kN}$: (a) with zero initial conditions, (b) with initial displacement and velocity

6.4.2.7 Fundamental resonance for damping ratio $\zeta=0.5\%$

Similarly, for damping ratio $\zeta=0.5\%$, the threshold of the load amplitude can be calculated:

$$(P_0)_{m,\text{peak}} \leq 2 \cdot 25.52\text{kNsec}^2 \text{ m}^{-1} \cdot 0.005 \cdot (8.22 \text{sec}^{-1})^2 \cdot 3.975\text{m} = 68.54\text{kN} \quad (6-103)$$

which is much smaller than in the case of damping ratio $\zeta=2\%$. This load corresponds to load amplitude for the MDOF cable net:

$$(P_0)_{p,\text{peak}} = 68.54\text{kN} \cdot \left(\frac{2}{26}\right)^2 = 0.40\text{kN} \quad (6-104)$$

A smaller load amplitude is chosen for the prototype equal to $(P_0)_p=0.31\text{kN}$, corresponding to a nodal load for the SDOF model, equal to:

$$(P_0)_m = 0.31\text{kN} \cdot \left(\frac{26}{2}\right)^2 = 52.39\text{kN} \quad (6-105)$$

For this load amplitude the maximum amplitude of the steady-state response is:

$$a_{\text{peak}} = \frac{52.39\text{kN}}{2 \cdot 25.52\text{kNsec}^2 \text{ m}^{-1} \cdot 0.005 \cdot (8.22 \text{sec}^{-1})^2} = 3.04\text{m} \quad (6-106)$$

and the corresponding value of the detuning $\varepsilon\sigma$:

$$\varepsilon\sigma_{\text{peak}} = \frac{3 \cdot (52.39\text{kN})^2 \cdot 4211697.6\text{kN/m}^2}{2 \cdot (25.52\text{kNsec}^2 \text{ m}^{-1})^3 \cdot 0.005^2 \cdot (8.22 \text{sec}^{-1})^5 \cdot (100\text{m})^3} = 1.11 \text{sec}^{-1} \quad (6-107)$$

almost equal to the one for damping ratio $\zeta=2\%$. Hence, the peak steady-state response amplitude occurs for loading frequency:

$$\Omega = \omega_m + \varepsilon\sigma = 8.22\text{sec}^{-1} + 1.11\text{sec}^{-1} = 9.33\text{sec}^{-1} = 1.14\omega_m \quad (6-108)$$

The response curve is based on Eq. (6-39):

$$\begin{aligned} \varepsilon\sigma &= \frac{6a^2}{8.22 \text{ sec}^{-1}} \cdot \frac{4211697.6 \text{ kN}}{25.52 \text{ kN sec}^2 \text{ m}^{-1} \cdot (100 \text{ m})^3} \pm \\ &\pm \sqrt{\frac{(52.39 \text{ kN})^2}{4 \cdot (25.52 \text{ kN sec}^2 \text{ m}^{-1})^2 (8.22 \text{ sec}^{-1})^2 \cdot a^2} - (0.005 \cdot 8.22 \text{ sec}^{-1})^2} \Rightarrow \\ \varepsilon\sigma &= \left(0.12a^2 \pm \sqrt{\frac{0.016}{a^2} - 0.002} \right) \text{ sec}^{-1} \end{aligned} \quad (6-109)$$

The backbone curve of the system, independent of the damping ratio, remains:

$$\varepsilon\sigma = 0.12a^2 (\text{sec}^{-1}) \quad (6-110)$$

The instability region is now defined by:

$$\begin{aligned} 2B - \sqrt{B^2 - (\zeta\omega_m)^2} < \varepsilon\sigma < 2B + \sqrt{B^2 - (\zeta\omega_m)^2} \Rightarrow \\ 2B - \sqrt{B^2 - (0.005 \cdot 8.22 \text{ sec}^{-1})^2} < \varepsilon\sigma < 2B + \sqrt{B^2 - (0.005 \cdot 8.22 \text{ sec}^{-1})^2} \Rightarrow \\ 2B - \sqrt{B^2 - (0.0411 \text{ sec}^{-1})^2} < \varepsilon\sigma < 2B + \sqrt{B^2 - (0.0411 \text{ sec}^{-1})^2} \end{aligned} \quad (6-111)$$

where B is calculated by Eq. (6-44). The amplitude of the steady-state response with respect to the ratio of the loading frequency over the eigenfrequency is plotted in Figure 6-17. The bending of the curve is the same as in case of $\zeta=2\%$, because the backbone curve, defining this bending, is independent of the damping ratio. In the case of smaller damping ratio, though, the perturbation from the equilibrium state is smaller, meaning that the response curve approaches more the backbone curve, which represents the equilibrium state.

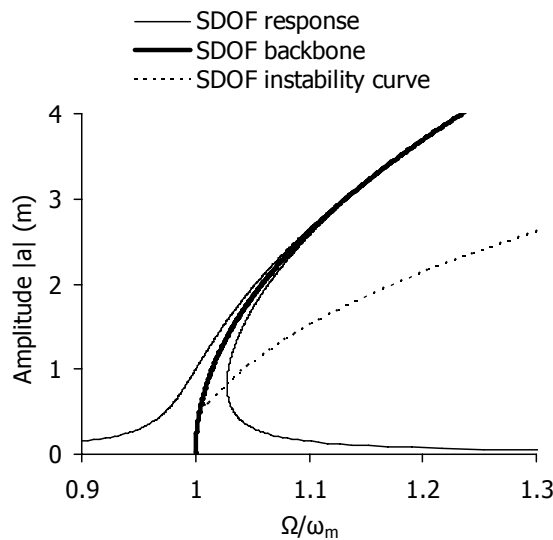


Figure 6-17: Fundamental resonance: response curve of the SDOF model for $\zeta=0.05\%$ and load amplitude $(P_0)_m=52.39 \text{ kN}$

6.4.2.8 Superharmonic resonance for damping ratio $\zeta=0.5\%$

In case of superharmonic resonant conditions, the peak amplitude of the free oscillation term is calculated from Eq. (6-49):

$$a_{\text{peak}} = \frac{16 \cdot 4211697.6\text{kN}}{25.52\text{kN sec}^2 \text{ m}^{-1} \cdot (100\text{m})^3} \cdot \frac{\Lambda^3}{0.005 \cdot (8.22 \text{ sec}^{-1})^2} = (7.82 \cdot \Lambda^3)(\text{m}) \quad (6-112)$$

The value of Λ that causes a deflection equal to the maximum permissible one is:

$$\Lambda_0 = 0.69\text{m} \quad (6-113)$$

and the threshold of the load amplitude can be calculated as:

$$\begin{aligned} (P_0)_{\text{m,peak}} &= 2 \cdot 25.52\text{kN sec}^2 \text{ m}^{-1} \cdot 0.69\text{m} \cdot \left((8.22 \text{ sec}^{-1})^2 - (2.74 \text{ sec}^{-1})^2 \right) \Rightarrow \\ (P_0)_{\text{m,peak}} &= 2115.20\text{kN} \end{aligned} \quad (6-114)$$

which corresponds to load amplitude for the MDOF cable net:

$$(P_0)_{\text{p,peak}} = 2115.20\text{kN} \cdot \left(\frac{2}{26} \right)^2 = 12.52\text{kN} \quad (6-115)$$

A smaller load amplitude is chosen for the prototype equal to $(P_0)_p=10\text{kN}$, corresponding to a nodal load for the SDOF model, equal to:

$$(P_0)_m = 10\text{kN} \cdot \left(\frac{26}{2} \right)^2 = 1690\text{kN} \quad (6-116)$$

meaning:

$$\begin{aligned} \Lambda &= \frac{1690\text{kN}}{2 \cdot 25.52\text{kN sec}^2 \text{ m}^{-1}} \cdot \frac{1}{(8.22 \text{ sec}^{-1})^2 - (2.74 \text{ sec}^{-1})^2} \Rightarrow \\ \Lambda &= 0.552\text{m} \end{aligned} \quad (6-117)$$

The amplitude of the free oscillation term for this nodal load is:

$$a_{\text{peak}} = (7.82 \cdot \Lambda^3)(\text{m}) = 7.82\text{m}^{-2} \cdot (0.552\text{m})^3 = 1.30\text{m} \quad (6-118)$$

occurring for frequency detuning:

$$\begin{aligned} \varepsilon\sigma_{\text{peak}} &= \frac{48 \cdot 4211697.6\text{kN}}{8.22 \text{ sec}^{-1} \cdot 25.52\text{kN sec}^2 \text{ m}^{-1} \cdot (100\text{m})^3} \cdot (0.552\text{m})^2 \cdot \\ &\cdot \left(1 + \frac{1}{8 \cdot 0.005^2 \cdot (8.22 \text{ sec}^{-1})^4} \left(\frac{16 \cdot 4211697.6\text{kN}}{25.52\text{kN sec}^2 \text{ m}^{-1} \cdot (100\text{m})^3} \right)^2 \cdot (0.552\text{m})^4 \right) \Rightarrow \\ \varepsilon\sigma_{\text{peak}} &= 0.50 \text{ sec}^{-1} \end{aligned} \quad (6-119)$$

The maximum steady-state amplitude is:

$$w_{\text{max,super,m}} = a + 2\Lambda = (7.82 \cdot \Lambda^3 + 2\Lambda)(\text{m}) = 1.30\text{m} + 2 \cdot 0.552\text{m} = 2.40\text{m} \quad (6-120)$$

The diagram of the steady-state response is defined as:

$$\begin{aligned}
\varepsilon\sigma &= \frac{48 \cdot (0.552\text{m})^2}{(8.22 \text{sec}^{-1})} \cdot \frac{4211697.6\text{kN}}{25.52\text{kNsec}^2 \text{m}^{-1} \cdot (100\text{m})^3} + \\
&+ \frac{6a^2}{(8.22 \text{sec}^{-1})} \cdot \frac{4211697.6\text{kN}}{25.52\text{kNsec}^2 \text{m}^{-1} \cdot (100\text{m})^3} \pm \\
&\pm \sqrt{\frac{(0.552\text{m})^6}{(8.22 \text{sec}^{-1})^2 a^2} \cdot \left(\frac{16 \cdot 4211697.6\text{kN}}{25.52\text{kNsec}^2 \text{m}^{-1} \cdot (100\text{m})^3}\right)^2 - [0.005 \cdot (8.22 \text{sec}^{-1})]^2} \Rightarrow \\
\varepsilon\sigma &= 0.293 \text{sec}^{-1} + 0.12a^2 (\text{sec}^{-1}) \pm \sqrt{\frac{0.003}{a^2} (\text{sec}^{-2}) - 0.002 (\text{sec}^{-2})}
\end{aligned} \tag{6-121}$$

and the frequency detuning is calculated for a given response amplitude. The total response amplitude is:

$$w_m = a + 2\Lambda \tag{6-122}$$

where Λ this time is:

$$\begin{aligned}
\Lambda &= \frac{1690\text{kN}}{2 \cdot 25.52\text{kNsec}^2 \text{m}^{-1}} \cdot \frac{1}{(8.22 \text{sec}^{-1})^2 - \Omega^2} \Rightarrow \\
\Lambda &= \frac{33.11\text{m/sec}^2}{(8.22 \text{sec}^{-1})^2 - \Omega^2}
\end{aligned} \tag{6-123}$$

with

$$\Omega = \frac{\omega_m + \varepsilon\sigma}{3} \tag{6-124}$$

The response diagram is plotted in Figure 6-18.

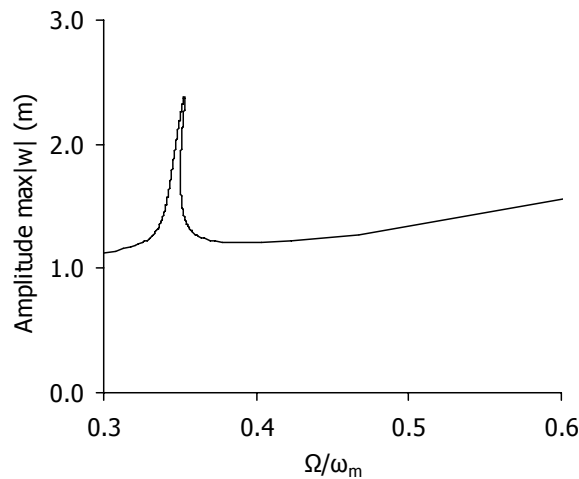


Figure 6-18: Superharmonic resonance: response curve of the SDOF model for $\zeta=0.5\%$ and load amplitude $(P_0)_m=1690\text{kN}$

6.4.2.9 Subharmonic resonance for damping ratio $\zeta=0.5\%$

Subharmonic solutions exist only if:

$$\begin{aligned} \varepsilon\sigma &\geq \frac{126\Lambda^2}{8.22 \text{ sec}^{-1}} \cdot \frac{4211697.6 \text{ kN}}{25.52 \text{ kNsec}^2 \text{ m}^{-1} \cdot (100 \text{ m})^3} + \\ &+ \frac{25.52 \text{ kNsec}^2 \text{ m}^{-1} \cdot (100 \text{ m})^3}{8 \cdot 4211697.6 \text{ kN}} \cdot \frac{0.005^2 \cdot (8.22 \text{ sec}^{-1})^3}{\Lambda^2} \Rightarrow \\ \varepsilon\sigma &\geq 2.53\Lambda^2 (\text{sec}^{-1}) + \frac{0.01}{\Lambda^2} (\text{sec}^{-1}) \end{aligned} \quad (6-125)$$

for a given quantity of Λ . The amplitude of the oscillation is calculated as:

$$a^2 = c \pm \sqrt{c^2 - D \cdot E} \quad (6-126)$$

where c and D are taken from Eqs. (6-99) and (6-100), respectively, and

$$\begin{aligned} E &= \left(\varepsilon\sigma - \frac{9\Lambda^2}{8.22 \text{ sec}^{-1}} \cdot \frac{16 \cdot 4211697.6 \text{ kN}}{25.52 \text{ kNsec}^2 \text{ m}^{-1} \cdot (100 \text{ m})^3} \right)^2 + \\ &+ 9 \cdot (0.005 \cdot 8.22 \text{ sec}^{-1})^2 \Rightarrow \\ \Rightarrow E &= \left[(\varepsilon\sigma - 2.89\Lambda^2)^2 + 0.015 \right] (\text{sec}^{-2}) \end{aligned} \quad (6-127)$$

Thus, Eq. (6-126) becomes:

$$\begin{aligned} a^2 &= (2.77\varepsilon\sigma - 6\Lambda^2)(\text{m}^2) \pm \\ &\pm \sqrt{\left[(2.77\varepsilon\sigma - 6\Lambda^2)(\text{m}^2) \right]^2 - 7.66 \cdot \left[(\varepsilon\sigma - 2.89\Lambda^2)^2 + 0.015 \right] (\text{m}^4)} \end{aligned} \quad (6-128)$$

In Figure 6-19, the curve defining the region of the subharmonic solutions is plotted, by means of Λ and $(P_0)_m$ with respect to the frequency ratio, while in Figure 6-20 the same charts are plotted for values of load amplitude up to the maximum permissible static one. Figure 6-21 shows the response amplitude with respect to the frequency ratio and the loading amplitude, while in Figure 6-22 the same charts are plotted for values of the response amplitude up to the maximum permissible one.

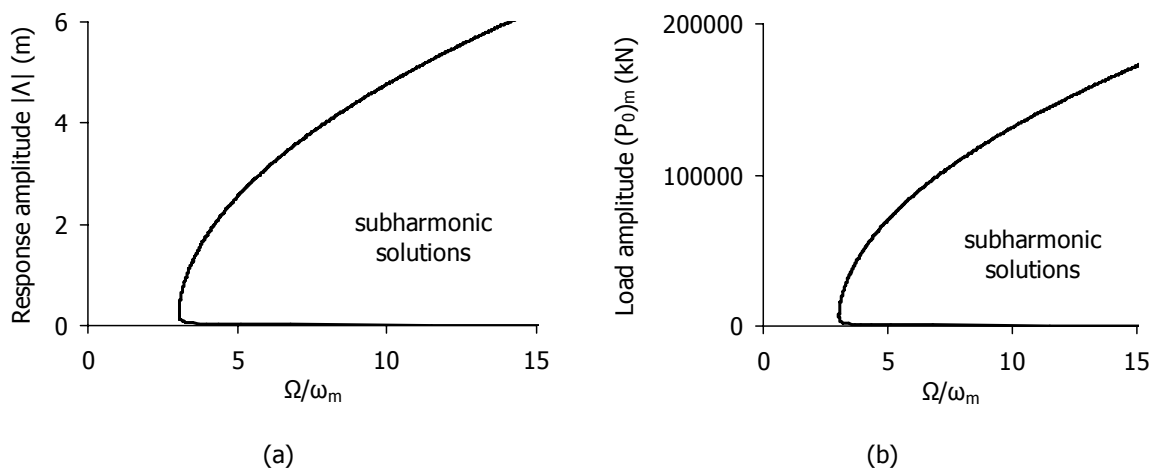


Figure 6-19: Subharmonic resonance of the SDOF model for $\zeta=0.5\%$: (a) Λ vs. frequency ratio, (b) $(P_0)_m$ vs. frequency ratio

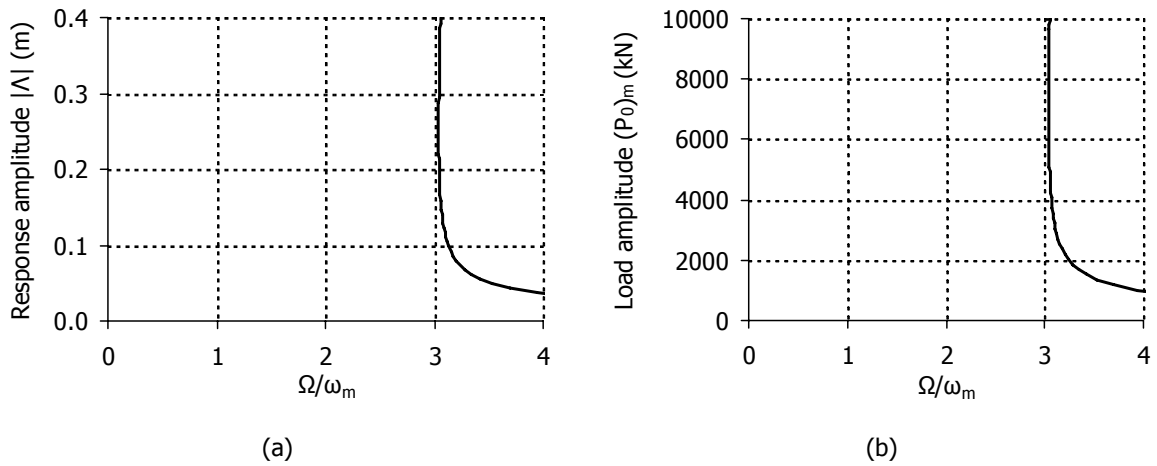


Figure 6-20: Subharmonic resonance of the SDOF model for $\zeta=0.5\%$ for loads up to the maximum permissible static one: (a) Λ vs. frequency ratio, (b) $(P_0)_m$ vs. frequency ratio

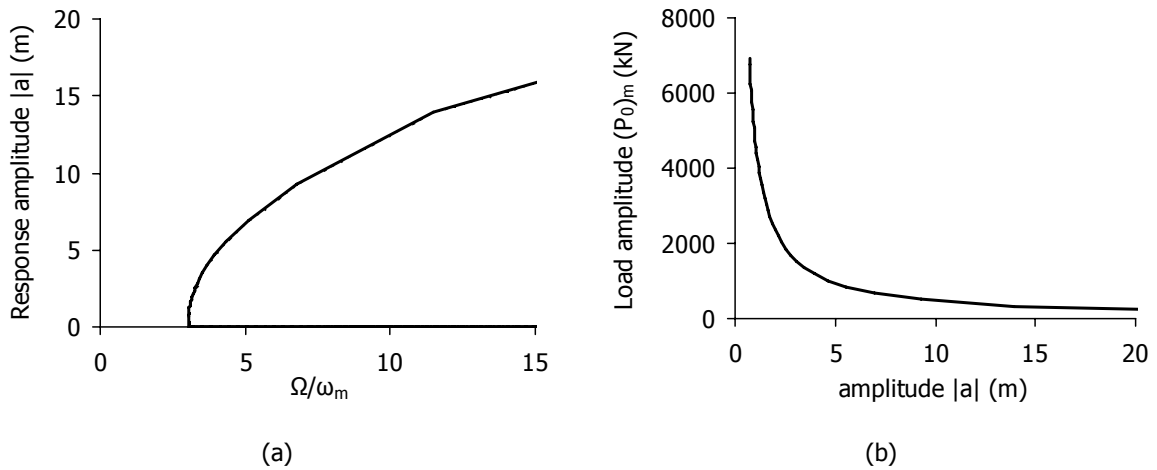


Figure 6-21: Subharmonic resonance of the SDOF model for $\zeta=0.5\%$: (a) response amplitude vs. frequency ratio, (b) load amplitude $(P_0)_m$ vs. response amplitude

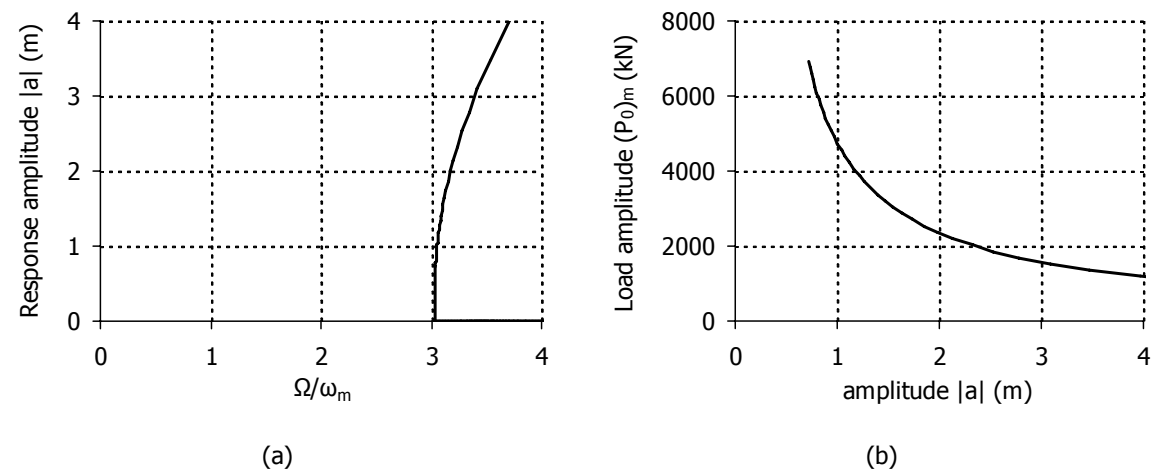


Figure 6-22: Subharmonic resonance of the SDOF model for $\zeta=0.5\%$ for loads up to the maximum permissible static one: (a) response amplitude vs. frequency ratio, (b) load amplitude $(P_0)_m$ vs. response amplitude

For this damping ratio and for an initial deflection smaller than the maximum permissible one equal to $w_{\max,m}=3.975\text{m}$, the load amplitude that can cause a subharmonic resonance must be larger than 1180kN. A load amplitude, almost equal to the maximum permissible for superharmonic resonance, i.e. $(P_0)_m=2500\text{kN}$ and a frequency ratio larger than 3.15, may cause subharmonic resonance. Taking into account initial deflection 1.50m and an initial velocity 25.50m/sec, for $(P_0)_m=2535\text{kN}$, which corresponds to a load for the MDOF system equal to 15kN, the frequency ratio that causes a subharmonic resonance is $\Omega/\omega_m=3.37$, giving an amplitude of steady-state oscillation equal to 2.98m, which is smaller than the maximum permissible one, meaning that no cable tensile failure occurs. For zero initial conditions the steady-state amplitude is only 0.14m (Figure 6-23).

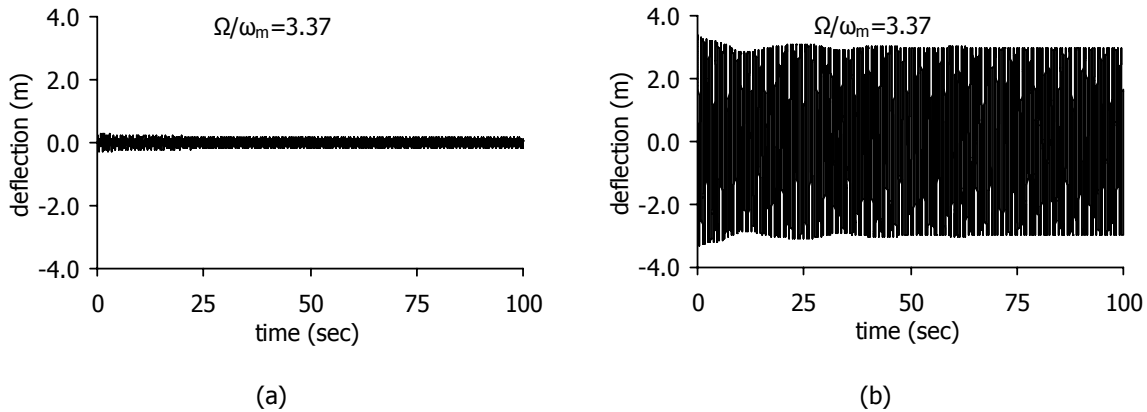


Figure 6-23: Time-history diagrams of the central node deflection for $\Omega/\omega_m=3.37$ and $(P_0)_m=2535\text{kN}$: (a) with zero initial conditions, (b) with initial displacement and velocity

6.4.3 Numerical results for the MDOF prototype

In order to evaluate the accuracy of this method, numerical analyses are conducted to calculate the dynamic response of the MDOF cable net, being the prototype for this example.

6.4.3.1 Static response

The maximum cable tension for the prototype is:

$$N_{\max,p}=A_p\sigma_y=0.00196\text{m}^2\cdot 157000\text{kN/m}^2=3082\text{kN} \quad (6-129)$$

Loading uniformly the structure and conducting a numerical analysis of the MDOF prototype, the load that leads to tensile failure of the cables is calculated equal to $P_{\max}=55.68\text{kN}$, causing also a maximum static deflection at the central node equal to 3.20m. The load-displacement curve for the central node of the net is plotted in Figure 6-24 and the tension distribution at the cables when the load reaches the maximum value, is illustrated in Figure 6-25, where the slackening of the cables is noted. The magnified deformed shape is also shown in Figure 6-25.

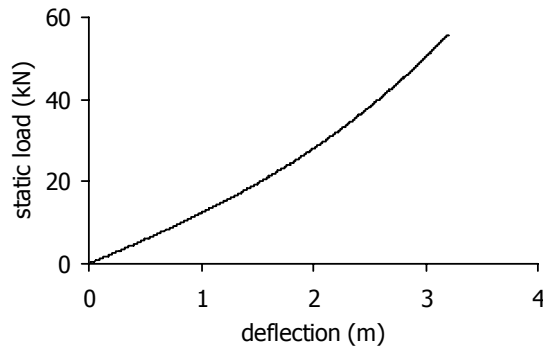


Figure 6-24: Load-displacement diagram for the central node

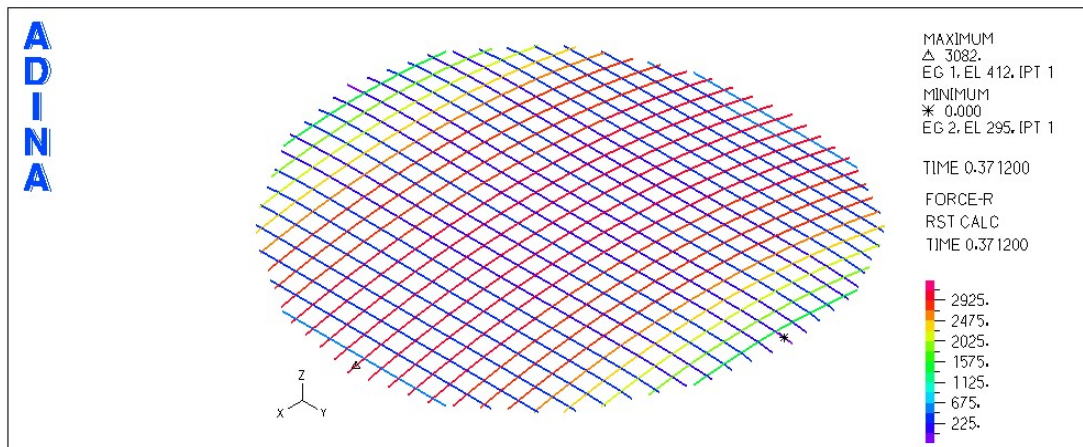


Figure 6-25: Cable tension of the deformed structure

The maximum permissible load for the SDOF model of Eq. (6-66) is transformed to the load for the MDOF prototype according to similarity relation (6-18):

$$P_{\max,p} = P_{\max,m} \left(\frac{N_m + 1}{N_p + 1} \right)^2 = 10939 \text{ kN} \cdot \left(\frac{2}{26} \right)^2 = 64.73 \text{ kN} \quad (6-130)$$

and the maximum permissible deflection of Eq. (6-64), calculated for the model, is transformed to the one for the prototype according to similarity relation (6-26):

$$w_p = w_m = 3.975 \text{ m} \quad (6-131)$$

The permissible load and deflection of the MDOF prototype provided by the method of the equivalent SDOF model is, respectively, 16% and 24% larger than the magnitudes obtained by the numerical simulation. The difference is rather large, because the difference between the model and the prototype, regarding the number of cables is also large. Nevertheless, this method is not used here to calculate with accuracy the maximum deflection and cable tension, but it is proposed to detect the occurrence of nonlinear phenomena.

6.4.3.2 Eigenfrequencies and eigenmodes of the prototype

For this example, the non-dimensional parameter λ^2 is:

$$\lambda^2 = \left(\frac{f}{L}\right)^2 \frac{EA}{N_0} = \left(\frac{1}{35}\right)^2 \frac{165000000\text{kN/m}^2 \cdot 0.00196\text{m}^2}{600\text{kN}} = 0.44 \tag{6-132}$$

which means that the first mode of the system is the symmetric mode with a vertical component having no internal nodes with zero displacements. A modal analysis is performed to calculate the vibration modes and the natural frequencies of the system. The first twelve vibration modes are shown in Figure 6-26, while the symmetric ones among the first 55 vibration modes are shown in Figure 6-27. The first vibration mode is the first symmetric mode (1S) with frequency $\omega_p=9.902\text{sec}^{-1}$.

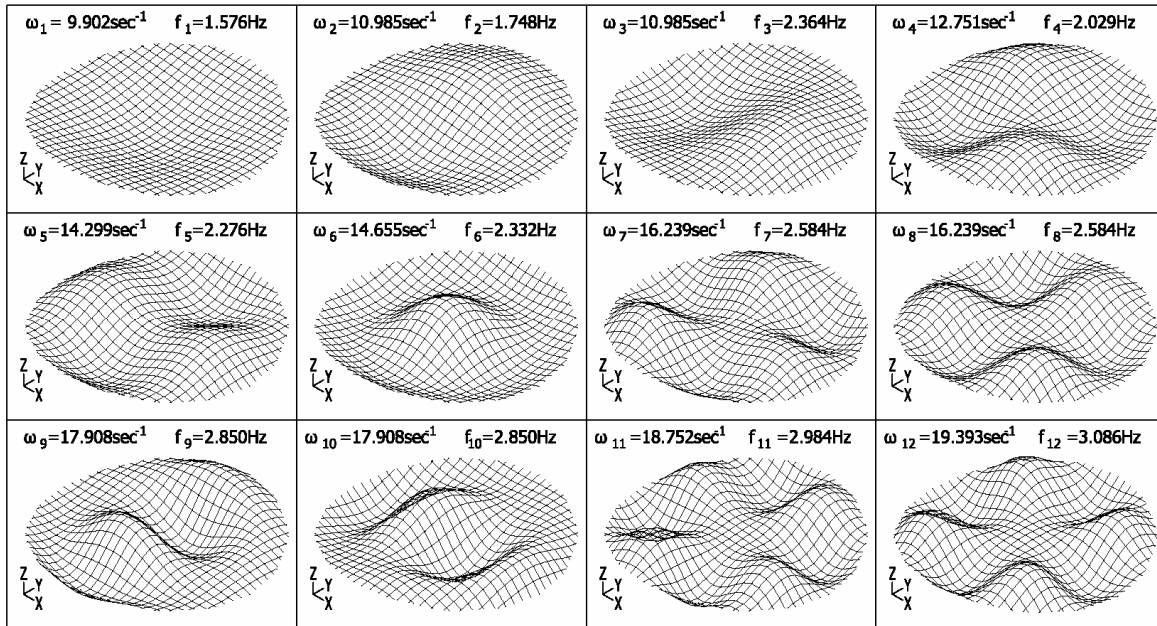


Figure 6-26: The first twelve vibration modes of the prototype

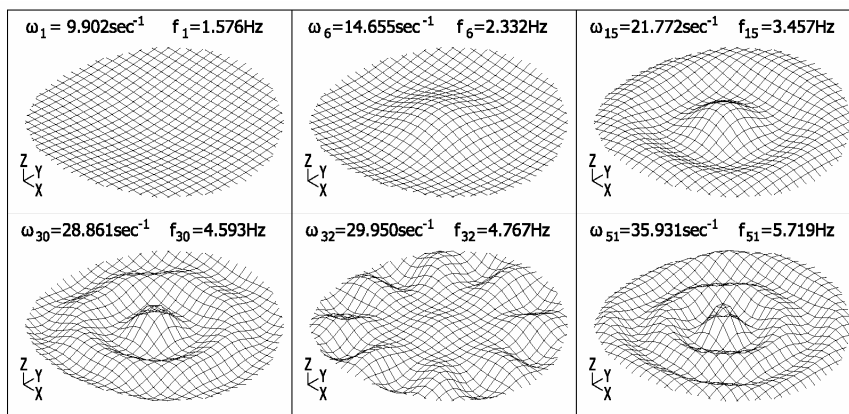


Figure 6-27: Symmetric vibration modes of the prototype

According to similarity relation (6-27) the natural frequency of the model should be equal to the prototype's one. The natural frequency of mode 1S, obtained by the equivalent SDOF model, is 17% smaller than the one calculated by modal analysis of the MDOF system. The difference is considered again as large.

6.4.3.3 Fundamental resonance for damping ratio $\zeta=2\%$

A dynamic load $P_p(t)=(P_0)_p \cos(\Omega t)$ is applied on every node. The load amplitude is chosen in section 6.4.2.4, equal to $(P_0)_p=1.30\text{kN}$. The load frequency varies between $0.90\omega_p$ and $1.30\omega_p$. The damping ratio, according to similarity relation (6-29), is equal to $\zeta_p=\zeta_m=\zeta=2\%$. Considering equal damping ratios for the first four modes, the coefficients for the Rayleigh damping are calculated, taking into consideration the first and the fourth eigenfrequencies, as also explained in chapter 2:

$$\alpha_0 = \frac{2\zeta\omega_1\omega_4}{\omega_1 + \omega_4} = \frac{2 \cdot 0.02 \cdot 9.902 \text{ sec}^{-1} \cdot 12.751 \text{ sec}^{-1}}{9.902 \text{ sec}^{-1} + 12.751 \text{ sec}^{-1}} = 0.22 \text{ sec}^{-1} \quad (6-133)$$

$$\alpha_1 = \frac{2\zeta}{\omega_1 + \omega_4} = \frac{2 \cdot 0.02}{9.902 \text{ sec}^{-1} + 12.751 \text{ sec}^{-1}} = 0.0018 \text{ sec} \quad (6-134)$$

The amplitude of the steady-state response for the central node of the MDOF prototype with respect to the ratio of the loading frequency over the eigenfrequency is plotted in Figure 6-28. In the same diagram the response of the SDOF model of Figure 6-6 is also illustrated for comparison reasons. In this diagram each dot corresponds to the steady-state deflection amplitude of the central node, obtained by one numerical analysis with zero initial conditions. The circles define the steady-state response of one numerical analysis considering initial conditions. It is noted that the equivalent SDOF model can predict with very good accuracy the response of the MDOF system.

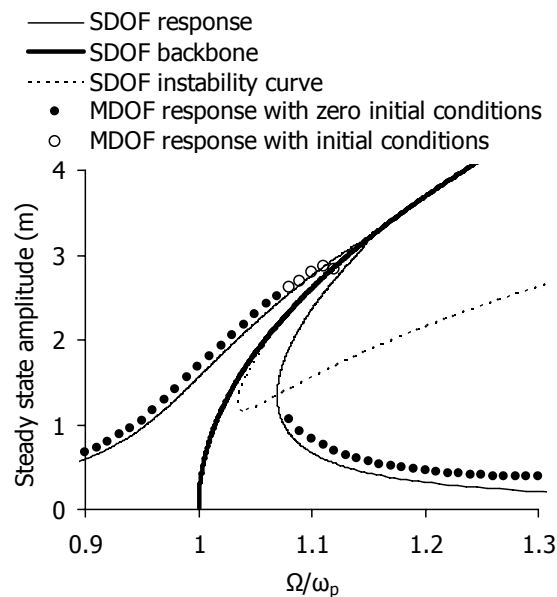


Figure 6-28: Fundamental resonance: response curve of the MDOF prototype for $\zeta=2\%$ and load amplitude $(P_0)_p=1.30\text{kN}$

According to similarity relation (6-25), the nodal dynamic deflection of the prototype should be equal to the one of the model. For frequency ratios between $\Omega/\omega_p=0.90$ and $\Omega/\omega_p=1.10$, the error of the calculation is not more than 10%, which is considered as satisfactory. After the peak amplitude and as the frequency ratio increases, the error increases too, arising at 45% for $\Omega/\omega_p=1.30$. This occurs because the sixth mode of the MDOF system is another symmetric mode, having a frequency $\omega_6=14.655\text{sec}^{-1}=1.48\omega_1=1.48\omega_p$. Thus, as the loading frequency approaches the frequency of this mode, the amplitude increases, leading to a fundamental resonance for the sixth mode. Using the equivalent SDOF model, which has a unique frequency, is not possible to predict this second fundamental resonance.

The bending of the response curve for the MDOF system is obvious from the diagram of Figure 6-28. If zero initial conditions are assumed, when the frequency ratio is $\Omega/\omega_p=1.07$ the steady-state amplitude is 2.52m, while for $\Omega/\omega_p=1.08$, the amplitude drops suddenly to 1.06m, verifying the jump phenomenon. However, if initial conditions are assumed, the amplitude of the steady-state deflection for $\Omega/\omega_p=1.08$ is 2.62m, verifying that the dynamic response of the MDOF prototype depends on the initial conditions. The initial conditions are deformations and velocities with respect to the three global axes, applied on every node, taken from the response of the MDOF system for $\Omega/\omega_p=1.07$ (Figure 6-29).

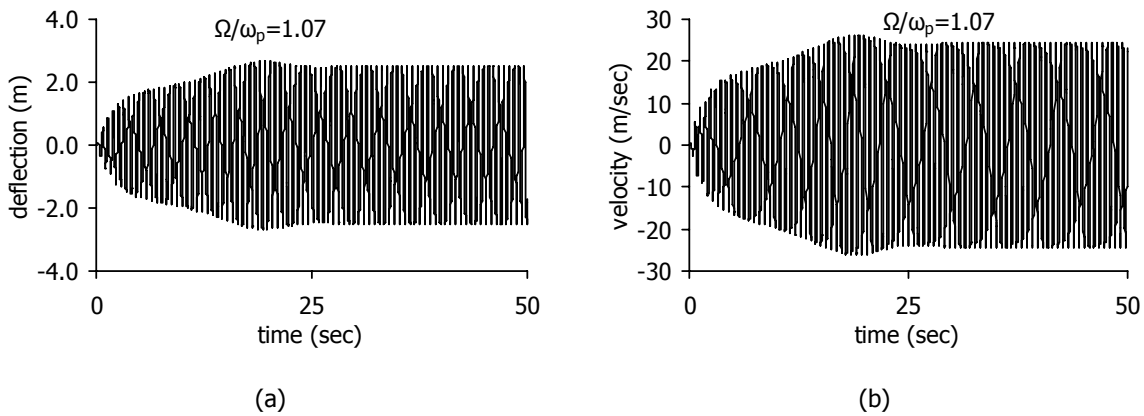


Figure 6-29: Time-history response of the central node for $\Omega/\omega_p=1.07$: (a) deflection diagram and (b) vertical velocity diagram

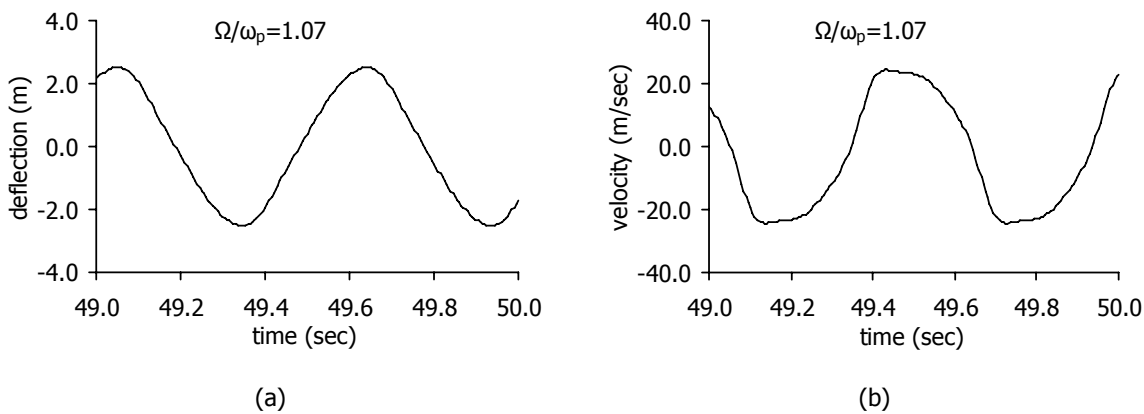
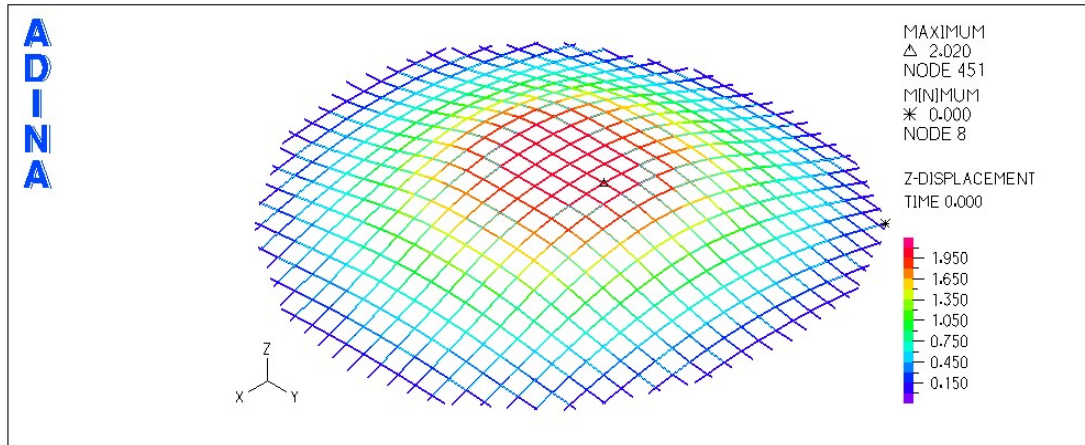
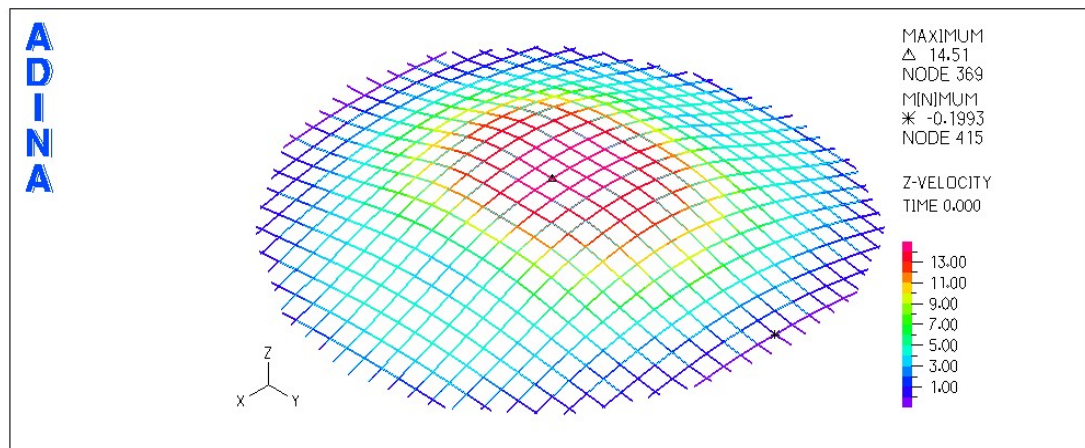
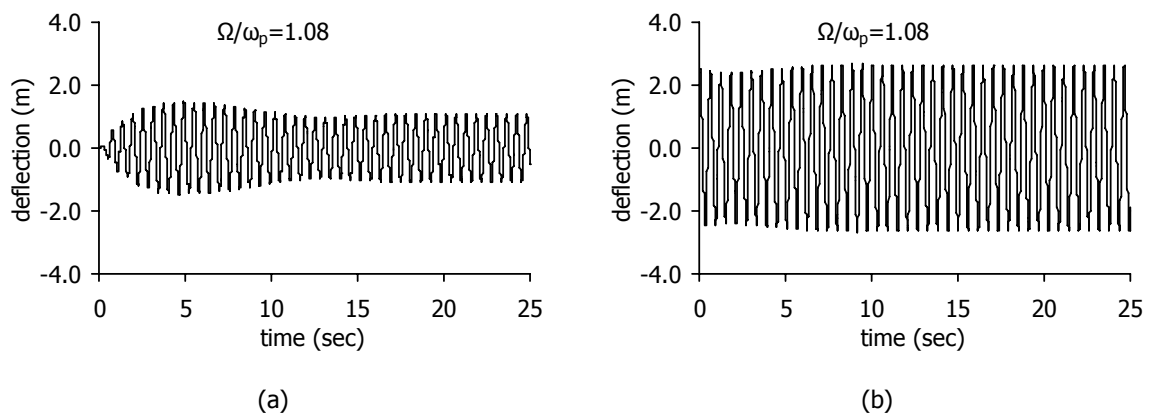


Figure 6-30: Time-history response of the central node for $\Omega/\omega_p=1.07$ at time interval 49sec-50sec: (a) deflection diagram and (b) vertical velocity diagram

At time $t=49.58\text{sec}$, both vertical displacement and velocity are considerable (Figure 6-30), thus the deflection (Figure 6-31) and the velocity (Figure 6-32) at that time are chosen as initial conditions for the next frequency step.

Figure 6-31: Vertical initial deflection for $\Omega/\omega_p=1.08$ Figure 6-32: Vertical initial velocity for $\Omega/\omega_p=1.08$

The time-history diagrams for $\Omega/\omega_p=1.08$, for these two cases of initial conditions, are plotted in Figure 6-33. It is worth mentioning that for $\Omega/\omega_p=1.12$, taking into account initial conditions, the steady-state deflection of the central node for the first 15 seconds is 2.87m, but after $t=20\text{sec}$, it becomes much smaller (Figure 6-34). For larger frequency ratios, the initial conditions do not play an important role in the steady-state response of the system.

Figure 6-33: Time-history diagrams of the central node deflection for $\Omega/\omega_p=1.08$: (a) with zero initial conditions, (b) with initial displacement and velocity

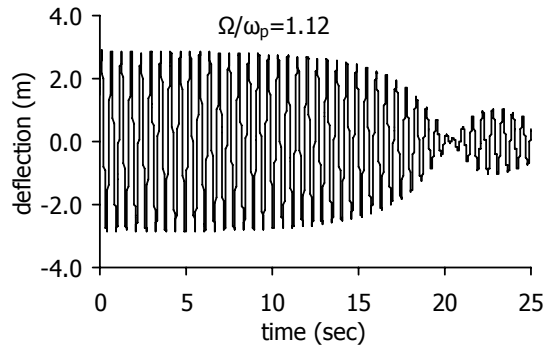


Figure 6-34: Time-history deflection diagram of the central node for $\Omega/\omega_p=1.12$

These phenomena, namely the maximum steady-state amplitude occurring for frequency ratio larger than 1, leading to the bending of the curve, the jump and the multiple response amplitudes dependent on the initial conditions, also verified by the numerical simulation, confirm the intense nonlinearity of the MDOF cable net, which was predicted by the SDOF model. Using the equivalent SDOF model, it is possible to estimate, for specific load amplitudes, the frequency ratio for which the maximum dynamic response of the MDOF system is expected.

6.4.3.4 Superharmonic resonance for damping ratio $\zeta=2\%$

In case of superharmonic resonance the load amplitude for the MDOF prototype is chosen in section 6.4.2.5, equal to $(P_0)_p=14\text{kN}$. The load frequency varies between $0.30\omega_p$ and $0.60\omega_p$. The amplitude of the steady-state response for the central node of the MDOF prototype with respect to the frequency ratio, and the response of the equivalent SDOF model of Figure 6-7, are plotted together in Figure 6-35. The steady-state amplitudes, estimated by the method of the SDOF model, are between 25% and 48% larger than the ones obtained by numerical analysis. This estimation cannot be considered as satisfactory.

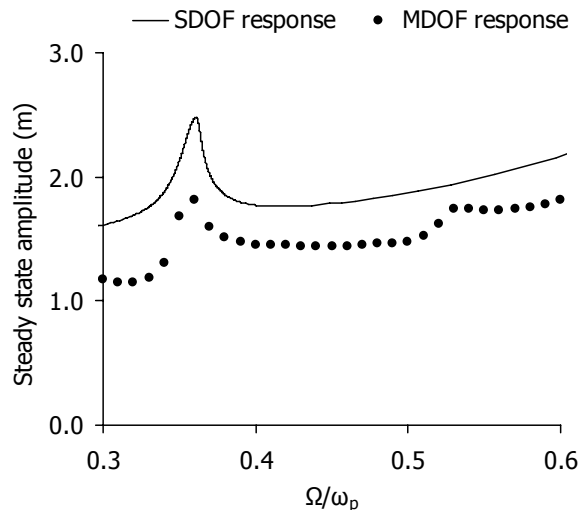


Figure 6-35: Superharmonic resonance: response curve of the MDOF prototype for $\zeta=2\%$ and load amplitude $(P_0)_p=14\text{kN}$

On the other hand, the peak amplitude for frequency ratio $\Omega/\omega_p=0.36$, predicted by the equivalent SDOF model, is verified for the prototype, confirming the occurrence of the order-three superharmonic resonance for the first symmetric mode. In Figure 6-36 the response of the central node is depicted by means of time-history diagrams and response spectra, verifying this nonlinear resonance. The

steady-state response, obtained after 20sec, is an oscillation of at least two different frequencies. This is also illustrated in the response spectrum, where two peaks are noted for frequencies 0.56Hz (3.52sec^{-1}), which is close to the loading frequency ($\Omega=0.36\cdot\omega_p=3.56\text{sec}^{-1}$) and 1.68Hz (10.56sec^{-1}), which is almost equal to the frequency of the first symmetric mode ($\omega_1=\omega_{15}=\omega_p=9.902\text{sec}^{-1}$). However, in Figure 6-35, a second peak of the amplitude is observed for frequency ratio $\Omega/\omega_p=0.53$ for the MDOF system, corresponding to an order-two superharmonic resonance for the same mode. In this case, the loading frequency is $\Omega=0.53\cdot\omega_p=5.525\text{sec}^{-1}=0.36\omega_6$, where ω_6 is the frequency of the sixth mode equal to $\omega_6=14.655\text{sec}^{-1}$. Hence, this second peak indicates also an order-three superharmonic resonance for the sixth mode being the second symmetric mode of the system.

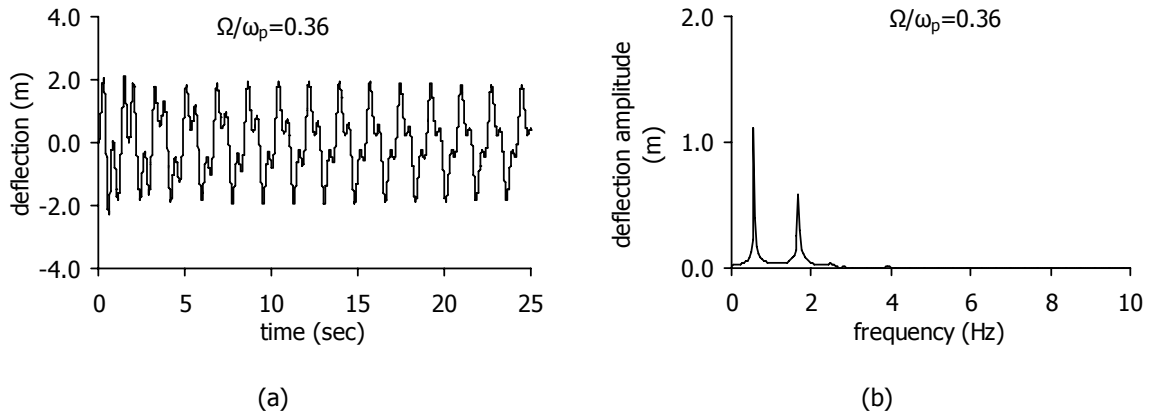


Figure 6-36: Response diagrams of the central node deflection for $\Omega/\omega_p=0.36$: (a) time-history diagram, b) response spectrum

In Figure 6-37a, the time-history diagram of the central node deflection is plotted. In Figure 6-37b, the response spectrum of the central node deflection illustrates that the oscillation of the central node is characterised by three frequencies: at 0.84Hz (5.28sec^{-1}), which is close to the loading frequency ($\Omega=0.53\cdot\omega_p=5.25\text{sec}^{-1}$), at 1.72Hz (10.81sec^{-1}), being close to the frequency of the first symmetric mode ($\omega_1=\omega_{15}=\omega_p=9.902\text{sec}^{-1}$) and at 2.52Hz (15.83sec^{-1}), which is close to the frequency of the second symmetric mode ($\omega_6=14.655\text{sec}^{-1}$).

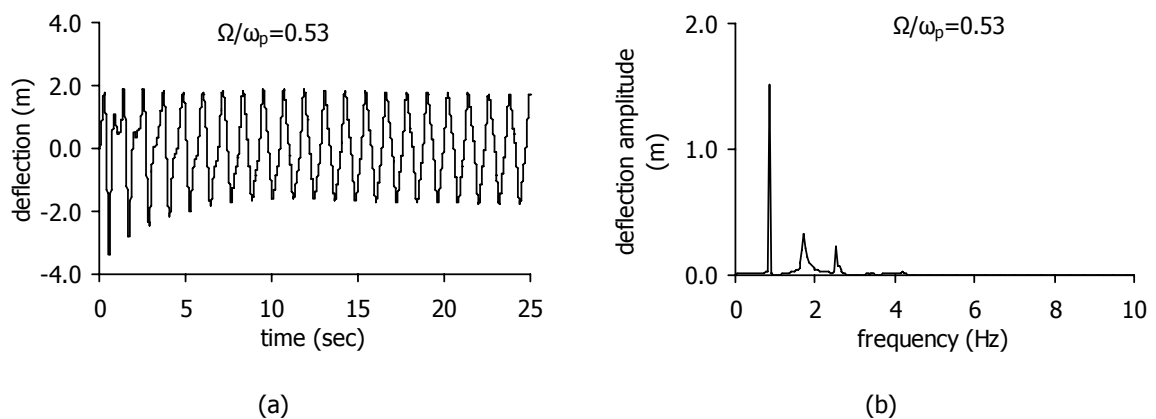


Figure 6-37: Response diagrams of the central node deflection for $\Omega/\omega_p=0.53$: (a) time-history diagram, b) response spectrum

Thus, both modes are activated and the occurrence of the order-three superharmonic resonance and order-two for the first and the second symmetric mode, respectively, is verified. With the equivalent SDOF model having only one frequency, it is not possible to predict this second superharmonic

resonance for the mode of higher order. In addition, the SDOF model, having only a cubic nonlinear term, cannot detect order-two superharmonic resonances.

6.4.3.5 Subharmonic resonance for damping ratio $\zeta=2\%$

Based on the parametric analysis of section 6.4.2.6, a load amplitude equal to $(P_0)_p=51\text{kN}$ applied on every node, with a load frequency equal to $\Omega=3.44\omega_p$ and initial conditions that correspond to an initial deflection of the central node 2.28m and initial velocity of the same node 16m/sec, should cause subharmonic resonance. In order to apply the initial conditions the diagram of Figure 6-31 is scaled so that the deflection of the central node is 2.28m, while the one of Figure 6-32 is magnified so that the central node velocity results in 16m/sec. Conducting a numerical analysis for the prototype, before the first cycle of the oscillation concludes, the nodal deflection reaches the maximum permissible one, causing cable tensile failure. The same also occurs for load amplitude $(P_0)_p=56\text{kN}$, loading frequency $\Omega=3.32\omega_p$ and initial conditions, corresponding to a deflection and velocity for the central node, 1.48m and 16m/sec, respectively (Figure 6-38). For smaller load amplitudes, larger initial deflection is required, and for smaller initial deflection, only larger load amplitude can cause subharmonic resonance. Both cases lead to cable tensile failure. Thus, for this cable net, with damping ratio 2%, it is impossible for the subharmonic resonance to evolve, because the large load amplitude and the large initial conditions required for such a resonance, cause cable tensile failure as soon as the vibration starts.

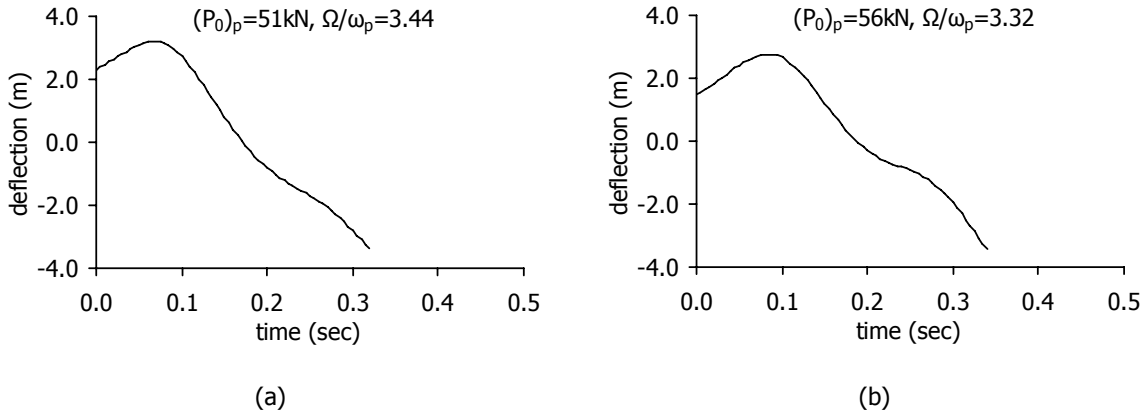


Figure 6-38: Time-history response of the central node for: (a) $(P_0)_p=51\text{kN}$ and $\Omega/\omega_p=3.44$, (b) $(P_0)_p=56\text{kN}$ and $\Omega/\omega_p=3.32$

6.4.3.6 Fundamental resonance for damping ratio $\zeta=0.5\%$

For damping ratio $\zeta=0.5\%$, the load amplitude is chosen in section 6.4.2.7, equal to $(P_0)_p=0.31\text{kN}$. The load frequency varies again between $0.90\omega_p$ and $1.40\omega_p$. The coefficients for the Rayleigh damping are calculated, taking into consideration the first and the fourth eigenfrequencies:

$$\alpha_0 = \frac{2\zeta\omega_1\omega_4}{\omega_1 + \omega_4} = \frac{2 \cdot 0.005 \cdot 9.902 \text{ sec}^{-1} \cdot 12.751 \text{ sec}^{-1}}{9.902 \text{ sec}^{-1} + 12.751 \text{ sec}^{-1}} = 0.0557 \text{ sec}^{-1} \quad (6-135)$$

$$\alpha_1 = \frac{2\zeta}{\omega_1 + \omega_4} = \frac{2 \cdot 0.005}{9.902 \text{ sec}^{-1} + 12.751 \text{ sec}^{-1}} = 0.0018 \text{ sec} \quad (6-136)$$

The amplitude of the steady-state response for the central node of the MDOF prototype with respect to the ratio of the loading frequency over the eigenfrequency is plotted in Figure 6-39, along with the response diagram of the SDOF model of Figure 6-17. In this case the error of the estimated response

amplitude, based on the method of the equivalent SDOF model, is approximately 10%, which is considered as satisfactory. In addition, the instability region, the jump phenomenon, the double response dependent on the initial conditions and the frequency ratio for which the maximum steady-state response occurs are predicted by the SDOF model. The diagram is narrower than the one for damping ratio $\zeta=2\%$, approaching the backbone curve. As a consequence, the existence of the sixth mode will increase the steady-state amplitude of the response for frequency ratios near $\Omega/\omega_p=1.48$, causing a divergence between the results of the equivalent model with the ones obtained numerically, due to the fundamental resonance for this second symmetric mode. But for values up to $\Omega/\omega_p=1.30$, this mode does not influence the response curve, resulting in very good agreement between the analytical solution for the SDOF model and the numerical one for the MDOF prototype. For frequency ratios between $\Omega/\omega_p=1.04$ and $\Omega/\omega_p=1.06$, two response amplitudes are obtained, depending on the initial conditions.

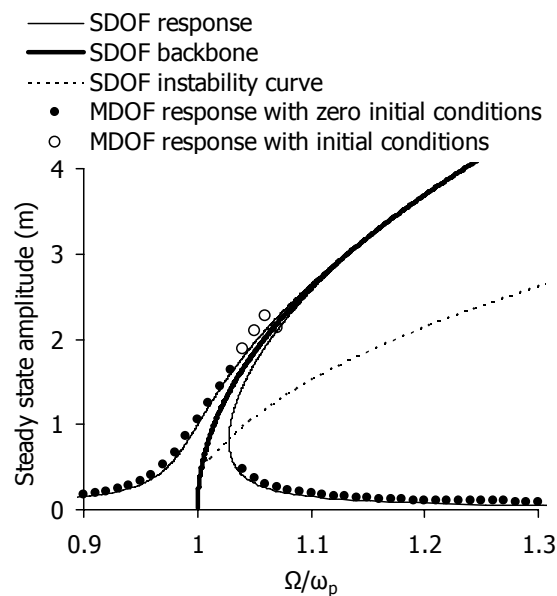


Figure 6-39: Fundamental resonance: response curve of the MDOF prototype for $\zeta=0.5\%$ and load amplitude $(P_0)_p=0.31\text{kN}$

The deflection distribution at the nodes considered as initial condition is shown in Figure 6-40, while the vertical initial velocity distribution, in Figure 6-41. The time-history diagrams of the response for $\Omega/\omega_p=1.04$, taking into account initial conditions or not, are plotted in Figure 6-42.

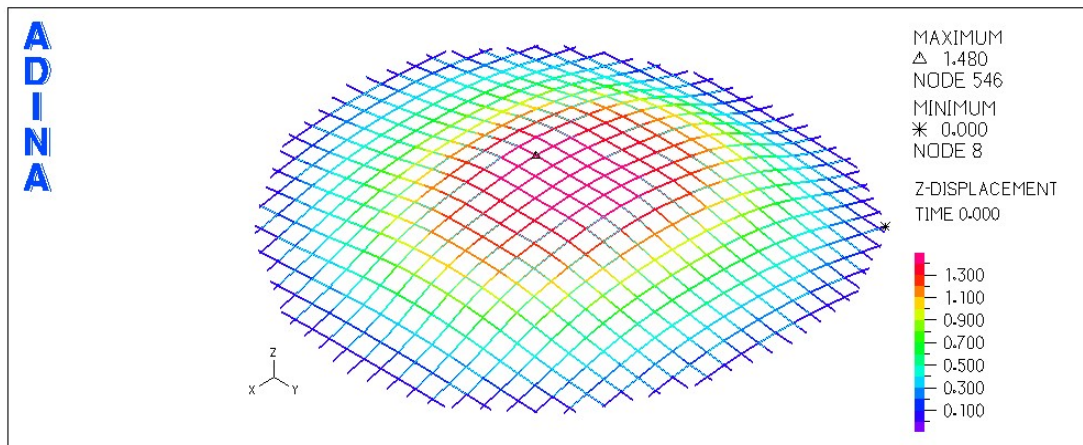


Figure 6-40: Vertical initial deflection for $\Omega/\omega_p=1.04$

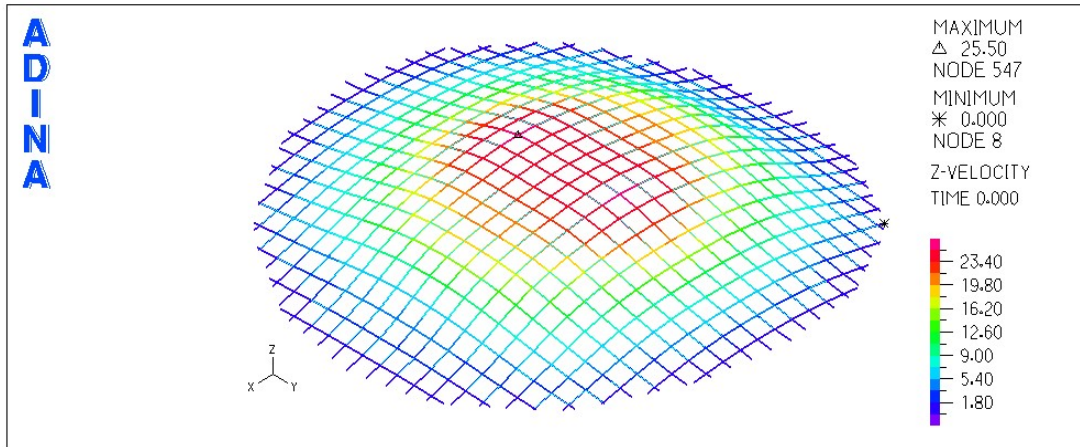


Figure 6-41: Vertical initial velocity for $\Omega/\omega_p=1.04$

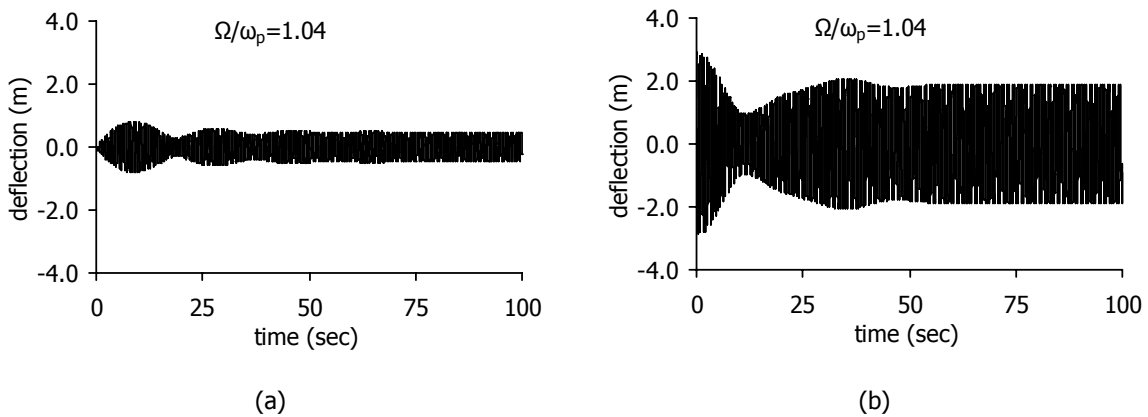


Figure 6-42: Time-history diagrams of the central node deflection for $\Omega/\omega_p=1.04$: (a) with zero initial conditions, (b) with initial displacement and velocity

For $\Omega/\omega_p=1.07$, taking into consideration initial conditions, the steady-state deflection of the central node for the first 20sec is 2.13m, but then it drops with beat phenomenon until the steady-state amplitude corresponding to zero initial conditions is reached (Figure 6-43). For frequency ratios larger than $\Omega/\omega_p=1.07$, the initial conditions do not influence the steady-state response of the system.

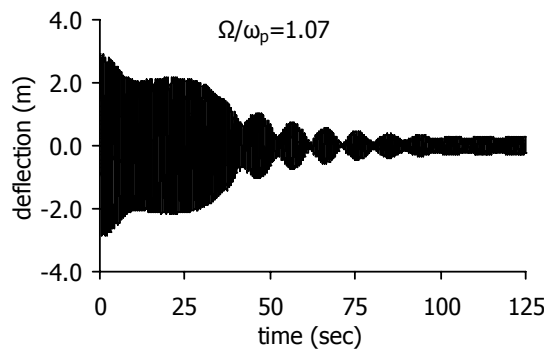


Figure 6-43: Time-history deflection diagram of the central node for $\Omega/\omega_p=1.07$

6.4.3.7 Superharmonic resonance for damping ratio $\zeta=0.5\%$

For superharmonic resonant conditions, the load amplitude for the MDOF prototype is chosen in section 6.4.2.8, equal to $(P_0)_p=10\text{kN}$. The amplitude of the steady-state response for the central node

of the MDOF prototype with respect to the frequency ratio, varying between $0.30\omega_p$ and $0.60\omega_p$, and the response of the equivalent SDOF model of Figure 6-18, are plotted together in Figure 6-44. The estimation of the steady-state amplitudes by the method of the SDOF model, is again non satisfactory, being 16%-45% larger than the ones obtained by numerical analysis. Two peaks of the steady-state amplitude are noted for the prototype. The first one occurs for frequency ratio $\Omega/\omega_p=0.35$, as predicted by the equivalent SDOF model, confirming the order-three superharmonic resonance for mode 1S. In Figure 6-45 the deflection time-history and response spectrum are plotted, verifying the phenomenon of this nonlinear resonance. In the second chart, two peaks are noted for frequencies 0.55Hz (3.45sec^{-1}), which is almost equal to the loading frequency ($\Omega=0.35\cdot\omega_p=3.47\text{sec}^{-1}$) and 1.66Hz (10.43sec^{-1}), which is close to the frequency of mode 1S ($\omega_{1S}=\omega_p=9.902\text{sec}^{-1}$).

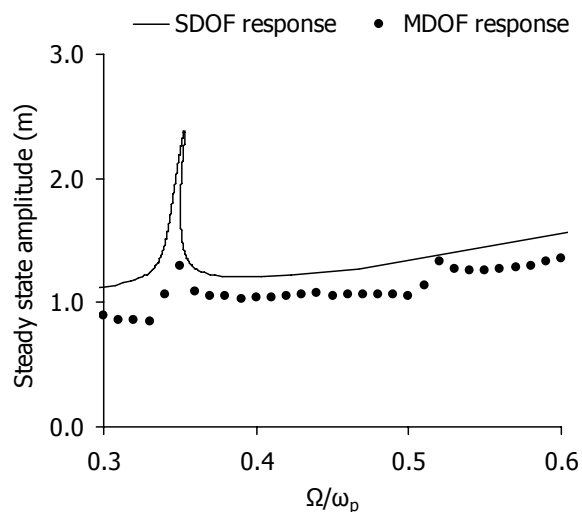


Figure 6-44: Superharmonic resonance: response curve of the MDOF prototype for $\zeta=0.5\%$ and load amplitude $(P_0)_p=10\text{kN}$

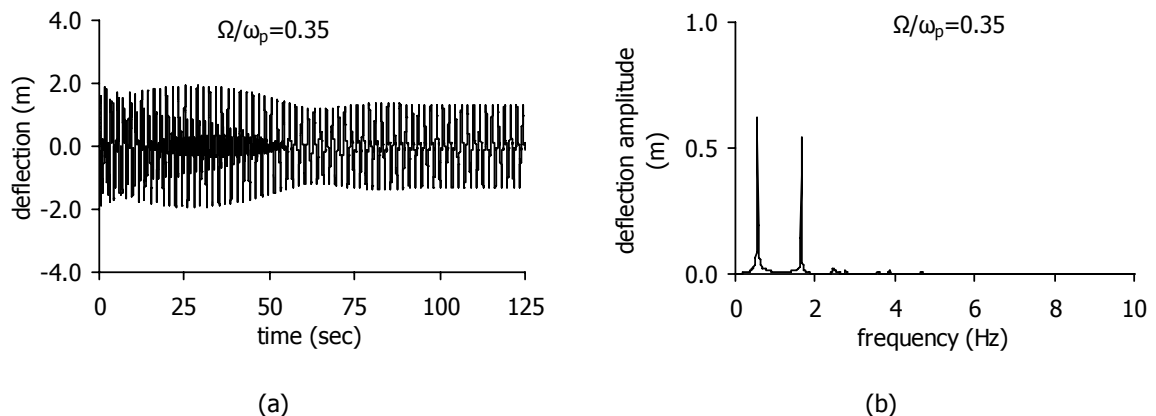


Figure 6-45: Response diagrams of the central node deflection for $\Omega/\omega_p=0.35$: (a) time-history diagram, (b) response spectrum

The second peak of the steady-state amplitude is observed for $\Omega/\omega_p=0.52$, corresponding to order-two superharmonic resonance for mode 1S and an order-three superharmonic resonance for the sixth mode, verified also by the charts of Figure 6-46, which present the time-history diagram and the response spectrum of the central node deflection. In the second chart three frequencies of the oscillation are noted: at 0.82Hz (5.15sec^{-1}), which is equal to the loading frequency ($\Omega=0.52\cdot\omega_p=5.15\text{sec}^{-1}$), at 1.66Hz (10.43sec^{-1}), being close to the frequency of the first symmetric mode ($\omega_1=\omega_{1S}=\omega_p=9.902\text{sec}^{-1}$) and at 2.47Hz (15.52sec^{-1}), which is close to the frequency of the

sixth mode ($\omega_6=14.655\text{sec}^{-1}$). None of these two nonlinear resonances can be predicted by the method of the equivalent SDOF model.

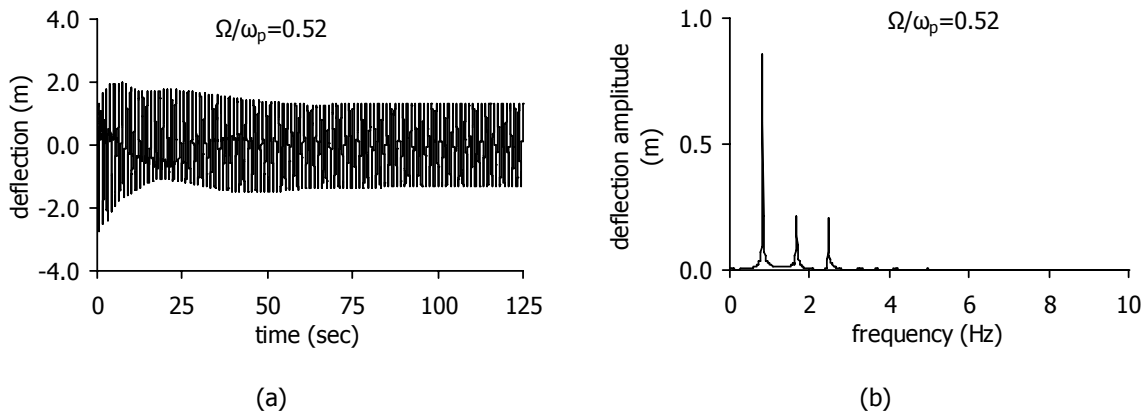


Figure 6-46: Response diagrams of the central node deflection for $\Omega/\omega_p=0.52$: (a) time-history diagram, b) response spectrum

6.4.3.8 Subharmonic resonance for damping ratio $\zeta=0.5\%$

In order to detect subharmonic resonance, the conditions of section 6.4.2.9 are adopted. Thus, the load amplitude takes the value $(P_0)_p=15\text{kN}$, while the frequency ratio is $\Omega/\omega_p=3.37$. The time-history diagram of the central node deflection for zero initial conditions is shown in Figure 6-47a, while in Figure 6-47a the diagram of the central node motion is plotted, taking into account the initial deflection shown in Figure 6-40 and the initial velocity illustrated in Figure 6-41, which are close to the corresponding ones, assumed in section 6.4.2.9.

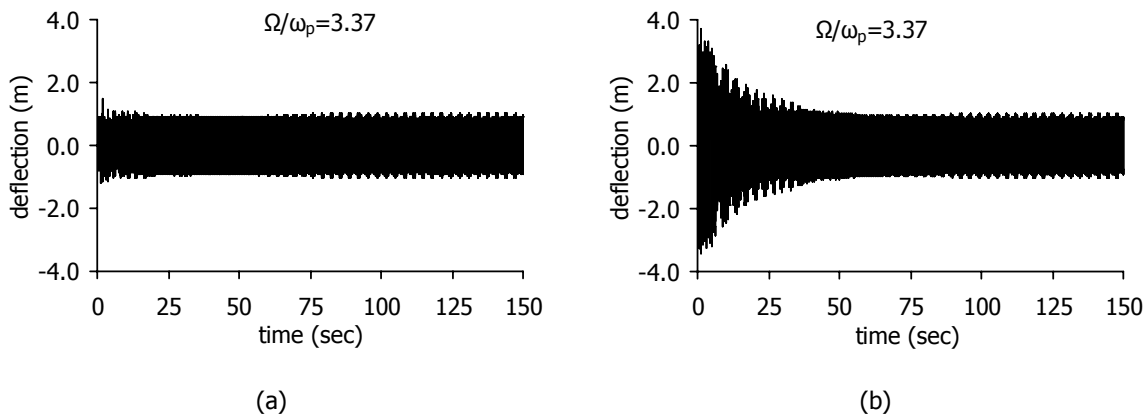


Figure 6-47: Time-history diagrams of the central node deflection for $\Omega/\omega_m=3.37$ and $(P_0)_p=15\text{kN}$: (a) with zero initial conditions, b) with initial displacement and velocity

For these diagrams, an infinitely linear material is assumed, in order to avoid the end of the calculation due to cable tensile failure. Indeed, in case initial conditions are considered, the maximum deflection measured is 3.71m at time 1.215sec, exceeding the maximum permissible one, which is 3.20m, leading to a maximum cable tension equal to 3077kN (Figure 6-48). For a material 1670/1860MPa though, the maximum permissible cable tension would be equal to:

$$N_{\text{cmax,p}}=A_p\sigma_y=0.00196\text{m}^2\cdot 167000\text{kN/m}^2=3273\text{kN} \quad (6-137)$$

which means that, for this steel category, the deflection of 3.71m would be possible to occur without causing cable tensile failure.

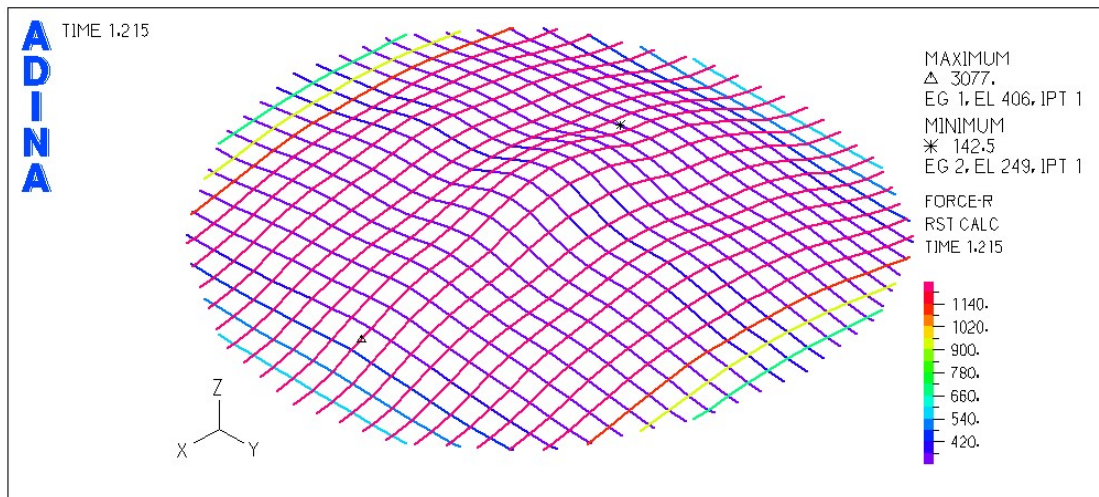
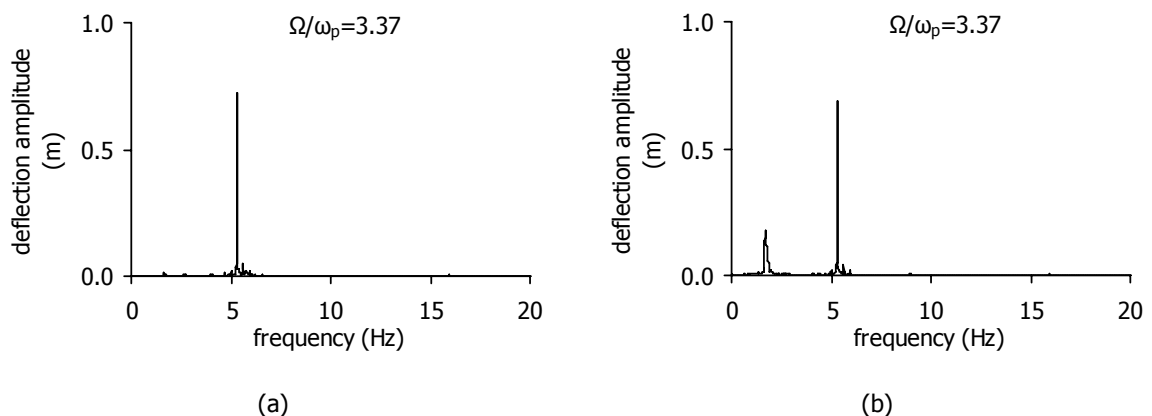


Figure 6-48: Maximum cable tension of the deformed structure

Comparing the diagrams of Figure 6-47 with the ones of Figure 6-23, it is obvious that the response of the MDOF prototype is not well predicted by the equivalent SDOF model. For zero initial conditions, the steady-state amplitude of the prototype is almost 1.00m, while for the SDOF model it is 0.14m. Considering initial conditions, the steady-state amplitude of the prototype does not differ from the one calculated with zero initial conditions, in contrast to the response of the SDOF model, for which, due to the subharmonic resonance, the oscillation amplitude arises at 2.98m.

Plotting the response spectra of the central node deflection in Figure 6-49, it is noted that for zero initial conditions, the vibration of the central node has only one dominant frequency, equal to 5.31Hz, which is the loading frequency, corresponding to $\omega=33.36\text{sec}^{-1}$, which is near the frequency of the 51st mode ($\omega_{51}=35.931\text{sec}^{-1}$), shown in Figure 6-27. This means that a fundamental resonance for this mode occurs, which explains the large amplitude of the MDOF prototype, with respect to the one of the SDOF model. The SDOF model, having only one eigenmode, cannot predict this fundamental resonance. In case initial conditions are assumed, two vibration frequencies are noted, one at 1.71Hz ($\omega=10.74\text{sec}^{-1}$) and one at 5.31Hz ($\omega=33.36\text{sec}^{-1}$). The first one is very close to the frequency of the first symmetric mode ($\omega_{15}=9.902\text{sec}^{-1}$), while the second one is the loading frequency.

Figure 6-49: Response spectra of the central node deflection for $\Omega/\omega_p=3.37$: (a) with zero initial conditions, (b) with initial displacement and velocity

In Figure 6-50, the time-history diagram of the central node amplitude is plotted again, zoomed at the time interval from the beginning of the analysis until 20sec. In this chart, the amplitude of the motion is almost 3.00m until the time of 6sec, when, with a beat phenomenon, it begins to reduce. This

means that for the first 6sec, a subharmonic resonance occurs with steady-state amplitude equal to 3.00m, as predicted by the SDOF model, but then the fundamental resonance for the 51st mode prevails.

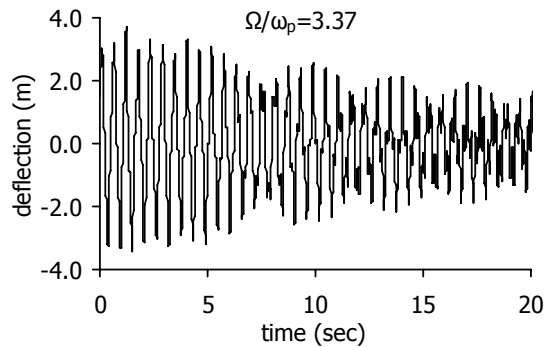


Figure 6-50: Time-history diagram of the central node deflection for $\Omega/\omega_p=3.37$ with initial displacement and velocity

6.5 EXAMPLE 2: CABLE NETS WITH SAG-SPAN RATIO $f/L=1/20$

6.5.1 Characteristics of the cable nets

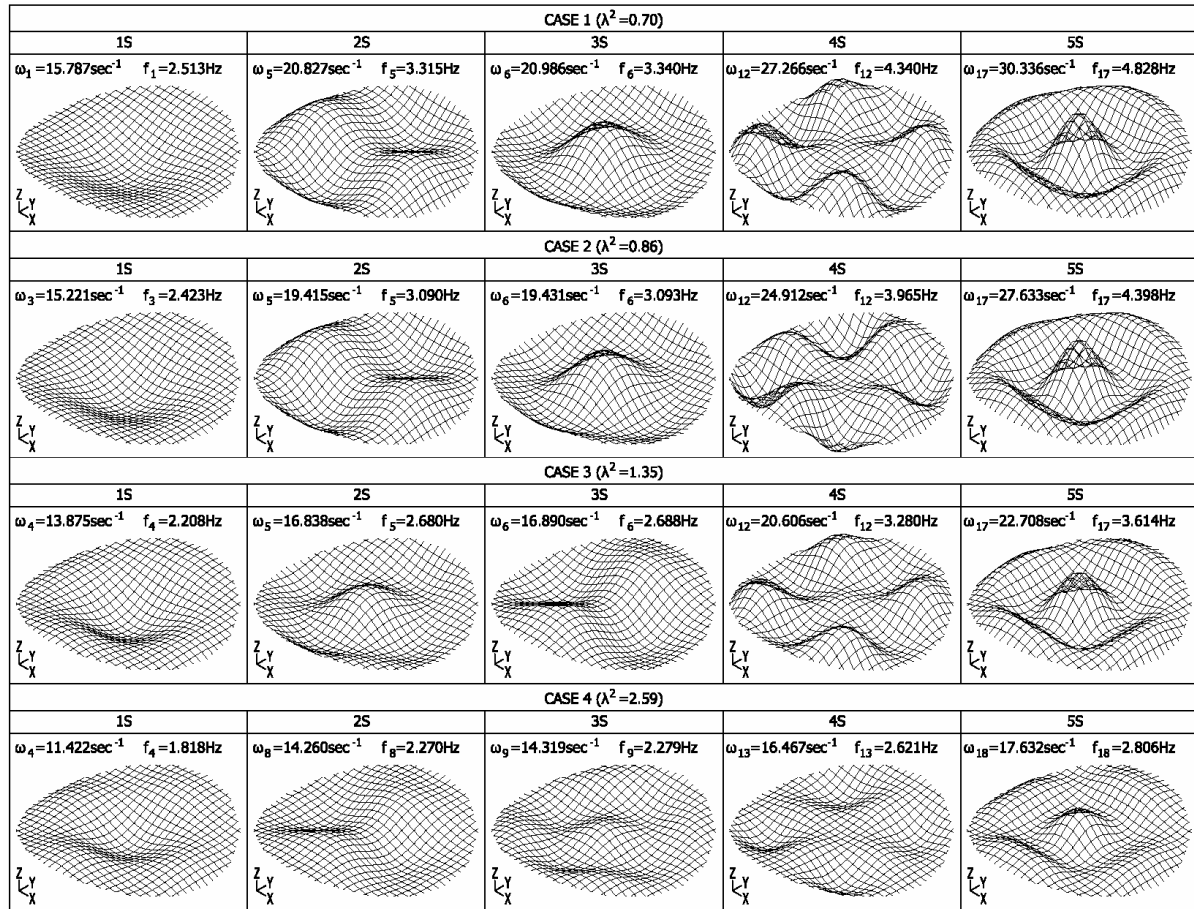
Another cable net is assumed, with sag-to-span ratio equal to $f/L=1/20$, Young modulus $E=165\text{GPa}$, and four different cases of cable diameter D and initial pretension N_0 , accounting for three different levels of initial cable stress. The cable diameter, the initial pretension and the yield stress are chosen appropriately resulting in characteristic values of the non-dimensional parameter λ^2 . The load amplitude in each case is chosen large enough to cause bending of the response curve, but small enough to avoid cable tensile failure. The characteristics of the nets for these cases are tabulated in Table 6-1.

Table 6-1: Characteristic cases for cable net with $f/L=1/20$ and $E=165\text{GPa}$

Cases	P_0 [kN]	D [mm]	N_0 [kN]	σ_y [MPa]	$N_0/(A\sigma_y)$	λ^2
1	1.3	40	735	1670	0.35	0.70
2	1.2	40	600	1570	0.30	0.86
3	2.0	50	600	1570	0.20	1.35
4	5.0	80	800	1570	0.10	2.59

6.5.2 Eigenfrequencies

The first five symmetric modes of the cable nets are illustrated in Figure 6-51, where it is noted that the shapes of these modes are similar for all cases but do not follow always the same sequence of appearance.

Figure 6-51: Eigenmodes and eigenfrequencies of the cable nets with sag-to-span ratio $f/L=1/20$

The relation between the frequencies of these modes is tabulated in Table 6-2. In all cases the second and third symmetric modes (2S and 3S) have frequencies close to the one of mode 1S, while the frequencies of the fourth and fifth symmetric modes (4S and 5S) are considered close to the previous three symmetric modes only in the last two cases. This, as will be shown, influences the response of the system, for loading frequencies close to the one of the second and third symmetric modes.

Table 6-2: Relation between the eigenfrequencies of the first symmetric modes

Cases	ω_{2S}/ω_{1S}	ω_{3S}/ω_{1S}	ω_{4S}/ω_{1S}	ω_{5S}/ω_{1S}
1	1.32	1.33	1.73	1.92
2	1.28	1.28	1.64	1.82
3	1.21	1.22	1.49	1.64
4	1.25	1.25	1.44	1.54

6.5.3 Fundamental resonance

Following the same procedure, as described in section 6.4, a damping ratio $\zeta=2\%$ is considered and the case of fundamental resonance for the first symmetric mode (1S) is addressed. The diagrams of the steady-state amplitude of the central node deflection of the MDOF system, along with the ones of the equivalent SDOF cable net, for different frequency ratios, are illustrated in Figure 6-52. In all charts, two peaks appear in the response curve of the MDOF system. The first one, for frequency ratio close to 1, corresponds to the fundamental resonance of the first symmetric mode, while the second peak describes the fundamental resonance for the second symmetric mode.

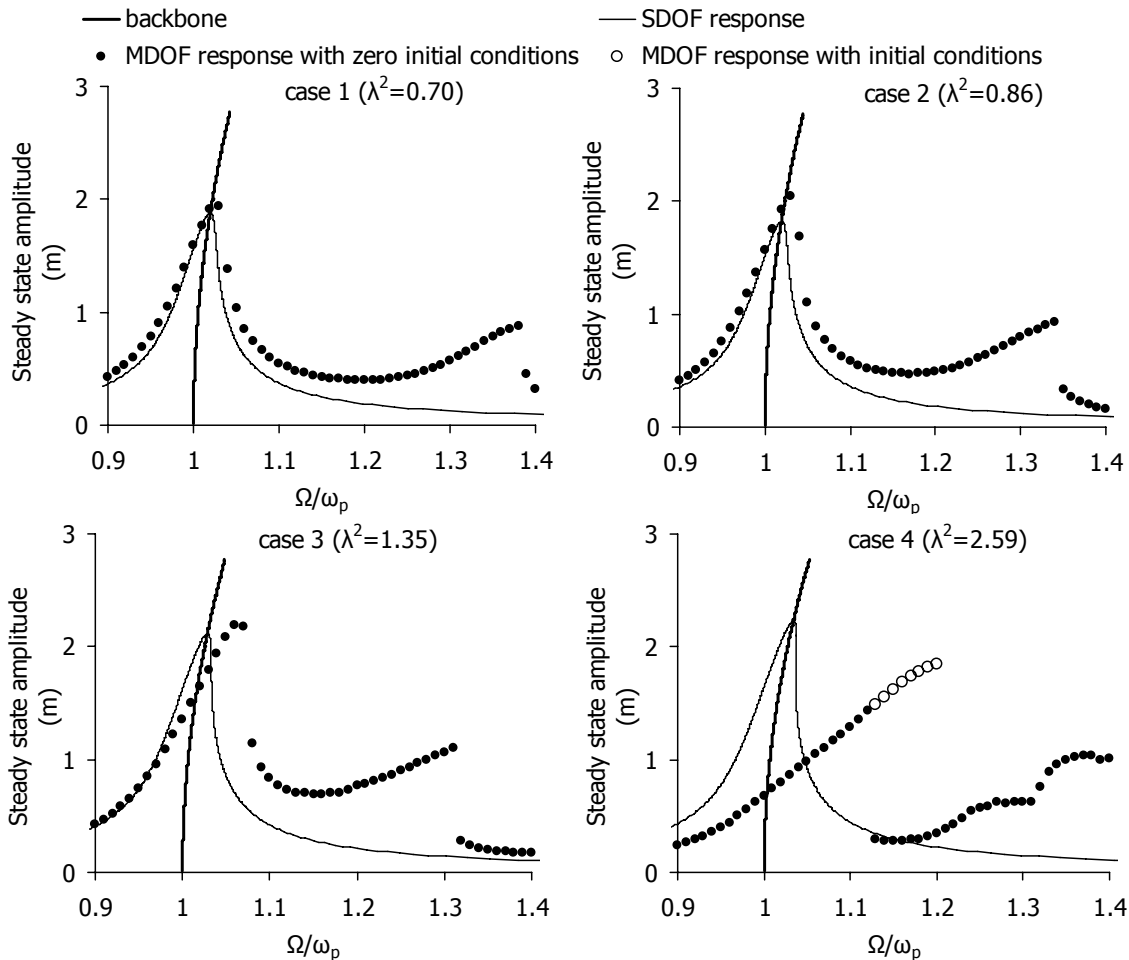


Figure 6-52: Fundamental resonance: response curve of the MDOF prototype and SDOF model for $\zeta=2\%$

For the first two cases, the maximum steady-state response of the central node of the MDOF system, as well as the frequency ratio for which this occurs, are predicted with satisfactory accuracy by the method of the SDOF system. For the third case, the response diagram bends more than the one of the equivalent SDOF cable net, while for the fourth case the method does not provide accurate results. In this case, the bending of the response curve for the MDOF system is more intense and the maximum steady-state amplitude of the central node is smaller than the one predicted by the method. This occurs because for the third and fourth cases the parameter λ^2 is larger than 1.17, meaning that the first symmetric mode presents internal nodes with zero displacements, as explained in chapter 5. Thus, the vibration mode of the SDOF cable net cannot describe well the one of the MDOF system, and the results do not agree. The analysis of the equivalent SDOF cable net, having only one degree of freedom, cannot predict the fundamental resonance for the second symmetric mode. In the last two cases, following fundamental resonance for the first symmetric mode a beat phenomenon characterises the time-history diagrams of the central node deflection, meaning that more than one modes participate in the motion of the node. This occurs for frequency ratios between $\Omega/\omega_p=1.14$ and $\Omega/\omega_p=1.20$ for the third case and between $\Omega/\omega_p=1.20$ and $\Omega/\omega_p=1.40$ for the fourth case. The beat phenomenon is very intense in the fourth case, in which all five symmetric modes have frequencies close to the loading frequencies, resulting in the irregular increase of the response amplitude, as shown in Figure 6-52. For example, the time-history diagram and the response spectrum of the central node deflection for frequency ratio $\Omega/\omega_{15}=1.25$ are plotted in Figure 6-53. The beat phenomenon is obvious in the time-history diagram during the 100 seconds of the analysis, which

does not decay, although damping is included. In the response spectrum, several peaks are distinguished, corresponding to each one of the symmetric modes illustrated in Figure 6-51, proving that all symmetric modes are activated during the oscillation of the net.

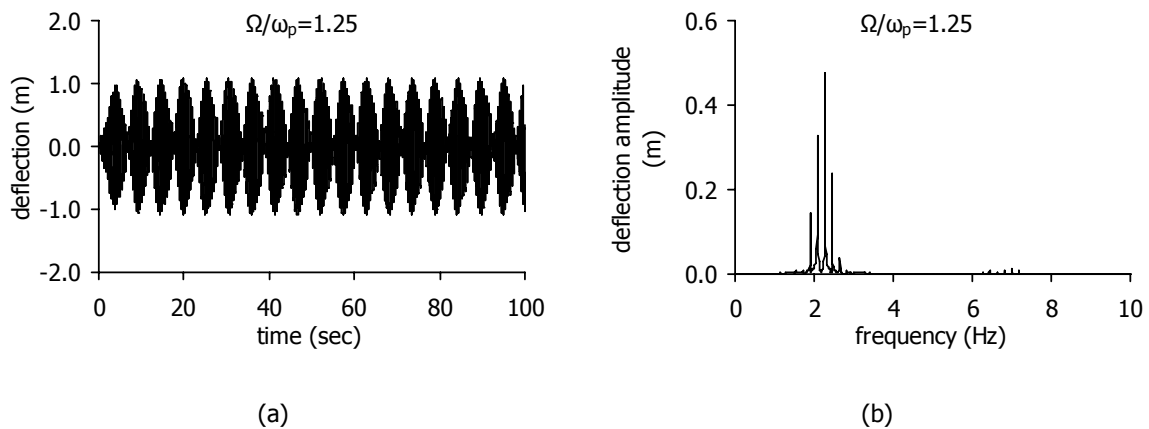


Figure 6-53: Response diagrams of the central node deflection for $\Omega/\omega_p=1.25$ (case 4): (a) time-history diagram, (b) response spectrum

Observing the diagrams of Figure 6-52, it is worth mentioning that in order to obtain similar oscillations amplitudes, the load amplitude for the fourth case is much larger than the one of the other cases, as listed in Table 6-1. Thus, for the same load amplitude, larger parameters λ^2 lead to smaller oscillation amplitudes. In the next chapter, the response of the second case is thoroughly investigated.

6.6 EVALUATION OF THE METHOD

The pros of this method are the following:

- The intensity of the geometrical nonlinearity of the MDOF system can be estimated very satisfactorily, by means of the bending of the response curve, the jump phenomena and the existence of double response amplitude due to the initial conditions.
- The loading frequency detuning, for which fundamental, superharmonic or subharmonic resonances for the first symmetric mode occur, can be estimated with good accuracy.
- The load amplitude, for which cable tensile failure occurs under fundamental, superharmonic or subharmonic resonant conditions, can be estimated with small error.
- The occurrence of subharmonic resonance can be excluded if the system is highly damped or weakly nonlinear.
- The computational time required to solve the equation of motion and have an assessment of the response of the MDOF system is minimal. On the contrary, the creation of a response diagram for the MDOF system requires a large number of nonlinear dynamic analyses.

The cons of this method are the following:

- The solution of the equation of motion, derived for the SDOF cable net, cannot consider cable slackening or cable tensile failure during the dynamic motion.
- The equivalent SDOF model, having only one eigenfrequency and eigenmode, can detect neither resonances for higher modes for a MDOF cable net, nor internal resonances.
- The equivalent SDOF model, having only a cubic nonlinear term, cannot predict superharmonic or subharmonic resonances of order two for the large system.

- The analytical solution of the SDOF cable net is provided for the vertical load applied on the central node, causing a vertical vibration. Thus, only the oscillation amplitude of the central node of the MDOF system can be estimated.
- In addition, this vertical motion corresponds to the first symmetric mode of the cable net. Hence, the method of the equivalent SDOF model cannot estimate the response of the MDOF cable net for other modal shapes, or for other spatial loading distributions, such as antisymmetric ones.
- The analytical solution of the SDOF cable net describes the steady-state amplitude of the response but not the maximum transient one, for which a cable tensile failure is possible to occur, before the steady-state response is reached.
- The results of this method are not satisfactory when the parameter λ^2 is larger than 1.17 for the MDOF system. In this case, the first symmetric mode of the cable net presents internal nodes with zero displacements and cannot be simulated with accuracy by the one of the SDOF model. Thus, this method is not recommended for cable nets with sag-to-span ratio between 1/30 and 1/20, with low levels of initial cable stress or for deep cable nets with sag-to-span ratio larger than 1/20, independently of the initial cable stress.
- The accuracy of the response amplitude assessment is not satisfactory when, for the MDOF system, two or more modes with similar shapes have commensurable frequencies, leading to internal resonance.

6.7 SUMMARY AND CONCLUSIONS

A method of using an equivalent single-degree-of-freedom cable net is introduced in this chapter, in order to predict the nonlinear dynamic response of a multi-degree-of-freedom cable net. The geometrical and mechanical characteristics of the large cable net are transformed to the corresponding ones of the small cable net, using similarity relations. The analytical solution of the SDOF model is explored, in order to detect nonlinear phenomena, such as the bending of the response curve, the occurrence of superharmonic and subharmonic resonances, instability regions, jump phenomena and the double response amplitude with respect to the initial conditions. The results of the SDOF model, by means of the maximum load, the maximum deflection and the loading frequency, are transformed to the ones of the MDOF system, by using the inverse similarity relations. Conducting nonlinear dynamic analyses and numerical simulation of the MDOF cable net, the nonlinear phenomena are verified.

This investigation verifies that the saddle-form cable nets have cubic nonlinearities, but also quadratic ones. Near resonances, although damping exists, a small change of the loading frequency may cause large difference in the oscillation amplitude. The initial conditions influence significantly the response of the cable net, as occurs in nonlinear systems. Jump phenomena, superharmonic resonances are also confirmed. Concerning the subharmonic resonances, it is difficult to detect them for a MDOF system, because they require specific load amplitude, load frequency and initial conditions. It is impossible to know which load amplitude and frequency and which initial deflection and velocity can cause this kind of nonlinear resonance, because no analytical solutions are available. The investigation of the SDOF model showed that subharmonic resonances may occur under certain conditions, but for the MDOF they are unlikely to occur, because the large initial conditions and the large load amplitude required for this phenomenon lead to cable tensile failure at the beginning of the vibration. If this is avoided, the subharmonic resonance appears only in the first few seconds of the vibrations and then the energy is transmitted to other modes, leading to fundamental resonances for modes of higher order.

The numerical investigation of the overall nonlinear dynamic behaviour of a MDOF system can be obtained by a large number of nonlinear time-history analyses, for different load amplitudes and for

very small time steps and frequency steps. This method can detect the loading amplitudes and frequencies for which nonlinear phenomena occur, constituting a useful guideline for the design of such cable structures, in order to avoid nonlinear phenomena.

Part of the work developed in this chapter has been presented in [6-17].

6.8 REFERENCES

- [6-1] G. C. Mays and P. D. Smith, "Blast effects on buildings", Thomas Telford, Great Britain, 1995.
- [6-2] C. M. Morison, "Dynamic response of walls and slabs by single-degree-of-freedom analysis – a critical review and revision", *International Journal of Impact Engineering*, Vol. 32, pp. 1214-1247, 2006.
- [6-3] H. N. Li, F. Wang and Z. H. Lu, "Estimation of Hysteretic Energy of MDOF structures based on equivalent SDOF Systems", *Key Engineering Materials*, Vol. 340-341, pp. 435-440, 2007.
- [6-4] S. Resemini, S. Lagomarsino and S. Giovinazzi, "Damping factors and equivalent SDOF definition in displacement-based assessment of monumental masonry structures", *Proceedings of the 1st European conference on earthquake engineering and seismology*, Geneva, Switzerland, 2006.
- [6-5] G. E. Manoukas, A. M. Athanatopoulou and I. E. Avramidis, "Static pushover analysis based on an energy-equivalent SDOF system", *Proceedings of the 14th World Conference on Earthquake Engineering*, Beijing, China, 2008.
- [6-6] R. Zaharia and F. Taucer, "Equivalent period and damping for EC8 spectral response of SDOF ring-spring hysteretic models", *JRC Scientific and Technical Reports*, European Communities, 2008.
- [6-7] M. Aschheim and J. Browning, "Influence of cracking on equivalent SDOF estimates of RC frame drift", *Journal of Structural Engineering*, Vol. 134, No. 3, pp. 511-517, 2008.
- [6-8] A. J. A. Oviedo, M. Midorikawa and T. Asari, "An equivalent SDOF system model for estimating the response of R/C building structures with proportional hysteretic dampers subjected to earthquake motions", *Earthquake Engineering and Structural Dynamics*, Wiley online library, 2010.
- [6-9] E. Buckingham, "On physically similar systems; Illustrations of the use of dimensional equations", *Physical Review*, Vol. 4, pp. 345-376, 1914.
- [6-10] J. S. Gero, "The behaviour of cable network structures", *Structures Report SR8*, University of Sydney, Australia, 1975.
- [6-11] J. S. Gero, "The preliminary design of cable network structures", *Structures Report SR9*, University of Sydney, Australia, 1975.
- [6-12] I. Vassilopoulou and C. J. Gantes, "Behaviour and preliminary analysis of cable net structures with elastic supports", *Proceedings of the 4th National Conference on Metal Structures*, Patras, Greece, Vol. II, pp. 517-525, 2002.
- [6-13] I. Vassilopoulou and C. J. Gantes, "Behavior, analysis and design of cable networks anchored to a flexible edge ring", *Proceedings of the IASS Symposium on Shell and Spatial Structures from Models to Realization*, Montpellier, France, Extended Abstract, pp. 212-213, 2004.

-
- [6-14] I. Vassilopoulou and C. J. Gantes, "Cable nets with elastically deformable edge ring", *International Journal of Space Structures*, Vol. 20, No.1, pp. 15-34, 2005.
- [6-15] I. Vassilopoulou and C. J. Gantes, "Similarity relations for nonlinear dynamic oscillations of a cable net", *Proceedings of the 1st ECCOMAS Thematic Conference on Computational Methods in Structural Dynamics and Earthquake Engineering – COMPDYN 2007*, Rethymno, Crete, Greece, abstract pp. 373, 2007.
- [6-16] A. K. Chopra, "Dynamics of structures, theory and applications to earthquake engineering", Prentice Hall International, Inc., U.S.A., 1995.
- [6-17] I. Vassilopoulou and C. J. Gantes, "Nonlinear dynamic behaviour of a saddle form cable net modeled by an equivalent SDOF cable net", *Proceedings of the 3rd ECCOMAS Thematic Conference on Computational Methods in Structural Dynamics and Earthquake Engineering – COMPDYN 2011*, Corfu, Greece, 2011.

7 DYNAMIC RESPONSE OF MDOF CABLE NETS UNDER HARMONIC LOAD

7.1 INTRODUCTION

Tensile structures are much lighter than any other conventional steel or concrete structure, designed to span the same area and to carry the same permanent loads. This is their main advantage, but, on the other hand, their lightness renders them particularly susceptible to dynamic oscillations due to fluctuating loads. Their response under dynamic excitation may become unpredictable, as, apart from the primary resonance phenomena, secondary resonances may emerge as well, endangering the system's stability causing cable slackening, fatigue problems at the cable anchorages or even tensile failure of some cables.

Several researchers have investigated such phenomena for individual cables, with many applications in cable stayed or suspension bridges, electrical overhead transmission lines or guyed masts, but only a few have dealt with such phenomena for cable suspended roofs. Most of the pertinent publications present new computerised methods of analysis and other numerical techniques to calculate the nonlinear static or dynamic response of cable networks and membranes, by solving the governing equations of motion ([7-1] – [7-11]), several of them compared with experimental results. In [7-12] the authors, presenting several time-history analyses of a cable network oscillation, concluded that symmetric uniform loading produces an almost linear dynamic response, whilst for antisymmetric loads, the nonlinearity of the system is more intense. Lazzari et al. [7-13] studied the free vibrations of a real saddle-form cable net, its resonant behaviour and its dynamic response under wind action. They interpreted the beat phenomenon of the displacement time-history diagram, in case of primary resonance, as the change of stiffness due to increase of deformation, producing also a change of the resonance frequency and avoiding the well-known continuously increasing amplitude of vibration, which occurs for linear systems.

During the initial stage of the present work, the dynamic behaviour of an undamped cable net with fixed supports under fundamental resonance was explored in [7-14] and internal resonances were detected, indicated by the beat phenomena in the oscillation of the net. On the other hand, in [7-15] a damped cable net with rigid supports subjected to a uniform symmetric load was analysed for a wide range of values of the loading frequency, concluding that it is never sufficient to take into consideration only the first natural modes, as fundamental resonances of higher modes may lead to

cable nets' oscillations of large amplitudes, comparable to those generated by the fundamental resonance of the first symmetric mode. Moreover, in [7-16], some similarities and differences between a network with rigid cable supports and one with the cables anchored to a flexible edge ring were highlighted.

In this chapter, the nonlinear nature of a cable net is investigated through the occurrence of nonlinear dynamic phenomena, in order to ascertain whether it can be treated as a weakly nonlinear system. The net is subjected to harmonic excitations, considering three different spatial distributions regarding the sign of the dynamic nodal loads. Diagrams of nodal displacements and cable tension variation, obtained by nonlinear transient analyses, delineate the response of the system. The boundary conditions of the cables are also studied, underlining similarities and differences between a network with rigid cable supports and one with the cables anchored to a deformable edge ring, proving that simplifying assumptions lead in some cases to completely different results.

7.2 MODELLING ISSUES AND ASSUMPTIONS

The 3-dimensional cable network system, described in chapter 6, is utilised again for the investigation of the dynamic response under harmonic excitation. The cable net forms the surface of a hyperbolic paraboloid, with circular plan view of diameter $L=100\text{m}$. The net consists of $N=25$ cables in each direction, arranged in a quadratic grid. The sag of the roof is equal to $f=L/20=5\text{m}$. All cables have a circular cross-section with the same diameter $D=50\text{mm}$ and area $A=0.0019635\text{m}^2$, and mass density of the cables is $m=10\text{kN}\cdot\text{sec}^2\cdot\text{m}^{-4}$, while no concentrated additional masses are assumed. The influence of the edge ring on the cable net response under harmonic load is also investigated, using the cable net described above, as far as the cable characteristics are concerned, with a contour ring having a square box cross-section of width $b=6.00\text{m}$, wall thickness $b/10=0.60\text{m}$, unit weight $\rho_r=25\text{kN/m}^3$ and elastic modulus $E_r=39\text{GPa}$. The eventual cable slackening is taken into account assuming a constant modulus of elasticity $E=165\text{GPa}$ in the tension branch and zero compression branch. The initial cable pretension is $N_0=600\text{kN}$, which is introduced as initial strain in the cable, equal to $N_0/EA=0.001852$. The maximum cable stress is considered equal to the yield stress 1570MPa corresponding to a strain equal to 0.009515 and a maximum cable tension $N_{\max}=3082.68\text{kN}$.

Regarding the boundary conditions, the cable ends are considered either as fixed or anchored to a boundary ring, as described in chapter 5. The state under prestressing is taken into consideration as the initial state. As proved in chapter 5, the equilibrium at every node under pretension is reached at the first step of the analysis. Hence, introducing the same strain in all cable segments does not entail errors in the results. A lumped mass matrix is used and a damping ratio equal to $\zeta=2\%$ is assumed. The damping is introduced in the system as mass and stiffness proportional Rayleigh damping [7-17]. Linear modal analyses are performed to calculate the eigenfrequencies and the eigenmodes, while the dynamic response of the cable net is represented by nodal displacement and cable tension response diagrams, conducting time-history analyses, considering also the geometric nonlinearity of the structure. The geometry and the mechanical characteristics of this system are very close to the ones of the cable net roof of the Peace and Friendship Stadium in Athens, Greece [7-18].

The difference between the dynamic response and the static one is defined by the ratio of the dynamic magnitudes of the response over the static ones corresponding to the same load:

$$R_{\text{dyn}} = \frac{M_d}{M_{\text{st}}} \quad (7-1)$$

where M stands for the nodal deflection or the cable tension and the subscripts d and s denote dynamic and static results, respectively.

7.3 LOAD DESCRIPTION

Equal concentrated loads expressed as $P=P_0\cos(\Omega t)$, are exerted vertically on all nodes of the net, having the same amplitude and time variation. No permanent loads are taken into consideration. The frequency of the harmonic load Ω takes several values, aiming at resonance conditions. Two load amplitudes are considered for dynamic analysis, equal to $P_0=2\text{kN}$ and $P_0=24\text{kN}$, for loading frequencies near the natural frequency of the system, aiming at fundamental resonance, or smaller than that, aiming at superharmonic resonance, respectively. Thus, for $P_0=2\text{kN}$ the loading frequency Ω varies between 0.90ω and 1.40ω , and for $P_0=24\text{kN}$, Ω varies between 0.30ω and 0.60ω , where ω is the eigenfrequency of the cable net. The same loads are applied statically, in order to compare the static response with the dynamic one. These amplitudes are chosen so that phenomena of fundamental and superharmonic resonances appear, respectively, without cable tensile failure; thus, for load amplitudes larger than 2kN with loading frequencies close to the eigenfrequency of the system, and for load amplitudes larger than 24kN with loading frequencies smaller than the natural frequency, the cables reach the yield stress.

The spatial load distribution is assumed either uniform, signed according to the first symmetric mode (1S), or antisymmetric, signed either according to the first antisymmetric mode with respect to one horizontal axis (1A), or to both horizontal axes (2A). The nodes that exhibit the maximum deflection for each loading spatial distribution are node 15 (central node) for mode 1S (Figure 7-1), node 202 for mode 1A and node 458 for mode 2A (Figure 7-2). The deflection diagrams for these nodes will describe the response of the system.

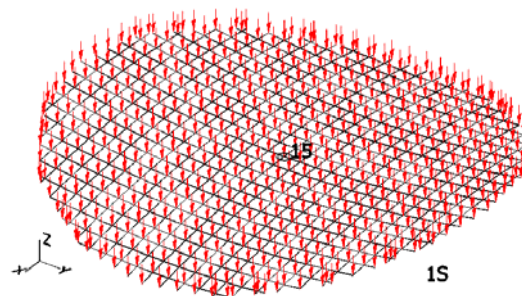


Figure 7-1: Uniform spatial load distribution and characteristic node

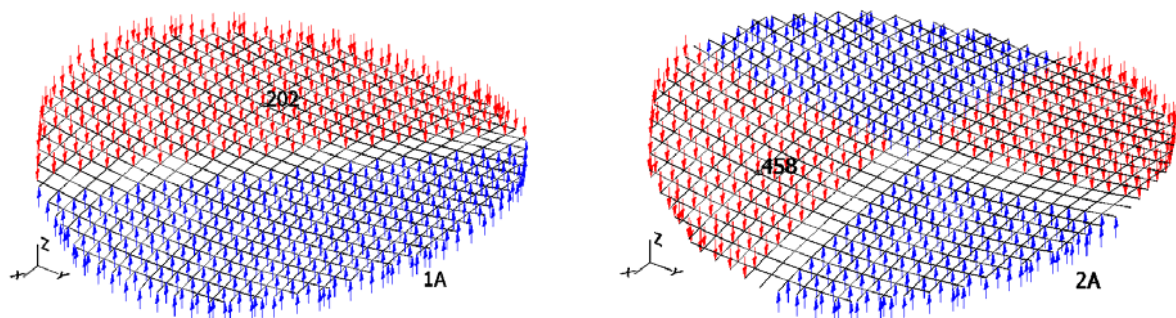


Figure 7-2: Antisymmetric spatial load distributions and characteristic nodes

7.4 CABLE NET WITH RIGID SUPPORTS

7.4.1 Eigenmodes and eigenfrequencies

The non-dimensional parameter λ^2 is:

$$\lambda^2 = \left(\frac{f}{L}\right)^2 \frac{EA}{N_0} = \left(\frac{1}{20}\right)^2 \frac{165000000 \cdot 0.00196}{600} = 1.35 \tag{7-2}$$

This value of the parameter λ^2 does not imply any crossover point. The first mode of the system is the antisymmetric mode with reference to both horizontal axes, (2A). The second and third modes are both antisymmetric with respect to y' or x' axis, respectively, with equal eigenfrequencies and similar shapes (1A). The auxiliary coordinate system with axes x' and y' is shown in Figure 7-3.

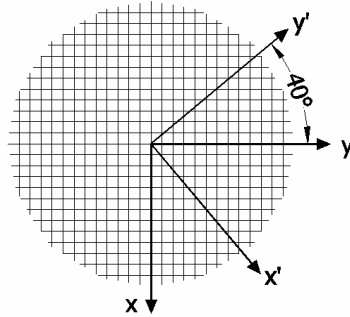


Figure 7-3: Auxiliary axes x' and y'

The first symmetric mode of the system (1S) is the fourth mode. The first twelve vibration modes and the corresponding natural frequencies are shown in Figure 7-4. The appearance sequence of the eigenmodes is as expected, based on the value of parameter λ^2 (see Chapter 5).

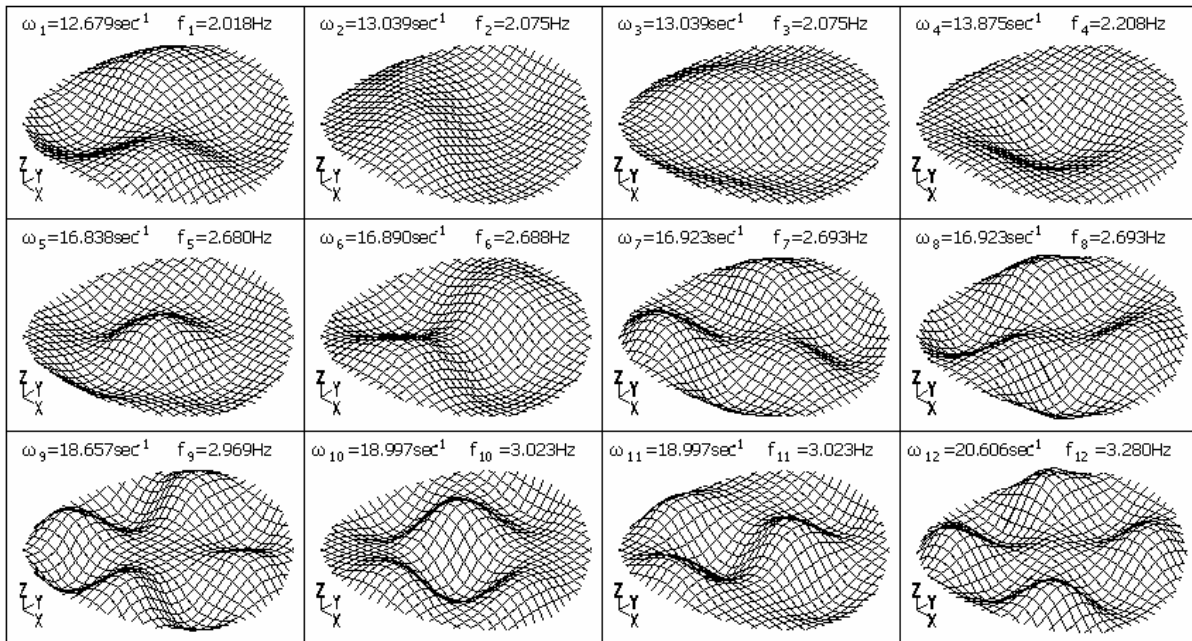


Figure 7-4: Vibration modes and natural frequencies of the cable net with rigid supports

7.4.2 Uniform spatial load distribution (1S) – Static response

For spatial load distribution signed according mode 1S, the load-deflection diagram for the central node as well as the variation of the maximum tension in the longest cable, are plotted in Figure 7-5 for load up to 24kN. The response appears to be practically linear up to a load level of 18.5kN but then, the stiffness of the system decreases, due to the slackening of some cables. The geometric nonlinearity of the system is proved to be weak for this load level, causing almost linear diagrams,

instead of curved ones as in highly nonlinear systems. The two loads that are considered for dynamic analysis, equal to $P=2\text{kN}$ and $P=24\text{kN}$, cause a maximum static deflection at node 15 equal to 0.067m and 0.838m , respectively. In addition, these two loads cause maximum static cable tension, equal to 676kN and 1433kN , respectively, developed in cable segment 40 (Figure 7-6). The magnified deformed shape of the net for $P=24\text{kN}$ is shown in Figure 7-7.

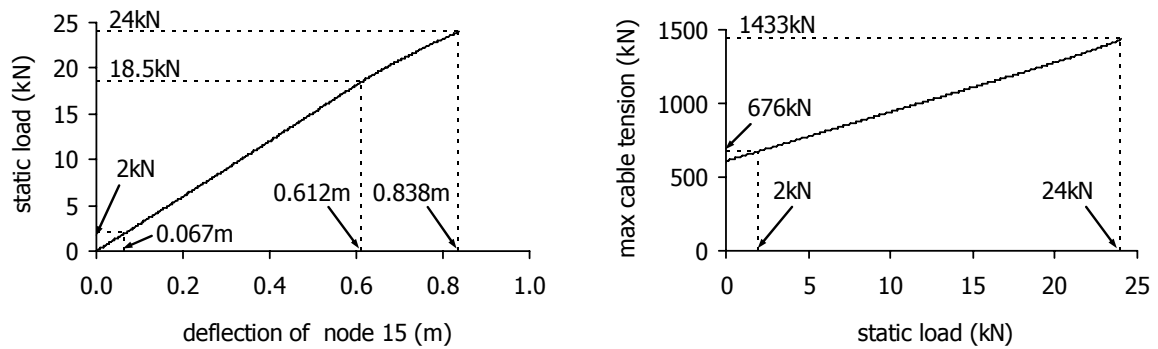


Figure 7-5: Static response of the cable net with rigid supports for uniform spatial load distribution (1S)

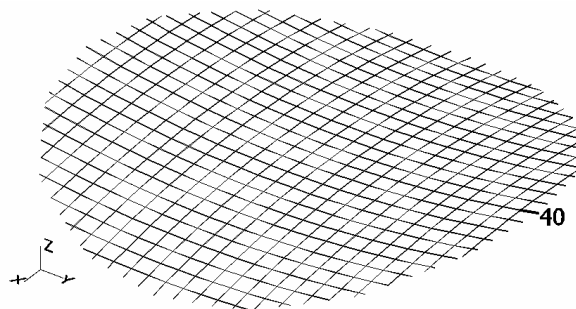


Figure 7-6: Cable segment 40 developing the maximum tension

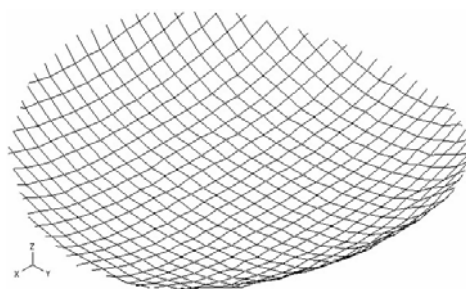


Figure 7-7: Magnified deformed shape for uniform spatial load distribution (1S)

7.4.3 Uniform spatial load distribution (1S) – Dynamic response

For a uniform spatial load distribution of the dynamic loads, the steady-state response amplitude of node 15 with respect to the ratio of the loading frequency over the frequency of mode 1S is illustrated in Figure 7-8, for loading amplitude $P_0=2\text{kN}$ and loading frequency between $0.90\omega_{1S}$ and $1.40\omega_{1S}$, where $\omega_{1S}=\omega_4=13.875\text{sec}^{-1}$ ($f_4=2.208\text{Hz}$, $T_4=0.45\text{sec}$).

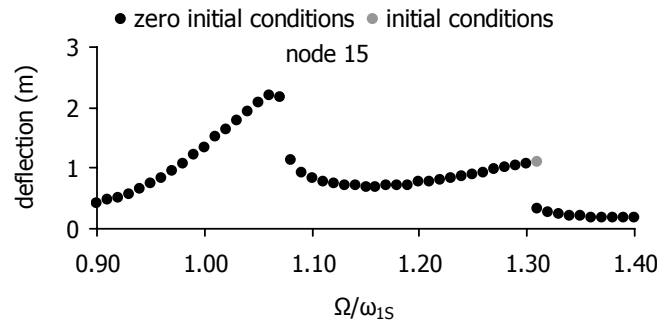


Figure 7-8: Steady-state response of the cable net with rigid supports under fundamental resonance for mode 1S ($P_0=2\text{kN}$)

The maximum steady-state oscillation amplitude occurs for $\Omega/\omega_{1S}=1.07$, equal to 2.18m, which is much larger ($R_{dyn}=32.54$) than the static one caused by a load of the same amplitude $P=2\text{kN}$. For $\Omega/\omega_{1S}=1.08$, the steady-state amplitude drops to 1.14m, indicating the bending of the curve and the jump phenomenon. The time-history diagrams and response spectra of the central node deflection are illustrated in Figure 7-9 for these frequency ratios. It is noted that the response for $\Omega/\omega_{1S}=1.07$ is larger than the one corresponding to $\Omega/\omega_{1S}=1.08$. From the response spectra it is confirmed that only one frequency characterises the oscillation of node 15, equal to 2.37Hz, which is the loading frequency and close to the frequency of mode 1S. The maximum tension is calculated for cable segment 129, shown in Figure 7-10. The tension time-history diagrams for these frequency ratios are illustrated in Figure 7-11. The maximum cable tension of the longest cable is 2410kN ($R_{dyn}=3.56$) for $\Omega/\omega_{1S}=1.07$.

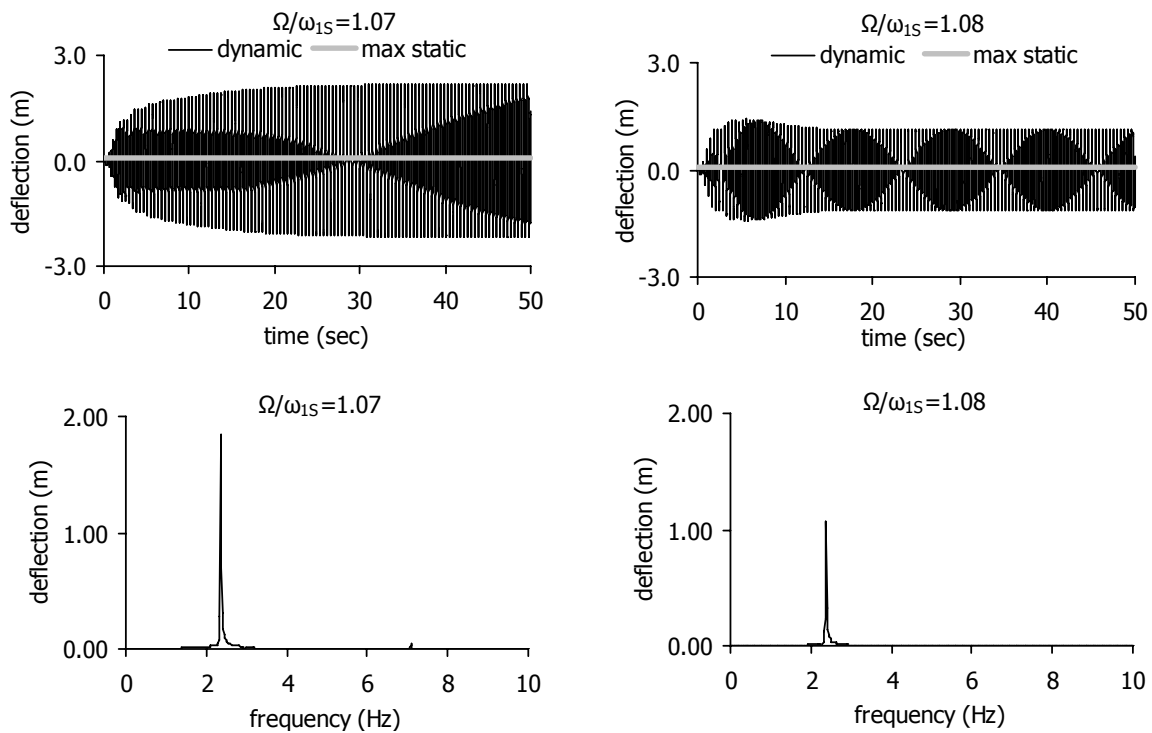


Figure 7-9: Deflection diagrams for node 15 of the cable net with rigid supports under fundamental resonance for mode 1S ($P_0=2\text{kN}$)

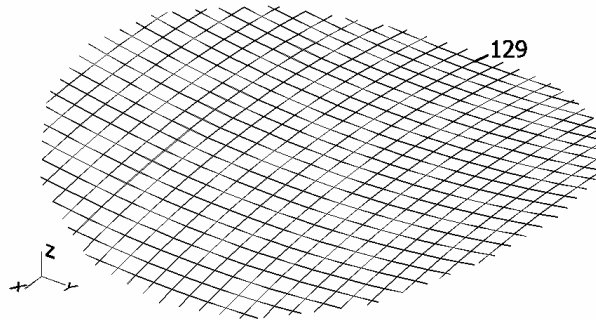


Figure 7-10: Cable segment 129 developing the maximum tension

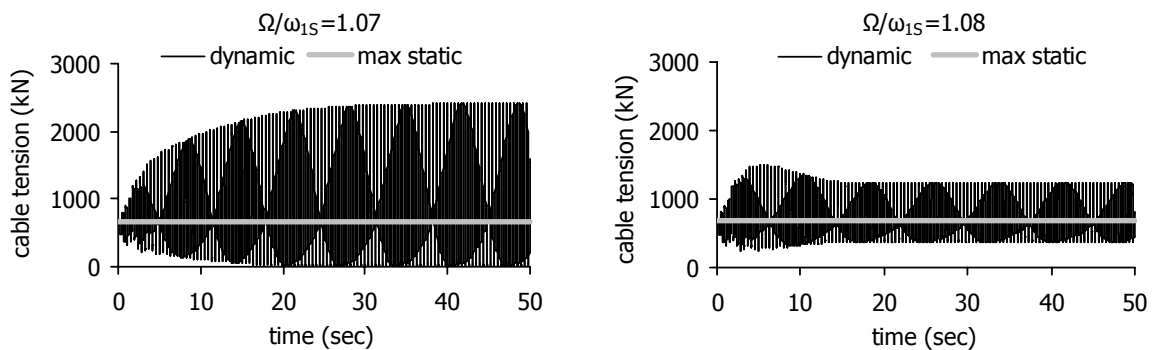


Figure 7-11: Tension diagrams of the cable net with rigid supports under fundamental resonance for mode 1S ($P_0=2\text{kN}$)

The initial conditions influence the response only when $\Omega/\omega_{1S}=1.31$, meaning $\Omega=18.18\text{sec}^{-1}$ (2.89Hz). For this frequency ratio another peak of the response is observed in Figure 7-8. This loading frequency corresponds to a frequency ratio $\Omega/\omega_5=1.08$ ($\omega_5=16.838\text{sec}^{-1}$) for the fifth mode, which is the second symmetric mode of the system, as illustrated in Figure 7-4. Thus, the second peak indicates a fundamental resonance for this mode. The response diagrams for this frequency ratio, considering initial conditions, are plotted in Figure 7-12. It is verified that the main peak in the response spectrum corresponds to the fifth mode. For larger values of this frequency ratio, the response amplitude suddenly decreases, indicating again jump phenomena.

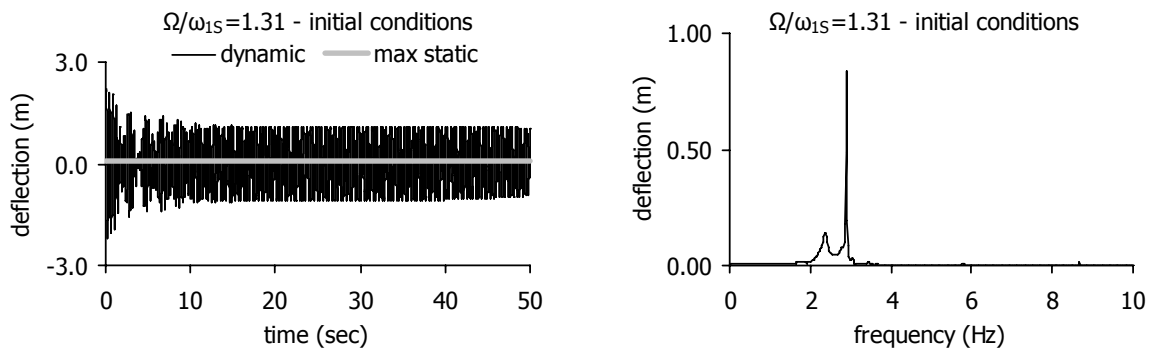


Figure 7-12: Deflection diagrams for node 15 of the cable net with rigid supports under fundamental resonance for mode 1S ($P_0=2\text{kN}$, $\Omega/\omega_{1S}=1.31$, initial conditions)

For loading amplitude $P_0=24\text{kN}$ and frequencies between $0.30\omega_{1S}$ and $0.60\omega_{1S}$, the steady-state response is shown in Figure 7-13. In this chart, two peaks of the response are noted: one for $\Omega=0.33\omega_{1S}=4.57\text{sec}^{-1}$ (0.73Hz), and one for $\Omega=0.42\omega_{1S}=5.83\text{sec}^{-1}$ (0.93Hz). The first one, equal to 1.203m, indicates an order-three superharmonic resonance for the fourth mode, while the second

one, equal to 1.257, corresponds to an order-three superharmonic resonance for the fifth node. This is verified by the frequency ratio $\Omega/\omega_5=0.35$ where $\omega_5=16.838\text{sec}^{-1}$. For frequency ratios between 0.33 and 0.42 smaller steady-state amplitudes are observed. Thus, a small change of the loading frequency results in significantly different response amplitudes, due to the superharmonic resonance.

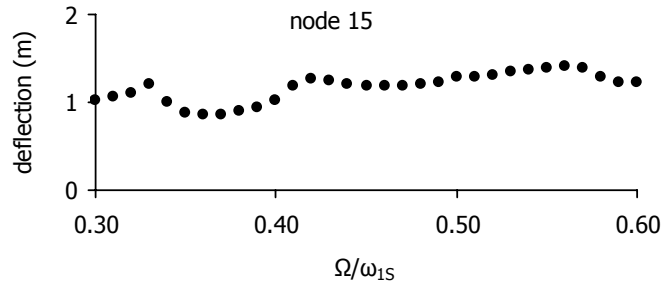


Figure 7-13: Steady-state response of the cable net with rigid supports under superharmonic resonance for mode 1S ($P_0=24\text{kN}$)

The deflection diagrams of node 15 for these two frequency ratios are illustrated in the diagrams of Figure 7-14. The maximum oscillation amplitude is observed during the transient response and it is equal to -2.13m for $\Omega/\omega_{1S}=0.33$ and -2.72m for $\Omega/\omega_{1S}=0.42$, with $R_{\text{dyn}}=2.54$ and $R_{\text{dyn}}=3.25$, respectively. The response spectrum for the first frequency ratio shows two significant frequencies, one at 0.75Hz , being the loading frequency, and another one at 2.20Hz , being equal to the one of mode 1S, verifying the order-three superharmonic resonance for this mode. The frequencies of the oscillation for $\Omega/\omega_{1S}=0.42$, shown in the response spectrum, are 0.95Hz , being close to the loading frequency, 2.25Hz , near the frequency of mode 1S, and 2.80Hz , which is close to the frequency of the fifth mode, confirming the order-three superharmonic resonance for these two modes.

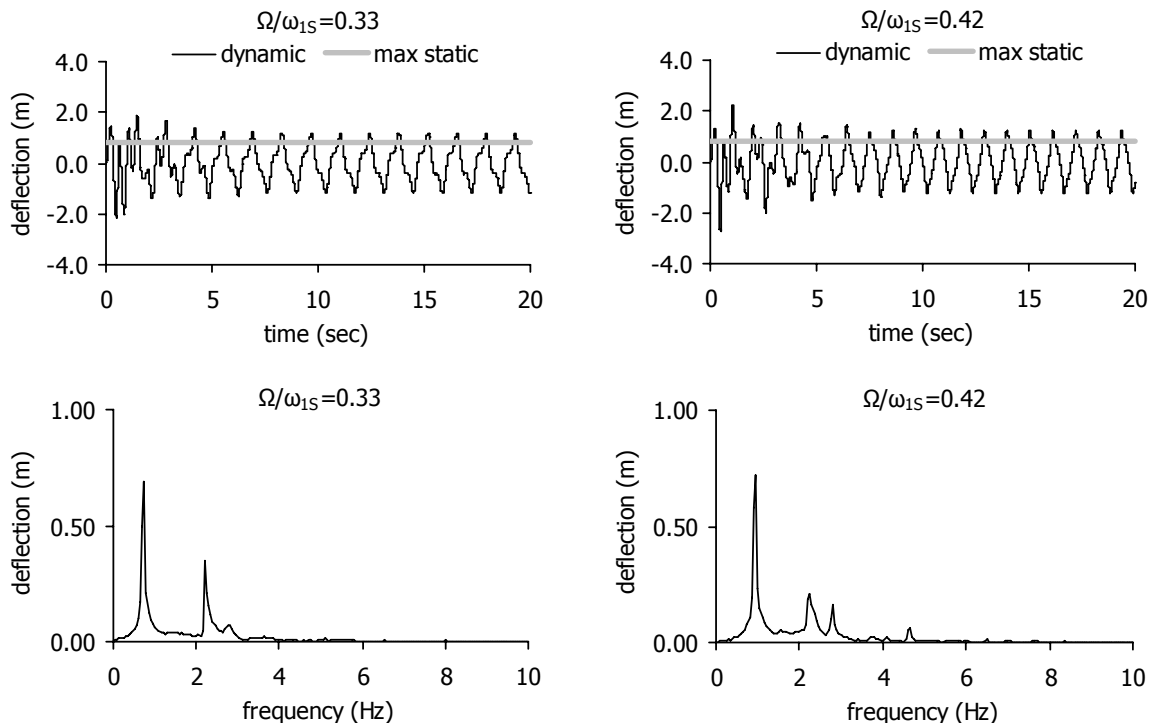


Figure 7-14: Deflection diagrams for node 15 of the cable net with rigid supports under order-three superharmonic resonance for mode 1S ($P_0=24\text{kN}$)

The cable tensions of the segments presenting the maximum magnitude for these two frequency ratios are plotted in Figure 7-15. For $\Omega/\omega_{1S}=0.33$ and 0.42 , the maximum tension is 2117kN ($R_{\text{dyn}}=1.48$) and 2470kN ($R_{\text{dyn}}=1.72$), respectively. In these diagrams it is noted that cable slackening and re-tensioning take place.

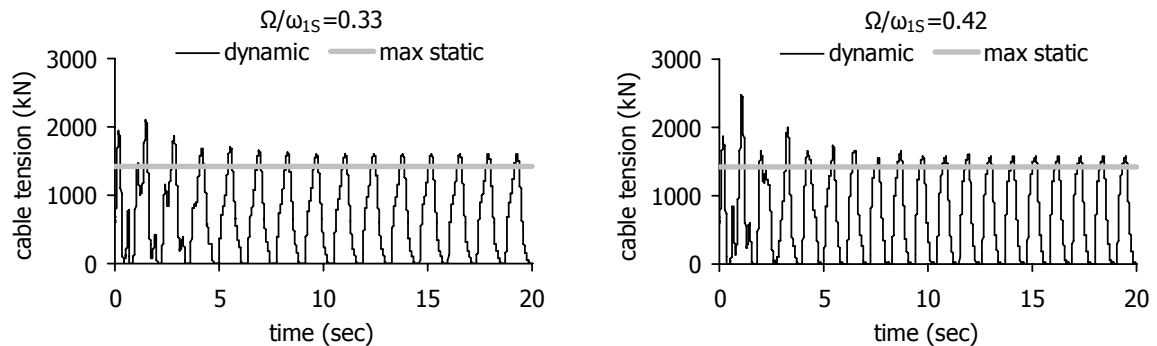


Figure 7-15: Tension diagrams for the cable net with rigid supports under order-three superharmonic resonance for mode 1S ($P_0=24\text{kN}$)

Two other smaller peaks are also observed in Figure 7-13 for $\Omega/\omega_{1S}=0.50$ and $\Omega/\omega_{1S}=0.57$ corresponding to order-two superharmonic resonances for the same two symmetric modes. The deflection diagrams of node 15 for these two frequency ratios are plotted in Figure 7-16, with maximum deflection -2.96m for $\Omega/\omega_{1S}=0.50$ and -3.00m for $\Omega/\omega_{1S}=0.57$, with $R_{\text{dyn}}=3.53$ and $R_{\text{dyn}}=3.58$, respectively. The response spectra show that in case of $\Omega/\omega_{1S}=0.50$, the two frequencies characterising the oscillation of node 15 are the loading frequency and the one of mode 1S, verifying the order-two superharmonic resonance for this mode, while for $\Omega/\omega_{1S}=0.57$, three frequencies are noted, the loading one, and the frequencies for mode 1S and the fifth mode, confirming this time the order-two superharmonic resonance not only for the fourth mode but also for the fifth one.

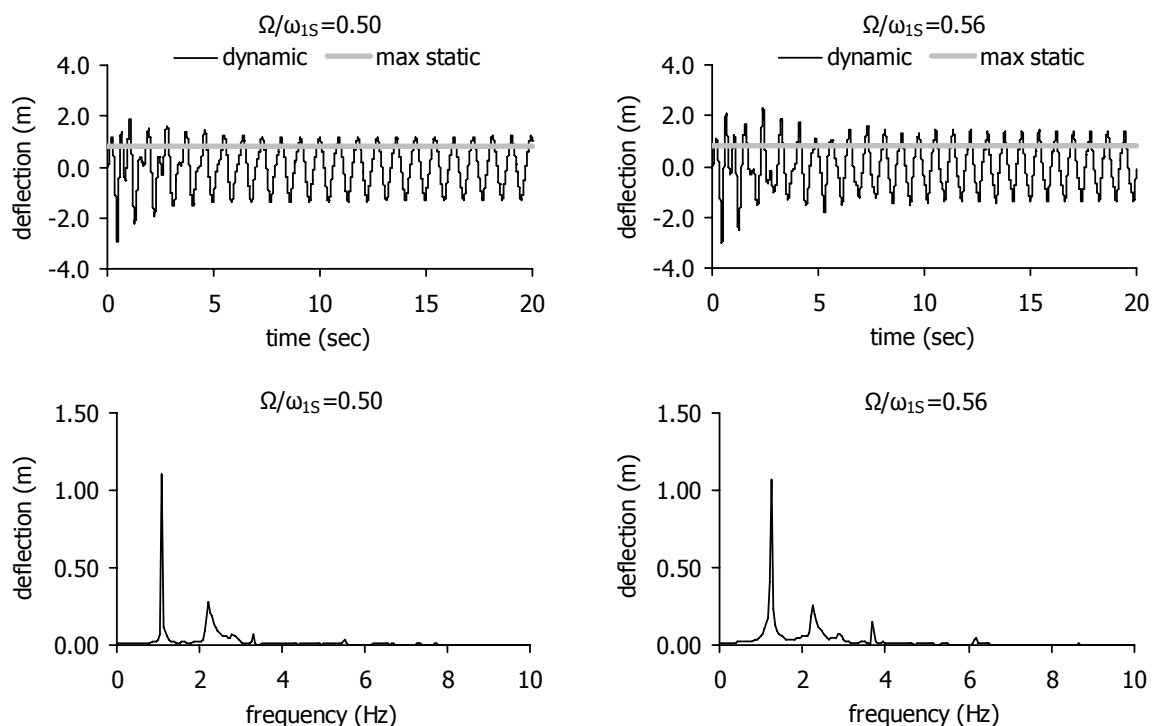


Figure 7-16: Deflection diagrams for node 15 of the cable net with rigid supports under order-two superharmonic resonance for mode 1S ($P_0=24\text{kN}$)

The cable tension diagrams for these two frequency ratios are illustrated in Figure 7-17. For $\Omega/\omega_{15}=0.50$ and 0.56 , the maximum tension is 2077kN ($R_{\text{dyn}}=1.45$) and 2457kN ($R_{\text{dyn}}=1.71$), respectively. In these diagrams cable slackening and re-tensioning are noted again.

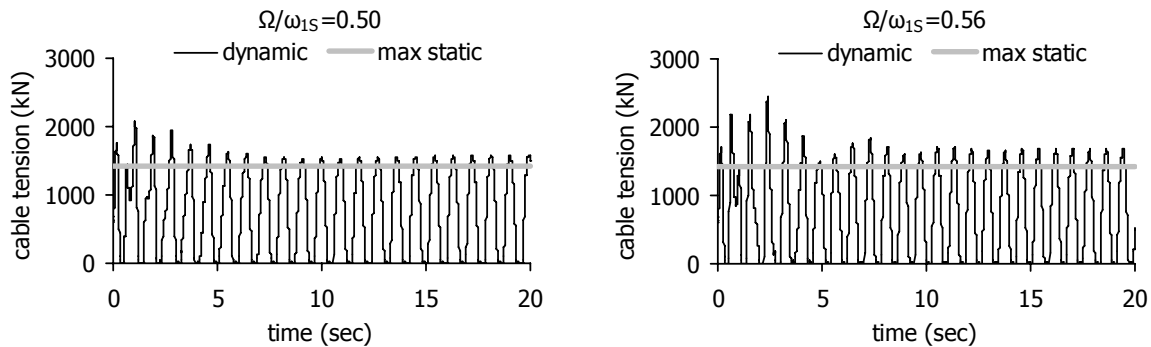


Figure 7-17: Tension diagrams for the cable net with rigid supports under order-two superharmonic resonance for mode 1S ($P_0=24\text{kN}$)

The same conclusions are drawn if smaller load amplitude is assumed, in order to avoid cable slackening if the load is applied statically. Thus, for loading amplitude $P_0=18\text{kN}$ the steady-state response is shown in Figure 7-18. Within the range of $\Omega/\omega_{15}=0.30$ and $\Omega/\omega_{15}=0.60$, three peaks are observed for frequency ratios 0.34 , 0.42 , 0.53 . As expected, they are smaller than the ones of Figure 7-13. As explained in chapter 3, for small load amplitudes, superharmonic resonances cannot cause large oscillation amplitudes.

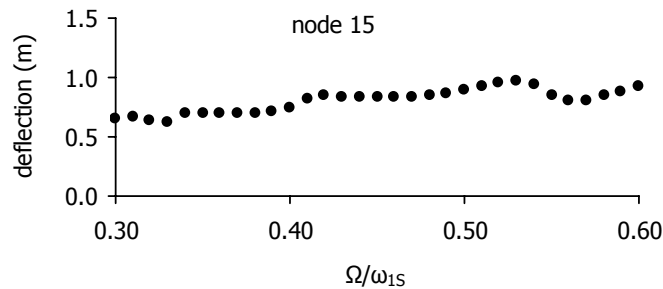


Figure 7-18: Steady-state response of the cable net with rigid supports under superharmonic resonance for mode 1S ($P_0=18\text{kN}$)

Although based on the static response the system could be considered as weakly nonlinear, the response to dynamic loads is proved to be highly nonlinear, characterised by superharmonic resonances, bending of the response curve, dependence on the initial conditions and jump phenomena.

7.4.4 Antisymmetric spatial load distribution (1A) – Static response

The net is now uniformly loaded with a vertical static nodal load equal to $P=2\text{kN}$, applied on every node. The sign of the nodal loads follows mode 1A. The maximum vertical displacement is observed for node 202 (Figure 7-2), while the maximum tension develops in cable segment 217 (Figure 7-19).

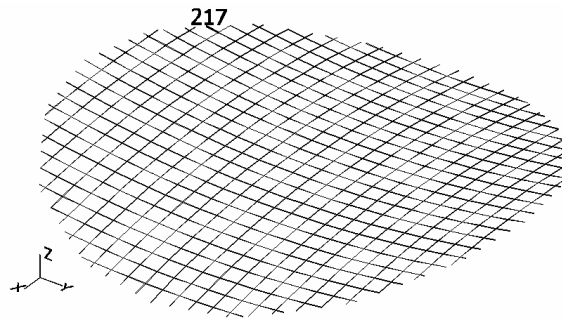


Figure 7-19: Cable segment 217 developing the maximum tension

The load-deflection diagram for node 202, as well as the variation of the maximum tension are illustrated in Figure 7-20 for load up to $P=24\text{kN}$. The first diagram is slightly curved, meaning that for this spatial load distribution the nonlinearity of the cable system is stronger with respect to the previous consideration of uniform load. The two load amplitudes $P=2\text{kN}$ and $P=24\text{kN}$, which will be considered for dynamic analysis, cause maximum deflection 0.10m and 1.01m , respectively, and maximum cable tension 665kN and 1349kN , respectively. No cable slackening occurs for this load level. The magnified deformed shape of the net is shown in Figure 7-21.

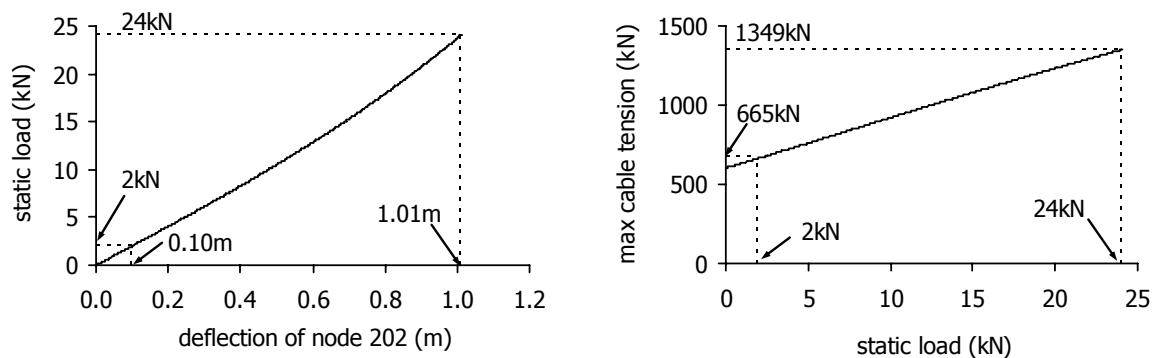


Figure 7-20: Static response of the cable net with rigid supports for antisymmetric spatial load distribution (1A)

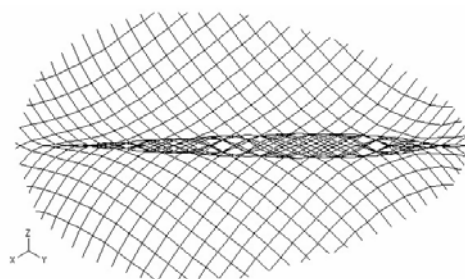


Figure 7-21: Magnified deformed shape for antisymmetric spatial load distribution (1A)

7.4.5 Antisymmetric spatial load distribution (1A) – Dynamic response

For a dynamic load with loading amplitude $P_0=2\text{kN}$, and spatial antisymmetric distribution signed according to mode 1A, the steady-state response amplitude of node 202 (Figure 7-2) with respect to the ratio of the loading frequency over the frequency of mode 1A is plotted in Figure 7-22 for loading frequency between $0.90\omega_{1A}$ and $1.40\omega_{1A}$, where $\omega_{1A}=\omega_2=\omega_3=13.039\text{sec}^{-1}$, corresponding to $f_{2,3}=2.075\text{Hz}$ and $T_{2,3}=0.48\text{sec}$.

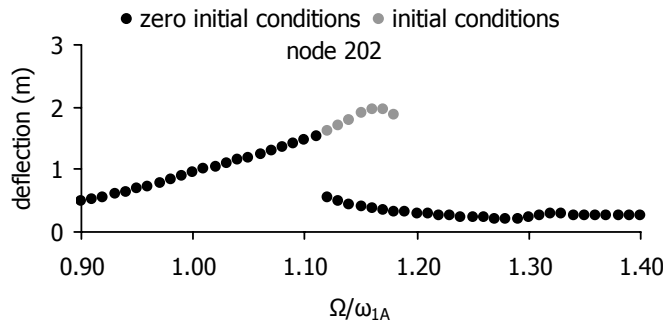


Figure 7-22: Steady-state response of the cable net with rigid supports under fundamental resonance for mode 1A ($P_0=2\text{kN}$)

For frequency ratios between $\Omega/\omega_{1A}=1.12$ and $\Omega/\omega_{1A}=1.19$, two steady-state responses are calculated. Considering as initial deflection and initial velocity the ones calculated for $\Omega/\omega_{1A}=1.12$, the large vibration amplitudes are obtained, while the small ones are obtained with zero initial conditions. The maximum steady-state oscillation amplitude occurs for $\Omega/\omega_{1A}=1.17$ and it is equal to 1.972m ($R_{dyn}=19.72$), much larger than the static deflection for the same load amplitude. The maximum steady-state deflection of the net for this load distribution is smaller than the one of the uniform distribution for the same load amplitude. On the other hand, the bending of the response curve for the antisymmetric spatial load distribution is more intense than the one for the uniform load shown in Figure 7-8, signifying a more intense nonlinear behaviour, as was also observed for static loads.

For $\Omega/\omega_{1A}=1.18$, considering initial conditions, the steady-state amplitude is 1.88m, but suddenly it decreases to 0.33m, which corresponds also to the steady-state amplitude for zero initial deflection and velocity. The response for this frequency ratio is shown in Figure 7-23, for the two assumptions regarding the initial conditions. The response spectra show that only one oscillation frequency exists, 2.45Hz, equal to the loading frequency.

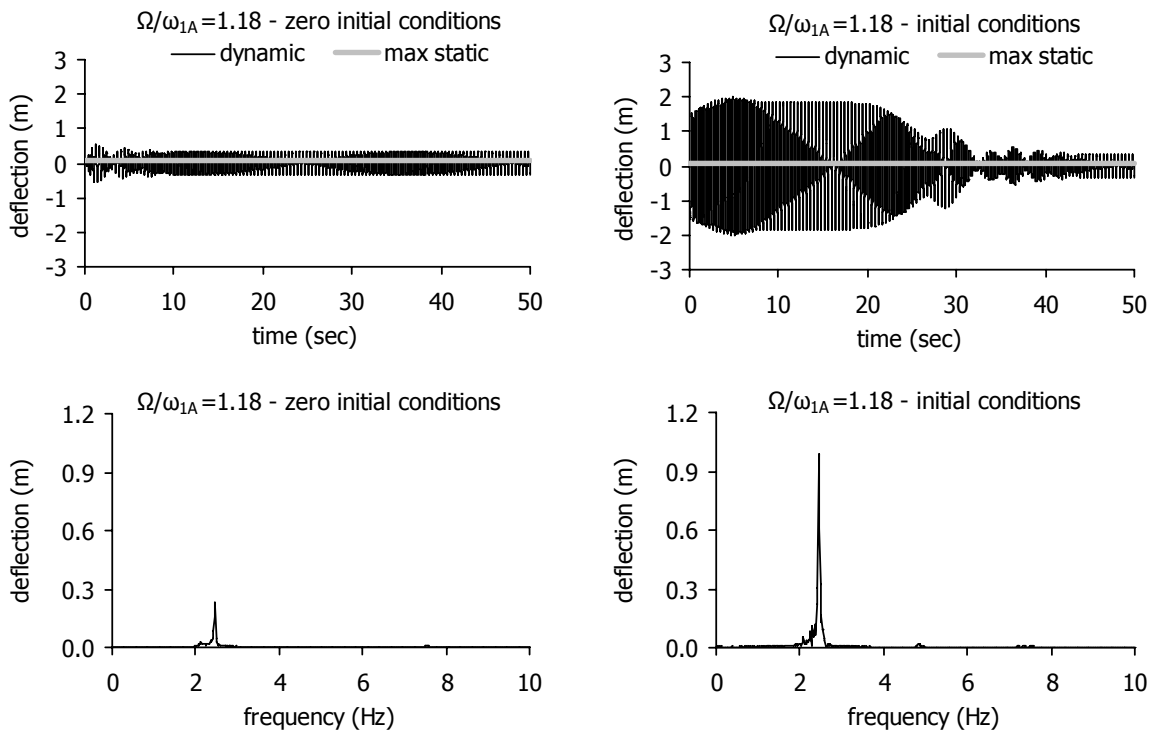


Figure 7-23: Deflection diagrams for node 202 of the cable net with rigid supports under fundamental resonance for mode 1A ($P_0=2\text{kN}$)

The maximum cable tension is 895kN for cable segment 121 and zero initial conditions, while taking into account initial conditions the maximum cable tension develops in cable segment 524, equal to 2155kN with $R_{dyn}=3.24$. The aforementioned cable segments are illustrated in Figure 7-24, while the corresponding diagrams are plotted in Figure 7-25.

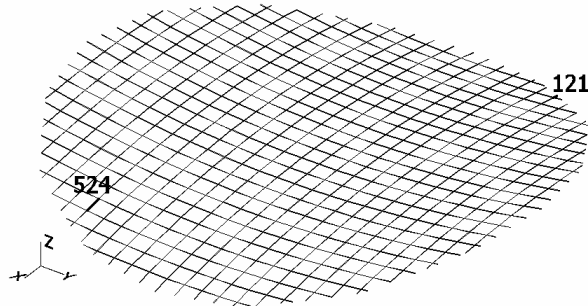


Figure 7-24: Cable segments 121 and 524 developing the maximum tension

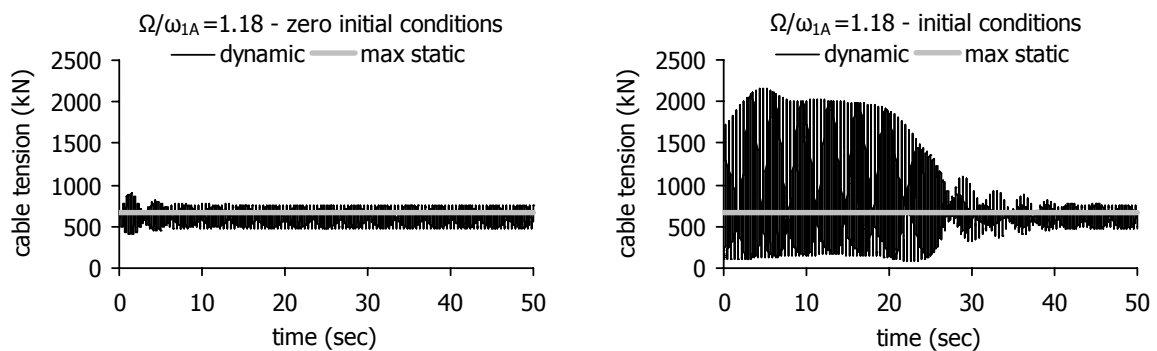


Figure 7-25: Tension diagrams for the cable net with rigid supports under fundamental resonance for mode 1A ($P_0=2kN$)

The deflection diagram of the net for loading amplitude $P_0=24kN$ and loading frequency between $0.30\omega_{1A}$ and $0.60\omega_{1A}$ is plotted in Figure 7-26. The maximum steady-state amplitude is 1.803m for $\Omega=0.40\omega_{1A}=5.22sec^{-1}$ (0.83Hz), indicating an order-three superharmonic resonance for mode 1A. The deflection diagrams of node 202 are illustrated in Figure 7-27, while the time-history diagram of the maximum cable tension is plotted in Figure 7-28.

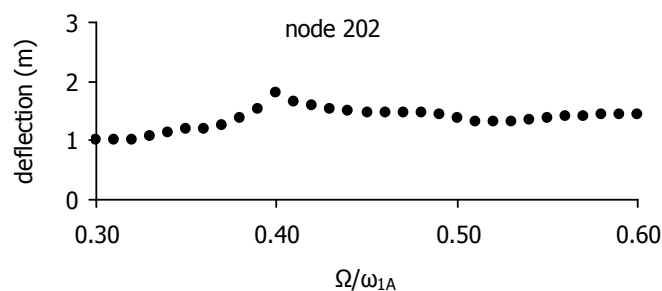


Figure 7-26: Steady-state response of the cable net with rigid supports under superharmonic resonance for mode 1A ($P_0=24kN$)

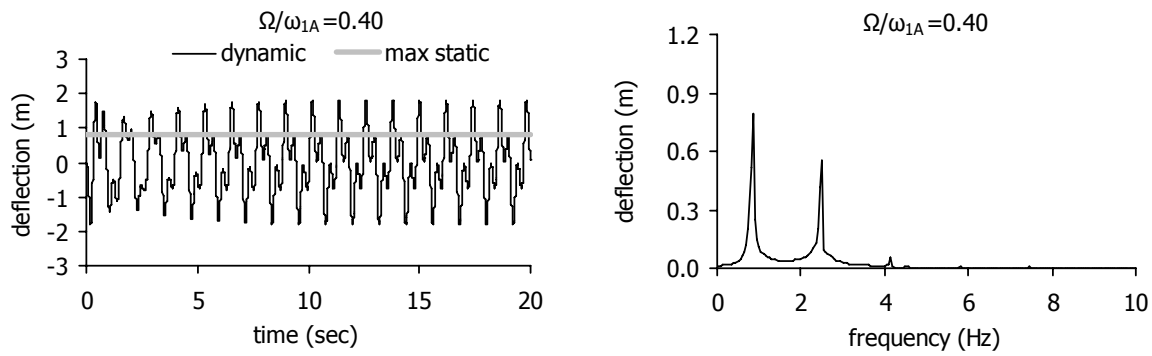


Figure 7-27: Deflection diagrams for node 202 of the cable net with rigid supports under superharmonic resonance for mode 1A ($P_0=24\text{kN}$)

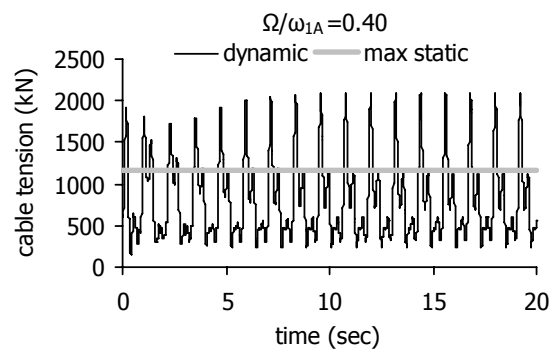


Figure 7-28: Tension diagram for the cable net with rigid supports under superharmonic resonance for mode 1A ($P_0=24\text{kN}$)

The response spectrum shows two significant frequencies of oscillation, one at 0.85Hz, being close to the loading frequency, and another one at 2.50Hz, which corresponds to the one of mode 1A, verifying the occurrence of order-three superharmonic resonance for this mode. The maximum cable tension is 2091kN presenting a ratio $R_{\text{dyn}}=1.55$.

7.4.6 Antisymmetric spatial load distribution (2A) – Static response

For an antisymmetric spatial load distribution signed according to mode 2A, the maximum tension develops in cable segment 405, shown in Figure 7-29. The load-deflection diagram for node 458, as well as the variation of the maximum tension, are shown in Figure 7-30, for load amplitude up to $P=24\text{kN}$.

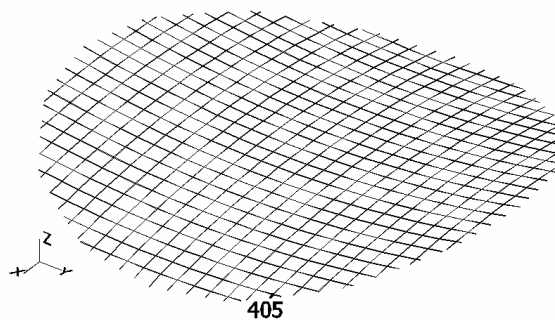


Figure 7-29: Cable segment 405 developing the maximum tension

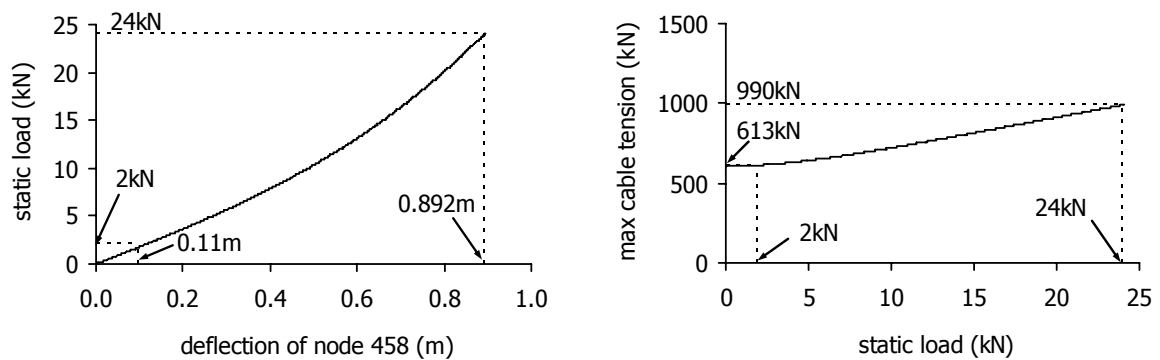


Figure 7-30: Static response of the cable net with rigid supports for antisymmetric spatial load distribution (2A)

The first diagram is more curved than the corresponding ones for the uniform load (Figure 7-5) and the antisymmetric spatial load distribution (1A) (Figure 7-20), meaning that in this case the geometric nonlinearity of the cable system is more intense than in any other consideration of load distribution. The two load amplitudes considered for dynamic analysis, $P=2\text{kN}$ and $P=24\text{kN}$, cause maximum static deflection 0.11m and 0.892m , respectively and maximum static cable tension 613kN and 990kN , respectively. This level of load does not cause any cable slackening. The magnified deformed shape of the net is shown in Figure 7-31.

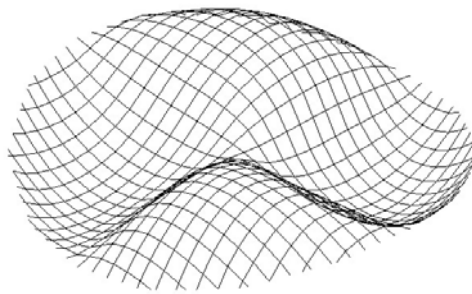


Figure 7-31: Magnified deformed shaped for antisymmetric spatial load distribution (2A)

7.4.7 Antisymmetric spatial load distribution (2A) – Dynamic response

Assuming now an antisymmetric spatial load distribution signed according to mode 2A and applied dynamically, the steady-state response amplitude of node 458 (Figure 7-2), with respect to the ratio of the loading frequency over the frequency of the antisymmetric mode 2A, is plotted in Figure 7-32, for loading amplitude $P_0=2\text{kN}$ and loading frequency between $0.90\omega_{2A}$ and $1.40\omega_{2A}$, where $\omega_{2A}=\omega_1=12.679\text{sec}^{-1}$ ($f_1=2.018\text{Hz}$, $T_1=0.50\text{sec}$). For frequency ratios between $\Omega/\omega_{2A}=1.17$ and $\Omega/\omega_{2A}=1.33$, there are two steady-state responses depending on the initial conditions. The large amplitudes are obtained taking into consideration as initial deflection and initial velocity the ones calculated for $\Omega/\omega_{2A}=1.16$, while the small amplitudes are obtained without initial conditions. The maximum steady-state oscillation amplitude occurs for $\Omega/\omega_{2A}=1.33$ and it is equal to 1.461m with ratio $R_{\text{dyn}}=13.28$. The deflection diagrams for these two responses are shown in Figure 7-33.

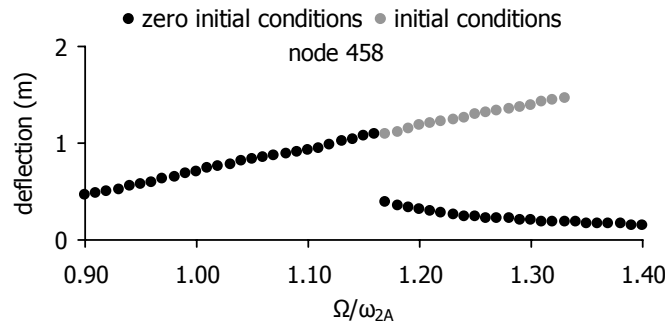


Figure 7-32: Steady-state response of the cable net with rigid supports under fundamental resonance for mode 2A ($P_0=2\text{kN}$)

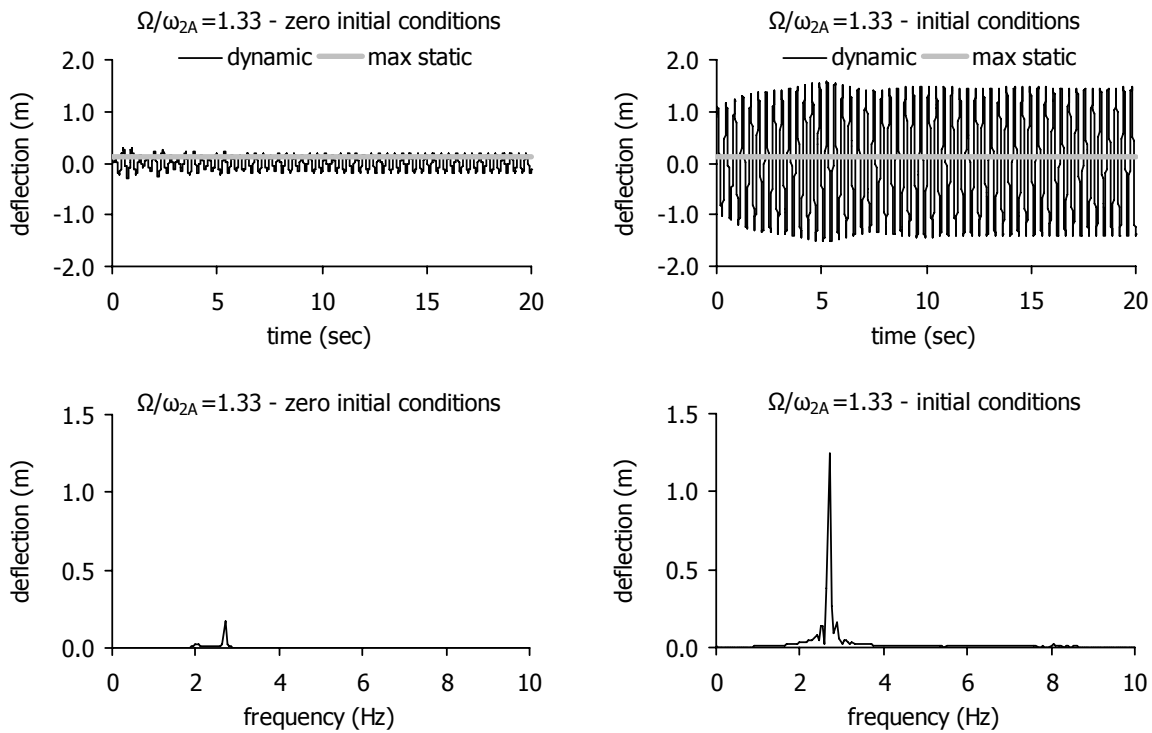


Figure 7-33: Deflection diagrams for node 458 of the cable net with rigid supports under fundamental resonance for mode 2A, for $\Omega/\omega_{2A}=1.33$ ($P_0=2\text{kN}$)

The maximum cable tension is 651kN for cable segment 121 and zero initial conditions, while taking into account initial conditions the maximum cable tension develops in cable segment 222, equal to 1706kN corresponding to $R_{dyn}=2.78$. These cable segments are illustrated in Figure 7-34. The tension diagrams for both assumptions regarding the initial conditions are shown in Figure 7-35. The different oscillation and tension amplitudes are noted, according to the assumed initial conditions. The main vibration frequency is the loading frequency, but in case zero initial conditions are considered, there is another frequency at 2.05Hz, which is almost equal to the frequency of mode 2A. For zero initial conditions the amplitude for the same frequency ratio is only 0.18m. The maximum cable tension for this frequency ratio, considering initial conditions, is 1706kN for which the ratio R_d results equal to $R_{dyn}=2.78$.

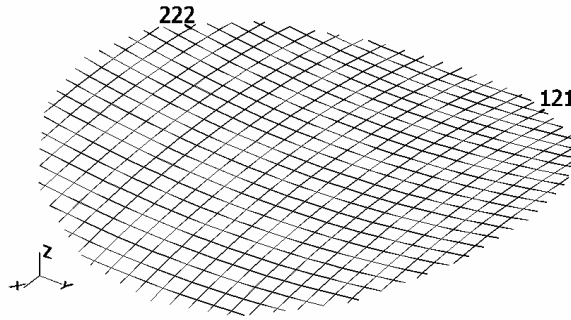


Figure 7-34: Cable segments 121 and 222 developing the maximum tension

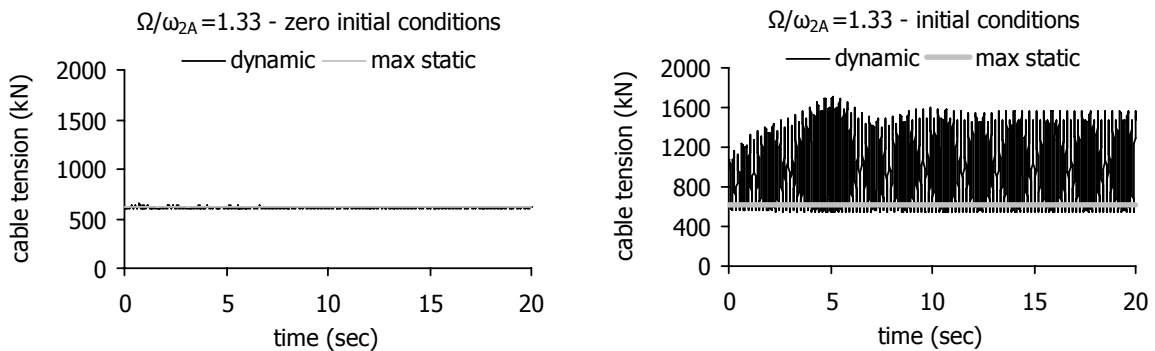


Figure 7-35: Tension diagrams for the cable net with rigid supports under fundamental resonance for mode 2A ($P_0=2\text{kN}$, $\Omega/\omega_{2A}=1.33$)

For larger frequency ratios the initial conditions do not influence the steady-state response. For example, for $\Omega/\omega_{2A}=1.34$, the steady-state response is the same with or without initial deflection and velocity, but not the transient response. In Figure 7-36 these two responses are plotted, by means of time-history diagrams of the deflection for node 458.

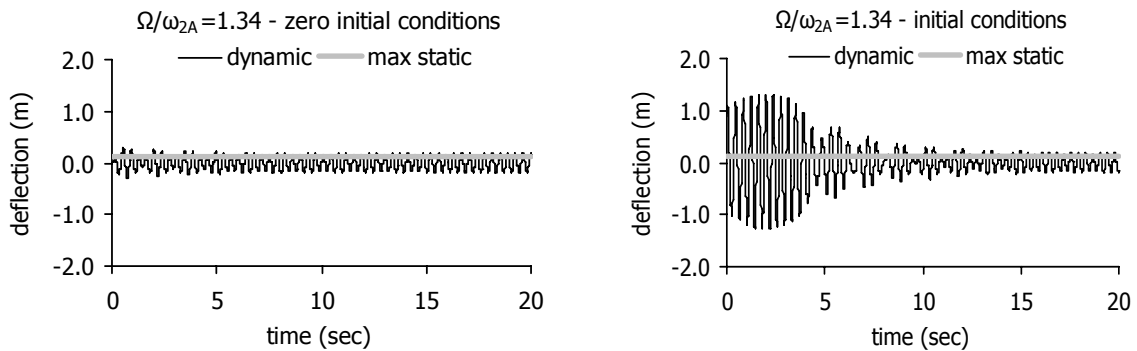


Figure 7-36: Deflection diagrams for node 458 of the cable net with rigid supports under fundamental resonance for mode 2A ($P_0=2\text{kN}$, $\Omega/\omega_{2A}=1.34$)

Considering a loading amplitude $P_0=24\text{kN}$ and loading frequency between $0.30\omega_{2A}$ and $0.60\omega_{2A}$, the steady-state response of the net is plotted in Figure 7-37. The maximum steady-state amplitude is 1.588m for $\Omega=0.47\omega_{2A}=5.96\text{sec}^{-1}$ (0.95Hz), indicating an order-three superharmonic resonance for mode 2A.

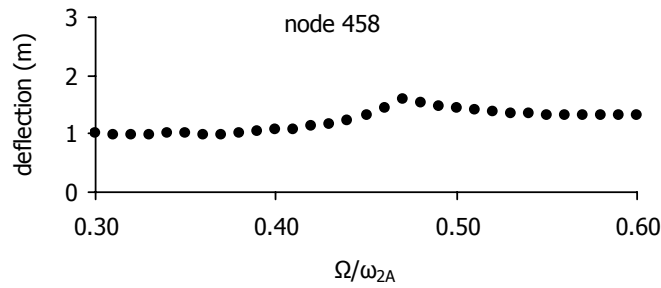


Figure 7-37: Steady-state response of the cable net with rigid supports under superharmonic resonance for mode 2A of the net ($P_0=24\text{kN}$)

The deflection diagrams of node 458 are illustrated in Figure 7-38, while the time-history diagram of the maximum cable tension is shown in Figure 7-39. The maximum oscillation amplitude for $\Omega/\omega_{2A}=0.47$ is 1.774m ($R_{\text{dyn}}=1.99$), while in the response spectrum two significant frequencies appear, one at 0.95Hz, being the loading frequency, and another one at 2.85Hz, which is close to the one of mode 2A, indicating the order-three superharmonic resonance for this mode. The maximum cable tension is 1979kN with $R_{\text{dyn}}=2.00$.

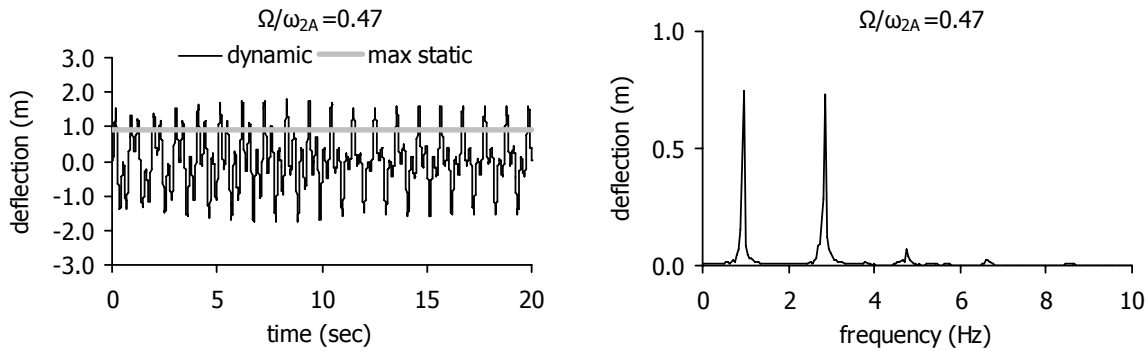


Figure 7-38: Deflection diagrams for node 458 of the cable net with rigid supports under superharmonic resonance for mode 2A ($P_0=24\text{kN}$)

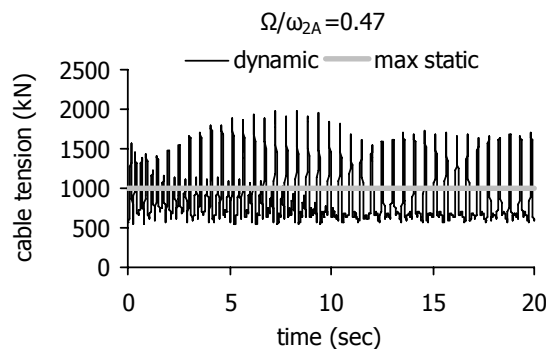


Figure 7-39: Tension diagram for the cable net with rigid supports under superharmonic resonance for mode 2A ($P_0=24\text{kN}$)

This load distribution results in smaller response with respect to the other two for the same load amplitude, but for a large range of frequency ratio Ω/ω_{2A} the initial conditions influence the response of the net, in contrast to the other two spatial load distributions. Hence, among the three spatial load distribution considerations, this case leads to the most intense bending of the response curve and thus to the highest nonlinearity.

7.5 CABLE NET WITH BOUNDARY RING

7.5.1 Eigenmodes and eigenfrequencies

For the cable net with a deformable boundary ring, the first twelve vibration modes of the system, with the corresponding natural frequencies, are shown in Figure 7-40.

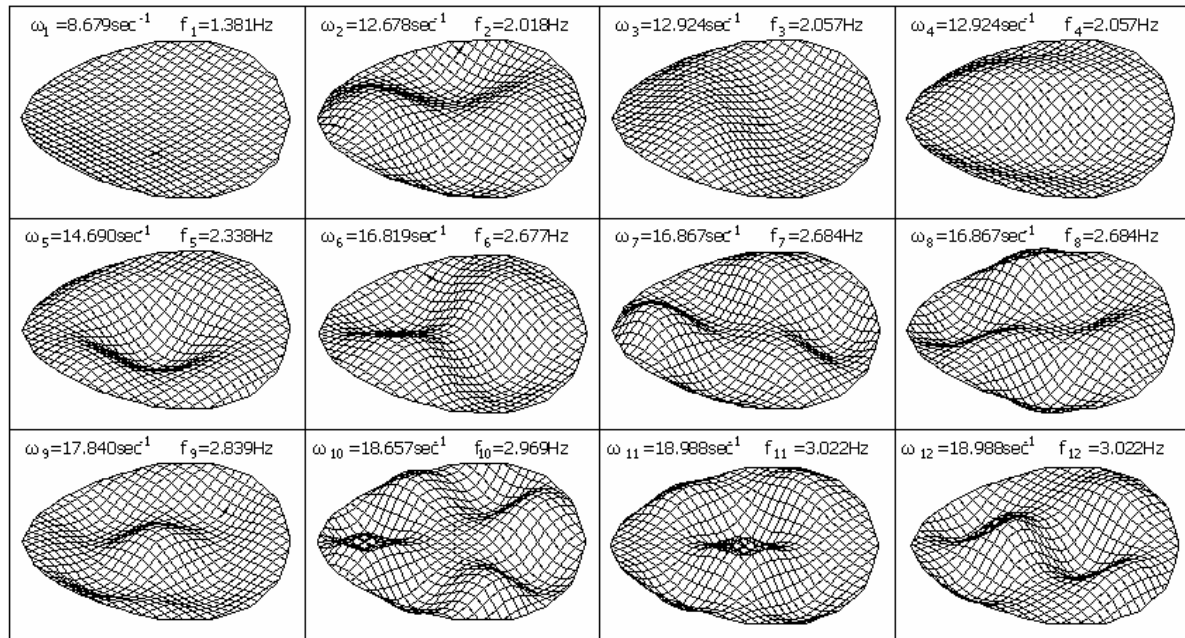


Figure 7-40: Vibration modes and natural frequencies of the cable net with deformable boundary ring

The first mode of the system is the ring's in-plane mode, the second is mode 2A, the third and fourth are modes 1A and the fifth one is mode 1S. Comparing these eigenfrequencies with the ones of the first cable net with rigid supports (Figure 7-4), it is noted that the 2A frequency remains unaltered whether the ring is taken into account or not, the 1A frequencies decrease by about 1%, while the presence of the ring increases the 1S frequency by about 6%.

7.5.2 Uniform spatial load distribution (1S) – Static response

For a uniform spatial distribution, the load-deflection diagram for node 15 as well as the variation of the maximum cable tension, are illustrated in Figure 7-41, for load amplitude up to $P=24\text{kN}$. The deformability of the ring renders the system more flexible, thus, the deflection is larger and the cable tension is smaller than the corresponding ones calculated for the cable net with fixed ends (Figure 7-5). For the two load amplitudes assumed, $P=2\text{kN}$ and $P=24\text{kN}$, the maximum static deflection at node 15 is equal to 0.105m and 1.21m, respectively. Moreover, these two loads cause maximum static cable tension equal to 667kN and 1411kN, respectively.

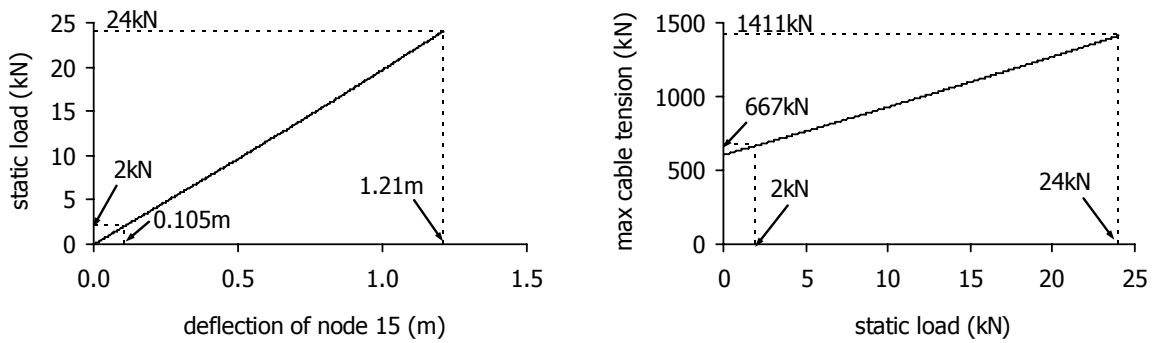


Figure 7-41: Static response of the cable net with flexible supports for uniform spatial load distribution (1S)

7.5.3 Uniform spatial load distribution (1S) – Dynamic response

For a dynamic load, $P(t)=P_0\cos(\Omega t)$, having a uniform spatial load distribution, the steady-state response amplitude of node 15 with respect to the ratio of the loading frequency over the frequency of mode 1S is given in Figure 7-42, for loading amplitude $P_0=2\text{kN}$ and loading frequency between $0.90\omega_5$ and $1.40\omega_{1S}$, where $\omega_{1S}=\omega_5=14.690\text{sec}^{-1}$ ($f_5=2.338\text{Hz}$, $T_5=0.43\text{sec}$). In the same chart, the response of the cable net with rigid supports is also plotted, for comparison reasons.

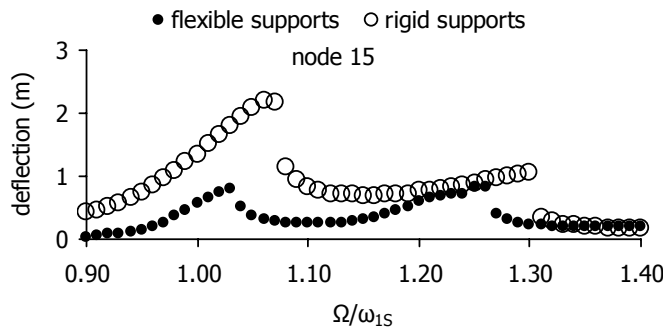


Figure 7-42: Steady-state response under fundamental resonance for mode 1S ($P_0=2\text{kN}$)

As for the cable net with rigid supports, two peaks of the response are noted, one occurring for $\Omega=1.03\omega_{1S}=15.13\text{sec}^{-1}$ (2.41Hz), corresponding to the fundamental resonance for the mode 1S, and one for $\Omega=1.26\omega_{1S}=18.51\text{sec}^{-1}$ (2.95Hz), for which a fundamental resonance for the ninth mode occurs, which is also a symmetric one (Figure 7-40). It should be mentioned that, in contrast to the static response, smaller dynamic deflection is observed for the cable net with the boundary ring, although this cable net is more flexible than the one with fixed cable ends. This is explained next.

For frequency ratio $\Omega/\omega_{1S}=1.03$ the deflection diagrams of node 15 are illustrated in Figure 7-43 and the time-history diagram of the maximum tension in Figure 7-44. The maximum net deflection is 0.814m ($R_{\text{dyn}}=7.75$), being only 37% of the one calculated for the cable net with rigid cable ends (Figure 7-9). The response spectrum shows that the main oscillation frequency is 2.42Hz, which is the loading frequency and close to the frequency of mode 1S. The maximum cable tension, developed in cable segment 40 (Figure 7-6), is 1031kN ($R_{\text{dyn}}=1.55$), which is 43% of the corresponding one for the cable net with rigid cable ends (Figure 7-11).

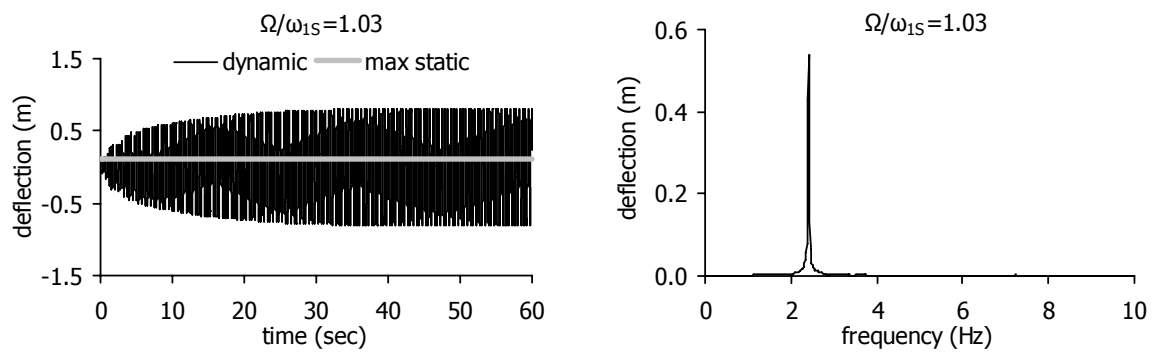


Figure 7-43: Deflection diagrams for node 15 of the cable net with flexible supports under fundamental resonance for mode 1S ($P_0=2\text{kN}$)

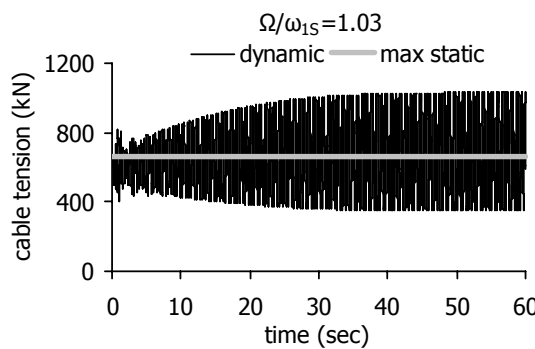


Figure 7-44: Tension diagram of the cable net with flexible supports under fundamental resonance for mode 1S ($P_0=2\text{kN}$)

Two more time-history diagrams are plotted; one for the highest ring node 563, with coordinates $(0, -L/2)$ (Figure 7-45) and one for the lowest ring node 318, with coordinates $(L/2, 0)$ (Figure 7-46). In the response spectra diagrams of the horizontal displacement of the ring nodes, the highest peak is for the loading frequency, but a much smaller one, for $f_1=1.38\text{Hz}$ which is the frequency of the ring in-plane mode, indicates that the symmetric loading activates also the symmetric in-plane ring mode, even though there is no internal resonance between the two first symmetric modes.

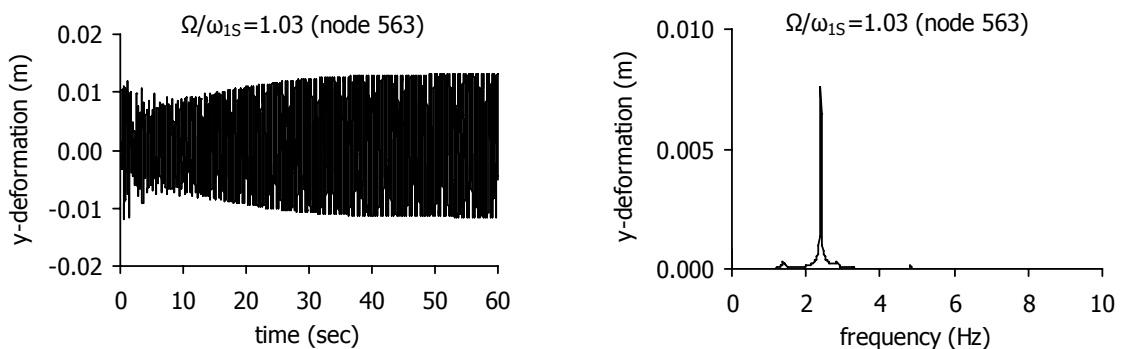


Figure 7-45: Response of the ring's highest node 563 under fundamental resonance for mode 1S

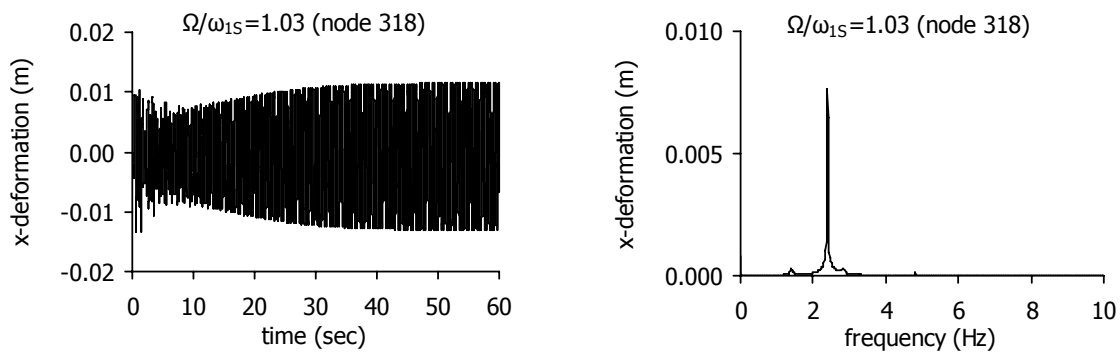


Figure 7-46: Response of the ring's lowest node 318 under fundamental resonance for mode 1S

A detail of the above time-history diagram of the net deflection is shown in Figure 7-47, while for the ring's nodes in Figure 7-48, zooming at the last second of the analysis. Observing the diagrams, it can be explained why the ring oscillation influences favourably the system, by decreasing the net vibration amplitude and the cable tension. When the net deflection is positive (upwards), the horizontal displacements of nodes 563 and 318 are also positive, which means that the highest nodes of the ring approach each other, while the lowest ones are moving apart. Both motions of the ring generate a net deflection downwards, as illustrated in Figure 7-49. Hence, an in-plane vibration of the ring of several centimetres may cause a vertical oscillation to the net of opposite sign with respect to the one produced by the external load, reducing the absolute magnitude of the net deflection and the cable tension.

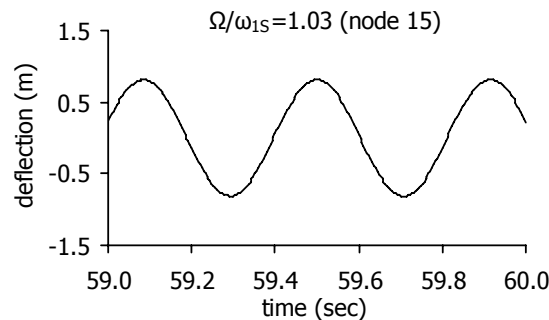


Figure 7-47: Detail of the deflection time-history diagram for the central node of the net under fundamental resonance for mode 1S

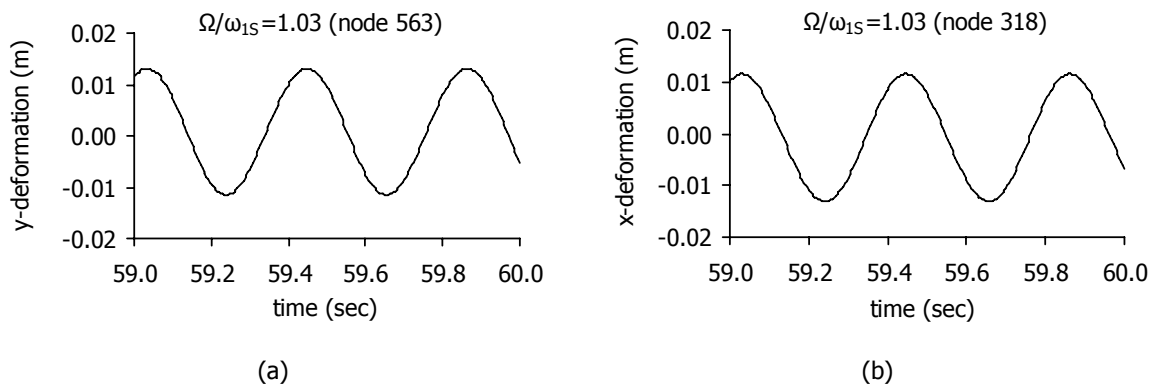


Figure 7-48: Detail of the horizontal displacement time-history diagrams for the (a) highest node of the ring, (b) lowest node of the ring under fundamental resonance for mode 1S

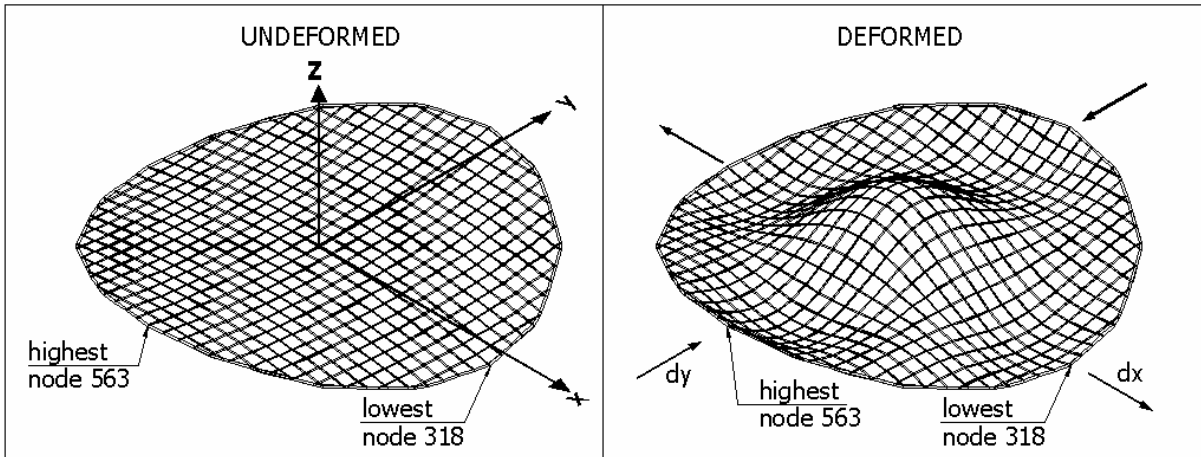


Figure 7-49: Deformation of the ring and the net under fundamental resonance for mode 1S

For loading amplitude $P_0=24\text{kN}$ and loading frequency between $0.30\omega_{1S}$ and $0.60\omega_{1S}$, where $\omega_{1S}=\omega_5=14.690\text{sec}^{-1}$, the steady-state response is shown in Figure 7-50, for both cable nets, with rigid or flexible supports. In case the boundary ring is considered, the response is larger. The maximum steady-state amplitude is calculated for loading frequency $\Omega=0.53\omega_{1S}=7.786\text{sec}^{-1}$ (1.24Hz).

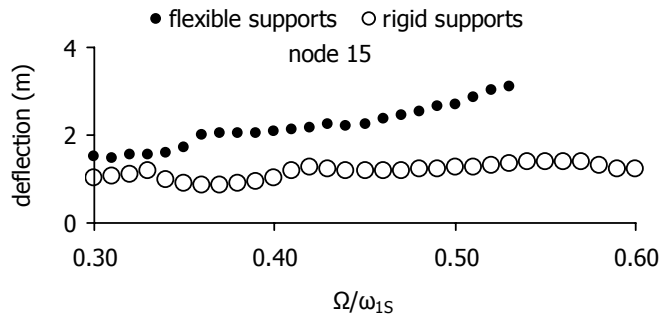


Figure 7-50: Steady-state response under superharmonic resonance for mode 1S ($P_0=24\text{kN}$)

For frequency ratios larger than $\Omega/\omega_{1S}=0.53$, cable tensile failure occurs during the transient vibration of the first steps of the numerical analysis. The response of the system for this frequency ratio is plotted by means of deflection diagrams of node 15 (Figure 7-51), time-history diagrams of the maximum cable tension (Figure 7-52), and diagrams of the horizontal displacement for the ring's highest node 563 (Figure 7-53) and lowest one 318 (Figure 7-54).

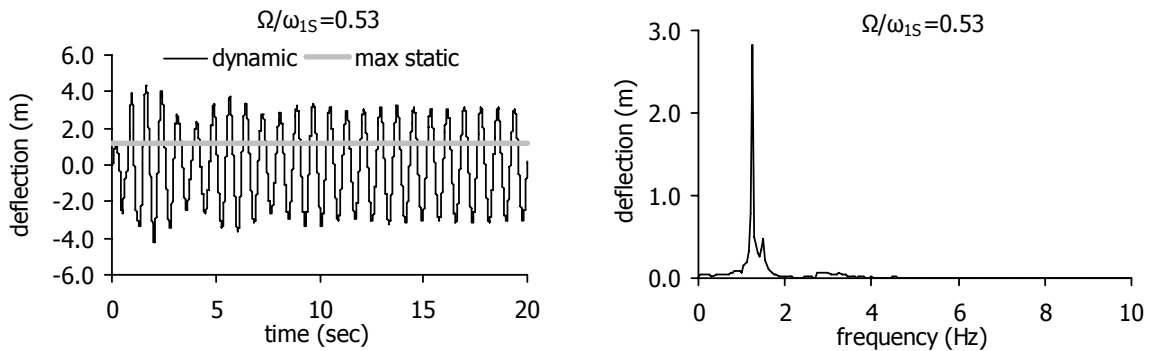


Figure 7-51: Deflection diagrams for node 15 of the cable net with flexible supports under superharmonic resonance for mode 1S ($P_0=24\text{kN}$)

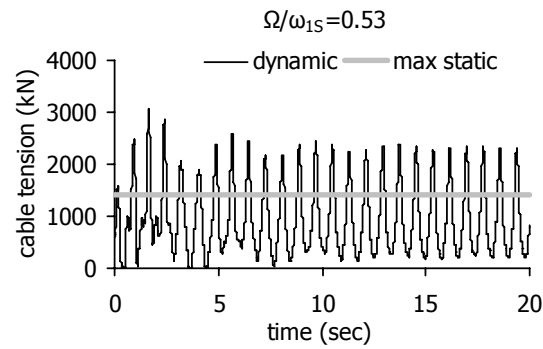


Figure 7-52: Tension diagram for the cable net with flexible supports under superharmonic resonance for mode 1S ($P_0=24\text{kN}$)

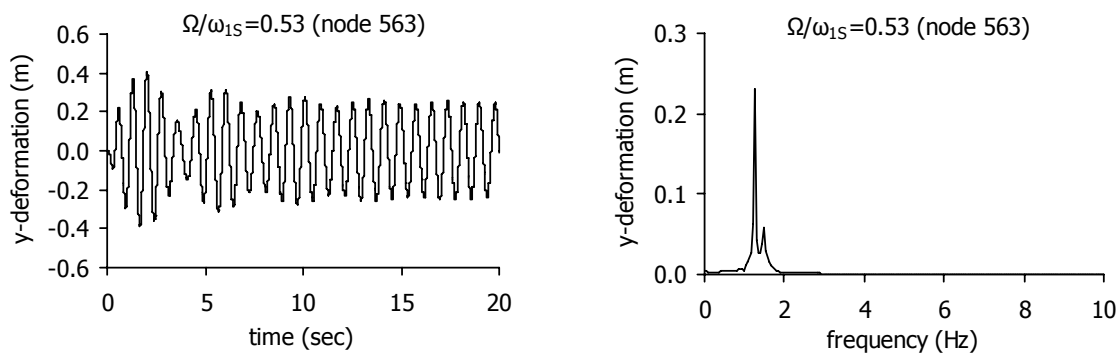


Figure 7-53: Response of the ring's highest node 563 under superharmonic resonance for mode 1S

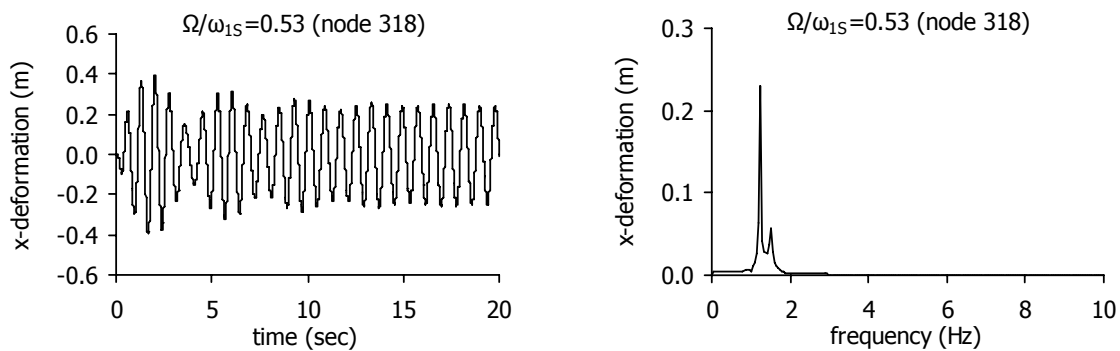


Figure 7-54: Response of the ring's lowest node 318 under superharmonic resonance for mode 1S

Both ring and net oscillate with the loading frequency, which is close to the frequency of the first in-plane mode of the ring (1.381Hz). Thus, for larger loading frequencies, the cable failure occurs due to the fundamental resonance for the first mode of the system. Zooming at the last second of the analysis, a detail of the time-history diagrams is drawn again for the net deflection in Figure 7-55, and for the ring's nodes in Figure 7-56. In this case, when the net deflection is negative (downwards), the horizontal displacement of nodes 563 and 318 are positive. The highest nodes approach each other, while the lowest ones are moving apart. Both motions generate a net deflection downwards, reinforcing the deflection of the net.

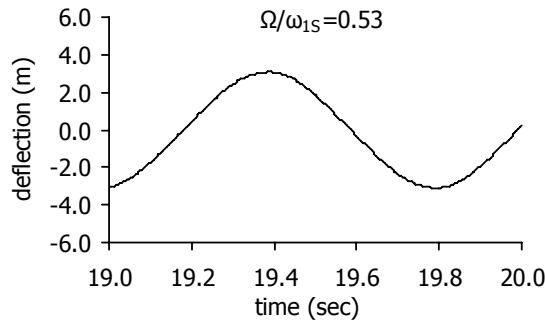


Figure 7-55: Detail of the deflection time-history diagram for the central node of the net under superharmonic resonance for mode 1S

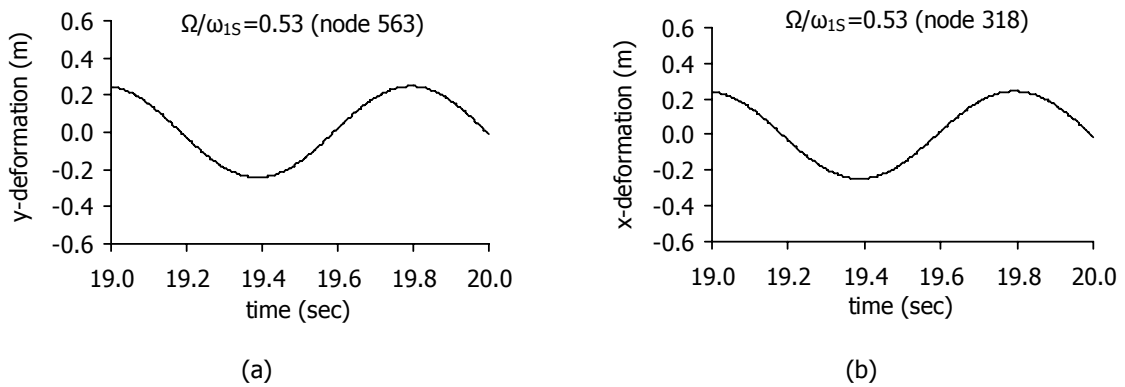


Figure 7-56: Detail of the horizontal displacement time-history diagrams for the (a) highest and (b) lowest node of the ring under superharmonic resonance for mode 1S

7.5.4 Antisymmetric spatial load distribution (1A) – Static response

For a load distribution signed as mode 1A, the load-deflection diagram for node 202 as well as the variation of the maximum cable tension for nodal load up to $P=24\text{kN}$ are shown in Figure 7-57. For $P=2\text{kN}$ and $P=24\text{kN}$ the maximum deflection calculated for node 202 is 0.10m and 1.02m , respectively, while the maximum cable tension is 659kN and 1336kN , respectively, being slightly different with respect to the ones for the cable net with rigid supports.

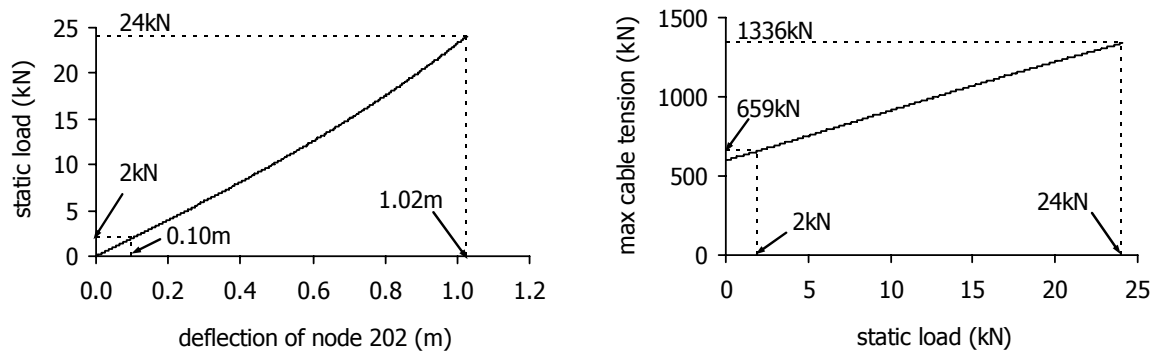


Figure 7-57: Static response of the cable net with flexible supports for antisymmetric spatial load distribution (1A)

7.5.5 Antisymmetric spatial load distribution (1A) – Dynamic response

The dynamic response of the cable net with boundary ring, subjected to a dynamic load $P(t)=P_0\cos(\Omega t)$ with a spatial load distribution signed according to mode 1A does not differ

significantly from the one of the net with fixed cable ends, meaning that the ring does not influence the response of the net for this load distribution. The steady-state response amplitude of node 202 with respect to the ratio of the loading frequency over the frequency of mode 1A, for both systems, is shown in Figure 7-58, where two charts are plotted: one for load amplitude $P_0=2\text{kN}$ and fundamental resonance for mode 1A, meaning that the frequency ratio varies between $\Omega/\omega_{1A}=0.90$ and $\Omega/\omega_{1A}=1.40$, where $\omega_{1A}=\omega_3=\omega_4=12.924\text{sec}^{-1}$, and one for $P_0=24\text{kN}$ and frequency ratio between $\Omega/\omega_{1A}=0.30$ and $\Omega/\omega_{1A}=0.60$, leading to superharmonic resonance for the same mode.

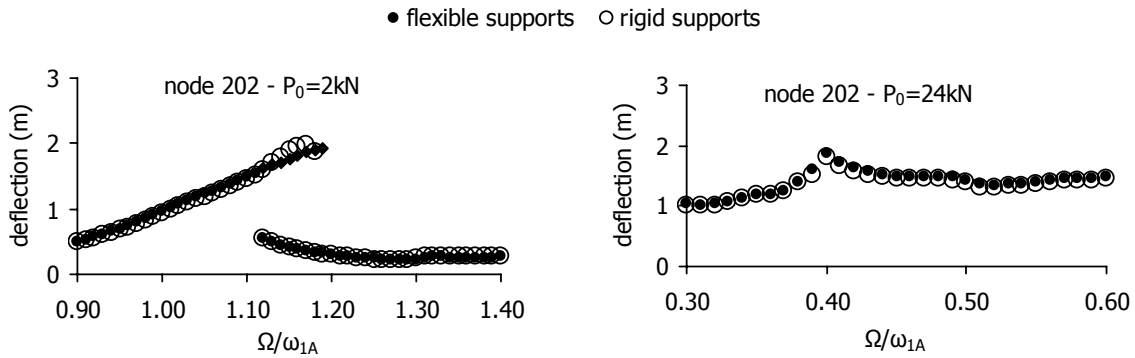


Figure 7-58: Steady-state response under fundamental and superharmonic resonance for mode 1A

7.5.6 Antisymmetric spatial load distribution (2A) – Static response

For a static load up to $P=24\text{kN}$, having a spatial distribution signed according mode 2A, the load-deflection diagram for node 458 as well as the variation of the maximum cable tension are plotted in Figure 7-59. For $P=2\text{kN}$ and $P=24\text{kN}$ the maximum deflection calculated for node 458 is 0.11m and 0.897m , respectively, while the maximum cable tension is 608kN and 986kN , respectively. The difference with the corresponding magnitudes of the cable net with rigid supports is negligible.

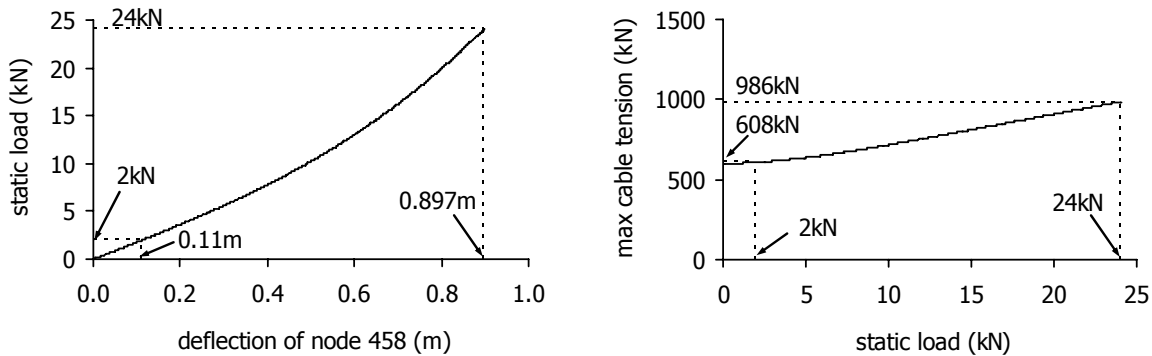


Figure 7-59: Static response of the cable net with flexible supports for antisymmetric spatial load distribution (2A)

7.5.7 Antisymmetric spatial load distribution (2A) – Dynamic response

In case the dynamic load $P(t)=P_0\cos(\Omega t)$ has spatial load distribution signed according to mode 2A, the ring does not influence the response of the net. The steady-state response amplitude of node 458 with respect to the ratio of the loading frequency over the frequency of mode 2A, is plotted in Figure 7-60 for both systems: (i) for load amplitude $P_0=2\text{kN}$ and frequency ratio between $\Omega/\omega_{2A}=0.90$ and $\Omega/\omega_{2A}=1.40$, where $\omega_{2A}=\omega_2=12.679\text{sec}^{-1}$, accounting for fundamental resonance for mode 2A, and (ii) for $P_0=24\text{kN}$ and frequency ratio between $\Omega/\omega_{2A}=0.30$ and $\Omega/\omega_{2A}=0.60$, concerning the superharmonic resonance for the same mode.

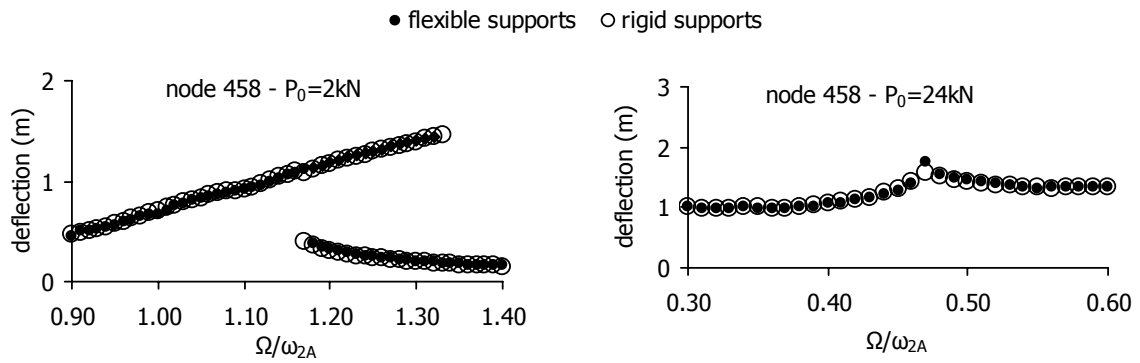


Figure 7-60: Steady-state response under fundamental and superharmonic resonance for mode 2A

7.6 PARAMETRIC ANALYSES

7.6.1 Influence of the initial cable stress

In the example presented in section 7.2, the initial strain assumed causes an initial cable stress equal to 19% of the yield stress. Changing the initial pretension and the cable cross-sectional area, but keeping the sag-to-span ratio equal to 1/20 as well as all other parameters of section 7.2, the influence of the initial cable stress on the nonlinearity of the dynamic behaviour is studied. Considering cable nets that approximate realistic structures, two more cases are studied. In the first one, the cables have diameter $D=80\text{mm}$, initial pretension $N_0=800\text{kN}$, corresponding to an initial cable stress equal to 10% of the yield stress, while in the second one, the cable diameter is $D=40\text{mm}$, and the initial pretension $N_0=600\text{kN}$, corresponding to 30% of the yield stress. The natural frequencies of the cable nets for the first symmetric mode are listed in Table 7-1. The load amplitude is chosen appropriately to cause nonlinear phenomena, without cable tensile failure.

Table 7-1: Characteristics and frequencies of the cable nets for the first symmetric mode ω_{1S}

D [mm]	N_0 [kN]	σ_y [MPa]	$N_0/(A\sigma_y)$	λ^2	ω_{1S} [sec ⁻¹]	f_{1S} [Hz]
80	800	1570	0.10	2.59	11.422	1.818
40	600	1570	0.30	0.86	15.221	2.423

The steady-state response of both systems for uniform spatial load distribution and loading frequencies close to the frequency of mode 1S is shown in Figure 7-61, accounting for fundamental resonance.

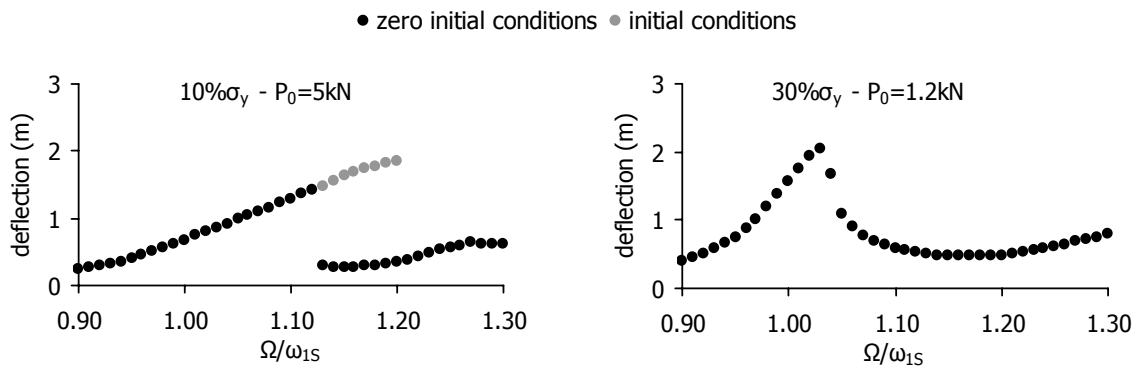


Figure 7-61: Steady-state response of the cable nets with initial cable stress $10\%\sigma_y$ and $30\%\sigma_y$ under fundamental resonance for mode 1S

It is noted that small levels of initial cable stress lead smaller eigenfrequencies and to intense nonlinear phenomena, such as jump phenomena and dependence on the initial conditions, while large initial cable stresses, rendering the system stiffer, lead to an almost linear behaviour. However, the maximum steady-state amplitude is observed in both cases for frequency ratio larger than 1, meaning that even for large values of initial stress the bending of the response curve characterises the dynamic behaviour of the cable net. Fundamental resonances for the second symmetric mode occur for both cable nets.

For loading frequencies smaller than the frequency of mode 1S (Figure 7-62), superharmonic resonances occur for the system with low levels of initial cable stress, as explained in section 7.4.3, while for high levels of initial cable stress the peaks observed in the diagram are very small. This investigation leads to the conclusion that high levels of pretension render the system stiff enough to respond in an almost linear way.

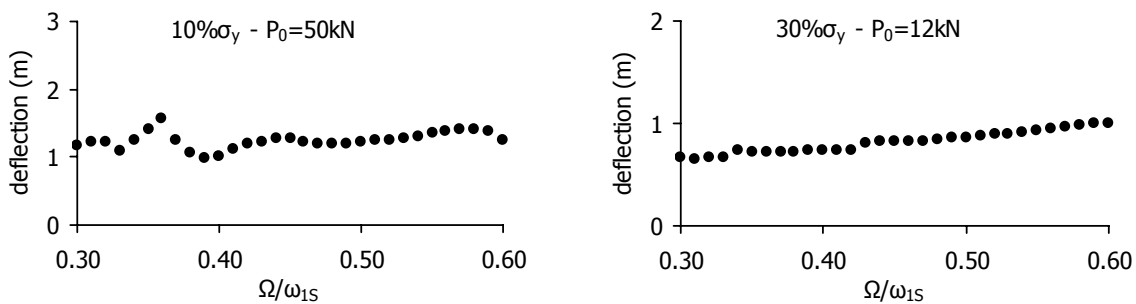


Figure 7-62: Steady-state response of the cable nets with initial cable stress $10\%\sigma_y$ and $30\%\sigma_y$, under superharmonic resonance for mode 1S

7.6.2 Influence of the sag-to-span ratio

In order to investigate the influence of the sag-to-span ratio on the nonlinearity of the dynamic response of such systems, two more cable nets are considered with $f/L=1/35$ and $f/L=1/10$, representing a shallow and a deep cable net, respectively. The number of cables in each direction, the diameter of the circular plan view L , the cable diameter D , cross-sectional area A and unit weight ρ , the Young modulus E , the initial pretension N_0 , and the damping ratio ζ remain as given in section 7.2. The natural frequencies of the cable nets for the first symmetric mode are listed in Table 7-2.

Table 7-2: Characteristics and frequencies of the cable nets for the first symmetric mode ω_{1S}

f/L	λ^2	ω_{1S} [sec ⁻¹]	f_{1S} [Hz]
1/35	0.44	9.902	1.576
1/10	5.40	17.061	2.715

For a uniform harmonic load with amplitude that is large enough to cause resonant phenomena without cable failure, and a loading frequency close to the frequency of the first symmetric mode, the response diagrams of the central nodes of these two cable nets are illustrated in Figure 7-63. Comparing these diagrams with the one of Figure 7-8 it is noted that as the sag-to-span ratio decreases, the eigenfrequency decreases and the system becomes more flexible leading to an intense bending of the response curve. As a consequence, for small values of the sag-to-span ratio, the initial conditions play an important role in the steady-state amplitude. Thus, for the cable net with $f/L=1/35$, for a wide range of frequency ratios, two responses are expected, depending on the initial conditions, while for $f/L=1/20$ the corresponding range of the frequency ratio is limited, as shown in Figure 7-8 and explained in section 7.4.3. For the cable net with $f/L=1/10$ the response is more linear, with a slight bending of the curve and no dependence on the initial conditions, while the fundamental

resonance for the second symmetric mode causes larger oscillation amplitudes than the ones corresponding to the fundamental resonance for mode 1S.

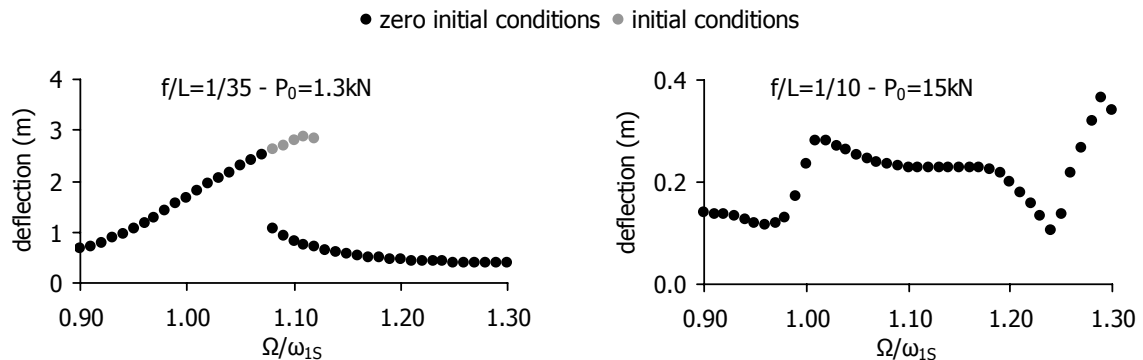


Figure 7-63: Steady-state response of the cable nets with sag-to-span ratio $f/L=1/35$ and $f/L=1/10$ under fundamental resonance for mode 1S

Superharmonic resonances occur for both systems when the loading frequency is equal to one third or half of the frequency of mode 1S (Figure 7-64), even for the second system, which could be considered as weakly nonlinear.

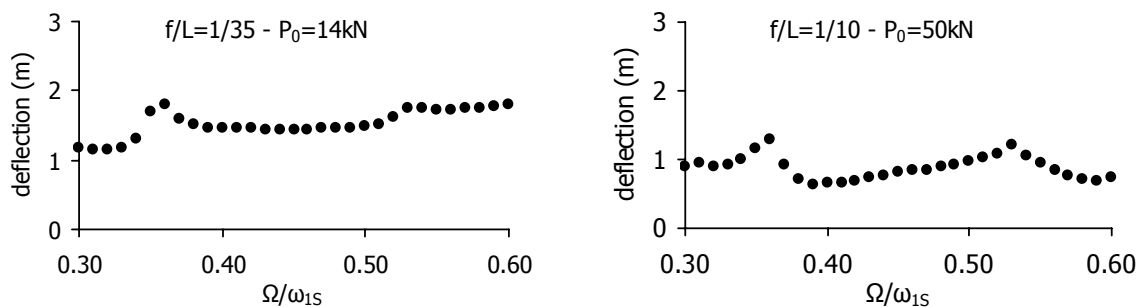


Figure 7-64: Steady-state response of the cable nets with sag-to-span ratio $f/L=1/35$ and $f/L=1/10$ under superharmonic resonance for mode 1S

7.7 SUMMARY AND CONCLUSIONS

The nonlinear dynamic response of two saddle-shaped cable net systems is studied in this chapter. The first system is a net with fixed cable ends and the second one takes into consideration the deformability of the edge ring. In order to compare the results, the systems have the same geometry, a circular plan view with diameter $L=100\text{m}$ and a sag-to-span ratio equal to $f/L=1/20$, similar to the geometry of the Peace and Friendship Stadium in Athens, Greece. The cable nets are subjected to a harmonic excitation, considering three different spatial load distributions, regarding the sign of the load, which is determined by the first symmetric and antisymmetric vibration modes of the net. The loading frequency varies, in order to trace several kinds of resonances in the response of the net, such as fundamental and superharmonic resonances. A nonlinear static analysis is also conducted, in order to compare the dynamic response with the static one.

The present investigation proves that cable networks having the shape of a hyperbolic paraboloid exhibit strongly nonlinear dynamic behaviour, in spite of their significant stiffness compared to simple cables, even for low levels of loading amplitude, which, applied statically, would lead to an almost linear behaviour. Bending of the response curve, jump phenomena, sudden drops of the response amplitude, response peaks for small loads confirm the nonlinearity of the system and the occurrence

of secondary resonances. In addition, fundamental resonance occurs for frequency ratio larger than 1, indicating the hardening nonlinear behaviour of the system. Such systems cannot be characterised as weakly nonlinear systems, even if their static response is almost linear. Their analysis should not be approached by linear or quasi-static methods, but only by nonlinear dynamic methods, such as time domain analysis, considering the geometric nonlinearity of the system. In addition, response curves should be plotted in order to detect the loading frequency for which nonlinear phenomena take place. All these phenomena occur for both shallow and deep cable nets and for medium or low levels of initial pretension. Only for high levels of initial cable stress does the response of the cable net approach the linear one.

This work also proves the sensitivity of cable nets with respect to the assumptions regarding their boundary conditions. Modelling the edge ring is indispensable, because it inserts new vibration modes, which may transform the entire behaviour of the net and modify the results with respect to the ones referring to the net with rigid supports. It is verified that the existence of the in-plane mode of the ring influences significantly the amplitude of the net oscillation for uniform spatial distribution of the load, while for antisymmetric spatial load distribution the presence of the ring does not alter the dynamic response of the net.

It is finally noted that the dynamic response of the net, regarding its oscillation amplitude and the tension developed in the cables, depends on the spatial load distribution. It is important to determine a realistic spatial distribution of dynamic loads, in order to proceed in a correct design, without either very conservative or unsafe assumptions, especially if the dynamic load is due to wind, with a pressure distribution over the roof surface depending on its inclination and the wind direction.

Part of this work has been published in [7-19].

7.8 REFERENCES

- [7-1] N. F. Morris, "Dynamic response of cable networks", *Journal of the Structural Division*, Vol. 100, No. ST10, pp. 2091-2108, 1973.
- [7-2] N. F. Morris, "Modal analysis of cable networks", *Journal of the Structural Division*, Vol. 101, No. ST1, pp. 97-108, 1975.
- [7-3] C. Birnstiel, "Analysis and design of cable structures", *Computers and Structures*, Vol. 2, pp. 817-831, 1972.
- [7-4] H. Ozdemir, "A finite element approach for cable problems", *Computers and Structures*, Vol. 15, pp. 427-437, 1979.
- [7-5] G. R. Monforton and N. M. El-Hakim, "Analysis of truss-cable structures", *Computers and Structures*, Vol. 11, pp. 327-335, 1980.
- [7-6] L. F. Geschwindner, "Nonlinear dynamic analysis by modal superposition", *Journal of the Structural Division*, Vol. 107, No. ST12, pp. 2325-2336, 1981.
- [7-7] M. Papadrakakis, "Inelastic dynamic response of cable networks", *Journal of Structural Engineering*, Vol. 109, No. 5, pp. 1139-1154, 1983.
- [7-8] S. Swaddiwudhipong, C. M. Wang, K. M. Liew and S. L. Lee, "Optimal pretensioned forces for cable networks", *Computers and Structures*, Vol. 33, No. 6, pp. 1349-1354, 1989.
- [7-9] G. D. Stefanou, E. Moossavi, S. Bishop and P. Koliopoulos, "Conjugate gradients method for calculating the response of large cable nets to static loads", *Computers and Structures*, Vol. 49, No. 5, pp. 843-848, 1993.

- [7-10] G. D. Stefanou, "Dynamic response analysis of nonlinear structures using step-by-step integration techniques", *Computers and Structures*, Vol. 57, No. 6, pp. 1063-1070, 1995.
- [7-11] G. D. Stefanou, "The response of large cable nets to general dynamic loads based on step-by-step time integration techniques", *Journal of the International Association for Shell and Spatial Structures, IASS*, Vol. 38, No. 123, pp. 53-64, 1997.
- [7-12] L. F. Geschwindner and H. H. West, "Forced vibrations of cable networks", *Journal of the Structural Division*, Vol. 106, No. ST9, pp. 1885-1898, 1980.
- [7-13] M. Lazzari, A. V. Saetta and R. V. Vitaliani, "Non-linear dynamic analysis of cable-suspended structures subjected to wind actions", *Computers and Structures*, Vol. 79, pp. 953-969, 2001.
- [7-14] I. Vassilopoulou and C. J. Gantes, "Similarity relations for nonlinear dynamic oscillations of a cable net", *Proceedings of the 1st ECCOMAS Thematic Conference on Computational Methods in Structural Dynamics and Earthquake Engineering – COMPDYN 2007*, Rethymno, Crete, Greece, abstract pp. 373, 2007.
- [7-15] I. Vassilopoulou and C. J. Gantes, "Modal transition and dynamic nonlinear response of cable nets under fundamental resonance", *Proceedings of the 8th HSTAM International Congress on Mechanics*, Patras, Greece, Vol. 2, pp. 787-794, 2007.
- [7-16] I. Vassilopoulou and C. J. Gantes, "Vibration modes and dynamic response of saddle form cable nets under harmonic excitation", *Proceedings of the Euromech Colloquium 483, Geometrically Non-linear Vibrations of Structures*, FEUP, Porto, Portugal, pp. 129-132, 2007.
- [7-17] A. K. Chopra, "Dynamics of structures, theory and applications to earthquake engineering", Prentice Hall International, Inc., U.S.A., 1995.
- [7-18] M. Majowiecki, "Tensostrutture progetto e verifica", Edizioni CREA, Italy, 1994, (in italian).
- [7-19] I. Vassilopoulou and C. J. Gantes, "Nonlinear dynamic behavior of saddle-form cable nets under uniform harmonic load", *Engineering Structures*, Vol. 33, pp. 2762-2771, 2011.

8 WIND PRESSURE DISTRIBUTION ON SADDLE-FORM ROOFS

8.1 INTRODUCTION

The two most important dynamic actions acting on structures are due to wind and earthquake, but suspended cable structures may exhibit large deformations mostly due to wind, rather than earthquake, because of their small mass. In order to analyse correctly such structures subjected to wind pressures, it is important to know the spatial distribution of these pressures over the surface of the structure, as well as the frequency spectrum and magnitude of wind velocity.

The wind pressure on a surface can be expressed as:

$$w=0.5c_p\rho V^2 \quad (8-1)$$

where ρ is the air density, V is the wind velocity at the surface altitude and c_p is the pressure coefficient, which depends on the geometry and the orientation of the surface with respect to the wind flow. The wind pressure coefficient is usually obtained experimentally. Eurocode 1, Part 1.4 [8-1], constitutes a useful guideline for wind pressures on roofs, proposing the coefficients of wind internal and external pressures for flat, duopitch, monopitch, hipped and vaulted rectangular roofs and domes, considering also eventual wall openings. Each surface is divided in zones according to their location as well as their orientation with respect to the wind direction and the external pressure coefficients are provided, which include local coefficients and global ones, named as overall coefficients. Local coefficients, defined as $c_{pe,1}$, refer to loaded areas of $A=1\text{m}^2$ or less e.g. for the design of small elements and fixings, while for loaded areas larger than $A=10\text{m}^2$, overall coefficients, denoted as $c_{pe,10}$, can be used. For $1\text{m}^2 < A < 10\text{m}^2$, the pressure coefficient is calculated as:

$$c_{pe} = c_{pe,1} - (c_{pe,1} - c_{pe,10}) \log_{10} A \quad (8-2)$$

However, Eurocode 1 does not cover roofs with circular plan view or with unusual shapes, such as hyperbolic paraboloids. Thus, cable nets having the shape of hyperbolic paraboloids cannot be designed for wind according to Eurocode 1. For these structures wind tunnel experiments are recommended as the only reliable technique for calculating wind pressures.

Results from wind tunnel experiments can be found in the literature, concerning simple suspended cables ([8-2], [8-3]), unique geometries of actual design projects, such as stadium roofs ([8-4] – [8-7]), hangars [8-8], or roofs with common shapes ([8-9] – [8-19]). Few publications refer to roofs with hyperbolic paraboloid surface. Tabarrok and Qin in [8-20] and [8-21] proposed an approximate procedure to estimate the wind pressure distribution upon saddle roofs, by assuming the wind pressure coefficient to be equal to the minus cosine of the angle α between the wind direction and the outward normal to the element surface.

$$c_p = -\cos\alpha \quad (8-3)$$

This model gives zero pressures on horizontal surfaces ($\alpha=90^\circ$), positive values (wind pressure) on windward surfaces ($\cos\alpha < 0$) and negative values (wind suction) on leeward surfaces ($\cos\alpha > 0$). However, this approach has not been proved experimentally and cannot be considered as accurate. A wind tunnel study of cable roofs was described in [8-22], where the Calgary Olympic Coliseum in Canada was used as the prototype. In this study, the frequency and damping ratios were measured, and found to be dependent on the area of lateral openings. The maximum deflection of the net was also reported, but no pressure coefficients were given. Buchholdt [8-23] referred to a wind tunnel study carried out by Beutler [8-24], as the most comprehensive one and he reported some pressure distribution diagrams for a rhomboid saddle-form roof with rectilinear or curvilinear boundaries and for different directions of the wind. Buchholdt also gave a diagram of the pressure coefficient for an open saddle-shaped cable roof, with circular plan view, very similar to the ones under investigation in this work. Wind tunnel test results were also summarised in [8-25] – [8-27] referring to saddle-shaped suspended roofs of rhomboid plan view. Rizzo et al. in ([8-28] – [8-30]) referred to wind tunnel experiments on tension roofs of hyperbolic paraboloid shape with rectangular, square and circular plan view. Although several geometries were considered, they only presented diagrams with the wind pressure coefficients of roofs with a square plan view. In [8-31] though, several results were presented regarding all three shapes of plans.

This chapter includes an attempt to compare the very few reported experimental data offered by wind tunnel tests and the proposed pressure coefficients, which are recommended by Eurocode 1 for similar shapes. Several simplifying assumptions are made, in order to apply these recommendations on a surface of a hyperbolic paraboloid. Firstly, circular flat roofs are considered confirming that the pressure coefficients given by Eurocode 1 for rectangular roofs can be applied also for circular ones. Secondly, the comparison between the wind tunnel results for a vaulted roof and the coefficients proposed by Eurocode 1 are discussed. Subsequently, the wind tunnel results of hyperbolic paraboloid surfaces are compared with Eurocode 1, using the pressure coefficients for duopitch and vaulted roofs. Finally, evaluating the conclusions of the above comparisons, a spatial distribution of the wind pressure upon saddle-form cable nets is proposed, which will be used next for an investigation of their dynamic behaviour under wind loads.

8.2 CIRCULAR FLAT ROOFS

8.2.1 Wind tunnel experiment

Stefanou in [8-17] gave a wind pressure diagram on a circular roof, but no further information was provided about the dimensions of this roof, the height of the building, or whether it referred to a closed building or to a structure with lateral openings. More information is available, instead, from the wind tunnel test of circular flat roofs, reported in [8-19]. The geometry of the model used in the experiment is shown in Figure 8-1a. It represents a cylindrical building without wall openings. The diameter D of the model was 267mm and the height-to-span ratio H/D varied between 1/16 and

16/16. The wind pressure coefficient was determined with respect to the velocity pressure at the roof height H. A diagram of the mean fluctuating wind pressure coefficient is illustrated in Figure 8-1b.

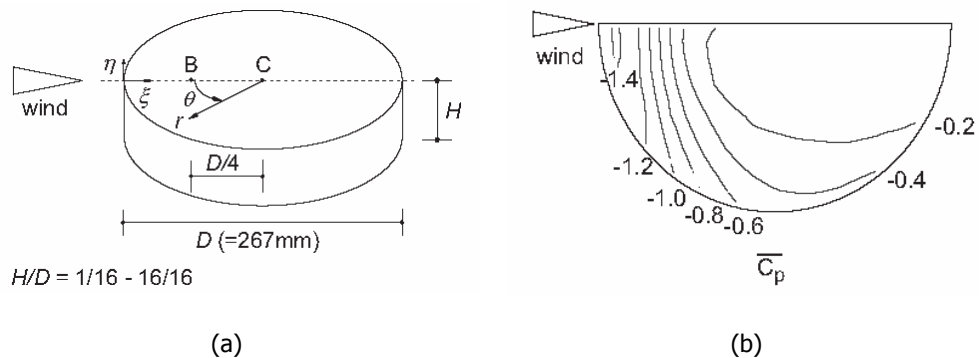


Figure 8-1: (a) Geometry of the wind tunnel circular flat roof model, (b) Pressure coefficient diagram for $H/D=4/16$, (from [8-19])

8.2.2 Comparison with Eurocode 1

Eurocode 1 provides the pressure coefficients for flat rectangular roofs with parapets, sharp, curved or mansard eaves. In the case of the circular building described in section 8.2.1 the eaves are sharp. The surface is divided in zones according to the dimensions and the height of the building (Figure 8-2).

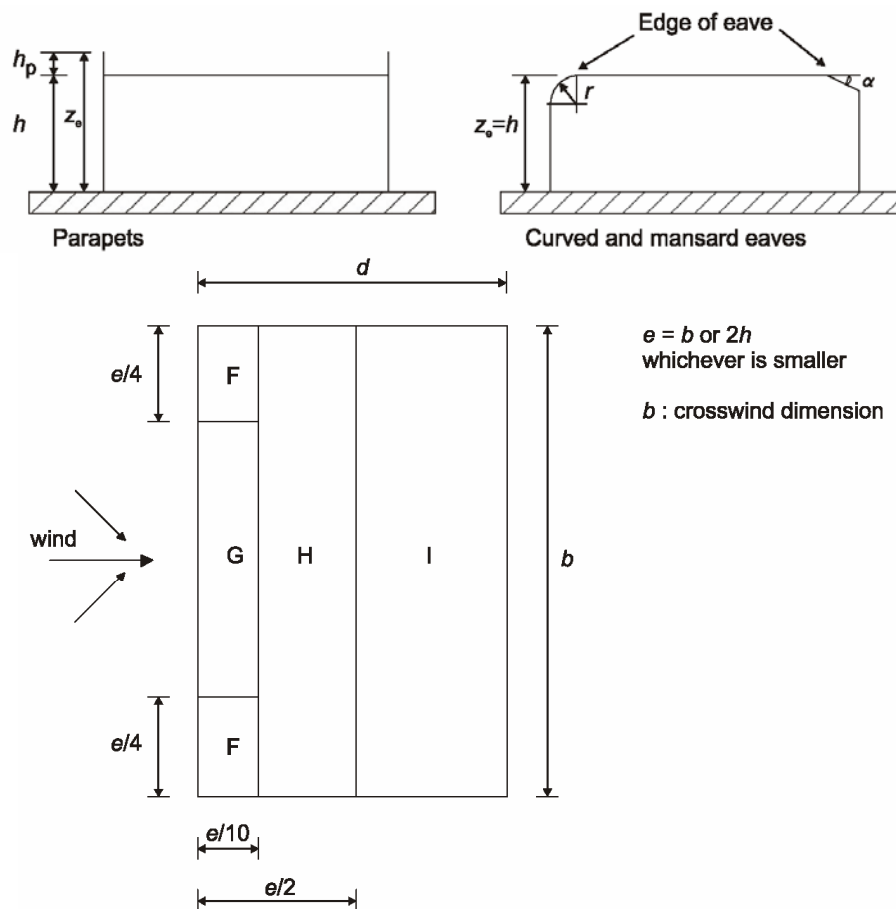


Figure 8-2: Key for flat roofs (from [8-1])

Values for the pressure coefficients $c_{pe,10}$, which may be used for the overall loaded structure, are listed for each zone of the surface in Table 8-1. The positive values correspond to wind pressure and the negative ones to wind suction. Applying these coefficients to a circular roof inscribed in a rectangular flat roof, taking into account the regions defined in Figure 8-2, the corresponding diagram of the pressure coefficients will be as shown in Figure 8-3, which is very close to the diagram of Figure 8-1b, if the negative value of region I is considered. Thus, the methodology proposed by Eurocode 1 can be adopted for circular flat roofs.

Table 8-1: External pressure coefficient for flat roofs (from [8-1])

Roof type	Zone			
	F	G	H	I
	$c_{pe,10}$	$c_{pe,10}$	$c_{pe,10}$	$c_{pe,10}$
Sharp eaves	-1.8	-1.2	-0.7	+0.2
				-0.2

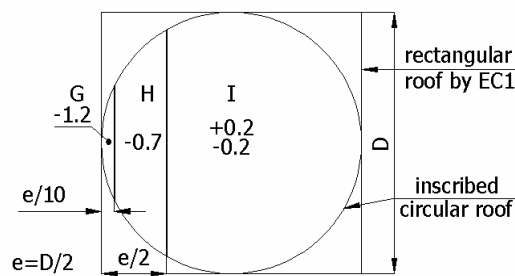


Figure 8-3: Pressure coefficient diagram for $H/D=4/16$ according to Eurocode 1

8.3 VAULTED ROOFS

A comparison between the coefficients suggested by Eurocode 1 for vaulted or curved roofs and the ones obtained by wind tunnel experiments was discussed in [8-16]. The models tested in the wind tunnel had rise/width ratios (r/d) from 0.05 to 0.5 and wall height/width ratios (h/d) from 0.06 to 1.0. That study also included a range of building length/width (L/d) ratios from 1 to 10 in order to study the effect of two-dimensional flow at $L/d=10$ and three-dimensional flow at $L/d=1$. Figure 8-4 shows a schematic representation of the model used for the wind tunnel test. Averaged pressure coefficients were obtained for each of the zones defined in Figure 8-5. The authors concluded that the suggested pressure coefficients by Eurocode 1 (Figure 8-6) do not match with the experimental results in all cases considered and they proposed some amendments in the diagram of the recommended coefficients. The modified pressure diagram proposed by the authors is illustrated in Figure 8-7.

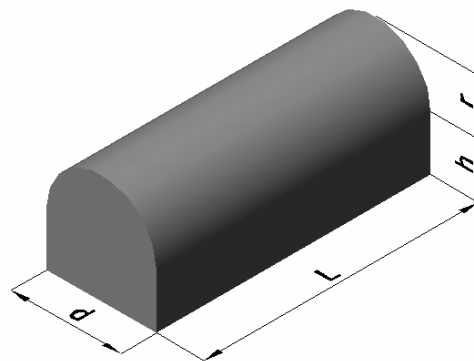


Figure 8-4: Geometry of the wind tunnel vaulted roof model [8-16]

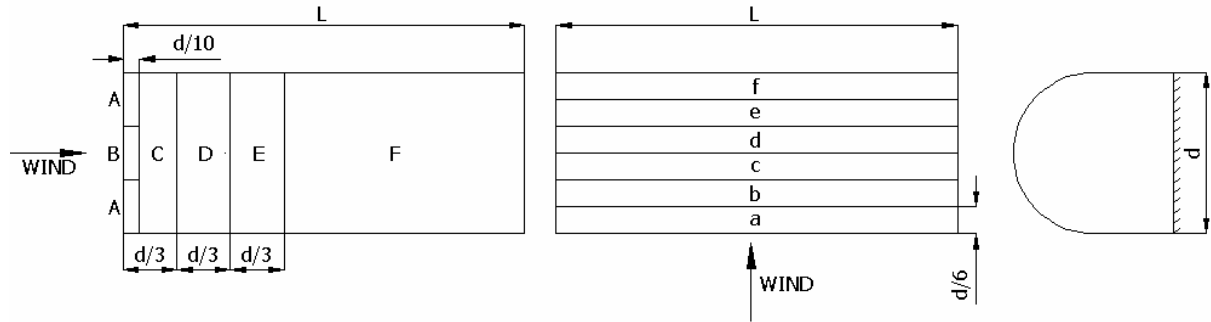


Figure 8-5: Definition sketch with key to loaded areas (from [8-16])

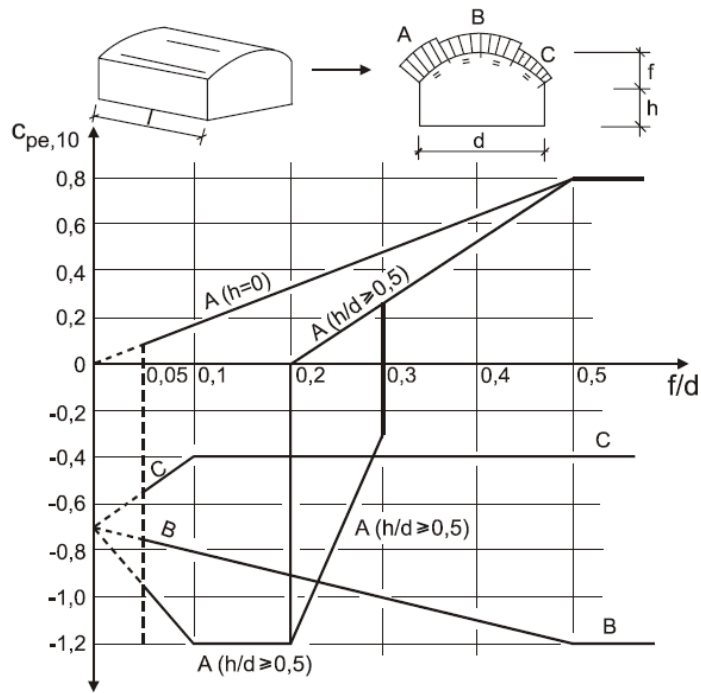


Figure 8-6: External pressure coefficients $c_{pe,10}$ for vaulted roofs with rectangular base according to Eurocode 1, (from [8-1])

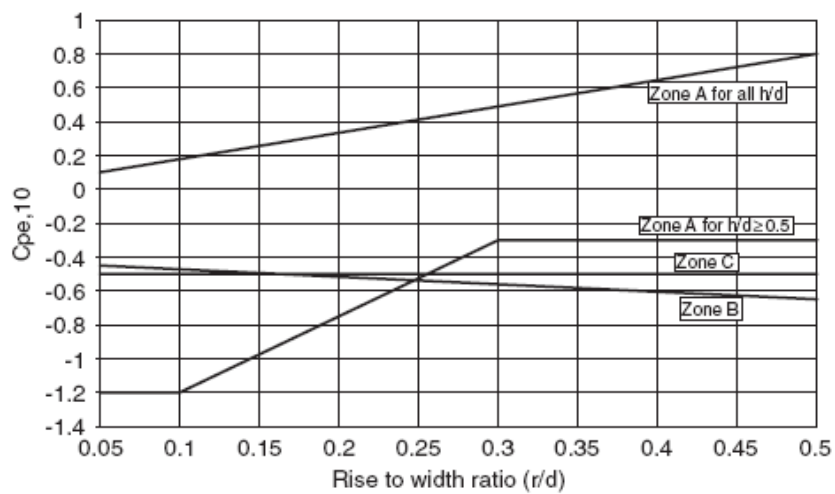


Figure 8-7: Proposed revision to Eurocode 1 diagram for pressure coefficients on vaulted roofs, (from [8-16])

Eurocode 1 does not give any guidance for wind blowing onto the eaves of vaulted roofed buildings, but the authors in [8-16] proposed that, for the purposes of codification, the data for duopitch roofs may approximate wind pressures, assuming that the effective pitch angle α of the vaulted roofs is taken as $\alpha = \arctan(2f/d)$. A comparison between the experimental data and those referred to Eurocode 1 is plotted in Figure 8-8.

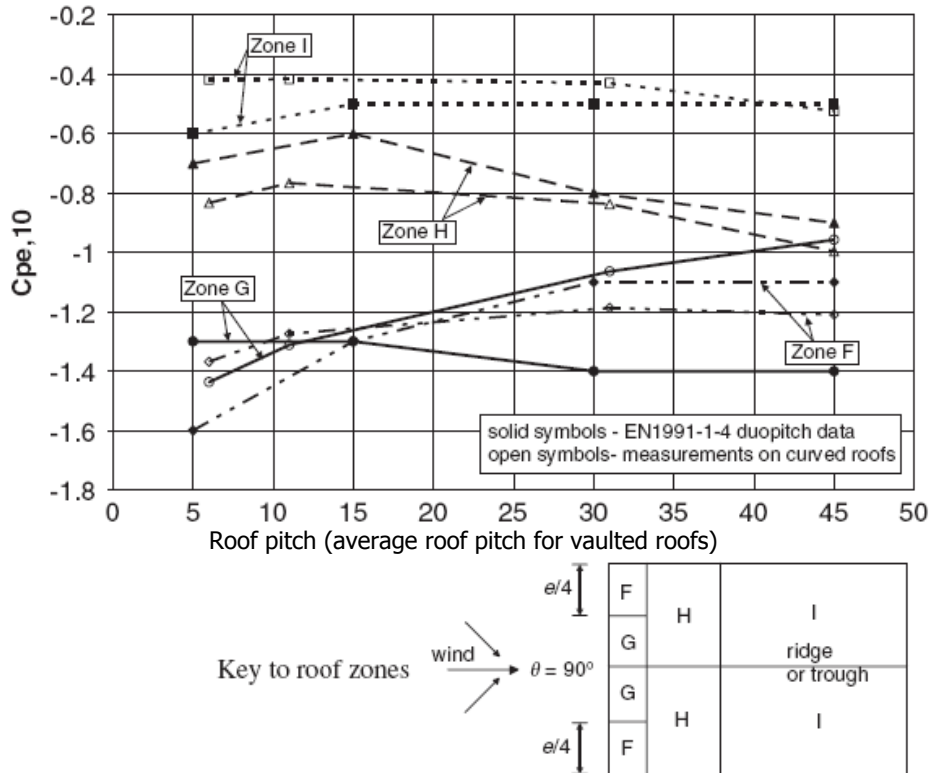


Figure 8-8: Comparison between vaulted roof measurements and duopitch data for wind direction 90° (from [8-16])

8.4 SADDLE-FORM CANOPY

8.4.1 Wind tunnel experiment

Buchholdt [8-23] gave some wind tunnel results for a cable net, having the surface of a hyperbolic paraboloid, with 100% wall openings. The model had a circular plan view of diameter $L=120\text{m}$ (Figure 8-9) and a sag-to-span ratio equal to $f/L=3\%$ for both main and secondary cables. The mean height of the roof was 20m. The self-weight of the roof, including the net and the cladding, was equal to 0.6kN/m^2 , and an additional air mass was assumed to be vibrating with the roof, only in resonant conditions, equal to 60kg/m^2 . The rigid model was tested in the wind tunnel and the resulted pressure coefficients are illustrated in Figure 8-10.

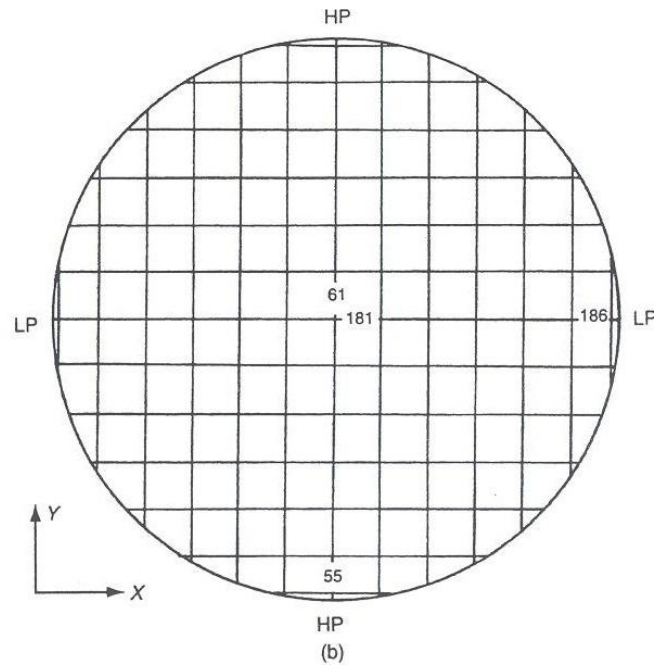


Figure 8-9: Plan view of the model used in the wind tunnel (LP: Low Points, HP: High Points) (from [8-23])

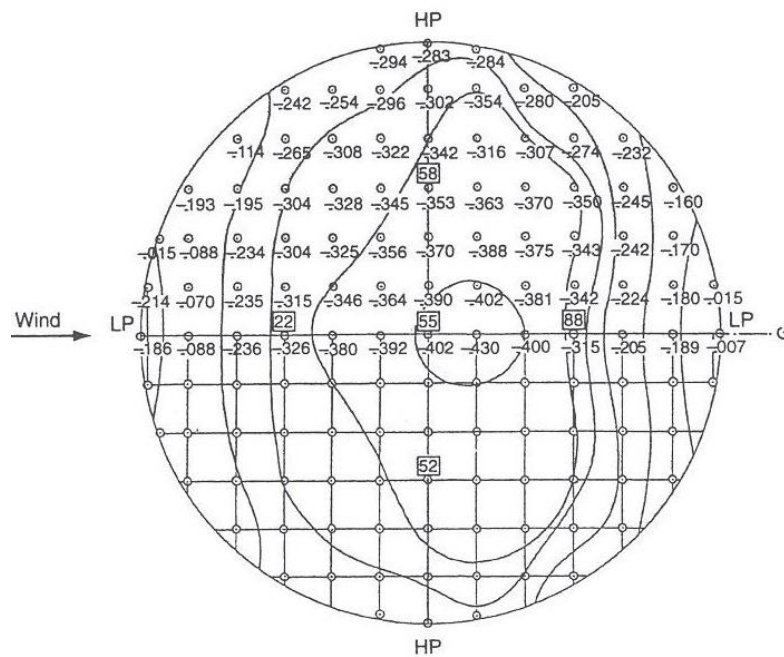


Figure 8-10: Diagram of wind pressure coefficient (LP: Low Points, HP: High Points) (from [8-23])

8.4.2 Comparison with Eurocode 1

Provided that Eurocode 1 does not give values for the pressure coefficients for this kind of structure, the ones suggested for an open canopy will be used and compared with the experimental results. The maximum angle of the canopy, at the lowest points of the boundary, which lie on the windward of the canopy, is assumed to be equal to $\alpha = \arctan(2f/L) = \arctan(0.06) = 3.4^\circ$. According to Eurocode 1, for pitch angles between $\alpha = -5^\circ$ and $\alpha = +5^\circ$, the roof should be considered as flat. Thus, the values of Table 8-2 are adopted, for angle 0° and for blockage ϕ equal to zero, representing an empty canopy.

Table 8-2: Values of the coefficients $c_{p,net}$ and c_f for flat canopies (from [8-1])

			Net pressure coefficient $c_{p,net}$		
Roof angle α	Blockage φ	Overall force coefficient c_f	Zone A	Zone B	Zone C
0°	Min $\varphi = 0$	- 0.5	- 0.6	- 1.3	- 1.4

Applying these coefficients to a circular canopy inscribed in a rectangular canopy, taking into consideration the regions defined in Table 8-2, the corresponding diagram of the pressure coefficients are those of Figure 8-11. The diagram for the overall force coefficient is very close to the one of Figure 8-10. The net pressure coefficient diagram can be considered again close to the experimental data, if the extreme zones B and C are neglected. In any case the wind pressure distribution according to Eurocode 1 is a little more conservative than the wind tunnel results.

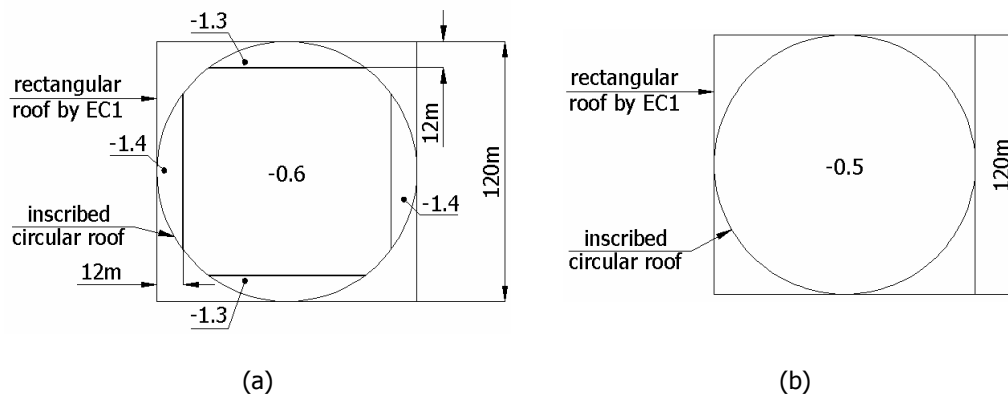


Figure 8-11: (a) Overall force coefficient c_f (b) Net pressure coefficient diagram for flat canopy according to Eurocode 1

8.5 SADDLE-FORM ROOFS

8.5.1 Wind tunnel experiment

Buchholdt again in [8-23] referred to a wind tunnel study, performed by Beutler [8-24]. A part of this work deals with rhomboid saddle-shaped surfaces. A parametric analysis was carried out for different curvatures, corresponding to $H=A/2$, $A/3$, $A/4$, $A/6$, $A/8$ and $A/10$ and for three different wind directions (Figure 8-12).

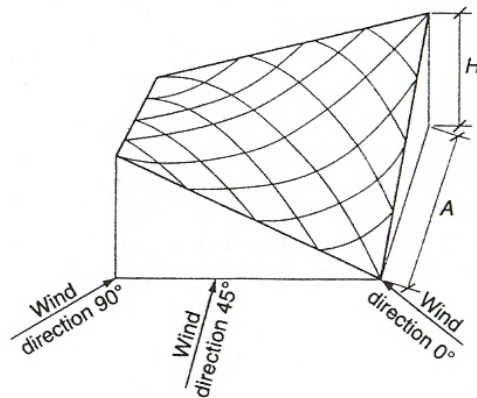


Figure 8-12: Wind directions and geometry of the wind tunnel model (from [8-23])

Buchholdt in his book gave some pressure distribution diagrams, regarding only the case of $H=A/2$, as the most complete. The longest cable span is equal to $L = \sqrt{2}A$ and the sag of the roof is $f=H/2=A/4$, corresponding to a sag-to-span ratio f/L equal to 17.7%. The diagrams for the wind pressure distribution presented in Figure 8-13, concern a closed roof for wind direction at 0° , 45° and 90° . In these diagrams, HP stands for the Highest Points and LP for the Lowest Points.

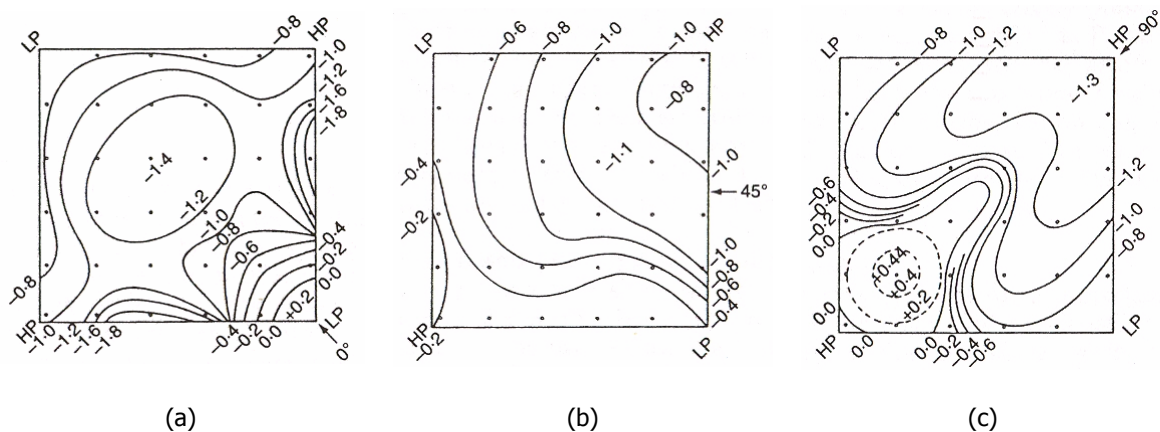


Figure 8-13: Saddle roof with edge beams and walls (from [8-23]): pressure distribution above the roof surface for wind direction at (a) 0° , (b) 45° and (c) 90° (HP: Highest Points, LP: Lowest Points)

8.5.2 Comparison with Eurocode 1

8.5.2.1 The roof modelled as duopitch roof in both directions

For these structures, the recommended pressure coefficients for a duopitch roof will be adopted and compared with the experimental results. Four cases are distinguished and combined in Eurocode 1, regarding a duopitch roof: a) positive pitch angle of the roof, b) negative pitch angle of the roof, c) wind direction $\theta=0^\circ$ and d) wind direction $\theta=90^\circ$. According to which case is considered, the zones are defined on the roof and the overall pressure coefficients $c_{pe,10}$ are taken from the corresponding Tables of Eurocode 1. These four cases are illustrated in Figure 8-14.

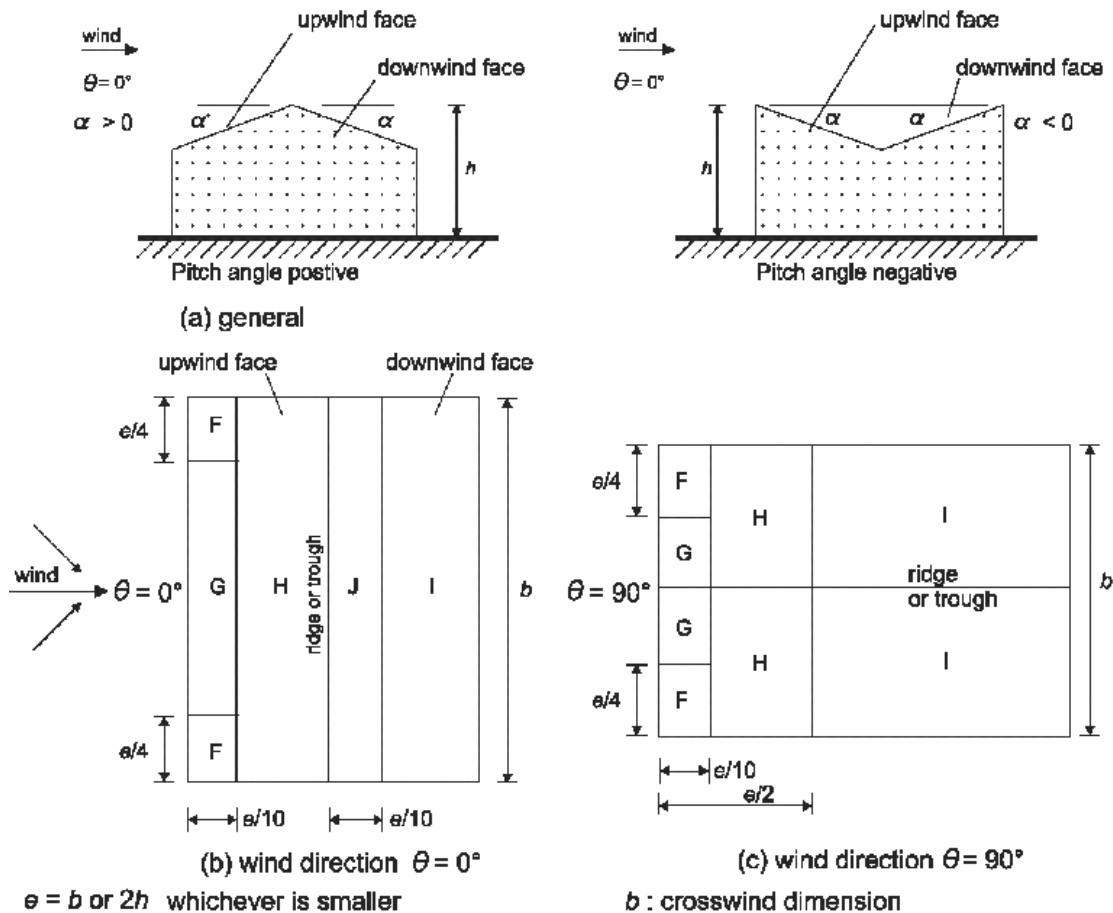


Figure 8-14: Key for duopitch roofs (from [8-1])

In order to adopt the proposed methodology of Eurocode 1 to the saddle-form roof, the following assumptions are made:

- The angle of the roof is assumed to be equal to $\alpha = \arctan(2f/L) = \arctan(0.354) = 19.5^\circ$.
- The surface of the saddle-shaped roof is divided into four zones, as shown in Figure 8-15.
- Two vertical sections A and B are defined, as shown in Figure 8-16.
- Zones 1 and 2, referring to section A, have a positive pitch angle, and zones 3 and 4, referring to section B have a negative one.
- For wind direction 0° , section A is parallel to the wind, and thus zones 1 and 2 refer to the Table of Eurocode 1 for $\theta = 0^\circ$, while the section B is perpendicular to the wind and zones 3 and 4 refer to the Table of Eurocode 1 for $\theta = 90^\circ$.
- Respectively, for wind direction 90° , section A is perpendicular to the wind, and thus zones 1 and 2 refer to the Table of Eurocode 1 for $\theta = 90^\circ$, while section B is parallel to the wind and zones 3 and 4 refer to the Table of Eurocode 1 for $\theta = 0^\circ$.
- For wind direction 45° , no pressure coefficients are available. In this case, the wind is analysed into two equal components, one at direction 0° and one at 90° and the above assumptions with the corresponding pressure coefficients multiplied by $\cos 45^\circ$, are adopted again. Thus, the resultant of the two pressure diagrams produces the diagram for this wind direction.
- Zone J of Figure 8-14 is not taken into account, because there is no acute ridge or trough. This zone is incorporated in zone I. Zone F cannot be defined, because of the rhomboid shape of the roof. Zone G is very small and it is not taken into consideration.

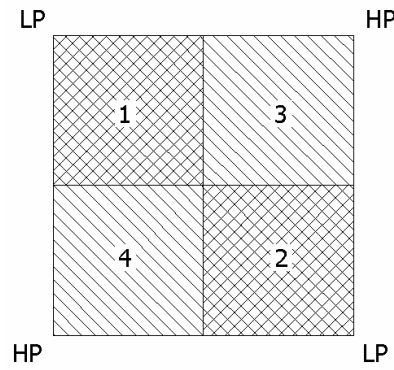


Figure 8-15: Zones on the hyperbolic paraboloid surface (HP: Highest Points, LP: Lowest Points)

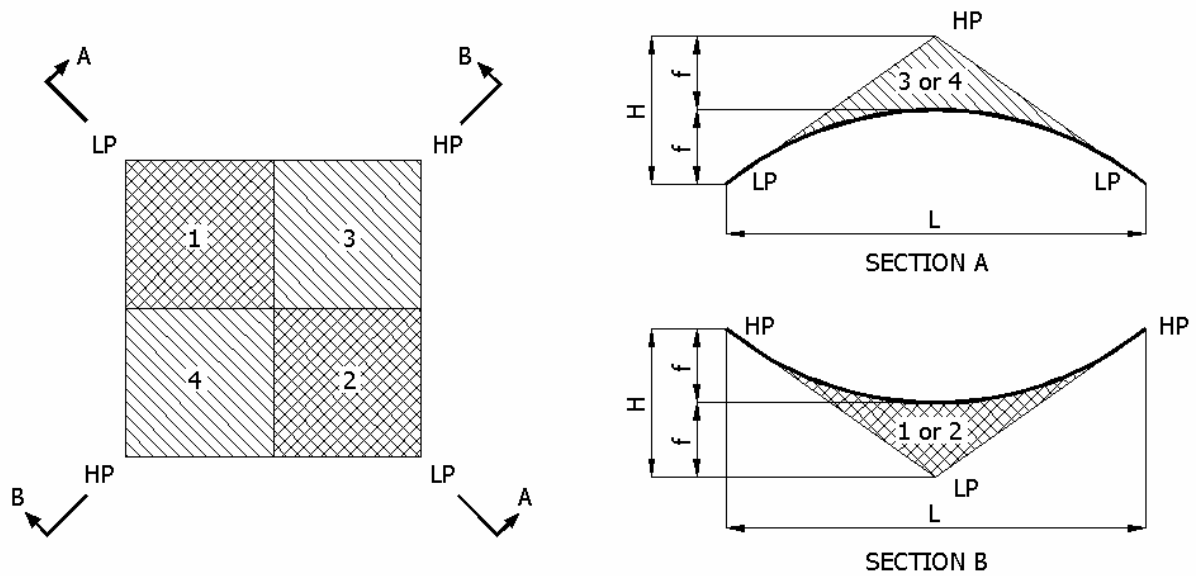


Figure 8-16: Vertical sections (HP: Highest Points, LP: Lowest Points)

Table 8-3 and Table 8-5 give the pressure coefficient for wind direction $\theta=0^\circ$ and $\theta=90^\circ$, respectively, reported from Eurocode 1. For pitch angle $\alpha \approx \pm 20^\circ$ a linear interpolation between the available values is proposed, tabulated in Table 8-4 and Table 8-6, respectively.

Table 8-3: External pressure coefficient for wind direction $\theta=0^\circ$ (from [8-1])

pitch angle α	Zone for wind direction $\theta = 0^\circ$				
	F	G	H	I	J
-30°	$C_{pe,10} = -1.1$	$C_{pe,10} = -0.8$	$C_{pe,10} = -0.8$	$C_{pe,10} = -0.6$	$C_{pe,10} = -0.8$
-15°	$C_{pe,10} = -2.5$	$C_{pe,10} = -1.3$	$C_{pe,10} = -0.9$	$C_{pe,10} = -0.5$	$C_{pe,10} = -0.7$
15°	$C_{pe,10} = -0.9$	$C_{pe,10} = -0.8$	$C_{pe,10} = -0.3$	$C_{pe,10} = -0.4$	$C_{pe,10} = -1.0$
30°	$C_{pe,10} = +0.2$	$C_{pe,10} = +0.2$	$C_{pe,10} = +0.2$	$C_{pe,10} = 0$	$C_{pe,10} = 0$
	$C_{pe,10} = -0.5$	$C_{pe,10} = -0.5$	$C_{pe,10} = -0.2$	$C_{pe,10} = -0.4$	$C_{pe,10} = -0.5$
	$C_{pe,10} = +0.7$	$C_{pe,10} = +0.7$	$C_{pe,10} = +0.4$	$C_{pe,10} = 0$	$C_{pe,10} = 0$

Table 8-4: External pressure coefficient for pitch angle $\pm 20^\circ$ and for wind direction $\theta=0^\circ$

pitch angle α	Zone for wind direction $\theta = 0^\circ$				
	F	G	H	I	J
	$C_{pe,10}$	$C_{pe,10}$	$C_{pe,10}$	$C_{pe,10}$	$C_{pe,10}$
-20°	-2.0	-1.1	-0.9	-0.5	-0.7
$+20^\circ$	-0.8	-0.7	-0.2	-0.4	-0.8
	+0.4	+0.4	+0.3	0	0

Table 8-5: External pressure coefficient for wind direction $\theta=90^\circ$ (from [8-1])

Pitch angle α	Zone for wind direction $\theta=90^\circ$			
	F	G	H	I
	$C_{pe,10}$	$C_{pe,10}$	$C_{pe,10}$	$C_{pe,10}$
-30°	-1.5	-1.2	-1.0	-0.9
-15°	-1.9	-1.2	-0.8	-0.8
15°	-1.3	-1.3	-0.6	-0.5
30°	-1.1	-1.4	-0.8	-0.5

Table 8-6: External pressure coefficient for pitch angle $\pm 20^\circ$ and for wind direction $\theta=90^\circ$

Pitch angle α	Zone for wind direction $\theta=90^\circ$			
	F	G	H	I
	$C_{pe,10}$	$C_{pe,10}$	$C_{pe,10}$	$C_{pe,10}$
-20°	-1.8	-1.2	-0.8	-0.8
$+20^\circ$	-1.2	-1.3	-0.7	-0.5

Hence the diagrams of Figure 8-17 are produced, regarding the three directions of the wind. Comparing these diagrams with the ones given in Figure 8-13, it is obvious that the consideration of dividing the roof into two vertical sections, and taking the values from Eurocode 1, retaining each section as a duopitch roof, with positive or negative pitch angle, results in 43% smaller values than the ones obtained by the experiments, at the centre of the roof, for wind direction 0° . At the corners of the roof for this wind direction, the pressures are not far from the ones obtained in the wind tunnel. For the other directions of the wind, the maximum pressure coefficients according to Eurocode 1 are approximately 18% and 31% smaller for 45° and for 90° , respectively, than the ones from the wind tunnel.

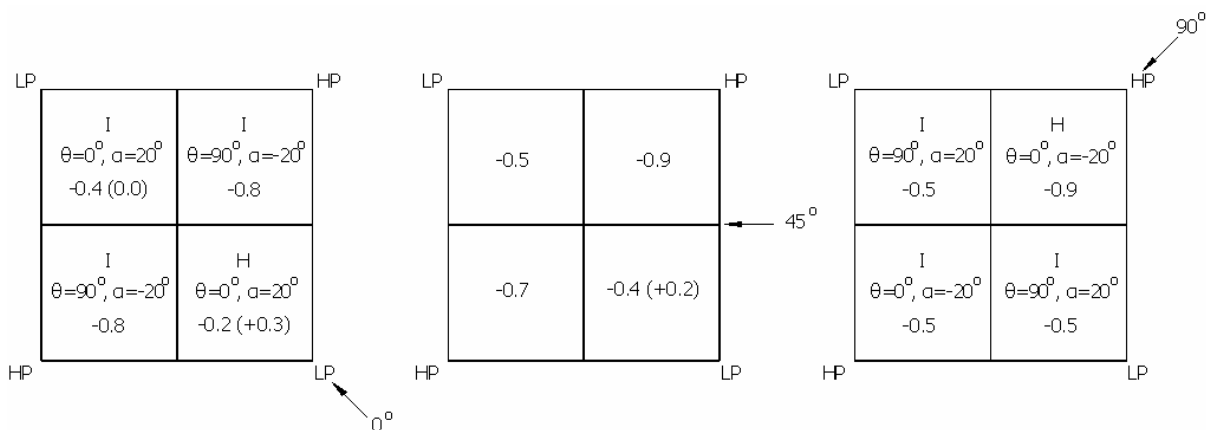


Figure 8-17: Diagrams of the wind pressure distribution taking into account the values suggested by Eurocode 1 for duopitch roofs (HP: Highest Points, LP: Lowest Points)

8.5.2.2 The roof modelled as vaulted and duopitch roof in the two directions

For wind direction 0° , for which the largest difference is observed, the roof is assumed as vaulted. Thus, new zones are defined, shown in Figure 8-18. For zones 1', 2', 5, 6, 7 and 8 the pressure coefficients are calculated from the diagram of Figure 8-6 for $h=0$ and $f/d=f/L=0.177$, while zones 3

and 4 remain as defined before. For the wind direction 90° , the assumptions made before regarding the zones remain the same.

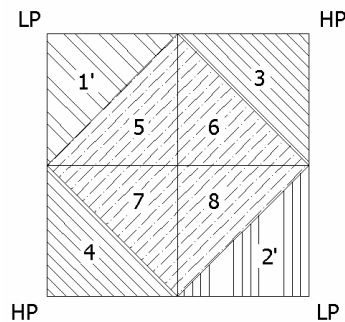


Figure 8-18: Zones for wind direction 0° on the hyperbolic paraboloid surface (HP: Highest Points, LP: Lowest Points)

The new pressure diagrams are shown in Figure 8-19 for the three directions of the wind. In these diagrams, the pressure distribution is closer to the ones of Figure 8-13 and the difference for the wind direction 0° is smaller than before, arising at 36% for the maximum value. Thus, the assumption of treating the hyperbolic as vaulted roof, when the wind blows from the lowest parts, is considered as the most appropriate.

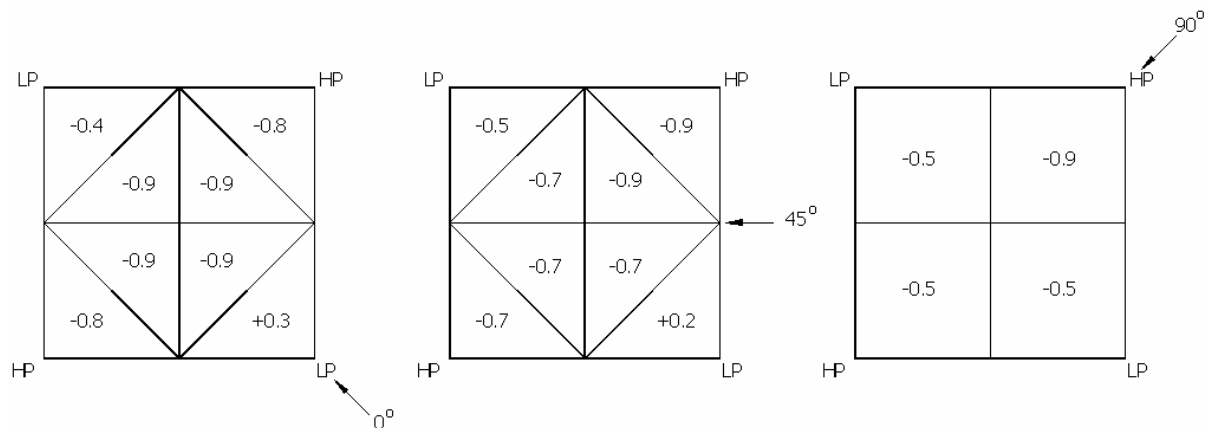


Figure 8-19: Diagrams of the wind pressure distribution taking into account the values suggested by Eurocode 1 for duopitch and vaulted roofs (HP: Highest Points, LP: Lowest Points)

8.6 PROPOSED PRESSURE DISTRIBUTION

Based on the above investigation concerning the wind tunnel results on circular, flat, vaulted or saddle roofs, several assumptions are made in order to apply the wind pressure coefficients, recommended by Eurocode 1, to a symmetric cable net with circular plan view, having the geometry of a hyperbolic paraboloid, in order to represent a more realistic wind pressure distribution. The global coordinate system and the geometry of the model is shown in Figure 8-20, in which L is the projected diameter, f is the sag and z is the height of the roof's centre. The angle α of the roof is defined as $\alpha = \arctan(2f/L)$ and it is positive for a vertical section at $y=0$ and negative for a vertical section at $x=0$. These vertical sections are chosen because they correspond to the two main wind directions 0° (parallel to axis x) and 90° (parallel to axis y) as illustrated in Figure 8-21.

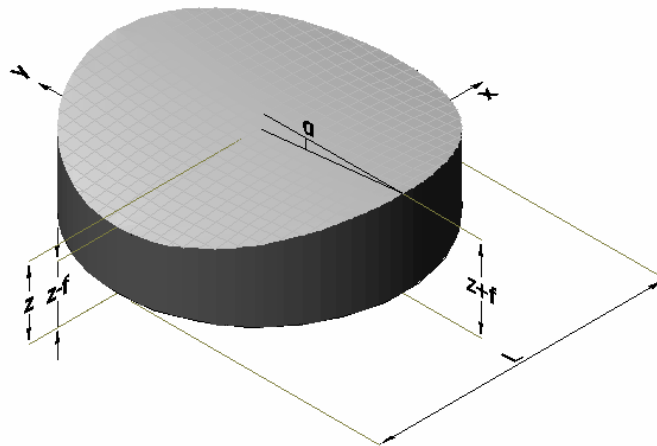


Figure 8-20: Geometry of the cable net under investigation

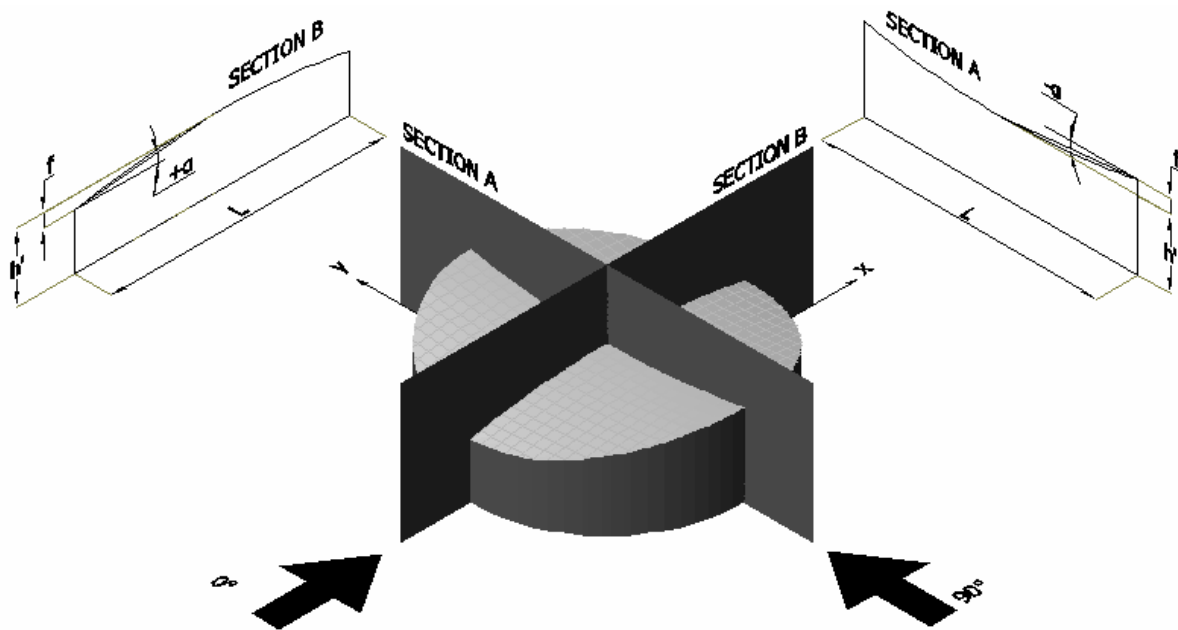


Figure 8-21: Pitch angles for the vertical sections at $x=0$ and $y=0$

For pitch angles $\alpha < -5^\circ$ and $\alpha > +5^\circ$, corresponding to $f/L > 1/22$, the roof is divided in eight zones (Figure 8-22). Each zone is treated differently, according to the wind direction. Three wind directions are studied, at 0° , at 90° and at 45° with respect to axis x . The third one, as explained already, is considered to be analysed into the two main directions of 0° and 90° , thus, no pressure coefficients are provided, but it is recommended to apply the resultant of the values given for the other two wind directions.

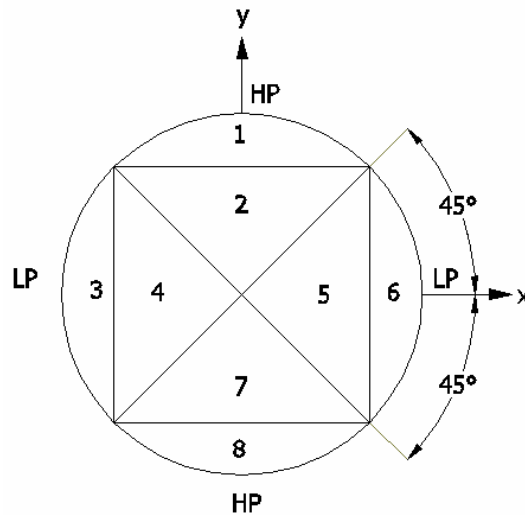


Figure 8-22: Zones on the hyperbolic paraboloid surface with circular plan view and $f/L > 1/22$ (HP: Highest Points, LP: Lowest Points)

For wind direction parallel to x-axis (direction 0°), zones 2 – 7 refer to a vaulted roof and correspond to zones A, B and C of a vaulted roof given by Eurocode 1, as defined in Figure 8-6. Zones 1 and 8, instead, correspond to zone I of a duopitch roof according to Eurocode 1, for wind direction parallel to the trough ($\theta=90^\circ$), as shown in Figure 8-14. The correspondence of the eight zones with the ones of Eurocode 1 is listed in Table 8-7.

Table 8-7: Cable nets considered as vaulted and duopitch roofs for wind direction 0°

Hyperbolic Paraboloid		Eurocode 1		
Zone	Pitch angle	Zone	Wind direction θ	Vaulted roof
1	(-)	I	90° (parallel to the trough)	
2				B
3				A
4				B
5				B
6				C
7				B
8	(-)	I	90° (parallel to the trough)	

For wind direction parallel to y-axis (direction 90°), zones 3, 4, 5 and 6, represented by section B (Figure 8-21), correspond to a duopitch roof with positive pitch angle α . Thus, the pressure coefficients for these zones are derived from Eurocode 1 for wind direction parallel to the ridge ($\theta=90^\circ$), as shown in Figure 8-14. Zones 1, 2, 7 and 8, instead, represented by section A, correspond to a duopitch roof with negative pitch angle α , with pressure coefficients, derived from Eurocode 1, which refer to a wind direction perpendicular to the trough ($\theta=0^\circ$), as also shown in Figure 8-14. The correspondence of the eight zones with the ones of Eurocode 1 is tabulated in Table 8-8. In these tables, zones G and J, and in some cases zone H shown in Figure 8-14, are not included. As they are dependent on the parameter e , which is equal to the minimum of the values L , or $2h$, where h is the height of the structure in the windward wall, usually small with respect to the span L , the parameter $e/10$ defines zones of very small areas, which can be neglected. Zones F are also neglected, because they are not included in the circular plan view of the structure.

Table 8-8: Zones of cable nets considered as duopitch roofs for wind direction 90°

Hyperbolic Paraboloid		Eurocode 1		
Zone	Pitch angle	Duopitch roof		Vaulted roof
		Zone	Wind direction θ	
1	(-)	I	0° (perpendicular to the trough)	
2	(-)	I	0° (perpendicular to the trough)	
3	(+)	I	90° (parallel to the ridge)	
4	(+)	I	90° (parallel to the ridge)	
5	(+)	I	90° (parallel to the ridge)	
6	(+)	I	90° (parallel to the ridge)	
7	(-)	H	0° (perpendicular to the trough)	
8	(-)	H	0° (perpendicular to the trough)	

The values of the pressure coefficients given by Eurocode 1 are reported here for the zones used. Hence, Table 8-9 provides the coefficients of zone I, needed for zones 1 and 8 with negative pitch angle when the wind direction is 0° and for the central zones 3 – 6 with positive pitch angle when the wind direction is 90°. In Table 8-10 the pressure coefficients for zones I and H are tabulated, needed for zones 1, 2, 7 and 8 with negative pitch angle for wind direction 90°.

Table 8-9: External pressure coefficient for duopitch roofs for wind direction parallel to the ridge or the trough ($\theta=90^\circ$ Eurocode 1)

	Zone for wind direction $\theta=90^\circ$
pitch angle α	I
-45°	-0.9
-30°	-0.9
-15°	-0.8
-5°	-0.6
5°	-0.6
15°	-0.5
30°	-0.5
45°	-0.5
60°	-0.5
75°	-0.5

Table 8-10: External pressure coefficient for duopitch roofs for wind direction perpendicular to the ridge or the trough ($\theta=0^\circ$ Eurocode 1)

	Zone for wind direction $\theta = 0^\circ$	
pitch angle α	H	I
-45°	-0.8	-0.7
-30°	-0.8	-0.6
-15°	-0.9	-0.5
-5°	-0.8	+0.2
		-0.6

For pitch angles $-5^\circ < \alpha < +5^\circ$, corresponding to $f/L < 1/22$, the roof can be considered as flat. Having in both directions equal sag-to-span ratios, the pressure coefficients depend only on the wind direction. Thus, the roof is divided in two zones, as shown in Figure 8-23. Zones H and I of Figure 8-2 for flat roofs with sharp eaves correspond to zones 1 and 2 of Figure 8-23, respectively, as listed in Table 8-11. The pressure coefficients are listed in Table 8-12.

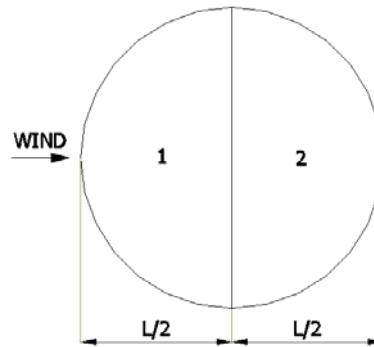


Figure 8-23: Zones on the hyperbolic paraboloid surface with circular plan view and $f/L < 1/22$

Table 8-11: Cable nets considered as flat roofs

Hyperbolic Paraboloid	Eurocode 1
	Flat roof
Zone	Zone
1	H
2	I

Table 8-12: External pressure coefficient for flat roofs

Roof type	Zone	
	H	I
	$C_{pe,10}$	$C_{pe,10}$
Sharp eaves	-0.7	-0.2

8.7 VALIDATION OF THE PROPOSED PRESSURE DISTRIBUTION

The results of the only wind tunnel test found in the literature concerning saddle-form cable nets with circular plan view are studied in order to evaluate the accuracy of the proposed pressure distribution.

8.7.1 Wind tunnel experiment

Rizzo et al. in [8-31] presented a summary of their work, regarding wind tunnel experiments on tension roofs of hyperbolic paraboloid shape with rectangular, square and circular plan view, performed in the CRIACIV's (Interuniversity research Centre of Aerodynamic and Wind Engineering) wind tunnel in Prato (Italy). Fourteen different geometries were considered, regarding the shape and the dimensions L_1 and L_2 of the plan, the sags in the direction of the main and stabilising cables f_1 and f_2 , respectively, the height of the roof, defined as $H=f_1+f_2$, and the height of the walls from the base to the lowest point of the roof, noted as H_b (Figure 8-24). In order to simplify the three-dimensional problem, they assumed a two-dimensional model, represented by two zones C1 and C2, which refer to the dimension L_1 and L_2 , respectively (Figure 8-25).

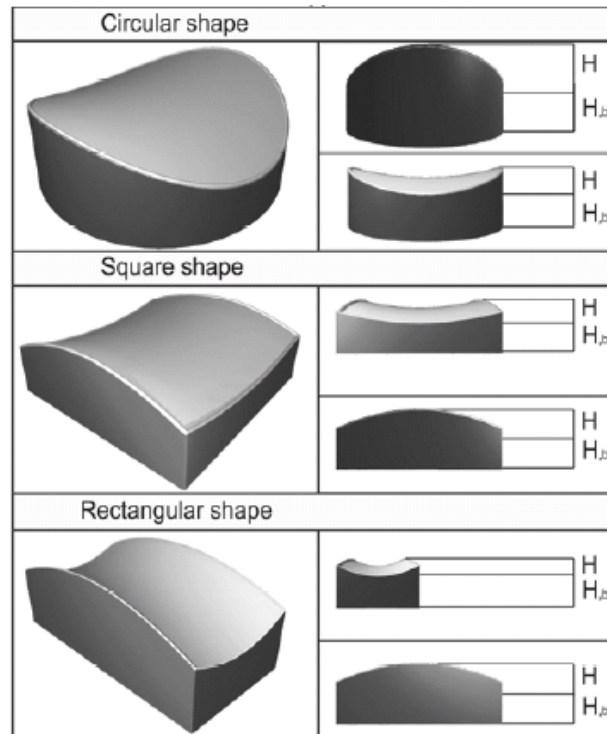


Figure 8-24: Wind tunnel models (from [8-31])

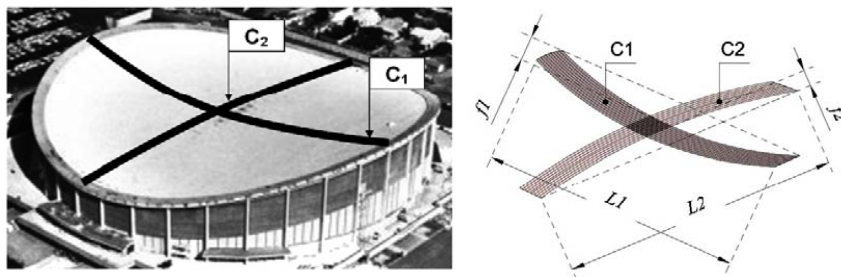


Figure 8-25: Defined zones (from [8-31])

Regarding the wind direction, the results of three angles were reported, at 0° , 45° and 90° . The wind direction at 0° was parallel to C2 cable zone, denoted as direction 1, while the 90° wind direction was parallel to C1 cable zone, named as direction 2 (Figure 8-26).

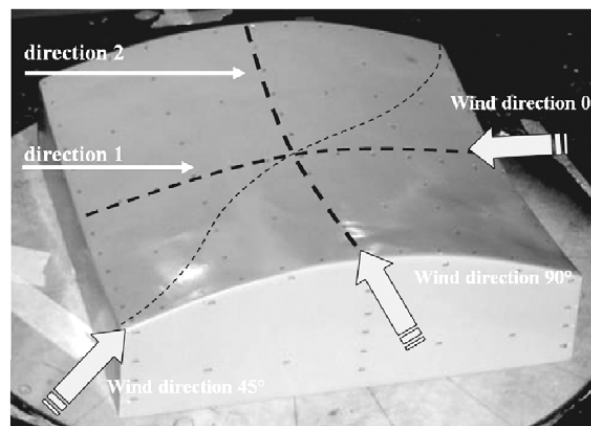


Figure 8-26: Wind direction according to the roof's orientation (from [8-31])

The six examples of the roofs with circular plan view, presented in this work, had the characteristics of Table 8-13. Two of the models (P.9 and P.10) have two different degrees of side roughness in order to include the influence of the Reynolds number. The results of P.11 are reported here (Figure 8-27).

Table 8-13: Characteristics of the roofs with circular plan view (from [8-31])

Model number	L (m)	f_1 (m)	f_2 (m)	H (m)	H_b (m)
P.9/P.9 w.r.	80.00	4.44	8.89	13.33	13.33
P.10/P.10 w.r.	80.00	4.44	8.89	13.33	26.66
P.11	80.00	2.67	5.33	8.00	13.33
P.12	80.00	2.67	5.33	8.00	26.66

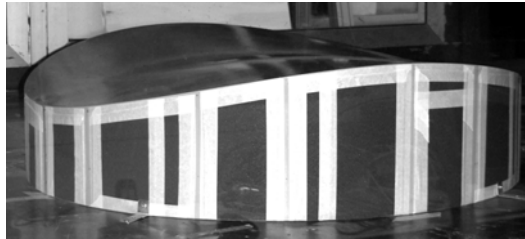


Figure 8-27: Wind tunnel test for a hyperbolic paraboloid with circular plan view (from [8-31])

For wind direction 0° , parallel to the stabilising cables (direction 1 – zone C2) the mean pressure coefficient distribution over the surface is illustrated in Figure 8-28, varying between -0.85 and -0.15. The diagrams of Figure 8-29 show the variation of the maximum, minimum and mean value of the coefficients c_p along the zones C1 and C2. For wind direction 90° , parallel to the main cables (direction 2 – zone C1) the mean pressure coefficient distribution over the surface is presented in Figure 8-30, ranging between -1.20 and 0.00. In Figure 8-31 the charts demonstrate the variation of the maximum, minimum and mean value of the coefficients c_p along zones C1 and C2. Finally, for wind direction at 45° the mean pressure coefficient distribution varies between -1.50 and -0.11 (Figure 8-32), while the charts of Figure 8-33, plotting the variation of the maximum, minimum and mean value of the coefficients c_p only along zones C1 and C2, do not provide sufficient information about the maximum absolute values of the wind pressure, which is observed at 45° .

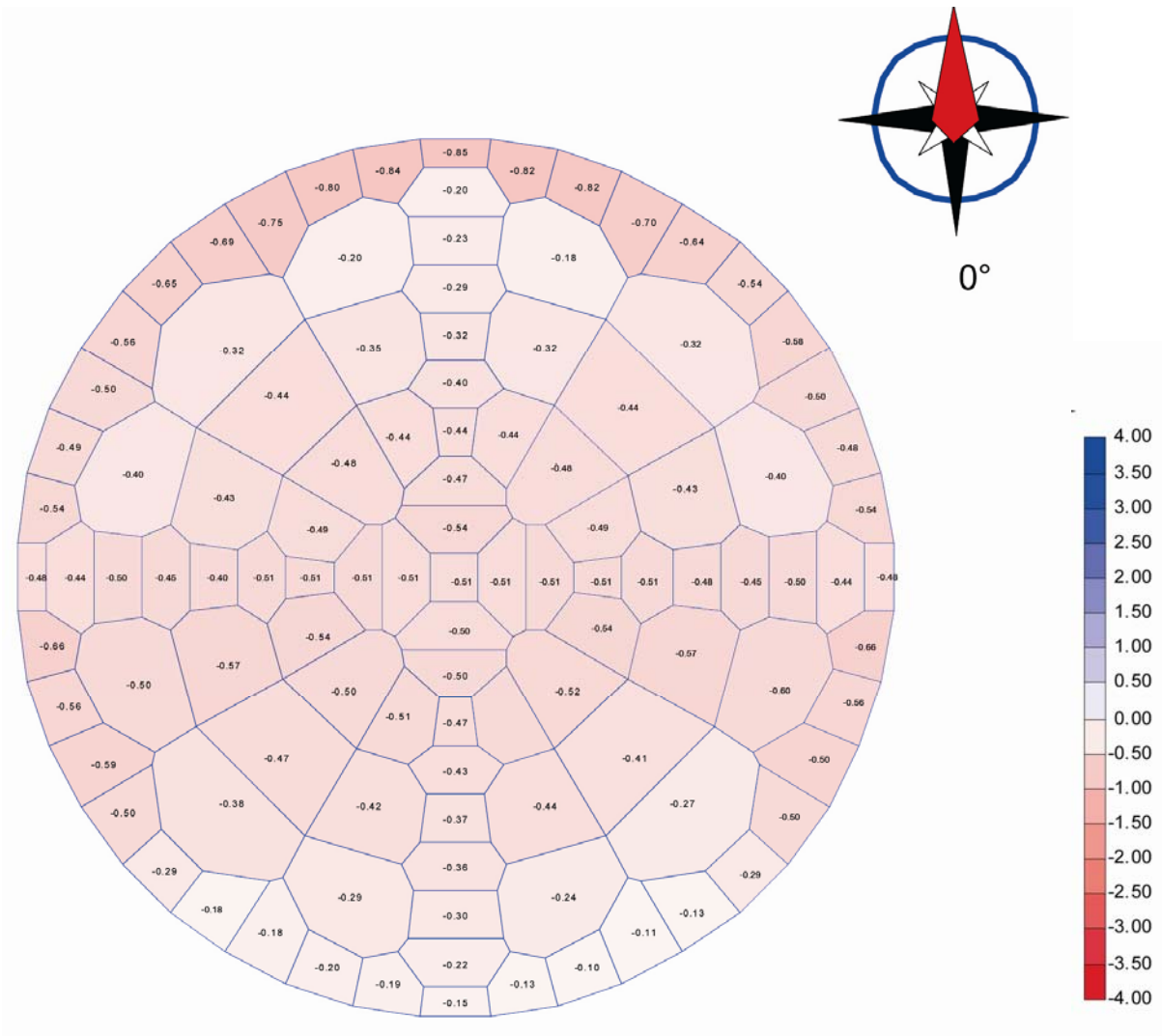


Figure 8-28: Mean pressure coefficients over a circular plan view for wind direction 0° (from [8-31])

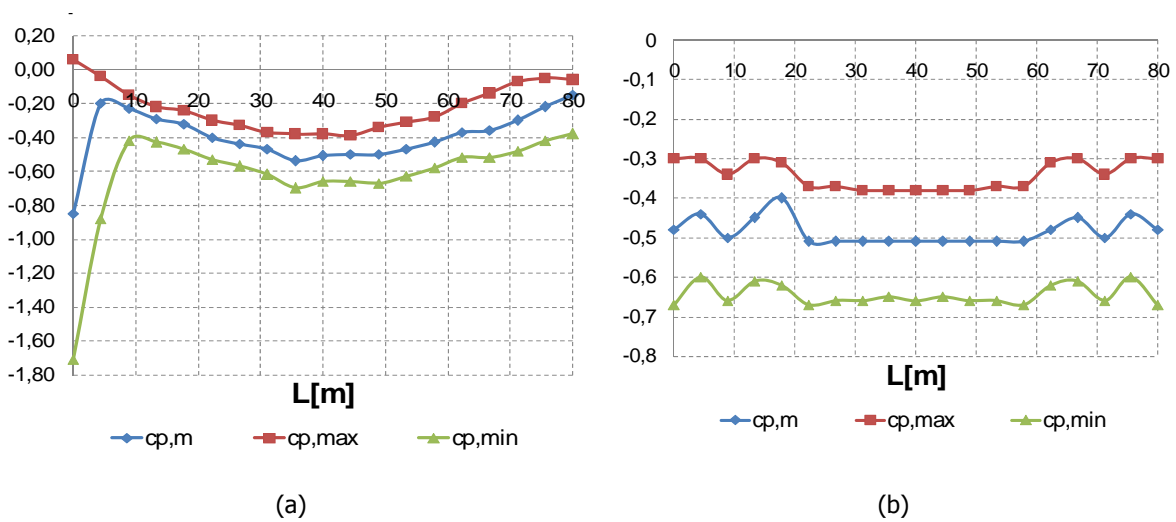


Figure 8-29: Pressure coefficient variation over a circular plan view for wind direction 0° (a) direction 1 parallel to C2, (b) direction 2 parallel to C1 (from [8-31])

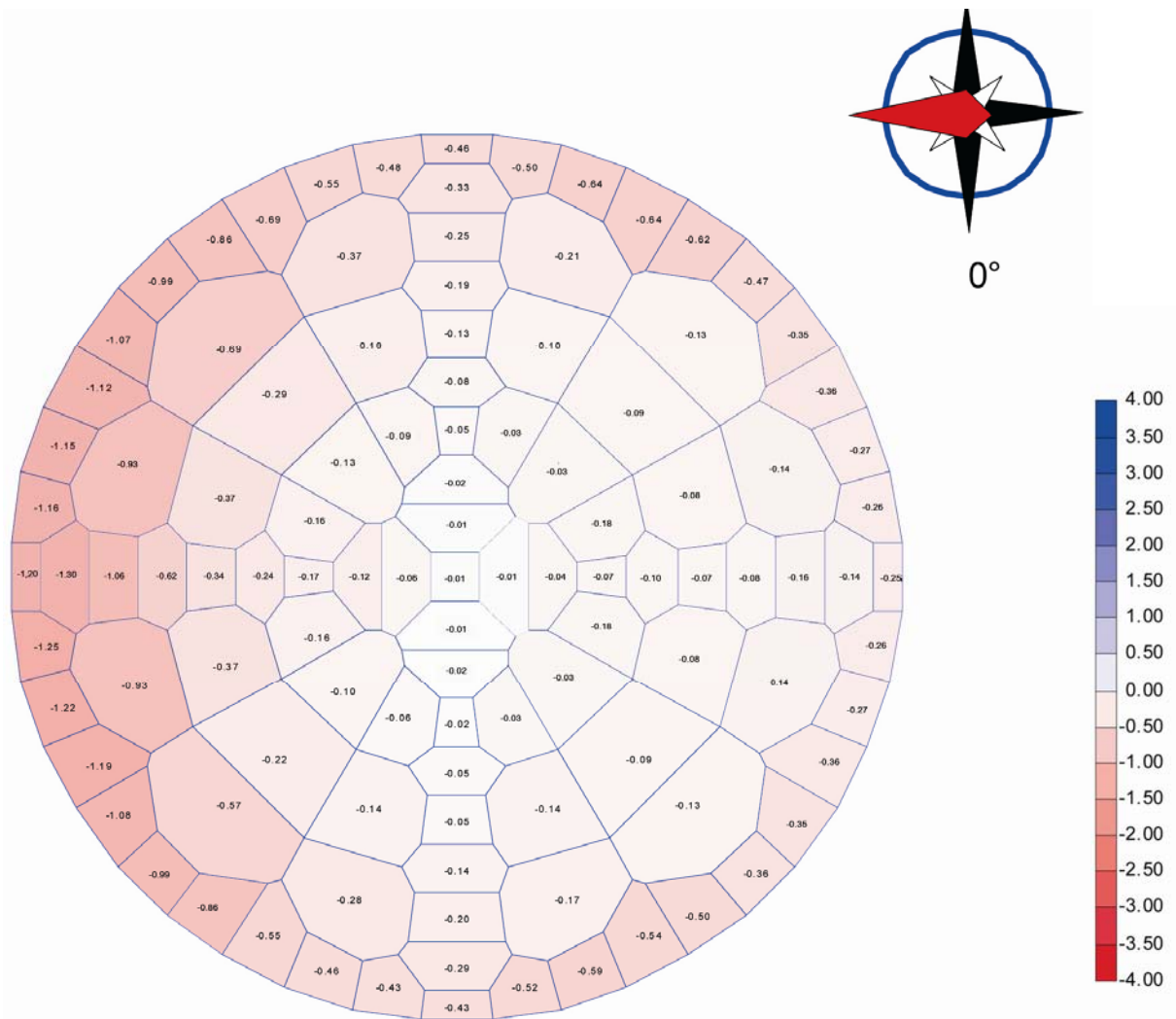


Figure 8-30: Mean pressure coefficients over a circular plan view for wind direction 90° (from [8-31])

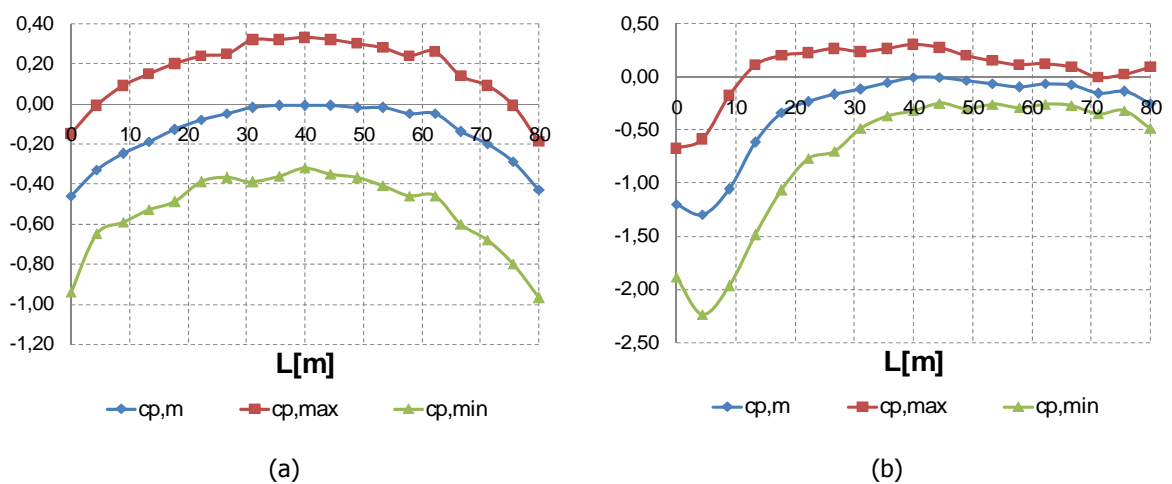


Figure 8-31: Pressure coefficient variation over a circular plan view for wind direction 90° (a) direction 1 parallel to C2, (b) direction 2 parallel to C1 (from [8-31])

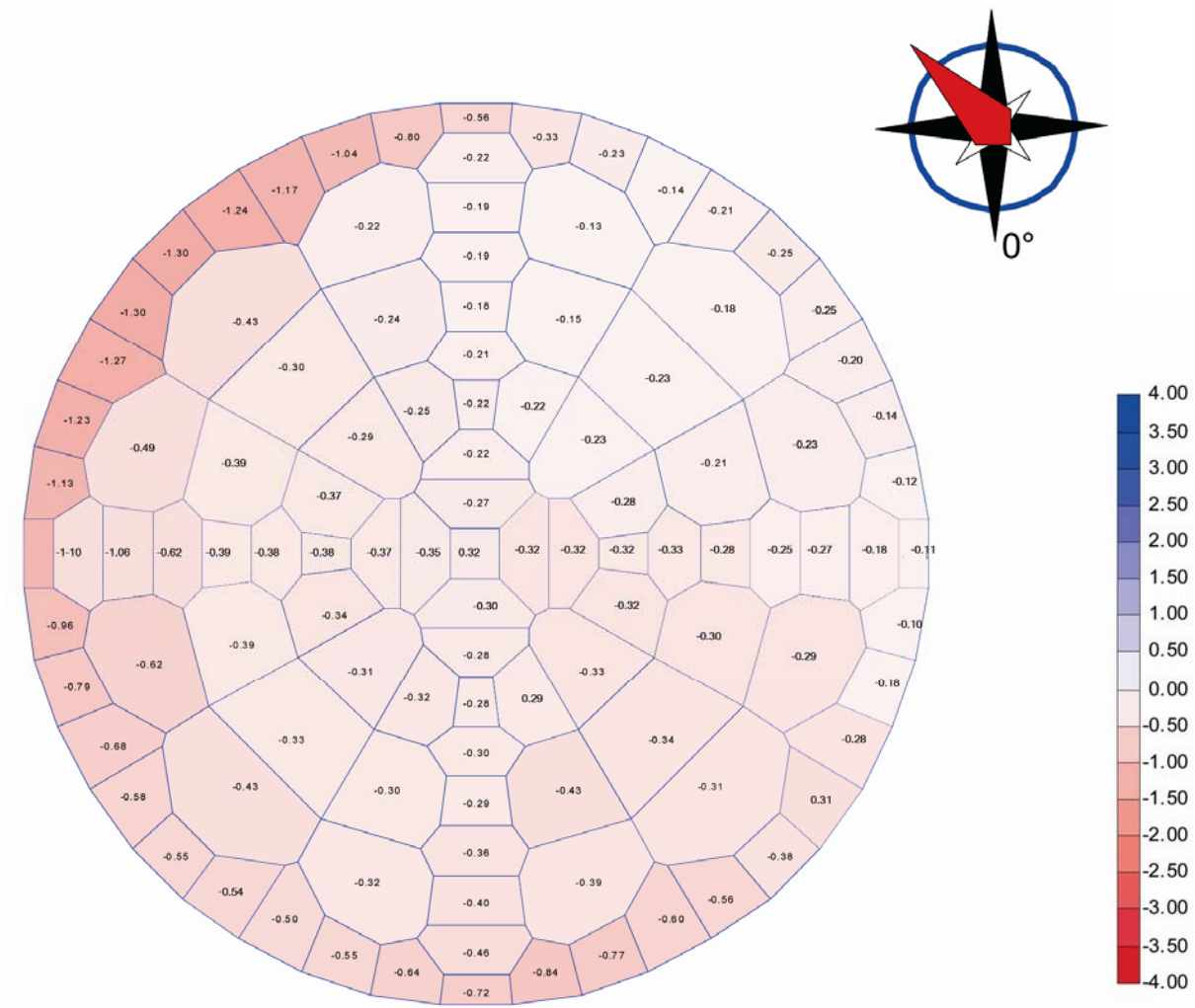


Figure 8-32: Mean pressure coefficients over a circular plan view for wind direction 45° (from [8-31])

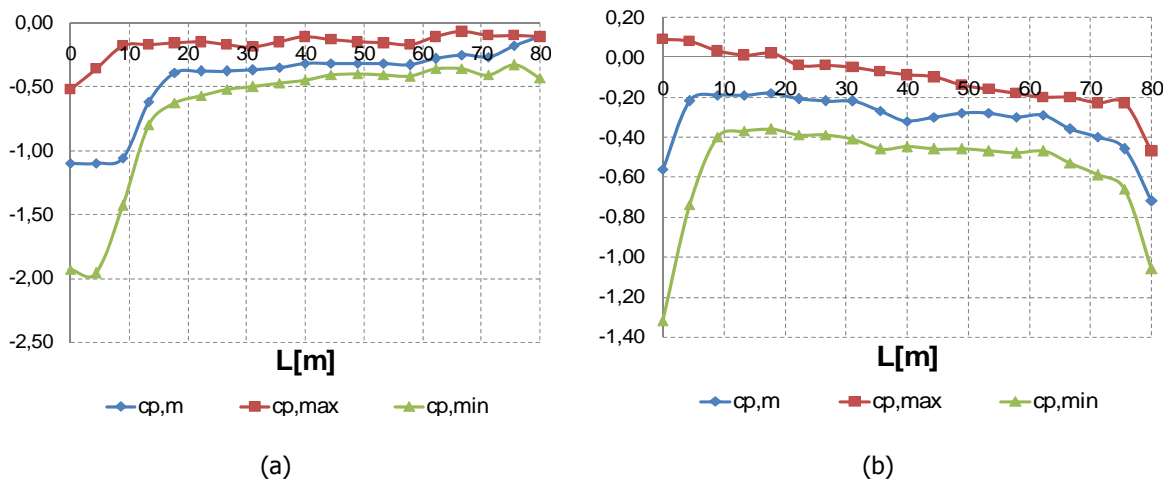


Figure 8-33: Pressure coefficient variation over a circular plan view for wind direction 45° (a) direction 1 parallel to C2, (b) direction 2 parallel to C1 (from [8-31])

A comparison between all models with circular plan view studied in this work show that for wind direction 0° the mean pressure coefficients are negative, indicating wind suction all over the roof

(Figure 8-34), while for wind direction 90° , only a small central part of the surface presents small wind pressure (positive pressure coefficient c_p), while, in the rest of the surface, wind suction occurs.

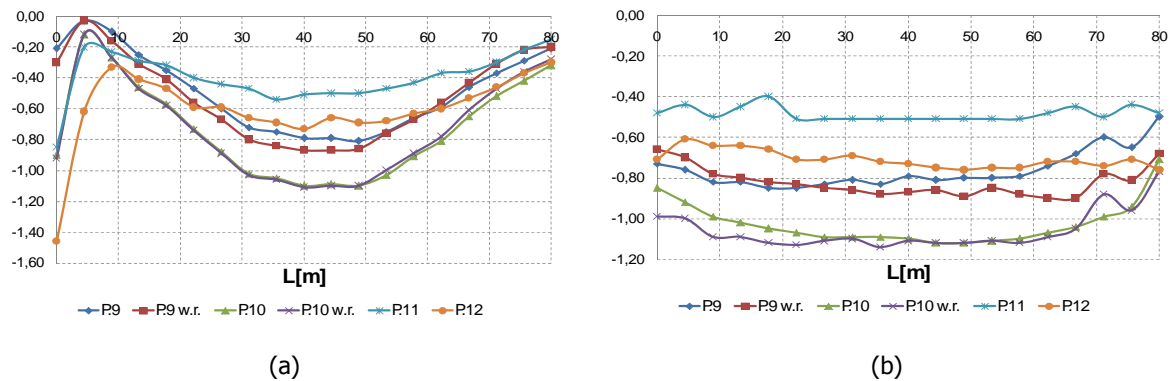


Figure 8-34: Mean pressure coefficient variation over a circular plan view for wind direction 0° for all models: (a) direction 1 parallel to C2, (b) direction 2 parallel to C1 (from [8-31])

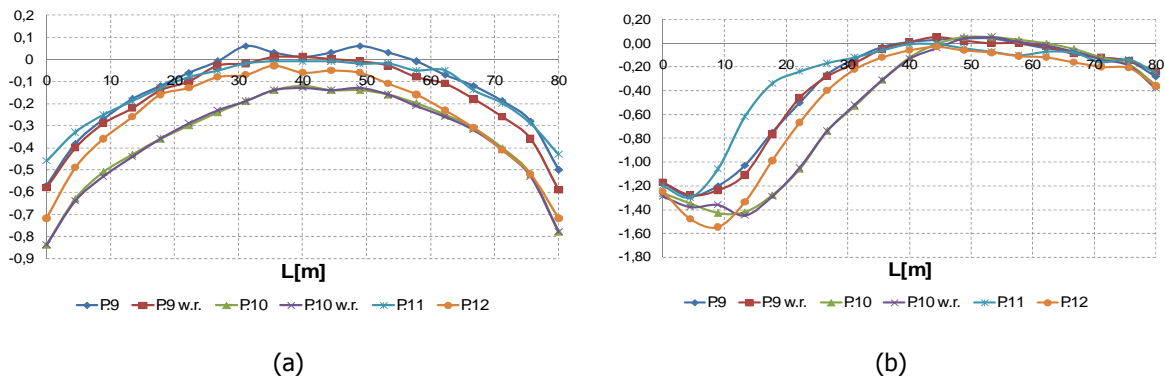


Figure 8-35: Mean pressure coefficient variation over a circular plan view for wind direction 90° for all models: (a) direction 1 parallel to C2, (b) direction 2 parallel to C1 (from [8-31])

8.7.2 Comparison with the proposed pressure distribution

8.7.2.1 Geometry

The sag-to-span ratio of the main cables (zone C1) is $f_1/L=1/30$ and the angle of the roof is assumed to be equal to $\alpha=-\arctan(2f_1/L)=-\arctan(0.067)=-3.81^\circ$. In this direction the roof is considered either as flat, or as duopitch with pitch angle $\alpha=-5^\circ$. The sag-to-span ratio of the stabilising cables (zone C2) is $f_2/L=1/15$ which corresponds to a pitch angle $\alpha=\arctan(2f_2/L)=\arctan(0.13)=7.59^\circ$. The height of the walls is $H_b=L/6$ and $H_b/f_2=15/6=2.5$.

8.7.2.2 Wind direction 0°

When the wind direction is parallel to the stabilising cables, the roof is modelled as duopitch or flat roof in direction C1 and as vaulted in direction C2. According to Figure 8-6, for $h/d=H_b/f_2=2.5>0.5$ and $f_2/L=1/15=0.067$, the pressure coefficients for zones A, B and C of the vaulted roof are -1.2, -0.85 and -0.4, respectively. According to Table 8-12 the pressure coefficient for zone I is -0.6 if it is considered as duopitch roof and -0.2, if it is considered as flat roof. The pressure coefficient distribution over the surface is illustrated in Figure 8-36. Comparing these diagrams with the one of Figure 8-28 it is noted that the proposed pressure distribution results in a correct distribution regarding the peaks of the wind suction. Regarding the direction of the stabilising cables, the pressure coefficients are between $c_{p,m}$ and $c_{p,min,r}$ while near the highest points of the surface, where the main

cables are anchored, the values approach $c_{p,m}$ for a duopitch roof assumption, or $c_{p,max}$ considering a flat roof (Figure 8-29).

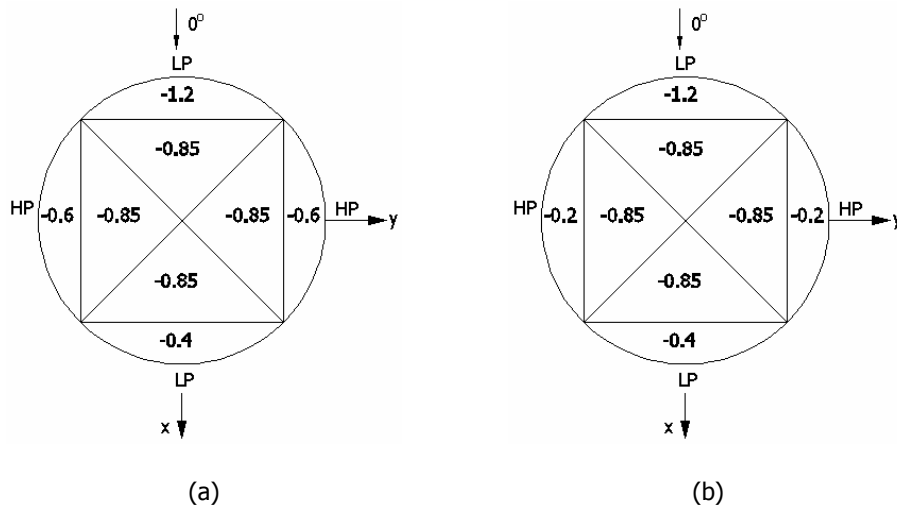


Figure 8-36: Pressure coefficient distribution for wind direction 0° with C1 zone (y-direction) considered as (a) duopitch roof, (b) flat roof

8.7.2.3 Wind direction 90°

When the wind direction is parallel to the main cables, the roof is modelled as flat or duopitch roof in direction C1 and as duopitch with positive pitch angle $\alpha=7.59^\circ$ in direction C2. According to Table 8-10 the pressure coefficient for zone I and for pitch angle 7.59° is -0.60 or $+0.20$. According to Table 8-12 the pressure coefficient for zones H and I of a flat roof are -0.7 and -0.2 , respectively. The pressure coefficient distribution over the surface is illustrated in Figure 8-37.

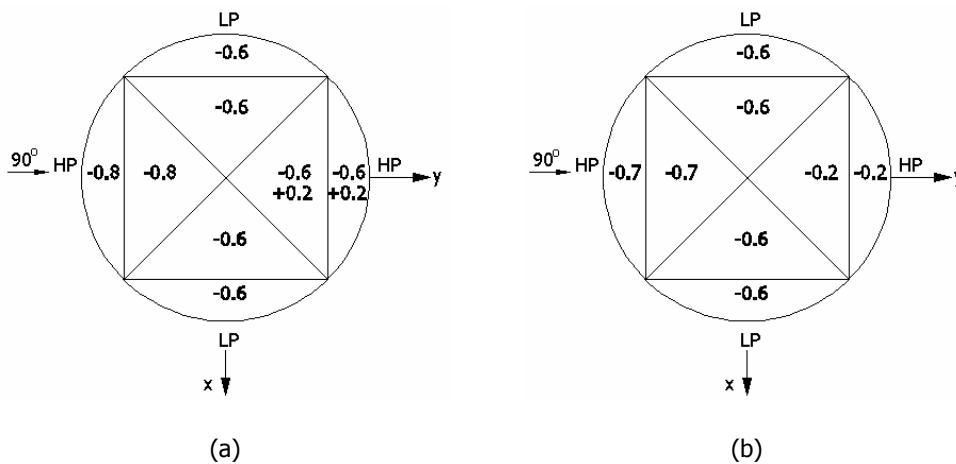


Figure 8-37: Pressure coefficient distribution for wind direction 90° with C1 zone (y-direction) considered as (a) duopitch roof, (b) flat roof

Comparing this diagram with the one of Figure 8-30 it is noted that the proposed pressure distribution predicts again a correct distribution, while a comparison with the charts of Figure 8-31 shows that the pressure coefficients are close to $c_{p,min}$ regarding the direction of the stabilising cables. If a duopitch roof is considered along the main cables, the pressure coefficients of the leeward side vary between $c_{p,min}$ and $c_{p,max}$. If instead a flat roof is assumed, they approach $c_{p,m}$. The values of the windward side in both cases are between $c_{p,max}$ and $c_{p,m}$.

8.7.2.4 Wind direction 45°

Considering as the two components of the wind direction 45° the ones given for wind direction 0° (Figure 8-36) and 90° (Figure 8-37) the resultant creates pressure coefficient distributions as the ones shown in Figure 8-38, considering as duopitch or flat the zone C1. Comparing this diagram with the one of Figure 8-32 and the values of pressure coefficients for the two characteristic zones C1 and C2 (Figure 8-33), it can be noted that the proposed approach predicts a satisfactory distribution of the wind suction, but the pressure coefficients are more conservative regarding the central zone.

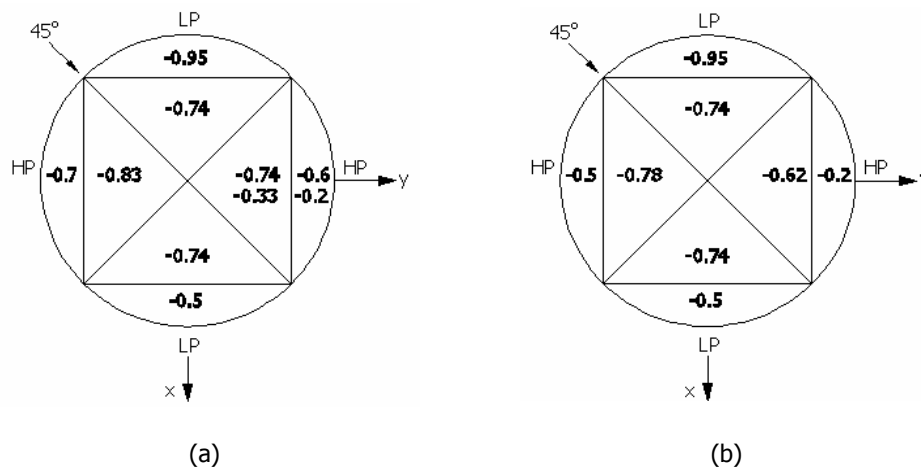


Figure 8-38: Pressure coefficient distribution for wind direction 45° with C1 zone (y-direction) considered as (a) duopitch roof, (b) flat roof

In all cases, the use of the pressure coefficients suggested by Eurocode leads to a satisfactory distribution of the wind pressure and can be adopted to assess the pressure coefficients.

8.8 NUMERICAL EXAMPLES

The cable nets that will be used in the next chapter have a circular plan view of diameter $L=100\text{m}$ and sag-to-span ratio for both main and stabilising cables f/L , corresponding to a pitch angle $\alpha=\arctan(2f/L)$, being positive for the direction of the stabilising cables and negative for the direction of the main cables. The height of the central node of the roofs is equal to $z=25\text{m}$ and the smallest height of the lateral walls is $h=z-f$. The ratio h/L , which will be needed to assess the pressure coefficients for the vaulted roof, is equal to $h/L=0.2$. The characteristics of these cable nets are tabulated in Table 8-14.

Table 8-14: Characteristics of the numerical examples

L (m)	f/L	f (m)	α (degrees)	h/L
100	1/10	10.00	$11.31 \approx 10^\circ$	0.15
100	1/20	5.00	$5.71 \approx 5^\circ$	0.20
100	1/35	2.86	$3.27 \approx 0^\circ$	-

According to the pressure distribution presented in section 8.6, the distribution of the pressure coefficients over the roofs, taking into consideration the maximum and minimum values suggested by Eurocode 1, are illustrated in Figure 8-39 for the first example and in Figure 8-40 for the second and third examples, for three wind directions.

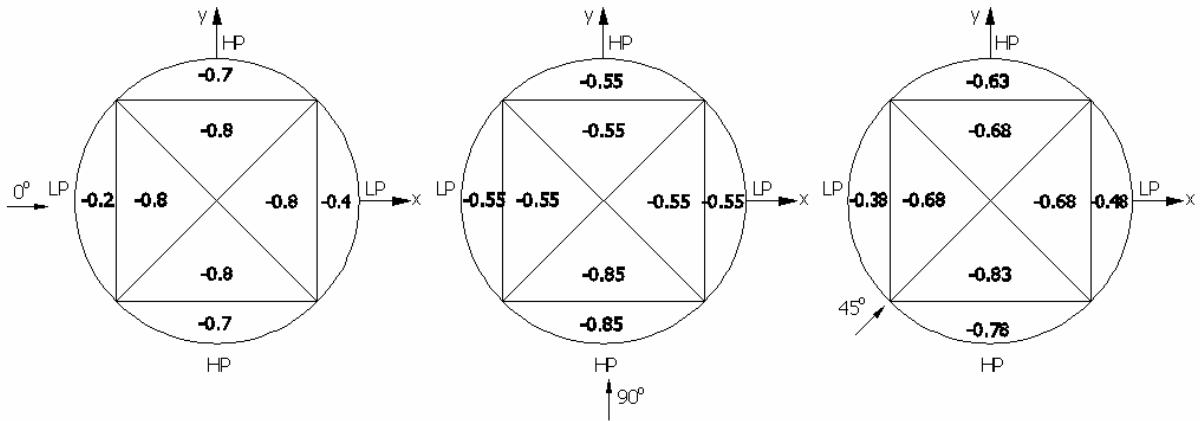


Figure 8-39: Pressure coefficients for the cable net with $f/L=1/10$

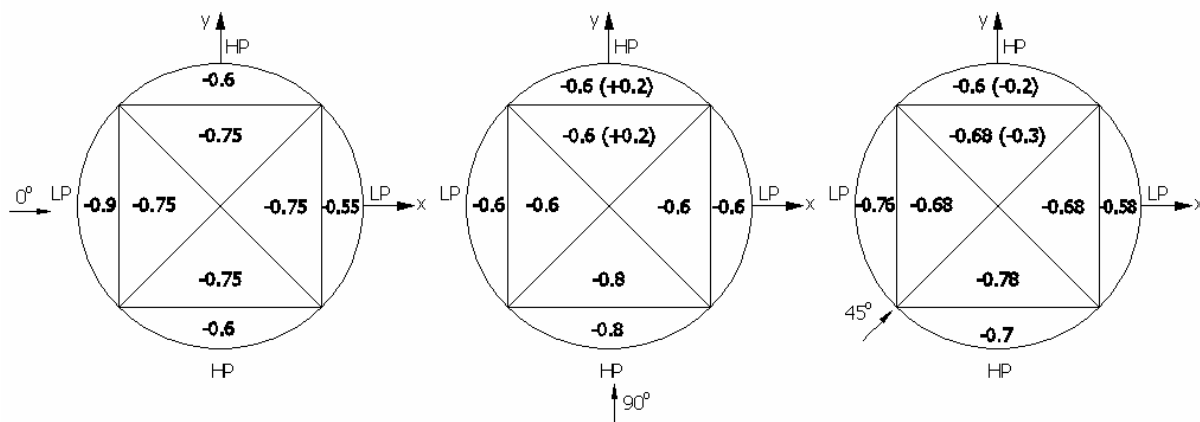


Figure 8-40: Pressure coefficients for the cable net with $f/L=1/20$

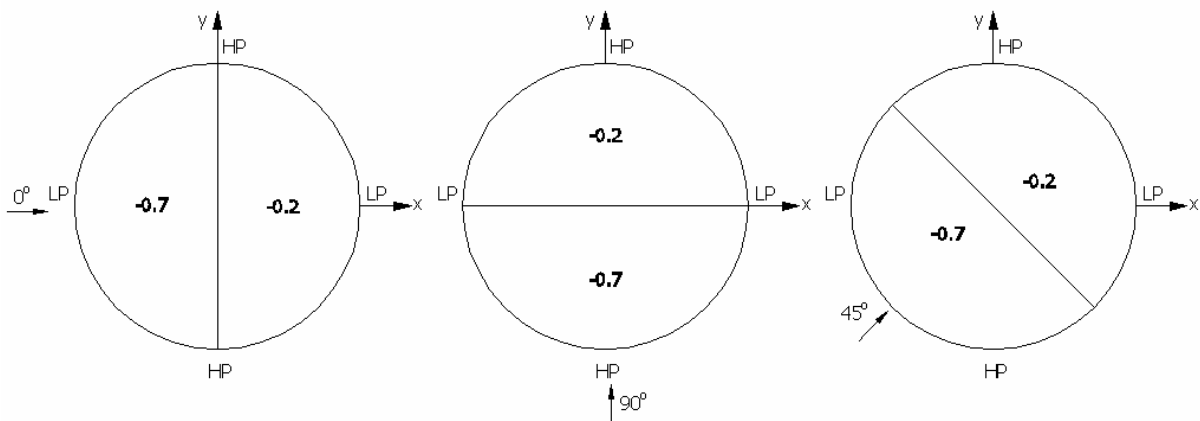


Figure 8-41: Pressure coefficients for the cable net with $f/L=1/35$

8.9 SUMMARY AND CONCLUSIONS

In this chapter, wind tunnel test results providing wind pressure distribution on roofs are compared with the pressure coefficients recommended by Eurocode 1, Part 1-4 for wind actions on structures. The experiments concerning circular flat roofs, vaulted roofs and saddle-form canopies with circular plan view and good agreement between the tests and Eurocode 1 is observed. In case of a saddle-

form roof with rhomboid plan view, several assumptions are made in order to obtain a correspondence between the pressure coefficients from Eurocode 1 and the ones measured for the hyperbolic paraboloid surfaces. Eight different zones are defined on a saddle-shaped roof with circular plan view and a relation between these zones and the pressure coefficients of Eurocode 1 is delineated, with respect to the wind direction and the sag-to-span ratio of the roof. The only data found in the literature, concerning wind tunnel tests of similar structures, are compared with the results of the proposed approach, giving satisfactory agreement with the proposed pressure coefficients and wind pressure distribution over the surface.

8.10 REFERENCES

- [8-1] EUROCODE 1, PART 1.4, "General actions – Wind actions", 2003.
- [8-2] S. Cheng, H. Tanaka, P. A. Irwin, J. B. Jakobsen, "Aerodynamic instability of inclined cables", Proceedings of the 5th International Symposium on cable dynamics, Santa Margherita Ligure, Italy, pp. 69-76, 2003.
- [8-3] G. Bartoli, F. Cluni, V. Gusella and L. Procino, "Dynamics of cable under wind action: Wind tunnel experimental analysis", Journal of Wind Engineering and Industrial Aerodynamics, Vol. 94, pp. 259-273, 2006.
- [8-4] C. Borri, M. Majowiecki and P. Spinelli, "Wind response of a large tensile structure: the new roof of the Olympic stadium in Rome", Journal of Wind Engineering and Industrial Aerodynamics, Vol. 41-44, pp. 1435-1446, 1992.
- [8-5] B. J. Vickery and M. Majowiecki, "Wind induced response of a cable supported stadium roof", Journal of Wind Engineering and Industrial Aerodynamics, Vol. 41-44, pp. 1447-1458, 1992.
- [8-6] P. Biagini, C. Borri and L. Facchini, "Wind response of large roofs of stadiums and arena", Journal of Wind Engineering and Industrial Aerodynamics, Vol. 95, pp. 871-887, 2007.
- [8-7] O. Flamand, J. Biétry, C. Barré, E. Germain and P. Bourcier, "Fatigue calculation on the roof sustaining cables of a large stadium in Paris", Journal of Wind Engineering and Industrial Aerodynamics, Vol. 64, pp. 127-134, 1996.
- [8-8] M. Kazakevitch, "The aerodynamics of a hangar membrane roof", Journal of Wind Engineering and Industrial Aerodynamics, Vol. 77-78, pp. 157-169, 1998.
- [8-9] B. Natalini, J. O. Marighetti and M. B. Natalini, "Wind tunnel modeling of mean pressures on planar canopy roof", Journal of Wind Engineering and Industrial Aerodynamics, Vol. 90, pp. 427-439, 2002.
- [8-10] Y. Uematsu, E. Iizumi and T. Stathopoulos, "Wind force coefficients for designing free-standing canopy roofs", Journal of Wind Engineering and Industrial Aerodynamics, Vol. 95, pp. 1486-1510, 2007.
- [8-11] Y. Uematsu, T. Stathopoulos and E. Iizumi, "Wind loads on free-standing canopy roofs: Part 1 local wind pressures", Journal of Wind Engineering and Industrial Aerodynamics, Vol. 96, pp. 1015-1028, 2008.
- [8-12] Y. Uematsu, T. Stathopoulos and E. Iizumi, "Wind loads on free-standing canopy roofs: Part 2 overall wind forces", Journal of Wind Engineering and Industrial Aerodynamics, Vol. 96, pp. 1029-1042, 2008.

- [8-13] Y. L. Xu and G. F. Reardon, "Variations of wind pressure on hip roofs with roof pitch", *Journal of Wind Engineering and Industrial Aerodynamics*, Vol. 73, pp. 267-284, 1998.
- [8-14] J. G. Zhao and K. M. Lam, "Characteristics of wind pressures on large cantilevered roofs: effect of roof inclination", *Journal of Wind Engineering and Industrial Aerodynamics*, Vol. 90, pp. 1867-1880, 2002.
- [8-15] S. Franchini, S. Pindado, J. Meseguer and A. Sanz-Andrés, "A parametric, experimental analysis of conical vortices on curved roofs of low-rise buildings", *Journal of Wind Engineering and Industrial Aerodynamics*, Vol. 93, pp. 639-650, 2005.
- [8-16] P. A. Blackmore and E. Tsokri, "Wind loads on curved roofs", *Journal of Wind Engineering and Industrial Aerodynamics*, Vol. 94, pp. 833-844, 2006.
- [8-17] G. D. Stefanou, "Dynamic response of tension cable structures due to wind loads", *Computers and Structures*, Vol. 43, No. 2, pp. 365-372, 1992.
- [8-18] Y. Uematsu, k. Watanabe, A. Sasaki, M. Yamada and T. Hongo, "Wind-induced dynamic response and resultant load estimation of a circular flat roof", *Journal of Wind Engineering and Industrial Aerodynamics*, Vol. 83, pp. 251-261, 1999.
- [8-19] Y. Uematsu, T. Moteki and T. Hongo, "Model of wind pressure field on circular flat roofs and its application to load estimation", *Journal of Wind Engineering and Industrial Aerodynamics*, Vol. 96, pp. 1003-1014, 2008.
- [8-20] B. Tabarrok and Z. Qin, "Nonlinear analysis of tension structures", *Computers and Structures*, Vol. 45, No. 5/6, pp. 973-984, 1992.
- [8-21] B. Tabarrok and Z. Qin, "Dynamic analysis of tension structures", *Computers and Structures*, Vol. 62, No. 3, pp. 467-474, 1997.
- [8-22] I. Elashkar and M. Novak, "Wind tunnel studies of cable roofs", *Journal of Wind Engineering and Industrial Aerodynamics*, Vol. 13, pp. 407-419, 1983.
- [8-23] H. A. Buchholdt, "An introduction to cable roof structures", Thomas Telford, 2nd Edition, Great Britain, 1999.
- [8-24] N. Esquillan and Y. Saillard (Editors), "Proceedings of the IASS Colloquium on Hanging Roofs, Continuous Metallic Shell Roofs and Superficial Lattice Roofs, Paris, France, 1962", North Holland Publishing Company, Amsterdam, 1963.
- [8-25] X. Y. Sun, Y. Wu, Q. S. Yang and S. Z. Shen, "Wind tunnel tests on the aeroelastic behaviors of pretensioned saddle-shaped suspended roofs", *Proceedings of the BBAA VI International Colloquium on Bluff Bodies Aerodynamics and Applications*, Milan, Italy, 2008.
- [8-26] Y. Uematsu, F. Arakatsu, S. Matsumoto and F. Tekeda, "Wind force coefficients for the design of a hyperbolic paraboloid free roof", *Proceedings of the 7th Asia-Pacific Conference on Wind Engineering*, Taipei, Taiwan, 2009.
- [8-27] F. Li, M. Gu and J. Pan, "Practical wind-resistant design of large space flexible cable net", *Proceedings of the 7th Asia-Pacific Conference on Wind Engineering*, Taipei, Taiwan, 2009.
- [8-28] F. Rizzo, P. D' Asdia and L. Procino, "Wind action evaluation on tension roofs of hyperbolic paraboloid shape", *Proceedings of the BBAA VI International Colloquium on Bluff Bodies Aerodynamics and Applications*, Milan, Italy, 2008.
- [8-29] F. Rizzo, P. D' Asdia and M. Lazzari, "Aerodynamic behaviour of hyperbolic paraboloid shaped roofs: wind tunnel tests", *Proceedings of the EACWE 5*, Florence, Italy, 2009.

- [8-30] F. Rizzo, P. D' Asdia, M. Lazzari and G. Olivato, "Aerodynamic behaviour of hyperbolic paraboloid shaped roofs: POD and CFD analysis", Proceedings of the EACWE 5, Florence, Italy, 2009.
- [8-31] F. Rizzo, P. D' Asdia, M. Lazzari and L. Procino, "Wind action evaluation on tension roofs of hyperbolic paraboloid shape", Engineering Structures, Vol. 23, pp. 445-461, 2011.

9 DYNAMIC RESPONSE OF CABLE NETS UNDER WIND ACTION

9.1 INTRODUCTION

Wind action is the main load dominating the dynamic response of lightweight structures. The main concern of the researchers dealing with wind actions on such structures is to find an equivalent static procedure for estimating the nonlinear dynamic response, avoiding the large computational time required for nonlinear dynamic analyses. For example in [9-1] a simplified frequency domain approach was proposed to estimate the maximum probable wind response of a weakly nonlinear cable roof network. In [9-2] it was concluded that the dynamic deflections of cable structures due to wind might exceed twice the static deflections. A review covering cantilevered, enclosed, free edged, arched and suspended roof systems subjected to wind load was presented in [9-3]. It was proved that for relatively conventional configurations of cantilevered, enclosed and free edged roofs the code leads to reasonable design loads. However, it was proposed that for arched and suspended roofs complex static design loads are required to achieve equivalent displacements. In [9-4] the dynamic response of cable-stayed masts to wind action was compared with the one calculated by assuming the patch load method, proposed by Eurocode 3 [9-5], which is an equivalent static analysis. It was concluded that the nonlinearity considerably influences the dynamic response of the tower. In [9-6] an actual cable net structure was analysed, considering a time-history diagram of the wind velocity. Large oscillation amplitudes were calculated, concluding that larger curvatures could improve the dynamic response, while larger values of the initial pretension would not alter the results significantly.

The nonlinear dynamic behaviour of saddle-shaped cable nets subjected to wind actions is studied in this chapter. Time-history analyses are performed, considering the geometric nonlinearity of the system. The maximum dynamic response, expressed by means of the maximum nodal amplitude and cable tension, is compared with the response provided by quasi-static analysis methods. The static wind loads are calculated according to the quasi-static analysis for wind loads proposed by Eurocode 1 [9-7], while the dynamic ones are based on measured wind velocity records [9-8] as well as artificial ones. Modal analyses are also conducted in order to calculate the natural frequencies of the cable net, taking into account additional masses due to permanent loads. The wind direction, the sag-to-span ratio, the initial cable stress, and the boundary conditions are parameters that influence the dynamic response. Three different geometries and three different levels of initial cable stress are assumed,

thus covering the range between deep and shallow, overstressed and under-stressed cable nets. The influence of the deformability of the boundary ring is also investigated.

9.2 MODELLING ISSUES

The cable net utilised for the investigation of the dynamic response under wind action is the one described in section 7.2. It has a hyperbolic paraboloid surface with a circular plan view of diameter $L=100\text{m}$ and sag-to-span ratio $f/L=1/20$. The height of the central node is assumed equal to $z=25\text{m}$. The angle of the roof is defined as $\alpha=\arctan(2f/L)$ (Figure 9-1). The net consists of 25 cables in each direction, arranged in a quadratic grid; thus, the distance of the cables is 3.846m . Both carrying and stabilising cables have a circular cross-section of diameter $D=50\text{mm}$, mass density $m=7.85\text{kN}\cdot\text{sec}^2\cdot\text{m}^{-4}$ and initial pretension $N_0=600\text{kN}$. The cable material has a constant modulus of elasticity $E=165\text{GPa}$ in the tension branch and zero compression branch. The maximum permissible cable stress is assumed equal to the yield stress of the material, $\sigma_y=1570\text{MPa}$. Rayleigh damping is also introduced for the dynamic analysis [9-9] with damping ratio $\zeta=2\%$. No openings at the lateral walls of the roof are considered.

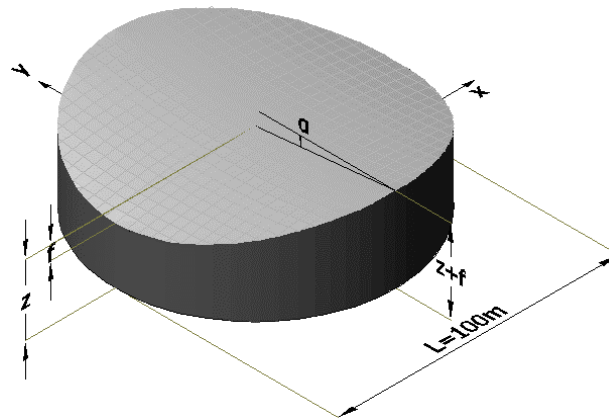


Figure 9-1: Geometry of the cable net

9.3 INITIAL STATE UNDER PERMANENT LOADS

9.3.1 Nonlinear static analysis

Firstly, the deformed state under pretension, self-weight of the cables and additional permanent loads equal to 0.36kN/m^2 is calculated, in order to be used as the initial state for the subsequent analyses. These permanent loads, corresponding to cladding and electromechanical equipment, were also considered for the design of the Peace and Friendship Stadium in Greece [9-10]. In this case the maximum negative (downward) deflection of the net is -0.22m , the minimum cable tension is 388kN and the maximum one 826kN . The deformed shape of the net is shown in Figure 9-2, where the maximum and minimum cable tensions are also plotted.

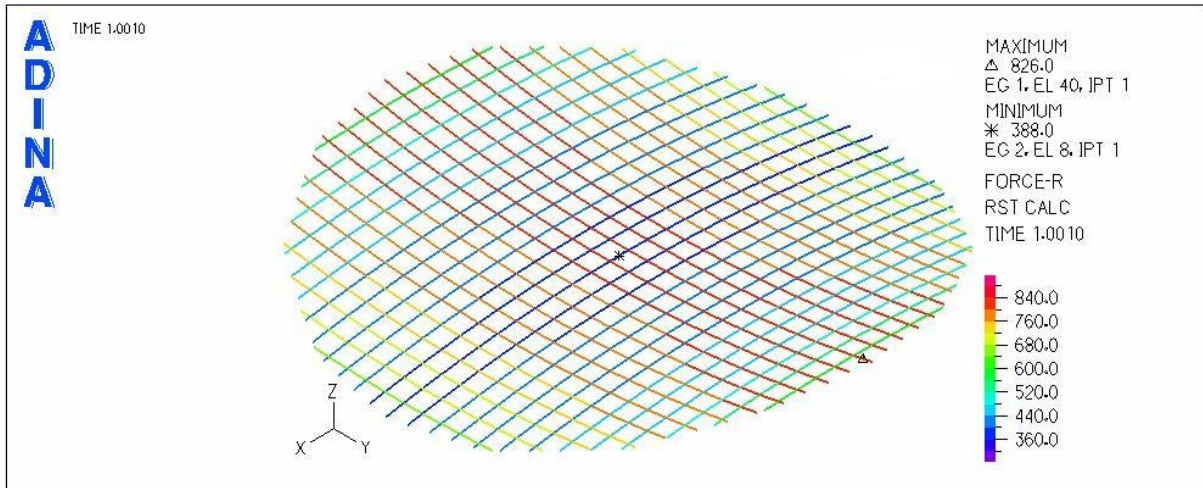


Figure 9-2: Deformed state and cable tensions under permanent loads

9.3.2 Modal analysis

Modal analysis is conducted in order to calculate the natural frequencies for the cable net considering as initial state the one under permanent loads. Additional masses are assumed, corresponding to the additional permanent loads. The mass matrix is considered as lumped. The first mode of the system is an antisymmetric one with respect to both horizontal axes with natural frequency 0.976Hz. The second and third modes are antisymmetric with reference to y and x axes, respectively, with natural frequencies 0.991Hz and 1.013Hz, respectively. The fourth vibration mode is a symmetric one with frequency 1.059Hz. The subsequent modes have symmetric or antisymmetric shapes. The modal shapes and the corresponding natural frequencies of the first nine modes are shown in Figure 9-3.

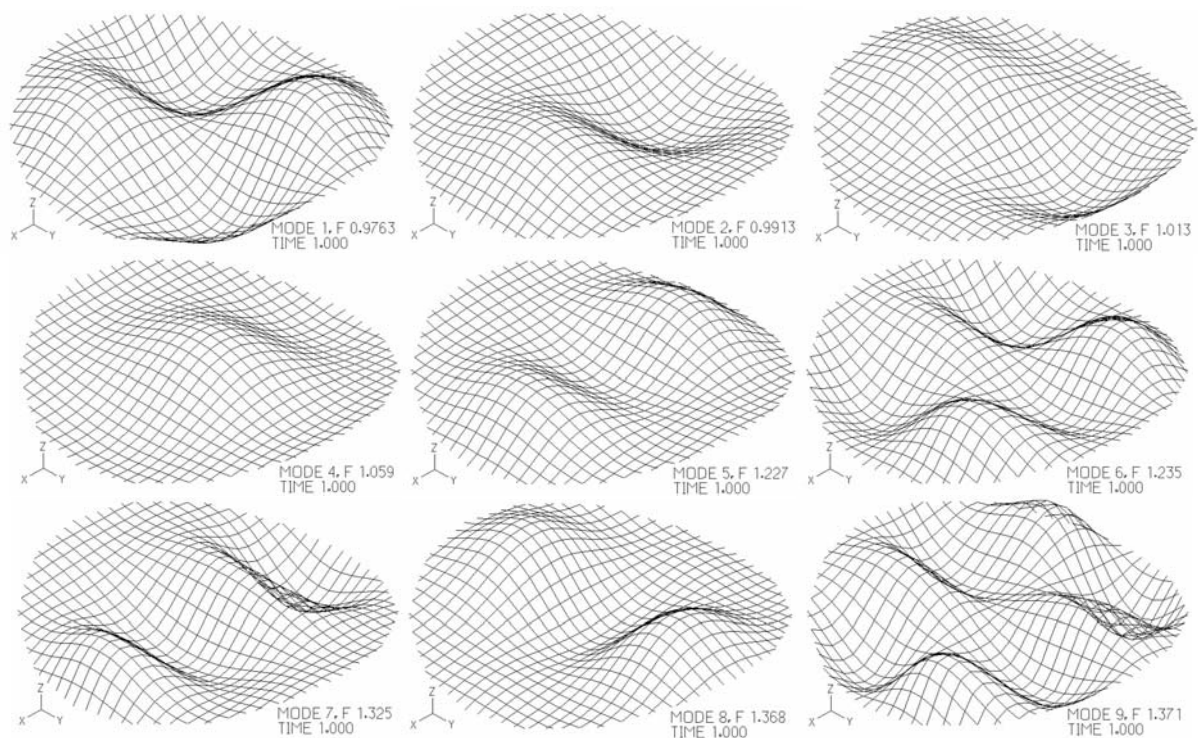


Figure 9-3: First nine vibration modes and natural frequencies

9.4 WIND DIRECTION AND SPATIAL DISTRIBUTION

A wind direction towards +x axis and parallel to the secondary cables (wind 0°) is considered, shown in Figure 9-4a. In chapter 8 the pressure coefficients were defined for this example and for this wind direction, illustrated in Figure 9-4b, where HP stands for High Points and LP for Low Points. The negative values of c_{pe} indicate suction all over the surface of the roof.

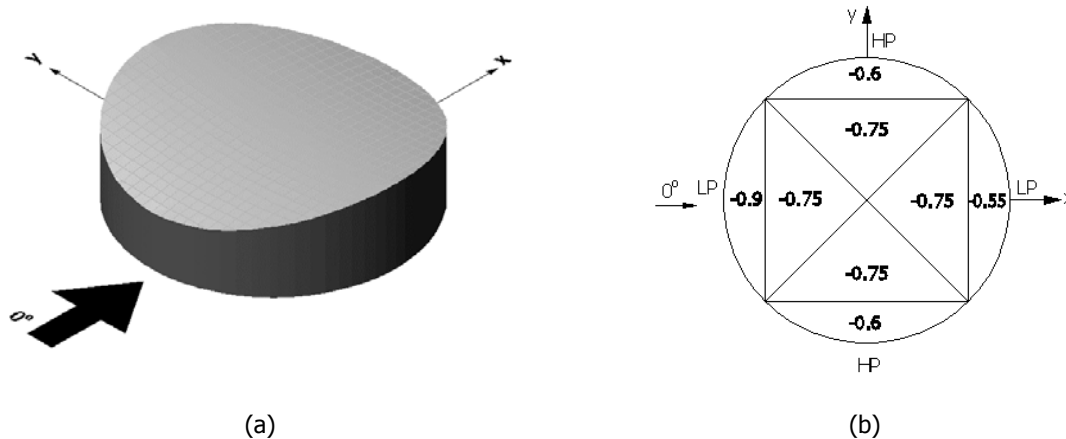


Figure 9-4: (a) Wind direction 0°, (b) Pressure coefficients

9.5 WIND ACTION

9.5.1 Wind velocities

According to Eurocode 1 [9-7], the mean wind velocity $V_m(z)$ at a height z above the terrain depends on the terrain roughness (expressed by c_r) and orography (expressed by c_o , taken as 1) and on the basic wind velocity, v_b . Considering a basic wind velocity $v_b=v_{b,0}=30\text{m/sec}$, terrain category III with $z_0=0.3\text{m}$, $z_{0,II}=0.05\text{m}$ and $z_{\min}=5\text{m}$, and height of the roof $z=25\text{m}$, the coefficients k_r and c_r are calculated:

$$k_r=0.19(z_0/z_{0,II})^{0.07}=0.19(0.3\text{m}/0.05\text{m})^{0.07}=0.215 \quad (9-1)$$

$$c_r(z)=k_r \ln(z/z_0) \Rightarrow c_r(25\text{m})=0.215 \ln(25\text{m}/0.3\text{m})=0.953 \quad (9-2)$$

and the mean velocity is:

$$V_m(z)=c_r(z) c_o(z) v_b \Rightarrow V_m(25\text{m})=0.953 \cdot 1.00 \cdot 30\text{m/sec}=28.58\text{m/sec} \quad (9-3)$$

9.5.2 Wind velocity variation with time

Finding a real wind record with a small recording time step is proved to be difficult. A common time step of such measurements is one or two minutes, usually obtained for meteorological purposes. Such time steps though are very large for analysing cable nets with eigenfrequencies close to 1.00Hz, because if a structure is subjected to a dynamic load with frequency much smaller than the lowest eigenfrequency, the response is practically static in nature and no dynamic motions are observed [9-11].

The wind velocity time-history diagram used for the nonlinear dynamic analyses of the cable net is retrieved from an experiment during the program Long-term Inflow and Structural Test (LIST) [9-8]. This program is collecting long-term, continuous inflow and structural response data to characterise

the extreme loads that drive the design of wind turbines. A heavily instrumented Micon 65/13M turbine is being used as the test turbine for this program (Photo 9-1, [9-12]). The experiment included measurements on three similar turbines, called the central tower, the north and the south ones, located in Bushland, Texas (Photo 9-2, [9-12]). Three components of wind velocity, U , V , and W , were recorded, referring to the along, across, and vertical components of the wind velocity, respectively. Data from the various instruments are sampled at a rate of 30Hz, using a newly developed data acquisition system that features a time-synchronised continuous data stream that is telemetered from the turbine rotor [9-13]. The data, taken continuously, are divided into 10-minute segments and archived for analysis.



Photo 9-1: LIST test turbine, reported from [9-12]



Photo 9-2: LIST turbines in Bushland, Texas, reported from [9-12]

The location of the measurement instruments are shown in Figure 9-5, reported from [9-12]. On the central tower, there were recordings at three different heights: at 14.4m (Figure 9-6), at 22.9m (Figure 9-7), and at 31.4m (Figure 9-8); on the north (Figure 9-9) and south (Figure 9-10) towers, recordings were only at height of 22.9m.

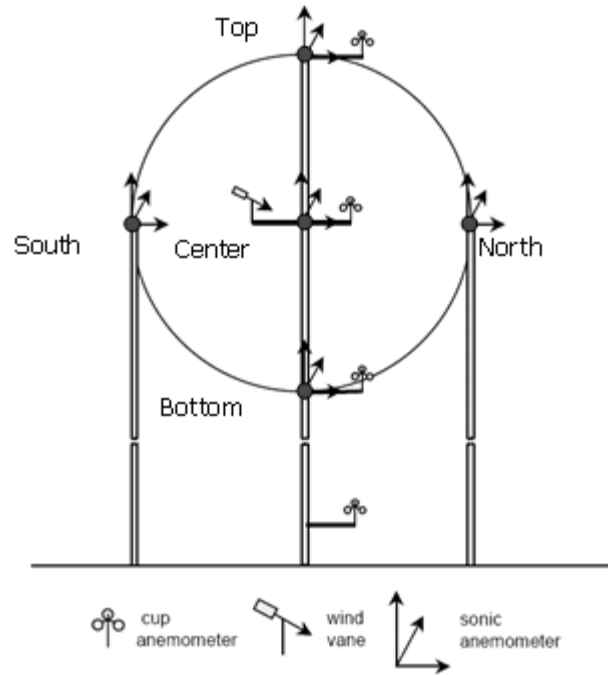


Figure 9-5: LIST turbines: location of measurement instruments, reported from [9-12]

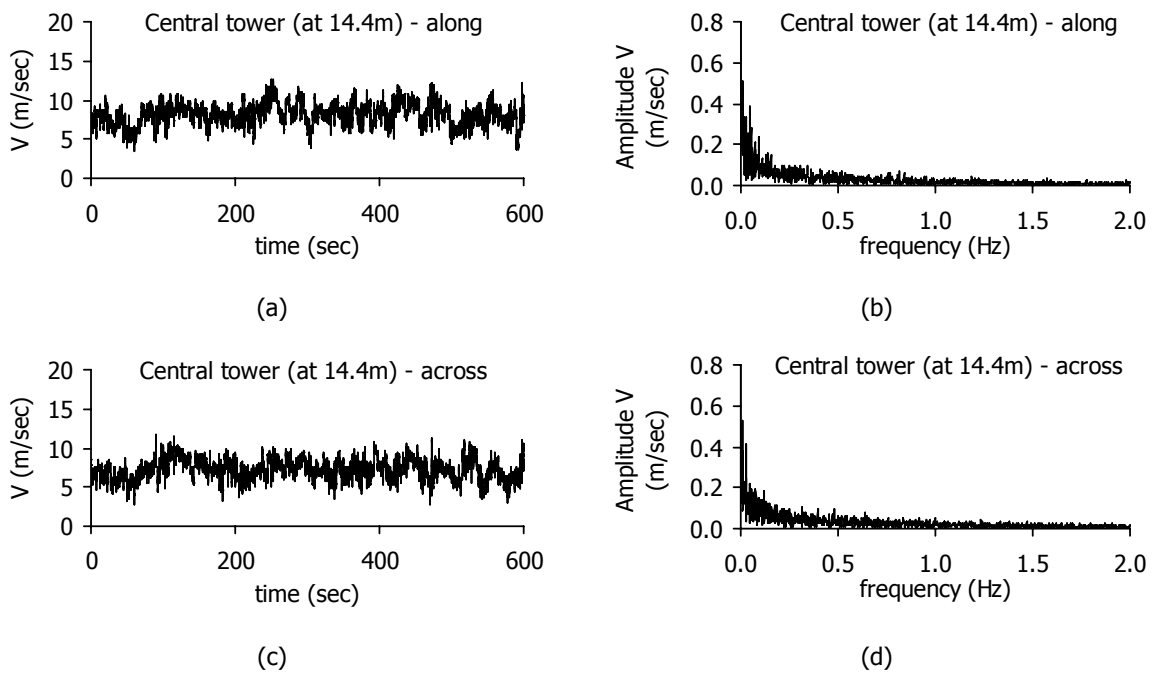


Figure 9-6: Central tower recording at height 14.4m: (a) time-history diagram of the along velocity, (b) Fourier diagram of the along velocity, (c) time-history diagram of the across velocity, (d) Fourier diagram of the across velocity

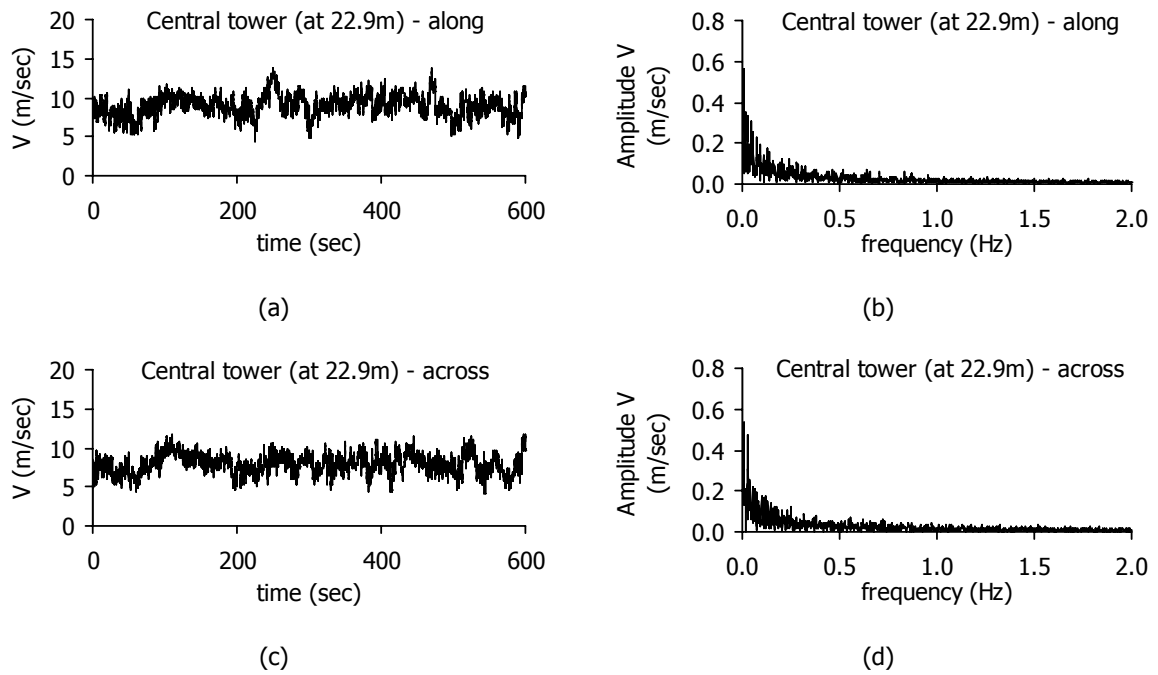


Figure 9-7: Central tower recording at height 22.9m: (a) time-history diagram of the along velocity, (b) Fourier diagram of the along velocity, (c) time-history diagram of the across velocity, (d) Fourier diagram of the across velocity

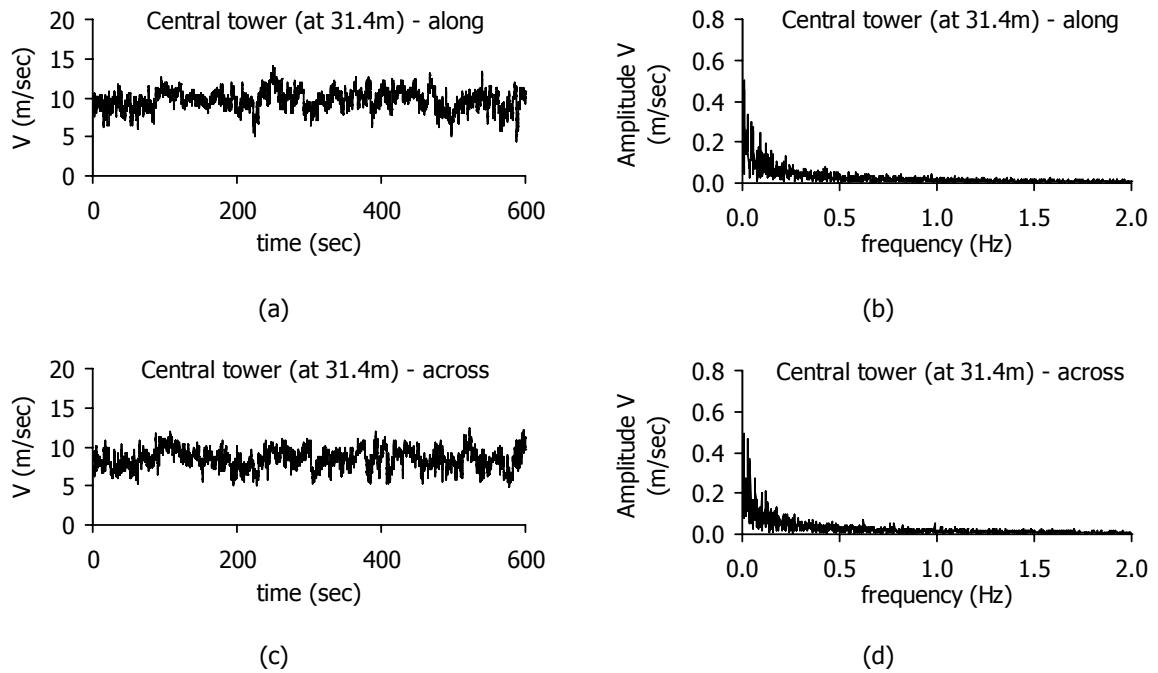


Figure 9-8: Central tower recording at height 31.4m: (a) time-history diagram of the along velocity, (b) Fourier diagram of the along velocity, (c) time-history diagram of the across velocity, (d) Fourier diagram of the across velocity

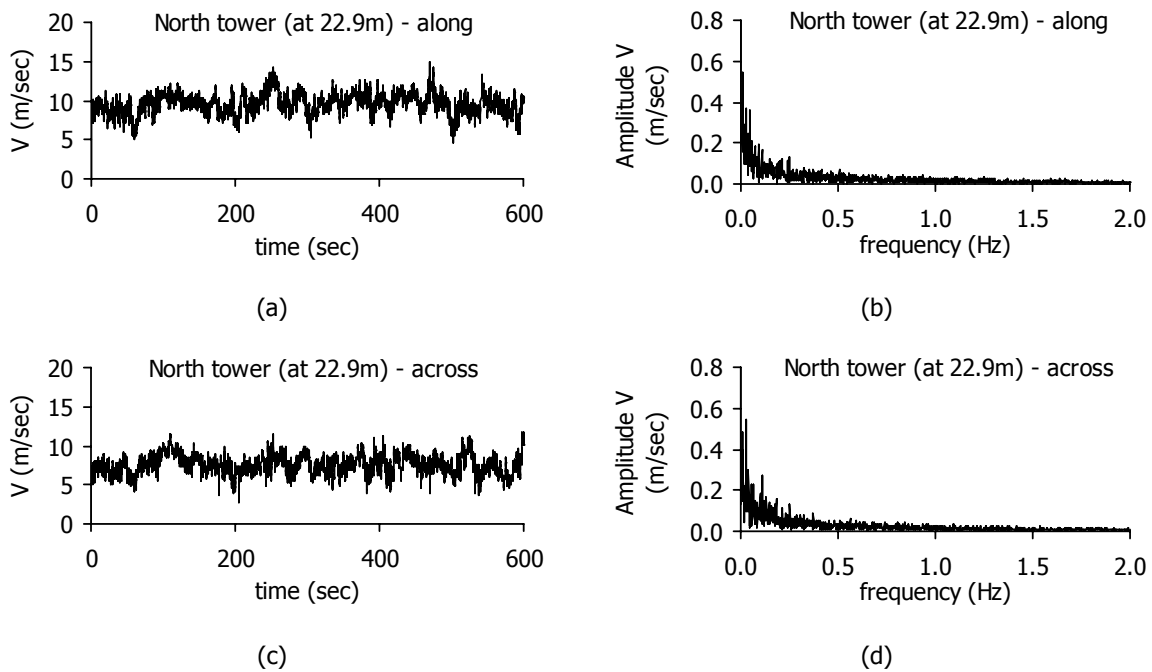


Figure 9-9: North tower recording at height 22.9m: (a) time-history diagram of the along velocity, (b) Fourier diagram of the along velocity, (c) time-history diagram of the across velocity, (d) Fourier diagram of the across velocity

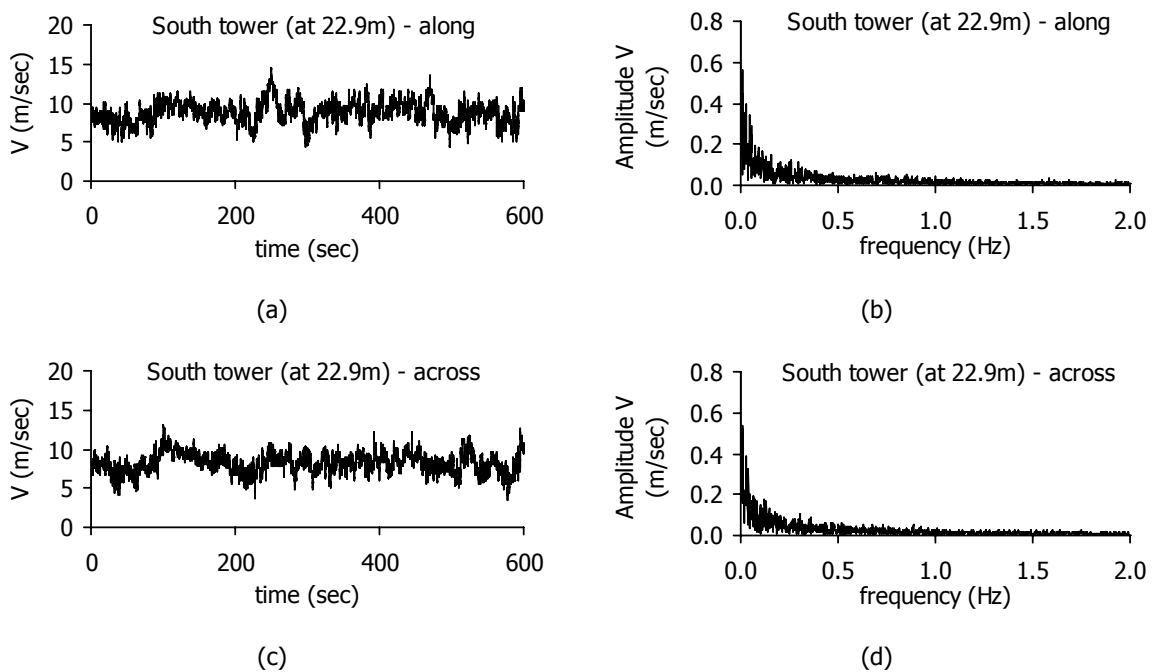


Figure 9-10: South tower recording at height 22.9m: (a) time-history diagram of the along velocity, (b) Fourier diagram of the along velocity, (c) time-history diagram of the across velocity, (d) Fourier diagram of the across velocity

It is noted that there are no significant differences between the records. For all diagrams the values of wind velocity are smaller than 15m/sec. Moreover, their main frequencies are smaller than 0.50Hz, while no significant amplitudes of wind velocity are observed for frequencies larger than 1.00Hz. The velocity diagram used in this chapter is the one of the along velocity recorded on the south tower (Figure 9-10a) presenting the maximum value of the wind velocity. The actually measured values are

scaled so that the mean value of the diagram equals to $V_m(25m)=28.58\text{m/sec}$, which is the mean velocity calculated by Eq. (9-3). The time-history of the scaled wind velocity, as well as its spectrum are plotted in Figure 9-11. The minimum and maximum values of the wind velocity are 14.35m/sec and 47.41m/sec , respectively.

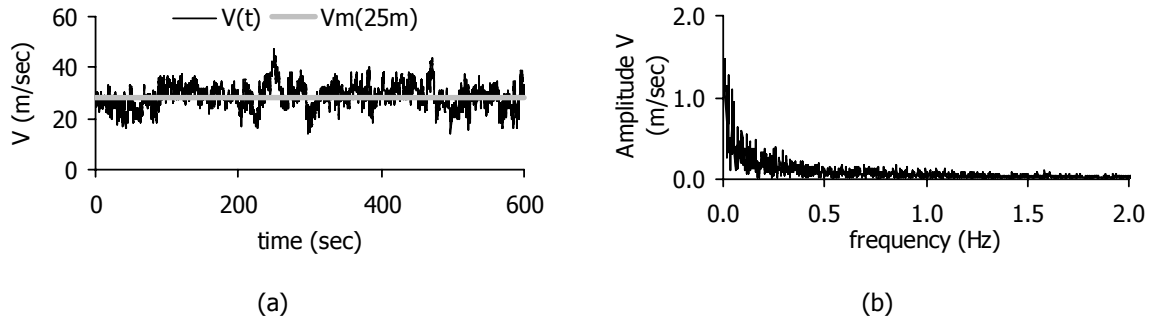


Figure 9-11: Wind velocity diagrams: (a) time-history diagram, (b) Fourier diagram

9.5.3 Static wind pressure and nodal force

The peak velocity pressure $q_p(z)$ at height z includes mean and short-term velocity fluctuations. The turbulence intensity of the wind is defined as [9-7]:

$$I_v(z) = 1 / \{ \ln(z/z_0) \cdot c_0(z) \} \Rightarrow I_v(25m) = 1 / \{ \ln(25m/0.3m) \cdot 1.00 \} = 0.23 \quad (9-4)$$

According to Eurocode 1 [9-7], taking into account the air density equal to $\rho = 1,25\text{kg/m}^3$ at height $z = 25\text{m}$, the peak velocity pressure is calculated as:

$$q_p(z) = 1/2 [1 + 7I_v(z)] \rho (V_m(z))^2 \Rightarrow$$

$$q_p(25m) = \frac{1}{2} [1 + 7 \cdot 0.23] \cdot \frac{0.0125\text{kN/m}^3}{10\text{m/sec}^2} \cdot (28.58\text{m/sec})^2 = 1.32\text{kN/m}^2 \quad (9-5)$$

Applying the quasi-static analysis method of Eurocode 1 [9-7], the wind pressure acting on the external surface of the roof is expressed as:

$$w(z) = q_p(z) c_{pe} \Rightarrow w(25m) = 1.32 c_{pe} (\text{kN/m}^2) \quad (9-6)$$

where c_{pe} is the pressure coefficient. The size factor is defined as:

$$c_s = \frac{1 + 7 \cdot I_v(z_e) \cdot \sqrt{B^2}}{1 + 7 \cdot I_v(z_e)} \quad (9-7)$$

Assuming the background factor $B^2 = 1$, on the safe side as recommended by Eurocode 1, $c_s = 1$. The turbulent length scale at height $z = 25\text{m} > z_{\min} = 5\text{m}$ is:

$$L(z) = L_t \cdot \left(\frac{z}{z_t} \right)^{\alpha} \Rightarrow L(25m) = 300\text{m} \left(\frac{25\text{m}}{200\text{m}} \right)^{[0.67 + 0.05 \ln(0.3)]} = 84.41\text{m} \quad (9-8)$$

Considering that the main vibration mode of the net is the first symmetric one, with eigenfrequency $n = 1.059\text{Hz}$, the non-dimensional frequency of the wind velocity is defined as:

$$f_L(z, n) = \frac{n \cdot L(z)}{V_m(z)} \Rightarrow f_L(25m, 1.059\text{Hz}) = \frac{1.059\text{Hz} \cdot 84.41\text{m}}{28.58\text{m/sec}} = 3.128 \quad (9-9)$$

Taking into consideration the turbulence factor equal to $k_T=1.00$ as recommended in Eurocode 1 and $k_r=0.215$, as calculated from Eq. (9-1), the standard deviation of the turbulence is:

$$\sigma_v = k_r \cdot v_b \cdot k_T = 0.215 \cdot 30 \text{m/sec} \cdot 1.00 = 6.45 \text{m/sec} \quad (9-10)$$

The non-dimensional power spectral density suggested by Eurocode 1 is expressed as:

$$S_L(z,n) = \frac{6.8 \cdot f_L(z,n)}{\sqrt[3]{[1 + 10.2 \cdot f_L(z,n)]^5}} \Rightarrow$$

$$S_L(25\text{m}, 1.059\text{Hz}) = \frac{6.8 \cdot 3.128}{\sqrt[3]{[1 + 10.2 \cdot 3.128]^5}} = 0.063 \quad (9-11)$$

Considering that the height and the width of the structure are $h=25\text{m}$ and $b=100\text{m}$, respectively, the reference height z_e for the external pressure is equal to the height of the central node of the roof, that is $z_e=z=25\text{m}$, and that the frequency of the first symmetric mode represents the frequency $n_{1,x}=1.059\text{Hz}$, the aerodynamic admittance functions are calculated as:

$$R_h = \frac{1}{\eta_h} - \frac{1}{2 \cdot \eta_h^2} (1 - e^{-2 \cdot \eta_h}) = \frac{1}{4.26} - \frac{1}{2 \cdot 4.26^2} (1 - e^{-2 \cdot 4.26}) = 0.207 \quad (9-12)$$

$$R_b = \frac{1}{\eta_b} - \frac{1}{2 \cdot \eta_b^2} (1 - e^{-2 \cdot \eta_b}) = \frac{1}{17.05} - \frac{1}{2 \cdot 17.05^2} (1 - e^{-2 \cdot 17.05}) = 0.057 \quad (9-13)$$

with

$$\eta_h = \frac{4.6 \cdot h}{L(z_e)} \cdot f_L(z_e, n_{1,x}) = \frac{4.6 \cdot 25\text{m}}{84.41\text{m}} \cdot 3.128 = 4.26 \quad (9-14)$$

$$\eta_b = \frac{4.6 \cdot b}{L(z_e)} \cdot f_L(z_e, n_{1,x}) = \frac{4.6 \cdot 100\text{m}}{84.41\text{m}} \cdot 3.128 = 17.05 \quad (9-15)$$

The resonance response factor R^2 is defined as:

$$R^2 = \frac{\pi^2}{2 \cdot \delta} \cdot S_L(z_e, n_{1,x}) \cdot R_h(\eta_h) \cdot R_b(\eta_b) = \frac{\pi^2}{2 \cdot 0.02} \cdot 0.063 \cdot 0.207 \cdot 0.057 = 0.183 \quad (9-16)$$

where δ is the total logarithmic decrement of damping, taken equal to 2%. The up-crossing frequency v is expressed as:

$$v = n \sqrt{\frac{R^2}{B^2 + R^2}} = 1.059\text{Hz} \sqrt{\frac{0.183}{1.00 + 0.183}} = 0.417\text{Hz} > 0.08\text{Hz} \quad (9-17)$$

The peak factor k_p is obtained by:

$$k_p = \sqrt{2 \cdot \ln(v \cdot T)} + \frac{0.6}{\sqrt{2 \cdot \ln(v \cdot T)}} =$$

$$\sqrt{2 \cdot \ln(0.417\text{Hz} \cdot 600 \text{sec})} + \frac{0.6}{\sqrt{2 \cdot \ln(0.417\text{Hz} \cdot 600 \text{sec})}} = 3.504 \quad (9-18)$$

where T is the averaging time for the mean wind velocity and is equal to $T=600$ seconds. Thus, the dynamic factor c_d is:

$$C_d = \frac{1 + 2 \cdot k_p \cdot I_v(z_e) \cdot \sqrt{B^2 + R^2}}{1 + 7 \cdot I_v(z_e) \cdot \sqrt{B^2}} = \frac{1 + 2 \cdot 3.504 \cdot 0.23 \cdot \sqrt{1 + 0.183}}{1 + 7 \cdot 0.23 \cdot \sqrt{1}} = 1.054 \quad (9-19)$$

Considering a reference area for each node $A_{ref}=(3.846\text{m})^2$ and taking into consideration the external wind pressure calculated from Eq. (9-6), the force applied on every node of the cable net is:

$$F = c_s C_d w(z) A_{ref} = 1.054 \cdot 1.32 \cdot (3.846\text{m})^2 c_{pe} = 20.58 c_{pe} \text{ (kN/node)} \quad (9-20)$$

Since no openings are considered, the internal wind pressure is equal to zero. In addition, friction forces are not taken into account.

9.5.4 Dynamic wind pressure and nodal force

Considering the wind velocity time variation $V(t)$ of Figure 9-11, the wind pressure acting on the external surface is a function of time:

$$w(t) = q(t) c_{pe} = 0.000625 \cdot V(t)^2 \cdot c_{pe} \quad (9-21)$$

where:

$$q(t) = 1/2 \rho V(t)^2 \Rightarrow q_p(t) = \frac{1}{2} \cdot \frac{0.0125 \text{ kN/m}^3}{10 \text{ m/sec}^2} \cdot V(t)^2 = 0.000625 \cdot V(t)^2 \quad (9-22)$$

and the load applied on every node of the cable net is:

$$F(t) = w(t) A_{ref} = 0.000625 \cdot V(t)^2 \cdot (3.846\text{m})^2 \cdot c_{pe} = 0.00924 c_{pe} [V(t)]^2 \text{ (kN/node)} \quad (9-23)$$

The time-history diagram of the wind load is plotted in Figure 9-12. The maximum load on the nodes of the cable net is $F_{max} = 20.78 c_{pe}$ (kN/node), which is very close to the one caused by the static wind pressure, given by Eq. (9-20).

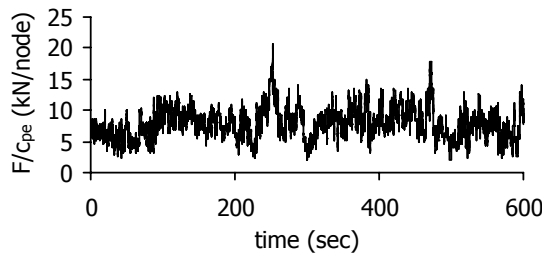


Figure 9-12: Time-history diagram of the wind force acting on every node of the net

9.6 RESPONSE TO COMBINED PERMANENT LOADS AND WIND ACTION

9.6.1 Nonlinear static analysis

The static wind load is applied on every node of the net, considering also the short-term velocity fluctuations, as calculated in section 9.5.3. The loads applied on every node are shown in Figure 9-13, according to the zones with different pressure coefficients. The load direction is assumed vertical, while the negative sign denotes wind suction. It is worth mentioning that the wind load considered for the static analysis of the Peace and Friendship Stadium was -1.10 kN/m^2 , uniformly distributed, corresponding to nodal loads -16.30 kN , which is very close to the values of Figure 9-13.

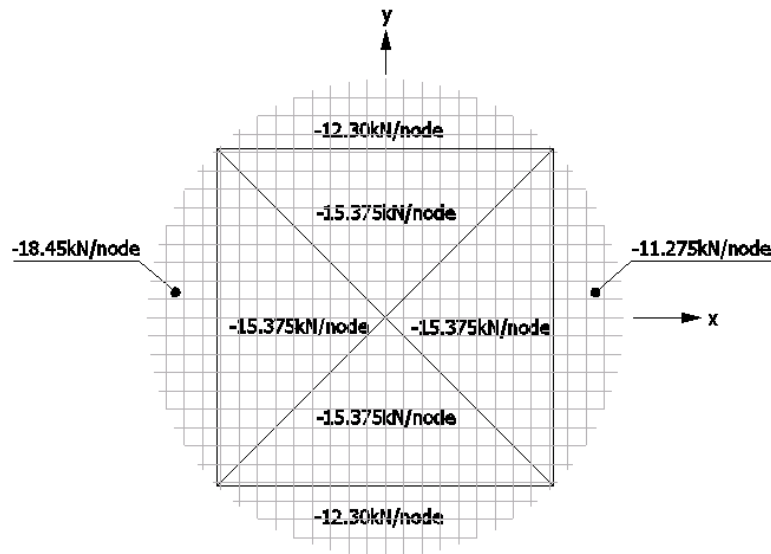


Figure 9-13: Static wind load on the nodes of the cable net for wind direction 0°

As initial state, the one under pretension and permanent loads is considered. Since the pressure coefficients define wind suction all over the surface, the wind load causes an upward z-displacement of the net equal to 0.306m. The minimum cable tension is 329kN and the maximum one 909kN. The deformed shape of the net is shown in Figure 9-14, where the maximum and minimum cable tensions are also plotted.

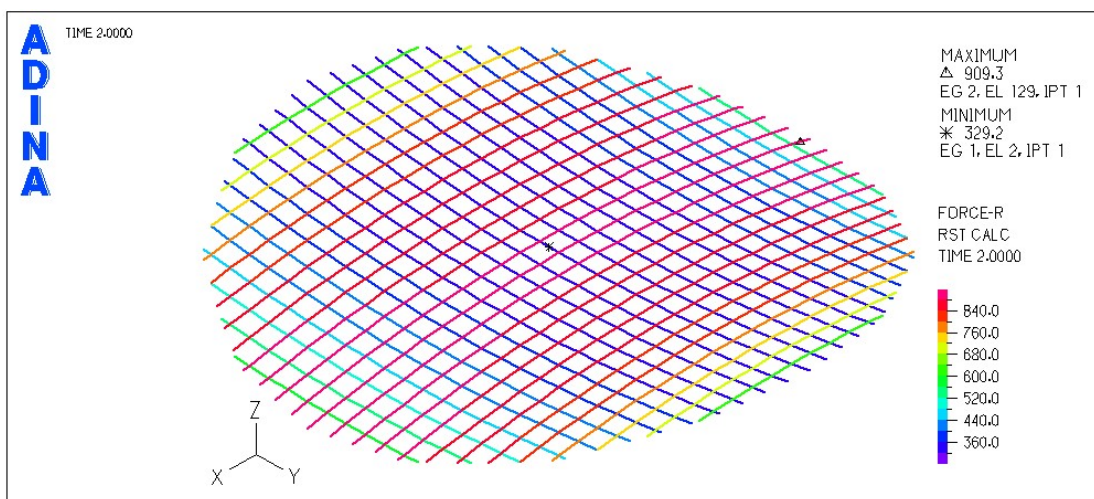


Figure 9-14: Deformed state and cable tensions under permanent and wind loads

9.6.2 Nonlinear dynamic analysis

Taking into account the velocity diagram of Figure 9-11 and applying the wind action on the net as described in section 9.5.4, the dynamic response of the cable net is calculated, considering again additional nodal masses due to permanent loads. Assuming that the damping ratio is the same for the first four modes, the Rayleigh damping coefficients [9-9] are calculated taking into consideration the first and fourth natural frequencies. The frequency of the first and fourth vibration modes are $\omega_1=6.134\text{sec}^{-1}$ and $\omega_4=6.654\text{sec}^{-1}$, respectively. For damping ratio $\zeta=2\%$, the Rayleigh damping coefficients are:

$$\alpha_0 = \zeta \frac{2\omega_i\omega_j}{\omega_i + \omega_j} = 0.02 \frac{2 \cdot 6.134 \cdot 6.654}{6.134 + 6.654} = 0.12767 \text{ sec}^{-1} \quad (9-24)$$

$$\alpha_1 = \zeta \frac{2}{\omega_i + \omega_j} = \frac{2 \cdot 0.02}{6.134 + 6.654} = 0.00313 \text{ sec} \quad (9-25)$$

The difference between the dynamic response and the static one is defined by the ratio of the dynamic magnitudes of the response over the static ones corresponding to the same load, denoted in chapter 7 as R_{dyn} . Thus, node 15, which is the central node of the net, exhibits the maximum deflections, which are -0.649m (downwards) and 0.302m (upwards). The maximum negative deflection is not predicted by the static analysis, while the maximum positive one is accurately assessed by the static one. The deflection diagrams of node 15 are plotted in Figure 9-15.

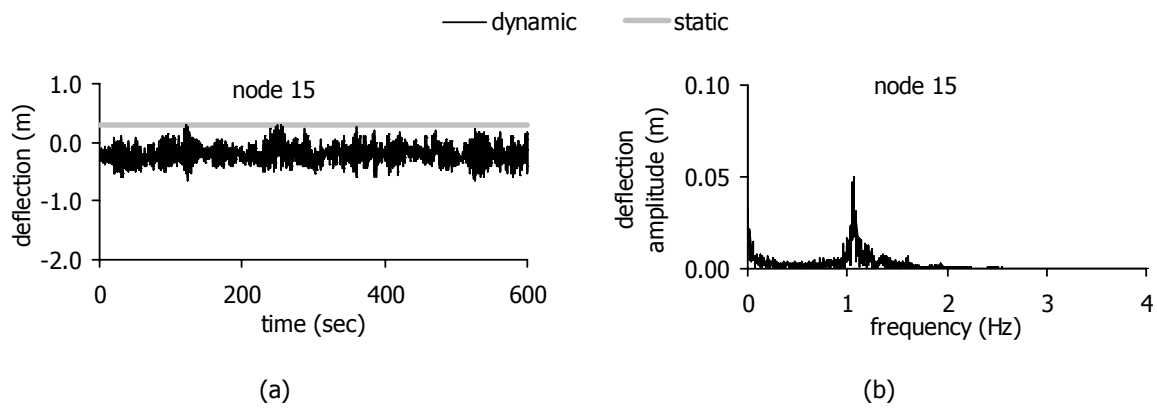


Figure 9-15: Deflection of the central node: (a) time-history diagram, (b) response spectrum

Cable segments 418 and 40, shown in Figure 9-16, develop the minimum and maximum tension, respectively. The minimum cable tension is 137kN, being 42% of the minimum static one ($R_{\text{dyn}}=0.42$) and the maximum cable tension is 1117kN, with $R_{\text{dyn}}=1.23$. The tension diagrams are shown in Figure 9-17. It is noted that the tension response spectra present two main frequencies, one at 1.04Hz, being close to the natural frequency of the system of the first symmetric mode, and one at 1.20Hz for the minimum cable tension and 1.38Hz for the maximum one, corresponding to the fifth mode with natural frequency 1.23Hz and the eighth one with 1.37Hz, respectively, being both symmetric modes, as shown in Figure 9-3. Significant amplitudes are also observed for frequencies smaller than 1.00Hz, while, for frequencies larger than 2.00Hz, the amplitudes are very small.

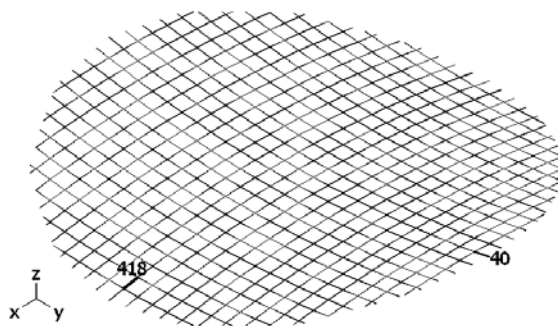


Figure 9-16: Cable segments 418 and 40

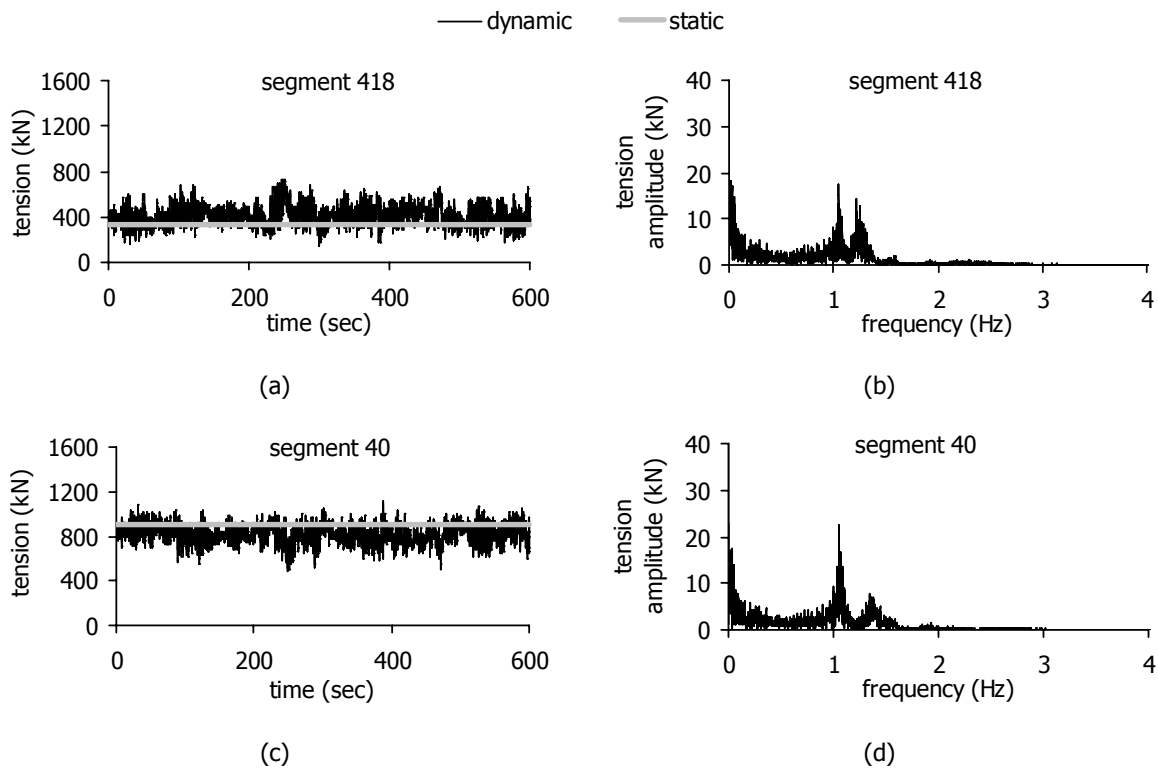


Figure 9-17: Minimum cable tension: (a) time-history diagram, (b) response spectrum, Maximum cable tension: (c) time-history diagram, (d) response spectrum

Some snapshots of the dynamic motion, where the three symmetric modes appear, are illustrated in Figure 9-18, in which the deformation is magnified. Although the spectrum of the wind velocity presents large amplitudes for frequencies much smaller than the eigenfrequencies and much smaller amplitudes for frequencies close to the natural frequencies, the symmetric modes of the system are activated. This occurs because even small amplitudes of the wind velocity cause fundamental resonances with large oscillation amplitudes, despite the presence of damping. In addition, due to the small frequencies of the wind, superharmonic resonances evolve, triggering the oscillation of the net with small frequencies, as the ones of the wind, but also with frequencies larger than the ones of the external excitation. Both kinds of resonances lead to larger dynamic response with respect to the static one, as observed from the cable tension time-histories.

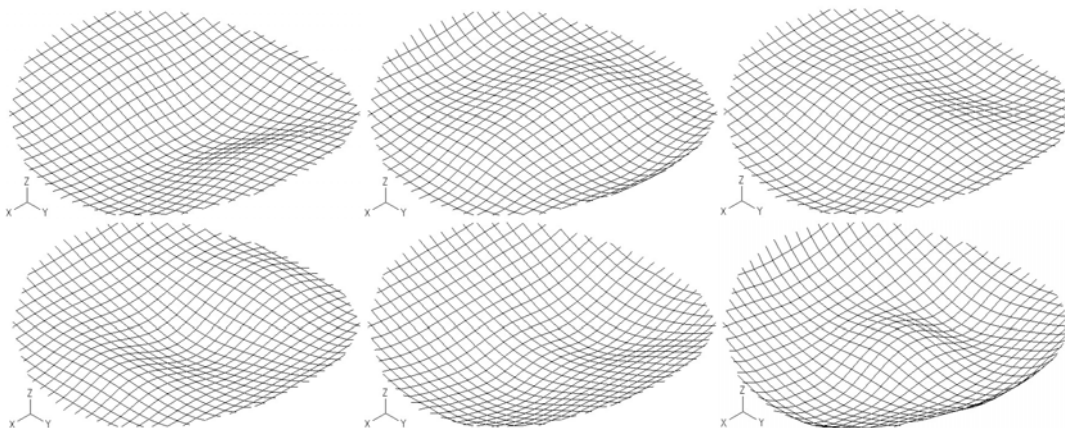


Figure 9-18: Snapshots of the dynamic motion for wind direction 0°

9.7 PARAMETRIC ANALYSES

9.7.1 Influence of the wind direction

The wind direction towards +y axis and parallel to the main cables (wind 90°) is considered, shown in Figure 9-19a. The pressure coefficients are illustrated in Figure 9-19b, retrieved from chapter 8. In two leeward zones the coefficient c_{pe} takes two values, one positive ($c_{pe}=+0.20$) and one negative ($c_{pe}=-0.60$). The negative one corresponds to a spatial distribution of the wind pressure similar to the one for wind direction 0°, thus only the positive value is taken into account in this section resulting in an antisymmetric spatial distribution.

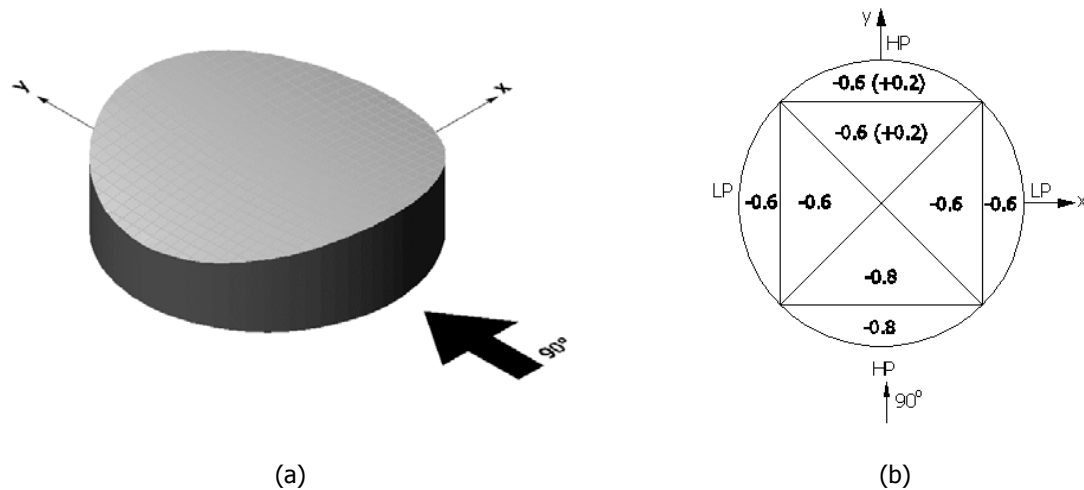


Figure 9-19: (a) Wind direction 90°, (b) Pressure coefficients

In this case the main vibration mode is assumed to be the third one, which is antisymmetric with respect to x-axis, with eigenfrequency 1.013Hz. Following the procedure described in section 9.5.3, considering $n=1.013\text{Hz}$, the dynamic factor c_d results equal to 1.06. Thus, according to Eq. (9-20), the wind force on every node is:

$$F = c_s c_d w(z) A_{ref} = 1.06 \cdot 1.32 \cdot (3.846\text{m})^2 c_{pe} = 20.70 c_{pe} \text{ (kN/node)} \tag{9-26}$$

Taking into consideration the pressure coefficients of Figure 9-19b, the loads applied on every node are shown in Figure 9-20. The positive sign denotes a downward direction, while the negative sign an upward one. The load direction is assumed again as vertical. The state under pretension and permanent loads is considered again as initial state, calculated in section 9.3.1. Node 27 exhibits the maximum downward z-displacement, with negative value, equal to -0.502m, while the maximum upward one, with positive value, is for node 35 and it is equal to 0.470m, as plotted in Figure 9-21, being both larger than the deflection calculated in section 9.6.1. The minimum cable tension is 291kN and the maximum one 972kN.

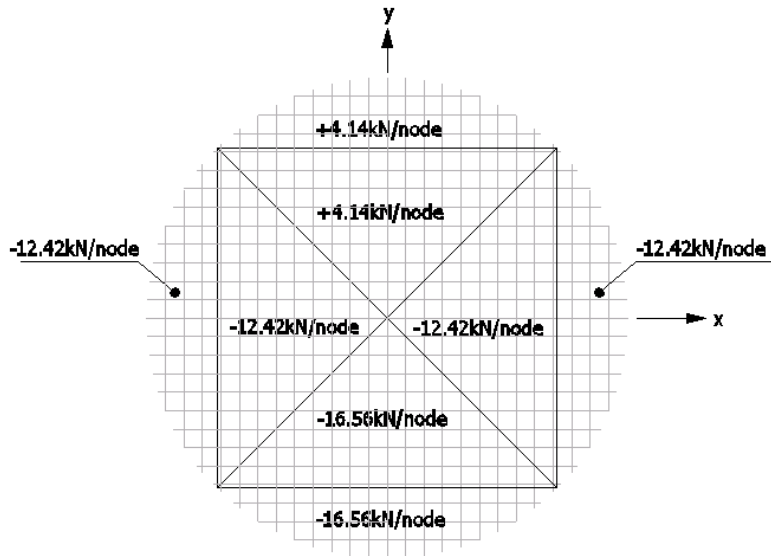


Figure 9-20: Static wind load on the nodes of the cable net for wind direction 90°

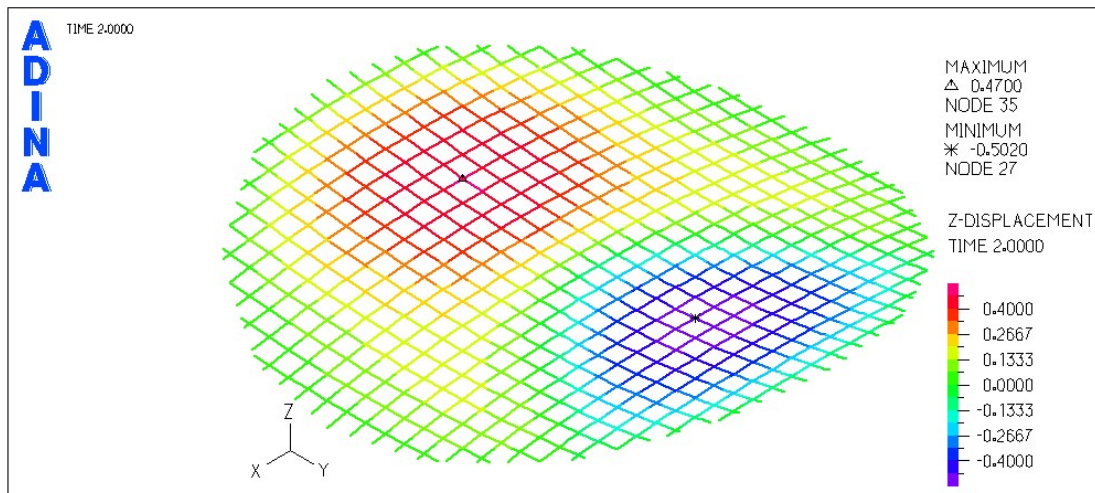


Figure 9-21: Vertical nodal displacements due to the static wind load for wind direction 90°

The dynamic response of the cable net is calculated considering the velocity diagram of Figure 9-11. The maximum negative vertical nodal displacement is -0.772m (downwards) for node 27, with $R_{\text{dyn}}=1.54$. The maximum positive one is 0.394m (upwards) for node 35, with $R_{\text{dyn}}=0.84$. The diagrams for the two nodes exhibiting the maximum negative and positive deflections are plotted in Figure 9-22. Cable segments 35 and 40 develop the minimum and maximum tension, respectively, shown in Figure 9-23. The minimum cable tension is 157kN with $R_{\text{dyn}}=0.54$ (Figure 9-24) and the maximum cable tension is 1060kN with $R_{\text{dyn}}=1.09$ (Figure 9-25). These differences are smaller than the corresponding ones for wind direction 0° , rendering the wind direction parallel to the secondary cables more unfavourable than the one parallel to the main cables.

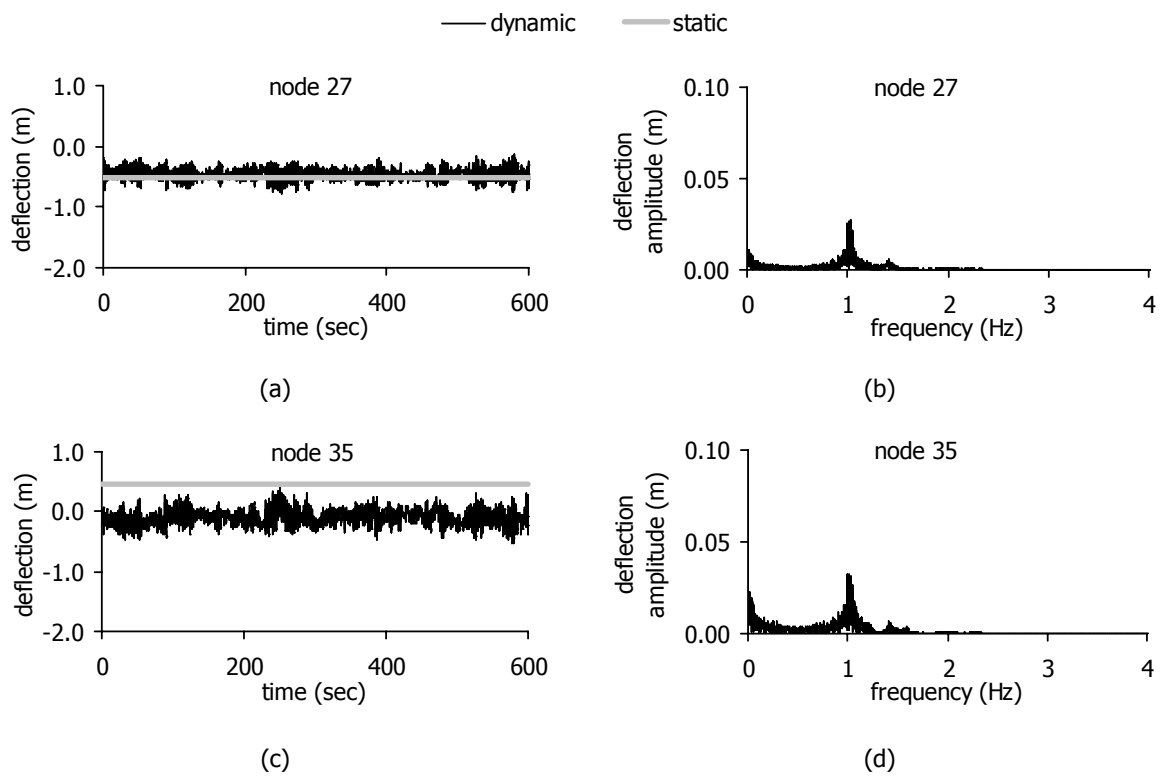


Figure 9-22: Wind direction 90°: maximum negative deflection: (a) time-history diagram, (b) response spectrum, maximum positive deflection: (c) time-history diagram, (d) response spectrum

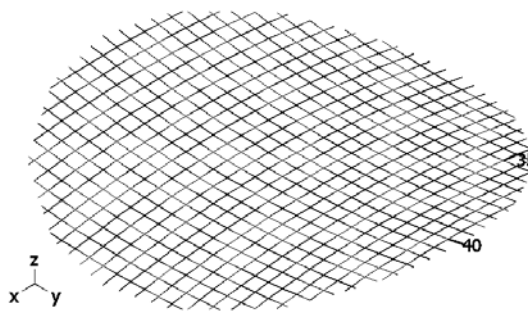


Figure 9-23: Cable segments 35 and 40

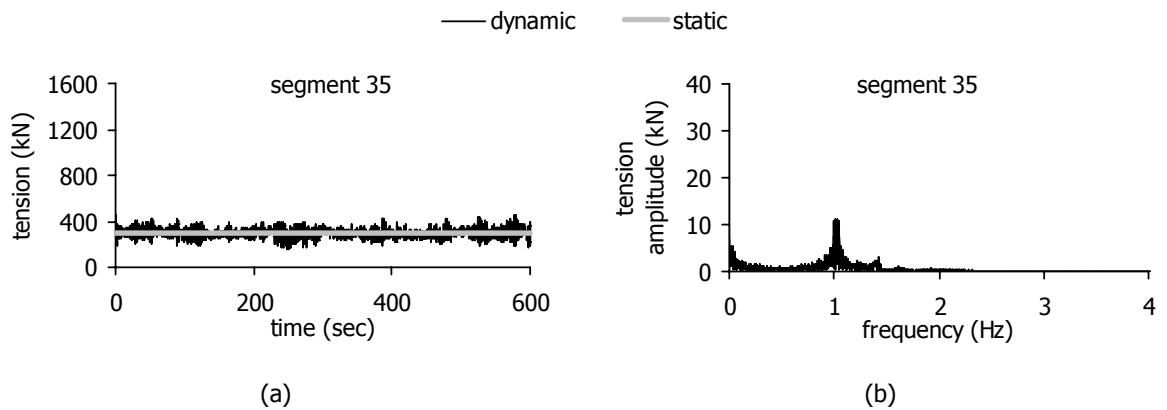


Figure 9-24: Wind direction 90°: minimum cable tension: (a) time-history diagram, (b) response spectrum

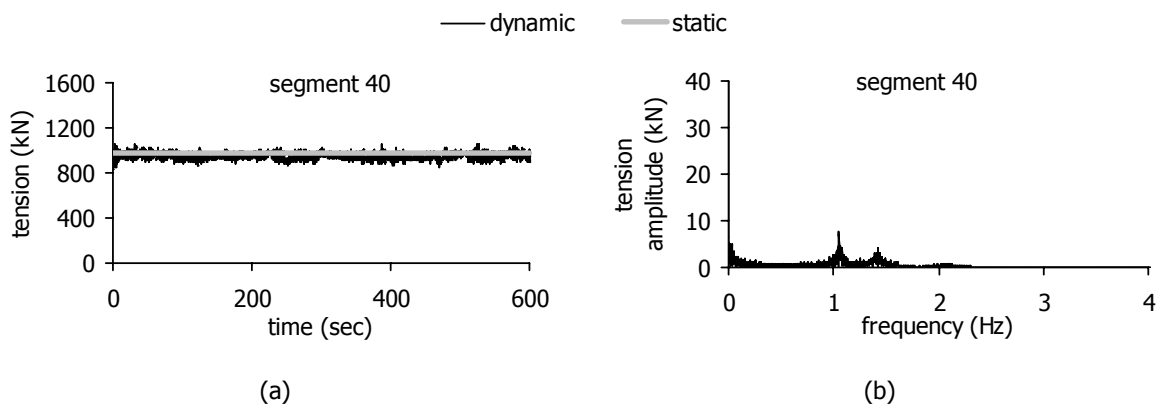


Figure 9-25: Wind direction 90°: maximum cable tension: (a) time-history diagram, (b) response spectrum

All response diagrams verify that the main vibration frequency of the cable net is close to the eigenfrequency of the system for the antisymmetric mode with respect to x-axis (1.013Hz), confirming once again the fundamental resonance caused by small loading amplitudes and the superharmonic one, due to the small frequencies of the wind. As a result of these two kinds of resonances, the dynamic response of the net is larger than the static one. The snapshots of the dynamic motion with magnified deformations, shown in Figure 9-26, confirm the antisymmetric deformed shape.

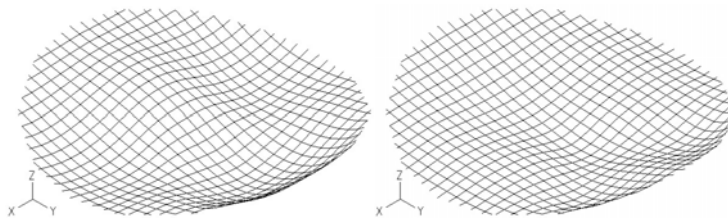


Figure 9-26: Snapshots of the dynamic motion for wind direction 90°

The maximum absolute values of the net deflection and cable tension for both assumptions regarding the wind direction are tabulated in Table 9-1.

Table 9-1: Static (st) and dynamic (d) response with respect to the wind direction

wind direction	Max net deflection			Max tension		
	w_{st} (m)	w_d (m)	w_d/w_{st}	N_{st} (kN)	N_d (kN)	N_d/N_{st}
0°	0.306	0.649	2.12	909	1117	1.23
90°	0.502	0.772	1.54	972	1060	1.09

A comparison of the maximum deflection diagrams for the two wind direction assumptions is shown in Figure 9-27. The maximum deflection is noticed for wind direction 90°, but the maximum variance of the response, which can cause fatigue problems, is observed for wind direction 0°, verified also by the larger oscillation amplitude in the response spectra.

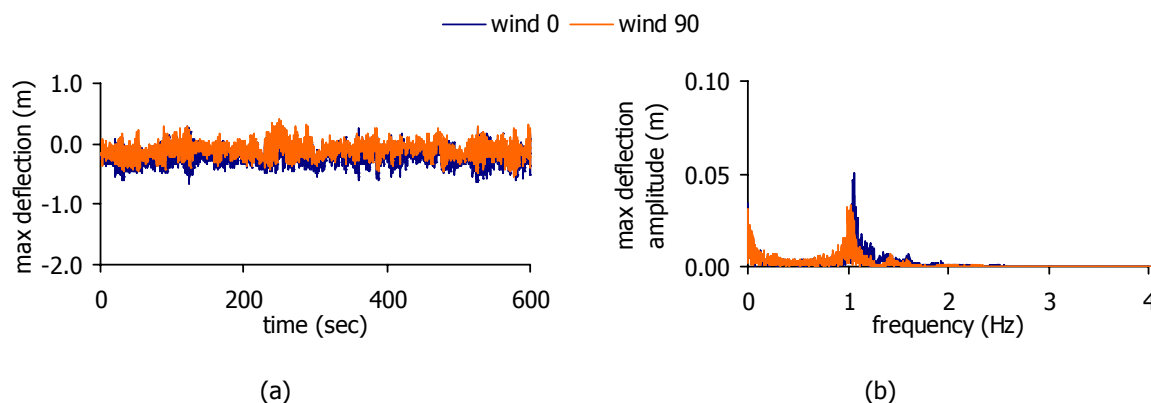


Figure 9-27: Maximum nodal deflection according to the wind direction: (a) time-history diagrams, (b) response spectra

9.7.2 Influence of the parameter λ^2

In this section the influence of the non-dimensional parameter λ^2 on the dynamic response of the cable nets is investigated. The initial pretension of the cable net described in section 9.2 corresponds to an initial cable stress, equal to 19% of the yield stress σ_y , which is a common level of prestressing for this kind of structures. In this section, two more cases are studied regarding the initial pretension and the cable cross-sectional area for the same geometry, accounting for different levels of stiffness due to the initial prestressing. Considering cable nets that approximate realistic structures, in the first case the cables have diameter $D=80\text{mm}$ and initial pretension $N_0=800\text{kN}$, corresponding to an initial cable stress equal to $10\%\sigma_y$, while in the second one, the cable diameter is $D=40\text{mm}$, and the initial pretension $N_0=600\text{kN}$, corresponding to initial cable stress $30\%\sigma_y$.

Changing the initial cable stress, the non-dimensional parameter λ^2 and the natural frequencies of the nets change too, as well as the sequence of the corresponding vibration modes, as proved in chapter 5. For the first cable net, although the initial stress is smaller than the one of the previous example, the frequency of the first symmetric mode is larger, due to the large cable diameter, axial stiffness EA and cable mass. The cable net with cable diameter $D=40\text{mm}$ and initial stress $30\%\sigma_y$, instead, has smaller eigenfrequency and parameter λ^2 than both other systems. A comparison between the different characteristics of the three systems is provided in Table 9-2.

Table 9-2: Characteristics of the nets with different cable diameters and initial cable stress

Cable net	D [mm]	N_0 [kN]	$N_0/(A\sigma_y)$ [%]	λ^2	ω_{1S} [sec^{-1}]	f_{1S} [Hz]
1	80	800	10	2.59	7.696	1.225
2	50	600	19	1.35	6.654	1.059
3	40	600	30	0.86	6.085	0.968

For the first cable net the dynamic factor c_d results equal to 1.038 taking into account the frequency of the first symmetric mode. Considering wind direction parallel to x-axis (wind 0°), the static response due to the wind load results in a maximum upward z-displacement 0.095m, a minimum cable tension 515kN and a maximum one 1097kN. The maximum and minimum dynamic deflection is observed for node 182, shown in Figure 9-28. The dynamic load of the wind causes maximum negative z-displacement of the net (downwards) equal to -0.273m and a positive one (upwards) equal to 0.069m. The deflection diagrams are illustrated in Figure 9-29. The static analysis gives conservative results regarding the maximum upward displacement, but it still cannot predict the maximum downward one.

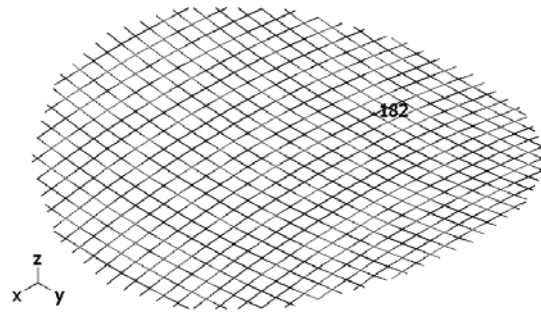
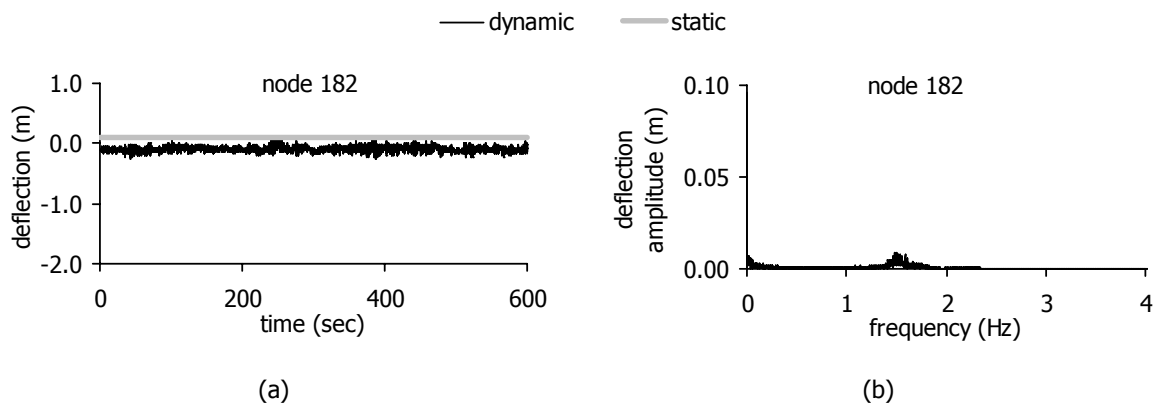


Figure 9-28: Node 182

Figure 9-29: Cable net with $\lambda^2=2.59$: maximum and minimum nodal deflection: (a) time-history diagram, (b) response spectrum

The minimum and maximum cable tensions are 253kN ($R_{\text{dyn}}=0.49$) and 1385kN ($R_{\text{dyn}}=1.26$), respectively, leading to larger differences between the static and dynamic responses, with respect to the ones of the first example given in section 9.6.2. Cable segment 27 exhibits the minimum tension, while the maximum one develops in cable segment 40 (Figure 9-30).

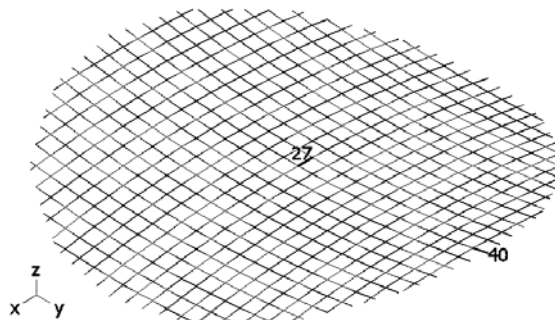


Figure 9-30: Cable segments 27 and 40

The tension diagrams are plotted in Figure 9-31. In the response spectra of the cable tensions significant tension amplitudes are observed again for small frequencies due to superharmonic resonances. The three peaks, at 1.18Hz, 1.53Hz, and 1.93Hz, confirm resonances for at least three modes.

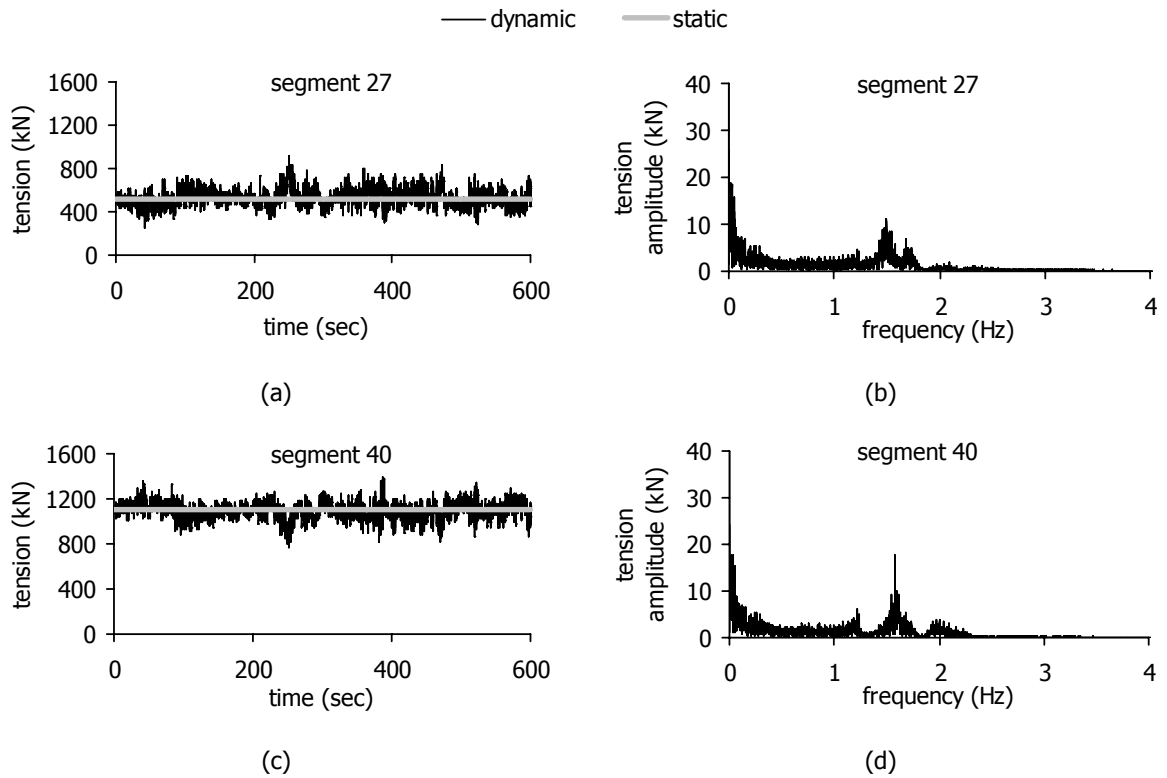


Figure 9-31: Cable net with $\lambda^2=2.59$: minimum cable tension: (a) time-history diagram, (b) response spectrum, maximum cable tension: (c) time-history diagram, (d) response spectrum

Similar differences between static and dynamic results arise for the cable net with the smallest parameter λ^2 . The dynamic factor c_d is equal to 1.067 taking into account again the frequency of the first symmetric mode. For wind direction parallel to x-axis (wind 0°), the maximum static upward z-displacement is 0.492m, the minimum cable tension 331kN and the maximum one 916kN. The dynamic wind load causes a maximum negative (downward) z-displacement of the central node of the net equal to -0.990m and a positive (upward) one 0.621m (Figure 9-32). The maximum downward deflection cannot be calculated by the static analysis while the maximum upward dynamic deflection is close to the static one.

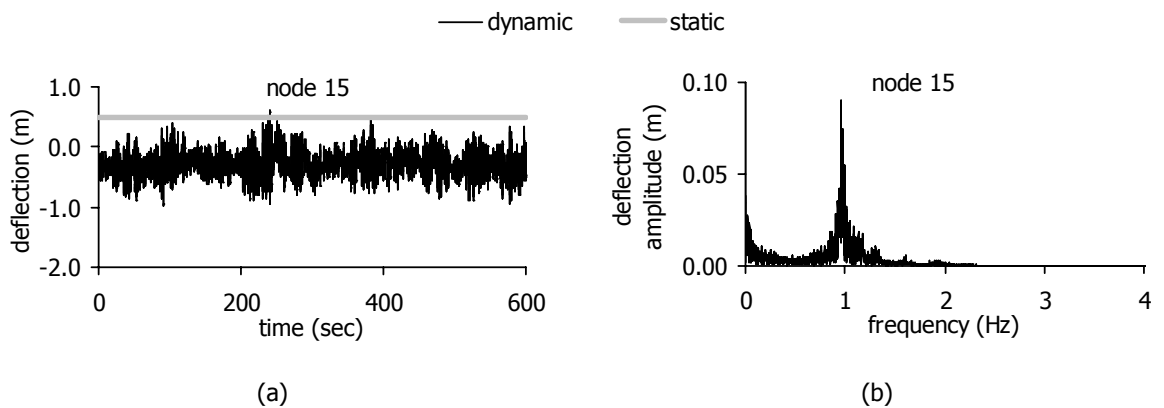


Figure 9-32: Cable net with $\lambda^2=0.86$: maximum and minimum nodal deflection: (a) time-history diagram, (b) response spectrum

The minimum and maximum cable tensions, observed in cable segments 418 and 40, respectively (Figure 9-16), are 208kN ($R_{dyn}=0.63$) and 1105kN ($R_{dyn}=1.21$), respectively. The tension time-history diagrams and response spectra are plotted in Figure 9-33. Superharmonic and fundamental resonances are verified again by the response spectra.

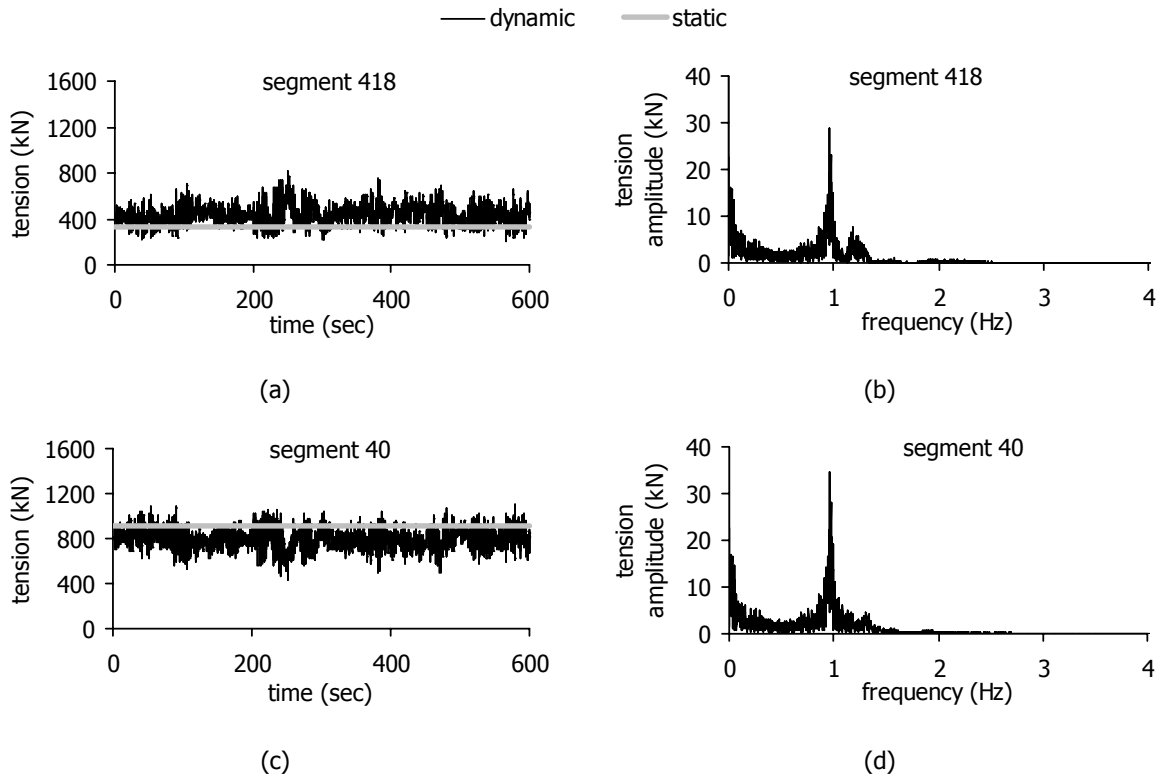


Figure 9-33: Cable net with $\lambda^2=0.86$: minimum cable tension: (a) time-history diagram, (b) response spectrum, maximum cable tension: (c) time-history diagram, (d) response spectrum

The maximum absolute values of the results for the three cable nets are listed in Table 9-3. A comparison of the maximum deflection diagrams for the three cable nets is illustrated in the charts of Figure 9-34. The largest difference between static and dynamic results is noted for the first cable net with the minimum initial cable stress. However, the maximum response is noticed for the cable net with the minimum cable diameter and the maximum initial cable stress, having the smallest parameter λ^2 . The maximum variance of the response is also observed for the same cable net. This parametric analysis shows that, although the larger initial stress increases the system’s stiffness, it does not result in smaller dynamic oscillation amplitudes and in general in a smaller dynamic response of the net. The cable diameter is also important, which as proved in chapter 3 influences the nonlinear term. In addition, a smaller cable diameter decreases the axial stiffness of the system and the total mass. As λ^2 increases the oscillation amplitudes decrease. For the first cable net, parameter λ^2 equals to 2.59 indicating that the first symmetric mode has internal nodes with zero vertical displacements, resulting thus in smaller oscillation amplitudes.

Table 9-3: Static (st) and dynamic (d) response with respect to parameter λ^2

Cable net	λ^2	Max net deflection			Max tension		
		w_{st} (m)	w_d (m)	w_d/w_{st}	N_{st} (kN)	N_d (kN)	N_d/N_{st}
1	2.59	0.095	0.273	2.87	1097	1385	1.26
2	1.35	0.306	0.649	2.12	909	1117	1.23
3	0.86	0.492	0.990	2.01	916	1105	1.21

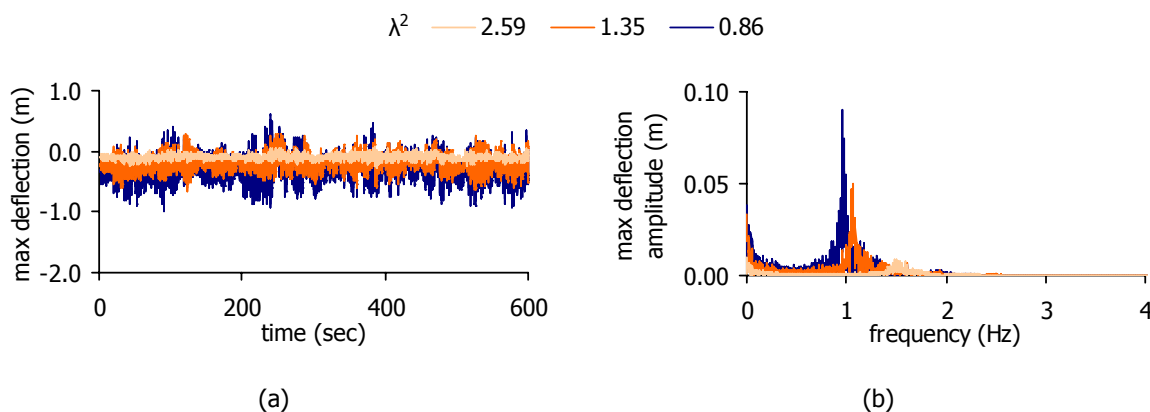


Figure 9-34: Maximum nodal deflection according to parameter λ^2 : (a) time-history diagrams, (b) response spectra

9.7.3 Influence of the sag-to-span ratio

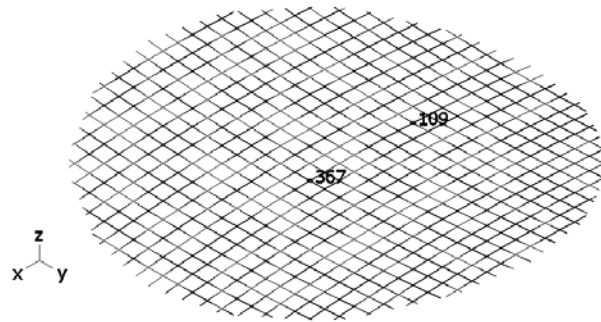
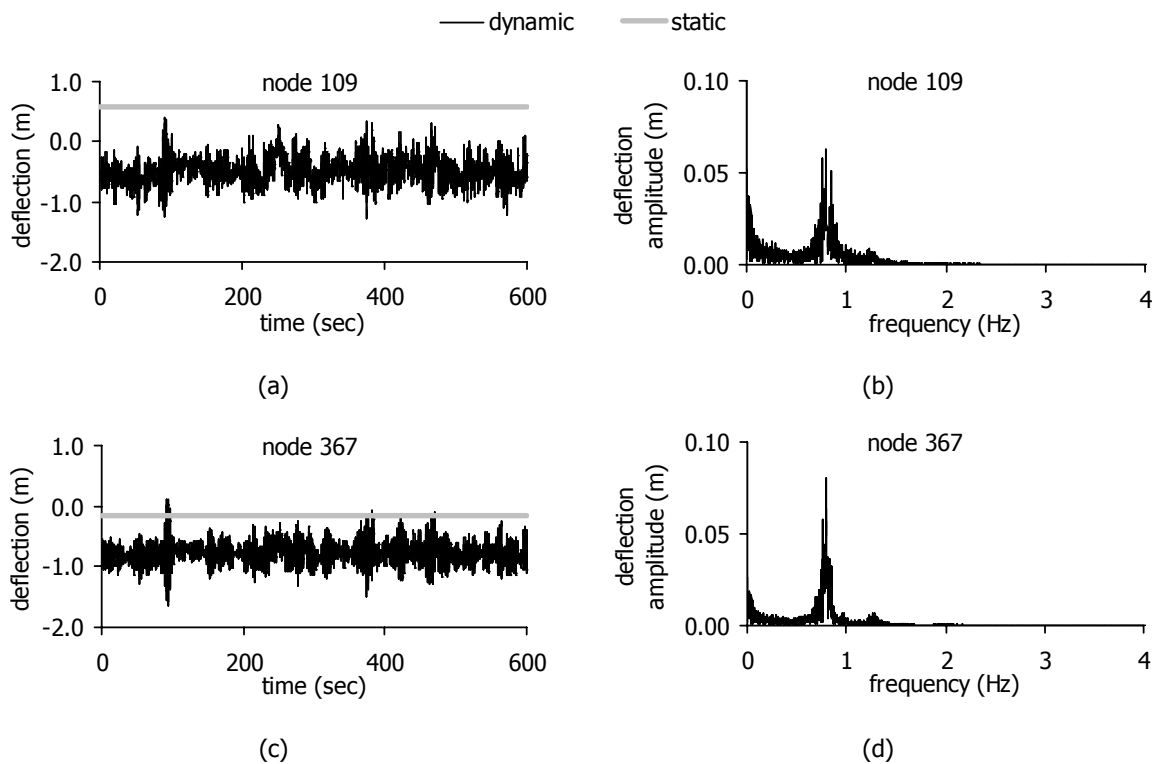
In order to investigate the influence of the roof's curvature on the dynamic response of such systems, two more cable nets are considered with $f/L=1/35$ and $f/L=1/10$, representing a shallow and a deep cable net, respectively. The number of cables in each direction, the diameter of the circular plan view L , the height of the central node of the net z , the cable diameter D and mass density m , the Young modulus E , the initial pretension N_0 and the damping ratio ζ remain as defined in section 9.2. The wind direction is parallel to the secondary cables (wind 0°). The equivalent pitch angle for the cable net with $f/L=1/35$ is $\alpha=3.27^\circ$, which is smaller than 5° . According to Eurocode 1, this roof can be considered as flat and it can be divided in two zones regarding the pressure coefficients. For $f/L=1/10$, this angle is $\alpha=11.31^\circ$ and the roof is divided in the eight zones. The pressure coefficients c_{pe} for both cable nets are given in chapter 8.

The first vibration mode of the shallow cable net with $f/L=1/35$ is the first symmetric one with frequency 0.777Hz, and the second one is the antisymmetric with respect to x-axis, with frequency 0.836Hz, being both closer to the wind frequencies. Due to the wind spatial distribution, it is expected that the antisymmetric mode will be the main vibration mode, thus the dynamic coefficient, taking into consideration the frequency of this antisymmetric mode, results in $c_d=1.093$. For the deep cable net with $f/L=1/10$, the frequency of the first symmetric mode is 1.306Hz, which is away from the frequencies of the excitation, leading to a dynamic coefficient $c_d=1.032$. For comparison reasons, the parameter λ^2 and the eigenfrequencies of the main vibration modes for these two systems and the one with $f/L=1/20$ described in section 9.3.2 are listed in Table 9-4.

Table 9-4: Characteristics of the nets with different f/L

Cable net	f/L	λ^2	ω_{1S} [sec^{-1}]	f_{1S} [Hz]	ω_{1A} [sec^{-1}]	f_{1A} [Hz]
1	1/35	0.44	-	-	5.253	0.836
2	1/20	1.35	6.654	1.059	-	-
3	1/10	5.40	8.205	1.306	-	-

Applying the dynamic load of the wind on the shallow cable net, the maximum dynamic positive (upward) and negative (downward) deflections are observed for node 109 and 367, respectively, shown in Figure 9-35. The maximum positive deflection is 0.408m (with $R_{dyn}=0.70$ where the maximum static one is equal to 0.587m) and the maximum negative one is -1.635m (with $R_{dyn}=9.97$ where the corresponding static one is equal to -0.164m). The deflection diagrams for nodes 109 and 367 are plotted in Figure 9-36.

Figure 9-35: Cable net with $f/L=1/35$: nodes 109 and 367Figure 9-36: Cable net with $f/L=1/35$: maximum positive deflection: (a) time-history diagram, (b) response spectrum, maximum negative deflection: (c) time-history diagram, (d) response spectrum

The minimum and maximum tensions, due to the static wind load, are 334kN and 804kN, respectively, while the corresponding dynamic ones are 61kN and 1513kN, leading to large differences between the two analyses and thus unsafe estimation of the response if the analysis is based on equivalent static methods. The minimum and maximum cable tensions are observed for cable segments 97 and 297, respectively, shown in Figure 9-37. The tension diagrams for both cable segments are plotted in Figure 9-38. Snapshots of the dynamic motion with magnified deformed shapes are illustrated in Figure 9-39, where symmetric and antisymmetric motions are noted.

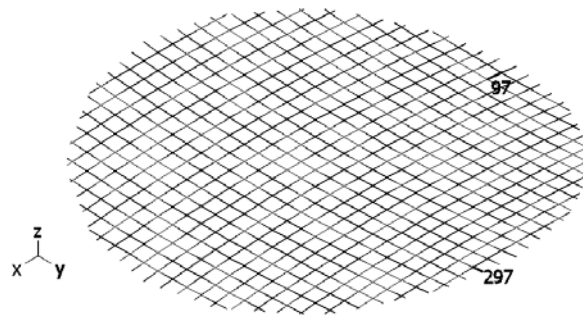


Figure 9-37: Cable net with $f/L=1/35$: cable segments 97 and 297

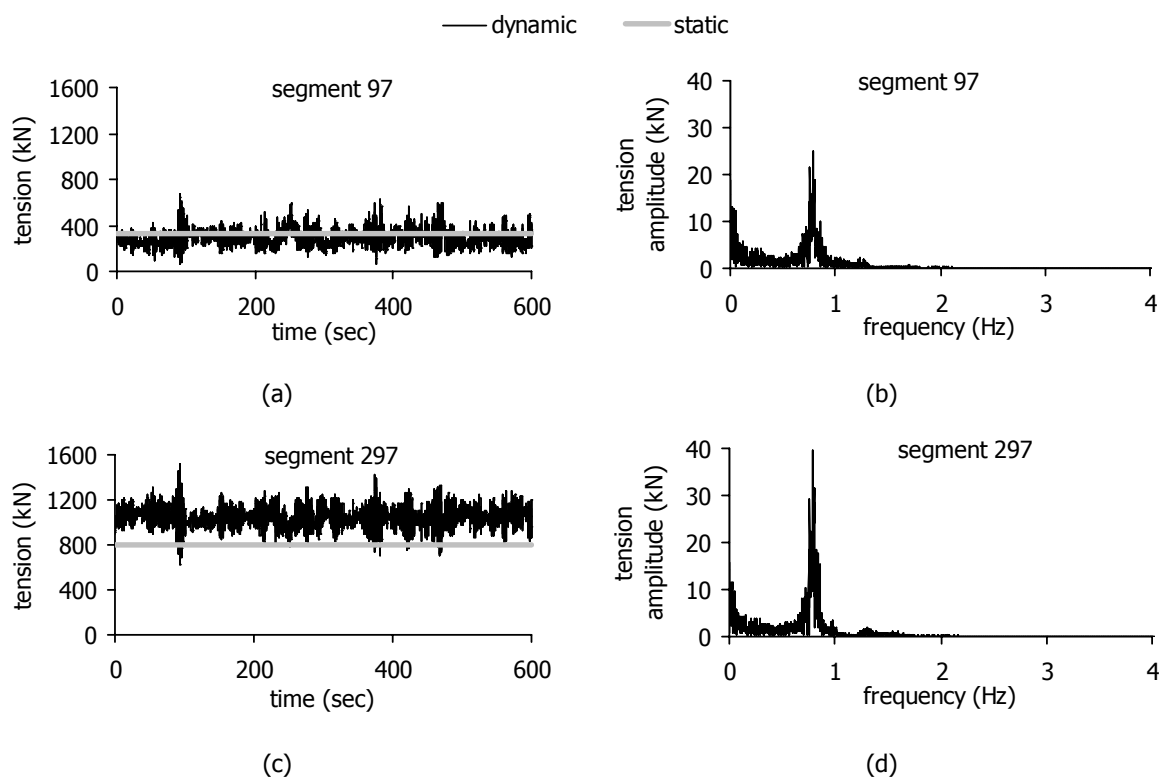


Figure 9-38: Cable net with $f/L=1/35$: minimum cable tension: (a) time-history diagram, (b) response spectrum, maximum cable tension: (c) time-history diagram, (d) response spectrum

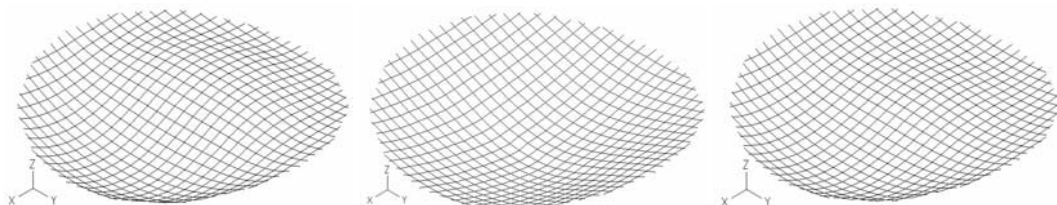


Figure 9-39: Snapshots of the dynamic motion for the cable net with $f/L=1/35$

The wind load is also applied on the deep cable net statically and dynamically and the two responses are compared again. Node 400 oscillates with the maximum amplitude, shown in Figure 9-40. As expected, due to the high level of stiffness obtained by the large sag-to-span ratio, the amplitudes of the deflection are very small with respect to the cable nets with smaller curvatures. The maximum upward deflection is 0.10m, equal to the static one, while the maximum downward deflection equals to -0.16m. The deflection diagrams of node 400 are illustrated in Figure 9-41. In the deflection

response diagram, it is shown that the main vibration frequencies are close to 1.70Hz and 2.00Hz, meaning that higher modes than the first symmetric one are activated. This is verified by the motion of the net, snapshots of which are shown in Figure 9-42 with magnified deformed shapes, while the corresponding vibration modes are illustrated in Figure 9-43.

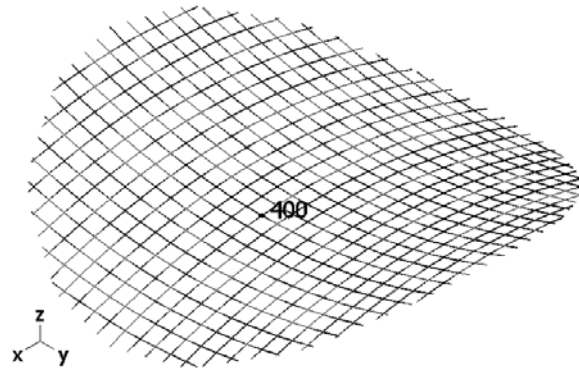


Figure 9-40: Cable net with $f/L=1/10$: node 400

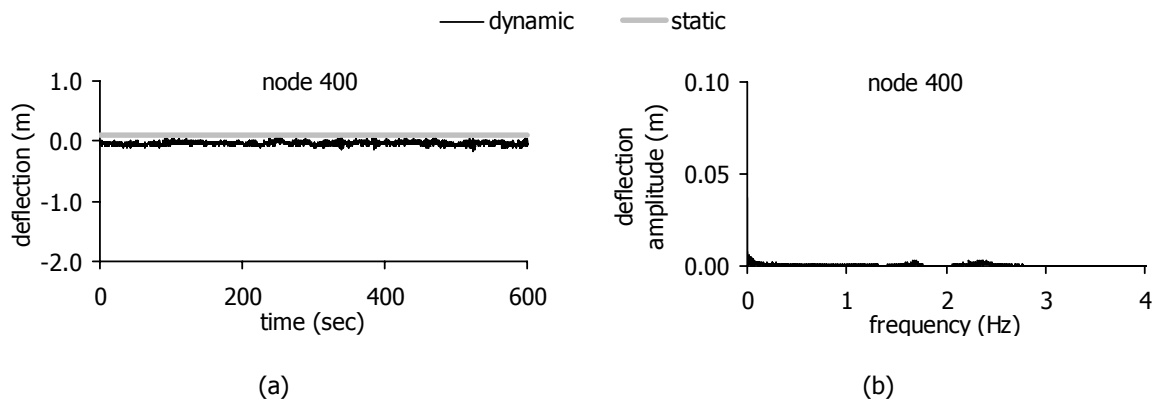


Figure 9-41: Cable net with $f/L=1/10$: maximum and minimum nodal deflection: (a) time-history diagram, (b) response spectrum

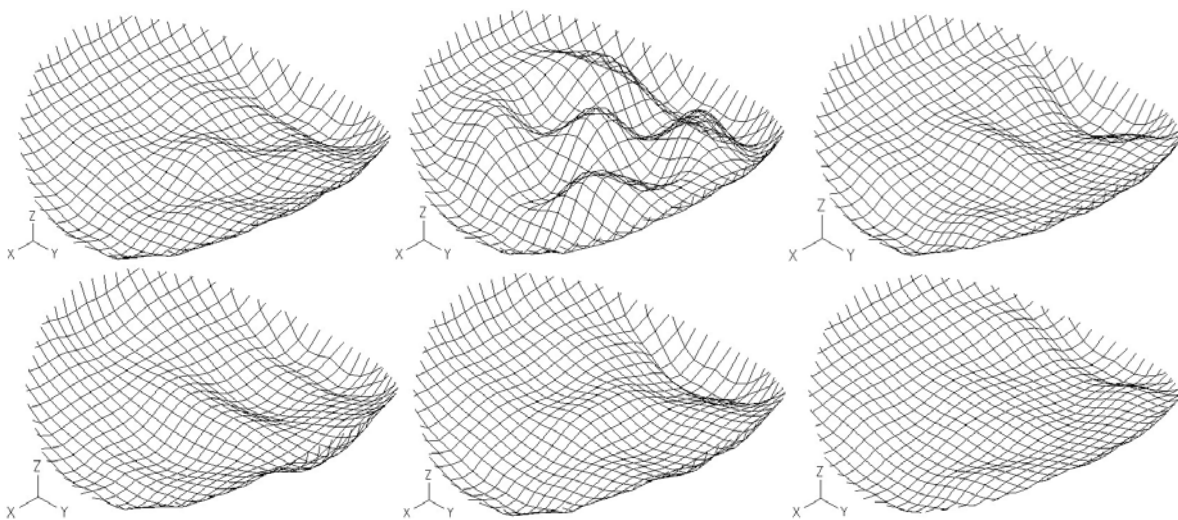


Figure 9-42: Snapshots of the dynamic motion for the cable net with $f/L=1/10$

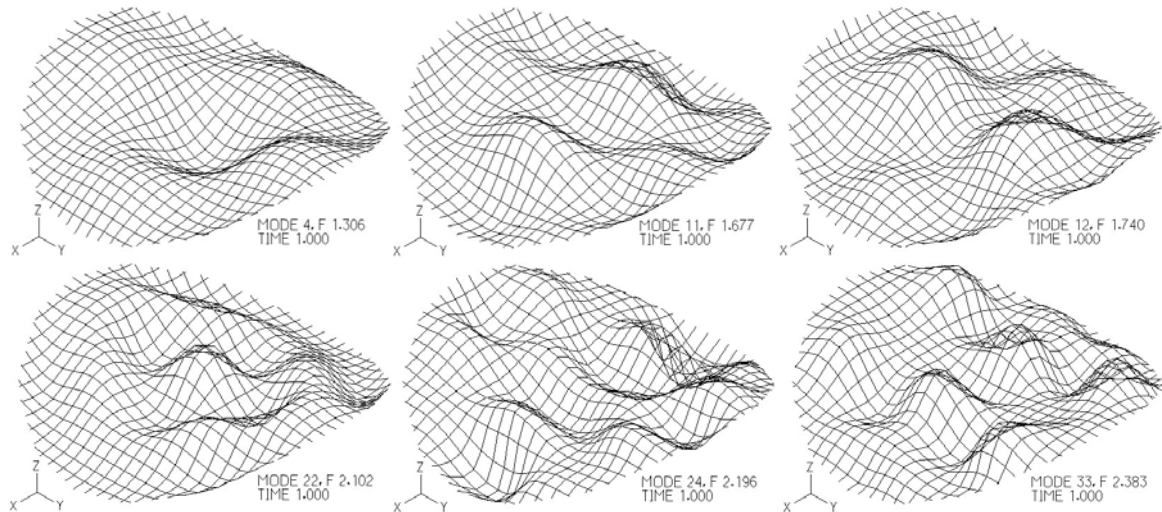


Figure 9-43: Activated vibration modes and natural frequencies for the cable net with $f/L=1/10$

Cable segments 6 and 59 develop the minimum and maximum tension, respectively. These segments are shown in Figure 9-44. The minimum dynamic cable tension is 347kN (Figure 9-45), with $R_{dyn}=0.83$ where the static one is 418kN. The maximum dynamic cable tension arises at 870kN (Figure 9-46), while the static one is 782kN, leading to a ratio $R_{dyn}=1.11$. These differences are small with respect to the corresponding ones of the previous examples. The main vibration frequencies close to 2.00Hz are also verified by the tension response diagrams.

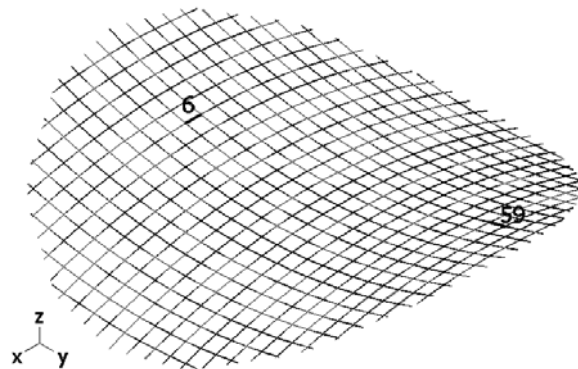


Figure 9-44: Cable net with $f/L=1/10$: cable segments 6 and 59

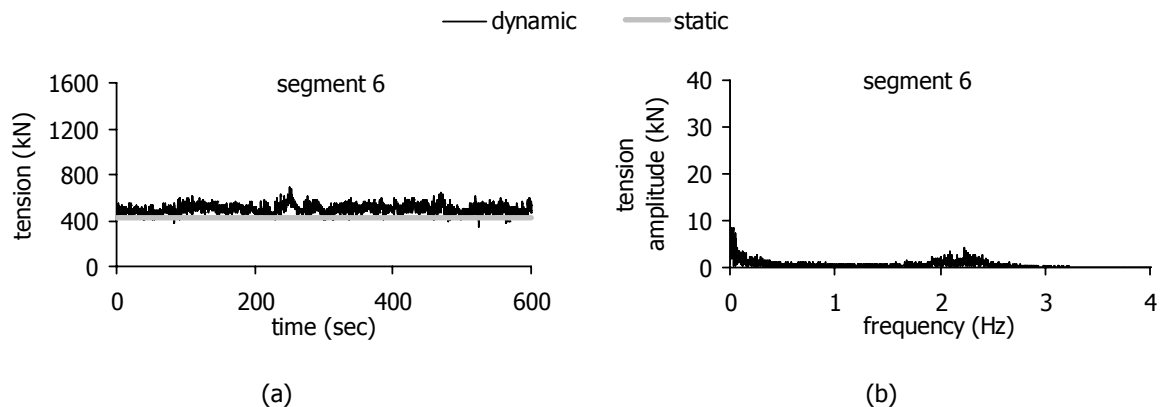


Figure 9-45: Cable net with $f/L=1/10$: minimum cable tension: (a) time-history diagram, (b) response spectrum

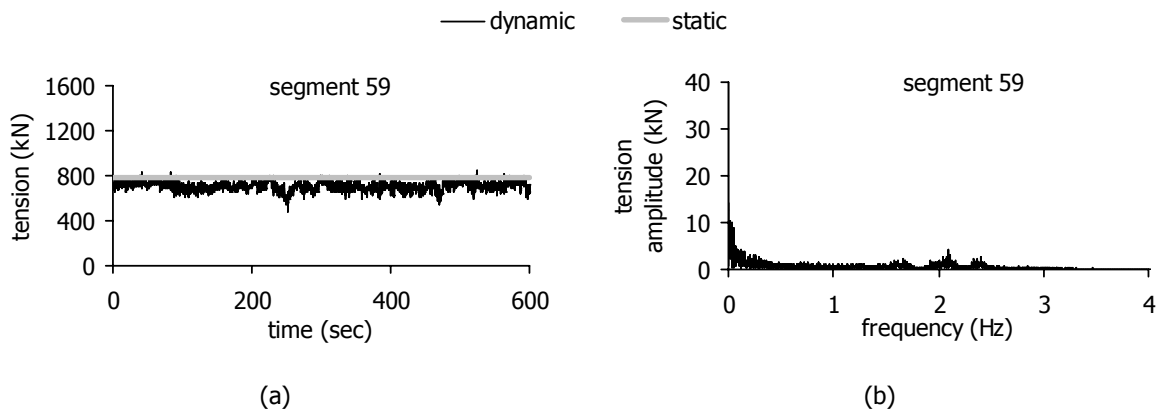


Figure 9-46: Cable net with $f/L=1/10$: maximum cable tension: (a) time-history diagram, (b) response spectrum

The maximum absolute values of the results for all three sag-so-span ratios are listed in Table 9-5.

Table 9-5: Static (st) and dynamic (d) response with respect to the sag-so-span ratio

Cable net	f/L	λ^2	Max net deflection			Max tension		
			w_{st} (m)	w_d (m)	w_d/w_{st}	N_{st} (kN)	N_d (kN)	N_d/N_{st}
1	1/35	0.44	0.587	1.635	2.78	804	1513	1.88
2	1/20	1.35	0.306	0.649	2.12	909	1117	1.23
3	1/10	5.40	0.100	0.160	1.60	782	870	1.11

The maximum nodal deflection diagrams for all three sag-to-span ratios are compared in the charts of Figure 9-47. As expected, the shallow cable net, being more flexible than the other systems, exhibits the maximum variance of the response, which can cause severe fatigue problems to the cable anchorages. Comparing also the response of these cable nets with the ones of section 9.7.2, it is verified that as parameter λ^2 becomes larger, the cable nets exhibit smaller oscillation amplitudes.

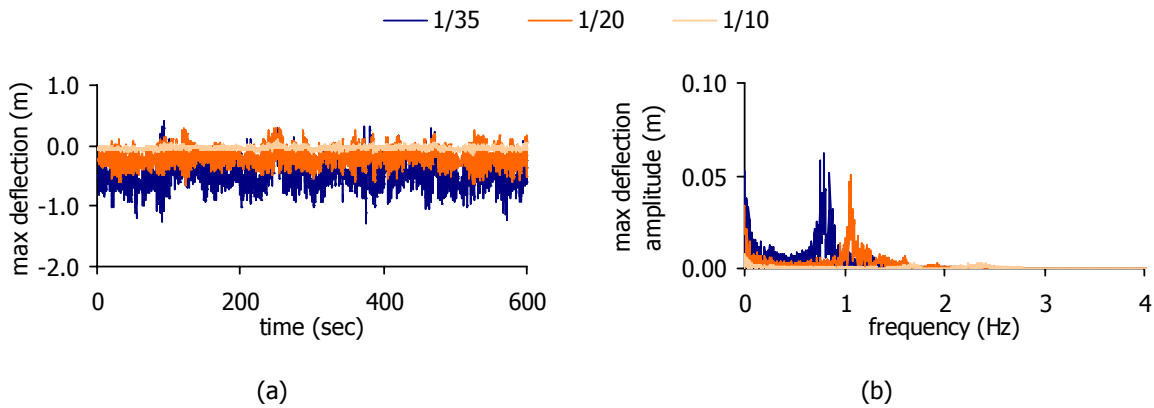


Figure 9-47: Maximum nodal deflection according to the sag-to-span ratio: (a) time-history diagrams, (b) response spectra

9.7.4 Influence of the boundary conditions

In all previous examples, the cable ends are considered as fixed. In this section the influence of the cable supports on the net’s dynamic response is compared with respect to the one of section 9.6.2. Thus, keeping the same geometry and mechanical characteristics of the net given in section 9.2, a boundary ring is added in the model having a square box cross-section, with width $b=6.00\text{m}$, wall thickness 0.60m and unit weight $\rho_r=25\text{kN/m}^3$. The Young-modulus of the ring’s material is assumed equal to $E_r=37\text{GPa}$. The boundary conditions are assumed as described in chapter 5, in such way that

the radial deformation of the ring is allowed, but not the overall rotation about the z global axis. The ring's first vibration mode is the first mode of the system with eigenfrequency $\omega_r=5.54\text{sec}^{-1}$ (0.882Hz), while the first symmetric mode of the cable net is the fifth mode of the system with eigenfrequency $\omega_{15}=7.358\text{sec}^{-1}$ (1.171Hz). Considering the first vibration mode, as the main vibration mode for the wind action the dynamic coefficient c_d is calculated equal to 1.083. The static load of the wind causes a maximum upward deflection equal to 0.496m. The minimum and maximum cable tensions are 345kN and 921kN, respectively. The dynamic load of the wind is also applied, calculated as described in section 9.5.4. The central node oscillates with the maximum amplitude, assuming a maximum negative value equal to -1.109m (downward deflection) and a positive one 0.502m (upward deflection), being both almost 170% of the corresponding ones calculated in section 9.6.2. The diagrams of the central node deflection are plotted in Figure 9-48.

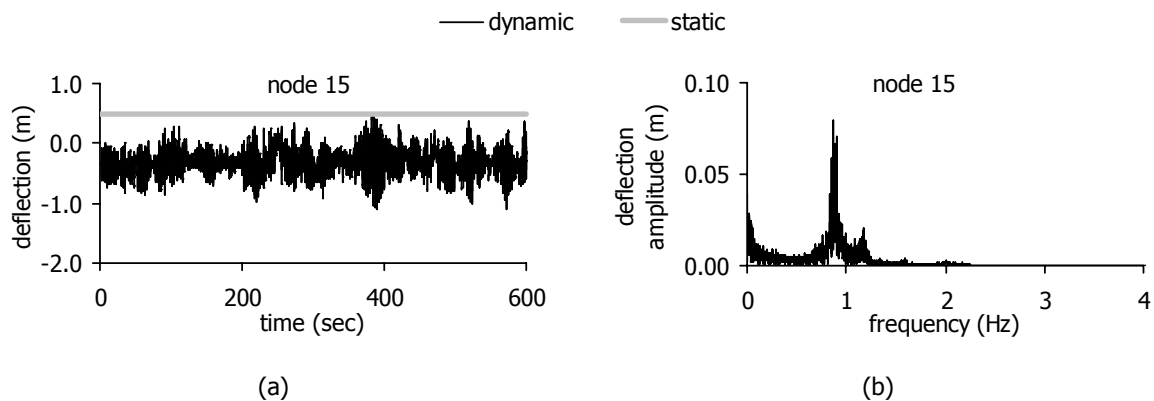


Figure 9-48: Cable net with boundary ring: maximum and minimum nodal deflection: (a) time-history diagram, (b) response spectrum

Both static and dynamic deflections are larger than the ones of the system with fixed cable ends, due to the activation of the ring's vibration mode and the first symmetric mode of the cable net. This is shown in the response spectrum, in which two main peaks are observed corresponding to these two symmetric modes. Even for this system the upward maximum deflection is estimated with accuracy by the quasi-static method, but not the downward one.

Cable segments 416 and 40 develop the minimum and maximum cable tension, respectively (Figure 9-49). The minimum cable tension is 140kN and the maximum cable tension is 1177kN (Figure 9-50), which are both very close to the ones calculated for the system with fixed cable ends, but the difference from the static corresponding ones is larger.

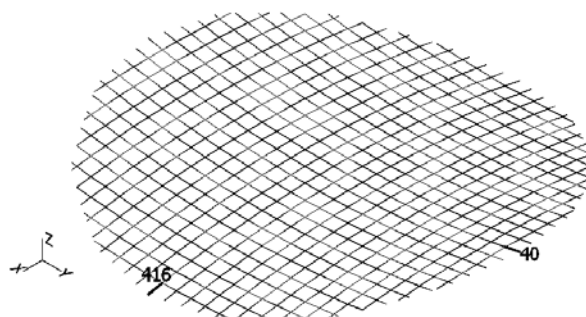


Figure 9-49: Cable net with boundary ring: cable segments 416 and 40

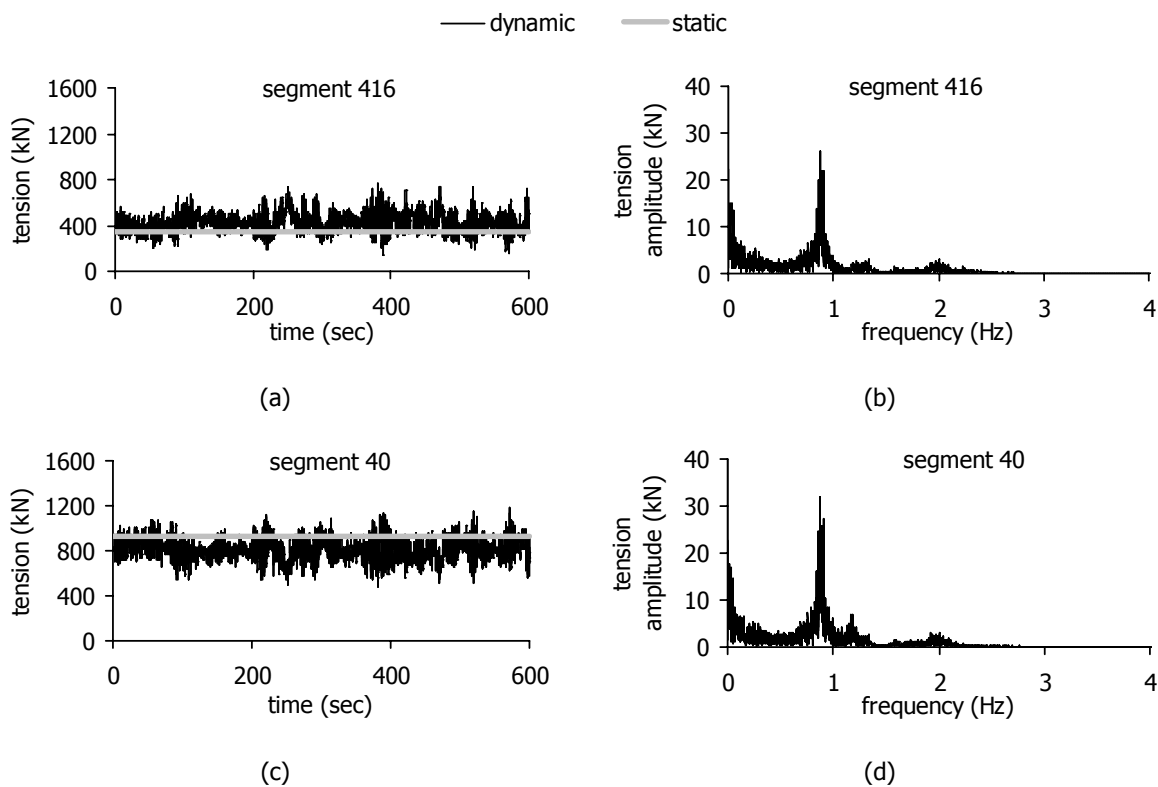


Figure 9-50: Cable net with boundary ring: minimum cable tension: (a) time-history diagram, (b) response spectrum, maximum cable tension: (c) time-history diagram, (d) response spectrum

As proved in chapter 7, fundamental resonance for the first symmetric mode of the net, results in smaller response for the cable net with the edge ring than for the one with rigid supports, because the vibration of the ring suppresses the net’s oscillation amplitude, while superharmonic resonance has opposite results. For the wind load considered, both kinds of resonances occur, resulting in similar responses for both models regarding the cable tensions. The response diagrams verify that the main vibration mode is the one of the ring, with frequency 0.882Hz. Modes of higher order, with frequencies close to 2.00Hz, also appear. In Figure 9-51, some snapshots of the cable net dynamic motion are illustrated with magnified deformed shapes, where it is evident that several symmetric modes are activated. Table 9-6 gives the maximum absolute values of the results for the two assumptions regarding the boundary conditions.

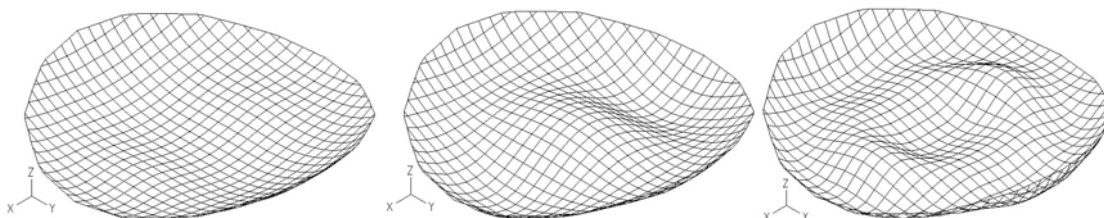


Figure 9-51: Snapshots of the dynamic motion of the cable net with boundary ring

Table 9-6: Static (st) and dynamic (d) response with respect to the boundary conditions

Cable net with	Max net deflection			Max tension		
	w_{st} (m)	w_d (m)	w_d/w_{st}	N_{st} (kN)	N_d (kN)	N_d/N_{st}
rigid supports	0.306	0.649	2.12	909	1117	1.23
ring	0.496	1.109	2.23	921	1177	1.28

In Figure 9-52 a comparison of the nodal deflections is given for the two boundary assumptions, where it is shown that the cable net with the ring experiences larger deflection than the one with fixed cable ends. The maximum variance of the response is also observed for the same system.

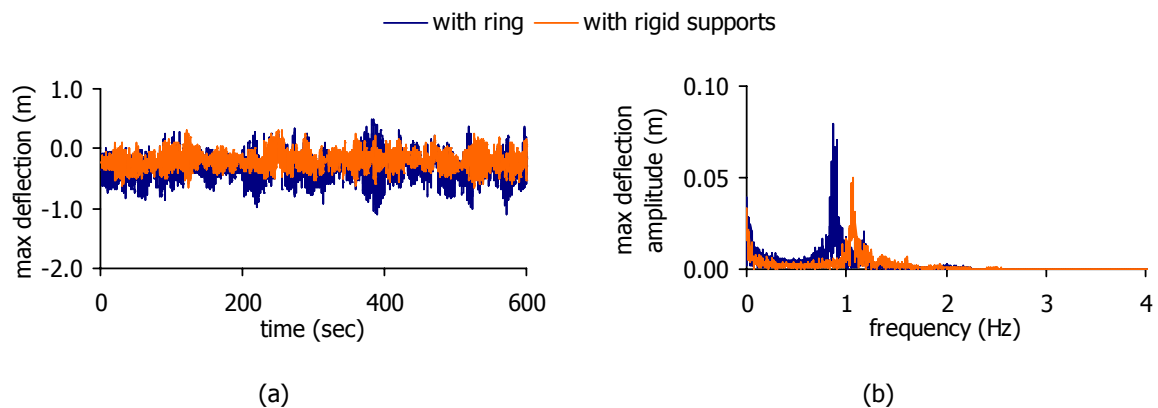


Figure 9-52: Maximum nodal deflection according to the boundary assumptions: (a) time-history diagrams, (b) response spectra

9.7.5 Artificial wind function

An artificial function of the turbulent wind velocity is created as described in chapter 2, based on the procedure proposed in [9-14]. For a mean value of the wind velocity equal to 28.58m/sec, as calculated from Eq. (9-3), the diagrams of an artificial wind velocity function are plotted in Figure 9-53.

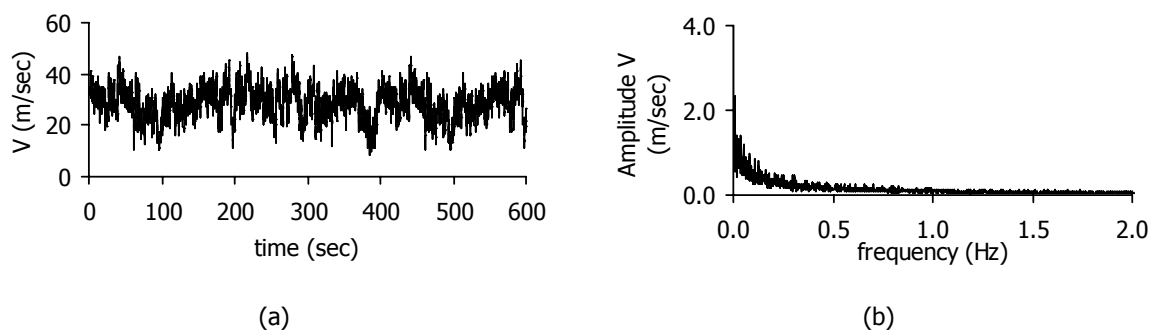


Figure 9-53: Artificial wind velocity: (a) time-history diagram, (b) Fourier diagram

The maximum and minimum values of the time-history diagram are 48.01m/sec and 8.47m/sec, respectively. The maximum value is very close to the corresponding one of the real record of Figure 9-11a, while the minimum one is smaller than the one of the real record, causing more intense variance. The main frequencies of the wind velocity are smaller than 1.00Hz as in the Fourier diagram of Figure 9-11b. Thus, this artificial wind velocity diagram approaches very satisfactorily real records of the wind. Two cable nets are subjected to this wind load; the first one is the cable described in section 9.2 and the second one is the cable net with a boundary ring having the characteristics of section 9.7.4.

The deflection diagrams of the central node of the cable net with rigid supports are plotted in Figure 9-54. The maximum negative deflection (downwards) is -0.898m, while the positive one (upwards) is 0.674m, being both larger than the corresponding ones of the analysis with the real wind record, shown in Figure 9-15, although the response diagram of the deflection do not present significant differences. The ratio R_{dyn} for the maximum upward deflection is $R_{dyn}=2.20$. Thus, not only the

maximum and minimum values of the wind velocity, but also its fluctuations play an important role in the dynamic response of the net.

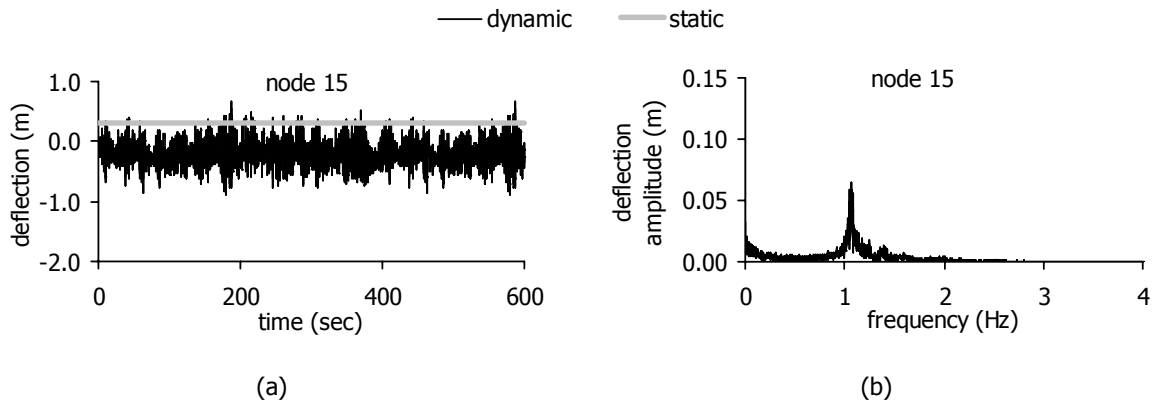


Figure 9-54: Cable net with rigid supports and artificial wind diagram: maximum and minimum nodal deflection: (a) time-history diagram, (b) response spectrum

Cable segments 368 and 40, shown in Figure 9-55, develop the minimum and maximum cable tension, respectively. The minimum cable tension is 43kN (Figure 9-56) and the maximum one is 1296kN (Figure 9-57), being more conservative than the corresponding ones for the real wind record, given in Figure 9-17, causing thus larger differences from the static results. However, the response frequencies for both wind considerations are the same. In Table 9-7 the maximum absolute values of the results for the real and the artificial wind diagrams are listed.

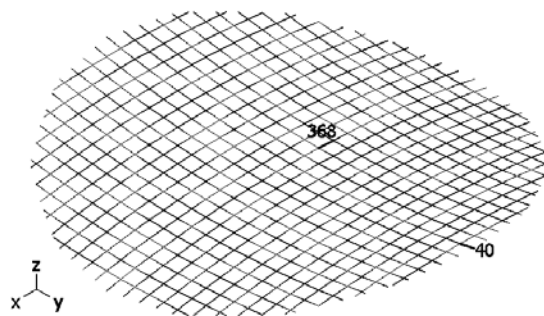


Figure 9-55: Cable net with rigid supports: cable segments 368 and 40

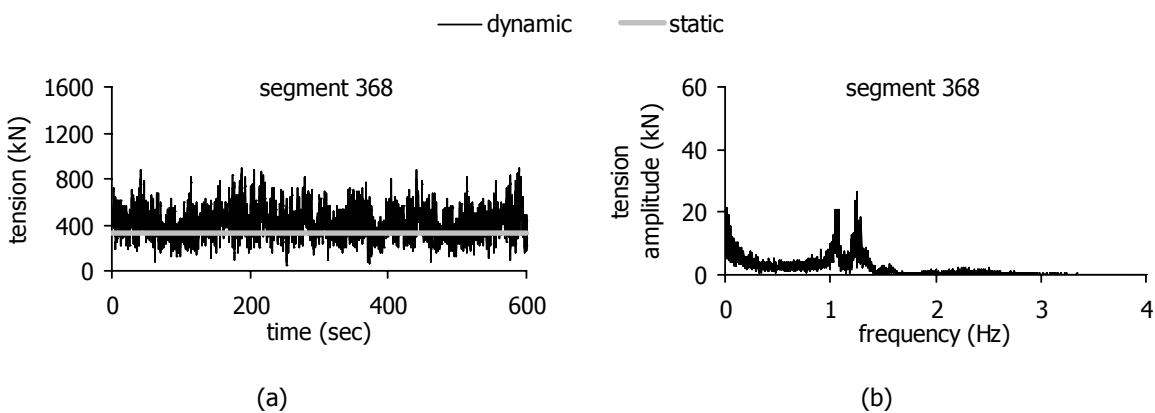


Figure 9-56: Cable net with rigid supports and artificial wind diagram: minimum cable tension: (a) time-history diagram, (b) response spectrum

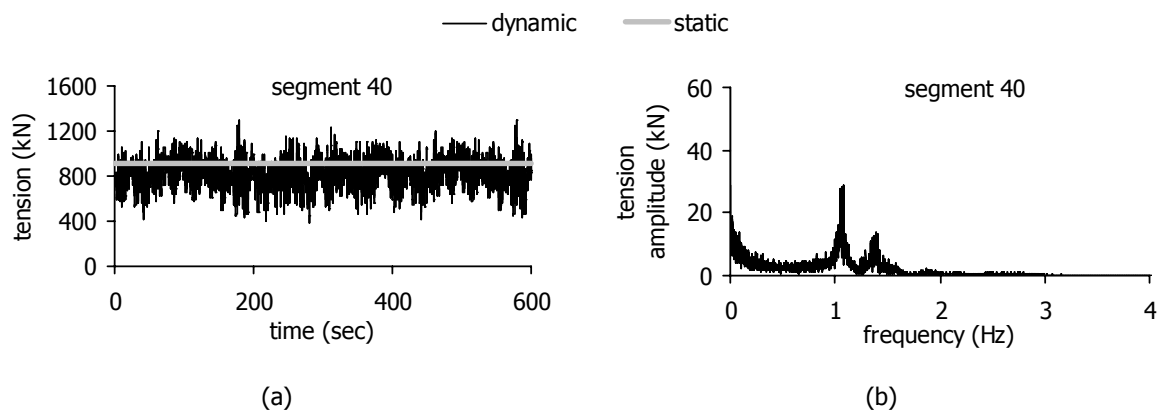


Figure 9-57: Cable net with rigid supports and artificial wind diagram: maximum cable tension: (a) time-history diagram, (b) response spectrum

Table 9-7: Static (st) and dynamic (d) response of the cable with rigid supports with respect to the wind diagram

Wind diagram	Max net deflection			Max tension		
	w_{st} (m)	w_d (m)	w_d/w_{st}	N_{st} (kN)	N_d (kN)	N_d/N_{st}
real	0.306	0.649	2.12	909	1117	1.23
artificial	0.306	0.898	2.93	909	1296	1.43

In the charts of Figure 9-58 the maximum nodal deflection is compared for this cable net subjected to the wind action of the real record, plotted in Figure 9-11 and the artificial one of Figure 9-53. The amplitude of the response is larger for the artificial wind but the main vibration frequencies are the same for both wind diagrams.

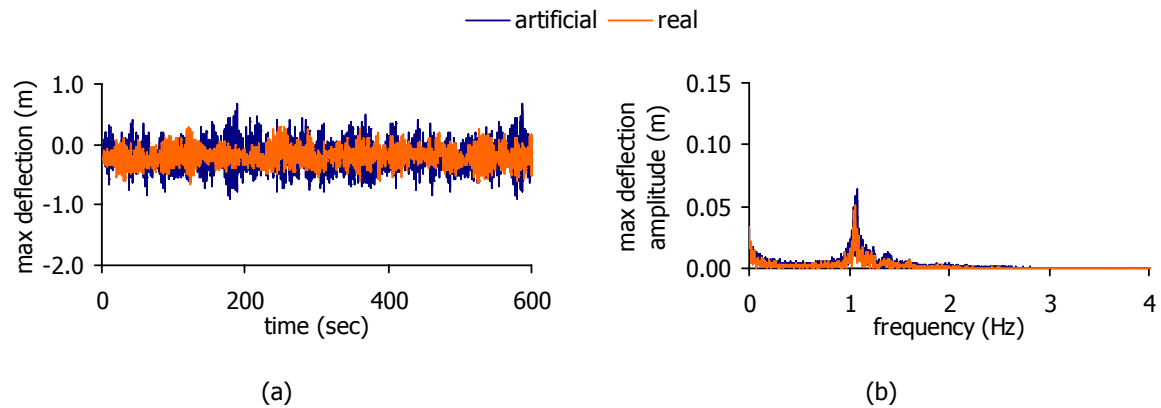


Figure 9-58: Maximum nodal deflection for a cable net with rigid supports considering real and artificial wind diagrams: (a) time-history diagrams, (b) response spectra

Regarding the cable net with boundary ring, the deflection diagrams of the central node are plotted in Figure 9-59, with maximum negative value -1.606m (downward deflection) and a positive one 0.984m (upward deflection), leading to larger response amplitudes with respect to the ones caused by the real wind record. The minimum and maximum cable tension diagrams are plotted in Figure 9-60 for cable segments 416 and 40, respectively, shown in Figure 9-49. The minimum one is 104kN and the maximum one is 1420kN. In this case, the boundary ring influences significantly the response of the net, not only in terms of the net deflection but also in terms of the cable tension. The difference of the results between this analysis and the one of section 9.7.4 is also considerable. This difference is attributed to the intense fluctuations of the produced wind. The ring’s vibration mode prevails again during the dynamic motion, as proved by the main oscillation frequency of the response diagrams. In

Table 9-8 the maximum absolute values of the results for the real and the artificial wind diagrams are listed.

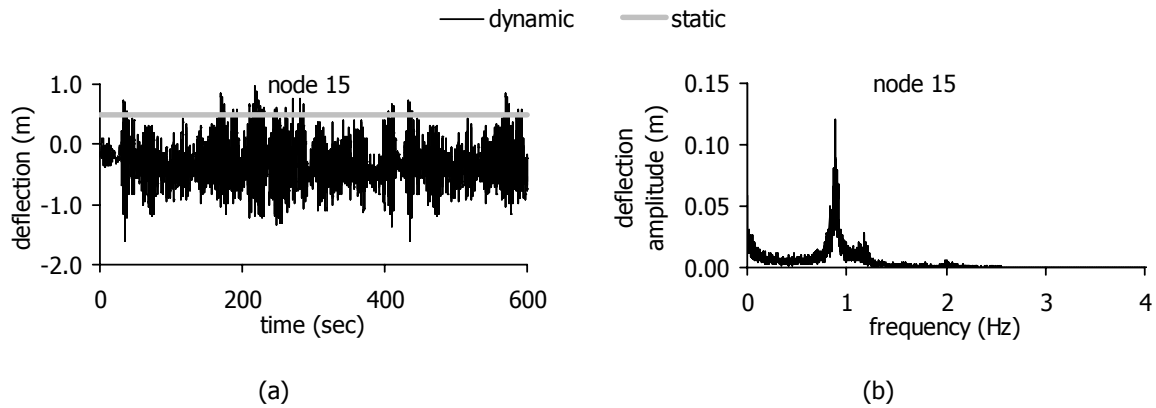


Figure 9-59: Cable net with boundary ring and artificial wind diagram: maximum and minimum nodal deflection: (a) time-history diagram, (b) response spectrum

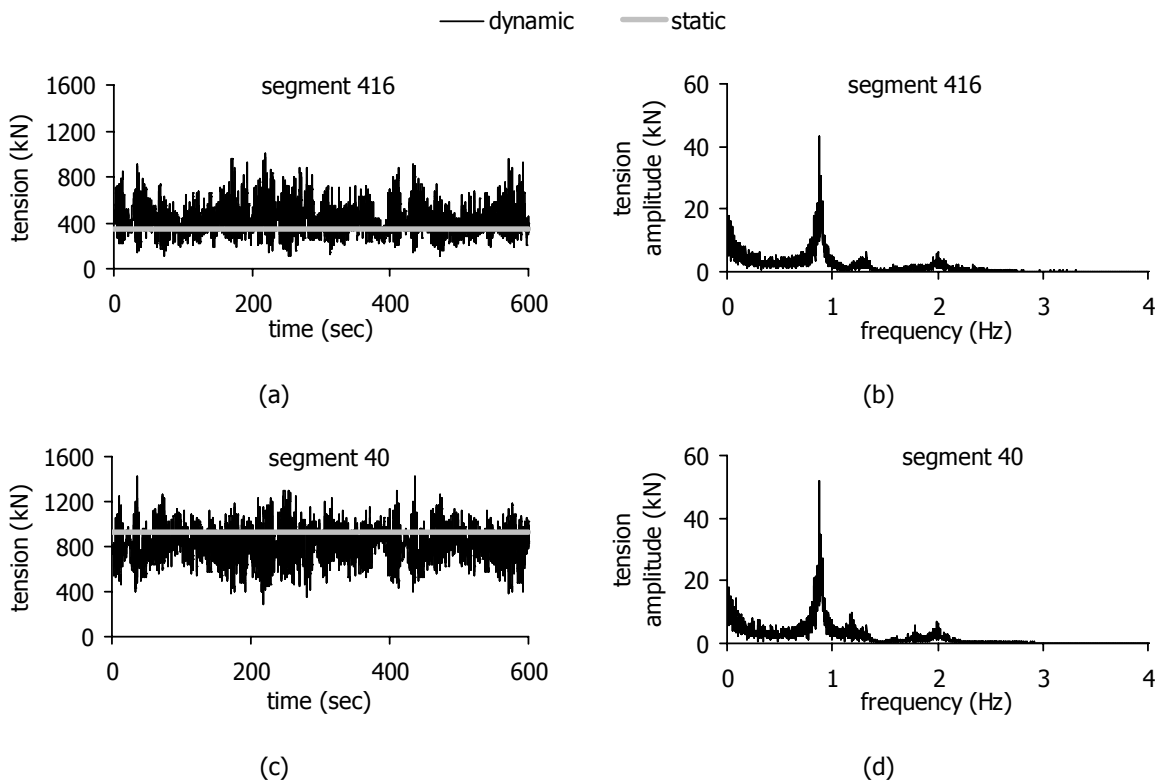


Figure 9-60: Cable net with boundary ring and artificial wind diagram: minimum cable tension: (a) time-history diagram, (b) response spectrum, maximum cable tension: (c) time-history diagram, (d) response spectrum

Table 9-8: Static (st) and dynamic (d) response of the cable with boundary ring with respect to the wind diagram

Wind diagram	Max net deflection			Max tension		
	w_{st} (m)	w_d (m)	w_d/w_{st}	N_{st} (kN)	N_d (kN)	N_d/N_{st}
real	0.496	1.109	2.23	921	1177	1.28
artificial	0.496	1.606	3.24	921	1420	1.54

The charts of Figure 9-61 compare the maximum nodal deflection diagram for the cable net with rigid supports or with boundary ring for the artificial wind function. The response of the cable net with the deformable boundary ring is again the larger one. The response spectra show the different vibrations

frequencies for the two systems, corresponding to the first symmetric mode and the in-plane mode of the ring.

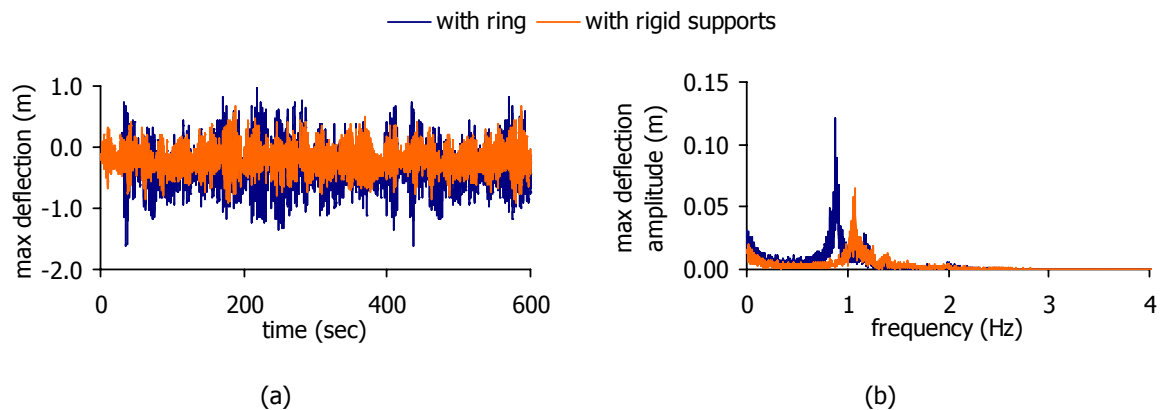


Figure 9-61: Maximum nodal deflection according to the boundary assumptions considering the artificial wind diagram: (a) time-history diagrams, (b) response spectra

Figure 9-62 gives the comparison of the maximum nodal deflection diagram for the cable net with boundary ring for the real record and the artificial one. The artificial wind function results again in larger oscillation amplitudes, but the main vibration frequencies coincide for both wind diagrams. Thus, in the lack of real wind records, the creation of a wind diagram according to the procedure described in [9-14] gives reliable results.

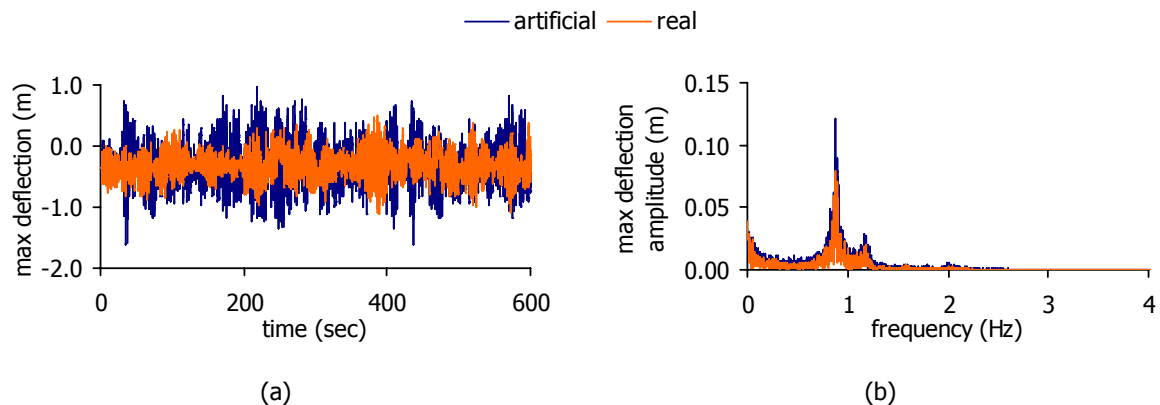


Figure 9-62: Maximum nodal deflection for a cable net with boundary ring considering real and artificial wind diagrams: (a) time-history diagrams, (b) response spectra

9.8 SUMMARY AND CONCLUSIONS

In this chapter, the dynamic response of saddle-shaped cable nets under wind action is studied. Accounting for different stiffness levels, several cable nets with different characteristics are assumed. Two different wind directions are also considered, leading to different deformed shapes of the net. The influence of the boundary conditions of the cables on the dynamic response of the net is also investigated. The time-history of the wind velocity is obtained from real records and scaled so that the mean velocity equals the one suggested from Eurocode 1 for the height of the net's central node. An artificial wind function is also created, taking into account the wind velocity spectrum proposed by Eurocode 1. Both velocity diagrams lead to similar results. Nonlinear dynamic analyses are performed considering the geometric nonlinearity of the system. Nonlinear static analyses are also conducted, based on the methodology proposed by Eurocode 1. The dynamic response of the cable nets is

compared with the static one, by means of the maximum deflection as well as the maximum and minimum cable tension.

Although the wind main frequencies are much smaller than the natural frequencies of the cable nets, the response spectra indicate the occurrence of superharmonic and fundamental resonances, causing oscillations with large amplitudes and frequencies not only equal to the wind frequencies but also equal to the natural frequencies. Superharmonic resonances, which amplify the dynamic response, cannot be assessed by the quasi-static methods. The dynamic analysis results in larger response with respect to the static one. The difference is significant for shallow or medium cable nets. For deep cable nets, the difference arises at 10%. In addition, it is proved that as parameter λ^2 increases, the oscillation amplitudes become smaller. The modelling of the boundary ring affects the maximum deflection of the net, leading to larger responses. Finally, artificial wind functions can reliably be used in the lack of real wind records.

Part of this work has been presented in [9-15] and [9-16].

9.9 REFERENCES

- [9-1] S. A. G. Oskoei and G. McClure, "Dynamic analysis of cable roofs under transient wind: a comparison between time domain and frequency domain approaches", *Tsinghua Science and Technology* ISSN 1007-0124 09/67, Vol. 13, No. S1, pp. 53-57, 2008.
- [9-2] G. D. Stefanou, "Dynamic response of tension cable structures due to wind loads", *Computers and Structures*, Vol. 43, No. 2, pp. 365-372, 1992.
- [9-3] W. H. Melbourne, "The response of large roofs to wind action", *Journal of Wind Engineering and Industrial Aerodynamics*, Vol. 54-55, pp. 325-335, 1995.
- [9-4] A. L. Materazzi and I. Venanzi, "A simplified approach for the wind response analysis of cable-stayed masts", *Journal of Wind Engineering and Industrial Aerodynamics*, Vol. 95, pp. 1272-1288, 2007.
- [9-5] EUROCODE 3, PART 3.1, "Towers, masts and chimneys – towers and masts", 2005.
- [9-6] M. Lazzari, A. V. Saetta and R. V. Vitaliani, "Non-linear dynamic analysis of cable-suspended structures subjected to wind actions", *Computers and Structures*, Vol. 79, pp. 953-969, 2001.
- [9-7] EUROCODE 1, PART 1.4, "General actions – wind actions", 2003.
- [9-8] H. J. Sutherland, P. L. Jones and B. A. Neal, "The long-term inflow and structural test program", *Proceedings of the Wind Energy Symposium 2001*, ASME, AIAA-2001-0039, Reno, Nevada, U.S.A., pp. 1-11, 2001.
- [9-9] A. K. Chopra, "Dynamics of structures, theory and applications to earthquake engineering", Prentice Hall International, Inc., U.S.A., 1995.
- [9-10] R. Alessi, D. Bairaktaris, F. Caridakis, M. Majowiecki and F. Zoulas, "The roof structures of the new sports arena in Athens", *Proceedings of the World Congress on Shell and Spatial Structures*, Spain, pp. 6.107-6.123, 1979.
- [9-11] J. W. Leonard, "Tension structures, behavior & analysis", McGraw-Hill, Inc., U.S.A., 1988.
- [9-12] L. Manuel, "Analysis of the Long-Term Inflow and Structural Test (LIST) Data", Site Coordination Meeting, Bushland/Amarillo, Texas, U.S.A., 2004.

- [9-13] H. J. Sutherland, "Preliminary analysis of the structural and inflow data from the LIST turbine", Proceedings of the Wind Energy Symposium 2001, ASME, AIAA-2001-0041, Reno, Nevada, U.S.A., pp. 1-11, 2001.
- [9-14] M. Shinozuka and C. M. Jan, "Digital simulation of random processes and its applications", Journal of Sound and Vibration, Vol. 25, No. 1, pp. 111-128, 1972.
- [9-15] I. Vassilopoulou and C. J. Gantes, "Nonlinear dynamic behaviour of saddle shaped cable nets under wind action", Proceedings of IABSE-IASS Symposium, London, Great Britain, 2011.
- [9-16] I. Βασιλοπούλου, Χ. Ι. Γαντές και Η. Γκιμούσης, "Απόκριση δικτύων καλωδίων υπό φορτία ανέμου", Πρακτικά 7^{ου} Εθνικού Συνεδρίου Μεταλλικών Κατασκευών Βόλος, Ελλάδα, 2011 (in greek).

10 SUMMARY AND CONCLUSIONS

10.1 SUMMARY

In the last decades many researchers have dealt with the dynamic response of simple suspended cables. Analytical solutions are provided in the literature describing the nonlinear phenomena that govern their behaviour and several experiments have been conducted to confirm the theory. A few publications refer to the nonlinear dynamic behaviour of larger cable structures such as cable nets. Most of them present innovative computerised methods of analysis and other numerical techniques to calculate their nonlinear dynamic response, or include results from parametric analyses concerning their eigenmodes and eigenfrequencies. Others draw their conclusions about the nonlinear manner in which such structures behave, either from isolated time-history analyses, or comparing the results obtained from linear and nonlinear analyses. Nevertheless, one can hardly find a systematic study of nonlinear dynamic phenomena in cable nets.

The aim of this research is to investigate the response of cable nets to dynamic loads such as harmonic loads or wind actions, focusing on the dynamic phenomena that characterise nonlinear structures, such as hardening or softening behaviour, dependence of the dynamic response on the initial conditions, bending of the response curve, instability regions, jump phenomena, internal and secondary resonances.

Firstly a simple cable net, consisting of two crossing cables, is studied and the equation of motion is derived. Neglecting small terms of its equation of motion, this single-degree-of-freedom (SDOF) system is proved to be similar to a Duffing oscillator with a cubic nonlinear term of the displacement. A thorough study of this oscillator can be found in the literature. The analytical solution of its steady-state response is adopted for the simple cable net and the occurrence of fundamental and secondary resonances, such as superharmonic or subharmonic resonances, is verified for this system, as well. The response diagrams are plotted for different resonant conditions showing bending of the response curve, hardening behaviour and dependence on the initial conditions. This response is confirmed by solving numerically the equation of motion as well as using finite element software and performing time-history analyses considering also the geometric nonlinearity of the cable net.

Proceeding to multi-degree-of-freedom (MDOF) systems, a saddle-form cable net with circular plan view is assumed. The boundary of the net is considered either as rigid, with cable ends modelled as pinned, or as flexible, modelling the deformable edge ring. The first symmetric and antisymmetric

vibration modes and the corresponding natural frequencies are calculated. A parametric analysis shows that changing the sag-to-span ratio of the net and the mechanical characteristics of the cables, regarding their axial stiffness and their pretension, the sequence of the first modes changes, as also occurs in simple cables. A non-dimensional parameter λ^2 , similar to the one used for simple cables to describe this phenomenon, is also introduced for cable nets in this study. It is confirmed that this parameter determines the sequence of their vibration modes, as in simple cables. For specific values of this parameter two or more vibration modes have equal frequencies although they have different shapes, leading to internal resonances. Based on a wide range of parametric analyses, semi-empirical formulae are proposed to estimate the frequencies of the first vibration modes of the system.

Regarding MDOF systems, nonlinear dynamic phenomena cannot be detected by performing single numerical analyses. The hardening behaviour of simple cable nets confirms that such systems experience fundamental resonances for loading frequencies slightly larger than the natural frequency of the system. For specific load amplitudes, the exact value of loading frequency causing the maximum response depends on the characteristics of the system and the initial conditions. On the other hand, secondary resonances occur for loading frequencies away from the eigenfrequency. Although, it is well-known that a frequency ratio Ω/ω (Ω : loading frequency, ω : natural frequency) close to $1/3$ or/and $1/2$ for a system having cubic or/and quadratic nonlinear terms may lead to superharmonic resonance, the exact frequency of the load is not known and it is not sure whether the load amplitude under consideration is large enough to cause this phenomenon. Subharmonic resonance may also evolve for frequency ratios close to 2 or/and 3 , but the exact loading frequency and amplitude and the initial conditions, which play the most important role in this phenomenon, are unknown. Only a specific combination of these parameters forces a certain system to nonlinear resonances, but obtaining this combination numerically is a time consuming procedure.

Having the analytical solution of the simple cable net, the idea of an equivalent SDOF system to assess the dynamic response of a MDOF system is introduced. The transformation of the characteristics from the large system to the smaller one is obtained by similarity relations adopted from a preliminary method used at the first steps of this research, which is extended here for this purpose. Response diagrams are plotted for both SDOF and MDOF systems, based on the analytical solutions and conducting time-history analyses, respectively. The two responses are compared for several geometries and cable initial stresses in order to define the field of application of this method, concluding that this method can be used for flexible cable nets with sag-to-span ratio between $1/30$ and $1/20$ and with high levels of initial cable stress.

Next, the influence of the spatial load distribution on the response of a cable net subjected to harmonic loads is investigated. Three different spatial load distributions are assumed: a symmetric one, and two antisymmetric ones with respect to one or both horizontal axes. Response diagrams are plotted for loading frequencies either close to the natural frequency, leading to fundamental resonances, or smaller than the eigenfrequency, aiming at superharmonic resonances. The influence of the boundary ring on the net oscillation is also investigated for the same spatial load distributions.

In order to analyse the behaviour of such structures subjected to actual dynamic loads such as wind actions, the wind pressure distribution on surfaces of this type is defined, based on the recommendations of Eurocode 1. The saddle-form roof is divided into eight zones and pressure coefficients are provided for each zone according to the wind direction. The proposed wind pressure distribution is also compared with experimental results in order to verify the accuracy of the assumptions made. It is proved that the approach adopted in this thesis results in slightly larger pressure coefficients in some cases, but the spatial distribution of the wind pressure is satisfactory.

Finally, an actual wind record and an artificial one are considered, resulting in a time-history diagram of the wind load, and nonlinear time-history analyses are performed to detect nonlinear resonant phenomena for the wind action, as well, using the spatial distribution proposed before. The dynamic behaviour of the cable nets is compared with the static one, which is calculated according to the quasi-static procedure recommended by Eurocode 1.

10.2 CONCLUDING REMARKS

Exploring the equation of motion of the simplest cable net with two crossing cables is an important first step towards understanding the dynamic response of cable nets. The opposite curvatures between the two cables, which is the main difference between cable nets and simple cables, double the stiffness of the system but they do not render it stiff enough so as to behave as a weakly nonlinear system. Nonlinear dynamic phenomena, established for simple cables, are also detected for cable nets. Although the Duffing oscillator with a cubic nonlinear term describes a simplified cable net model, providing only the steady-state response and not the transient one, and neglecting an eventual cable slackening, it is found to be reliable regarding the frequency and the amplitude of the load for which nonlinear phenomena take place.

Regarding MDOF cable net systems, the non-dimensional parameter λ^2 , which depends on the sag-to-span ratio of the cable net and the initial strain of the cable, is an important parameter that can be used to indicate internal resonances and modal transition, while it also determines the sequence of the modes. Knowing the importance of this parameter, it is possible to choose appropriately the mechanical and geometric characteristics of the cable net in order to avoid internal resonances, which increase the oscillation amplitude activating more than one vibration modes. The semi-empirical formulae, proposed to be used for the preliminary design stage, estimate satisfactorily the first natural frequencies of the cable net and the boundary ring. The modelling of the boundary ring influences significantly the symmetric vibration mode of the net, due to the ring's in-plane mode, which induces a symmetric oscillation to the net, while the antisymmetric modes of the net remain unaltered whether the cable supports are considered as fixed or as flexible.

The method of the equivalent SDOF model is proved to estimate satisfactorily the response of a MDOF cable net for common geometries of cable nets. The main advantage of this method is that it can define with small error and minimum computational time the loading amplitude and frequency for which nonlinear phenomena develop. It is also noted that, in order to have a superharmonic or a subharmonic resonance, large amplitudes of the load are required. Especially for subharmonic resonances, large initial conditions are also required. The combination of these two conditions leads to cable tensile failure during the transient response at the beginning of the analysis. Thus, it is unlikely for a cable net to experience a subharmonic resonance.

Applying a harmonic load on every node of a MDOF cable net, nonlinear phenomena are also verified for different spatial load distributions. The bending of the response curve, which indicates a hardening nonlinear behaviour, is more intense when the net is loaded antisymmetrically rather than symmetrically. As a result, the initial conditions influence the response for a large range of the loading frequency. The behaviour of the net, when it is uniformly loaded, is altered significantly if the deformability of the boundary ring is also taken into consideration in the simulation, while, for antisymmetric loading, it remains unchanged. It is concluded that the harmonic load, following any spatial distribution, causes nonlinear phenomena to shallow and deep cable nets, with medium or low levels of initial pretension. High levels of initial cable stress, instead, lead to a more weakly nonlinear response.

These nonlinear phenomena are clear and can be identified when the external excitation has only one frequency, as in case of harmonic loads. If large oscillation amplitudes are observed, the relation between the loading frequency and the natural frequency of the system defines the kind of resonance that occurs. The response spectra show the activated modes and confirm internal, fundamental or secondary resonances. Changing the frequency of the load by small steps and plotting the steady-state response, bending of the response curve may appear, leading to the conclusion that probably the initial conditions influence the response amplitude. Thus, the results of many numerical analyses indicate the nonlinear behaviour.

Although loading a structure with a harmonic load, having the spatial distribution of a mode of vibration as well as the appropriate frequency to cause resonances, provides substantial information about the behaviour of the system, it is an ideal situation and a very conservative assumption for the design of such structures. The actual dynamic load that affects this kind of structures is due to wind and they should be designed for this load. Hence, if a wind load acts on a structure, including many frequencies, it is impossible to detect such phenomena, because a single analysis cannot show the evolution of the hardening response, or a jump phenomenon. Only the response spectra that plot the oscillation frequencies can provide information about nonlinear phenomena such as internal or secondary resonances.

Regarding real or artificial wind velocity diagrams, the nonlinear dynamic analyses result in large oscillation amplitudes with respect to the static ones produced by the equivalent static method proposed by Eurocode 1. Large oscillation amplitudes are also observed in the response spectra for frequencies equal to the eigenfrequencies, although the main frequencies of the wind are much smaller than the eigenfrequencies of the cable nets, even though for frequencies close to the natural frequencies, the amplitude of the wind load is small. This leads to the conclusion that the small frequencies with large amplitudes of the wind load cause superharmonic resonances to the net, while a weak excitation with frequency near the eigenfrequency enforces the system to experience fundamental resonance, although damping is considered. Quasi-static methods cannot predict these nonlinear dynamic phenomena and thus they cannot be considered as accurate for the analysis and design of such structures. Large differences between static and dynamic responses are observed for all cable nets, while decreasing the parameter λ^2 , the oscillation amplitudes become larger, proving that this parameter influences not only the vibration modes but also the response of the cable nets to dynamic loads.

10.3 CONTRIBUTION OF THE RESEARCH

Cable nets are routinely considered as much stiffer structures than simple cables due to the opposite curvatures and in many cases they are treated as weakly nonlinear systems. However, this study shows that they present many similarities with simple cables and exhibit an intense nonlinear dynamic behaviour under certain conditions. Their response to static loads can be calculated with accuracy performing static analyses, which take into account geometric nonlinearity, but their overall dynamic behaviour cannot be approached by single numerical analyses. Knowing how the simple cable net responds to harmonic loads, a similar behaviour is expected from MDOF systems. The study of the simple cable net, thus, provides insight and useful guidelines for investigating the strong nonlinearity of a cable net, as well as detecting and interpreting the phenomena that characterise nonlinear systems.

It is of utmost importance to know the natural frequencies of a cable net before the final design stage of analysis, because they provide valuable information about the system's dynamic response, although they are calculated by linear modal analyses. The relation between the eigenfrequencies of a system

and the ratio of the loading frequency over the natural frequency determines whether nonlinear resonances should be expected or not. The semi-empirical formulae proposed for the estimation of the first natural frequencies of the cable net and the boundary ring can be useful in preliminary design stage. With these formulae it is possible to choose appropriately the mechanical characteristics of the cable net in order to avoid internal resonances, which may increase the oscillation amplitude.

The method of the equivalent SDOF cable net constitutes an important tool in order to confirm the occurrence of nonlinear phenomena for specific values of the loading characteristics. Otherwise, detecting numerically the conditions that cause a nonlinear phenomenon requires a large number of nonlinear time-history analyses changing in very small steps the load amplitude and frequency, as well as the initial conditions. Knowledge of the exact loading frequency and amplitude that may cause a nonlinear response can lead to better design of such structures.

For weakly nonlinear systems equivalent static methods, using dynamic coefficients, can estimate with satisfactory accuracy the response under dynamic loads, but for intensely nonlinear systems, the time-history analysis, considering also geometric nonlinearity, is the only reliable method.

Designers who deal with conventional structures presenting linear behaviour are not familiar with nonlinear dynamic phenomena. Being aware of the nature of such phenomena, they can detect and interpret them. Changing the parameters that influence the dynamic response of a nonlinear system, they can design such structures knowing what to look for, what to expect from a cable net system subjected to dynamic loads and what to avoid.

10.4 SUGGESTIONS FOR FUTURE RESEARCH

Closing this thesis, some suggestions for future research are summarised:

- Parametric analyses of Computational Fluid Dynamics (CFD) are suggested to evaluate with more accuracy the wind pressure coefficient on such roofs, changing the height of the roof, the sag-to-span ratio, the diameter of the plan view, the basic wind velocity and the wind direction.
- It would be interesting to investigate the influence of these nonlinear phenomena on the fatigue at the cable anchorages.
- In this research it is shown that the presence of the edge ring plays an important role in the vibration of the net. Simulating the exact boundary conditions is necessary in order to have accurate results. This study is based on the structure of the Peace and Friendship Stadium in Athens, Greece, including a ring, which is seated on the pylons, being free to vibrate in-plane. Other assumptions regarding the ring's support (e.g. fixed on the pylons) or shape (e.g. arches similar to the ones of the Raleigh Arena in North Carolina, U.S.A.) are expected to influence more or less the net's behaviour and they should also be considered.
- In this study, due to the small angles of the roof, the wind is applied vertically on each node of the net. However, the actual direction of the wind load is perpendicular to the surface. It would be interesting to compare the results of both assumptions, in order to evaluate the error introduced by the vertical direction adopted.
- The main analytical solution of the simplified cable net described as a Duffing oscillator cannot consider an eventual cable slackening. It is proposed to be studied whether this drawback could be eliminated by considering this system as a non-smooth one, whose solution is not everywhere differentiable, and may possess discontinuities.

ΒΙΟΓΡΑΦΙΚΟ ΣΗΜΕΙΩΜΑ

ΙΣΑΒΕΛΛΑ ΒΑΣΙΛΟΠΟΥΛΟΥ
ΠΟΛΙΤΙΚΟΣ ΜΗΧΑΝΙΚΟΣ (ΔΟΜΟΣΤΑΤΙΚΟΣ)
ΝΟΕΜΒΡΙΟΣ 2011

ΓΕΝΙΚΕΣ ΠΛΗΡΟΦΟΡΙΕΣ

Διεύθυνση κατοικίας Λεωφ. Ειρήνης 12, Πεύκη, 151 21, Αθήνα, Ελλάδα
Ημερομηνία γέννησης 12/06/1970
Τόπος γέννησης Αθήνα, Ελλάδα
Εθνικότητα Ελληνική
E-mail isabella@central.ntua.gr

ΣΠΟΥΔΕΣ

Διδακτορικό Δίπλωμα Διδάκτωρ, Νοέμβριος 2011
Εργαστήριο Μεταλλικών Κατασκευών, Τομέας Δομοστατικής, Σχολή Πολιτικών Μηχανικών, Εθνικό Μετσόβιο Πολυτεχνείο (www.ntua.gr)
Τίτλος: **“Μη γραμμική δυναμική απόκριση και σχεδιασμός δικτύων καλωδίων”**.
Επιβλέπων Καθηγητής: Χ. Γαντές, Αναπληρωτής Καθηγητής Ε.Μ.Π.

Μεταπτυχιακό Δίπλωμα Ειδίκευσης (ΜΔΕ) **Δομοστατικός Σχεδιασμός και Ανάλυση Κατασκευών** (2000-2001)
(www.postgrad.structural.civil.ntua.gr/pclab_eng/index_eng.htm)
Τομέας Δομοστατικής, Σχολή Πολιτικών Μηχανικών, Εθνικό Μετσόβιο Πολυτεχνείο.
Βαθμός διπλώματος 9,04/10.
Διπλωματική Εργασία: **Συμπεριφορά και Μελέτη Δικτύων Καλωδίων**
(εφαρμογή: καλωδιωτή στέγη Σταδίου Ειρήνης και Φιλίας).
Βαθμός διπλωματικής: 10
Επιβλέπων Καθηγητής: Χ. Γαντές, Αναπληρωτής Καθηγητής Ε.Μ.Π.

Δίπλωμα Πολιτικού Μηχανικού (Δομοστατικού) (1989-1995)
Τομέας Δομοστατικής, Σχολή Πολιτικών Μηχανικών, Εθνικό Μετσόβιο Πολυτεχνείο.
Βαθμός διπλώματος 8,29/10.
Διπλωματική Εργασία: **Ανελαστική Ανάλυση Επιπέδων Πλαισίων υπό Σεισμική Ένταση**.
Βαθμός διπλωματικής: 10
Επιβλέπων Καθηγητής: Β. Κουμούσης, Καθηγητής Ε.Μ.Π.

Πτυχίο Πιάνου, Ωδείο “Νίκος Σκαλκώτας”, Αθήνα Ιούνιος 1994. Βαθμός πτυχίου ΑΡΙΣΤΑ.

ΕΙΔΙΚΕΥΣΗ

Δομοστατικός σχεδιασμός και ανάλυση κατασκευών. Ευστάθεια στατικού συστήματος, αντοχή μελών και διατομών. Δυναμική απόκριση συμβατικών κατασκευών από χάλυβα, ωπλισμένο ή προεντεταμένο σκυρόδεμα υπό σεισμικές φορτίσεις, ή καλωδιωτών κατασκευών που υπόκεινται σε φορτία ανέμου, λαμβάνοντας υπόψη τη γεωμετρική μη γραμμικότητα του συστήματος. Γραμμική ή μη γραμμική στατική ανάλυση, ιδιομορφική ανάλυση, φασματική ανάλυση, μη γραμμική δυναμική ανάλυση με εν χρόνω ολοκλήρωση. Χρήση λογισμικών πεπερασμένων στοιχείων.

ΕΠΑΓΓΕΛΜΑΤΙΚΗ ΕΜΠΕΙΡΙΑ

- 2000 – σήμερα Ελεύθερη επαγγελματίας. Συμμετοχή στην εκπόνηση στατικών μελετών σε στάδιο προκαταρκτικής μελέτης, προμελέτης και οριστικής μελέτης. Μελέτες σηράγγων, μελέτες οδικών και σιδηροδρομικών γεφυρών απλά οπλισμένων και προεντεταμένων, Cut & Covers, μόνιμων επενδύσεων σηράγγων, μεμβρανών, καλωδιωτών στεγών, μεταλλικών στεγών, γερανογεφυρών, καλωδιωτών ιστών, προκατασκευασμένων κτιρίων από οπλισμένο σκυρόδεμα. Έλεγχος ολυμπιακών έργων στο ΟΑΚΑ Αττικής.
- 1999 – 2001 Συνεργάτης σε τεχνικό μελετητικό γραφείο. Συμμετοχή στην εκπόνηση στατικών μελετών δημοσίων και ιδιωτικών έργων (σχολείων, κολυμβητηρίων, γυμναστηρίων, κατοικιών κλπ) σε στάδιο οριστικής μελέτης και στάδιο εφαρμογής, σύμφωνα με τους ελληνικούς κανονισμούς: Κανονισμούς Ωπλισμένου Σκυροδέματος (Κ.Ω.Σ.) και Νέος Ελληνικός Αντισεισμικός Κανονισμός (Ν.Ε.Α.Κ.). Μελέτη για αποκατάσταση βλαβών σε κτίρια που επλήγησαν από το σεισμό της 7^{ης} Σεπτεμβρίου 1999 (σχολεία, εργοστάσια κλπ). Έλεγχος αντοχής του φέροντα οργανισμού παλαιών πέτρινων κτιρίων με σκοπό την επανάχρησή τους. Μελέτες πλακών επί εδάφους, οχετών, δεξαμενών βιολογικών καθαρισμών, πισινών κλπ. με τη μέθοδο των πεπερασμένων στοιχείων.
- 1995 – 1999 Στατικές Μελέτες τεχνικών έργων οδοποιίας (γέφυρες, τοίχοι αντιστήριξης, κιβωτιοειδείς οχετοί, σήραγγες, Cut & Covers κλπ), σύμφωνα με τους γερμανικούς κανονισμούς DIN. Μελέτες χωροδικτυωμάτων, μεταλλικών οδηγών ανελκυστήρων, μεταλλικών ικριωμάτων σύμφωνα με τον EC-3.
- 1993 - 1995 Palindrome Ε.Π.Ε., Παλλήνη. Μετάφραση λογοτεχνικών βιβλίων από την Αγγλική

ΔΙΔΑΚΤΙΚΗ ΕΜΠΕΙΡΙΑ

- 2005 – 2011 Συμμετοχή στην προετοιμασία σημειώσεων και διδασκαλία ασκήσεων στα μαθήματα "ΣΙΔΗΡΕΣ ΚΑΤΑΣΚΕΥΕΣ Ι" & "ΣΙΔΗΡΕΣ ΚΑΤΑΣΚΕΥΕΣ ΙΙ" στο Ε.Μ.Π.
- 2000 – 2007 Καθηγήτρια ιταλικών, παράδοση μαθημάτων κατ' οίκον
- 1994 – 2009 Δασκάλα πιάνου στο Ωδείο "Μουσική Εκπαιδευτική", Αθήνα

ΔΗΜΟΣΙΕΥΣΕΙΣ ΣΕ ΕΠΙΣΤΗΜΟΝΙΚΑ ΠΕΡΙΟΔΙΚΑ ΚΑΙ ΒΙΒΛΙΑ

- 2011 Vassilopoulou, I. and Gantes, C. J., "**Assessment of nonlinear phenomena of a MDOF cable net using an equivalent SDOF model**", (προς υποβολή)
- Οκτώβριος 2011 Vassilopoulou, I. and Gantes, C. J., "**Nonlinear dynamic behavior of cable nets subjected to wind loading**", (έχει υποβληθεί)
- Σεπτέμβριος 2011 Vassilopoulou, I. and Gantes, C. J., "**Nonlinear dynamic phenomena in a SDOF model of cable net**", *Archive of Applied Mechanics*, (δεκτό για δημοσίευση)
- Ιούλιος 2011 Vassilopoulou, I. and Gantes, C. J., "**Nonlinear dynamic behavior of saddle form cable nets under uniform harmonic load**", *Engineering Structures*, Vol. 33, pp. 2762-2771.
- Ιανουάριος 2010 Vassilopoulou I. and Gantes C. J., "**Vibration modes and natural frequencies of saddle form cable nets**", *Computers and Structures*, Vol. 88, pp. 105-119.
- Μάρτιος 2005 Vassilopoulou, I. and Gantes, C.J., "**Cable nets with elastically deformable edge ring**", *International Journal of Space Structures*, Vol. 20, Number 1, pp. 15-34. (Θωμάϊδείο βραβείο).
- Ιούνιος 2002 Tassios, T. P. and Vassilopoulou, I., "**Shear transfer capacity along a R.C. crack, under cyclic sliding**" in *Befestigungstechnik Bewehrungstechnik, (Rolf Eligehausen zum 60. Geburtstag), W. Fuchs, H. W. Reinhardt (Ed.), Ibidem – Verlag, Stuttgart, 2002*, pp. 405-414.

ΔΗΜΟΣΙΕΥΣΕΙΣ ΣΕ ΕΠΙΣΤΗΜΟΝΙΚΑ ΣΥΝΕΔΡΙΑ

- Σεπτέμβριος 2011 Βασιλοπούλου, Ι., Γαντές, Χ. Ι. και Γκιμούσης, Η., **"Απόκριση δικτύων καλωδίων υπό φορτία ανέμου"**, 7^ο Εθνικό Συνέδριο Μεταλλικών Κατασκευών, Βόλος, Ελλάδα, Σεπτέμβριος 29 – Οκτώβριος 1, 2011, Τόμος 1, σελ. 416-423.
- Σεπτέμβριος 2011 Vassilopoulou, I. and Gantes, C. J., **"Nonlinear dynamic behaviour of saddle shaped cable nets under wind action"**, IABSE-IASS Symposium 2011, London, UK, Σεπτέμβριος 20-23, 2011, abstract pp.479.
- Σεπτέμβριος 2011 Seferoglou, K., Proutzopoulos, G., Chrysochoidis, F., Fortsakis, P., Vasilopoulou, I. & Perleros, V., **"Rehabilitation of a landslide in NW Greece - from the investigation to the geotechnical design"**, 15th European Conference on Soil Mechanics and Geotechnical Engineering, Αθήνα, Ελλάδα, Σεπτέμβριος 12-15, 2011, Vol. 3, pp. 1395-1400.
- Μάιος 2011 Vassilopoulou, I. and Gantes, C. J., **"Nonlinear dynamic behaviour of a saddle form cable net modeled by an equivalent SDOF cable net"**, 3rd ECCOMAS Thematic Conference on Computational Methods in Structural Dynamics and Earthquake Engineering – COMPDYN 2011, Κέρκυρα, Ελλάδα, Μάιος 26-28, 2011.
- Σεπτέμβριος 2009 Vassilopoulou, I., **"Natural frequencies and dynamic response of saddle form cable nets with rigid or flexible supports"**, SICON-CF, International Conference: Nonlinear Dynamics, Stability, Identification and Control of Systems and Structures, University of Rome "La Sapienza", Rome, Italy, Σεπτέμβριος 21-25, 2009.
- Οκτώβριος 2008 Βασιλοπούλου, Ι., Σεφέρογλου, Κ. και Βάγιας, Ι., "Σύμμικτη γέφυρα Κάτω Διάβασης Σιδηροδρομικών γραμμών στην Εθνική Οδό Τρίπολης - Μεγαλόπολης", ΣΤ' Εθνικό Συνέδριο Σιδηρών Κατασκευών, Ιωάννινα, Οκτώβριος 2-4, 2008, Τόμος 1, σελ. 418-425.
- Οκτώβριος 2008 Βασιλοπούλου, Ι. και Γαντές, Χ. Ι., "Ευπάθεια δικτύων καλωδίων σε κόπωση λόγω ανεμοπίεσης", ΣΤ' Εθνικό Συνέδριο Σιδηρών Κατασκευών, Ιωάννινα, Οκτώβριος 2-4, 2008, Τόμος 2, σελ. 135-141. (αίτηση για Θωμαΐδειο βραβείο).
- Ιούλιος 2007 Vassilopoulou I. and Gantes C. J., "Modal transition and dynamic nonlinear response of cable nets under fundamental resonance", 8th HSTAM International Congress on Mechanics, Patras, Greece, July 12 – 14, 2007, Vol. 2, pp. 787-794.
- Ιούλιος 2007 Vassilopoulou I. and Gantes C. J., "Vibration modes and dynamic response of saddle form cable nets under sinusoidal excitation", Euromech Colloquium 483, Geometrically Non-linear Vibrations of Structures, FEUP, Porto, Portugal, July 9 – 11, 2007, pp. 129-132.
- Ιούνιος 2007 Vassilopoulou I. and Gantes C. J., "Similarity relations for nonlinear dynamic oscillations of a cable net", First International Conference on Computational Methods in Structural Dynamics and Earthquake Engineering – (COMPDYN2007), Rethymno, Crete, Greece, June 13–16, 2007, abstract pp. 373. (Θωμαΐδειο βραβείο).
- Σεπτέμβριος 2005 Βασιλοπούλου, Ι., Χατζηφώτη, Α. και Γαντές, Χ. Ι., "Μελέτη και κατασκευή του μεταλλικού στεγάστρου εισόδων στο Ο.Α.Κ.Α", Ε' Εθνικό Συνέδριο Σιδηρών Κατασκευών, Δημοκρήτειο Πανεπιστήμιο Ξάνθης, 29/9-2/10 2005, Τόμος 2, σελ. 77-84. (Θωμαΐδειο βραβείο).
- Σεπτέμβριος 2004 Vassilopoulou I. and Gantes C. J., "Behavior, analysis and design of cable networks anchored to a flexible edge ring", International Symposium on Shell and Spatial Structures from Models to Realization (IASS 2004), Montpellier, France, September 20-24, 2004, abstract pp. 212-213.

ΔΗΜΟΣΙΕΥΣΕΙΣ ΣΕ ΕΠΙΣΤΗΜΟΝΙΚΑ ΣΥΝΕΔΡΙΑ (ΣΥΝΕΧΕΙΑ)

- Μάιος 2003 Vassilopoulou I. and Tassios, T. P., "**Shear transfer capacity along a R.C. crack, under cyclic sliding**", *fib2003 Symposium: Concrete Structures in Seismic Regions, Athens, Greece, May 6-9, 2003*, abstract pp. 108-109. (Θωμαΐδειο βραβείο).
- Μάιος 2002 Vassilopoulou I. and Gantes C.J., "**Behaviour and preliminary analysis of cable net structures with elastic supports**", *Δ' Εθνικό Συνέδριο Σιδηρών Κατασκευών, Πανεπιστήμιο Πατρών, Μάιος 24-25, 2002*, Τόμος II, σελ. 517-525. (Θωμαΐδειο βραβείο).

ΣΥΜΜΕΤΟΧΗ ΣΕ ΣΕΜΙΝΑΡΙΑ

- Σεπτέμβριος 2009 Υπότροφος Marie Curie "**SICON-CF: Nonlinear Dynamics, Stability, Identification and Control of Systems and Structures**", *SICON, University of Rome "La Sapienza", Ρώμη, Ιταλία, Σεπτέμβριος 21-25, 2009*.
- Ιούνιος 2008 Υπότροφος Marie Curie "**TC3: Experimental Dynamics, Model Identification and Damage Detection**", *SICON, University of Rome "La Sapienza", Ρώμη, Ιταλία, Ιούνιος 9-13, 2008*.
- Φεβρουάριος 2008 Υπότροφος Marie Curie "**TC2: Nonlinear Dynamics and Control of Structural and Mechanical Systems**", *SICON, Vienna University of Technology, Βιέννη, Αυστρία, Φεβρουάριος 18-22, 2008*.
- Ιούλιος 2007 Υπότροφος Marie Curie "**TC1: Stability and Bifurcations of Nonlinear Dynamical Systems**", *SICON, University of L' Aquila, Department of Structural, Hydraulic and Geotechnical Engineering, L' Aquila, Ιταλία, Ιούλιος 2-6, 2007*.
- Νοέμβριος 2005 "**New codes for bridge engineering & new developments in computational modelling**", *Ελληνικό Κέντρο Πληροφόρησης και Επιμόρφωσης, Χ. Μαραβέας & Συνεργάτες, TDV Technische Datenverarbeitung GmbH, Αθήνα, Νοέμβριος 11, 2005*.
- Μάιος 2004 "**Επεμβάσεις ενίσχυσης, επισκευής και επανάχρησης ιστορικής και παραδοσιακής κατασκευής σε σεισμογενές περιβάλλον**", *Ελληνικό Κέντρο Πληροφόρησης και Επιμόρφωσης & Σύλλογος Πολιτικών Μηχανικών Ελλάδος, Πάτρα, Μάιος 14-15, 2004*.
- Ιούλιος 2001 "**Wind Effects on Structures and on the Built Environment**", *SOCRATES – ERASMUS, Università degli Studi di Firenze, Facoltà di Ingegneria, Φλωρεντία, Ιταλία, Ιούλιος 13-21, 2001*.

ΠΑΡΟΥΣΙΑΣΗ ΣΕΜΙΝΑΡΙΩΝ

- Απρίλιος 2010 Εισηγήτρια σεμιναρίου "**EN 1993: Σχεδιασμός Κατασκευών από Χάλυβα και EN 1994: Σχεδιασμός Σύμμικτων Κατασκευών: 1. Μέθοδοι ανάλυσης – Κατάταξη διατομών, 2. Εφελκόμενα και καμπτόμενα μέλη, Ασκήσεις για θέματα αντοχής και ευστάθειας**", *IEKEM-TEE, Αθήνα, 12 – 26 Απριλίου, 2010*.
- Μάρτιος–Απρίλιος 2009 Εισηγήτρια σεμιναρίου "**EN 1993: Σχεδιασμός Κατασκευών από Χάλυβα και EN 1994: Σχεδιασμός Σύμμικτων Κατασκευών: 1. Μέθοδοι ανάλυσης – Κατάταξη διατομών, 2. Εφελκόμενα και καμπτόμενα μέλη, Ασκήσεις για θέματα αντοχής και ευστάθειας**", *IEKEM-TEE, Αθήνα, 30 Μαρτίου – 14 Απριλίου, 2009*.
- Νοέμβριος 2007 Εισηγήτρια σεμιναρίου "**EN 1993: Σχεδιασμός Κατασκευών από Χάλυβα και EN 1994: Σχεδιασμός Σύμμικτων Κατασκευών: Ασκήσεις για θέματα αντοχής και ευστάθειας**", *IEKEM-TEE, Αθήνα, Νοέμβριος 5-14, 2007*.

ΞΕΝΕΣ ΓΛΩΣΣΕΣ

- Άριστες γνώσεις ιταλικών "**Diploma di lingua e cultura italiana - Istituto Italiano di Cultura di Atene**" (1999) (Επάρκεια γλώσσας)
- Άριστες γνώσεις αγγλικών "**Certificate of Proficiency in English, University of Cambridge**" (1990) (Επάρκεια γλώσσας)
- Μέτριες γνώσεις γαλλικών "**Certificat de langue française – Premier Cycle, Institut Français d' Athènes**" (1985)

ΜΕΛΟΣ ΕΠΑΓΓΕΛΜΑΤΙΚΩΝ ΚΑΙ ΕΠΙΣΤΗΜΟΝΙΚΩΝ ΟΡΓΑΝΙΣΜΩΝ

- Μέλος Τεχνικού Επιμελητηρίου Ελλάδος (Τ.Ε.Ε. - www.tee.gr) (1995)
- Μέλος Ελληνικού Τμήματος Αντισεισμικής Μηχανικής (Ε.Τ.Α.Μ. - www.eltam.gr) (2003)
- Μέλος International Association for Shell and Spatial Structures (IASS - www.iass-structures.org) (2004)
- Μέλος International Council on Monuments and Sites (ICOMOS - www.icomoshellenic.gr) (2003)

ΆΛΛΑ

- Μελετητικό πτυχίο κατηγορίας στατικών μελετών (08) Β' τάξης
- Μελετητικό πτυχίο κατηγορίας γεωτεχνικών μελετών και ερευνών (21) Β' τάξης
- Χειρισμός Η/Υ σε περιβάλλον Windows, 2000, XP
- Άριστες γνώσεις των προγραμμάτων Sofistik, MS Office, Autocad 2008 (2D και 3D), Cadisi, ADINA v.8.3
- Μερικές γνώσεις των προγραμμάτων Statik3, Fagus3, Larix2, Space-32bit, Othisis-32bit, Micro Study, SCADA, MGI Photosuite 8.06, Matlab, MAPLE, Easy, SAP2000.
- Γνώσεις internet
- Μέτριες γνώσεις προγραμματισμού σε FORTRAN
- Τυφλό σύστημα δακτυλογράφησης στην ελληνική, την ιταλική και την αγγλική
- Διεθνές δίπλωμα ιστιοπλοΐας ανοικτής θαλάσσης – Ελληνική Ιστιοπλοϊκή Σχολή (1994)

CURRICULUM VITAE

ISABELLA VASSILOPOULOU

STRUCTURAL ENGINEER

NOVEMBER 2011

GENERAL INFORMATION

Address 12, Irinis Avenue, Pefki, GR-151 21, Athens, Greece
Date of birth 12/06/1970
Place of birth Αθήνα, Ελλάδα
Nationality Ελληνική
E-mail isabella@central.ntua.gr

EDUCATION

Doctoral degree (Ph.D.) **Civil Engineering.** November 2011,
Laboratory of Metal Structures, School of Civil Engineering,
National Technical University of Athens (NTUA, www.ntua.gr).
Thesis: "**Nonlinear dynamic response and design of cable nets**" in English.
Supervisor: Assoc. Prof. Charis Gantes, NTUA.

Postgraduate degree of specialization (PDS) **Interdisciplinary Graduate Program of Studies**
Structural Analysis and Design (2000-2001)
(www.postgrad.structural.civil.ntua.gr/pclab_eng/index_eng.htm)
School of Civil Engineering, NTUA. GPA 9.04/10.
Thesis: **Behavior and analysis of cable net roofs**, Grade: 10/10
Supervisor: Assoc. Prof. Charis Gantes, NTUA.

Diploma **Civil Engineering** (with specialization in Structural Engineering), (1989-1995)
School of Civil Engineering, NTUA. GPA 8.29/10.
Thesis: **Inelastic analysis of frames under seismic conditions**, Grade: 10/10
Supervisor: Prof. Vlasios Koumoussis, NTUA.

Diploma **Piano**, Conservatory "Nikos Skalkotas", June 1994, Athens. GPA 10/10.

AREAS OF SPECIALIZATION

Structural analysis and design with emphasis on infrastructure design. Mainly focused on bridges made of reinforced or prestressed concrete or steel. Stability of the structural system, resistance of the elements and the cross-sections. Investigation and solution proposal for earthquake-resistant design with real life experience in the local industry planning and execution. Involvement in analysis and design of structures under extreme loading conditions, including both seismic and wind settings. Inspection and assessment of nonlinear static and dynamic structural behavior. Concentration on tension structures with the engagement of finite element method.

PROFESSIONAL EXPERIENCE

1995 – today

Conceptual, preliminary and final structural design of tunnels, cut & covers, road, railway and pedestrian bridges made of reinforced or prestressed concrete, composite bridges, cast-in-situ and prefabricated concrete elements, retaining walls, culverts, according to the German DIN codes or the European codes.

Geotechnical design of tunnels, cut & covers, road and railway bridges.

Design verification study of the Entrance Canopies of the Athens Olympic Sports Complex according to the European codes.

Analysis and design of membranes, cable net roofs, steel roofs, guyed masts, masonry structures, metal scaffolding, according to the European codes.

Preliminary and final design of precast buildings, schools, stadiums, swimming pools, residential buildings, according to the Greek codes.

Restoration study and seismic strengthening of residential buildings, schools, factories damaged by the earthquake of September 7th 1999 in Athens.

TEACHING EXPERIENCE

- 2005 – today Participation in preparation of class notes and teaching of the compulsory courses: Steel structures I (7th semester) & Steel structures II (8th semester), School of Civil Engineering, NTUA.
- 2000 – 2007 Italian Instructor – private tutoring
- 1994 – 2009 Piano tutor at the conservatory "Mousiki Ekpedeutiki" (<http://musicacademy.gr>)

JOURNAL AND BOOK PUBLICATIONS

- 2011 Vassilopoulou, I. and Gantes, C. J., "**Assessment of nonlinear phenomena of a MDOF cable net using an equivalent SDOF model**", (in preparation)
- October 2011 Vassilopoulou, I. and Gantes, C. J., "**Nonlinear dynamic behavior of cable nets subjected to wind loading**", (submitted)
- September 2011 Vassilopoulou, I. and Gantes, C. J., "**Nonlinear dynamic phenomena in a SDOF model of cable net**", *Archive of Applied Mechanics*, (accepted for publication) (www.springer.com/materials/mechanics/journal/419)
- July 2011 Vassilopoulou, I. and Gantes, C. J., "**Nonlinear dynamic behavior of saddle form cable nets under uniform harmonic load**", *Engineering Structures*, Vol. 33, pp. 2762-2771. (www.sciencedirect.com/science/article/pii/S0141029611002367)
- January 2010 Vassilopoulou, I. and Gantes, C. J., "**Vibration modes and natural frequencies of saddle form cable nets**", *Computers and Structures*, Vol. 88, pp. 105-119. (www.sciencedirect.com/science/article/pii/S0045794909001898)
- March 2005 Vassilopoulou, I. and Gantes, C. J., "**Cable nets with elastically deformable edge ring**", *International Journal of Space Structures*, Vol. 20, No. 1, pp. 15-34. (<http://multi-science.metapress.com/content/q1x15u7472750887>)
- June 2002 Tassios, T. P. and Vassilopoulou, I., "**Shear transfer capacity along a R.C. crack, under cyclic sliding**" in *Befestigungstechnik Bewehrungstechnik, (Rolf Eligehausen zum 60. Geburtstag), W. Fuchs, H. W. Reinhardt (Ed.), Ibidem – Verlag, Stuttgart, 2002*, pp. 405-414.

CONFERENCE PAPERS

- September 2011 Vassilopoulou, I., Gantes, C. J. and Gkimousis, I., "**Response of cable nets under wind loads**", *7th National Conference on Metal Structures, Volos, Greece, September 29th – October 1st, 2011*, Vol. 1, pp. 416-423.
- September 2011 Vassilopoulou, I. and Gantes, C. J., "**Nonlinear dynamic behaviour of saddle shaped cable nets under wind action**", *IABSE-IASS Symposium 2011, London, UK, September 20-23, 2011*, abstract pp.479.
- September 2011 Seferoglou, K., Proutzopoulos, G., Chrysochoidis, F., Fortsakis, P., Vasilopoulou, I. & Perleros, V., "**Rehabilitation of a landslide in NW Greece - from the investigation to the geotechnical design**", *15th European Conference on Soil Mechanics and Geotechnical Engineering, Athens, Greece, September 12-15, 2011*, Vol. 3, pp. 1395-1400.
- May 2011 Vassilopoulou, I. and Gantes, C. J., "**Nonlinear dynamic behaviour of a saddle form cable net modeled by an equivalent SDOF cable net**", *3rd ECCOMAS Thematic Conference on Computational Methods in Structural Dynamics and Earthquake Engineering – COMPDYN 2011, Corfu, Greece, May 26-28, 2011*.
- September 2009 Vassilopoulou, I., "**Natural frequencies and dynamic response of saddle form cable nets with rigid or flexible supports**", *SICON-CF, International Conference: Nonlinear Dynamics, Stability, Identification and Control of Systems and Structures, University of Rome "La Sapienza", Rome, Italy, September 21-25, 2009*.
- October 2008 Vassilopoulou I., Seferoglou K., Vayas I., "**Composite railway underpass bridge in the Tripoli - Megalopoli Highway**", *6th National Conference on Metal Structures, Ioannina, Greece, October 2-4, 2008*, Vol. 1, pp. 418-425.

CONFERENCE PAPERS (CONTINUED)

- October 2008 Vassilopoulou I. and Gantes C. J., "**Sensitivity of cable nets to wind-induced fatigue**", *6th National Conference on Metal Structures, Ioannina, Greece, October 2-4, 2008*, Vol. 2, pp. 135-141.
- July 2007 Vassilopoulou I. and Gantes C. J., "**Modal transition and dynamic nonlinear response of cable nets under fundamental resonance**", *8th HSTAM International Congress on Mechanics, Patras, Greece, July 12 – 14, 2007*, Vol. 2, pp. 787-794.
- July 2007 Vassilopoulou I. and Gantes C. J., "**Vibration modes and dynamic response of saddle form cable nets under sinusoidal excitation**", *EUROMECH Colloquium 483, Geometrically Non-linear Vibrations of Structures, FEUP, Porto, Portugal, July 9 – 11, 2007*, pp. 129-132.
- June 2007 Vassilopoulou I. and Gantes C. J., "**Similarity relations for nonlinear dynamic oscillations of a cable net**", *First International Conference on Computational Methods in Structural Dynamics and Earthquake Engineering – (COMPADYN2007), Rethymno, Crete, Greece, June 13–16, 2007*, abstract pp. 373.
- September 2005 Vassilopoulou I., Chatzifoti A., Gantes C. J., "**Design and construction of the Athens Olympic Sports Complex Entrance Canopies**", *5th National Conference on Metal Structures, Xanthi, Greece, September 29– Oct 2, 2005*, Vol. 2, pp. 77-84.
- September 2004 Vassilopoulou I. and Gantes C. J., "**Behavior, analysis and design of cable networks anchored to a flexible edge ring**", *International Symposium on Shell and Spatial Structures from Models to Realization (IASS 2004), Montpellier, France, September 20-24, 2004*, abstract pp. 212-213.
- May 2003 Vassilopoulou I. and Tassios T. P., "**Shear transfer capacity along a R.C. crack, under cyclic sliding**", *fib2003 Symposium: Concrete Structures in Seismic Regions, Athens, Greece, May 6-9, 2003*, abstract pp. 108-109.
- May 2002 Vassilopoulou I. and Gantes C. J., "**Behaviour and preliminary analysis of cable net structures with elastic supports**", *4th National Conference on Metal Structures, Patras, Greece, May 24-25, 2002*, Vol. 2, pp. 517-525.

PARTICIPATION IN SEMINARS

- September 2009 Marie Curie fellowship in "**SICON-CF: Nonlinear Dynamics, Stability, Identification and Control of Systems and Structures**", *SICON, University of Rome "La Sapienza", Rome, Italy, September 21-25, 2009. (www.sicon.ing.univaq.it)*
- June 2008 Marie Curie fellowship in "**TC3: Experimental Dynamics, Model Identification and Damage Detection**", *SICON, University of Rome "La Sapienza", Rome, Italy, June 9-13, 2008.*
- February 2008 Marie Curie fellowship in "**TC2: Nonlinear Dynamics and Control of Structural and Mechanical Systems**", *SICON, Vienna University of Technology, Vienna, Austria, February 18-22, 2008.*
- July 2007 Marie Curie fellowship in "**TC1: Stability and Bifurcations of Nonlinear Dynamical Systems**", *SICON, University of L' Aquila, Department of Structural, Hydraulic and Geotechnical Engineering, L' Aquila, Italy, July 2-6, 2007.*
- November 2005 "**New codes for bridge engineering & new developments in computational modelling**", *Hellenic Center of Information and Education, C. Maraveas & Partners, TDV Technische Datenverarbeitung GmbH, Athens, November 11, 2005.*
- May 2004 "**Strengthening, restoration and reuse of historic and traditional structures in seismic areas**", *Hellenic Center of Information and Education & Association of Civil Engineers of Greece, Patras, May 14-15, 2004.*
- July 2001 "**Wind Effects on Structures and on the Built Environment**", *SOCRATES – ERASMUS, Università degli Studi di Firenze, Facoltà di Ingegneria, Florence, Italy, July 13-21, 2001.*

PRESENTATION OF SEMINARS

- April 2010 Instructor of the seminar **"EN 1993: Design of steel structures and EN 1994: Design of composite steel and concrete structures – 1. Methods of analysis - Classification of cross sections, 2. Resistance of cross-sections: Tension and bending, applications about resistance and sensitivity issues"**, *IEKEM-TEE* (<http://www.iekemtee.gr>), *Athens, Greece, April 12-26, 2010.*
- March – April 2009 Instructor of the seminar **"EN 1993: Design of steel structures and EN 1994: Design of composite steel and concrete structures – 1. Methods of analysis - Classification of cross sections, 2. Resistance of cross-sections: Tension and bending, applications about resistance and sensitivity issues"**, *IEKEM-TEE, Athens, Greece, March 30 – April 14, 2009.*
- November 2007 Instructor of the seminar **"EN 1993: Design of steel structures and EN 1994: Design of composite steel and concrete structures – Applications about resistance and sensitivity issues"**, *IEKEM-TEE, Athens, Greece, November 5-14, 2007.*

PROFESSIONAL AND SCIENTIFIC SOCIETIES MEMBERSHIP

- Technical Chamber of Greece (TEE - www.tee.gr) (1995)
- Hellenic Society for Earthquake Engineering (HSEE - www.eltam.gr) (2003)
- International Association for Shell and Spatial Structures (IASS - www.ias-structures.org) (2004)
- International Council on Monuments and Sites (ICOMOS - www.icomoshellenic.gr) (2003)

LANGUAGES

- Greek (native)
- Italian: **"Diploma di lingua e cultura italiana, Istituto Italiano di Cultura di Atene"** (1999)
(Proficient knowledge)
- English **"Certificate of Proficiency in English, University of Cambridge"** (1990)
(Proficient knowledge)
- French **"Certificat de langue française – Premier Cycle, Institut Français d' Athènes"** (1985)
(Fair knowledge)

OTHER

- Fluent knowledge of the software: Sofistik, Autocad (2D και 3D), MS Office, Cadisi, ADINA v.8.4.
- Working knowledge of the software: Statik3, Fagus3, Larix2, Space-32bit, Othisis-32bit, Micro Study, SCADA, MGI Photosuite 8.06, Matlab, MAPLE, Easy, SAP2000.
- International sailing diploma (skipper) – Hellenic Sailing School (1994)

